ISSN 0288-4534
CODEN: KONAE7

KONA

POWDER AND PARTICLE

No. 17 (1999)
Published by Hosokawa Powder Technology Foundation

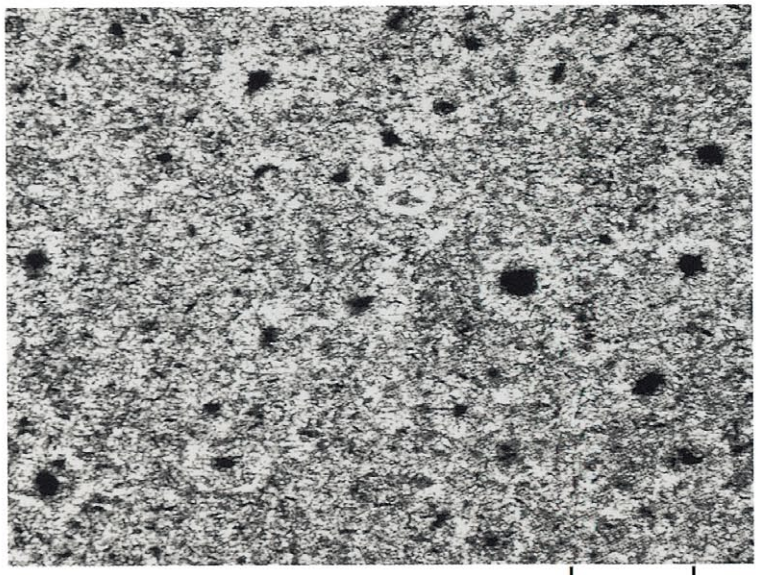

Internal structure of sintered body by transparent optical microscopy

100 μ m

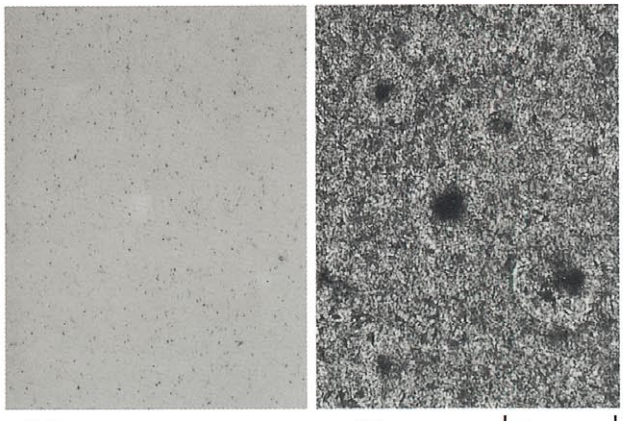

(a) (b)

100 μ m

a) Observed in reflection mode
b) Observed in transmission mode

KONA

POWDER AND PARTICLE

KONA is a refereed scientific journal that publishes articles on powder and particle sciences and technology. KONA has been published annually since 1983 by the Hosokawa Powder Technology Foundation in Japan. KONA is distributed to researchers, members of the scientific community, universities and research libraries throughout the world.

About the Cover of Journal "KONA"

The Chinese character "粉" is pronounced "KONA" in Japanese, and means "Powder". The hand written "粉" is after the late Mr. Eiichi Hosokawa, founder of the Hosokawa Micron Corporation.

Hosokawa Micron Corporation and its R&D Center

■ **Publication Office**

Hosokawa Powder Technology Foundation (Japan) in Hosokawa Micron Corporation
No. 9, 1-chome, Shoudai Tajika, Hirakata-shi, Osaka 573 Japan

■ **Notes**

○ Hosokawa Powder Technology Foundation has entrusted the editorial duty to the editorial board organized by the Council of Powder Technology, Japan.

(Complimentary Copy)

Printed in Japan

Obituary

It is with deep regret that we inform the readers of the KONA journal of the death of Professor Genji Jimbo, President of the Council of Powder Technology Japan and the former Editor-in-Chief of this Journal. He passed away on 27th May, 1999 at the age of 69, following a short illness. Within half a year we lost two great leaders of particle science and technology in Japan, Professors Jimbo and Iinoya.

Professor Jimbo was born in Tokyo on 10th July 1929. He graduated from the Doctor Course in the Department of Chemical Engineering of the University of Tokyo in 1958 and began his career as a Research Associate in the same university. He was a British Council Scholar for one year at Kings College, University of London, starting September 1961. He moved to Nagoya University, Department of Chemical Engineering, as an Associate Professor in 1966 and he was promoted to a full Professor in 1967. He retired from Nagoya University in 1993 and founded a consulting company called Chubu Powtech Plaza Laboratory. In 1994 he was appointed to a Professor of Gifu Keizai (Economics) University.

He was a distinguished leader and one of the founding fathers of particle science and technology in Japan. He served as Editor-in-Chief of the Journal of the Society of Powder Technology Japan from 1967-1976 and as President of this Society from 1989-1993. During his career, he was involved in numerous professional society committees. Among all his contributions to international societies were worthy of special mention. In 1986 he served as the Co-chairman of Organizing Committee for the 1st World Congress on Particle Technology in Nurnberg, Germany. In 1990, he served as the Chairman of Organizing Committee for the 2nd World Congress on Particle Technology held in Kyoto, Japan. Professor Jimbo also served as editors or advisory boards of international journals such as: "Powder Technology", "Particle and Particle Systems Characterization", "KONA" and "Advanced Powder Technology". He was an international advisor of International Fine Particle Research Institute. In the last issue of this KONA journal he wrote in the obituary admiring Professor Iinoya's achievement in internationalization of Japanese particle science and technology. Professor Jimbo himself greatly contributed to the internationalization as Professor Iinoya did.

Throughout his career, Professor Jimbo was recognized for his achievements in the field of particle science and technology. In 1990 he received the Hausner Award from the Fine Particle Society during the 2nd World Congress on Particle Technology. He received the Iinoya Award posthumously in June, 1999. He also won the awards from the Society of Chemical Engineering in 1990 and from the Association of Powder Process Industry and Engineering in Japan in 1991. He was also recognized by the Japanese Government for his contributions to domestic, environmental protection.

We were surprised when he became a Professor of "Gifu Keizai (Economics) University". There he was teaching the subjects of: "History of Scientific Technique", "Resources and Environment" and "Introduction to Natural Science". His attainments qualified him to teach in these fields since his 200 publications include papers on these subjects.

He was conscientious in supervising young research workers. His questions and comments to young speakers in academic meetings were always acute and constructive. They were both stimulated and encouraged by him. He was respected and loved not only by young researchers but by everyone for his open minded character. Personally, I am privileged to have been influenced by him.

We lost a brilliant scientist who pioneered many aspects of particle science and technology and I, myself, lost a teacher whom I admired and respected.

Yasuo Kousaka
Vice Chairman of Asia/Oceania Editorial Board
(Osaka Prefecture University)

In Memory of Prof. Naoya Yoshioka

Emeritus Professor of Kyoto University, Dr. Yoshioka passed away on Sept. 10. He served as the first editor-in-chief of KONA and was the former administrative senior vice-president of the Hosokawa Powder Technology Foundation. Until April he was out playing tennis with his wife and was enjoying a very active lifestyle and seemed to be in good health until the discovery of a polyp in June, unfortunately his health deteriorated rapidly. He was at the age of 78, but I wish that he lived longer because there was so much more for me to learn from him.

Prof. Yoshioka graduated from the former Naniwa High School and entered Kyoto Imperial University, Faculty of Eng. Dept. of Chem. Eng. in 1941. Upon finishing his doctorate studies he started working as an assistant professor in 1946. He devoted 38 years to research and education in mechanical unit operations in the field of chemical engineering. During this period he played a major role in the Society of Chemical Engineering, Japan, serving as administrator, Director and Vice-director of the Kansai branch, Editor-in-chief of the Japanese journal, Kagaku Kougaku Ronbunshu, Chairman of the Education Committee, Chairman of the Award committee, etc. Upon retiring from Kyoto Univ. in 1984 he became a professor at Okayama Science University and taught there for 10 years. Meanwhile, he put his efforts into the publication of the premiere issue of KONA and became the first editor-in-chief and built the foundations for an excellent journal.

His research interests in chemical engineering covered a wide range of mechanical unit operations, such as, thickening of slurry, liquid cyclones, aerosol filtration, and flow characteristics of non-Newtonian fluids. He was a researcher who was always ahead of his times. I had the privilege of being under his supervision during my doctorate studies, while I was a research associate as well as Assist Professor for a total of 8 years (1961-1969). At that time he was famous as an authority of thickener and liquid cyclone. When I entered graduate school he was busy working on his doctor dissertation putting together all of his great achievements. While I helped with his drawings and figures I read his dissertation and noticed how logical his writing was although I could not fully understand the contents. At that time unit operations were at a peak and everything was put away with dimensionless parameters, he always grasped the core of the phenomena, which triggered me to learn his attitude toward knowledge.

Being a quiet gentleman he never forced me to do anything. Anytime I had a question he answered with great patience and helped me find splendid solutions to my problems. Being humble and engaged in the study of wet powders he seldom attended the meetings of the Society of Powder Technology. But his contribution to chemical engineering was the bridging of theory and practice, which is well documented in "Kagaku Kikai no Riron to Keisan", which is so called the bible of chemical engineering text book. This will be remembered for many years together with his other fine achievements.

His life would not be complete without mentioning baseball. As a high school student he played against the famous Japanese professional baseball player, Kaoru Betto. Even after he became professor, students were unable to get a hit from him because he threw such an amazing straight fast ball and also a steep drop ball. Should a student get lucky and find himself on first he would be thrown out by Prof. Yoshioka's quick flick of the wrist. Until he retired he was director of semi-hard Baseball Club of Kyoto University. After retirement he surprised everybody at the opening game by throwing his straight fast ball, a strike right down the middle.

The last time I saw him was on Aug. 19 and I spent an hour talking with him. It is hard to believe that he is no longer here with us and I hope that he is resting in peace now.

Hitoshi Emi
(Kanazawa University)

The Letter from the Editor

Kei Miyanami
Editor-in-Chief

It is with our deep regrets that we inform you of the death of Professors Genji Jimbo and Naoya Yoshioka. Professor Jimbo passed away on Thursday, May 27, 1999 (the pancreas cancer) and Professor Yoshioka on Friday, September 10, 1999 (the lungs cancer). We have been very surprised and so sorry to hear their sudden death.

On behalf of the KONA editorial committee, we all lament their death and extend our condolences heartily.

The passing of Professors Jimbo and Yoshioka, the pride of our academic fields, is a great loss to us all. Their accomplishments being so well-known worldwide, and their influences on their junior colleagues so deep, their death is truly a great loss.

We are greatly thankful to them for their enormous contributions to the publication of KONA journal since the first issue. Both of them were the chartered members of the Council of Powder Technology, Japan and the Board of Hosokawa Powder Technology Foundation. They also experienced the President of the CPT and the chairman of the KONA Editorial Committee.

More importantly, we have lost friends and respected colleagues who have left each of us with many fond memories. We would like to pay our respects to their achievements here anew. May they rest in peace.

KONA

GENERAL INFORMATION

HISTORY OF THE JOURNAL

KONA journal has been published by the Council of Powder Technology, Japan. (CPT), from No.1 to No.12 issues, under the sponsorships of Hosokawa Micron Corporation (No.1 to No.9) and Hosokawa Powder Technology Foundation (No.10 to No.12).

The CPT has been established in 1969 as a non-profit organization to enhance the activities of research and development on powder science and technology in Japan under the sponsorship of Hosokawa Micron Corporation. In 1983, the CPT has decided to issue an international journal named "KONA", which publishes the excellent articles appeared in Japanese journals concerning powder science and technology, after translated into English, throughout the world. After the seventh volume issued in 1989, the CPT has changed its policy to internationalize the "KONA" from the 8th issue (1990) and on by incorporating the monographs originally written in English from the authors throughout the world. Immediately, the present editorial board including Asian, Americas' and European Blocks has been organized.

From the 13th issue and on, the Hosokawa Powder Technology Foundation has taken over the role of KONA publisher from the CPT and the Foundation has entrusted the editorial duty to the present KONA editorial board organized by the CPT without requesting any shift in our present editorial policies. This switching of publisher has been simply and only to make the aim and scope of the Foundation definite. Essentially no change has been observed in continuously editing and publishing this journal except in the designation on a part of the journal cover.

AIMS AND SCOPE OF THE JOURNAL

KONA Journal is to publish the papers in a broad field of powder science and technology, ranging from fundamental principles to practical applications. The papers discussing technological experiences and critical reviews of existing knowledge in specialized areas will be welcome.

These papers will be published only when they are judged, by the Editor, to be suitable for the progress of powder science and technology, and are approved by any of the three Editorial Committees. The paper submitted to the Editorial Secretariat should not have been previously published except the translated papers which would be selected by the Editorial Committees.

CATEGORY OF PAPERS

- Invited papers
  Original research and review papers invited by the KONA Editorial Committees.
- Contributed papers
  Original research and review papers submitted to the KONA Editorial Committees, and refereed by the Editors.
- Translated papers
  Papers translated into English, which were previously published in other languages, selected by the KONA Editorial Committees with the permission of the authors and / or the copyright holder.

SUBMISSON OF PAPERS

Papers should be sent to each KONA Editorial Secretariat.

- Asia / Oceania Editorial Secretariat
  F. Nakagawa
  Hosokawa Micron Corporation Micromeritics Laboratory 1-9, Shoudai Tajika, Hirakata 573 JAPAN
- Europe / Africa Editorial Secretariat
  Dr. P. van der Wel or Mrs. P. Krubeck
  Hosokawa MikroPul GmbH
  Welserstr. 9-11, 51149 Köln
  Postfach 900749, 51117 Köln
  GERMANY
- Americas Editorial Secretariat
  Dr.I. Pikus or D.A. Scort
  Hosokawa Micron International Inc.
  10 Chatham Road, Summit, NJ 07901 USA

PUBLICATION SCHEDULE

KONA is published once a year.

SUBSCRIPTION

KONA is distributed free of charge to senior researchers at universities and laboratories as well as to institutions and libraries in the field throughout the world. The publisher is always glad to consider the addition of names of those who wish to obtain this journal regularly to the mailing list. Distribution of KONA is made by each Secretariat.

INSTRUCTIONS TO AUTHORS

(1) Manuscript format

- Two copies should be submitted to the Editorial Secretariat, in double-spaces typing on pages of uniform size.
- Authorship is to give author's names, and the mailing address where the work has been carried out on the title page.
- Abstract of 100-180 words should be given at the beginning of the paper.
- Nomenclature should appear at the end of each paper. Symbols and units are listed in alphabetical order with their definitions and dimensions in SI units.
- Literature references should be numbered and listed together at the end of paper, not in footnotes. Alphabetical order is accepted. Please give information as in the following examples:
  1) Carslaw, H.C. and J.C. Jaeger: "Conduction of Heat in Solids", 2nd ed., Clarendon Press, Oxford, England (1960).
  2) Howell, P.A.: US Patent, 3,334,603 (1963).
  3) Rushton, J.H., S.Nagata and D.L. Engle: AlChEJ., 10. 294 (1964).
  4) Seborg, D.E.: Ph.D. Dissertation, Princeton Univ., N.J., U.S.A. (1969).
- Original figures with each single copy should be submitted, on separate sheets. Authors' names and figure numbers are marked in the corner.
- Figure numbers and captions are listed on a separate sheet.
- Place of figure insertion is to be indicated in the margin of the manuscript.
- Tables should be typed on separated sheets.
- Submit an IBM-readable floppy disk ($3_{1/2}$) with your unformatted text file in ASCII code. If you use either WORD or WORD PERFECT–as word processing system, please add the formatted text file.

(2) Reprints

- The authors shall receive 50 free reprints. Additional reprints will be furnished when ordered with return of galley proofs.

(3) Publication policy

- All papers submitted for publication become immediately the property of the CPT and remain so unless withdrawn by the author prior to acceptance for publication or unless released by the Editor. Papers are not to be reproduced or published in any form without the written permission of the CPT.

KONA Powder and Particle No. 17 (1999)

Contents

Explanation of the Cover Photograph

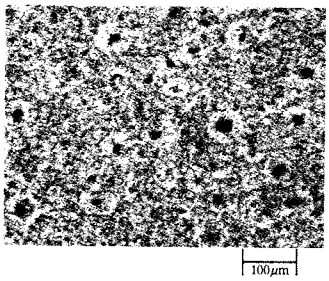

Internal structure of sintered body
by transparent optical microscopy

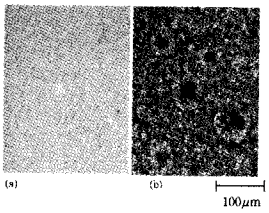

a) Observed in reflection mode
b) Observed in transmission mode

Ceramics have a keen interest as one of materials, which have advantages in using at high temperature, high wear resistance and good mechanical strength. However, the lack of reliability remains as the highest barrier to its wide application in ceramics, owing to their brittleness. One of reason for this limitation is the difficulty to understand the relevance among the fracture origin in ceramics and their brittle characteristics. These detrimental flaws could be very minor, so then, highly careful structure investigation is needed to examine this subject because of appropriate characterization deficiency. Recently, the fracture origin can be successfully studied by examining with optical microscopy. Specimens are thinned to tens of microns to make them transparent, and are observed optically in transmission mode (see/ right photomicrograph). The volume of specimen under the examination is a few cubic millimeters, which is large enough to contain some large, but very few, processing defects (see/ left photomicrograph). The tool has been successfully applied to solve various problems in ceramics such as the direct correlation between defect size distribution and flexural strength. The method is expected to realize a new evaluation strategy which directly reveals characteristics in the powder and their processing to construct the structural features of compact and sintered bodies.

Tadashi HOTTA and Makio NAITO, Japan Fine Ceramics Center
Nobuhiro SHIINOHARA and Masataro OKUMIYA, Asahi Glass Co. Ltd.
Keizo UEMATSU, Nagaoka University of Technology

Review

A Review of CA-Silo: Concerted Action for Silo Research†

J. Nielsen+ and C.J. Brown*
*Brunel University, Uxbridge, UK**

Abstract

The origins of a collaborative project on silo research (CA-Silo) are given, along with some of the background case for support. The activities described include contributions on a state of the art in silo research, and brief descriptions on some collaborative research work that was carried out. The ways in which industry was involved with CA-Silo are explained. Research requirements are identified in terms of both general objectives, and short-term requirements for pre-normative research. Finally, some of the project management issues are raised, and the project outcomes are described.

1. Introduction

This paper describes the origins, activities and outcomes of a co-ordination activity that was funded under the auspices of the European Community's BRITE/EuRam research programme. CA-Silo was the acronym adopted for a Concerted Action into Silo Research. It commenced in 1992, and was completed in 1997. The total project budget was 370 kECU. (£300,000 approx.)

The silo business is technically complex. In spite of this, relatively few researchers are active in the field. Silo technology is used in many industrial sectors, and expertise lies within a number of different disciplines. Knowledge therefore tends to be diffuse, and research work replicated. The CA-Silo programme was established to bring together the current research in Europe and to form a network of researchers willing and able to collaborate so that future activity would be better informed and a more co-ordinated inter-disciplinary approach possible.

This paper is structured to:

- briefly outline some of the key problems in silo technology,
- explain how and why CA-Silo was conceived,
- describe the activities undertaken as part of the project,
- give the authors' perspective on the importance and relevance of these activities,
- present the achievements of the project,
- describe some of the lessons learned from running such a project, and finally,
- outline the challenges for future research work.

This paper intends to give an outline of work that has been carried out, and why it was carried out. The reader is referred to Ref. 1 in which extensive technical information and references are given. Further technical information on the collaborative projects can be obtained from the contacts named (§12).

2. The Importance of Silo Research

Silos store materials ranging from fine powders to quarried rocks – all worth many million ECU. The cost of the stored material frequently exceeds the cost of the silo. Silo users range from industrial giants to numerous small and medium-sized enterprises.

Silo problems occur in many industrial sectors. In agriculture the storage of harvested produce is important, while in the mining industry there is the need to store mined material or a by-product after separation. The chemical and petro-chemical industries use such structures, as does the pharmaceutical industry where large volumes of product storage may be less important than quality and process control.

Information about silo failures is scarce and somewhat difficult to obtain. Operators and designers are often reluctant to reveal details of "their" failures.

Silo failures can be broadly classified as either structural failure or flow failure. Occasionally structural failures are gross and dramatic, and unfortunately may lead to loss of life. In such cases data may become available through official inquiries, but there are many other cases with less dramatic damage or unacceptable operating conditions which are less well publicised.

Human safety is the primary concern arising from structural failures of silos, but failures can often result in considerable loss of income. In the most extreme

+ Danish Building Research Institute, Hørsholm
* Department of Mechanical Engineering, Brunel University, Uxbridge, Middlesex UB8 3PH, UK
† Received: May 17, 1999

cases structural failure may result in heaps of spilled material and piles of twisted metal or concrete rubble. However, the structural failure will often take more subtle forms, where defects such as local buckling in a metal silo or splitting and cracking in a reinforced-concrete silo will make the structure unsafe for use or unserviceable.

Flow failure is less visual but may lead to equally dramatic consequences, particularly if remedial efforts are ill judged. Many injuries are reputed to occur as a result of ill-considered efforts to make material flow from a silo. The loss of flow may completely disrupt a mixing or chemical process, resulting in waste material rather than usable product – often with considerable economic consequences. Reasons for loss of flow are various. Among the less complicated phenomena are arching (where the stored material forms a self-supporting area within the material, thus preventing flow through an apparently clear orifice) and ratholing (where a clear pipe of material from top to bottom of the silo is emptied from the silo, again leaving blocks of stationary material within the silo). Such stationary material – from whatever cause – is prone to collapse suddenly and such collapses may have fatal consequences. This is just one example of how flow and structural failures may be linked.

Many of the fundamental load and flow phenomena in silos are very complicated and still poorly understood. Silos therefore suffer a disproportionately large number of structural failures compared with many other forms of construction. Silos continue to fail, even though the designers and operators may be working within available guidelines and accepted best practice. Designs that appear to have been effective within their previous design experience may turn out to be inappropriate; furthermore, silos that have been in good operational condition for many years can suddenly develop severe problems. The lack of appropriate and accurate design guidance is therefore clearly detrimental to silo users.

Many of the technical problems are not easily resolved. Numerical and experimental tools are used to study the phenomena involved. Analysts are striving to generate more accurate models for the prediction of pressures and flow in complex silo geometries and under complex flow regimes. Experimental techniques to determine physical parameters for the stored material, to determine strains and stresses in the stored bulk solid or in the silo structure, and to model silos and their related phenomena all involve techniques that are very complicated to both develop and implement. Many of the techniques that have been developed have lacked certainty and in consequence many results have been questioned.

3. The CA-Silo Project

There is clearly justification for research into silo problems. What is equally apparent is the need for a co-ordinated approach to silo research. This section outlines how CA-Silo was conceived, and how the activity planning for the project was undertaken.

3.1 Origins of the Project

It is often difficult to look back and determine the starting point for such projects, but in this case it was an informal discussion at a silo meeting (Silos – Forschung und Praxis, Tagung '88, SFB219) held in Karlsruhe in 1988. A group from the researchers present identified some silo research that was being duplicated; further, it was evident that some existing research knowledge had not been well disseminated or had not been widely enough understood. The potential inefficiencies were obvious.

Funding sources for silo research are both limited and scattered, as the solution to problems in the storage or processing of bulk materials tends to be specific to the different industries involved. The number of active research groups in Europe is limited and the technical and research expertise that does exist is diverse. Many branches of engineering are involved with the design and manufacture of silos. Agricultural Engineers, Chemical Engineers, Civil Engineers, Mechanical Engineers and Structural Engineers have all applied their knowledge to silo problems. The dissemination of understanding is therefore correspondingly diluted. However, in practice, most design problems are inter-related and effective solutions require expertise from more than one traditional discipline.

The group therefore concluded that international collaboration between disciplines would extend fundamental understanding of silo problems significantly.

3.2 Concerted Actions

Bringing together research activity from different member states was an important strategic element of the EC Research Programme in the early 1990s. A first project proposal was not successful, but a revised proposal was put forward by seven partners from five different member states. They were Danish Building Research Institute, Denmark; Technische Universität Braunschweig, Germany; University of Karlsruhe, Germany; University of Edinburgh, UK; T.N.O. Building & Construction Research, The Netherlands; Labora-

toire Central des Ponts et Chaussées, France; and Building Research Establishment, UK. The proposal was accepted with a start date of September 1992 and duration of 4 years. The Project Co-ordination was originally carried out by the Building Research Establishment, UK, and completed by Brunel University, UK.

3.3 CA-Silo Objectives and Activities

The primary objective of CA-Silo was to bring "concerted action to the silo research community". It was the task of the Steering Committee (§12) to outline activities that would enable these objectives to be met.

The first activity was to bring together all those known to have an active interest in silo technology at a plenary meeting. This was held in Delft in 1993. Researchers were asked to make presentations outlining the strategic objectives of their work; industrialists were asked to formulate their main interests, and to identify substantive problems. After the meeting the Steering Committee embarked on a number of activities grouped in a number of broad headings:

- determining the current "state of the art",
- initiating collaborative projects between active laboratories,
- supporting exchanges between established groups,
- involving industry, and
- identifying research requirements for Codes of Practice, Standards and design guides.

"Working Groups" were established as a mechanism to administer the CA-Silo project. Each working group had an influential researcher as its Chairman. The scope of the working groups was then somewhat pragmatic, based on a mixture of the Chairman's interests and the subject area as well as the logistics of meetings in limited available time. Each working group was required to produce its own state-of-the-art report. Discussion within the group led to the formulation of sets of working papers, which were then distributed to non-attending members for comment and agreement on remaining technical problems. In some groups the discussions were extensive, in others less so. It was not possible in all cases to remove disagreements, but where these occurred, to recognise them and use them creatively. An outline of the activities is given below (§4).

Having established the state of the art, the groups were invited to move on to active collaboration on agreed objectives, create links and exchanges, and involve industry in the determination of best design practice and the future needs of European codes. These subsequent collaborations were carried out by the research groups then most active, based on proposals approved by the Steering Committee, and are described later in this paper (§5).

4. The State-of-the-Art Report

There were seven working groups, and in effect each has contributed to a part of the resulting book (Ref. 1) – the form in which the reports were eventually published. There are over 40 contributors to the 56 Chapters, resulting in over 800 pages in the final form. In addition to the six parts outlined below in this section (§4), the seventh part describes an industrial survey that was carried out, and a synopsis of the research work needed to support ongoing code work. These were also part of the CA-Silo project, and are described in §6 and §7 below.

4.1 Silo Flow

Of all the areas of work covered by CA-Silo, the one covered by the working group on "Silo Flow" was perhaps the broadest and most difficult to define. "Silo Flow" covered not only the work associated with the determination of conditions for flow to occur in silos, but also the sophisticated testing needed to determine characteristics of the stored bulk solid. There was a potential overlap between the work related to material characteristics for determining flow, and that related to constitutive relations for numerical models. However, the material characteristics (and appropriate methods) have been outlined in both contributions to the state of the art with relevant emphasis.

Silo flow is an area in which industry is actively involved, and the development of continuous monitoring, control and flow promoting devices has been industry led. Wherever there is an industrial lead, there can often be commercial considerations to the research carried out. Nevertheless, this state of the art (Ref. 1, Part 1) has produced extremely useful contributions from a variety of sources.

The state of the art on silo flow is divided into three major parts. The first deals with the testing associated with the stored material and/or the silo material, looking at the problem from both the fundamental and the practical point of view.

In steep-walled mass-flow silos, the flow pattern of the material is well known, and based on the work of Jenike in the 1960s can be confidently predicted. The first-in, first-out characteristic is useful, particularly for biodegradable materials. No stagnant zones form during discharge of bulk solids.

In funnel-flow silos, a flow channel is formed within stagnant material, the funnel-like shape of the flow

channel being less predictable. A pressure peak can occur at the intersection of the boundary line with the silo wall (and is often thought to be the cause of many silo structural failures). Knowledge of the shape of the flow channel and its dependence on the flow properties is therefore required, as it may have a substantial impact on the economic structural design of silos.

In either case, knowledge of the properties of both bulk solid and silo is necessary to predict flow within the silo.

The second section deals with the flow pattern within a silo. This can be influenced by placing inserts into the silo, by aeration, by vibration or by mechanical activation. Inserts may be needed not only for improvements of the flow pattern but also for introduction of purge or drying gases or for blending purposes. These can have a significant impact on the pressure distribution in the silo. Many codes and standards do not give rules for loads on or from inserts because of the lack of fundamental understanding of their behaviour, and some recent research on this topic is also presented.

Finally, the state of the art provides a critical review of the discharge and flow metering equipment currently available.

The breadth and change occurring in this field are noted by the leaders of this working group, and the suggestion is made that such a project should be run "every 5-10 years" to ensure updates of the information available. Clearly this evinces the need for such collaborative projects, and for some joint industry/government funding on a co-ordinated scale.

4.2 Concrete Structures

Creating two separate sub-sections for concrete and metal structures, each one identifying structural actions and the effect of those actions, caused some concern. However, with silos the division is justified by some of the fundamentally different characteristics of concrete and metal structures.

Concrete silos are relatively stiff structures, often formed by using slipforming, a continuously sliding formwork technique. Other forms of concrete silos include rectangular or polygonal silos, possibly using precast panels. Concrete silos are especially sensitive to tensile stresses. Tensile stresses are introduced mainly by load perpendicular to the structure. However, because of the stiffness of the structure, tensile stresses may also be introduced by thermal action and by differential settlements.

This group consequently focused (Ref. 1, Part 2) on loads particular to the silo form, including bottom loads, and to the structural consequences of temperature changes and differential settlements. Attention is also paid to earthquakes and dust explosions.

Dust explosions can occur spontaneously with disastrous consequences if appropriate conditions arise in the silo and sufficient energy dissipation cannot take place. This is a more significant problem with concrete structures, and so a proposed design method for vent openings has been outlined.

The key topics for research in concrete silo technology are given in a final section. They include soil-structure interaction, earthquake effects, temperature effects in multi-cell silos, and concrete performance in relation to wear.

4.3 Metal Silos

Metal silos are used for storing a wide range of bulk solids and are built in many different forms and sizes. The mechanisms for load carrying and the potential failure modes are generally governed by the thin-walled nature of the structure.

In steel and aluminium silos the critical load patterns are different from those in concrete silos. Many potential failure modes are both sudden and catastrophic and can occur under rather unpredictable conditions.

The two common structural forms have different characteristics. In the curved shells associated with circular planform structures, there is a complex structural response; less well known is the sensitivity to small imperfections that, under some conditions, can be critical. Bursting failures are rare, and metal silo design is mainly governed by other criteria. Rectangular planform steel silos are also used for their simplicity of construction and adaptability, but they are not as intrinsically efficient as shell structures. However, greater economy might be achieved from them with the development of new design philosophies.

The state of the art (Ref. 1, Part 3) addresses in turn the main design problems for metal structures. For efficiently designed metal silos, buckling failure will be a major design criterion. Axial compression occurs not only from frictional traction, but also from unsymmetrical lateral loads from the stored bulk solid. Alone or in combination, these effects can produce high vertical stresses in the wall of the silo. Minor deviations in the wall, the presence of residual stress, local pressure variations within the silo and local variations in stiffness of the stored bulk solid can all affect the buckling load.

Conical shells are used for hoppers and for roofs in circular planform silos, and their design – often a

rather specialist function – is described.

Wind loading can sometimes be the design criterion for empty metal silos; particularly in squat silos, wind pressures can be more significant than those imposed from the stored bulk solid.

The Working Group again identified key areas where future research was needed. These include the effect of real geometric imperfections on silo strength, wall stress patterns caused by unsymmetrical pressures, conditions for buckling under high local stresses, eccentric discharge and how to determine when failure might occur, and criteria for economic designs of rectangular silo structures.

4.4 Numerical Simulation

The inclusion of the state of the art in numerical modelling (Ref. 1, Part 4) is essential, but also to some extent one of the most contentious areas of work. The area is not mature, and developments are still relatively rapid. Many research workers have been active in the development of various numerical modelling approaches. Any concerted action needed to ensure these groups conversed, and it was recognised from the outset that the creation of the state of the art in this activity would be likely to produce a more varied outcome than in some other contributions, and that agreement within the group might be more difficult to obtain. For instance, while some models seek to represent every detail of a silo and to be "accurate", others may seek to sacrifice some of the accuracy in an attempt to simplify the characteristics of the model.

The different models focus on various aspects of silo technology such as the complex behaviour of the stored granular materials, the different silo geometries and characteristics, the interaction between the stored material and the silo walls, and the different process situations to be addressed (e.g. loading or unloading etc.).

Stored bulk solids exhibit particular mechanical behaviour. This may include non-linearity, stress or strain dependency, plasticity, and dilatancy. Such phenomena need sophisticated modelling. Cell geometry varies not only globally, but also because of local singularities such as eccentric outlets, inserts or internal ties.

The friction coefficient between the silo walls and the stored material is difficult to model, as it may in reality be extremely variable, and depend on the stress levels. Similarly, the load and structural response may be a coupled problem; wall deformations can drastically affect wall pressures.

The different mechanical actions of filling (increasing density, small strains) and emptying (dilation and large strains), and the switch from one to the other can lead to complex phenomena. Asymmetry resulting from apparently symmetric conditions can be difficult to model.

Many of these problems are dealt with in the state of the art, and in particular examples of the use of both the classical continuum approach (the Finite Element Method – FEM) and Discrete Particle Models (DPM) are presented. As in any numerical modelling, the choice of appropriate constitutive equations for the material model is critical, and some alternatives have been examined. In addition, stochastic finite element analysis has been introduced, and contributions looking at the basis for choice of model and method are presented.

Advanced models are able to deal with a range of problems, and an extensive initiative in Germany (the SFB programme) enabled significant progress to be made. Nevertheless, some apparently simple problems cause significant difficulties for the differing numerical models. These include:

- modelling of material behaviour during discharge,
- prediction of flow patterns and conditions of no arching,
- simulation of heterogeneities, segregation, and anisotropy due to the filling process,
- influence of eccentric filling and discharge.

Some of the projects described below (§5) endeavoured to produce further collaboration between active groups.

4.5 Silo Tests

The group working on silo tests was formed to represent those workers (research-based or from industry) who had a direct knowledge of the variety of output that could be obtained from tests on silos. In experimental conditions there is a great deal of variability. There is often an interaction between the behaviour of the stored bulk solid and the structural behaviour. An ideal objective of the group's work was to provide detailed guidance on features of silo tests that should be recorded for the benefit of all future applications of the results.

The state of the art (Ref. 1, Part 5) reviews the conditions of both the stored bulk solid and the silo itself that should be recorded in any silo test. Key elements of the data include the properties of the test silo, the properties of the stored material, the instrumentation of the silo, and the test conditions.

Along with proposals for data to be recorded, a mech-

anism for the presentation and processing of the collected data is presented. This might facilitate transfer of data between sites.

4.6 Experimental Techniques

The effectiveness of silo tests is heavily dependent on the experimental techniques employed. The techniques employed in the measurement of pressures and stresses in silos can differ noticeably from those used in other branches of experimental mechanics. For example, when dealing with relatively stiff elastic bulk solids, it is essential that only very small displacements occur in the cell face of pressure measurement devices. If cell face displacements are too large (in some cases this is of the order of microns), the measured pressure will be a significant underrepresentation of the pressure at that position. Conversely, if the stored material is very flexible, a stiff cell placed in the bulk solid may interfere with the development of stresses within the stored material.

The contributions to state of the art in Experimental Techniques (Ref. 1, Part 6) are from active researchers who have addressed such demanding problems. Along with criteria for the determination of various pressure readings in silos, alternative strategies are examined. Measurements of such phenomena as cracking, moisture and flow patterns are addressed by specialist techniques. Finally, the criteria for carrying out experiments are examined.

A survey of existing silo test facilities revealed that the number is small and that each facility is built for a specific function. The need for research collaboration could not be more emphasised than in this field.

The working group identified key problems as

- the inter-changeability and calibration of pressure measurement devices
- measurement of local density in situ
- measurement of interstitial and atmospheric air pressure
- measurement of moisture in stored bulk solids
- flow visualisation techniques
- the use of wall strain measurements
- model laws and scale errors

5. Collaborative Projects

A key objective of CA-Silo was to bring together groups or individuals that were already working on specific problems. The aim was to add value to existing projects. CA-Silo funded these collaborative activities after approval by the Steering Committee. They are described very briefly below. Fuller details and publications are available from the co-ordinators of each activity (indicated by the bracketed number [ ] in the sub-headings and listed in §12).

5.1 Imperfections in Metal Silos: Measurement, Characterisation and Strength Analysis [1]

There are several groups working on imperfection measurement and characterisation in Europe, but the application of the studies can vary considerably – from rocket science (conical shells) to more earth-bound silo structural problems. One of the strategic objectives of this project was to bring together a body of knowledge on the subject, and to identify criteria common to all applications that might be especially relevant to the design of silos.

The three technical objectives in this project were: to measure, characterise, and analyse imperfections in real metal silos; to perform buckling strength predictions for metal silos, identifying imperfection modes and amplitudes; and to examine the relationship between measurements and imperfection characterisation.

A Workshop held at INSA Lyon (France) provided the final focus for this project. Sixteen papers were presented, each forming an important output from the work of the contributor, and following discussion, agreement was reached on a number of issues relating to imperfection modelling.

Two of the key outcomes from this project relate to construction quality and modelling tools. It was agreed that construction quality was likely to be a significant feature in the design of silos, and in particular the presence of residual stress would be significant to the buckling strength of the shell. In terms of modelling techniques, in many cases axisymmetric imperfections remain a useful tool in modelling real imperfections.

5.2 Comparative Evaluation of Numerical Methods for Predicting Silo Phenomena [1]

There already existed a UK-based project to determine the state of the art in numerical modelling in silos. CA-Silo could add value to that project. The idea of the CA-Silo project was to bring researchers in this field together and ask them to attempt to solve an idealised identical problem using their own procedures. While anonymity would be retained, each researcher would be able to identify their own position in the "pack".

Both Discrete Element and Discrete Particle Models (DEM), and Finite Element Models (FEM) were used in the project. There were only a few full 3-D FEM models. DEM models could only handle relatively

small numbers of particles. Thus, plane strain 2-D analyses were a natural choice. The collaborating researchers were set two problems. The first was a filling problem, while the second involved discharge from a silo.

The project concluded that, in general, there is a very wide scatter in predictions from different programs even when given carefully defined identical initial data. The finite element method generally cannot represent the filling process at all, but must take this as an *a priori* assumption, while the discrete element method has difficulty in capturing such elementary properties as the angle of repose, or the stresses in the stored solid.

5.3 Finite Element Modelling of Real Silos: Comparison with Full-Scale Tests [2]

Some of the problems in silo research remain unaddressed. One of the challenges for the future will be the calibration of numerical models against reliable data from full-scale silo tests. This collaborative project was the tip of that iceberg. It took data from tests at Chartres (*France*), at Karpalund (*Sweden*) and at Watford (*UK*), and aimed to compare finite element predictions (essentially wall pressure) with experimental measurements from these instrumented real or large-scale model silos. Different modelling strategies were investigated.

The conclusion was that a satisfactory model does not readily exist: a dynamic calculation gives a suitable solution based on a sophisticated model, but it does not reach the permanent flow stage. Quasi-static approaches are more efficient for this, but they are not able to represent the evolution of the stress distribution just at the beginning of the discharging process. Neither of the two approaches reached acceptable comparisons to experimental data.

5.4 Improvement of Stress Measurement in Silos [3]

The problem of pressure measurement in silos is widely recognised as an extremely difficult and specialist task. A collaborative project was established to determine the extent to which the challenge of pressure measurement in silos was being met, and the initial survey of all potential CA-Silo participants revealed the known difficulties in constructing pressure cells and hence rarity of appropriate pressure cells. It was therefore entirely appropriate for this project to focus on technology transfer, and to ensure that the existing knowledge would be maintained among those interested.

The group identified a need for validation criteria when designing pressure cells (calibration of pressure cells with different stiffnesses), and used the project to form a comparison of the calibration procedures adopted in a special chamber and in a geotechnical centrifuge. A short-term exchange had shown that transfer of the techniques involved in the use of embedded normal stress cells was possible. The subsequent focus on factors enhancing the technology transfer (e.g. the effect of personal factors when mounting the cells and the need for standardisation of the placement procedure) was a natural progression.

The work has shown that suitable technology exists for the determination of in-situ stress, that calibration is possible, that with appropriate training the technology can be transferred, and that placement of the device is critical and can be made less variable by means of placement devices.

5.5 Patch Loads and their Use in Metal Silo Design [1]

This collaborative activity was based on existing work being carried out at the three laboratories involved. It was designed to focus this work, and bring it more rapidly to the state of being useful in codified rules. The work at the University of Edinburgh (UK) aimed to determine the effect of patch loads on circular metal silo structures, taking into account different forms and positions for the patch of pressure, while work at the Technical University of Graz (Austria) aimed to determine the effect of a patch load on silos that are stiffened, by comparing stiffened and unstiffened designs. Brunel University (UK) looked at the effect of a patch load on rectangular planform metal silos.

The study concluded that the patch load problem in metal silos is very complicated, and requires much more study if patch loads are to be used generally in silo design. With patch loads, there appear to be no simple ideas that can easily be used to generalise the effects of real pressures on silos of different geometry and thickness, which store different solids and which could be supported in different ways.

In general, the patch load is not needed in many rectangular silos, and the standards should be modified to identify the geometry where patch loads are really needed to ensure structural integrity.

In circular planform silos, use of a patch load concept aims at ensuring a robust design approach to deal with asymmetric actions in apparently symmetric systems. Yet the location, distribution of patch pressure and the effect of the patch adopted on the mod-

elled design may be inappropriate or disproportionate; care must be taken to model a realistic silo.

The results of this project are important in relation to the drafting of codes or guidelines for the design of silos. However, from this study it is clear that the relationship between measured silo non-symmetric pressures and suitable models for patch load definitions needs much more work.

5.6 Stochastic Behaviour of Loads from Bulk Solids [4]

In-line with the approach to structural loads adopted in the Eurocodes (CEN standards), it is clear that in the longer term, silo loads should be prescribed in probabilistic terms. To investigate these possibilities, a smaller (almost feasibility) study considered a set of wall pressure measurements taken from a full-scale concrete silo that had been used for storing soya meal.

It can be concluded that it will remain a challenge for some time to define load models for practical use based on the stochastic approach. Accurate and adequate collection of data from pressure and strain gauge measurements in a large range of silos with different stored solids are needed.

5.7 Load Parameters [5]

Parameters for representing the physical behaviour of stored bulk solids are included in all models of silo loads that are used in codes of practice, design recommendations and standards. However, such parameters are often not well defined and are dependent on the test methods used and the individual interpretations of results. As they are listed in official documents, safety considerations have influenced the published values of parameters. The new CEN, ENV 1991, part 4, Actions on Silos and Tanks, refers to load parameters determined directly from materials testing, but there is little experience with the accuracy of this approach.

This CA-silo project aimed at asking each of the contributors to provide data from their own work which, when combined with others, would form a major contribution to the European database on load parameters. It aimed:

- to compare the load parameters given in the proposed European standard with those obtained from material tests on some of the listed materials;
- to compare results obtained from different laboratories and methods;
- to evaluate safety levels obtained from using code values, as opposed to those obtained using load parameters from test results.

The material testing was carried out in different apparatus. These include triaxial tests, circular and square shear-boxes and apparatus for direct measurement of the pressure ratio, K. Some tests in the circular shear-box were carried out using the Jenike procedures and were intended for flow determination. For these tests the consolidation procedure deviates significantly from the soil mechanics tradition.

The project concludes that the load parameters listed in the ENV and those derived from the material tests conform reasonably well in many cases. There are, however, also cases where the agreement is not satisfactory, especially due to larger variability of the measured values than the so-called conversion factors can be assumed to take into account. This is certainly true for coal, and perhaps also for flour. Too few parameters have been obtained from triaxial tests and direct K-measurements to judge if these – presumably more accurate – tests give systematically different results. The measurement of reliable and relevant wall friction coefficients is a severe problem. If the wall friction depends on whether the normal load is increasing or decreasing, it is the value for increasing load that should be the relevant load parameter. However, for coal and wheat, it is seen that the wall friction measured directly in a silo may be significantly larger than the value obtained from shear tests.

From the results, it became clear that to date, there is a significant influence of both the testing method and the interpretation of the material tests in obtaining load parameters for the structural design of silos. This means that further actions are needed.

5.8 Concluding Comments on Collaborative Projects

The collaborative projects were particularly successful where individuals or groups were already active in the field. CA-Silo was not able to fund any substantive work, although some of the work necessary for the collaboration was funded. This essentially meant that participation was limited to those with current research grants, or time/funding available to work on the problems; consequently, the number of potential participants was limited. Further comment is made on this issue below (§10).

6. Short-Term Exchanges [6]

The CA-Silo Programme supported a number of short-term exchanges. A pre-condition was that the parties involved were essentially active researchers. Some of the short-term exchanges led to fuller collab-

orations in other elements of CA-Silo (e.g. one visit from Italy to UK led to a contribution to the work on imperfections in metal silos – see §4.1). In other cases, young researchers from one group have gained substantially from experiencing first-hand the work being carried out by another group. There are few enough active silo groups for this to have been an extensive activity.

Another short-term exchange funded a joint visit by an academic from Germany and an industrialist from UK to report on a Dutch silo with problems. By bringing their joint expertise to bear, this problem can now be fully reported with appropriate technical detail.

7. Industrial Involvement

Silo research needs industrial guidance; the majority of silo problems impact on industrial efficiency. Industry was encouraged to participate actively in the project from the outset. At the Delft meeting (see §3.3), industrialists were invited to make presentations and to participate in the discussions which formed the basis of the work programme. After Delft, some industry contributors were asked to sit on the Steering Committee and to sit on the working groups discussing the state of the art. Twenty-two of the contributions to the chapters are from industrial participants.

To obtain an industrial point of view on research requirements, a wide-ranging group of companies was asked to complete a questionnaire. This is also included in Ref. 1 and has been useful in helping shape conclusions on future research.

It is evident that the project generated interaction with elements of industry. However, it is also evident that no particular industry is prepared to take responsibility for major investments in the basic knowledge that still needs to be generated.

8. Research Requirements

As part of the work of each group, it was agreed that a common element of output should be the identification of research needs within that sphere of work. In each case, the work is identified in the appropriate summary of each part of Ref. 1. Research requirements are also evident from some of the conclusions from the collaborative projects. In consequence, the project has raised a number of questions for future workers, and a number of specific requirements for pre-normative research have been identified.

A survey carried out by CA-Silo identified those areas where significant improvements and further work are necessary for the effective implementation and acceptance by the silo community of CEN guidelines. Ten projects have been identified, and of these, the three with highest priority were:

- Calibration of parameters for stored materials
- Loads in silos with extreme eccentric outlets and/or inlets
- Silos with internal ties

An initial study of the calibration of material parameters has been carried out (see §5.7) but there is further work required. The other two areas require such significant efforts that these need separate funding. Other major areas requiring research are:

- Loads in squat silos
- Seismic actions in silos
- Calibration of Patch Loads with measured properties (again, some initial work has been carried out in a collaborative project)
- Dust explosions in silos
- Loads in silage silos
- Actions due to differential temperatures
- Buckling strength of metal silos under eccentric loads

Efforts to obtain funding for this work have, so far, been unsuccessful.

9. Project Outcomes

The completion of the state-of-the-art report in book form was a major achievement. The book (Ref. 1) contains contributions from not only major European silo researchers, but also a considerable number of industrialists. It is confidently expected that it will be used as a primer for many future researchers and designers.

The collaborative projects were limited, but the quality of work carried out was high. The added value to the projects from multi-national and multi-disciplinary participation would not have been possible without CA-Silo.

CA-Silo identified future research needs. Not only did the active researchers in CA-Silo identify research needs, but a survey of industrialists also provided insights into their perceived research requirements. Not surprisingly, there was much agreement between the two sets of responses.

10. Project Management Issues

A definable "silo industry" does not exist. There is a collection of industrialists with problems and queries from many sectors; the common interest is the need

for safe, reliable storage of bulk solids. The level of expertise varies tremendously from sector to sector; some industrial sectors lead research while for others research is the last tool to be used.

The Delft Workshop held by CA-Silo brought together a range of different interests, and provided a focus for potential contributions. All attendees were funded, and all (consultants, contractors, industrial users and researchers) provided a brief (2 or 3-minute) synopsis of their research, their industrial interest, or their current problem. This formed the diffuse basis from which CA-Silo was generated.

CA-Silo activity needed an operational focus, and this was initially the state-of-the-art report. Working groups had been established, and all those who attended the Delft meeting were kept involved at different levels.

A wider, more iterative and controlled process was part of the initial concept for the generation of the state of the art; this review process would have led to in-depth discussion of key issues, greater agreement on areas of conflict, and a more homogeneous coverage of the different items. However, this was not approved by EC as part of the project plan, and so the state of the art was brought to a premature conclusion in 1996. Despite this restriction, the contributors were motivated to maintain their engagement and complete the work.

Later in the project period, direct collaborations became a key activity. The collaborative projects were conceived as a method of bringing together active researchers and adding value to their joint work. This was achieved along the lines of the original CA-Silo proposals.

The difficulty here, however, was that research awards (whether academic grants or industry-based contract research) are quite carefully monitored with project management often an important aspect of any approved contract, and with time-scales, schedules and deliverables as key items. Lead times are often years rather than weeks. It is therefore difficult to take advantage of the potential added value unless chosen objectives are almost identical; but if objectives are that close, unwanted duplication is a potential problem.

CA-Silo resolved the duplication issue by bringing together different institutions working on related problems and by asking them to solve a common problem using their individual approach. Examples include the project where several institutions used different numerical models to solve the same problems, and the project where different institutions measured properties of stored bulk solids.

One feature that could not be resolved by a concerted action is the fundamentally disparate nature of the sectors with interests in silo research. Research funding is difficult to obtain without industrial support, and while a follow-on project in, say, powder testing may obtain support from process industries, it is unlikely that the different firms involved in the structural design process could be so united. To fund the fundamental research work needed to produce a pan-European design guide or Code of Practice, an even wider perspective is required.

Many failures could be avoided with improved understanding. Having reached consensus on the research need, it is frustrating that to date, no mechanism for carrying out the work is available.

11. Concluding Comments

It is now just over two years since the conclusion of the project, and it is an appropriate time to review the outcomes from such a significant project and to suggest ways forward from CA-Silo.

The CA-Silo project confirmed that many of the fundamental phenomena are very complicated and still poorly understood. These problems are too broad-ranging for any single nation state, and international collaboration is clearly needed if the essential potential gains and savings to industry are to be realised in the foreseeable future. This justification for concerted action remains after the project.

The CA-Silo project has shown that a collaborative action can be established to resolve the technically complex problems within this field. CA-Silo has built up a network of groups willing and able to collaborate. This network has involved major research groups as well as consultants and industrialists engaged in silo problems. Future international co-operation in this field has an improved starting point.

CA-Silo was a significant step along the road to greater harmonisation of research priorities, and to better understanding of some of the significant and challenging fundamental technical problems facing designers, producers and users of silos.

12. Acknowledgements and Contacts for further Information

The authors of this paper are particularly grateful to the members of the Steering Committee. Their timely and accurate reporting of elements of CA-Silo for which they were responsible has been a major source

of information for this review. The members of the Steering Committee were:

Prof. J. Schwedes, Technische Universitat Braunschweig, GERMANY
Prof. J. Eibl, University of Karlsruhe, GERMANY
Prof. J.M. Rotter, University of Edinburgh, UK
Prof. G. Rombach (to 1995), formerly Bilfinger+Berger, now Technische Universitat Hamburg-Harburg, GERMANY
Prof. J. Martinez (from 1995), I.N.S.A. Rennes, FRANCE
Dr. H. Stoffers, T.N.O. Building & Construction Research, THE NETHERLANDS
Prof. V. Askegaard (to 1995), Technical University of Denmark, DENMARK
Dr. J. Garnier, Laboratoire Central des Ponts et Chaussées, FRANCE
Dr. H. Wilms, Zeppelin Schuttguttechnik GmbH, GERMANY
Dr. N.D. Jarrett (to 1994), Building Research Establishment, UK
C.J. Brown (from 1994), Brunel University, UK
Dr. J. Nielsen (Chairman), Danish Building Research Institute, DENMARK

The project was supported by the European Community under the BRITE EuRam Programme, Contract BRE2-0128, Project BE 5021.

The four EC Project Officers throughout the duration of this project gave helpful advice, and in particular the authors would like to acknowledge the support of Dr L. Braganza and Dr S. Becker.

Contacts for papers, reports and further information on collaborative projects

[1] Prof. J.M. Rotter, Silos Research Group, University of Edinburgh, Dept. of Civil and Environmental Engineering, University of Edinburgh, The Kings Buildings, Edinburgh, EH9 3LJ, U.K. {e-mail J.Rotter@ed.ac.uk}
[2] Prof. E. Ragneau, I.N.S.A. Rennes, 20 Avenue des Buttes de Coesmes, F-35043 Rennes, FRANCE. {e-mail Ragneau@insa-rennes.fr}
[3] Dr J. Garnier, Laboratoire Central des Ponts et Chaussées, Route de Pornic, BP 19, F-44340 Bouguenais, FRANCE. {e-mail garnier@lcpc.inrets.fr}
[4] Dr H. Stoffers, T.N.O. Building & Construction Research, Lange Klelweg 5, Rijswijk, P.O. Box 49, NL-2600 AA Delft, THE NETHERLANDS
[5] Dr J. Nielsen, Danish Building Research Institute, P.O. Box 119, DK-2970, Horsholm, DENMARK. {e-mail JN@sbi.dk}
[6] C.J. Brown, CA-Silo Project Co-ordinator, Department of Mechanical Engineering, Brunel University, Uxbridge, UB8 3PH, U.K. {e-mail Chris.Brown@brunel.ac.uk}

11. Reference

1) Silos: Fundamentals of theory, behaviour and design. C.J. Brown and J. Nielsen Eds. (ISBN 0 419 21580 8) Spon, London (1998).

Author's short biography

Chris Brown

Chris Brown is a Senior Lecturer in Mechanical Engineering at Brunel University. He graduated in Civil Engineering from Leeds University. He joined The Department of Building Technology, Brunel University in 1974, and transferred to Mechanical Engineering in 1984. He is currently head of the Structural Mechanics Research Group in the department, and has active research interests in silos, in biomechanics and in mathematical modelling. He has completed over 70 industrial consultancies and is a chartered engineer.

Jørgen Nielsen

Jørgen Nielsen is head of the Division of Building Technology and Productivity at the Danish Building Research Institute. He is a structural engineer, having gained his PhD from the Technical University of Denmark in 1972. He has been an active researcher in silo technology for many years, working in a number of different countries. He is Chairman of the Committee revising ENV 1991-4, Actions in Silos and Tanks. He is an Associate Professor in the Mechanical Engineering Department at Brunel University.

Review

Electrophysical Characterisation of Powders†

R. Ciccu, M. Ghiani and A. Serci
*University of Cagliari, DIGITA Dpt.**
G. Ferrara
*University of Trieste, DICAMP Dpt.***
P. Massacci
*University of Rome "La Sapienza", ICMMPM Dpt.****

Abstract

The paper reviews methods for the electrophysical characterisation of powders and particles and describes in detail many of the laboratory units especially designed for this purpose at the Cagliari University. In particular, the following characteristics can be measured or calculated for powders and particles: (a) electrical conductivity as a function of temperature; (b) thermoelectric potential difference; (c) Seebeck coefficient; (d) electron work function; (e) position of the Fermi level referred to the valence band upper edge; (f) width of the forbidden energy gap; (g) either type of charge carrier concentration (n concentration of electrons in the conduction band, p concentration of free holes in the valence band); (h) either type of charge carrier mobility; (i) electrical charge of powders or single particles; (l) triboelectric charging with different systems. Detailed drawings of the laboratory equipment are provided for each unit used to measure the above-mentioned characteristics, as well as the experimental procedure for both fine powders and single particles. The paper also provides the theory on which the experimental procedure is based and the calculation methods.

1. Introduction

The electrophysical characterisation of powders is highly important in a number of processes involving mineral separation, dust collection, coating materials, handling bulk solids, transporting and mixing powders and particles, and agriculture among others. The influence of the powders' electrophysical characteristics on most of these processes was studied empirically in the past; more intensive studies were conducted only about 30 years ago using the solid-state physics. The most significant early studies dating back to the sixties, in particular related to flotation, electrostatic and triboelectric separation, are those by Plaksin et al. [1, 2], Hoberg [3], Carta et al. [4, 5, 6], Revnivtsev et al. [7], reported also by Schubert [8].

Since the sixties, the University of Cagliari has devoted great effort to conducting both theoretical and experimental research on the electrophysical characteristics of powders and particles and their influence on electrostatic and triboelectric separation, as well as on wet separation systems such as flotation. The collaboration of Professor P. Manca [9, 10, 11] at the Institute of Solid State Physics has been of great importance in this effort. A number of new laboratory units were designed and set up to measure certain physical quantities that make it possible to calculate the electrophysical parameters which describe both surface and bulk energy states of minerals, and powders and particles in general.

After a concise preliminary review of the solids' energy bands theory, this paper describes the laboratory equipment in detail; the mathematical relationships between the relevant physical quantities are also provided and discussed. In addition, the correlation between the electrophysical parameters and the energy exchange phenomena on which the behaviour of solid particles during the separation processes is based is explained and discussed. The laboratory equipment described in this paper was already presented in 1974 (Ciccu et al., [12]), although it had a very limited audience as it was published in Italian.

* Cagliari, Italy
** Trieste, Italy
*** Rome, Italy
† Received: June 11, 1999

2. Energy Level Band Theory

The behaviour of solids in electric conduction, can be described with the energy level band model [13, 14]. In solids, the electron energy levels can lie in allowed energy bands that may overlap or be separated by forbidden gaps. The uppermost allowed band is the conduction band where electrons move freely under the action of an electric field; in metals this band is only partially filled, while in semiconductors and insulators it is empty. A more or less wide forbidden gap separates the conduction band from the underlying valence band where the electrons are strictly bound to the atoms. At temperatures above 0°K, some electrons may acquire enough energy to jump up to the conduction band (if the forbidden gap is not too wide as in insulators), leaving *holes* in the valence band. In this way, electric conduction occurs through the movement of *electrons* in the conduction band and *holes* in opposite direction in the valence band, even if their mobility differs, as will be explained later.

The description above refers to ideal solids whose crystal lattice is perfect, i.e. it extends indefinitely and has no defects or impurities (intrinsic semiconductor). Actually, localised energy levels lie in the forbidden gap in real solids due to impurities or imperfections in the crystal lattice (natural or intentionally produced) [11, 15, 16], or due to the abrupt interruption of crystal lattice periodicity [17, 18]. These energy levels may be *donor* levels if occupied by electrons or *acceptor* levels if empty and hence able to receive electrons coming from the valence band. Accordingly, semiconductors are called *n-type* or *p-type* and the electric conduction occurs involving electrons in the conduction band and holes in the valence band. The two types of energy levels may also coexist in the forbidden gap: in this case, both electrons and holes independently contribute to electric conduction. In any case, the minimum energy needed for starting conduction equals the energy difference between the lower limit of the conduction band and the donor level, or between the acceptor level and the upper limit of the valence band.

The Fermi level E_f encompasses the energy status of a solid. It gives the average energy of the electrons involved in the exchanges taking place in electric and electrochemical phenomena. In a semiconductor without defects or impurities, the Fermi level lies exactly at the centre of the forbidden gap (*intrinsic semiconductor*). In a more general case, E_f may lie in the upper part of the forbidden gap if donor levels prevail or in the lower part if acceptor levels prevail (*extrinsic semiconductor*).

In addition to the Fermi level E_f, the other electrophysical parameters needed to define the energy status of a solid more completely are:

- the *work function*, Φ, the energy required to remove an electron from the Fermi level to the vacuum level (reference level);
- the width of the forbidden energy gap, E_g;
- the charge carrier concentration of either type (n, concentration of free electrons in the conduction band; p, concentration of holes in the valence band);
- the charge carrier mobility of either type, μ_n or μ_p.

Fig. 1 shows the energy band model where localised levels in the forbidden band occur as a consequence of impurities or crystal lattice defects. **Figs. 1 a)** and b) refer to an n-type semiconductor: at ambient temperature, electric conduction is only due to electrons which have jumped from the donor level to the conduction band where they move freely under the action of an electric field. As absolute temperature T increases, an increasing number of electrons in the valence band receive enough energy to overcome the energy gap E_g, so they jump to the conduction band. Thus, the semiconductor becomes an *intrinsic semiconductor* when electrons which have jumped from the valence to the conduction band prevail over the electrons coming from the donor levels in the forbidden gap (whose quantity is obviously limited). At the same time, a number of holes equal to the number of electrons which have jumped are generated in the valence band, further contributing to electric conduction with p-type carriers. The Fermi level initially lies between the donor level and the bottom of the conduction band; as the temperature increases, it gradually moves downwards towards the centre of the forbidden gap, which is reached when the ratio of electrons/holes involved in conduction practically reaches unity.

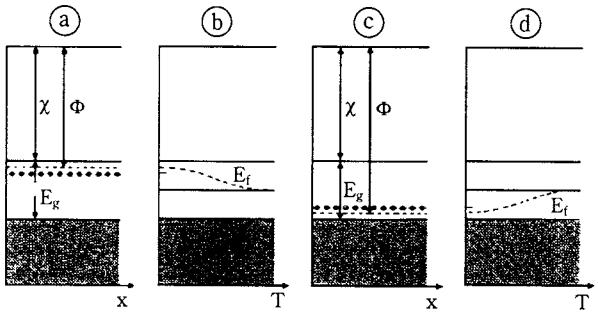

Fig. 1 Energy band model for: (a) n-type semiconductors; (c) p-type semiconductors. Figures (b) and (d) show how the Fermi level moves towards the centre of the forbidden band as absolute temperature increases.

Likewise, the acceptor levels lie in the lower part of the forbidden energy gap in p-type semiconductors (**Figs. 1 c)** and **d)**). Therefore, electrons in the valence band with relatively low energy can jump and fill the acceptor level, thus producing holes in the valence band capable of p-type electric conduction in the same band. As the absolute temperature T increases, an increasing number of electrons in the valence band receive enough energy to overcome energy gap E_g, and thus jump to the conduction band. The semiconductor becomes an *intrinsic semiconductor* when the electrons which have jumped from the valence band to the conduction band prevail over the holes left by the electrons which have jumped from the valence band to the acceptor energy levels in the forbidden gap (which can be rapidly filled). The Fermi level, initially lying between the top of the valence band and the acceptor level, gradually moves upwards towards the centre of the forbidden band as the temperature increases.

Fig. 1 also shows the energy levels (referring to the vacuum level) corresponding to work function Φ; this gives the mean energy needed to extract an electron from the crystal lattice. **Fig. 1** provides a simplified explanation of these phenomena as it refers only to the semiconductor surface, even if the internal part of the solid close to the surface is also involved. For a more detailed explanation, see the papers of Carta et al. [5], Revnivtzev et al. [7], and Schubert [8].

The relevant parameters can be determined by measuring electrophysical quantities such as:

- the difference in contact potential between the sample and a reference electrode; work function Φ can be calculated from this;
- the electric conductivity in the intrinsic zone of the semiconductor, whose gradient gives the forbidden gap width;
- the thermoelectric effect which makes it possible to determine the Fermi level and, hence, calculate the charge carrier concentrations and also to define the type of conduction.

Methods and units used for measuring such electrophysical quantities are illustrated in the following sections. The values of the parameters describing the surface energy status of powders and particles of solids can be calculated from these quantities. In addition, a special section is devoted to measuring the contact electric charge, a phenomenon that can be well explained by using the band energy model.

3. Measuring Electric Conductivity and Forbidden Gap Width

Electric conductivity depends on the number of charge carriers and their ability to move under the action of an electric field. It is expressed as [10, 19]:

$$\sigma = q.n.\mu_n + q.p.\mu_p \tag{1}$$

where:

σ	electric conductivity	$(S \cdot cm^{-1})$
n	concentration of free electrons	$(electrons \cdot cm^{-3})$
p	concentration of holes	$(holes \cdot cm^{-3})$
μ_n	mobility of free electrons	$(cm^2 \cdot V^{-1} \cdot s^{-1})$
μ_p	mobility of holes	$(cm^2 \cdot V^{-1} \cdot s^{-1})$
q	electron charge	$(1.602 \cdot 10^{-19}\ C)$

Eq. (1) is valid in the semiconductor's intrinsic zone. However, it is also valid in the extrinsic field when the number of minority charge carriers is significant compared with the number of majority carriers.

As in the intrinsic zone $n=p=n_i$, Eq. (1) becomes:

$$\sigma = n_i.q(\mu_n + \mu_p) \tag{2}$$

and, if the electron mobility is much higher than hole mobility:

$$\sigma = n_i.q.\mu_n \tag{3}$$

Since:

$$n_i = 2\frac{(2\pi mkT)^{3/2}}{h^3}\left(\frac{m_n \cdot m_p}{m^2}\right)^{3/4} \exp(-E_g/2kT) \tag{4}$$

where:

m	free electron mass	$(9.11 \cdot 10^{-31}\ kg)$
h	Planck's constant	$(6.624 \cdot 10^{-34}\ J \cdot s)$
m_n	effective mass of an electron	(kg)
m_p	effective mass of a hole	(kg)
T	absolute temperature	(°K)
k	Boltzmann's constant	$(1.38 \cdot 10^{-23}\ J \cdot K^{-1})$
E_g	forbidden gap width	(eV)

Eq. (3) becomes:

$$\sigma = q\frac{2(2\pi mkT)^{3/2}}{h^3}\left(\frac{m_n \cdot m_p}{m^2}\right)^{3/4} \exp(-E_g/2kT)\mu_n \tag{5}$$

If the product of the effective masses is constant and the mobility of free electrons is proportional to $T^{-3/2}$ (lattice diffusion), the result is:

$$\sigma = A \cdot \exp(-E_g/2kT) \tag{6}$$

where:

A	constant
E_g	$E_{g0} + aT$
E_{g0}	forbidden gap width at 0°K

According to Eq. (6), if conductivity σ is plotted in a logarithmic scale against the reciprocal absolute temperature, a straight line is obtained whose slope in the high temperature zone (where the semiconductor is intrinsic) gives the width of the forbidden band E_g (e.g., see **Fig. 1** of paper [6]).

The apparatus described in **Fig. 2** was developed to measure σ in powders. The sample is introduced into a cylindrical cavity delimited by a high-resistivity ceramic body between two cylindrical copper electrodes. The axes of the electrodes have been bored; so thermistors can be inserted to measure the temperature at the electrodes' ends (**Fig. 3**). The powder sample with the desired size composition is then

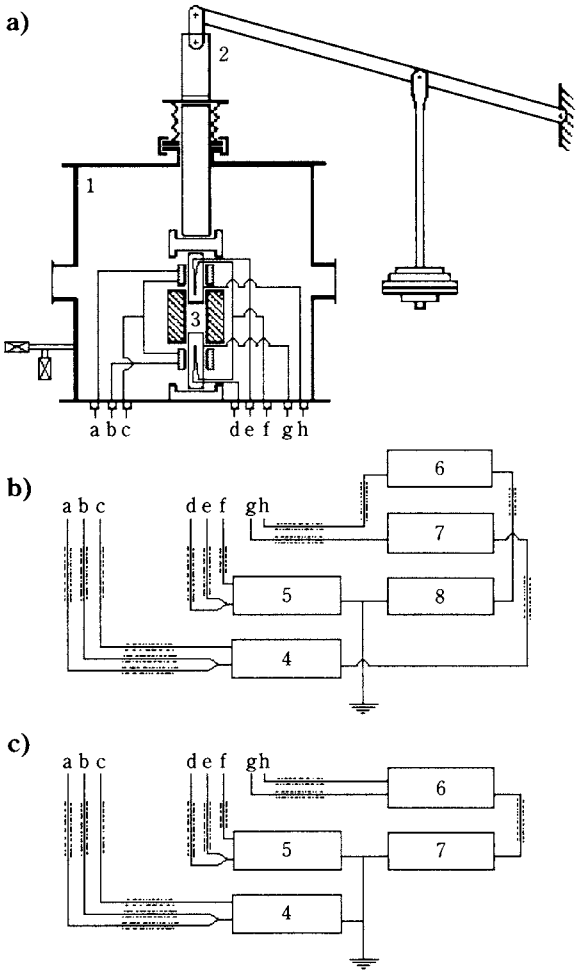

Fig. 2 Apparatus and circuits for measuring electric conductivity and thermoelectric potential difference.
Apparatus (a): 1 – vacuum-sealed stainless steel vessel; 2 – powder compression system; 3 – measuring cell.
Circuit (b) for measuring the electric conductivity: 4 – direct current generator; 5 – electronic voltmeter; 6 – electrometer; 7 – high-tension generator; 8 – recorder.
Circuit (c) for measuring the thermoelectric potential difference: 4 – direct current generator; 5 – electronic voltmeter; 6 – electrometer; 7 – recorder.

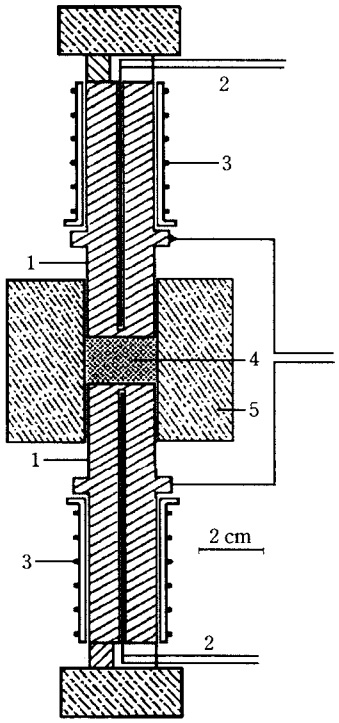

Fig. 3 Detail of the cell for measuring the electric conductivity and thermoelectric potential difference.
1 – copper electrodes; 2 – thermistors; 3 – electric resistance; 4 – sample; 5 – ceramic body.

pressed between the two electrodes. These electrodes can be heated up to 600-700°C with an electric resistance around a ceramic sleeve. The compression of the powder is obtained by applying a pressure with maximum load of 10 kN. The apparatus is located inside a vacuum-sealed stainless steel vessel with a control window. After the vacuum has been achieved, the vessel is filled with an inert gas (argon) and the heating of the electrodes begins.

The relevant data are measured forwards (as temperature increases), and backwards (as temperature decreases). Electrodes a, b, c, d, e, and f are connected to the circuit (b) in **Fig. 2** to measure the electric conductivity.

All the connections are made with shielded cables and Amphenol connectors. Earthing resistance must be less than 2 Ω.

Electric conductivity σ ($S \cdot cm^{-1}$) is calculated with the following equation:

$$\sigma = \frac{I \cdot l}{s}\left(\frac{2}{V_+ + V_-}\right) \qquad (7)$$

where:

I	electric current	(mA)
l	distance between the electrodes	(cm)
s	electrode's cross-section	(cm^2)

$V_+ \cdot V_-$ voltage (mV) measured according to the current direction.

After each measurement, the copper electrodes must be polished with abrasive paste and then washed in an ultrasound bath comprising twice-distilled water.

4. Measuring the Thermoelectric Effect

The thermoelectric potential difference between two extremities of a solid depends on the diffusion of electrons and holes inside the solid where a temperature gradient exists. The Seebeck coefficient α (mV/°C) is the ratio between the thermoelectric potential difference and the temperature difference between the extremities of the sample, connected to a high impedance voltmeter.

The Seebeck coefficient may be from 100 to 1,000 times higher in semiconductors than in metals. Hence, the metals in the circuit do not influence the measurement. This coefficient may vary rapidly with temperature and greatly depends on the concentration of impurities in the semiconductor. There are equations that give the Seebeck coefficient for both intrinsic and extrinsic semiconductors. For extrinsic semiconductors, Putley [20] gives:

$$\alpha = -\frac{k}{q}\left\{(P+5/2)-E_f/kT\right\} \tag{8}$$

where P is a constant and E_f is the Fermi level (eV) (referred to the valence band upper edge) given by:

$$E_f = kT \cdot \ln \frac{n \cdot h^3}{2(2\pi m^{\wedge} kT)^{3/2}} \tag{9}$$

The symbols are the same as in the preceding section.

When impurities prevail, the Seebeck coefficient is:

$$\alpha = \pm\frac{k}{q}(A-\eta) \tag{10}$$

where:

$$\eta = \frac{E_f}{kT} \qquad \text{for p-type semiconductors}$$

$$\eta = \frac{E_g - E_f}{kT} \qquad \text{for n-type semiconductors}$$

In Eq. (10), the + sign refers to p-type and the − sign to n-type semiconductors. Given α and E_g (eV), it is possible to calculate Fermi level E_f. Constant A is assumed equal to 2 in the case of diffusion processes due to thermal vibration of the crystal lattice, and equal to 4 in the case of diffusion processes due to impurities and crystal defects.

For intrinsic semiconductors, Johnson [21] developed an expression incorporating: ratio b between the mobility of electrons and holes, forbidden gap width and the ratio between the effective masses of electrons and holes:

$$\alpha = -\frac{k}{q}\left\{\frac{b-1}{b+1}(E_g/2kT)+\frac{2(b-1)}{b+1}+\frac{3}{4}\ln(m_n/m_p)\right\} \tag{11}$$

If the forbidden band amplitude and temperature are assumed to have a linear relationship, according to an arithmetic scale diagram where the Seebeck coefficient is plotted against the reciprocal absolute temperature, one can obtain slope Θ and intercept c which defines the straight line:

$$\alpha = \Theta/T + c \tag{12}$$

where:

$$\Theta = -\frac{k}{q}\left(\frac{b-1}{b+1}\right)\cdot E_{g_0}/kT$$

and $$c = -\frac{k}{q}\left\{\left(\frac{b-1}{b+1}\right)\cdot\left(\frac{a}{2k}+2\right)+\frac{3}{4}\ln(m_n/m_p)\right\}$$

Since E_g is known (calculated by measuring the electric conductivity), one can obtain ratio b between the electron and hole mobility using the equation:

$$b = \frac{E_{g_0}-2\Theta q}{E_{g_0}+2\Theta q} \tag{13}$$

or the approximate equation:

$$b = |m_p/m_n|^{5/2} \tag{14}$$

The thermoelectric potential difference can be measured with the same cell used for the electric conductivity according to circuit (c) of **Fig. 2**. The sample with the desired size composition is introduced into the measurement cell between the two copper electrodes: after the vacuum is achieved and the inert gas is introduced, only one electrode is heated up to 300-400°C. The thermoelectric potential difference is measured when the temperature decreases. The temperature difference between the electrodes is measured by the thermistors connected with an electrometer. All the connections are made with cables and Amphenol-type connectors. Grounding resistance is lower than 2 Ω. An example of determining the Seebeck coefficient is given in **Fig. 2** of paper [6].

5. Measuring the Electric Charge

When two solids (metals or semiconductors) are placed in contact, a flow of electrons moves from the material with the higher Fermi level (lower work function) to the other until the Fermi level energies of

both materials are equalised. For example, a semiconductor whose Fermi level is lower than a metal will extract electrons from the metal, and assumes a negative charge (not only on the surface but also in the layer near the contact). Conversely, a semiconductor whose Fermi level is higher than a metal will supply electrons to the metal, and assumes a positive charge.

In a nutshell, if Φ_m and Φ_s are the work functions of the metal and the semiconductor, we will have the following when the solids are placed in contact:

positive semiconductor
negative metal for $\Phi_m > \Phi_s$
negative semiconductor
positive metal for $\Phi_m < \Phi_s$

More details on this phenomenon and on the distribution of charges near the contact zone in semiconductors can be found in the paper of Carta et al. [5].

The contact charge can be obtained in the lab by letting the particles slide on vibrating chutes or by injecting them into an air cyclone where friction occurs in the inner wall.

5.1 Vibrating Chute Method

In general, the contact charge must be measured in a controlled atmosphere. The device sketched in **Fig. 4** has been used to achieve this. The compressed air, partially dehumidified in two collecting reservoirs (not shown in the figure), is fed into vessel G (controlling the pressure with needle valve V and manometer M), and is dehumidified to about 3% by passing it through many silica gel beds. Then, the air is fed to an electrically heated coil where the temperature can reach about 70°C, and finally it is fed into a Perspex box (internally shielded through an earthed copper cage) where the vibrating chute and the Faraday well

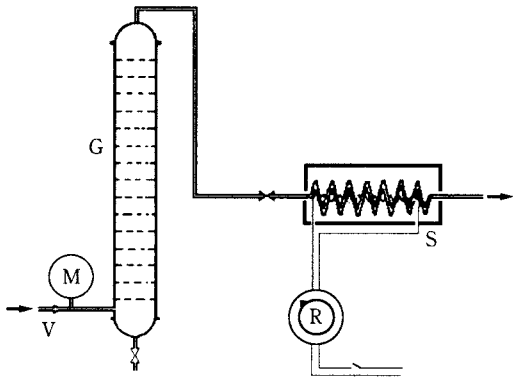

Fig. 4 System for humidity and temperature control of the atmosphere in the apparatus for measuring the electric charge of solid particles.
V – needle valve; M – manometer; G – dehumidifier; S – heated coil; R – rheostat.

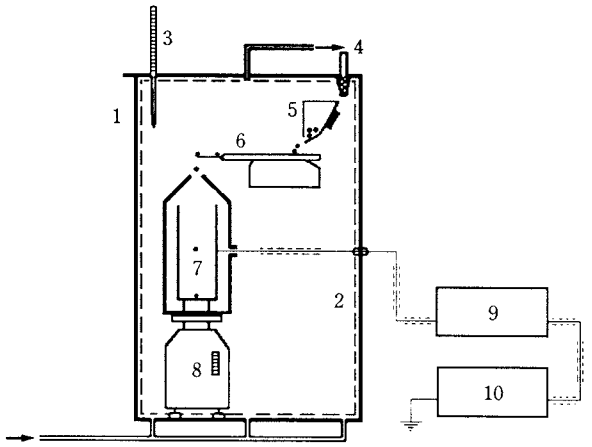

Fig. 5 Apparatus for measuring the particle charge with the vibrating chute method.
1 – Perspex vessel; 2 – earthed copper cage; 3 – thermometer; 4 – hygrometer; 5 – particle feeding device; 6 – vibrating chute; 7 – Faraday well; 8 – precision scale; 9 – electrometer; 10 – recorder.

are located (**Fig. 5**). This apparatus lies on a non-vibrating table. The air enters the vessel through many inlets in order to rapidly obtain constant characteristics inside the box. The requested conditions are controlled by a thermometer and a hygrometer. The chute on which the particles slide is earthed and rigidly fixed (though electrically insulated) to a vibrator capable of variable amplitude by means of a rheostat. The Faraday well consists of a metal cylinder (10 cm diameter, 30 cm height) shielded by an earthed coaxial cylinder with a conical frustum-shaped cover with a circular hole on top for the passage of the particles. A Teflon block insulates the two coaxial cylinders. The particles fall into the Faraday well connected to an electrometer, which measures the electric charges in coulomb. The electrometer is connected to a recorder. The Faraday well rests on a high-accuracy scale in order to weigh the particles and calculate the specific charge (C/g).

The charge of differently sized individual particles can be measured from about 2 mm down to 0.5 mm with statistical procedures. After at least one hour under controlled atmosphere, particles are fed through a suitable dosing device on the chute where they slide and fall one at a time into the Faraday well.

The particle charge can be determined under controlled atmosphere in air or inert gas with the apparatus of **Fig. 5**. A more recent version of the apparatus has been constructed for measurements in vacuum as well, and for a larger range of vibration frequency and amplitude, as well as contact time. In this way, different rubbing systems can be simulated from gentle sliding, to high-velocity impingement [22,23,24,25,26].

Fig. 6 shows a photo of the apparatus consisting of three parts: a system for charging the particles, a device for feeding charged particles into the Faraday well, and a system for containing particles before processing. This apparatus is hosted in a vacuum vessel.

The charging system consists of a vibrating plate suspended on two springs and actuated by a set of two opposite main electromagnets. The plate can be heated to a desired temperature controlled by a thermocouple, and an interchangeable surface manufactured using whatever material can be fixed over it for triboelectric charging. Surface vibration amplitude is set in each test, while frequency can vary between 2 and 24 Hz during the test. Retention time of the particle on the charging surface can vary from one second to one hour. The surface is kept horizontal during the charging phase, at the end of which it is inclined downwards, thus directing the particles towards the Faraday well when the electric charge must be measured.

Two additional electromagnets feed charged particles into the Faraday well. One of them inclines the surface, the second produces a controlled vibration. When particles stick to the surface due to the high acquired electric charge, the two main electromagnets can be deployed to detach these particles.

The particle dispenser consists of two independent superimposed stainless steel discs. The top disc has steel brushes attached under it that delimit a number of places (between the brushes) where single particles or groups of particles can be placed in a round channel engraved in the bottom disc. The bottom disc is fixed and has a hole where the particles fall onto the vibrating charging chute which drives them into the Faraday well. The top disc rotates by steps through a driving gear controlled by a photoelectric cell, so that particles are sent to the charging chute at spaced time intervals.

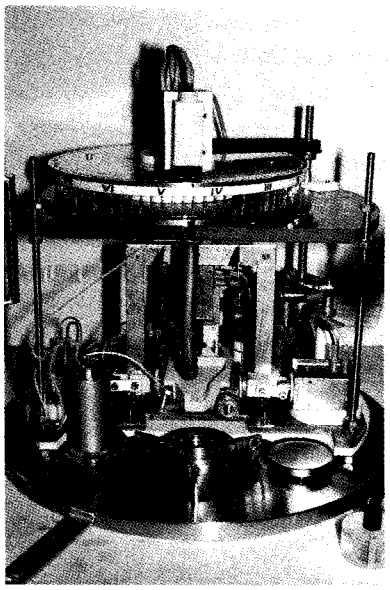

Fig. 6 Apparatus for measuring the triboelectric charge on individual particles. This apparatus is contained in a Leybold-Heraeus steel vacuum vessel.

All the operations in the steel vacuum vessel are controlled and monitored, and charges are measured by means of an electrometer and a recorder.

5.2 Air Cyclone Method

The air in the apparatus sketched in **Fig. 7** comes from a compressor with automatic pressure control and oil filter, and it is directed into two passive accumulators with total capacity of 0.1 m^3. A set of valves discharges the condensed water. A constant pressure of 0.5 MPa is obtained in the last accumulator. The air dehumidification system is indicated in **Fig. 7**, which also shows the hygrometer (4) for monitoring air humidity. The air flow rate is controlled by means of a rotameter and then sent to the cyclone charging system where the particles from the cyclone apex go directly into the Faraday well. Temperature and pressure are monitored in the charging system, and there are two systems for feeding particles: the first (12) for bulk feeding of fine powders and the second (13) for feeding single particles. In system (12) the particles are conditioned either with the air circulating in the cyclone or in the Perspex vessel; system (13) gives only the last possibility. In any case, particles should be heated at a given temperature before each test. Other gases can be used as an alternative to compressed air.

The terminal part of the apparatus, shown on the right in **Fig. 7**, can be manufactured with different materials; in particular, the cyclone can be replaced to study the behaviour of various materials in the contact charging as well as to study the influence of the cyclone geometry. Preferably, the solid to be charged must be classified in narrow size ranges, especially for study of charging single particles. Statistical significance for determining the average charge of single sized particles requires measurements on at least 200 particles.

The measurement results of the triboelectric charge may vary widely depending on different factors, for example:

- the contact system used and its energy: gentle or stronger sliding in a chute, rubbing in an air cyclone or rotating device, charging by impact;
- the crystal size, orientation and surface affected by charging;

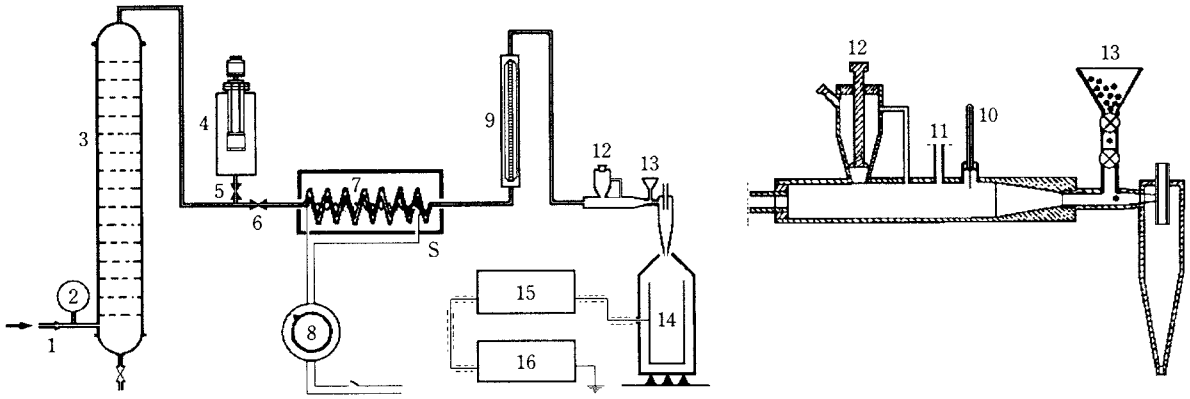

Fig. 7 Experimental set for the electric charge measurement using the air cyclone: whole experimental set (left), enlarged detail of the cyclone (right).
1 – needle valve; 2 and 11 – manometers; 3 – dehumidification vessel; 4 – hygrometer; 5 and 6 – needle valves; 7 – heated coil; 8 – rheostat; 9 – rotameter; 10 – thermometer; 12 and 13 – particle feeding systems; 14 – Faraday well; 15 – electrometer; 16 – recorder.

– the surrounding atmosphere in equilibrium with the crystal surface.

Therefore, different systems give different charge values [27]. For example, in an air cyclone, one obtains electric charges ten times higher than in a sliding chute [24]. However, the polarity of the charge chiefly depends on the work function difference between the solids in contact.

Recently, other charging systems have been studied, sometimes according to the needs of the research: charging single particles by impact [28], charging powders in pipes during pneumatic transport [29].

6. Measuring the Work Function

The Fermi level position, defined by the Work Function Φ, determines the polarity of electric charges. In the triboelectric charging of two solids, the one with the higher Fermi level (i.e., the lower work function) gives electrons to the other which becomes negatively charged, while the first solid becomes positively charged. The following methods can be used to determine the work function:
- photoelectric method,
- thermoionic method,
- ionisation method
- Kelvin method.

6.1 Fundamentals for Measuring the Work Function

a) Photoelectric Effect

The energy of electrons emitted from a surface subsequent to an incident monochromatic radiation can be determined by measuring the potential V needed to decrease down to zero the photoelectric current:

$$V \cdot q = h \cdot \nu - \Phi \tag{15}$$

where:
ν wavelength of the incident radiation (cm);
h Planck's constant ($6.624 \cdot 10^{-34}$ J·s);
Φ work function (eV);
q electron's charge ($1.602 \cdot 10^{-19}$ C).

b) Thermoionic Effect

Electrons are spontaneously emitted from a high-temperature solid. The current density of this emission is given by the Richardson-Fermi expression:

$$J_s = A \cdot t^2 \cdot e^{-\Phi/kT} \tag{16}$$

where:
A constant;
T absolute temperature (°K);
k Boltzmann's constant ($1.38 \cdot 10^{-23}$ J °K^{-1});
t time (s)

Φ can be calculated by measuring J_s and plotting log J_s against 1/T.

c) Ionisation

When ionised gas is present between two facing solids, the ions are attracted depending on the Fermi levels: positive ions migrate towards the surface with the higher Fermi level, negative ions towards the surface with the lower Fermi level. Consequently, ions act as an electric connection allowing the Fermi levels of the two solids to equalise. The contact potential difference between the solids is:

$$V_c = (\Phi_1 - \Phi_2)/q \tag{17}$$

where Φ_1 and Φ_2 are the work functions of the reference solid and unknown solid, and q is the electron charge.

d) Kelvin Method

According to the classical Kelvin method [30] (**Fig. 8a**), two facing samples A and B (A with known work function; B, unknown) form a capacitor with capacitance C_1. The two capacitor plates are electrically connected with switch K so that negative charge Q flows from A (with the lower work function) to B until the Fermi levels of the two solids equalise. In this way, the contact potential difference V_0 is established between the two plates.

When switch K is closed, the moved charge will be $Q=C_1 \cdot V_0$. When switch K is open and the distance between the plates is increased, the capacitance will be strongly reduced to C_2. Therefore, since Q is constant, the potential difference V_E becomes much higher than V_0, according to:

$$V_E = V_c(C_1/C_2) \tag{18}$$

The increasing distance between the capacitor plates only serves to increase the potential difference measured by electrometer E.

Another measuring system consists of inserting a potential difference just equal to V_0 into the circuit of **Fig. 8a)** to counteract the contact potential difference. This way, the increased distance between the plates with K open will not effect any increase in the potential difference measured by the electrometer, as the voltage applied to the circuit exactly compensates the contact potential difference. Hence we know $V_0=(\Phi_1-\Phi_2)/q$, and we obtain Φ_2 if Φ_1 is known.

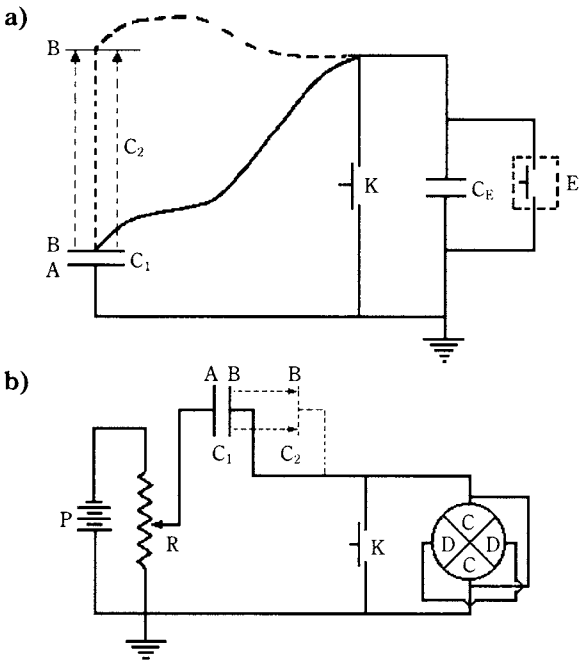

Fig. 8 Kelvin method for measuring the work function: (a) classic method; (b) modified method.

The modified Kelvin methods involve producing a relative motion of the plates (or the samples acting as plates) of the capacitor, thus generating an alternating current that can be nullified by applying a given voltage (counteracting the contact potential difference) (**Fig. 8b**) [31].

The following methods were set up to determine the work function:

- vibrating capacitor;
- rotating capacitor;
- ionisation.

6.2 The Vibrating Capacitor Method

If V_c is the contact potential difference between the plates of a vibrating capacitor, its capacity varies according to the equation $C(t)=C_0 \cdot \cos \omega t$ and the electric current will be:

$$i = V_c \cdot dC/dt = -V_c \cdot \omega \cdot C_0 \cdot \text{sen}\, \omega t$$

The following potential difference can be measured at the extremities of resistance R_1:

$$V_1 = -V_c \cdot \omega \cdot R_1 \cdot C_0 \cdot \text{sen}(\omega t + \varphi)$$

where ω is the angular frequency, and φ the phase shift produced by circuit capacitance C depending on capacitor C_s and R_1.

Potential difference V_1 is generally much lower than V_c because capacitance C is only a few pF; the vibration frequency $f=\omega/2\pi$ is about 100 Hz; the maximum value of R_1 is limited by C_s. In general, the required signal is highly disturbed subsequent to undesired noise in the apparatus. A phase-sensitive detector is used to eliminate the signals which do not correspond to the vibrating capacitor frequency, thus discriminating the signal from disturbances.

Fig. 10 shows the measuring circuit. The low-frequency oscillator (<100 Hz) (1) actuates the electromagnetic vibrator (9) through the power amplifier (2). Potential difference V_1 occurring at the extremities of resistance R_1 is amplified in the low-noise amplifier (5). As indicated before, the phase shifter (3) and the phase-sensitive detector (4) are needed:

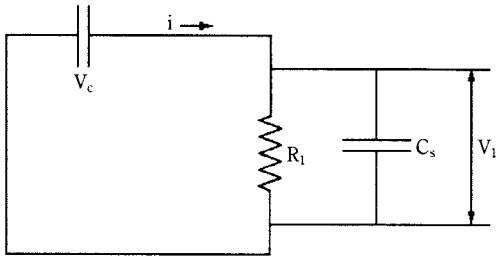

Fig. 9 Simplified circuit of the vibrating capacitor method for measuring the work function.

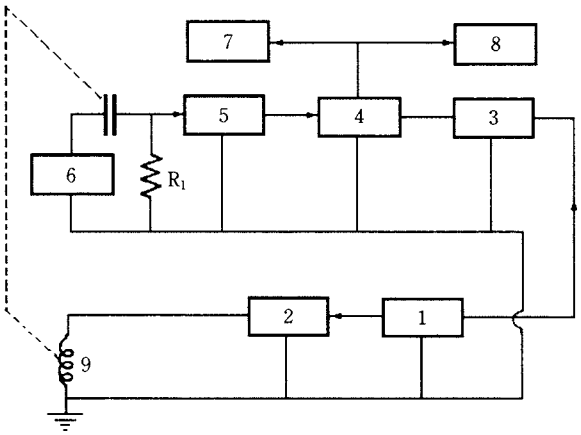

Fig. 10 Circuit for measuring the work function with the vibrating capacitor method.
1 – oscillator; 2 – power amplifier; 3 – phase shifter;
4 – phase-sensitive detector; 5 – low noise amplifier;
6 – potentiometric circuit; 7 – oscilloscope; 8 – recorder;
9 – electromagnetic vibrator.

during measurements, the phase shifter is used to maximise the phase-sensitive detector deviation. In fact, this maximum deviation is proportional to the contact potential difference, provided that other conditions are equal. The measuring method consists of using the potentiometer (6) to balance the contact potential difference V_c until the signal from the phase-sensitive detector reaches zero. The instruments used in the circuit in **Fig. 10** are:

- a high-frequency-range video oscillator (model TF 88S A/1, Marconi Instruments) with amplifier and continuously variable output;
- a cathode-ray oscilloscope with 1 MΩ input impedance (model 104, Hewlett-Packard);
- an electrometer with input impedance up to $10^{14}\Omega$ (model 610 B, Keithley Instruments);
- a potentiometer that can produce a minimum of 10^{-3} of the battery voltage; it is equipped with a voltmeter whose sensitivity is 10^{-3} V (model 2227, Yokogawa Electric Works);
- a phase shifter that can shift the phase by about 180° (model 421, Brookdeal);
- a phase-sensitive detector with a 1 Hz to 1 MHz frequency range (model 471, Brookdeal).

In practice, only gold or platinum can be used as reference metals to measure the work function of different materials due to their resistance to oxidation. In our case, gold was preferred as its work function is well known: measurements made by many researchers indicate that the gold work function is 4.71 eV, which is assumed as the reference value.

In **Fig. 11,** the reference electrode (1) is fixed at the lower extremity of a hollow Teflon rod and connected to the potentiometric circuit with a cable passing through the same rod. The sample (2) is pasted with a suspension of colloidal silver to a gold disc (3) which is fixed through the screw (4) to a site made in the support arms (6). The Teflon block (7) is an insulator; the shielded cable and amplifier connection is shown in (8). The disc (3) and the support arms (6) are gold-plated to avoid superimposing the potential contact differences of other metals. This apparatus is inside a vacuum container with vacuum-sealed electric connections.

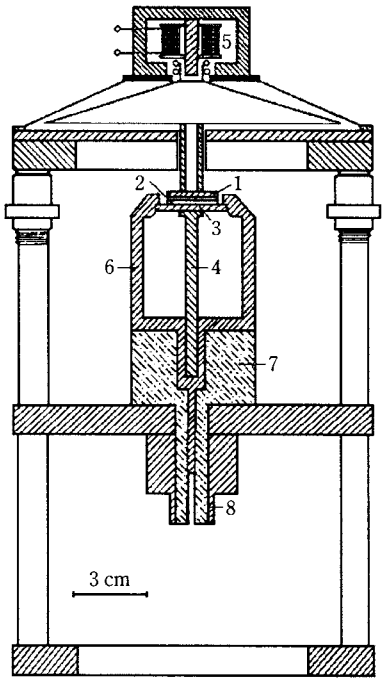

Fig. 11 Assembly drawing of the vibrating capacitor.
1 – reference electrode; 2 – sample; 3 – gold-plated disc;
4 – setting screw; 5 – electromagnetic vibrator;
6 – support arms; 7 – teflon;
8 – connection of the shielded cable.

6.3 The Rotating Capacitor Method

Fig. 12 shows the electric circuit. As in the vibrating capacitor method, a periodic current is generated with the rotating capacitor. Since the periodic current

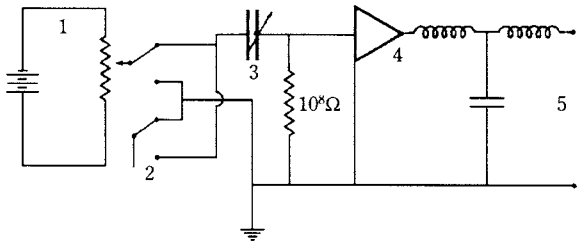

Fig. 12 Circuit for measuring the work function with the rotating capacitor method.
1 – potentiometer; 2 – selector switch;
3 – rotating capacitor; 4 – preamplifier; 5 – oscilloscope.

is weak, the signal must be amplified before being displayed on the oscilloscope. If a voltage balancing the contact potential difference V_c is applied to the plates of the rotating capacitor through a potentiometer, one obtains:

$$i = dq/dt = V \cdot dc/dt = 0$$

Hence, when the sine wave displayed by the oscilloscope is minimised by acting on the potentiometer, the voltage will equal the contact potential difference.

Since the voltage of the battery may not be constant, the potential difference must be measured in the potentiometric circuit using a high-precision electronic voltmeter. To reduce high-frequency disturbances, the signal is sent in a low-pass filter before the oscilloscope. The instruments used in the measuring circuit are:

- a potentiometer that can provide a minimum of 10^{-3} of the battery voltage; it is equipped with a voltmeter with sensitivity of 10^{-3} V (model 2227, Yokogawa Electric Works);
- an electronic voltmeter whose sensitivity is 10^{-4} V (model 419 A DC null voltmeter, Hewlett-Packard);
- an electrometer with input impedance up to $10^{14}\Omega$ (model 610 B, Keithley Instruments);
- a cathode-ray oscilloscope with 1 MΩ input impedance (model 104, Hewlett-Packard).

Fig. 13a) shows the assembly of the rotating capacitor and **Fig. 13b)** shows the gold rotating electrode with two symmetric reliefs on the plate (A electrodes). Plate B rotates through plate shaft D, joint E and drive shaft D. The electric connection with the electrodes A is obtained through a sliding contact (graphite brush). The connection with sample P is made through a shielded cable in T. H and F are insulating Teflon blocks. Sample holder S is gold-plated to avoid superimposing the potential contact differences of other metals. The rotating capacitor is shielded with an earthed Faraday cage; chassis L and the motor are earthed as well. The measurements can be made under ambient conditions or inside a vacuum container with vacuum-sealed electric connections.

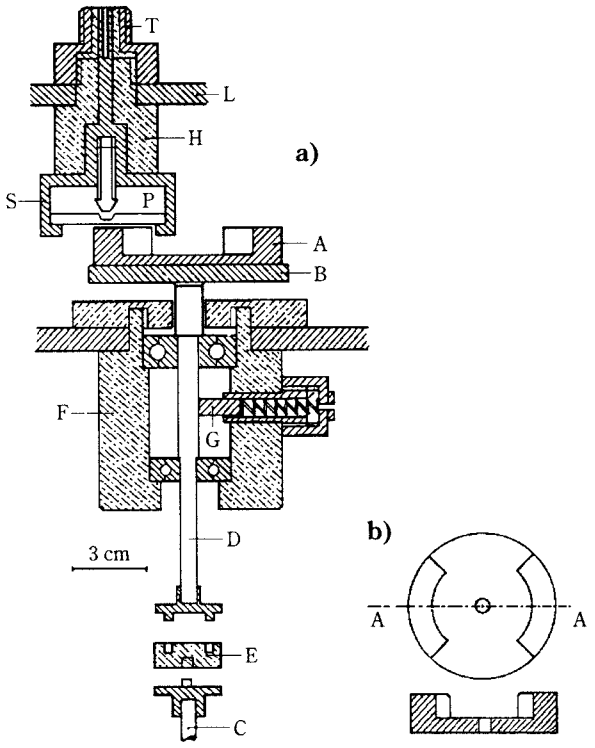

Fig. 13 Assembly drawing of the rotating capacitor (a) and detail of the rotating electrode (b).
A – reference electrode; B – rotating plate;
C – drive shaft; D – rotating plate axis; E – teflon joint;
F – teflon block; G – sliding contact; H – teflon block;
L – chassis; P – sample; S – gold plated specimen holder;
T – connection of the shielded cable.

6.4 Ionisation Method

Fig. 14 shows the electric circuit. The contact potential difference is:

$$V = i_1 \cdot R + e_1 = e_1(1 + R/r_1) \qquad (19)$$

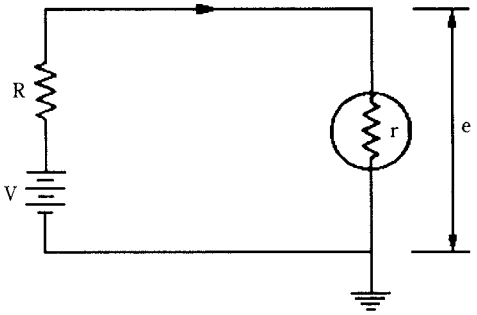

Fig. 14 Electric circuit of the ionisation method.

where:

R ionised air resistance (Ω);

e_1 voltage drop at the extremities of the r_1 resistance (mV);

V contact potential difference (mV),

i_1 current (mA).

Replacing resistance r_1 with resistance r_2 one obtains:

$$V = i_2 \cdot R + e_2 = e_2(1 + R/r_2) \qquad (20)$$

and by equating expressions (19) and (20), R can be calculated:

$$R = (e_1 - e_2)/(e_1/r_1 - e_2/r_2)$$

By substituting R in Eqs. (19) or (20), the contact potential difference V can be obtained. To this end, measuring the voltage drops e_1 and e_2 is sufficient.

The measuring circuit includes:

- a resistance varying from 10 Ω to 10^{11}Ω;
- an electrometer with input impedance up to 10^{14} Ω (model 610 B, Keithley Instruments);
- a low-impedance voltmeter recorder;
- an ionising source, consisting of a tablet activated with Radium-226 inserted into an Ag base plate and an Au plate, with a specific activity of 185,000 disintegrations per second.

Fig. 15 shows the assembly of the ionisation chamber. It consists of a metallic cylinder with two vacuum-sealed caps and four vacuum-sealed windows to inspect the ionising zone. Two pipes connect the vacuum pump and fill the cylinder with a gas as required. The sample is fixed to a holder in a colloidal silver paste. This holder is suspended by three adjusting screws and earthed. The ionising source is inserted into a cavity on a gold plate under the sample in order to reduce the radiation angle. In this way, only the space in front of the sample is irradiated. The base plate of the ionising source lays on a Teflon block and is connected to the external electric circuit by means of a shielded cable. The electric connection is vacuum-sealed. Measuring the distance between the electrodes and their parallel setting is very important. This can be obtained optically through the windows using a light source, a lens and a screen, where the distances are indicated.

The sample whose work function is being determined may be a metal, a mineral or a compacted powder. A powder can be compacted by using a press capable of reaching 60 MPa.

7. Measuring the Concentration of Electrons and Holes

The electrophysical characteristics below are necessary to define the energy structure of semiconductors in terms of average behaviour:

E_f Fermi level, referred to the valence band upper edge (eV);

E_g forbidden gap width (eV);

n, p concentration of charge carriers, n-type (electrons) and p-type (holes), expressed in number of charge carriers per cm^3;

μ_n, μ_p mobility of n-type and p-type charge carriers, expressed in $cm^2 \cdot V^{-1} \cdot s^{-1}$

The concentration of charge carriers n and p and their ratio can be determined by both indirect and direct (Hall effect) methods.

7.1 Indirect Method

The following equation links the quantities E_f, E_g and p/n [32]:

$$E_f = 1/2 \cdot E_g - 1/2 \cdot kT \cdot \ln p/n \qquad (21)$$

where k is Boltzmann's constant and T the absolute temperature.

Therefore, after calculating E_f and E_g through the experimental procedures described in sections 3 and 4, the p/n ratio can be calculated. In addition, if p/n is known, the absolute values of the charge carrier con-

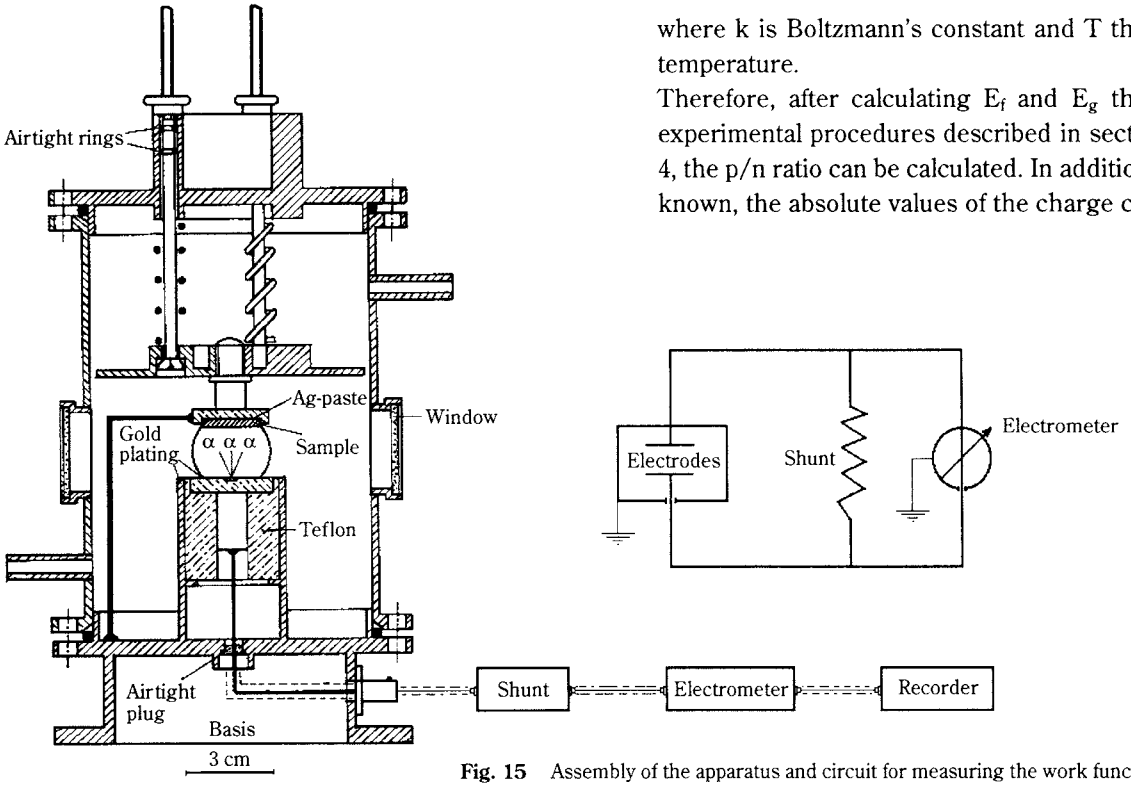

Fig. 15 Assembly of the apparatus and circuit for measuring the work function with the ionisation method. The detail of the ionisation chamber is shown.

centrations p and n can be calculated with the following equation [16, 19].

$$p \cdot n = (2U \cdot T^{3/2})^2 \exp(-E_g/kT) \quad (22)$$

where U is a constant equal to $2.42 \cdot 10^{15} \cdot cm^{-3} \cdot °K^{-3/2}$

7.2 Direct Method

If an electric current I_x (x axis) flows in a semiconductor (**Fig. 16**) of size d (y axis) and thickness h (z axis), a potential difference forms along the z axis when a magnetic field H_y is applied [19]:

$$V_z = V_H = 10^{-12} \frac{R_H \cdot I_x \cdot H_y}{d} \quad (23)$$

where:

V_H Hall voltage (mV);
I_x Hall current (mA);
H_y magnetic field strength (T);
d size of the sample (cm);
R_H Hall coefficient (cm^3/C)
R_H value (constant) depends on the material, the temperature and the impurity content.

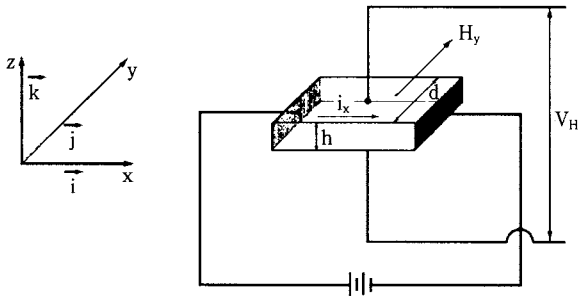

Fig. 16

Measuring the sign of the V_H voltage makes it possible to determine the conduction type: p-type (positive sign) or n-type (negative sign). R_H gives information on the sample characteristics. The general expression of R_H is:

$$R_H = -\beta \frac{n\mu_n^2 - p\mu_p^2}{q(n\mu_n + p\mu_p)^2} \quad (24)$$

where β equals $3\pi/8$ for diffusion due to thermic vibrations, and 1.93 for diffusion due to impurities.

When the semiconductor is in a temperature range where one type of charge carrier concentration predominates over the other, the following simple equations can be used to determine the charge carrier concentration n and p:

$$n = -\beta\left(\frac{1}{q \cdot R_H}\right) \quad \text{for n-type semiconductors} \quad (25)$$

$$p = +\beta\left(\frac{1}{q \cdot R_H}\right) \quad \text{for p-type semiconductors} \quad (26)$$

The charge carrier mobility can be calculated with the equations:

$$\mu_n = -\frac{R_H \cdot \sigma}{\beta} \quad \text{for n-type semiconductors} \quad (27)$$

$$\mu_p = +\frac{R_H \cdot \sigma}{\beta} \quad \text{for p-type semiconductors} \quad (28)$$

where σ is the electric conductivity determined as explained in section 3.

For intrinsic semiconductors, where $n=p=n_i$, we have:

$$\sigma = n_i \cdot q(\mu_n + \mu_p) \quad (29)$$

$$n_i = 2\frac{(2\pi mkT)^{3/2}}{h^3}\left(\frac{m_n \cdot m_p}{m^2}\right)^{3/4} \exp(-E_g/2kT) \quad (30)$$

$$R_H = -\beta\frac{\mu_n^2 - \mu_p^2}{n_i \cdot q(\mu_n + \mu_p)^2} = -\frac{\beta}{q \cdot n_i}\left(\frac{b-1}{b+1}\right) \quad (31)$$

where:

m mass of the electron ($9.11 \cdot 10^{-31}$ kg);
h Planck's constant ($6.624 \cdot 10^{-34}$ J·s);
m_n effective mass of an electron (kg);
m_p effective mass of a hole (kg);
b ratio between the mobility of electrons and holes.

Combining Eq. (29), (30) and (31), one obtains:

$$R_H = -\frac{\beta}{q}\left(\frac{b-1}{b+1}\right)\frac{h^3 \cdot \exp(E_g/2kT)}{2(2\pi mkT)^{3/2}(m_n \cdot m_p/m^2)^{3/4}} \quad (32)$$

that can be written in the form

$$R_H \cdot T^{3/2} = (\text{constant}) \exp(E_g/2kT) \quad (33)$$

The slope of line $\log R_H T^{3/2}$ versus T^{-1}, gives the value of $E_{g0}/4.61 \cdot k$, where k is Boltzmann's constant.

When both types of charge carriers have to be taken into consideration, the following equations can be used:

$$n \cdot \mu_n + p \cdot \mu_p = \frac{\sigma}{q} \quad (34)$$

$$n \cdot \mu_n^2 + p \cdot \mu_p^2 = -\frac{R_H \cdot \sigma^2}{\beta \cdot q} \quad (35)$$

$$n \cdot p = \text{constant} \quad (36)$$

Bearing in mind the equation:

$$p - n = 2 \cdot M \exp(-E_g/2kT)\sqrt{\frac{p}{n}} \quad (37)$$

(where $M = U \cdot T^{3/2}$) deriving from Fermi-Dirac's statistics, the equation system (34), (35), (36) and (37) can be solved.

The Hall effect can be detected using direct or alternating current. Due to the system asymmetry, a

small potential difference between the z-axis electrodes can be observed when voltage is applied to the x-axis electrodes (**Fig. 16**) using the direct current, even without a magnetic field. When the Hall effect is small, this potential difference may exceed the Hall voltage.

The following procedure can be used to overcome this drawback: when a direct current flows through the sample (x-axis electrodes), one measures voltage V_0 between the z-axis electrodes with a high-impedance voltmeter when the magnetic field is zero. The magnetic field is then applied and one measures $V_1=V_0+V_H$, where V_H is the Hall voltage. Reversing the magnetic field, the Hall voltage reverses as well and one measures $V_2=V_0-V_H$. Hence:

$$V_1-V_2=(V_0+V_H)-(V_0-V_H)=2V_H \qquad (38)$$

The Hall effect measurements with direct current were made using a DC generator (Keithley, model 240 A) and an electrometer (Keithley, model 610 B or model 640). Measurements were made in the vacuum with the cell illustrated in **Fig. 18**, on samples of minerals or other materials and compacted powders, up to temperatures of 700-800°C.

The use of alternating current is preferable when measurements are made on compacted powders [33]. The measuring circuit is sketched in **Fig. 17** and consists of the following units:

- a phase-sensitive detector with frequency range from 1Hz to 1 MHz (model 471, Brookdeal);
- an amplifier (model 450, Brookdeal),
- a phase shifter that can shift the phase by about 180° (model 421, Brookdeal);
- a signal generator (model 142, Watevek),
- an electronic filter (model 3750, Krohn-Hite), frequency range 0.02-20 kHz;
- an electromagnet (Systron-Donner) with low residual flux density (0.03 Tesla), capable of providing a magnetic field intensity up to 3 Tesla;
- a Hall probe (model 505, RFL Electronics) for measuring the magnetic field intensity.

When an alternating potential difference is applied to the x-axis electrodes (**Fig. 16**), an alternating current occurs in the sample. Since the magnetic field is along the y axis, an alternating voltage with the same frequency can be detected at the z-axis electrodes. In addition, a voltage with magnetic field zero as well as a voltage due to capacitive and inductive disturbances coming from the generator and connectors develops between the same electrodes. The electric signal at the z-axis electrodes is amplified and sent to the phase-sensitive detector. The reference signal is emitted by the generator through the phase shifter. When the magnetic field is reversed, the Hall voltage phase changes through 180°, and the signal component due to the Hall effect changes sign. The difference between the two measurements in the phase-sensitive detector is proportional to the Hall voltage only. Since the voltage at zero magnetic field does not change phase when the magnetic field is reversed, it does not influence the measurement. Likewise, capacitive and inductive disturbances do not change sign when the magnetic field is reversed. The reference signal must be in phase with the Hall effect signal to obtain a

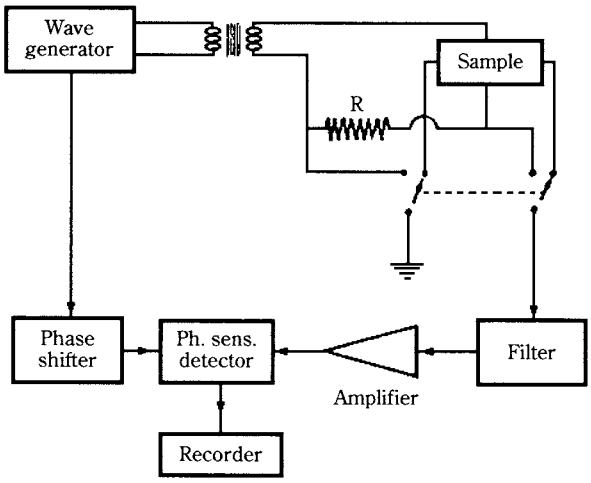

Fig. 17 Electric circuit to measure the Hall effect.

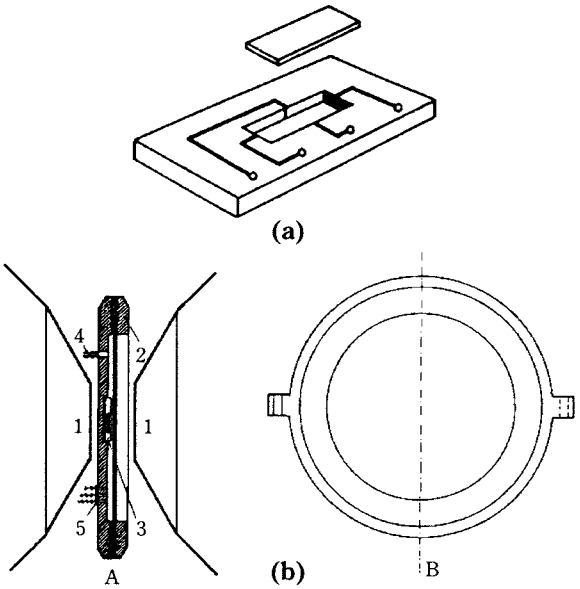

Fig. 18 Sketch of the apparatus for measuring the Hall effect: (a) detail of the sample holder; (b) cell cross-section A and plan B.
1 – electromagnet poles; 2 – bronze container;
3 – sample holder; 4 – pipe for connection with the vacuum pump; 5 – vacuum sealed electric connectors.

maximum intensity signal from the phase-sensitive detector.

The sample is placed in a special ceramic holder (**Fig. 18a**) and covered with a plate of the same material. The current and voltage electrodes have been printed in this holder using a laser procedure. There is also a thermistor for measuring the temperature. The sample holder is placed in the Hall effect measuring cell (**Fig. 18b**), where the vacuum is created and there is the electric resistance needed to increase the temperature.

Acknowledgements

This paper summarises the results of long-term research on the electrophysical characterisation of minerals and powders, and describes the main units the DIGITA Dpt. developed to achieve this under the aegis of MURST (Ministry of the University) and CNR (Italian Research Council) programmes.

Nomenclature

a	coefficient	
b	ratio between the charge carrier mobilities=μ_n/μ_p	dimensionless
C_0, C_1, C_2	capacitance	[F]
e_1, e_2	voltage drop	[mV]
E_f	Fermi level (referred to the valence band upper edge)	[eV]
E_g	width of the forbidden gap	[eV]
E_{g0}	width of the forbidden gap at 0 °K	[eV]
f	vibration frequency	[Hz]
h	Planck's constant	[J·s]
H_y	intensity of the magnetic field	[T]
I, I_x	current	[mA]
i, i_1, i_2	current	[mA]
k	Boltzmann's constant	[J·K^{-1}]
l	distance	[cm]
m	free electron mass	[kg]
m_n	effective mass of an electron	[kg]
m_p	effective mass of a hole	[kg]
q	charge of electron	[C]
r_1, r_2	electric resistance	[Ω]
R	resistance of ionised air	[Ω]
R_H	Hall coefficient	[cm^3·C^{-1}]
s	area	[cm^2]
t	time	[s]
T	absolute temperature	[°K]
U	constant	[cm^{-3}·K$^{-3/2}$]
V_+, V_-	potential difference	[V]
V_c, V_E	contact potential	[V]
V_H	Hall voltage	[V]
α	Seebeck coefficient	[V·K^{-1}]
β	constant	dimensionless
μ_n	mobility of free electrons	[cm^2·V^{-1}·s^{-1}]
μ_p	mobility of holes	[cm^2·V^{-1}·s^{-1}]
ν	wavelength	[cm]
Φ	work function (Fermi level referred to the vacuum level)	[eV]

References

1) Plaksin, I.N. and Shafeev, R.Sh.: Osobennost razdelenia mineralov, obladayouschchikh polyprovodinkovimn svoistvsmi b electrostaticheskov pole. *Instituta Gornovo Dela Skochinskovo*, Moscow, 1966, 18 p.
2) Plaksin, I.N.; Shafeev, R.Sh.; and Chanturia, V.A.: A relation between structure of mineral crystal and their flotation properties. *8th Intern. Mineral Process. Congress*, Leningrad, 1968, paper S-3, 8 p. (Russian text).
3) Hoberg, H.: Untersuchungen der Deutung der Änderung der Flotierbarkeit halbleitender Erzmineralien durch bestrahlung im Kernreaktor. *Aachener Blätter*, **17**, June 1967, 17 p.
4) Carta, M.; Ferrara, G.; Del Fa, C.; and Ciccu, R.: Progrés dans la theorie et l'application de la séparation triboéléctrique des minerais. *Revue de l'Industrie Minérale*, May 1969.
5) Carta, M.; Ciccu, R.; Del Fa, C.; Ferrara, G.; Ghiani, M.; and Massacci, P.: The influence of the surface energy structure of minerals on electric separation and flotation. *Proc., 9th Intern. Mineral Process. Congress*, Praha, 1970, pp. 47-57.
6) Carta, M., Ciccu, R., Del Fa, C., Ferrara, G., Ghiani, M.; and Massacci, P.: Improvement in electric separation and flotation by modification of energy levels in surface layers. *Proc., 10th Intern. Mineral Process. Congress*, London, 1973, pp. 349-376.
7) Revnivtsev, V.I.; Ul'janov, N.S.; Angelov, A.I. et al.: Theoretical principles and applications of the triboelectric separation of dielectric minerals. *Proc., 9th Intern. Mineral Process. Congress*, Praha, 1970, pp. 79-88, (Russian text).
8) Schubert, H.: Aufbereitung fester Stoffe- Band II: Sortierprocesse. Deutscher Verlag für Grundstoffindustrie, Stuttgart, 1996, ISBN 3-342-00555-6.
9) Manca, P.: A relation between the binding energy and the band-gap energy in semiconductors of diamond or zinc-blend structure. *J. Phys. Chem. Solids*, **20**, 1961, pp. 268-273.
10) Bailly, F. and Manca, P.: Corrèlation entre largeur de la bande interdite et l'énergie libre d'atomisation des matériaux semi-conducteurs. *J. Phys. Chem. Solids*, **27**, 1966, pp. 783-793.
11) Manca, P.: Legame interatomico e semiconduzione nei solidi. *Nuovo Cimento*, ser. 1,. **6**, Suppl., 1968, pp. 759-779.
12) Ciccu, R.; Del Fa, C.; Ghiani, M.; and Massacci, P.: Metodologie sperimentali per lo studio dei fenomeni all'interfase, dei relativi parametri influenti e del loro

ruolo nei processi di trattamento dei minerali. *Atti della Facoltà di Ingegneria dell'Università di Cagliari*, Vol. II, Maggio 1974, pp.29-107.
13) Finkenlburg, W.: Einführung in der Atomphysik, 12. Aufl., Springer-Verlag, 1976.
14) Schneider, H.A. und Zimmer, H.: Physik für Ingenieure, Bd. 2, Leipzig: Fachbuchverlag GmbH, 1991.
15) Pope, M.I.: The influence of lattice defects on the properties of solids. *Educ. Chem.*, **2**, 1965, pp.127-134.
16) Many, M.; Goldstein, Y.; and Grover, N.B.: Semiconductors surfaces. North Holland, 1965.
17) Tamm, I.: Über eine mögliche Art der Elektronenbindung an Kristalloberflächen. *Z. Phys.*, **76**, 1932; *Chem. Abstr.*, **26**, 1932, 5837.
18) Shockley, W.: On the surface states associated with a periodic potential. *Phys. Rev.*, **56**, 1939, pp. 317-323
19) Shive, J.: Semiconductors devices. Van Nostrand, Princeton, N.J., 1959.
20) Putley, E.H.: The Hall effect and related phenomena. Butterworths, London, 1960.
21) Johnson, V.A. and Lark-Horowitz, H.: *Physical Review*, **92**, 1953, pp. 226-232.
22) Serci, A.: I fenomeni di scambio energetico nei fenomeni di separazione elettrostatica. PhD Thesis, University of Cagliari, 1988.
23) Serci, A.: Ricerche sul caricamento triboelettrico dei minerali. *Atti, Facoltà di Ingegneria dell'Università di Cagliari*, **35**, N. XXI, 1992
24) Ciccu, R.; Ghiani, M.; Peretti, R.; Serci, A.; and Zucca, A.: Tribocharging studies of ground coal matter. *Processing and Utilisation of High-Sulfur Coals, IV*, P.R. Dugna, D.R.Quigley and Y.A. Attia Eds., Elsevier, Amsterdam, 1991, pp. 223-237.
25) Ciccu, R. and Foreman, W.E.: Sul caricamento triboelettrico dei minerali in relazione allo stato elettronico delle loro superfici. *L'Industria Mineraria*, **19**, 1968, pp. 523-531.
26) Ciccu, R.; Ghiani, M.; and Ferrara, G.: Selective tribocharging of particles for separation. *KONA-Powder and Particle*, **11**, 1993, pp. 5-16.
27) Ralston, O.C.: Electrostatic separation of mixed granular solids. Elsevier, Amsterdam, 1961.
28) Yamamoto, H. and Scarlett, B.: Triboelectric charging of polymer particles by impact. *Particle Characterisation*, **3**, 1986, pp. 117-121.
29) Ose, S.: Pneumatic transport electrostatic charging bench. *POSTEC Newsletter*, **17**, November 1998, pp. 19-31.
30) Kelvin, Lord: Roy. Inst. Proceed., **15**, 1897 p. 521.
31) Loeb, L.: Static electrification. Springer Verlag, Berlin, 1958.
32) O'Kane, D.F.: An investigation of ternary semiconducting compound. Ph.D. Thesis, University of Michigan, 1962.
33) Bragaglia, R.: Ricerca con metodi matematici e sperimentazioni su applicazioni di fisica dello stato solido, e segnatamente sull'effetto Hall, a problemi di separazione mineralurgica. MSc Thesis, University of Cagliari, 1973.

Author's short biography

Raimondo Ciccu

Raimondo Ciccu graduated in Mining Engineering at the University of Cagliari in 1965. Shortly after he served the National Research Council covering the position of Senior researcher until 1973. From 1974 to 1981 he was Chief Sector at the Sardinian Mining Board (EMSa) and meanwhile he acted as Managing Director of a major mining Company in Italy. In 1982 he joined the University of Cagliari as Associate Professor and from 1983 as Full Professor of Surface Mining and Land Reclamation.

The fields of interest range from excavation and cutting of rocks using traditional and advanced technologies (diamond tools and waterjet) to various subjects of mineral processing, especially electrostatic separation and comminution. Presently his research, teaching and consulting activity is chiefly focussed on stone quarrying and processing.

Professor Ciccu Authored about 200 scientific and technical papers, most of them discussed at International Conferences, and he is responsible of many research contracts with the industry as well as scientific coordinator of EEC-supported projects. He shares many patents for electrostatic separators of mineral matter

Languages spoken: Italian, English, French, Portuguese and Spanish.

Marcello Ghiani

Marcello Ghiani graduated in Mining Engineering at the University of Cagliari in 1958 and developed his entire Academic career at the same University. In 1966 he was abilitated as lecturer in the field mineral processing, and in 1975 he was appointed professor of mineral processing at the University of Cagliari, where from 1985 until 1992 was director of Mining and Mineral Processing Department. He carries out on a scientific activity within the frame of the research programs of the Department of Geoenrineering and Environmental Technologies and of the Mineral Science Study Centre of National Research Council at the University of Cagliari. He partecipated in various national and international conferences giving numerous contributions. He is author of more than 200 papers in the field of mineral beneficiation. As a consultant Dr. Ghiani has cooperated in the development of various projects and as a member of the scientific committee he is involved with the development of a general plan concerning the Sardinina mining sector.

Antonello Serci

SERCI ANTONELLO graduated in Mining Engineering in 1982 at the University of Cagliari (Italy) where he obtained the Ph.D. degree in 1988.

Formerly junior researcher of the National Research Council, presently senior researcher at the Department of Geoengineering and Enviromental Tecnologies of the University of Cagliari.

His research activity covers many fields of mineral processing with special focus in electric separation and flotation.

Dr. Serci is author of about 20 papers and shares a patent for a new electrostatic separator with researchers of the Department and of CSGM (National Research Council).

Author's short biography

Gianfranco Ferrara

Gianfranco Ferrara obtained his degree in Mining Engineering in 1954 at the University of Cagliari (Italy). At the same University he was appointed Research Assistant in 1955 and Assistant Professor in 1960. In 1971 he was appointed to his present position of Professor of Mineral Processing at the University of Trieste, where from 1979 to 1992 he was Chairman of the Mineral Engineering Division.
Consultant for the evaluation of the research activities financed by the European Community in the framework of the Primary Raw Materials and Recycling programme from 1980 to 1989. Member of the Steering Committee of the IMPC's. Regional Editor for Europe of the journal "Minerals Engineering" from 1988 to 1997. Member of the Editorial Board of the journals "Coal Preparation", "KONA-Powder and Particle" and "Minerals & Metallurgical Processing".
For the research activity he has been appointed Adjunct Professor of the West Virginia University, USA.
To date he has produced more than 120 publications concerning mineral and coal processing research, characterisation of particulate solids, mineral liberation, comminution, mechanical, hydraulic and pneumatic classification of solids, dense medium separation processes in centrifugal field of ores and coals, rheology of dense suspensions, electrostatic separation, modelling and simulation of the separation processes of minerals, coals and particulate solids, treatment of post-consumer plastics and recycling.
Author of a number of patents in the field of dynamic dense medium separation processes, which are applied in industrial plants operating in many countries of Europe, in Canada, South Africa, South America and China.

Paolo Massacci

Paolo Massacci obtained his degree in Mining Engineering in 1964 at the University of Cagliari (Italy). At the same University he was appointed Research Assistant in 1964 and Assistant Professor in 1970. In 1975 he was appointed to his present position of Professor of Raw Material Engineering at the University of Rome (Italy), where since 1978 has been Chairman of the Mineral Engineering Division. He is currently member of the Scientific Committee of the International Mineral Processing Congresses, designed as Chairman for the XXI Congress which will be held in Rome in 2000.
His research interests are principally concerned mineral processing, characterization of particulate solids, recycling of secondary raw materials, flotation and comminution.

Review

Sonocrystallization: The End of Empiricism?

A review on the fundamental investigations and the industrial developments†

Berthe Ratsimba, Béatrice Biscans, and Henri Delmas
*ENSIGC, Toulouse, France**
Jean Jenck
*Rhodia, France***

Abstract

Among many attractive effects on physicochemical processes; one of the most promising applications of power ultrasound concerns crystallization. This paper is a review of the previous work on sonocrystallization. Ultrasound has been used in crystallization to initiate primary nucleation by narrowing the metastable zone width. It influences secondary nucleation and crystal growth. It has beneficial effects on crystal habit and crystal size distribution. It can reduce or modify agglomeration and the subsequent liquid inclusions and improve product handling. A description of the available equipment will be given. Finally, from the previous work and the experience gained, the possible future developments in sonocrystallization will be examined.

1. Introduction

Ultrasound is understood to mean sinusoidal pressure waves whose frequency ranges between 1.6 10^4 Hz, the upper limit of audible sound, and 10^7 Hz, the lower limit of hypersound. Generally two large fields of application are considered: power ultrasound (low frequency and high power) to transform materials, and high-frequency ultrasound for diagnosis and scanning. Power ultrasound is usually characterized by frequencies between 1.6 10^4 Hz and 2 10^6 Hz. The interaction of the pressure wave with media containing liquids can generate chemical or physical changes due to acoustic cavitation.

When acoustic pressure exceeds the cavitation threshold, bubble nuclei entrapped in liquid impurities – and more often in cracks of the vessel wall or of the suspended particles – grow during the low-pressure half-period and decrease during the consecutive pressurisation. Cavitation bubble oscillations can produce microstirring, resulting in high mass transfer specially at liquid-solids interfaces toward which collapsing bubbles are attracted. At higher acoustic pressures, violent collapses occur, leading to shock wave emission, to solids erosion or disruption, and to extremely high temperatures and pressures in the compressed bubbles, thus generating highly reactive free radicals. So both mechanical and chemical effects are expected at high ultrasound power.

Crystallization is a unit operation combining particle formation and purification. It is used in the production of a wide range of materials ranging from chemicals to speciality chemicals and pharmaceuticals. The quality of a crystalline product is judged according to several criteria: crystal purity, crystal size distribution and crystal morphology. Some effects of power ultrasound on crystallization were observed several decades ago [1], but recently the manufacture of more complex molecules and the need of giving the desirable properties to the crystals generated research for new crystallization techniques. A renewed interest in systems that exploit acoustic forces was observed. It is why most practical applications and implementations have only recently been identified.

The first part of this paper is devoted to sonocrystallization. Ultrasound can be used beneficially in crystallization. The literature on ultrasonic crystallization, however, contains conflicting data, which are due in part to a lack of understanding of the crystallization process itself under ultrasound, and also to a lack of understanding of the influence of the ultrasound parameters.

The second part of this paper deals with a review on the existence and recognition of the effects of

* *Laboratoire de Génie Chimique UMR 5503 CNRS/UPS/INPT ENSIGC, 18 Chemin de la Loge, 31078 Toulouse, France*
**Rhodia, 24 avenue Jean Jaures, 69153 Décines Charpieu, France
† Received: June 15, 1999

ultrasound in liquid and liquid-solids-based systems. In particular, the fundamental background on the modelling of the sound propagation in suspensions will be summarized.

2. Sonocrystallization

2.1 The effects of ultrasound

2.1.1 On nucleation and growth

Supersaturation is the driving force of crystallization, a prerequisite of nucleus formation in solution and the principal factor influencing nucleus quality. Supersaturation of a solution can be generated by cooling, solvent evaporation, addition of an antisolvent and chemical reaction. The generation method of supersaturation is selected from some solubility data. For example, if the product solubility increases strongly with increasing temperature, the cooling crystallization could be applied.

The adjustment of any metastable state involves two consecutive steps: surmounting the energy barrier which defines this condition, and subsequent passage to a level of lower energy and greater stability. In the case of supersaturated solutions, these two general steps are tantamount to nucleation and growth, respectively. These two steps are considered to be independent, nucleation being more difficult and slower [2]. This distinction between nucleation and growth is evident in most of the early theories and experimental studies. Generally, the Gibbs-Thomson equation is sufficient to explain the metastability [2,3,4,5]. The kinetics of nucleation is represented by the general equation:

$$V = k_0 e^{-W/RT} \tag{1}$$

k_0 is a frequency factor and W the minimum energy required to form the nucleus.

Previous works have shown that the nucleation rate of crystals is increased by ultrasound. Yaminsky et al. [6] have shown that the nucleation rate of calcium sulphate is ten times higher with ultrasound. Moreover, the induction time of nucleation (latent period before the appearance of the nuclei) is highly reduced by the application of ultrasound for several compounds [7,8,9,10]. In some cases, ultrasound can replace seed crystals to initiate nucleation. For example, the process of nucleation of sugar solutions might be markedly influenced by a sonic field. In that case, nucleation could be carried out at low supersaturation [11]. The effect of ultrasound on the crystallization of a range of organic compounds was investigated by Price and coworkers [12,13]. For dodecanedioic acid, benzamide and sorbitol hexaacetate, all crystallized in methanol, these authors found that the width of the metastable zone (critical undercooling at which primary nucleation occurs) was reduced by the application of ultrasound. Residual supersaturation levels can also be reduced resulting in an increased yield.

So, nucleation can be induced in a crystal-free solution below the supersaturation at which primary nucleation would normally occur.

Most of these results were obtained on a laboratory scale, and an ultrasonic bath or an immersed probe tip (horn) was used for laboratory insonation.

Ultrasound can also generate substantial quantities of secondary nuclei. Secondary nuclei are generated from parent crystals pre-existing in the crystallizer. Two main mechanisms of secondary nucleation were identified: removal of semiordered surface layers from the parent crystal surface through fluid shear stresses, and contact nucleation due to collisions between crystals themselves and parts of the crystallizer. One of the mechanisms which influences secondary nucleation under ultrasound is cavitation [14]. It seems that cavitation takes place on or near crystal surfaces. So, the intense shear stresses at the collapse of cavitation bubbles can result in significant secondary nucleation.

Like nucleation, the crystal growth rate is driven by supersaturation and can be described by a simple equation [2]:

$$G = K\Delta C^g \tag{2}$$

G is the crystal growth rate and K the growth rate constant,

ΔC is the supersaturation and g the growth exponent.

This equation is a simplification of the complex mechanisms, but represents the industrial practice in the calculation of growth kinetics. The interaction of nucleation and growth phenomena defines the product properties (size distribution, morphology).

Several works have dealt with growth rate measurements under an ultrasonic field. Zhang Qiang et al. [11] have carried out growth measurement experiments on a single crystal of sugar and found that the growth rate was accelerated by ultrasound. For potassium alum according to Le Bras [1], the effects of ultrasound on the growth rate depend on crystal shape, temperature, supersaturation of the solution and on ultrasound frequency and intensity. When the intensity of ultrasound increases, the growth rate increases up to a given value and then decreases. Hofmann and Roubik [15] have noticed that the growth rate of

potassium sulphate crystals depends on their initial size, when an ultrasonic field is applied. For crystal sizes lower than 350 μm, the growth rate is similar to that found without ultrasound; for larger crystals, the growth rate is higher.

When the supersaturation is generated by chemical reaction (precipitation), the irradiation of the solution may accelerate the reaction [16,17]. Gatumel et al. [17] showed that the effect of ultrasound on barium sulphate precipitation is not due to an improvement in micromixing but that there must be a specific effect of ultrasound on nucleation and growth mechanisms.

Several remarks can be made on these previous works. Ultrasound can influence both nucleation and crystal growth, but the distinction between the nucleation and growth rates of crystals under an ultrasonic field is more difficult to perform than in classical crystallization. The influence of the operating parameters cannot be generalized because the small-scale nucleation correlation is often of limited value in predicting the nucleation rate in large-scale equipment and depends on the considered product.

2.1.2 On agglomeration

Ultrasound is well known to have an effect on the agglomeration of particles in suspensions. In some cases agglomeration is promoted or increased, but most often it is reduced. The morphology of the agglomerates obtained in an ultrasonic field is different from that of the agglomerates normally obtained.

Under ultrasound, Srinivasan et al. [18] obtained diphenyl oxide and di-methyl phenyl carbinol crystals from the melt with a higher purity. The crystals produced in an ultrasonic field are needle-like particles which are agglomerated in an ordered way (instead of randomly-shaped without ultrasound). In another study on the precipitation of aluminium sulphate, Enomoto and Nakagawa [19] produced particles agglomerated to larger sizes than those obtained without ultrasound.

2.1.3 On comminution

Kusters et al. [20] presented a theory on the ultrasonic comminution of agglomerate particles suspended in liquids. They found that collapsing cavitation bubbles disperse the agglomerates. An expression for the comminution rate as a function of the ultrasonic power (2.5 to 100 W) and agglomerate size was given for titania and silica powders. They showed that comminution increases with increasing ultrasound intensity.

Klink et al. [21] suggested that the comminution of particles by ultrasonic treatment takes place by particle collisions with the tip of the ultrasonic horn. This mechanism now seems very improbable, but although ultrasonic dispersion has been used for many years, a quantitative description of this comminution process has received little attention. Aoki et al. [22] proposed a simple quantitative model that describes the change of mean particle size in an ultrasonic dispersion process. The model is based upon the assumption that the dispersion results from the interaction of the agglomerates with the ultrasonically induced cavities.

2.1.4 On the product quality

• Crystal purity

Sonocrystallization can be used beneficially to improve the crystal properties and yield. One of the most important criteria is the purity specification. Several mechanisms of retention of impurities within the product were identified. Impurities may be deposited on crystal surfaces due to the incomplete removal of impure mother liquor. They can also be distributed in the crystal lattice by molecular substitutions. Another mechanism is the entrapment of impurities in the void between the crystals in agglomerates. Moreover, there may be inclusions of mother liquor within individual crystals.

For melt crystallisation, Srinivasab et al. [18] considered that the improvement of the purity of crystals under ultrasound is due to the existence of hot points existing for a few nanoseconds during the implosion of cavitation bubbles. These hot points enable the redissolution of impurities at a lower melting point. Price [14] proposed the same explanation for crystals in solution. These assumptions can be questioned because the hot spots are randomly distributed in the suspension and their duration is very short compared with dissolution times. More probably, ultrasound can lead to fewer inclusions of impurities by preventing or reducing agglomeration.

The amorphous phase of a product can be obtained under ultrasound. Enamoto et al. [19] found that the sonohydrolysis of aqueous solutions containing urea and aluminium sulphate generates an amorphous product and that ultrasound increases the agglomeration of the precipitates. These results were interpreted by considering the difference between the velocity of attraction among solute species (ions, molecules) and the velocity of orientation of the species deposited at bulk surfaces. When the first one is higher, the arrangement of the species in the precipitate is made randomly (amorphous product). When the tendency is reversed, a crystalline product is obtained. It was concluded that ultrasound increases the mobility of solute species in solution.

Polymorphism can also be considered as a purity problem. In general, metastable polymorphisms form more quickly than stable ones. As the crystallization progresses and the solution is desupersaturated, the crystals of the more stable polymorphic phases grow while the metastable ones dissolve. Only few data were available in the literature about polymorphism under ultrasound.

• **Crystal size distribution**

Crystal size distribution is often specified and imposed by the end user of the crystalline products. The control of crystal size distribution implies control of the nucleation, the growth phenomena and also the agglomeration as it occurs. Supersaturation is then a key parameter.

In their study, Enamoto et al. [23] observed the influence of the ultrasound frequency (200, 550 and 1740 kHz) and intensity (1.1, 2.1 and 9.2 $W.cm^{-2}$) on the crystal size distribution of alum in a "Cup-horn" reactor of 60 ml. The particle size distribution is shifted downwards and smaller particles are obtained in an ultrasonic field. But the width of the distribution is narrowed by the application of ultrasound. Mydlarz and Briedis [24] used a two-stage system. The sonicator is used in their work as a pre-nucleation device (mini-nucleator), the outlet of which was fed to a MSMPR (Mixed Suspension Mixed Product Removal) crystallizer. Experimental and theoretical studies of zinc oxalate precipitation in this system showed that the narrow crystal size distribution obtained from the MSMPR crystallizer is due to use of the ultrasonic mini-nucleator. Thus the mini-nucleator produces crystals of a very small size range and a very narrow crystal size distribution which continuously seed the crystallizer.

Ultrasound was also used in the preparation of catalysts. The internal specific surface and the size of the particles were fundamentally affected [25]. Precipitation in an ultrasonic bath (low intensities) leads to small particles with low specific surface. The preparation under the influence of the ultrasonic probe horn (high intensities) leads to catalysts of large particles with high surface areas. Conventional preparation techniques lead to intermediate particle size distributions.

Finally, one can conclude that the mechanisms by which ultrasound affects crystal size distribution are not at all well understood.

• **Crystal habit**

Crystal habit has a great influence on the bulk physical properties of the product. Together with size distribution, the shape and the aspect ratio of the crystals often affect many other properties such as the feasibility of solids-liquid separation, bulk density, flow behaviour, flow fracture behaviour or dust formation. The individual crystal faces have their own growth rate depending on the temperature, supersaturation and presence of impurities. Different crystal faces can have different behaviours. Specific impurities can act on certain crystal faces and not on the others. Ultrasound was found to favour the growth of one type of surface and not others [26].

2.2 Mechanisms of sonocrystallization

In previous works, all the investigated mechanisms by which ultrasound affects crystallization are related to cavitation induced by ultrasonic waves. They can be summarized in this section. The action of ultrasound on primary nucleation is expressed in terms of the probability of molecules of the solute colliding to form aggregates which are future nuclei. Mechanical stirring does not provide enough energy to the entities to allow collisions and therefore leads to a broad nuclei size distribution. On the contrary, the ultrasonic vibrations enable these collisions and a narrow size distribution of nuclei is obtained. Moreover, the vibration and implosion of cavitation bubbles create local hot points where supersaturation is reduced. This can explain the achievement of larger nuclei when the ultrasonic intensity increases.

According to several authors cited in [1], the effects of ultrasound on crystal growth are essentially due to the generation of high and variable pressures locally in the liquid. Others explain the actions of ultrasound by cavitation and gas bubble pulsation.

According to Price [14], the mechanism by which ultrasound acts on crystal growth is not well understood but it might be the consequence of the mass transfer enhancement at the crystal surfaces.

The mechanism of action of ultrasound on agglomeration is probably of the same type as for nucleation. Agglomeration increases with the increase of the collision probability. In that case, the time of contact between particles must be long enough.

As seen before, the comminution of agglomerates in an ultrasonic field is due to the interactions of the particles with the cavitation bubbles. Secondary nucleation could be induced by the same mechanism, because cavitation bubbles are preferentially localized on the liquid discontinuities near the crystalline surfaces. The intense forces which appear at bubble collapse may achieve substantial secondary nucleation.

3. Equipment for Sonocrystallization

3.1 Laboratory-scale equipment

3.1.1 Generation of ultrasound

The energy of vibrations dissipated in sonoreactors may have two sources: mechanical or electrical. One type of source can be transformed into the other by a transducer. The mechanical transducers enable transformation of the kinetic energy of a gas or a liquid flow into acoustic energy (whistle or siren transducers, [27]). This type of mechanical generator is mainly used for homogenisation and emulsification. Ultrasonic waves can also be produced either by piezoelectric or magnetostrictive transducers. Magnetostriction uses the change of the dimensions of some ferromagnetic materials such as nickel, cobalt, and ferrites when submitted to an electrical field. This type of transducer used for high ultrasonic powers is very robust but is limited in its frequency range which does not go up to 100 kHz and gives less power yield. Piezoelectric transducers are the most widely used at present.

3.1.2 Equipment

• Ultrasonic bath or immersed probe

Ultrasound reactors are composed of three parts:

- an electrical generator which enables the creation of a sinusoidal electrical signal from a 50-Hz current with high frequency and amplitude;
- a piezoelectric transducer which transforms the electrical signal of high frequency into a mechanical vibration of the same frequency; and
- a transmitter which transfers the piezoelectric vibrations to the medium.

On a laboratory scale, either an ultrasonic bath or horn consisting of an immersed probe tip are commonly used. An ultrasonic bath is made of a rectangular tank with piezoelectric transducers fixed at the bottom and on the lateral faces of the tank. For this equipment, the power is rarely variable and the frequency ranges from 20 to 50 kHz. The tank can be directly used as a reactor or another reactor can be located in the tank full of water. The main drawbacks of this equipment are the weak ultrasonic intensity in the range of 1 to 5 $W \cdot cm^{-2}$, and the difficulty of controlling the temperature in the sonicated medium.

For immersed probe tips, the wave is transmitted from the transducer to the sonicated medium via a shaped extension screwed on a nodal point of the vibration. The vibrating surface, generally a disc, can have a few millimetres to sixty centimetres in diameter. This probe enables amplifying the vibrations and increases the intensity. The frequency of ultrasound is often fixed at 20 kHz but the electrical generators can work with variable power. **Figure 1** shows the main geometries of the probes.

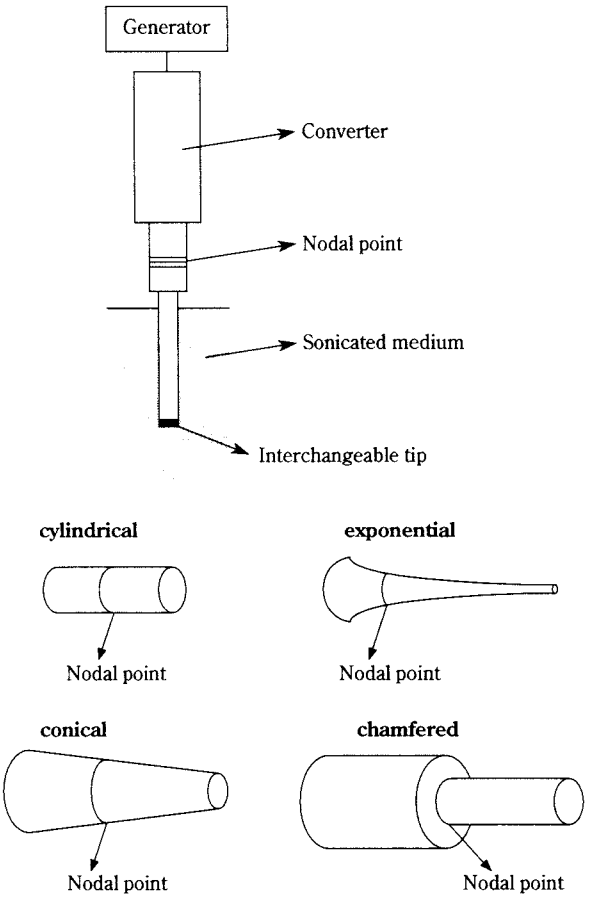

Fig. 1 Schematical representation of an immersed probe and examples of different geometries of probes

• Cup-horn reactor

A cup-horn reactor is a illustrated in **Figure 2**. It is a double-jacketed reactor, the bottom of which is made of a plane emitter surface. Ultrasound is emitted directly into the liquid at the bottom of a reactor. High frequencies can be used.

• Radial emission tubes

Several equipment companies offer vibrating tubes of selected length in order to create standing waves in the metal. Such a geometry involves non-homogeneous radial emission so that these devices are better used for a circulating liquid along the tube than as a continuous flow cell. The power can reach 4 kW for tubes of about one metre of length and 50 mm in diameter. Another device is made of an empty tube connected to the emitter by a radial collar. One of these

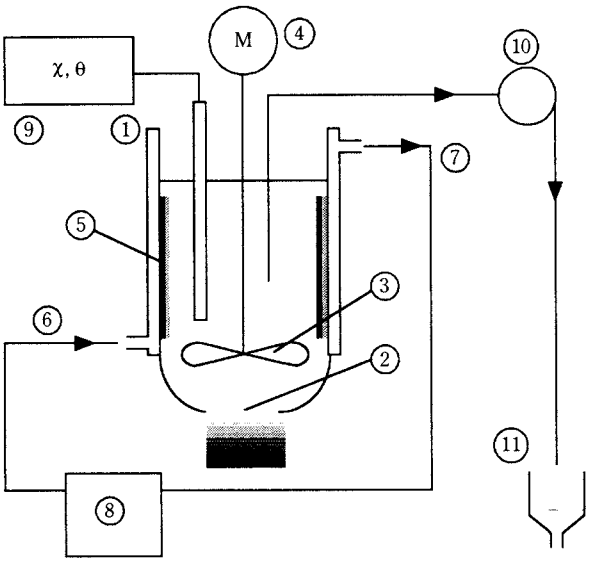

1–Crystallizer
2–Ultrasonic emitter
3–Propeller
4–Motor
5–Baffles
6–Cooling liquid inlet
7–Cooling liquid outlet
8–Programmable thermostated bath
9–Conductivity and temperature measurements
10–Peristaltic pump
11–Membrane filter

Fig. 2 Cup-horn reactor

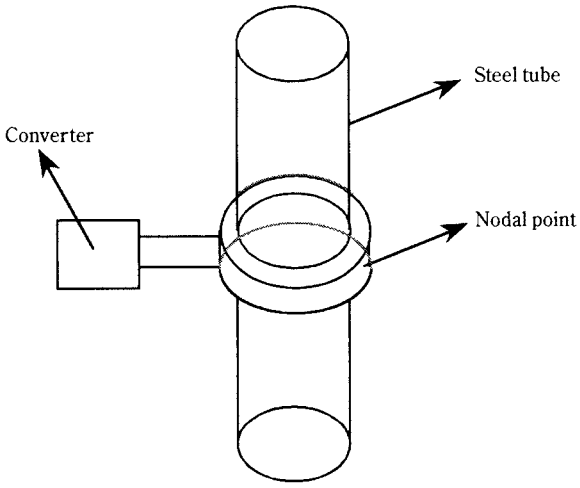

Fig. 3 Sodeva radial emission tube

systems is the Sodeva tube illustrated in **Figure 3**. For this configuration, the ultrasonic frequency is 20 kHz and the electrical power is adjustable up to 2000W. The internal diameter is 42 mm, the length of the tube can be 0.4 m up to several metres. The temperature inside the tube can be hardly checked.

Telsonic tubes are also available. They are made of an empty tube, the extremities of which are closed. The piezoelectric transducer is located at one of the ends.

3.2 Industrial-scale equipment

Currently, high-power ultrasound equipment is not available. Furthermore, a very high intensity is generally not desirable because of the probable break-up of crystals.

Industrial-scale sonocrystallizers are therefore often designed as recycled loops or flow-through devices which can irradiate conveniently the circulated liquid. This type of sonocrystallizer is then divided into "active" and "inert" volumes and has been designed empirically. Few detailed descriptions of the equipment are given in literature [12].

The sonoreactor developed by AEA technology consists of a conventional reactor vessel which contains a powerful "sonoreactor module" in a loop arrangement (see **Figure 4**). The sonoprocessor [28], schematically represented in **Figure 5**, consists of a cylindrical duct irradiated by three transducers and couplers located radially about the mid-plane.

Another apparatus patented by Anderson et al. [29] consists of a large agitation vessel containing baffles or a draft tube where only a zone above the draft tube is sonicated. According to the authors, this is equivalent to pulse-sonicating the entire crystallizer because of the continuous circulation of the slurry through this zone. The principle of this sonoreactor is shown in **Figure 6**.

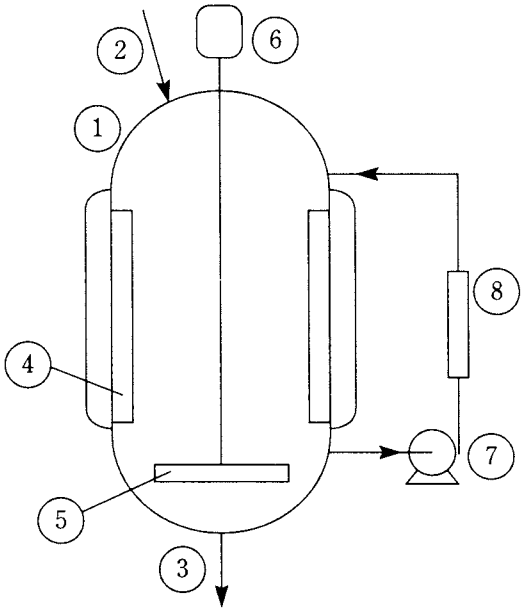

1–Double-jacketed reactor
2–Feed
3–Outlet of the suspension
4–Internal baffles
5–Stirrer
6–Motor of the stirrer
7–Pump
8–Ultrasound emitter

Fig. 4 Loop reactor for industrial sonocrystallization.

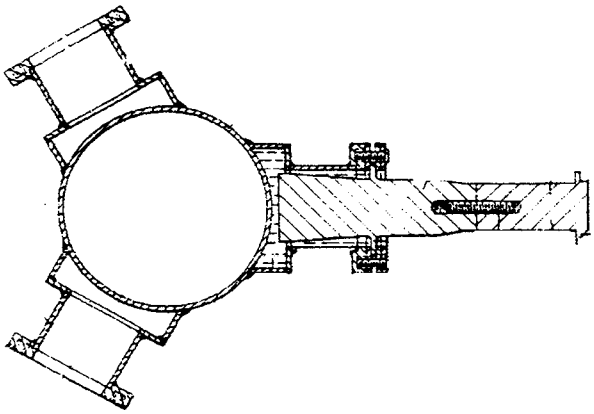

Fig. 5 Cross-sectional view of the irradiated part in the loop of the reactor [28].

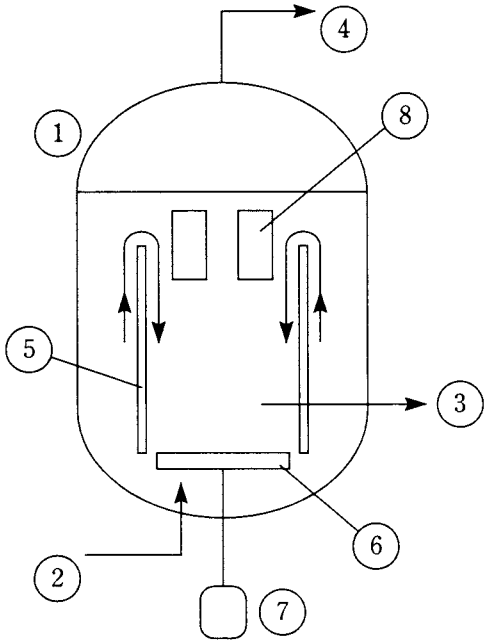

1–Cylindrical reactor
2–Feed
3–Outlet of the suspension
4–Outlet of vapour
5–Draft tube
6–Impeller
7–Motor of the stirrer
8–Ultrasound emitter

Fig. 6 Principle of the industrial sonoreactor according to Anderson et al. [29]

According to the operating conditions, major questions arise when dealing with industrial sonocrystallizers. Firstly, what is the level of intensity at which cavitation occurs in the crystallizers? Moreover, if cavitation exists, can it be stable or transient? The key operating parameter could be the ultrasonic power per volume unit or the ultrasonic intensity.

For the scale-up of the sonocrystallizer design from laboratory to industrial scale, knowledge of the relationship between ultrasonic intensity and the required cavitation per unit volume is necessary. The control of sonocrystallization needs the understanding of the physical phenomena occurring and of the way in which ultrasound acts during crystallization. Some fundamental background on sound propagation in suspensions is helpful for this purpose.

4. Sound Propagation in Suspensions

The design of sonophysico-chemical processes on a commercial scale should take into account wave damping which can be very strong especially in multiphase media.

4.1 Fundamental background

The laws of propagation of ultrasound are the classical laws used for the propagation of sound. The propagation of the sinusoidal wave in a given medium undergoes progressive damping: the amplitude of the wave decreases exponentially with the distance from the emitter. Sound absorption in a single-phase fluid is mainly due to viscous friction and thermal effects related to expansion-compression cycles. It is also proportional to the square of the wave frequency.

The absorption of ultrasound into a suspension is much faster and more complex than in single-phase media. When an incident wave reaches a particle in a solids-liquid suspension:

- the liquid surrounding the particle absorbs a part of the energy;
- a part of the ultrasonic energy is transmitted and another reflected;
- a part of the transmitted energy is absorbed by the solid;
- a part of the reflected energy is absorbed by the liquid.

Moreover, the reflected wave can interfere with the incidence wave or can be reflected again on another particle. A particle which is suspended in the liquid can oscillate under the influence of the acoustic pressure and move with a velocity different from that of the liquid. This is why friction appears on the solid surface, and energy is transformed into heat.

4.2 Modelling of the sound propagation in suspensions

The recent theories distinguish three main regimes of ultrasonic energy losses which result in an increase to the attenuation coefficients and a modification to the ultrasonic wave velocity [30, 31]:

- viscous regime

– inertial regime
– geometric scattering regime.

These three regimes can be delimited by using two parameters characterizing the ultrasonic field in the suspension: $k \cdot a$, where k is the wave number ($k=2\pi/\lambda$, λ is the wavelength of sound), and a is the particle radius, and an oscillatory Reynolds number. This Reynolds number is defined by:

$$Re = \frac{a}{\delta} \quad \text{with} \quad \delta = \sqrt{\frac{2\nu}{\rho_l \omega}}$$

δ is the viscous diffusion length around the particle,
ω is the wave pulsation,
ν is the dynamic viscosity of the fluid,
ρ_l is the density of the liquid.

The viscous regime of sound propagation prevails when the penetration (δ) by viscous diffusion length during one period is much greater than the particle radius a. This regime prevails when: $Re=a/\delta<<1$. Fluid inertia plays no role in this regime.

The geometric scattering regime prevails when the particles in a liquid-solids mixture are much larger than the wavelength of sound propagating through the mixture, causing the sound to scatter geometrically. This occurs when $k.a>>1$. In a suspension of finite solids concentration, the attenuation scales with the fourth power of frequency, resulting in poor penetration and a drop in the sound speed.

When the Reynolds number is large ($Re>>1$), the viscous boundary layer is very thin, and the inertia of the fluid surrounding the particle dominates the dynamic drag. This inertial regime is bounded by the viscous regime on one side and the multiple-scattering regime on the other, as shown in **Figure 7**.

There are several models describing the propagation of ultrasound through a solid – liquid dispersion

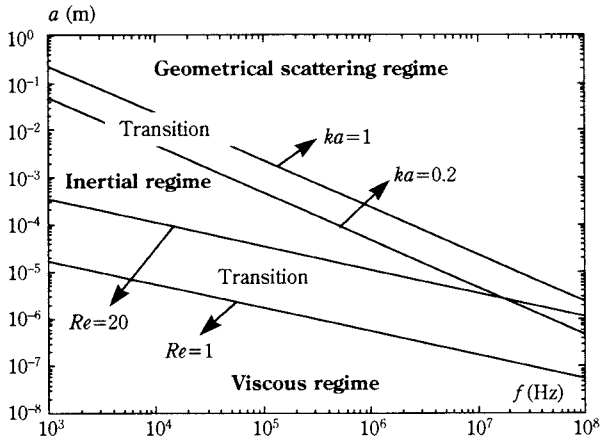

Fig. 7 The different regimes of the ultrasonic energy for suspensions, according to [31].

and from which the theoretical phase velocity, phase velocity dispersion and attenuation can be calculated. They differ from the physical mechanisms of ultrasonic propagation that they describe. The model by Urick [32,33,34] is phenomenological, the model of Harker et al. is hydrodynamical [35,36], and the model of Allegra and Hawley [37] is based on scattering.

4.3 Effects of cavitation

As already mentioned, ultrasound generates compressions and expansions in the liquid which, above a threshold, can generate cavitation. Acoustic cavitation results in successive growth and collapse of microbubbles formed from dissolved gases. The acoustic bubble population modifies the compressibility and sound absorption characteristics of the liquid in which cavitation occurs. This can result in dramatic changes of sound speed and attenuation, especially for bubble radii close to the resonant radius at the selected ultrasound frequency.

Several effects of the cavitation have been observed on immersed solids. The collapse of the bubbles increases the micromixing phenomena [38], which result in the increase of mass and heat transfer on small scales. Moreover, the solid surface can be eroded by the formation of violent microjets sent onto the surface and which can reach 500 $km.h^{-1}$ [39,40]. This last effect is used to clean surfaces with ultrasound and is also the source of the damage of the ultrasonic probes.

5. Conclusions

Ultrasound in crystallization and precipitation has been used for a long time. Several effects were observed. Ultrasound can influence both nucleation and crystal growth. Nucleation can be induced below the supersaturation at which primary nucleation would normally occur. This effect can be used to control nucleation and final crystal size distribution. Ultrasound can also generate secondary nucleation. One mechanism of action of ultrasound is cavitation. Ultrasound also affects crystal growth and agglomeration, but the mechanisms of both phenomena are not well understood. The benefits arising from the use of ultrasound are seen in changes of the crystal properties such as crystal size distribution, crystal purity or crystal habit.

Nowadays, ultrasound has the potential to be used as an industrial process control tool and some types of industrial crystallizers are available, but the influence of the operating parameters cannot be general-

ized and the mechanisms by which ultrasound affect crystal properties are not well known.

Finally, when dealing with sonocrystallization, despite the experience gained from widespread application, the problem is to go over the empiricism of this operation. The first step in this way is to understand the basics of the operation. The main problem is then to find the right methodology. In crystallization, usually the development of the process is divided into several stages. The first one is to gather basic data on solubility, nucleation and growth kinetics. Then, to perform batch crystallization tests on a laboratory scale to obtain data on the influence of the operating parameters. Finally, modelling of the operation for predicting crystal size distribution can be carried out.

In sonocrystallization, the same approach could be envisaged and one could study separately the two main steps for particles to be formed, nucleation and growth. As ultrasound can influence both phenomena, the distinction between the nucleation and growth rates of crystals under an ultrasonic field is more difficult to perform than in classical crystallization. So, fundamental studies with model substances for which primary nucleation may take place rather slowly under ultrasound could be necessary.

Several assumptions were made on the mechanisms of sonocrystallization, in which cavitation plays a major part. These assumptions must be checked, especially on nucleation and deagglomeration of the particles under cavitation. For this, one must be able to perform sonocrystallization without cavitation on the one hand and with cavitation on the other hand.

From an industrial point of view, even if the fundamental background of sonocrystallization is important, the scale-up is limited by the use of high-power devices and their reliability. In systems where the concentration of particles is high, attenuation is increased and the penetration of ultrasound is limited. So, the principle of the configuration of the sonocrystallizer as a pumped loop or flow-through device, which can irradiate a portion of the suspension, is better. The sonicated zone will then depend on the volume of suspension across which the intensity is applied.

Finally, the scale-up of sonocrystallizers depends on the understanding of conventional crystallization, sound physical principles and engineering innovation.

Nomenclature

a	: particle radius	[m]
f	: wave frequency	[Hz]
g	: growth exponent	[−]
G	: crystal growth rate	[ms^{-1}]
K	: growth rate constant	[ms^{-1}]
k_0	: frequency factor	
k	: wave number ($k=2\pi/\lambda$)	[$rad.m^{-1}$]
R	: gas constant	[$Jmol^{-1}K^{-1}$]
Re	: Reynolds number	[−]
T	: temperature	[K]
V	: primary nucleation rate	[$nuclei.m^{-2}s^{-1}$]
W	: minimum energy required to form the nucleus	[J]
ΔC	: absolute supersaturation	[$kmol.m^{-3}$]
δ	: viscous diffusion length around the particle	[m]
λ	: wavelength of sound	[m]
ν	: dynamic viscosity of the fluid	[Pa.s]
ρ_l	: density of the liquid	[$kg.m^{-3}$]
ω	: wave pulsation	[$rad.s^{-1}$]

References

1) Le Bras: "Action des ultrasons sur les processus physico-chimiques", Revue de chimie minérale, vol 4, (1967) 283-315.
2) Mullin J.W.: Crystallisation (3rd edition), Butterworth-Heinemann London (1993)
3) Jancic S.J. and Grootscholten P.A.: Industrial Crystallization, Delft University Press, published by D. Reidel (1984).
4) Mersmann A.: Crystallization technology handbook, Marcel Dekker, New York, ed A. Mersmann (1995)
5) Myerson A.S.: Handbook of industrial crystallization, Butterworth-Heinemann Series in Chemical Engineering (1993)
6) Yaminski V.V., Yaminskawa K.B., Pertsov A.V., and Shchukin E.D.: "Nucleation and coagulation effects of ultrasound during precipitation in solution" Kolloidnyi Zhurnal, 53-1 Jan-Feb, (1991) 100-104.
7) Kelly D.R.; Harrison S.J.; Jones S.; Masood M.A.; and Gwinfoer Morgan J.J.: "Rapid crystallization using ultrasonic irradiation-sonocrystallization", Tetrahedron Letters, 34 N°16, (1993) 2689-2690.
8) Ratsimba B.; Wilhelm A.M.; and Delmas H.: "Nucleation of potassium bitartrate under ultrasound", Proceedings of First European Congress of Chemical Engineering, Florence (Italy), (1997)
9) Kortnev A.V.; Martynovskawa N.V.: "Effect of ultrasound on the latent period of crystallization from supersaturated solutions", Sb., Mosk.Inst. Stali. Splavov, 77, (1974) 98-100.
10) Qiu Tai-Quin: "Nucleation of sucrose solution by sound field", International Sugar Journal, 95, N°1140, (1993) 513-519.

11) Zang Qiang; Huang Weijie; Shi Lei; Huang Rongbin; and Zheng Lansun: "Influence of sonic field on kinetics of solution" Huaxue Tongbao, (1), (1997) 44-46
12) Price C.: "Sonocrystallization: designing better crystals for the pharmaceuticals industry", presented at the AIChE annual meeting, topical conference on separation technology, Miami Beach Forida, USA, (1995) 12-17.
13) Martin P.D.; Phillips E.J.; and Price C.: "Power ultrasound. A new tool for controlling crystallization", IChemE Research Event, (1993) 516-518
14) Price C.: "Take some solid steps to improve crystallization" Chem. Eng. Progress, Sept (1997) 34-43.
15) Hofmann and Roubik, (1994)
16) Choi H.L.; Enomoto N.; and Nakagawa Z.E.: "Effect of ultrasonic irradiation on precipitation of lead oxalate from aqueous solution", Journal of Materials Science, 29, N°12, 15 Jun (1994) 3239-3242.
17) Gatumel C.; Espitalier F.; Schwartzentruber J.; Biscans B.; Wilhelm A.M.: "Nucleation control by ultrasound in precipitation processes", Kona, Powder and Particle, N°16, (1998), 160-169.
18) Srinivasan R.; Shirgaonkar I.Z.; and Pandit A.B.: "Effect of sonication on crystal properties", Separation Science and Technology, 30 N°10, (1995), 2239-2243;
19) Enomoto N. and Nakagawa Z.E.: "Effect of ultrasound on precipitation of basic alumina sulfate from homogeneous solution of orea", Report of the Research Laboratory of Engineering Materials, Tokyo Institute of Technology, n°20, (1995) 65-69.
20) Kusters K.A.; Pratsinis S.E.; Thoma S.G.; and Smith D.M.: "Ultrasonic fragmentation of agglomerate powders", Chem.Eng.Science, 48, N°24,(1993) 4119-4127.
21) Klink A.; Midler M.; and Allegretti J.: "A study of crystal cleavage by sonifier action", Chem. Eng. Proc. Symp. Ser., 67, (1972) 74-80.
22) Aoki M.; Ring T.A.; and Haggerty J.S.: "Analysis and modelling of the ultrasonic dispersion technique", Adv. Cer. Mat., 2,(1987) 209-212.
23) Enamoto N.; Sung T.H.; Nakagawa Z.; and Lee S.C.: "Effect of ultrasonic waves on crystallisation from a supersaturated solution of alum", Journal of Materials Science, 27, N°19 (1992), 5239-5243.
24) Mydlarz J.; and Briedis D.; "The narrowing of crystal size distributions in a sonicator-MSMPR crystalliser system", Chem. Eng. Comm.,104,(1991) 291-305.
25) Kunz U.; Binder C.; and Hoffmann U.: "Preparation of fine particles as catalysts and catalyst precursors by the use of ultrasound during precipitation", Preparation of Catalysts VI, Scientific bases for the preparation of heterogeneous catalysts, G. Poncelet et al (editors), Elsevier Science B.V.(1995) 869-879.
26) Shopova R.: "Shape of crystals during slow crystallization" in God. Vissh.Khim. – Tekhnol.Inst., Sofia, 26(2), (1979) 68-74.
27) Brown B. and Goodman J.E.: "High intensity ultrasonics; Industrial Applications" ed Iliffe Books LTD, London, (1965).
28) Desborough C.L.; Pike R.B.; Ward L.D.: "Sonochemical apparatus", Brit. Patent, Appn GB 243092A: Eur.PatAppn.EPO 449 008 A (1991).
29) Anderson H.W.; Carberry J.B.; Stauton H.F.; Sutradhar B.C.: "Crystallization of adipic acid", US Patent N°5471001, (1995)
30) Alba. F. and Herbst. A.: "Ultrasound absorption phenomena in slurries makes possible the estimation of complete particle size distributions and solid concentrations", Particulate and Multiphase Processes, 3: Colloidal and Interfacial Phenomena, (1987), 297-311.
31) Dersken J.S. and Kytomaa H.K.: "Acoustic properties of solid-liquid mixtures in the inertial regime: determination of the added mass coefficient", Proc. of 1994 ASME Fluid Engineering Division Summer Meeting. Part 11, FED v 189, (1994) 75-81.
32) Urick R.J.: "A sound velocity method for determining the compressibility of finely divided substance", J.Appl.Phys., 18, (1947) 983.
33) Urick R.J.: "The absorption of sound in suspensions of irregular particles", Journal of the Acoustical Society of America, 20, (1948) 283-289.
34) Urick R.J. and Ament W.S.: "The absorption of sound in composite media", Journal of the Acoustical Society of America, 21, (1949) 115-119.
35) Harker A.H. and Temple J.A.G.: "Velocity and attenuation of ultrasound in suspensions of particles in fluids", Journal of Physics D: Apll.Phys., 21, (1988) 1576-1588.
36) Harker A.H.; Schofield P.; Stimpson B.P.; Taylor R.G. and Temple J.A.G.: "Ultrasonic propagation in slurries", Ultrasonics, 29, (1991) 427-438.
37) Allegra J.R. and Hawley S.A.: "Attenuation of sound in suspensions ans emulsions: theory and experiments", Journal of Acoustical Society Of America, 51, n°5, (1971) 1545-1564.
38) Monnier H.: "Micromélange sous ultrasons", PhD thesis, INP Toulouse, France (1997)
39) Lauterborn W.: "Cavitation and inhomogeneities", ed Spinger Verlag, Berlin, (1980) 3-12.
40) Suslick K.S. and Doktycz S.J.: "Advances in sonochemistry", 1, (1990) 197-229.

Author's short biography

Berthe Ratsimba

Berthe Ratsimba is a Chemical engineer, assistant professor, at the Ecole Nationale Supérieure d'Ingénieurs de Génie Chimique of Toulouse (ENSIGC). She obtained her doctor's degree in 1990, in the field of crystallization. Now she is involved in projects on sonocrystallization.

Béatrice Biscans

Dr Béatrice BISCANS was born in 1958. She graduated from the Ecole Nationale Supérieure de Génie Chimique of Toulouse (ENSIGC) in 1982. She prepared a PhD thesis on the separation of proteins by ion exchange chromatography in the Chemical Engineering Laboratory of Toulouse (UMR CNRS 5503) and obtained her doctor's degree in 1985. She then undertook post-doctoral research on the electrophoretic separation technique.
Since 1987, she has developed and supervised several studies in the field of crystallization as a researcher of CNRS (French National Scientific Centre of Research), working in the Chemical Engineering Laboratory of Toulouse (UMR CNRS 5503). In particular, her work involves the development of research studies on spherical crystallization.

Henri Delmas

Henri Delmas is currently professor of Chemical Reaction Engineering at the National Polytechnic Institute of Toulouse. He received his degree in 1976 and his Doctor es Sciences degree in 1983. In addition to multiphase catalytic reaction engineering he developed a research devoted to sonochemistry: how to use ultrasound in physico chemical processes.

Jean Jenck

Jean Jenck is a Chemical Engineer. He received his Doctor degree in the field of homogeneous catalyst. Now he is senior process manager of Rhodia company.

The Behavior of Fine Particles in the Powder Particle Fluidized Bed†

Kunio Kato
*Gunma Univ.**

Abstract

The powder particle fluidized bed was invented for the processing of fine or very fine particles. In a powder particle fluidized bed, fine powders are continuously fed to a bed in which coarse particles have been fluidized. The fine powders are uniformly dispersed and fluidized in the bed, where they adhere to the surface of the coarse particles. Fine particles are then elutriated from the bed with gas.

This study entailed the use of a powder particle fluidized bed to investigate the holdup of fine particles in the bed, the elutriation rate constant of fine particles from the bed, and the average residence time of fine particles in the bed.

The holdup of fine particles increased linearly with an increase in the feed rate of fine particles and the holdup of fine particles increased with decrease in gas velocity and the particle size of fine particles.

The elutriation rate constant of fine particles increased when fine particle size and gas velocity increased, and decreased when coarse particle size increased. The average residence time of fine particles increased when gas velocity and fine particle size decreased. When fine particle size was smaller than several microns, the average residence time of fine particles in the bed was more than 1,000 times as long as that of the fluidized gas.

Introduction

Fluidized beds are used in gas-solid catalytic reactors, in gas-solid reactors, and for physical operations such as particle drying or granulation.

Fig. 1 shows Geldart's classification of fluidization patterns. **Fig. 2** shows the classification of fluidized beds. "A" particles are used in fluid beds, which are used as gas-solid catalytic reactors. "B" particles are used in teeter beds, which are employed as gas-solid reactors or for physical operations. "D" particles are used in spouted beds. However, "C" particles are usually not used in fluidized beds owing to the following two disadvantageous characteristics for fluidization. First, C particles are quite difficult to fluidize and in some cases they are fluidized by self-agglomeration. Second, because the terminal velocity of C particles is slower than 5 cm/s, if the superficial gas velocity in the bed is very high, all the particles in the bed are carried out with gas. But C particles have many attractive properties. If they are dispersed in the bed uniformly, the reaction between gas and particles is very fast. For example, if 100 μm particles complete the reaction in 100 s, 10 μm or 1 μm particles can complete the reaction in about 10 s or 1 s, respectively. If C particles are dispersed in the bed uni-

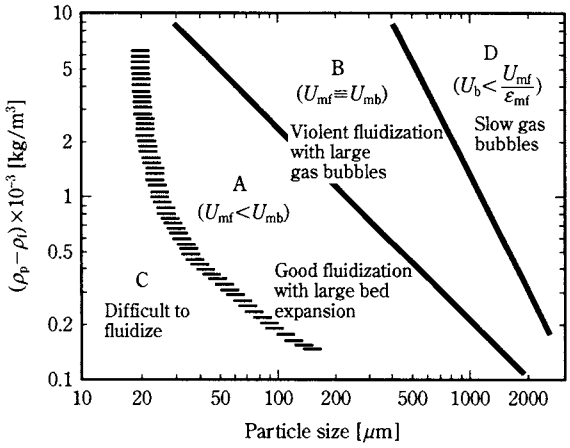

Fig. 1 Relation between fluidization pattern and particle size

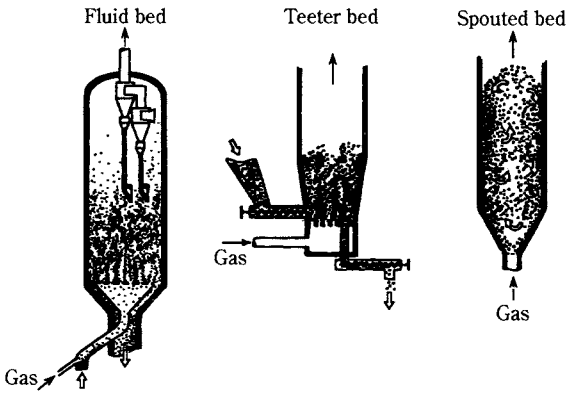

Fig. 2 Classification of fluidization patterns

* 1-5-1 Tenjin-cho, Kiryu-shi, Gunma-ken 376-8515, Japan
† Received July 9, 1999

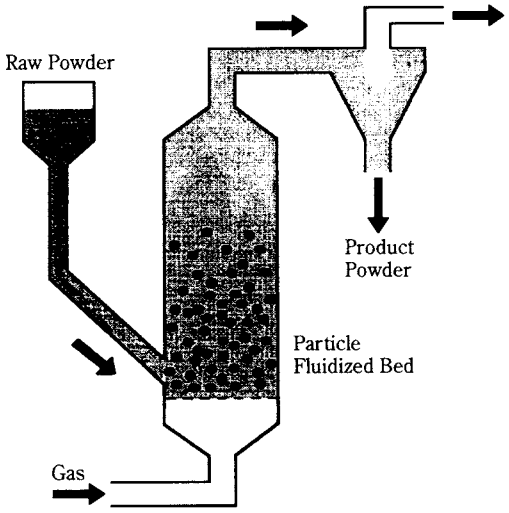

Fig. 3 Powder particle fluidized bed

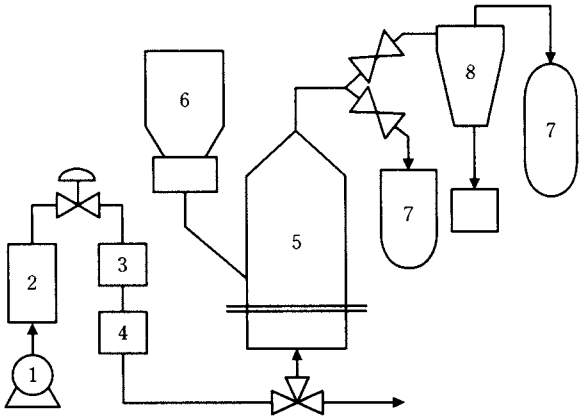

Fig. 4 Schematic diagram of the experimental apparatus

formly, the specific surface area of the particles is quite large and the heat or mass transfer rate between gas and particles is very fast.

Recently we invented a new type of fluidized bed, called a powder particle fluidized bed, for the processing of C particles. A diagram of the apparatus appears in **Fig. 3**. C particles are continuously fed to the bed in which coarse B or D particles have been fluidized. C particles are uniformly dispersed and fluidized in the bed, where they adhere to the surfaces of the coarse particles. The fine particles are elutriated from the bed with gas. A powder particle fluidized bed is used for the production of porous fine particles [1,2] and very fast reactions between particles and gas [3,4] and the reaction between fine particles, coarse particles and gas [5,6] and drying of slurry [7,8].

To analyze the reaction performance or physical operation in a powder particle fluidized bed, it is very important to investigate the behavior of fine particles in the bed.

This study used a powder particle fluidized bed to investigate the holdup of fine particles in the bed, the elutriation rate constant of fine particles from the bed, and the average residence time of fine particles in the bed.

Experimental apparatus and experimental method

Fig. 4 shows the experimental apparatus. The column used in this experiment was a vinyl chloride column with a 10 cm inside diameter and a height of 70 cm. Coarse particles several hundred μm in size were fed into the column until the static bed height became 10 to 30 cm and the particles were fluidized with air. Fine particles were continuously fed into the bed and fluidized with coarse particles, then elutriated from the bed. The elutriation rate of fine particles from the bed was measured by weighing the bag filter at certain time intervals. Once the elutriation rate of fine particles became constant, the system was considered to have achieved a steady state. At this point the feeds of both air and fine particles were immediately stopped, and the mixture of fine and coarse particles in the bed was removed to measure the content of fine particles, which was determined by separating the fine particles from the mixture in water.

Most of the fine particles in the bed had adhered to the surfaces of coarse particles. But some fine particles in the bed had agglomerated into secondary particles with sizes of 50-200 μm. The amount of these agglomerated particles was determined by the following procedure. The small amount of bed particles was screened with a sieve that had a smaller mesh size than the size of the coarse particles. Most of the agglomerated particles were screened out. Their weight was obtained by weighing the sample before and after screening. The holdup of fine particles X was calculated from Eq. (1) by measuring the total weight of fine particles W_p and total weight of coarse particles W_{cp} in the bed.

$$X = \frac{W_p}{W_{cp}} \tag{1}$$

The elutriation rate constant was calculated with the following equation.

$$R = KAX \tag{2}$$

If the holdup of fine particles X and the elutriation rate of fine particles R are measured in the steady

Table 1 Physical properties of particles

Particles	d_p [μm]	ρ_p [kg/m^3]	U_{mf} [m/s]
Silica sand	460		0.17
	550	2,650	0.26
	780		0.38
	920		0.51
Activated alumina	550	1,350	0.13
	780		0.23
Glass beads	550	2,600	0.24
$Al(OH)_3$	15	2,400	—
	3	2,400	—
Al_2O_3	3	4,000	—
	1.3	4,000	—
$CaCO_3$	10	2,710	—

state, the elutriation rate constant K is calculated from Eq. (2).

The average residence time of fine particles in the bed was obtained as follows.

$$\bar{\theta}_p = \frac{W_p}{R} \tag{3}$$

Table 1 shows the properties of the fine and coarse particles used in this experiment.

1. Holdup of fine particles in a powder particle fluidized bed (PPFB) [9]

The holdup of fine particles in a PPFB is determined by the balance between the rate by which fine particles adhere to the surface of coarse particles, and the rate by which fine particles separate from coarse particles due to coarse particle collisions. The holdup of fine particles in the bed is affected by the feed rate of fine particles, the size and density of fine and coarse particles, and the superficial gas velocity.

Fig. 5 shows the effect of superficial gas velocity on the holdup of fine particles in the bed. When gas velocity increased, coarse particle fluidization became violent, with frequent collisions of coarse particles and decreasing holdup of fine particles. **Fig. 6** shows the relationship between the fine particle feed rate and fine particle holdup, with coarse particle size as a parameter. Fine particle holdup increased linearly as the feed rate increased. When coarse particle size was small and gas velocity was constant, the holdup of fine particles in the bed became small. U-U_{mf} values became large when coarse particles were small, and when their size decreased, the fluidization of coarse particles became more violent and the holdup of fine particles decreased. **Fig. 7** shows the effect of superficial gas velocity on the holdup of fine particles in the bed, with fine particle size as a parameter. This figure

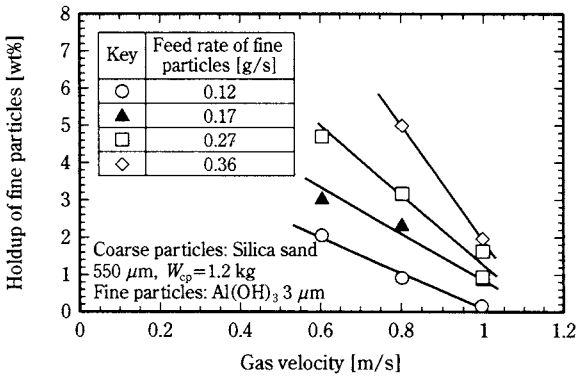

Fig. 5 Effect of gas velocity on the holdup of fine particles

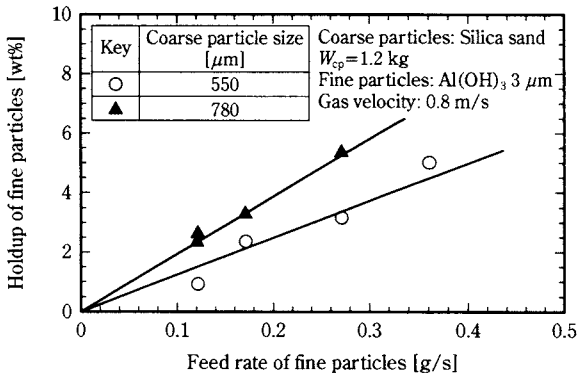

Fig. 6 Effect of coarse particle size and fine particle feed rate on the holdup of fine particles

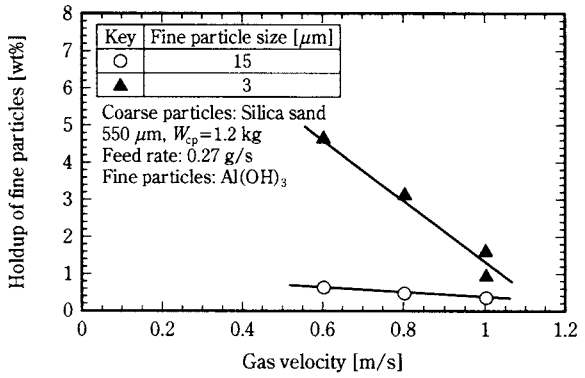

Fig. 7 Relationship between fine particle diameter and gas velocity on the holdup of fine particles

shows that when fine particle size decreased, their holdup in the bed increased remarkably. When fine particle size was small, the force by which fine particles adhered to coarse particles became large, and holdup increased greatly.

In a powder particle fluidized bed, fine particles are present in the bed in the following three situations. (1) Fine particles adhere to the surfaces of coarse particles. (2) Fine particles mutually agglomerate and form secondary particles with particle sizes of 50-200 μm. (3) Fine particles agglomerate with coarse

and fine particles to form very large secondary particles with sizes of 600-10^4 μm. When the holdup of fines in the bed was small, most of them adhered to the surfaces of coarse particles, but when the holdup of fine particles increased, the fractions of types (2) and (3) increased and in some instances steady state operation became impossible. The state of fine particles (3 μm $Al(OH)_3$) in the bed was investigated when 550 μm silica sand particles were fluidized with air. **Fig. 8** shows the relation between the total holdup of fine particles and the holdup in (1) (adhesion ratio). When the total holdup of fine particles was less than 3%, most of the holdup fine particles in the bed adhered to coarse particles, but when the holdup was larger than 3%, type (2) holdup increased as the total holdup of fine particles increased. When total holdup was larger than 8%, very large agglomerate particles formed in the bed and steady state operation became impossible. Therefore if fine particles are to come into contact with gas at the primary particle situation, the holdup of fine particles in the bed must be less than 3 or 4%.

2. Elutriation of fine particles from the powder particle fluidized bed [10]

When fine particles several μm in size were fed into a bed in which coarse particles have been fluidized, the fine particles were not elutriated from the bed at first. But the elutriation rate of fine particles increased as time passed, and it became constant after a certain period of time. When the fine particles were fed into a bed in which the coarse particles had been fluidized, the holdup of fine particles increased with the passage of time. When the separation rate of fine particles from coarse particles due to mutual collisions by coarse particles equalled the adhesion rate of fine particles to the surfaces of coarse particles, the elutriation rate of fine particles from the bed became constant. The rate constant K was calculated from Eq. (2) by measuring holdup X and the elutriation rate R.

Fig. 9 shows the relation between the superficial gas velocity and the elutriation rate constant, with coarse particle size as a parameter when 3 μm particles of $Al(OH)_3$ were fed into the bed. The rate constant increased as gas velocity increased. This tendency is the same as that of Geldart A and B particles. However, the elutriation rate constant of C particles was affected by the size of coarse particles, as shown in **Fig. 9**. This differs considerably from the elutriation rate of A or B particles. Much experimental or theoretical work has been performed on the elutriation rate constant for Geldart A or B particles, and many empirical equations for the rate constant have been proposed. In these equations, the rate constant of A or B particles is affected by the properties of the elutriated particles, the gas velocity, and gas properties, but it is not affected by the properties of coarse particles. The elutriation rate constant of C particles was affected by the properties of coarse particles as shown in **Fig. 9**. When coarse particles were small, the minimum fluidization gas velocity is small and the fluidization intensity U-U_{mf} increased at a constant gas velocity. The separation rate of fine particles from coarse particles increased, as did the rate constant of fine particles.

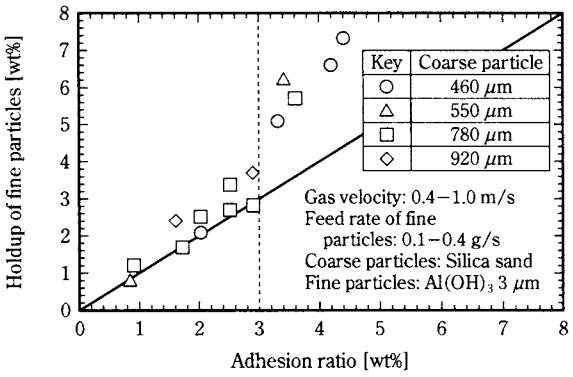

Fig. 8 Relationship between the holdup of fine particles and adhesion ratio

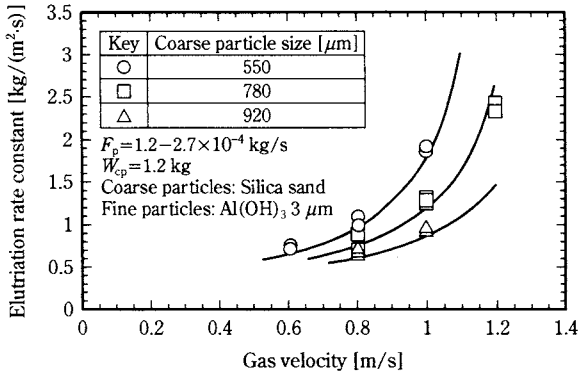

Fig. 9 Effect of gas velocity and coarse particle size on the elutriation rate constant

Fig. 10 shows the effect of superficial gas velocity on the elutriation rate constant, with the size of fine particles as a parameter. When the size of the particles elutriated was small, the rate constant decreased considerably as shown in **Fig. 10**. This tendency is quite different from the elutriation rate constant for Geldart A or B particles. The elutriation rate constant of particles at a constant superficial gas velocity attained the maximum value at the boundary between Geldart A particles and Geldart C particles [11]. In

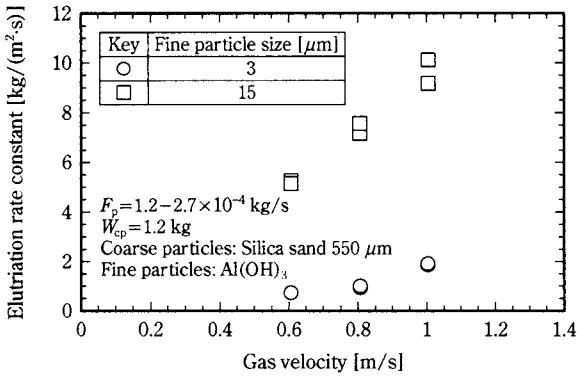

Fig. 10 Effect of fine particle size on the elutriation rate constant

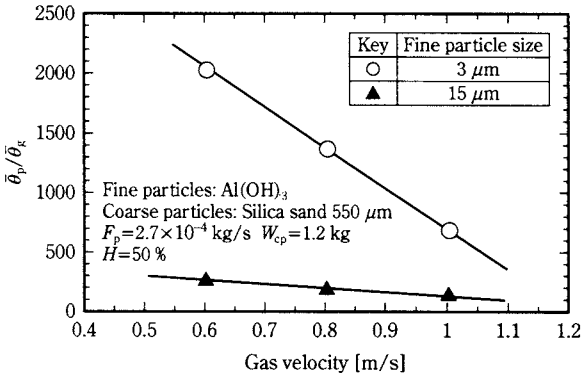

Fig. 11 Relationship between $\bar{\theta}_p/\bar{\theta}_g$ and gas velocity

the C particle region the elutriation rate constant decreased as particle size decreased owing to the adhesion force of fine particles. When the holdup X of fine particles in the bed was smaller than 8%, the elutriation rate constant was not affected by the holdup.

3. Average residence time of fine particles in the bed [12]

It is very important to investigate the average residence time of fine particles and the residence time distribution of fine particles in the bed in order to analyze the reaction between fine particles and gas or to analyze the drying of slurry in a powder particle fluidized bed. The average residence time of fine particles is calculated from Eq. (3) by measuring the elutriation rate of fine R and the total holdup of fine particles in the bed in a steady state. The average gas residence time in the bed is calculated as follows.

$$\bar{\theta}_g = \frac{AL_{mf}(1-\varepsilon_{mf})}{Q} = \frac{AL(1-\varepsilon)}{Q} \tag{4}$$

Where Q is the volume flow rate of fluidized gas and L_{mf} is the bed height at minimum fluidized gas velocity.

We investigated the effects of the properties of fine particles and the operating conditions upon $\bar{\theta}_p/\bar{\theta}_g$. **Fig. 11** shows the relation between $\bar{\theta}_p/\bar{\theta}_g$ and the superficial gas velocity, with fine particle size as a parameter. When the gas velocity increased, the dimensionless average residence time of fine particles $\bar{\theta}_p/\bar{\theta}_g$ decreased because of the violent fluidization of coarse particles. The value of $\bar{\theta}_p/\bar{\theta}_g$ was strongly affected by fine particle size. The dimensionless average residence time of fine particles increased as the size of fine particles decreased. When fine particles were several μm in size, the value of the dimensionless average residence time of fine $\bar{\theta}_p/\bar{\theta}_g$ was longer than 1,000 s. The dimensionless average residence time of fine particles was also affected by the size and density of coarse particles, and the humidity of the fluidizing gas.

From the foregoing we can see that the most important factor affecting the average residence time of fine particles in the bed was fine particle size.

When fine particle size was in the range of several to 20 μm, the dimensionless average residence time of fine particles in the bed was in the range of 1,000-100 s. In powder particle fluidized beds, fine particles less than 10 μm remained in the bed more than several hundred times longer than the average gas residence time in the bed with primary particle situation between gas and particle contacting. In gas-solid reactions, the time necessary to complete the reaction is very short when the particles are very small.

Powder particle fluidized beds are very good reactors for reactions between gas and fine particles, and for performing physical operations on fine particles.

Conclusion

The authors used a powder particle fluidized bed to investigate the holdup of fine particles in the bed, the elutriation rate constant of fine particle from the bed, and the average residence time of fine particles. Following are the results.

(1) The holdup of fine particles was affected by the fine particle feed rate, the properties of fine and coarse particles, and gas velocity. The state of fine particles in the bed was affected by the value of holdup in the bed.

(2) The elutriation rate constant of fine particles increased with increases in gas velocity and in fine particle size, and decreased with an increase in coarse particle size. However, it was not affected by the holdup of fine particles.

(3) The average residence time of fine particles in the bed increased when gas velocity and fine particle

size decreased. When the size of fine particles was smaller than 10 μm, their average residence time in the bed was more than several hundred times longer than that of gas residence time.

Nomenclature

A	: cross sectional area of the bed	(m^2)
d_i	: diameter of particle of size i	(μm)
d_p	: mean diameter of particle	(μm)
F_p	: fine particle feed rate	(kg/s)
H	: relative humidity of fluidization gas	(−)
K	: elutriation rate constant	(kg/m^2 s)
L	: bed height	(m)
L_{mf}	: bed height at minimum fluidization velocity	(m)
Q	: volume flow rate of fluidized gas	(m^3/s)
R_p	: elutriation rate of fine particles	(kg/s)
U	: superficial gas velocity	(m/s)
U_{mf}	: minimum fluidization velocity	(m/s)
W_{cp}	: weight of coarse particles	(kg)
W_p	: weight of fine particles	(kg)
X	: holdup of fine particles in the bed	(−)
$\bar{\theta}_g$	: average residence time of fluidized gas in the bed	(s)
$\bar{\theta}_p$	: average residence time based upon the average diameter of fine particles	(s)
ρ_p	: density of particles	(kg/m^3)
ε	: void fraction of fluidized bed	(−)
ε_{mf}	: void fraction at the minimum fluidization velocity	(−)

Literature Cited

1) T. Takarada, H. Sakamoto, K. Maehara, M. Ito, H. Tsutsui, N. Nakagawa and K. Kato, "Reduction of Iron Oxide Fine Particles from a Converter in a Powder Particle Fluidized Bed," *Kagaku Kogaku Ronbunsyu*, **19**, No. 3, 505-510 (1993).
2) T. Tashimo, T. Suto, J. Murota and K. Kato, "Calcination of Fine Limestone Particles by a Powder Particle Fluidized Bed," *J. Chem. Eng. Japan*, **32**, No. 3, 374-378 (1999).
3) K. Kato, T. Takarada, K. Koshinuma, I. Kanazawa and T. Sugihara, "Decarbonization of Silicon Carbide Carbon Fine Particles Mixture in Fluidized Bed," Proceedings of 6th International Fluidization Conference, pp. 351-358, Banf (1989).
4) Q. Guo and K. Kato, "The Effect of Operating Conditions on SO_2 Removal in Semidry Desulfurization Process by a Powder Particle Spouted Bed," *Kagaku Kogaku Ronbunsyu*, **24**, 279-284 (1998).
5) T. Takarada, T. Tonishi, H. Takezawa and K. Kato, "Pyrolysis of Yalloun Coal in Powder Particle Fluidized Bed," *Fuel*, **71**, 1087-1092 (1992).
6) K. Kato and S. Gao, "A New Dry Process for Simultaneous Removal of SO_2 and NO from Flue Gas by a Powder Particle Fluidized Bed," *Journal of the Japan Petroleum Institute*, **40**, 443-453 (1997).
7) N. Nakagawa, K. Ohsawa, T. Takarada and K. Kato, "Continuous Drying of Fine Particle Water Slurry in Powder Particle Fluidized Bed," *J. Chem. Eng. Japan*, **25**, 495-501 (1992).
8) J. Xu, S. Osada and K. Kato, "Limiting Efficiency for Continuous Drying of Microparticles Slurries in Powder Particle Spouted Bed," *J. Chem. Eng. Japan*, **31**, 35-40 (1998).
9) D. Taneda, H. Takahagi, S. Aoshika, N. Nakagawa and K. Kato, "Studies on Holdup and Agglomeration of Fine Particles in a Powder Particle Fluidized Bed," *Kagaku Kogaku Ronbunsyu*, **24**, 69-74 (1998).
10) D. Taneda, H. Takahagi, S. Aoshika, N. Nakagawa and K. Kato, "Studies on Elutriation of Fine Particles in a Powder Particle Fluidized Bed," *Kagaku Kogaku Ronbunsyu*, **24**, 418-424 (1998).
11) X. Ma, Y. Honda, N. Nakagawa and K. Kato, "Elutriation of Fine Particles from a Fluidized Bed of a Binary Particle Mixture," *J. Chem. Eng. Japan*, **29**, 330-335 (1996).
12) D. Taneda, T. Masagaki and K. Kato, "Studies on Mean Residence Time of Fine Particles in a Powder Particle Fluidized Bed," *Kagaku Kogaku Ronbunsyu*, **24**, 628-632 (1998).

Author's short biography

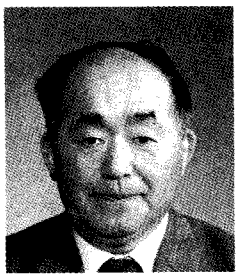

Kunio Kato

Kunio Kato graduated in Nagoya Institute of Technology in 1961 and finished Ph.D. in Tokyo Institute Technology in 1967.
He worked in Dept. of Chem. Eng. West Virginia Univ. from 1967 to 1969 as post doctoral fellow. He became associate professor Gunma Univ. in 1970. He became professor Gunma Univ. in 1980.
His major research field is the reaction engineering especially fluidization engineering. He invented new type of fluidization for the treatment of very fine particles, that is, powder particle fluidized bed (PPFB). Fundamentals and the application of PPFB is his recent major research works.

Arrangement of Microscale Particles by Electrification†

Hiroshi Fudouzi, Mikihiko Kobayashi and Norio Shinya
*STA National Research Institute for Metals**

Abstract

The assembly of particles is one of the built-up methods of fabricating an organized structure in the range from micro- to nanometer scales. We proposed a concept for particle assemblage and have been developing a new technique to assemble microscale particles for the fabrication of two- or three-dimensionally controlled micro structures.

In this paper, we describe the technique for arrangement of microscale particles that was published in previous papers. This technique is based on colloidal processing and can deposit microscale particles at specific areas on non-conductive substrates. The procedure is as follows: An electrified pattern is formed on a dielectric substrate by scanning of an electron or Ga^+ ion beams. The substrate is then dipped into a suspension in which the particles are dispersed The particles are attracted to the electrified pattern and adhere to the substrate.

Spherical silica particles of 5μm diameter were used as model particles in the experiments. Two-dimensional micropatterns were fabricated from the silica spheres by trial. This technique is potentially applicable to fabricate microdevices in electronic, magnetic and optical fields.

1. Introduction

The microstructured materials assembled with particles having diameters in the range from 0.1 to 10μm are expected to have unique and highly useful properties[1],[2]. Nevertheless, until recently, there have been few methods available for producing such materials[3],[4],[5]. The primary problem is the limitation of the available techniques for manipulating particles in this range.

Figure 1 shows an overview of the techniques for manipulating particles classified in the particle size. The techniques can be divided into two groups. One is to deposit single particles on a substrate one by one. A scanning probe microscope[6], a laser[7],[8] and microneedles[9],[10] are used for manipulation of ultra fine particles, fine particles and powder particles, respectively, as shown the upper part in **Fig. 1**. They can deposit particles at specified positions with high accuracy. However, the disadvantage is their low throughputs.

In contrast, the techniques in the other group[11],[12],[13] can deposit a great number of particles on a substrate by particle jets. However, they have a low accuracy for positioning of each particle. Therefore, a technique with high throughput and high accuracy positioning is required for manipulating microscale particles.

Figure 2 shows a conceptual process for the assembly of powder particles assisted by an electron beam drawing[14],[15]. The technique is fundamentally based on electrophotography[16]. At first, the electron beam drawing produces electrified patterns on a surface of

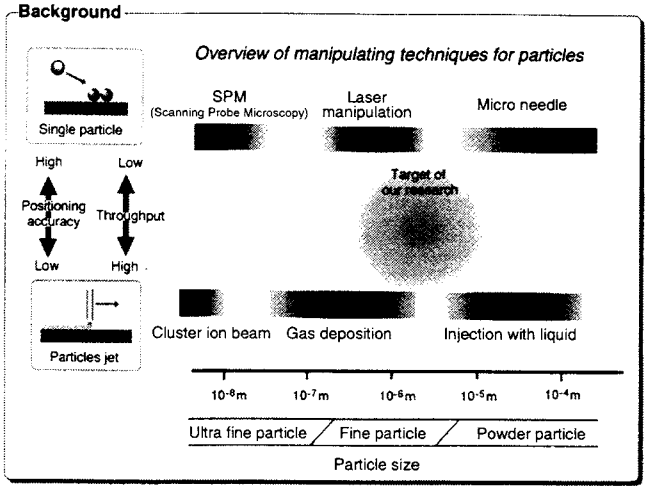

Fig. 1 Overview of manipulating techniques for solid particles.

* 1-2-1 Sengen, Tsukuba-shi, Ibaraki 305-0047, Japan
Corresponding to fudouzi@nrim.go.jp
† Received July 15, 1999

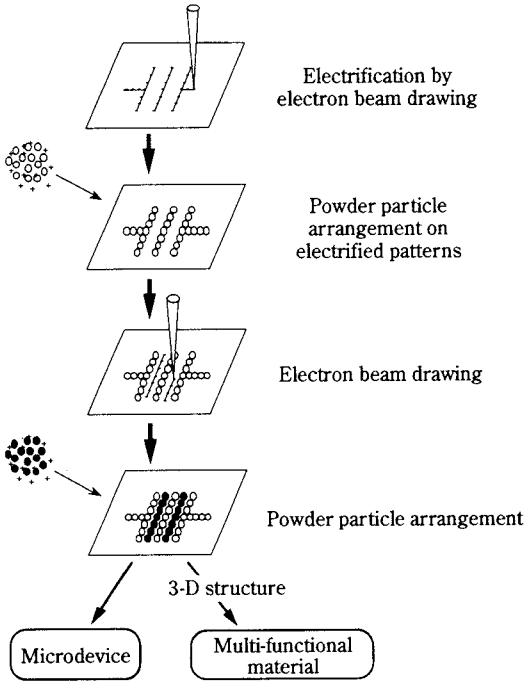

Fig. 2 Conceptual process for assembly of powder particles assisted by electron beam drawing.

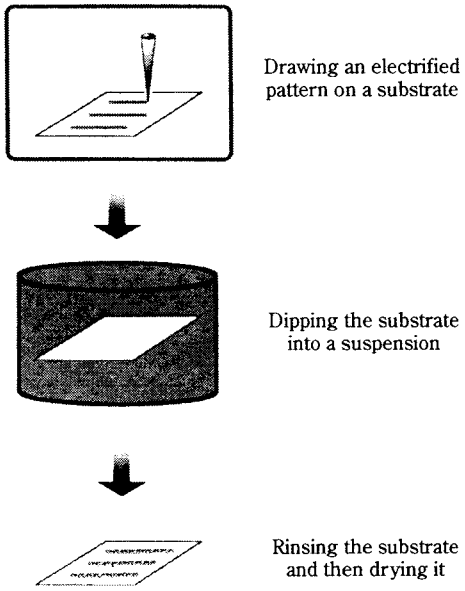

Fig. 3 Schematic illustration of the steps required for arrangement of microscale particles: (1) drawing an electrified pattern on an insulating substrate by drawing with a charged beam; (2) Dipping the substrate into a suspension in which particles are dispersed; (3) Rinsing the substrate and then drying it in air.

the substrates. Next, positively electrified powder particles are attracted by an electrostatic force to the electrified patterns and adhere to the substrates. By repetition of the drawing and adhesion using different particles, one can assemble various particles.

To realize the powder particle assembly, we have been investigating the processing of the drawing and adhesion. The drawing process forms electrified patterns using charged beams. Although it is well-known that irradiation of a charged beam cause charging up of the insulator, there are few papers on the formation of an electrified pattern using charged beams. J. Feder reported that negatively electrified patterns were formed on the thin Teflon foils using an electron beam in 1976[17]. However, no papers have reported on the formation of an electrified pattern on ceramic substrates. Therefore, we have developed a technique for the formation of an electrified pattern on non-conductive ceramics[18],[19],[20]. Next, the adhesion process deposits particles on the electrified pattern. We have developed a new process using a suspension[21],[22],[23]. This process is fundamentally based on the colloidal processing of powder particles.

The purpose of this paper is to describe a new method for manipulating microscale particles developed for the powder particle assembly. We believe that this process is simple and can be applied to wide fields related to the arrangement of microscale particles.

2. Procedure for Particle assembly

2.1 Developed process for particle arrangement

Figure 3 illustrates schematically the steps used to deposit microscale particles on a predetermined position on a substrate. The process consists of three steps, namely drawing, dipping and drying. In the first step, an electron beam drawing produces an electrified pattern on the surface of an insulating substrate. In the next step, the substrate is dipped in a suspension in which powder particles are dispersed. The electrified pattern attracts the powder particles in the suspension by electrostatic forces. Thus the particles migrate to the electrified pattern and deposit on the surface of the substrate along the pattern. In the final step, the substrate is rinsed with a low volatility solvent and then is dried in air. As a result, the adhered particles will form a particles array on the substrate.

2.2 Attraction force by electrification

Suppose that a non-conductive particle is placed near an electrified pattern on a substrate in an insulating solvent. The electrified pattern will attract the particle by an electrostatic force(F), which is expressed by equation 1.

$$F = F_{EP} + F_{DEP} \quad (1)$$

The first and second terms on the right side of the

equation represent the electrophoretic force (F_{EP})[24] and the dielectrophoretic force (F_{DEP})[25], respectively. They are expressed by the following equations.

$$F_{EP} = \pm q E \quad (2)$$

$$F_{DEP} = 2\pi r^3 \varepsilon_2 \varepsilon_0 [(\varepsilon_2 - \varepsilon_1)/(\varepsilon_2 + 2\varepsilon_1)] \nabla E^2 \quad (3)$$

where ε_1 is the permittivity of the solvent, ε_2 is the permittivity of a particle, r is the radius of a particle, E is the electric field caused by the electrified pattern and q is the charge of a particle. If the permittivity of the particle (ε_2) is larger than that of the solvent (ε_1), F_{DEP} plays a role in the attractive force. On the other hand, F_{EP} plays an important role in the attractive force, when the particle and the substrate are electrified in opposite polarity.

2.3 Materials

Properties and characteristics of the particle, the substrate and the solvent are shown in the **Table 1**. The silica spheres, SiO_2, were provided from UBE-NITTO KASEI Co.,Ltd. The SiO_2 spheres are monodispersed with a diameter of 5.1μm and a coefficient variation (Cv: the ratio of the standard deviation of particle size to the mean particle size) of 1.5%. This low Cv value indicates that the diameters of the SiO_2 spheres are almost the same.

The electrified pattern on the substrate will decay with time. Therefore, the electrical properties of the substrate are important for electrification[20]. The decay of the charge can be evaluated by the time constant of charge decay (τ) and is expressed by equation 4.

$$\tau = \varepsilon_r \varepsilon_0 \rho \quad (4)$$

where ε_r is the relative permittivity, ε_0 is the permittivity of a vacuum, and ρ is the volume resistance. The substrate should have a high permittivity and high resistivity. A calcium titanate ceramic ($CaTiO_3$; provided from KYOCERA Co.) is used as a substrate. The $CaTiO_3$ substrate has a high dielectric constant and a high resistivity as shown in **Table 1**. From equation 4, the τ of the $CaTiO_3$ substrate was estimated to be approximately 15 minutes. After drawing the electrified pattern, the arranging process should be finished within 15 minutes. Moreover, the $CaTiO_3$ substrates were mechanically polished and their flatness was less than 0.2μm as the average center height (Ra).

Table 1 Properties and characteristics of SiO_2 particle, $CaTiO_3$ substrate and Fluorinart FC-40 solvent.

SiO_2		Amorphous
	Relative permittivity	4.5
	Diameter	5.1μm
$CaTiO_3$		Polycrystalline
	Relative permittivity	108 (@1 kHz)
	Resistivity	10^{12} Ωm
	Surface flatness	Ra<0.2μm
Fluorinart FC-40		Liquid
	Relative permittivity	1.89
	Resistivity	4.0×10^{13} Ωm
	Boiling Point	155°C

The solvent must be a non-conductive and non-polar, because the electrified pattern will decay in a conductive liquid in a short time. In addition, if the dielectric constant of a solvent is larger than that of a particle, the dielectrophoresis will indicate a repulsive force. For this reason, a per-fluorocarbon (Fluorinert FC-40, SUMITOMO 3M) is used as a solvent. The solvent has a low permittivity (dielectric constant) and a high resistivity as shown in **table 1**.

2.4 Drawing and observing the electrified patterns[18], [19], [20]

Electrified patterns are formed by drawing with a focused charge beam at high energy. The electrified pattern is then observed with a scannng electron microsope (SEM) at low energies as a voltage contrast image[26]. In the voltage contrast image, a dark contrast means a positive potential region. On the other hand, a bright contrast means a negative potential region.

Negatively electrified patterns were formed on the $CaTiO_3$ substrates by drawing a focused electron beam (FEB; e^-) with a beam energy from 5 to 20keV. The electrified patterns were observed in-situ as a voltage contrast image with an SEM at 2keV. In contrast, positively electrified patterns were formed on the substrates by drawing a focused ion beam (FIB; Ga^+ ion) with the beam energy at 30keV. The electrified patterns were observed in-situ as a voltage contrast image with an SEM at 2.5keV.

2.5 Dipping, rinsing and drying[21], [22], [23]

To prepare a suspension, the SiO_2 spheres were introduced into a Fluorinert FC-40 solvent. The particle concentrations in the solvent were adjusted to the range from 1×10^6 to 5×10^6 count/ml. The SiO_2 spheres were well dispersed in the solvent by ultrasonication.

Substrates with the electrified images were dipped into SiO_2 sphere suspensions at room temperature. The dipping time was changed from 2 to 60 seconds. The substrates were then rinsed with a volatile liquid (Fluorinate FC-72; boiling point=56°C) and were dried in air.

The SiO_2 spheres arranged on the substrates were observed with an optical microscope or with an SEM at 2keV.

3. Electrified patterns by drawing with charged beams[18],[19],[20]

3.1 Negatively electrified patterns

Figure 4 shows a negatively electrified pattern formed by drawing with a focused electron beam (FEB). A grid pattern with 100μm spacing was drawn at 15keV of the FEB and its electron dose was 0.2pC/μm^2. The electrified pattern was observed in-situ with an SEM at 2keV. The bright grid image with a 100μm spacing corresponds to the pattern drawn by the FEB. In addition, the surface of the electrified pattern indicates negative polarity. Thus a negatively electrified pattern was obtained on the $CaTiO_3$ substrate by drawing with an electron beam.

3.2 Positively electrified patterns

Figure 5 shows a positively electrified pattern formed by drawing with a Ga^+-focused ion beam (FIB). A grid pattern with a 100μm spacing was drawn at 30keV and its Ga^+ ion dose was 0.08pC/μm^2. The electrified pattern was observed in-situ with an SEM at 2.5keV. The dark grid image with a 100μm spacing corresponds to the pattern drawn by the Ga^+-FIB. In addition, the surface of the electrified pattern indicates positive polarity. Thus a positively electrified pattern was obtained on the $CaTiO_3$ substrate by drawing with a Ga^+ ion beam. We can form negatively and positively electrified patterns on insulating ceramic substrates and observe them using a low energy SEM.

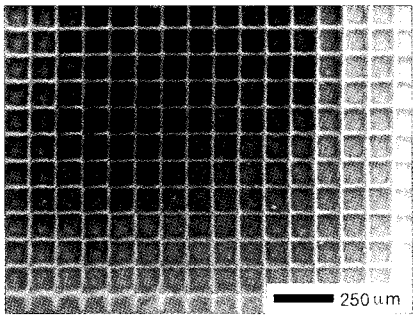

Fig. 4 Voltage contrast image of the negatively electrified pattern on a $CaTiO_3$ substrate. The pattern was drawn with a focused electron beam at 15keV. The image was observed in-situ with an SEM at 2keV.

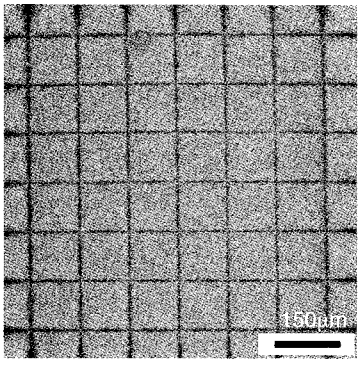

Fig. 5 Voltage contrast image of the positively electrified pattern on a $CaTiO_3$ substrate. The pattern was drawn with a focused Ga^+ ion beam at 30keV. The image was observed in-situ with an SEM at 2.5keV.

3.3 Comparison of the both electrified patterns

It appears that the positively electrified pattern shown in **Fig. 5** is finer than the negatively electrified pattern shown in **Fig. 4**. To compare the electrification by the Ga^+-FIB with that by FEB, the fineness of the electrified patterns was analyzed. A negatively electrified line and a positively electrified line were formed, and their exposure doses were 0.2pC/μm^2 and 0.02pC/μm^2, respectively. The value distribution of the voltage contrast line transverse to the line was obtained using image analysis software.

Figure 6 shows the results of the analysis. The line width of the electrified lines was determined as the full width at half maximum (FWHM). The FWHM of the positively electrified line was 4μm and that of the negatively electrified line was 14μm. Therefore, the drawing with a Ga^+ ion beam formed a fine electrified line less than one third that of the drawing with an electron beam.

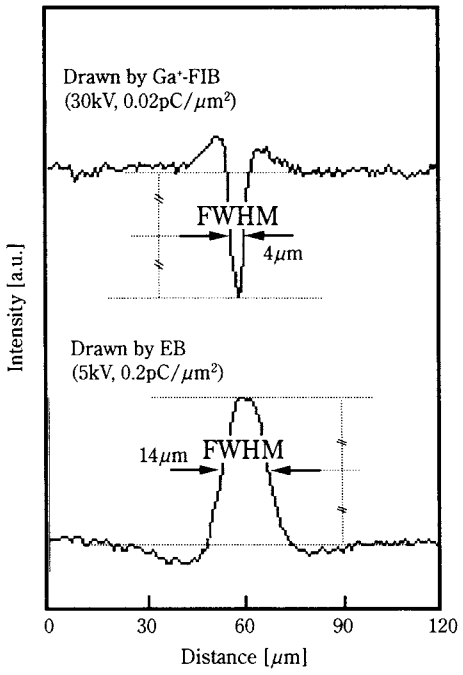

Fig. 6 Comparison of the line width of the positively electrified line and that of the negatively electrified line. The value distribution of the electrified line transverse to the line was obtained by line profiling using an image analysis on a computer. The line width is evaluated as the full width at half maximum (FWHM) and is shown in the figure.

4. Arranged particles on the substrates[21],[22],[23]

4.1 SiO_2 spheres arranged on the negatively electrified patterns

Figures 7 (a) and **(b)** show the SiO_2 spheres arranged on the negatively electrified pattern. Two electrified lines were formed on the $CaTiO_3$ substrate using the electron beam. The length of the line was 1600μm and the spacing of the two lines was 800μm. The SiO_2 spheres were deposited on the electrified lines. The adhered SiO_2 spheres formed two sphere lines as shown in **Fig. 7 (a)**. **Fig. 7 (b)** shows a part of the sphere lines as shown in **Fig. 7 (a)**. It is obvious that the SiO_2 spheres are aligned continuously. The sphere line is about 25μm in width.

4.2 Effect of electron dose of the pattern

We investigated two factors, electron dose and dipping time, that affect the count of spheres adhered to the negatively electrified patterns.

Figure 8 shows the relationship between electron dose and the count of adhered spheres. The experiments were carried out at primary electron energies of 5keV, 10keV, 15keV and 20keV. The count of adhered spheres linearly increases with the electron dose, and the slopes of the lines are approximately the same regardless of the primary electron energy. The linear correlation means that the count of the adhered spheres can be controlled by the electron dose.

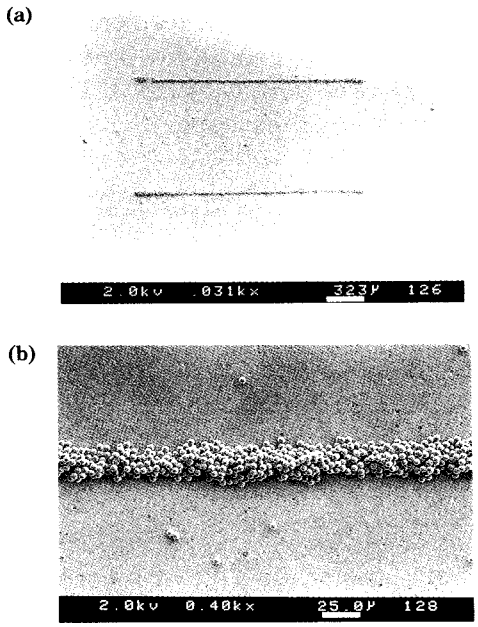

Fig. 7 SEM image of the silica (SiO_2) spheres arranged on negatively electrified lines. Photo(a) shows two lines composed of silica spheres on the substrate. The length of both lines is 1600μm and the spacing of the lines is 800μm. Photo(b) shows that SiO_2 spheres linearly arrayed along an electrified line on the substrate which is a part of the line shown in the photo (a).

4.3 Effect of dipping time in a suspension

Figure 9 shows the relationship between dipping time and the count of the adhered spheres for various electron doses. The electrified lines were formed by a 15keV electron beam drawing at doses of 0.2, 0.5 and 1.0 pC/μm^2. The count of adhered spheres linearly increases with the dipping time for the dose of 0.2 to 1.0pC/μm^2. This result means that the count of the adhered spheres can be controlled by the dipping time.

The experimental results showed that the electron

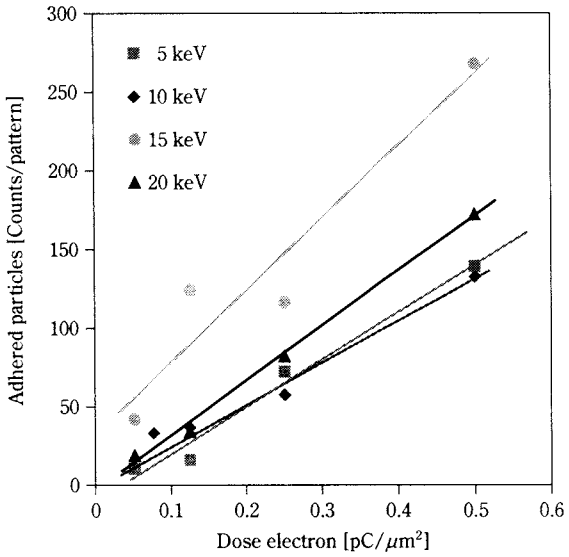

Fig. 8 Relationship between the dose electron density and density of particles adhered to the negatively electrified pattern.

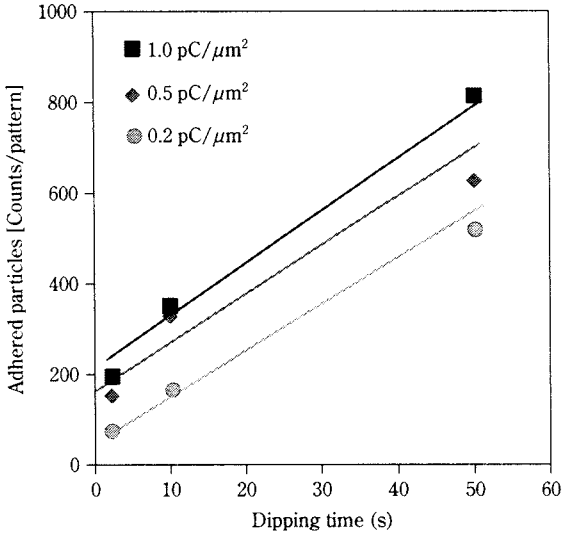

Fig. 9 Relationship between the dipping time of the substrate and density of particles adhered to the negatively electrified pattern.

dose and the dipping time can control the count of adhered spheres on the electrified patterns. We conclude that both are key factors in arranging microscale particles on the electrified pattern.

4.4 SiO_2 spheres arranged on the positively electrified pattern

Figure 10 shows examples of particle arrangements on the positively electrified patterns. **Fig. 10 (a)** shows a microstructure assembled with the SiO_2 spheres. The SiO_2 spheres were arranged on the electrified pattern on the $CaTiO_3$ substrate. The SiO_2 spheres formed a microstructure composed of particle lines. The line length and line spacing are 250μm and 50μm, respectively. Using Ga^+-FIB, we can fabricate a two-dimensional micro structure assembled with microscale particles.

Fig. 10 (b) shows an SEM image of another example. The adhered SiO_2 spheres are displayed as a three-dimensional bird's-eye view. An electrified pattern of a spot array 50μm apart was formed by a Ga^+-FIB on the $CaTiO_3$ substrate. The SiO_2 spheres preferentially adhered to the spot array and occupied over 90% of the spots. The average number of the adhered particles is 3.0 per single spot. The final goal of this arrangement is the formation a single particle array.

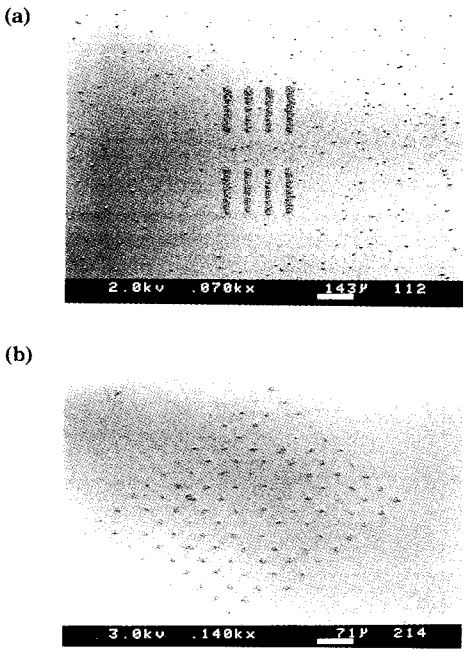

Fig. 10 SEM image of the SiO_2 spheres arranged on a positively electrified pattern formed by drawing Ga^+-FIB. Photo(a) shows eight lines composed of silica spheres on the substrate. The length of each line is 250μm and the spacing of the lines is 100μm. Photo(b) shows a bird's-eye view of silica spheres arrayed on the electrified spots. The distance spot-to-spot is 50μm.

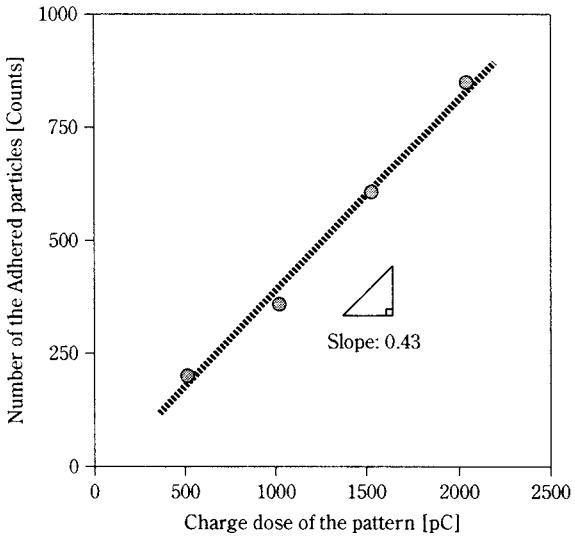

Fig. 11 Relationship between the amount of Ga^+ ion dose and the count of the particles adhered to the positively electrified pattern.

4.5 Effect of Ga^+ ion dose of the pattern

Figure 11 shows the relationship between the Ga^+ ion dose and the count of SiO_2 spheres adhered to the positively electrified pattern. The particle count is linearly increased with the charge dose. The linear correlation means that the adhered spheres can be controlled by the Ga^+ ion dose.

The line passes the origin and the slope of the line is 0.43 count/pC. This means that a dose charge of 2.3pC, the reverse of the slope, is required to deposit one particle on the electrified pattern.

4.6 Positioning of individual particles

Figure 12 (a) shows a voltage contrast image of the dotted line. Positively electrified dots with a 5μm spacing were formed by drawing with a Ga^+-FIB at 30keV. The dot-to-dot spacing is the same size as the diameter of the SiO_2 spheres, and the Ga^+ ion dose was set at 2.3 pC per dot.

Figure 12 (b) shows the SiO_2 sphere arrangement on the dotted line. The SiO_2 spheres adhered to the dots and formed a partly serial array. The electrostatic potential periodically changed along the line, and its intensity shows peaks at the center of each dot. Therefore, the SiO_2 spheres will preferentially deposit on the center of the electrified dots. As a result, the SiO_2 spheres will form a serial array of single particles like a pearl chain. We conclude that the dotted electrification is effective for site control of the particle arrangement.

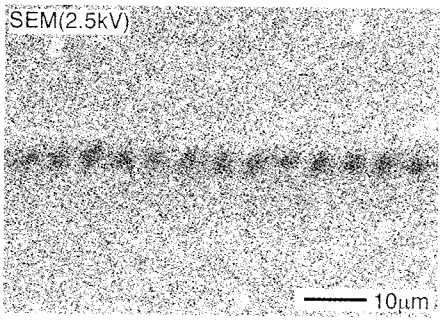

(a) Voltage contrast image of a dotted line formed by Ga^+-FIB drawing

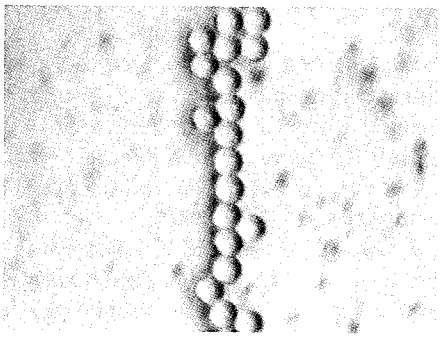

(b) Arranged silica spheres on the dotted line

Fig. 12 Precise arrangement of SiO_2 spheres on the pinpointed positions. Photo(a) shows a voltage contrast image of the dotted line formed by Ga^+-FIB drawing. The spacing of the dots was 5μm. Photo(b) shows the results arranged on the dotted electrified line in photo(a), and serially arrayed silica spheres like a pearl chain can be obtained.

5. Summary and outlook

A summary of this review paper is as follows:

(1) We have proposed a concept for the patterning process with micrometer particles and have developed a new technique to realize this concept.

(2) Electrified patterns were formed on insulating substrates by an electron beam and also by a focused Ga^+ ion beam, and were observed with a scanning electron microscope as voltage contrast images.

(3) The electrified pattern formed by a Ga^+ ion beam is finer than that by an electron beam. The line width is less than 5μm defined as an FWHM value.

(4) SiO_2 spheres of 5μm in diameter were arranged on the substrates along the positively or negatively electrified patterns. The count of adhered spheres linearly increased with the charge dose and the dipping time.

(5) The SiO_2 spheres arrayed in series like a pearl chain. This result indicated that micrometer-scale particles can be arranged on pinpointed positions on the insulating substrate.

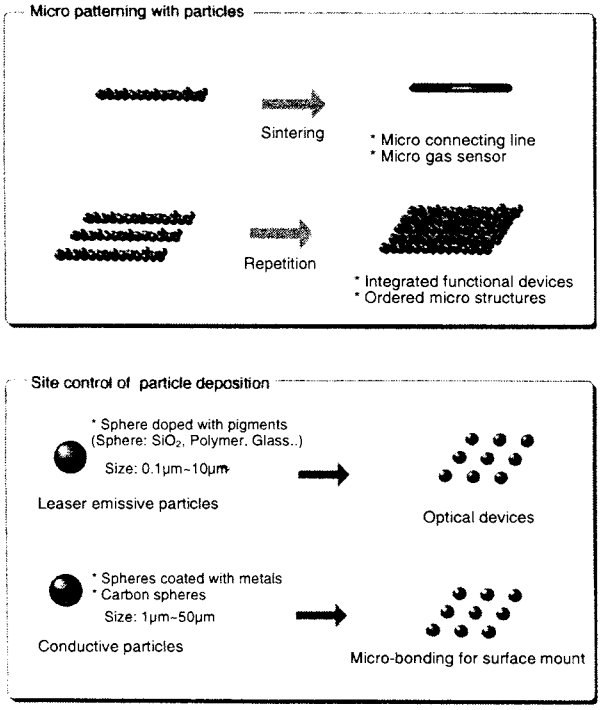

Fig. 13 Potential applications of the particle arranging technique.

Figure 13 shows the potential applications of this technique for the outlook of future work. We believe that this patterning technique can be applied to various fields; that is, it is possible to create microdevices and microstructures with multi-function. The applications are classified into two parts. The first part is the micropatterning with particles. One-dimensional patterning can be applied to a microconnecting line and a microgas sensor. Fabrication of two-dimensional microstructures can be applied to integrated functional devices and ordering of microstructured materials. On the other hand, the second part is fabrication of an optical device from microspheres and a microbonding with conductive particles for the surface mounting of electronic devices and materials.

Acknowledgements

The authors would like to thank Dr. Kishimoto, Dr. Hase and Mr. Egashira for their useful suggestions and discussions.

References

1) V. F. Janas and A. Safari, "Overview of fine scale piezoelectric ceramic/polymer composite processing," J. Ame. Ceram. Soc., **78**, 2945-55 (1995).
2) L. L. Hench and D. R. Ulrich, "Ultrastructure processing of ceramics, glasses, and composites," Wiley-Interscience, NY, 1984.

3) E. Kim, Y. Xia and G. M. Whitesides, "Two- and Three dimensional crystallization of polymeric microspherers by micromolding in capillaries," Advances Materials, **8**, 245-247 (1996).
4) J. Tien, A. Terfort and G. M. Whitesides, "Microfabrication through electrostatic self-assembly," Langmuir, **13**, 5349-55 (1997).
5) D. A. Saville and I. A. Aksay M. Trau, "Field-induced layering of colloid crystals," Science, **272**, 706-709 (1996).
6) T. Junno, K. Deppert, L. Montelius and L. Samuelson, "Controlled manipulation of nanoparticles with an atomic force microscope," Appl. Phys. Lett., **66**, 3627-3629 (1995).
7) A. Ashkin, "Acceration and trapping of particles by radiation pressure," Phys. Rev. lett., **24**, 156-159 (1970).
8) K. Sasaki, M. Koshioka, H. Misawa, N. Kitamura and H. Mashuhara, "Laser-scanning micromanipulation and spacial patterning of fine particles," Jpn. J. Appl. Phys., **30**, L907-909 (1991).
9) H. Miyazaki and T. Sato, "Mechanical assembly of three-dimensional microstructures from fine particles," Adv. Robot., **11**, 169-185 (1997).
10) N. Shinya, T. Konno and M. Egashira, "Micro-scale structure fabrication using micro-probe," Proc. of the smart structures and materials, pp. 36-44, SPIE, San Diego, 1996.
11) P. Calvert and R. Crockett, "Chemical solid free-form fabrication: making shapes without molds," Chem. Matter., **9**, 650-663 (1997).
12) C. Hayashi, S. Kashu, M. Oda and F. Naruse, "The use of nanoparticles as coatings," Mater. Sci. and Eng., **A163**, 157-161 (1993).
13) J. R. G. Evans P. F. Blazdell, M. J. Edirisinghe, P. Shaw and M. J. Binstead, "The computer aided manufucture of ceramics using multilayer jet printing," J. Mater. Sci. Lett., **14**, 1562-1565 (1995).
14) N. Shinya, M. Egashira and H. Fudouzi, "Powder particles assembly using electron beam for creation of multi-functional materials", Proc. of 2nd Int. Conf. on Intelligent Materials, pp. 1142-1151, Technomic Publishing Co., Williamsberg, 1994.
15) M. Kobayashi, T. Dan, H. Fudouzi and N. Shinya, "Development of new handling techniques for particle assemblage", J. Soc. Powder Technol., **35**, 125-134 (1998).
16) R. M. Schaffert, "Electrophotography," Focal Press Ltd., NY, 1965.
17) J. Feder, "Storage and examination of high-resolution charge images," J. Appl. Phys., **47**, 1741-1745 (1976).
18) H. Fudouzi, M. Egashira and N. Shinya, "Drawing and observating of electrified images on ceramic substrates using electron beam," J. Ceram. Soc. Japan, **104**, 556-561 (1996).
19) H. Fudouzi, M. Egashira and N. Shinya, "Formation of electrified images on ceramic substrates using focused ion beam," J. Ceram. Soc. Japan, **105**, 611-615 (1997).
20) H. Fudouzi, M. Egashira and N. Shinya, "Formation of electrified images using ion and electron beams", J. Electrostatics, **42**, 43-49 (1997).
21) H. Fudouzi, M. Kobayashi, M. Egashira and N. Shinya, "An arrangement of micrometer-sized powder particles by electron beam drawing," Advanced Powder Technol., **8**, 251-262 (1997).
22) H. Fudouzi, M. Kobayashi and N. Shinya, "An arrangement of micrometer-sized particles on substrate by electrified dots drawn with a focused ion beam," J. Soc. Powder Technol., **35**, 560-565 (1998).
23) M. Kobayashi, H. Fudouzi, M. Egashira and N. Shinya, "Assemblage of particles for intelligent materials," Smart Mater. Struct., **7**, 496-501 (1998).
24) Paul C. Hiemenz and Raj Rajagopalan "Principles of colloid and surface chemistry," Marcel Dekker, NY, 1997.
25) T. B. Jones, "Electromechanics of particles," Cambridge University Press, NY, 1995.
26) H. Seiler, "Secondary electron emission in the scanning electron microscope," J. Appl. Phys., **54**, R1-18 (1983).

Author's short biography

Hiroshi Fudouzi

Hiroshi Fudouzi is a researcher at the National Research Institute for Metals (NRIM), Japan. He received his bachelor of engineering (BE) and master of engineering (ME) from Kyushu Institute of Technology in 1991 and 1993, respectively. His research interests include advanced materials, particle assembly, patterning with micro-particles and self-assembly. He is a member of the Ceramic Society of Japan, The Chemical Society of Japan and The Japan Society of Applied Physics and the Society of Powder Technology, Japan. For more information, please send an E-mail to the following addressee: fudouzi@nrim.go.jp.

Mikihiko Kobayashi

Mikihiko Kobayashi is a leader of the first subgroup of the fifth Research Group in NRIM. He has served the Institute since 1977, and has taken the current position since April 1997. He obtained his BE and ME from Kyoto University in 1977 and 1979, respectively. He received his doctor of engineering (DE) in July 1988 from Kyoto University for a thesis entitled "Waste water treatment in the suspension systems." His current interests include intelligent materials, particle assemblage, and application of hydrometallurgical methods to the material processing. He is a member of the Mining and Materials Processing Institute of Japan.

Norio Shinya

Norio Shinya is a director of the fifth research group at NRIM. He received his BE from Waseda University in 1967 and his DE from Tokyo University in 1985. He proposed a concept of powder particle assembly and organized the fifth research group in 1994. His research interests include smart and intelligent materials, mechanical behavior and damage formations' process of materials at elevated temperature, and prediction and extension of residual life. He is a member of the Iron and Steel Institute of Japan, the Japan Institute of Metals, and the Society of materials science, Japan.

Scale-up of Agglomeration Processes using Transformations†

Paul Mort
*Procter & Gamble Co.**
Gabriel Tardos
*Department of Chemical Engineering, City University of New York***

Agglomeration is done with many different materials over many scales of production, from specialty materials and pharmaceuticals made in kg/day batches to continuous processes for detergents and fertilizers measured in tons/hour. Agglomeration is done to add value to the product, for example, to produce free-flowing, dust-free particles that are optimized for uses such as tabletting, dispersion/dissolution and compact delivery (i.e., increase the bulk density).

Transformations describe the many ways in which the raw materials are changed by the process to form the product. Agglomeration includes a complicated collection of transformations, typically including the mixing of powder feeds, binder atomization, dispersion of binder in powders, wetting and spreading of binder on particle surfaces, chemical reactions between binder and powder, particle growth by coalescence, consolidation, attrition and drying. This paper briefly reviews the agglomeration literature with the aim of summarizing transformations that typically have an important role in agglomeration processes, as well as to propose sets of process parameters and material properties that are critical to scale-up and process control.

There are many kinds of agglomeration processes. With a few exceptions such as smaller-scale fluid-bed agglomerators with glass risers, or, in some cases, pan agglomerators, most agglomeration processes are "black boxes" that do not allow the operator to visually observe the transformations as they occur. In the past, this has reinforced the perception of agglomeration as an "art" rather than a "science". Recently, much progress has been made towards the use of sophisticated on-line sensors and control in agglomeration processes.[1,2] On-line measurement capability of critical product attributes such as granule size, shape, moisture level, etc. presents an opportunity to approach granulation from a more scientific perspective. To harness the benefits of the scientific approach, one must be able to effectively translate fundamental knowledge collected at the lab scale, into industrial practice on a production scale. Because of this difference in scale, we need to identify the linkages between the important transformations in the agglomeration process. The linkages are made through relevant process parameters and the material properties in the agglomeration process, noting that key material properties often change during the process.

In order to make direct linkages between process parameters, material properties and the product attributes of the agglomerate, this paper seeks to examine fundamental interactions on a granular scale. The goal is to: 1) provide a framework of transformations covering the diverse set of agglomeration processes and products; and 2) use transformations as a basis for process scale-up.

The goal of scale-up is to maintain identical product attributes across production scales. Towards this goal, one can consider the granulation process from the perspective of the operating equipment (i.e., the *macro-scale*) or from the perspective of the product granules (i.e., the *micro-scale*).[3]

Macro-scale approach

One can consider scale-up of agglomeration processes based on equipment scale parameters, referred herein as the *macro-scale* approach. Typically, the macro-scale approach determines desired operating conditions over a range of geometrically-similar unit operations using dimensionless groups such as Froude Number, Reynolds Number and Power Number. A measurable process parameter, such as power draw in a vertical granulator used for pharmaceutical granulation, is used to determine the desired process residence time (e.g., endpoint in a batch mixer or fill level in a continuous mixer). This provides guidelines for scale-up of the equipment operation. Empirical

* Cincinnati, OH, U.S.A.
**NY, U.S.A.
† Received July 20, 1999

adjustment of parameters may still be required to achieve the desired granular product attributes such as granule size, size distribution and density.

In an example of a macro-scale type approach, dimensionless groups relating process parameters and wet-mass material properties over a series of vertical mixer-granulators (**Fig. 1**)[4], are defined. The Power Number (Np) relates the net power draw (ΔP) to mixer size (D), rotational speed of the agitator (N) and the instantaneous product bulk density (ρ). A pseudo-Reynolds Number (Re^*) describes the kinematic flow in the mixer in terms of product bulk density (ρ), agitator tip speed (ND), characteristic shear dimension (D) and a pseudo-viscosity (η^*). Here, η^* results from a torque measurement in a Mixer Torque Rheometer (MTR) used to measure the consistency of intermittent product samples. The MTR torque is assumed to relate to bulk flow behavior of the wet mass, in a way that is analogous to viscosity in a liquid system. The Froude Number (Fr) is the ratio of centrifugal to gravitational forces, and describes the state of fluidization in the mixer. The Fill Number describes the relative loading level of the mixer (**Fig. 1**).

For each scale of mixer, data were collected (see Ref. 4) at sets of N, D and h, with intermittent samples taken at various power draw conditions, and measured for density and pseudo-viscosity. The high x-axis data sampled at short times showed low density, low viscosity and a corresponding low power draw. At longer process times, the density, viscosity and power draw increase; these data are the low values on the x-axis. The overlap of the data at different scales implies that there is a consistent scale-up relationship between the power draw of the mixer and the wet-mass consistency of the mixture. Subsequent work has shown that this relationship can be extended across mixers that are not necessarily geometrically similar.[5] This approach demonstrates the use of MTR to obtain intermediate material properties sampled from the process. This is very important, as the relevant properties change as the bulk material is transformed during the agglomeration process. Although this approach does not directly address the scale-up of product attributes, the inclusion of product density and wet-mass viscosity in the dimensionless groups provide indirect linkages. More recently, good correlation has been shown between the wet-mass properties and subsequent dry-granule product attributes.[6]

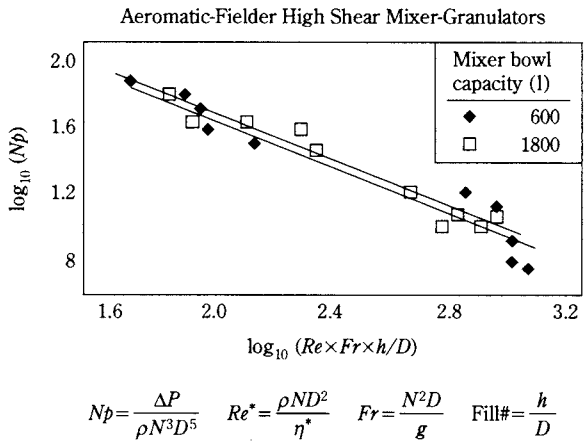

Fig. 1 Power law scale-up of high shear mixer-granulators using in-situ material properties: density (ρ) and wet-mass pseudo viscosity (η^*). Figure from Landin et al.[4]

In another example from the pharmaceutical literature, lab scale tests were done to define an optimum power level for endpoint control in the scale-up of a granulation process in a vertical mixer-granulator.[7] The granulation process was followed by tabletting. The critical properties of granular flow, tablet weight variation and tablet disintegration time were optimized together at a single power-draw endpoint on the lab scale. On scale-up to a larger mixer, however, several product attribute issues were encountered. In maintaining similar mechanical fluidization for binder/powder dispersion (i.e., constant Fr), more granular densification occurred, which led to negative impacts on tablet properties. Increased granular densification was due to the higher impeller tip speed that is invariably encountered on a Froude Number scale-up to a larger diameter mixer. To adjust the density, the rotational speed was reduced to approach tip speed (i.e., kinematic) similarity. The lower state of fluidization was balanced by reducing the binder spray-on flux (i.e., a longer batch time). It should be noted that the method of binder addition and its distribution in the powder typically becomes more and more critical at larger scales. In order to analyze the transformation of binder distribution and its effect on granulation, one needs to consider a micro-scale approach.

Micro-scale approach

The *micro-scale* approach to scale-up is based on defining the key transformations in an agglomeration process on a granular scale. This approach defines the key transformations (e.g., binder distribution, growth and consolidation) and establishes the main mechanistic linkages between the transformations and the desired product attributes (e.g., chemical homogeneity, granular size, size distribution and

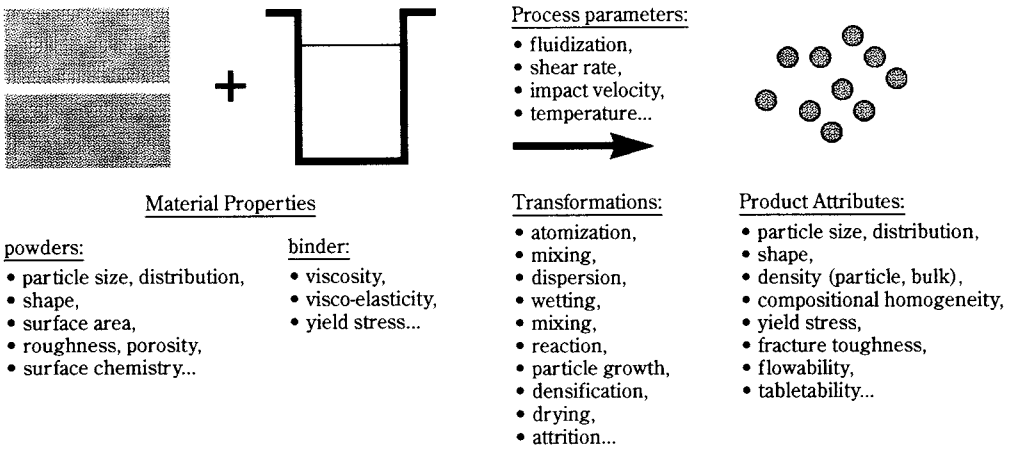

Fig. 2 Agglomeration process transformations defined as a function of material properties and process parameter groups.

granule density). The challenge is then to maintain the similarity of each transformation during scale-up. This approach helps in scale-up of specific product attributes, and helps in the adjustment of parameters needed to achieve the desired results.

Transformations describe the many ways in which the raw materials are changed by the process to form the product (**Fig. 2**). Atomization is key to binder sprays. Dispersion is the mixing of binder and powder. Wetting refers to the micro-scale spreading of binder on powder surfaces. Reactions may occur between binder and powders. Particle growth is generally regarded as the primary transformation in the agglomeration process; however, it is very much affected by many of the other transformations. Densification and consolidation of granules is intimately connected with growth and coalescence. Moisture removal is required to form a dry, flowable product from an aqueous binder system; drying may have a very strong impact on other transformations if it is done simultaneously. Attrition, or particle breakage, is often regarded as a negative transformation; it can also be used however, to advantage in limiting the breadth of particle size distributions.

Key powder properties include particle size, size distribution, shape, surface area, surface roughness, porosity and surface chemistry. Some of these, such as size distribution and surface area, can be characterized by fairly direct measurements. Others, such as shape and roughness are more qualitative measurements. Surface chemistry is a very important and often difficult area to characterize, where subtle changes can have significant effects on the agglomeration process. Binder properties are most commonly characterized in terms of viscosity, although viscoelasticity and yield stress are often relevant, especially in melt granulation.

There are a variety of adjustable process parameters covering the combined collection of agglomeration unit operations. Here, these have been compressed into a short list of key parameter groups. Certainly, fluidization is key to systems using binder sprays; shear rate is key to binder dispersion and agglomerate consolidation; and impact velocity affects consolidation and breakage. Material properties such as binder rheology, reaction rates and drying are sensitive to temperature.

Micro-scale transformations

The interaction between material properties and process parameters is illustrated on a series of simple transformation maps.

Dispersion

For high-shear mixers, the dispersion of a binder in a powder depends both on the binder viscosity and the applied shear rate of the process.[8] A combination of high shear and low viscosity will disperse the binder evenly throughout the powder mass (see **Figure 3**), while a viscous binder with insufficient shear results in a heterogeneous mixture of over-wet globules and dry powder.

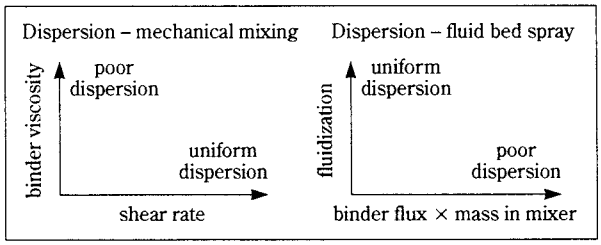

Fig. 3 Dispersion transformation map.

In top-spray fluid bed agglomeration, the dispersion of the binder depends on the spray coverage relative to the mass in mixer, as well as the turnover of the powder mass (i.e., fluidization). Here, the best dispersion is achieved with a large area of spray coverage and good fluidizaition.

Wetting and Binder Coverage

Wetting coverage refers to the local distribution of the binder on the particle surface. This depends on both the bulk dispersion of binder in the powder and the wetting chemistry between the binder and powder surface. Maximum binder coverage requires both good bulk dispersion and low binder-powder contact angle (**Fig. 4**).

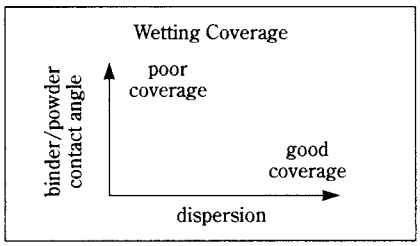

Fig. 4 Binder coverage depends on bulk binder dispersion (i.e., method of addition) as well as local wetting on the particle surface.

Interfacial Reaction and Drying

Some granulation systems involve reactions between a binder and a powder. For instance, an aqueous binder will hydrate starch excipients in a pharmaceutical granulation. In another example, granular detergents are made by an acid-base reaction between binder and powder. In such cases, reactions occur at the surface interface between the binder and powder; thus, the extent and rate of the reaction depends on the wetting coverage. Drying is somewhat analogous to this, except that the drying rate increases with increasing liquid-gas surface area. This occurs when the binder is thinly distributed over a large powder surface area. Both reaction and drying are very important transformations because they can significantly effect binder properties (e.g., viscosity, yield stress) and the effective binder loading (i.e., liquid saturation), which are key to the transformations of granule growth and consolidation (see **Figure 5**).

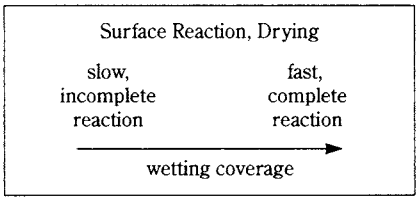

Fig. 5 Interface-limited reaction rates are limited by wetting coverage. This may also apply to drying in a fluid bed dryer/agglomerator.

Granule Growth

The primary factor controlling agglomerate growth is the relative binder loading level (**Fig. 6**). Kristensen, expressed this as a saturation ratio, relating the binder volume bridging between particles in an agglomerate to the total available pore and void space between particles.[9] The saturation ratio is increased by adding more binder and/or by consolidating agglomerates to reduce their internal porosity. The growth process depends on the success of particles sticking together upon collision. More growth occurs with increasing binder saturation, especially as the saturation approaches 100%. In the fully-saturated capillary state, rapid growth occurs by coalescence. Beyond 100% saturation, the particles are suspended in a continuous liquid phase and a slurry or over-wet mass results.

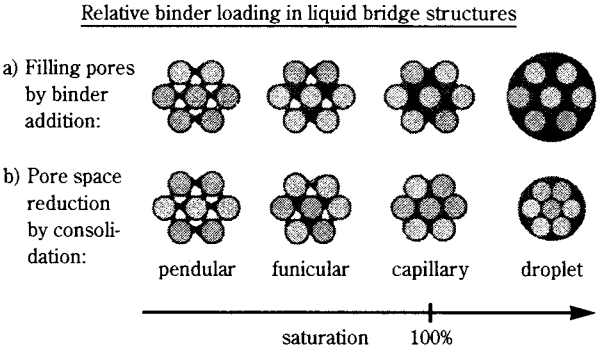

Fig. 6 Granular structure evolution with increasing binder saturation. Saturation increases by: a) additional binder loading and/or b) granular consolidation.

The growth process has been modeled using a force balance between colliding particles. Tardos and coworkers, developed the well-known Stokes Law criteria, which considers the force balance between colliding particles in an agglomeration process.[10] In this case, good binder coverage is assumed, and the success of the collision in producing an agglomerate depends on whether the collision energy is sufficiently dissipated by the viscous binder to prevent the elastic rebound from breaking the binder bridge between the particles. Further, it is assumed that the binder rheology is fluid enough to spontaneously form a liquid bridge on contact. The limitation to growth occurs when the viscous dissipation in the binder is not sufficient to absorb the elastic rebound energy of the collision, as with a low binder viscosity or high collision velocity (**Fig. 7a**). The Stokes crite-

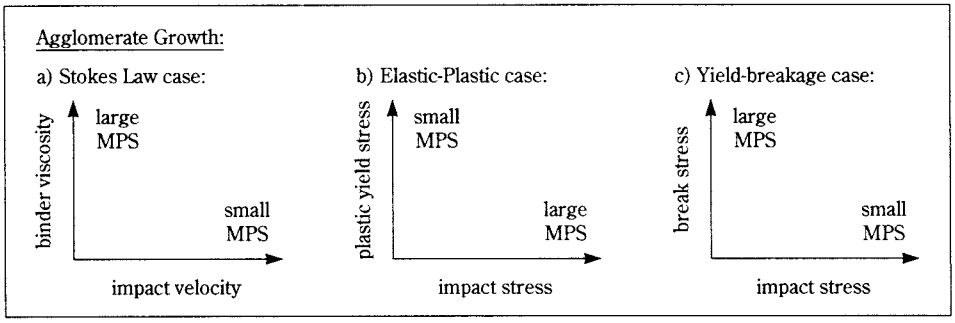

Fig. 7 Growth transformations analyzed in terms of force balances, where the extent of size growth is given by the mean particle size (MPS) of the granular distribution: a) Stokes Law case describes growth limited by viscous dissipation in binder layer; it assumes good binder coverage and the formation of liquid bridges on contact. b) In the elastic-plastic case, binder flow must be activated to form bridges between particles and/or embed particles into a binder droplet. To activate binder flow, the stress at impact must exceed the yield stress of the material (either binder or granular composite). In this case, it is assumed that the energy dissipation in plastic deformation of the material is large compared to the impact energy; therefore, no rebound occurs. c) The yield-deformation-breakage case describes an upper limit to growth based on granular breakage, where the impact shear stress increases with increasing granule size.

ria is expressed in the form of a viscous Stokes Number (St_v) which is the ratio of the collision energy to the energy of viscous dissipation (eq. 1). Here, $\tilde{a}$ is the reduced particle size in a collision of two particles (eq. 2), U is the collision velocity, ρ_p is particle density and η is the binder viscosity. The critical Stokes Number (St_v^*) accounts for binder loading in a system (eq. 3) where it is assumed that particles possess a solid core. Here e is the particle coefficient of restitution, h is the binder thickness at the collision surface and h_a is a characteristic length scale of surface asperities. The assumption of the existence of the solid core is only applicable in a limited number of cases (i.e., collision of very small, seed particles) and, in general, St_v^*, has to be computed numerically or measured experimentally. For conditions in which St_v is less than the critical value, St_v^*, collisions are successful and growth occurs. For $St_v > St_v^*$, viscous dissipation is insufficient and rebound occurs (**Fig. 8**).

$$St_v = \frac{8\rho_p U\tilde{a}}{9\eta} \tag{1}$$

$$\tilde{a}_v = \frac{a_1 \times a_2}{a_1 + a_2} \tag{2}$$

$$St_v^* = \left(1+\frac{1}{e}\right)\ln\left(\frac{h}{h_a}\right) \tag{3}$$

Binder rheology is not necessarily confined to Newtonian fluids. In fact, many binder systems exhibit yield-stress behavior. Examples include binder solutions containing longer-chain polymers, especially when the local concentration of the polymer on the particle surface increases due to water evaporation or hydration with the particulate solid. In such cases, small collision velocities and/or short collision times may be insufficient to allow for substantial binder flow and liquid bridge formation; more forceful particle impacts may be required to induce agglomerate growth. The combination of a high binder yield stress and a low collision velocity results in low growth while a low yield stress and higher collision velocity results in more growth (**Fig. 7b**), as long as the net viscous dissipation is sufficient to prevent rebound, as described by the Stokes criteria. It is important to note that binder rheology *at the time of collision* is relevant to this analysis; this is not necessarily the same as the rheology of the starting binder material, measured before addition to the agglomeration process. One must consider other transformations that may alter the binder rheology after it is added to the granulation, such as drying and hydration. Kinetics of these transformations must be considered in processes where binder rheology changes simultaneously with agglomerate growth and consolidation.

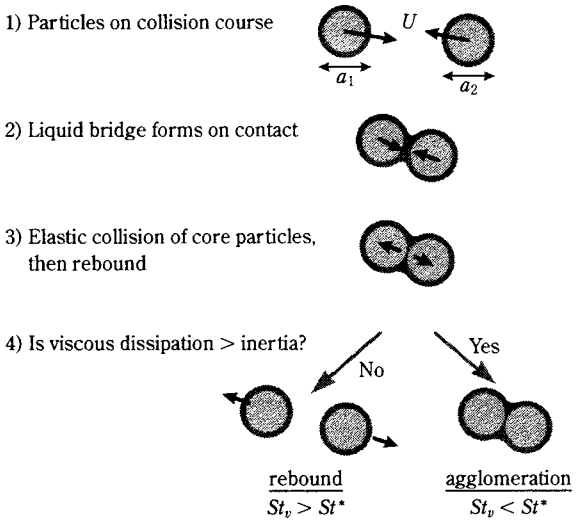

Fig. 8 Agglomeration sequence described by Stokes criteria.

Other examples of yield-stress binder rheology are found in melt agglomeration. Here, the binder is added as a powder or flake solid, mixed with the other powders, and then transformed into a binder by heating the entire mixture. In its' transformation from solid to liquid the binder typically passes through a critical semi-solid or glassy state where it exhibits a yield-stress rheology. In cases where the binder solids are larger in size than the other powders, melt-agglomeration may proceed according to an immersion mechanism, where the finer solids are embedded into the semi-solid binder particle.[11] The yield behavior of the binder, as measured by the thermo-mechanical analysis, is critical to the onset of growth.[12]

Granular deformation leading to coalescence is a well documented growth mechanism.[8,13,14] In coalescence, colliding granules stick together if the collision force is sufficient to plastically deform the granules, increasing the zone of contact, and consolidate the granular microstructures to the extent that enough binder is expressed into the contact zone (**Fig. 9**). Iveson and Litster recently proposed a granular growth regime map that shows increasingly rapid growth with increasing deformation at relatively high binder loading.[15] Assuming that there is enough fluid binder within the granular microstructure to hold the deformed parts together and prevent fracture, then growth will occur. Although rebound will occur if the collision is not of sufficient energy to induce elastic to plastic deformation, once the plastic yield stress is exceeded, the energy absorbed is typically quite high compared to the collision energy, minimizing the chance of an elastic rebound to break the formed bridge. Thus, the key transformation is the deformation of the granular microstructure and the flow of capillary binder to the contact zone, where the coalescence bridge is formed. Iveson and Litster describe this deformation propensity in terms of a deformation number (De), where Y_g is the granule dynamic yield stress, ρ_p is the granule density and U is a characteristic collision velocity for the granulator (eq. 4).

$$De = \frac{\rho_p U^2}{Yg} \tag{4}$$

The key material parameters relate to the deformation of the composite granular microstructure; typically, this is measured as an apparent plastic yield stress of the granular material (**Fig. 7b**). In addition, there may be time-dependent properties that are relevant depending on the time scale of collisions associated with a given agglomeration process.

In terms of process control parameters and material properties, the elastic-plastic transformation map for coalescence (**Fig. 7b**) and the Stokes criteria map (**Fig. 7a**) appear to be in opposition; in case a, the limiting size decreases with increased agitation while case b shows increasing growth with higher agitation. Although the growth-control response to the process used to affect agitation (e.g., impeller speed, gas velocity, etc.) is not straightforward, the micro-scale analyses are not necessarily contradictory. In the case of elastic-plastic collisions leading to coalescence, consider that the critical Stokes Number (St_v^*, eq. 3) accounts for binder loading in terms of the binder thickness at the zone of contact. During plastic deformation and microstructure consolidation, the binder thickness in the contact zone, h, substantially increases, thereby increasing the instantaneous value of St_v^* at the relevant interface. In addition, the coefficient of restitution, e, decreases on transforming from the elastic to plastic state, which also increases St_v^*. Thus, the force-balance analyses remain consistent when one treats St_v^* as a variable that can undergo instantaneous change during collisions involving the microstructural redistribution of binder and/or change in restitution due to elastic-plastic transition.

The yield-deformation-breakage case (**Fig. 7c**) considers the upper limit of growth in the process, beyond which breakage becomes dominant. To represent the process in mathematical terms, the present authors[19] proposed a "Stokes Number for Deformation-Breakage", St_{def}, as the ratio between the kinetic energy of a collision to the energy required for breakage (eq. 5), where τ_b is the shear stress required to

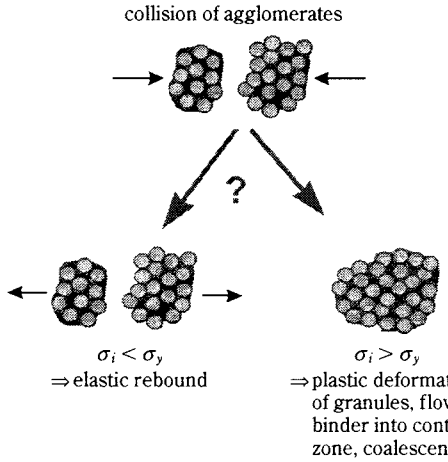

Fig. 9 Agglomerate growth by plastic deformation and coalescence. Plastic deformation occurs when the collision impact stress (σ_i) exceeds the plastic deformation yield stress of the composite granular material (σ_y). Plastic deformation of the granules increases the contact zone area. If sufficient binder flows into the contact zone, coalescence occurs.

deform and break the granule. Assuming that the local collision velocity is proportional to the shear rate and the particle size (eq. 6), and that the granule's yield strength is approximated by a Power-Law rheology model (eq. 7), a power-law relationship is predicted between the limiting size, a^*, and the shear rate in the mixer (eq. 8).

$$St_{def} = \frac{\rho_p U^2}{2\tau_b} \tag{5}$$

$$U \approx \dot{\gamma} \times a \tag{6}$$

$$\tau_b = k\dot{\gamma}^n \tag{7}$$

$$a^* = \dot{\gamma}^{((n/2)-1)} + c \tag{8}$$

Here, the force balance is between the collision force, the moment exerted on the granule, and the inherent *fracture stress* of the granular material. Large agglomerates are more prone to fracture than smaller ones for two reasons: 1) for a given impact force, the larger the size of the agglomerate, the greater the moment and the larger the stress that will be exerted on a weak point in the microstructure; and 2) as a composite material, larger agglomerates are more likely to contain a larger number of flaws through which cracks can propagate and cause fracture.

In terms of process control parameters and material properties, the elastic-plastic transformation map for coalescence (**Fig. 7b**) and the yield-breakage map (**Fig. 7c**) appear to be in opposition; in case b, the more growth occurs with increased agitation while in case c, the size limit decreases with higher agitation. Although both cases are driven by deformation of the granular materials, the product attribute result is very different. In the elastic-plastic deformation case, the granule is able to absorb all of the impact energy and dissipate it through plastic deformation and heat, resulting in coalescence. On the other hand, the material undergoing yield-breakage cannot absorb all the energy; it reaches a fracture point that limits its growth. [The ability of a material to absorb impact energy is related to its toughness – this is discussed further in the examples section.] The transition between plastic to breakage behavior can be strongly influenced by material properties such as moisture content and temperature. Thus, the relevant transformation map may change during a typical agglomeration process, e.g., progression in temperature and moisture level in a fluid-bed dryer-agglomerator may move the process from case 7b to 7c or viceversa.

Granule Consolidation

Agglomerate consolidation requires the plastic deformation of a granular structure into a more densely-packed structure. Plastic deformation occurs when the localized impact force exceeds the composite yield stress of the granule. Consolidation can increase the binder saturation ratio by reducing the void volume, without necessarily increasing the binder loading. As such, consolidation can trigger coalescence and growth when the saturation ratio reaches a critical point. Consolidation is integrally connected to the coalescence growth mechanism described in **Fig. 7b**.

If the yield stress occurs between an elastic and plastic regime, consolidation will occur. Alternatively, if the granule is brittle, the impact stress may exceed the fracture stress and attrition results. If the yield stress is significantly lower than the fracture stress, the granule will consolidate before it fractures. As a granular structure is consolidated, its strength typically increases.

The consolidation transformation is integral to the mechanism of growth coalescence by plastic deformation (see **Figure 10**). The linkage of consolidation and growth implies two feedback loops: 1) a small negative feedback to offset growth – as growth proceeds by coalescence, granular densification may cause an increase in the apparent yield stress, thereby limiting further coalescence; and 2) positive feedback which can potentially lead to runaway growth if consolidation increases binder saturation beyond the critical point (**Fig. 6b**) or if the yield stress is reduced as the result of the internal heat produced by the work of plastic deformation.

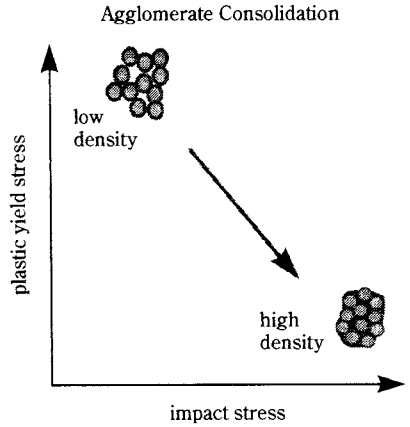

Fig. 10 Consolidation of granular microstructure and the elimination of intra-granular porosity.

Attrition

Granule attrition is a very complex subject. There are different mechanisms for surface breakage (i.e.,

erosion, abrasion) and particle breakage (fracture, shattering). These depend on material properties including elastic modulus, hardness and fracture toughness (i.e., the resistance to crack propagation), particle shape and impact conditions. In this illustration (**Figure 11**), a tough particle may survive a high level of impacts before it finally shatters, while a particle with a lower toughness and/or more irregular shape may progressively break into smaller fragments as impact stress is raised.

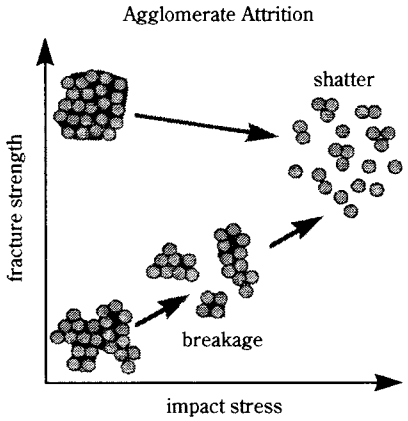

Fig. 11 Attrition of granules as a function of composite material toughness, flaw distribution (shape) and stress at impact. Note that shear stress is proportional to granular size.

Several important transformations may depend on single process parameters. For example, impeller speed in a vertical granulator affects binder dispersion (via fluidization and mixing, which scales with Froude number), consolidation and growth limit (via impact and breakage mechanisms, which scale with tip speed). Herein is a challenge for micro-based scale-up: one cannot increase the impeller diameter and keep both Froude Number and tip speed constant. When it is not possible to maintain similarity across all key transformations, it may be advisable to separate the transformations. For example, by staged processing in a batch unit or adding additional unit operations in a continuous process.

Scale-up examples using the micro approach

Several examples showing the effect of process parameters on product attributes are presented in this section. The examples use two different designs of agitated fluid beds. Both employ a fluid binder sprayed into a cylindrical gas-fluidized bed, equipped with a rotating arm or impeller mounted just above the gas distributor plate. The data by Watano et al.[16] are based on the Fuji-Paudal series of agitated fluid beds, which use an impeller with angled blade (**Fig. 12**);

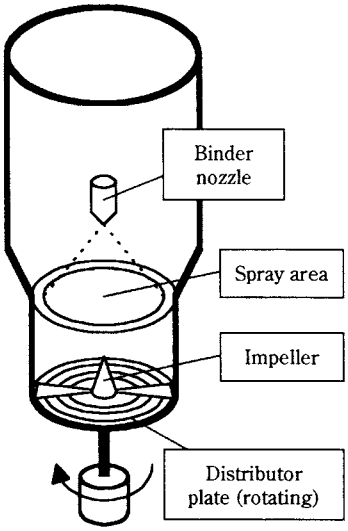

Fig. 12 Fuji-Paudal Agitated Fluid Bed Granulator, used by Watano et al.[16]

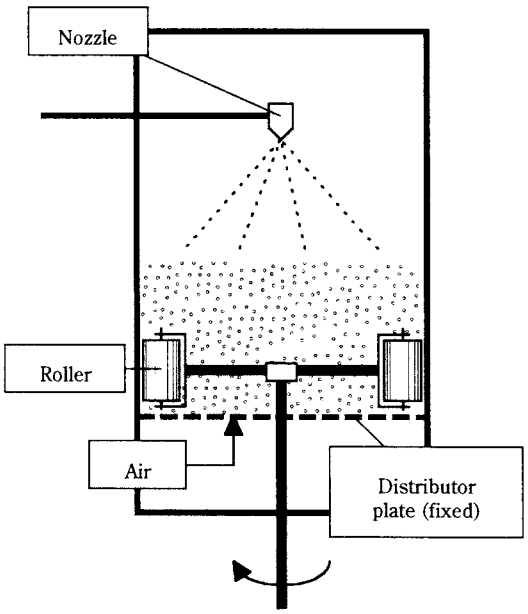

Fig. 13 Fluid Bed granulator with roller assembly, used by Dencs and Ormos[18]

these experiments were performed at three different scales. The data by Dencs and Ormos[17] were generated using a fluid bed with vertical rollers mounted on the ends of a rotating arm (**Fig. 13**); here only two scales were used.

Dispersion

In scale-up of a top-spray fluid bed agglomerator, it is hypothesized that the dispersion of the binder in the particle will be reflected in the product size distribution. If all particles contain an equal fraction of binder, then their physical properties will be equivalent and their growth will be the same, resulting in a

narrow size distribution. On the other hand, a heterogeneous dispersion favors larger growth of the more saturated granules and more limited growth of the binder-starved granules, resulting in a broader product distribution.

The link between dispersion and product size distribution is shown in the work of Watano et al. on the scale-up of agitated fluid bed agglomerators.[16] As the mixer scale increases, the spray surface area relative to the powder mass decreases. Experiments were done at different fluidization velocities for the different scales. The large-scale mixer at low fluidization velocity has the weakest dispersion, while the small scale mixer at high fluidization has the best. Analysis of the data (**Fig. 14**) show a clear trend between dispersion and the breadth of the granule size distribution, measured as the geometric standard deviation of the size distribution.[19]

Figure 14 illustrates one of the challenges in scale-up: it can be difficult to maintain the same degree of binder-powder dispersion on scaling up to larger batch mixers. This occurs because of increasing gradients in the shear rate within the mixer, as well as by the above spray area argument. An approach to correcting this problem is to reduce the spray flow rate in order to maintain the same flux/volume ratio. In this case, however, drying can have a significant complicating effect; a slower rate of binder addition with concurrent drying may not produce sufficient granule saturation for stable growth.

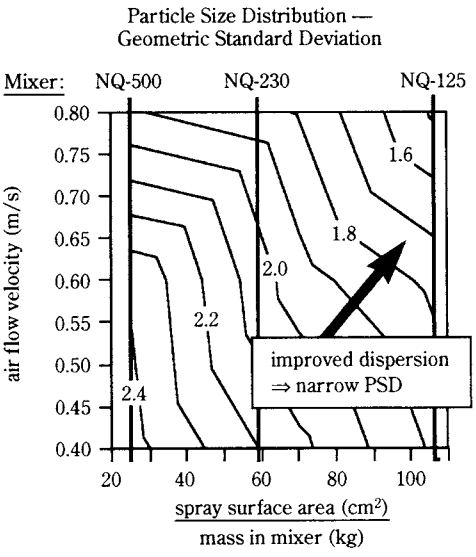

	Mixer Type		
	NQ-125	NQ-230	NQ-500
Powder feed (kg)	0.36	2.23	22.9
Spray area (cm²)	38.5	132.7	594
Spray area/Feed	107	60	26

Fig. 14 Experimental data[16] and analysis:[19] Breadth of particle size distribution (geometric standard deviation) of granules made in agitated fluid bed, as a function of spray area/product mass and fluidization in the bed. The distribution narrows as the spray is more uniformly applied to the mass of powder and the powder is more actively fluidized to the spray surface.

Growth with Yield-Deformation-Breakage Limit

To compare the results of Watano et al. to the Stokes analysis for breakage-limited growth, we use the theoretical result in equation (8). In the case of the Fuji-Paudal equipment, the maximum shear rate in the mixer is assumed to be proportional to the impeller tip speed. Substituting into the equation for critical particle size, a^*, gives a power-law relationship between the critical size and tip speed. The experimental data include median size (D_{50}) as a function of varying impeller speed at three independent gas fluidization velocities (U_f=0.4, 0.6, 0.8 m/s) at three machine scales (D=125, 230 and 500 mm); the data are given in **Figure 15**. The analytical expression predicts the limit to growth as a function of tip speed. This effect is counteracted somewhat by increased fluidization gas velocity which cushions granules from the impact of the impeller. Although the regression analysis in **Figure 15** is based on the absolute gas velocity, the excess fluidization velocity is probably the more relevant parameter.

Based on the slope of −0.25 on the log-log plot (see **Fig. 15**), a flow index value, n=1.5 is calculated. This corresponds to a shear-thickening behavior, i.e., the

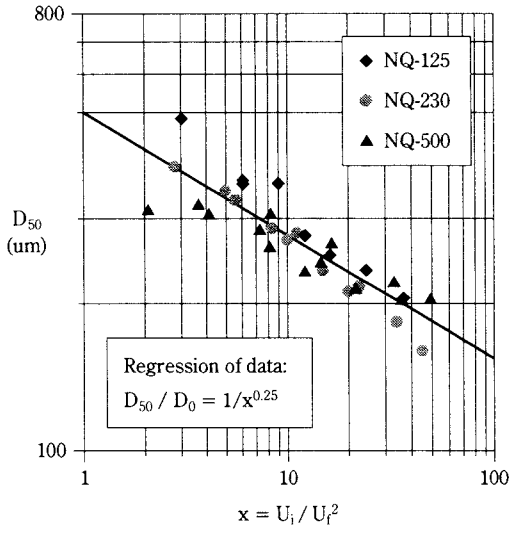

Fig. 15 Experimental data[16] and analysis:[19] Agglomeration of Lactose and Corn Starch with HPC and Water in an Agitated Fluidized Bed. Median agglomerate size is limited by shear rate (impeller tip speed) over three different mixer scales.

granule becomes tougher and more resistant to deformation as it is consolidated. The most important conclusion is that the slope and intercept take approximately the same value for the three different size granulators operated under different conditions.

Data by Dencs[17] show a similar trend, although the raw data show more variation than the Watano example (**Fig. 16a**). Note that several of the raw data sets appear to plateau at high values of rotational speed (see series with "vary N"). It is hypothesized that the actual shear rate in the roller gap starts to plateau at higher rotational speeds due to slip between the roller and the wall, caused by increased rotation of the rollers (**Fig. 13**) and/or product bypass of rollers at higher degrees of fluidization in the bed. Assuming that slip is proportional to fluidization, i.e., Froude Number (eq. 9), a modified shear-rate was calculated using the slip function, S, where Fr^* is a critical Froude Number for the slip function decay. The data collapse more tightly to the slip-corrected shear rate, using $Fr^*=0.17$ (**Fig. 16b**). However, the data from the sucrose experiments done in different diameter mixers do not fall exactly onto the same line; although their slopes are the same, the intercept for the larger diameter mixer is shifted higher than that of the smaller mixer. The difference in the intercept indicates that we lack some necessary element of a micro-scale model for the growth-limit in the roller-agitated bed. This is probably due to differences in flow patterns of the different scale mixers. With the fixed distributor plate design, the product mass in the larger diameter bed does not have as much interaction with the rollers at the perimeter compared to the smaller diameter bed. On the other hand, the slope (i.e., the shear-thickening exponent) is the same at both scales, indicating that the effect of material properties is the same across scales.

$$S = \frac{Fr^*}{Fr} \times \left(1 - \exp\left(-\frac{Fr}{Fr^*}\right)\right) \tag{9}$$

The Watano and Dencs data are summarized in terms of the power-law exponent in the rheological model. All appear to be shear thickening (**Table 1**). It is hypothesized that the apparent shear thickening is related to the strengthening of the granules as they are consolidated and compressed to a higher density. The value of the exponent may be a useful material-dependent index for agglomeration processing.

Consolidation

The experimental data of Watano et al. also support a micro-scale analytical treatment of granule consolidation. Here, the consolidation of a granule is approximated in terms of the Stokes Analysis, originally as reported by Ennis et al.[10] and modified here using the deformation criteria.[19]

The previous analysis of the Watano data found that the granule strength showed a power law behavior with $n=1.5$ (see **Table 1**). Combining this with the assumption of shear rate in proportion with tip speed, predicts that the consolidation should scale with square root of tip speed. Again, we find a good corre-

Table 1 Summary of power-law exponents for rheological models used in yield-breakage analysis.

Composition	n
Lactose and Corn Starch with HPC and Water (Watano et al.)	1.50
Sucrose and Water (Dencs)	1.56
Zinc Sulfate (Dencs)	1.80

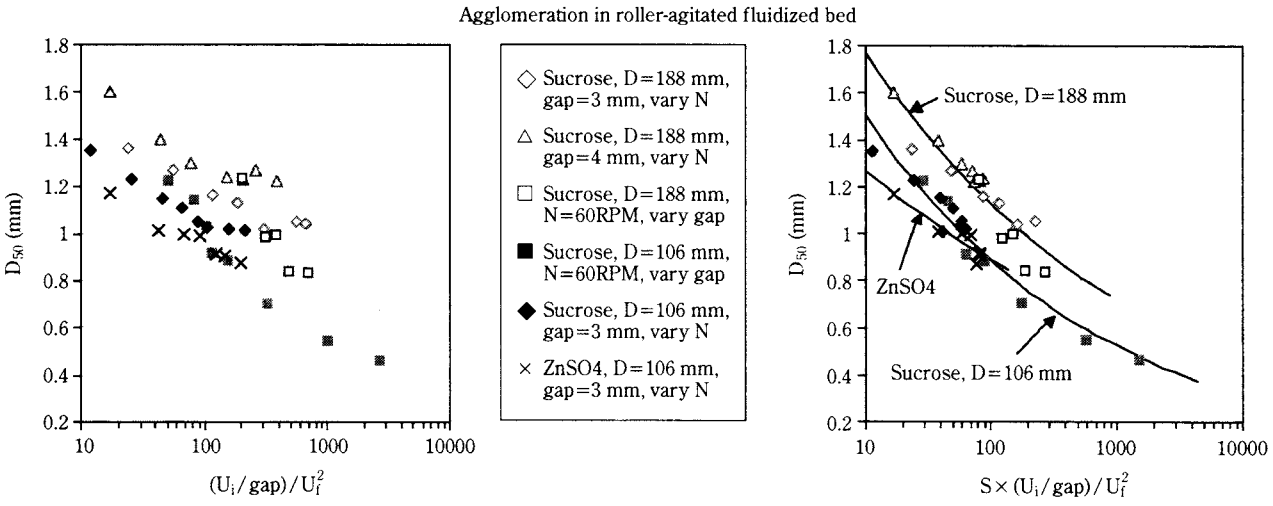

Fig. 16 Experimental data:[17] Agglomeration in Roller-Agitated Fluidized Beds with varying bed diameter, roller speed and roller gap: a) raw data of median granule size (D_{50}) versus calculated shear rate; b) data with slip function correction applied to shear rate calculation.

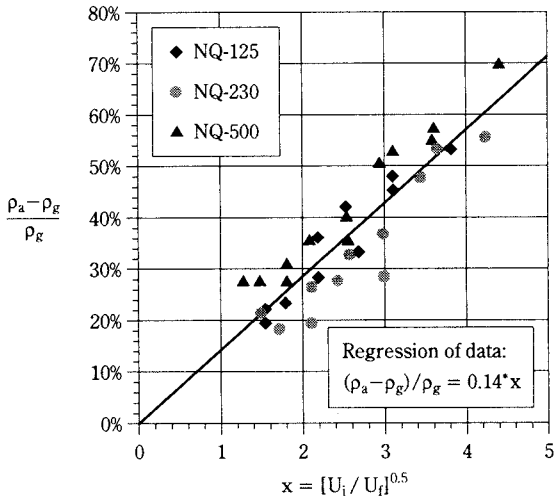

Fig. 17 Experimental data[16] and analysis:[19] Relative granule consolidation, $(\rho_a-\rho_g)/\rho_a$, versus impeller tip speed, U_i, and gas fluidization velocity, U_f, at three equipment scales.

lation between the experimental data and the analytical prediction (**Fig. 17**).

Conclusion

These examples show the potential usefulness of both macro and micro-scale approaches in predicting scale-up of agglomeration processes. With either approach, critical transformations depend on interactions between the process and material properties. Key material properties must be considered in all relevant states, including intermediate binder-powder mixtures. The examples discussed in this paper show the importance of identifying key properties and their in-situ measurement.

Scale-up is complicated by the many product transformations that may occur simultaneously in agglomeration processes. Although transformations may overlap and feedback among each other, they can be modeled discretely. Deeper understanding of discrete transformations lends insight to the fundamental mechanisms affecting the product attributes. Ideally, scale-up based on product attributes should be done by maintaining similarity across all transformations effecting all key product attributes. However, when it is not possible to maintain similarity across all transformations within a given unit operation, it may be advisable to separate the transformations, for example, by staged processing in a batch unit or adding additional unit operations for specific transformations in a continuous process.

Transformations depend on interactions between the process and material properties. Scale-up is often complicated because process parameters may effect more than one transformation. Additional complexity is introduced by the requirement to consider material properties in all relevant states, including intermediate binder-powder mixtures and local temperature conditions. To move ahead, we need to continue to link micro-scale analysis with key product transformations. Sorting out the complexities of *in-situ* material property transformations requires continued progress in on-line monitoring of process-parameters and material properties. This expanded capability of materials characterization is important for both micro-scale and macro-scale approaches.

Acknowledgements

The authors would like to thank Dr. Bela Dencs from the Research Institute for Chemical Engineering of the Pannon University of Agricultural Sciences in Veszprem, Hungary for the data in **Figure 16** and for fruitful discussions on the topic of granulation; collaboration with Dr. Dencs was partially supported by the US-Hungarian Joint Fund under project JFNo 593/96. We also appreciate the fruitful discussions with Dr. Satoru Watano from Osaka Prefecture University. The help of Dr. I.M. Khan and Mr. I. Talu from CCNY in performing some related experiments is also appreciated.

References

1) S. Watano and K. Miyanami, "Measurement and Control of Granule Growth in Fluidized Bed Granulation by a Newly Developed Image Processing System," World Congress on Particle Technology 3, Proceedings (1998).
2) S. Maronga and P. Wnukowski, "Establishing Temperature and Humidity Profiles in Fluidized Bed Particulate Coating," *Powder Technol.*, 94 (1997)
3) P.R Mort, "Dimensional Analysis of Agglomeration: Scale-up using Transformations," World Congress on Particle Technology 3, Proceedings (1998).
4) M. Landin, P. York, M.J. Cliff, R.C. Rowe and A.J. Wigmore, "Scale up of a pharmaceutical granulation in two production scale fixed bowl mixer-granulators," *Int. J. Pharm.*, 133 (1996).
5) P. York, Personal communication (June, 1997).
6) A. Faure, I.M. Grimsey, P. York, M.J. Cliff and R.C. Rowe, "Mixer Torque Rheometry: Relationships between Wet Mass Consistency in Pharmaceutical Wet Granulation Processes and Subsequent Dry Granule Properties," World Congress on Particle Technology 3, Proceedings (1998).
7) M.J. Cliff, "Granulation End Point and Automated Process Control of Mixer-Granulators," *Pharm. Tech.*, 112 (1990).
8) T. Schaefer and C. Mathiesen, "Melt pelletization in a

high shear mixer. VII. Effects of binder viscosity," *Int. J. Pharm.*, 139 (1996) 125.
9) H.G. Kristensen, "Particle Agglomeration," in Advances in Pharmaceutical Science (1995).
10) B.J. Ennis, G.I. Tardos and R. Pfeffer, "A microlevel-based characterization of granulation phenomena," *Powder Technology*, 65 (1991).
11) T. Schaefer and C. Mathiesen, "Melt pelletization in a high shear mixer. IX. Effects of binder particle size," *Int. J. Pharm.*, 139 (1996).
12) P.R Mort and R.E. Riman, "Hierarchically Ordered Particle Mixtures by Thermally-Triggered Granulation," *Kona*, 12 (1994).
13) H.G. Kristensen, P. Holm and T. Schaefer, "Granulation in High-Speed Mixers, Part VI. Effects of Process Conditions on Power Consumption and Granule Growth," *Powder Technol.*, 43 (1985) 225.
14) S.M. Iveson, J.D. Litster and B.J. Ennis, "Fundamental studies of granule consolidation, Part 1: Effects of binder content and binder viscosity", *Powder Technol.*, 88 (1996) 15.
15) S.M. Iveson and J.D. Litster, "Growth Regime Map for Liquid-Bound Granules," *AIChE Journal*, 44(7) (1998).
16) S. Watano, Y. Sato, K. Miyanami and T. Murakami, "Scale up of Agitation Fluidized Bed Granulation, Parts I-IV," *Chem. Pharm. Bull.* 43(7), (1995).
17) B. Dencs, Personal communication (April, 1998).
18) B. Dencs and Z. Ormos, "Particle size control in a fluidized bed spray-dryer and granulator during recovery of solids from liquids," *Hungarian Journal of Industrial Chemistry, Veszprem*, 21 (1993).
19) G.I. Tardos, M. Kahn and P.R Mort, "Critical parameters and limiting conditions in binder granulation of fine powders," *Powder Technology*, 94 (1997).

Author's short biography

Paul R Mort

Paul Mort is a Senior Engineer with the Procter & Gamble Company in Cincinnati, Ohio. His work is focused on Particle Technology, including agglomeration of powders for consumer products. He received a BS degree in Urban Planning from M.I.T. in 1978. Later, he returned to academia and earned a Ph.D. in Ceramic Science and Engineering from Rutgers University in 1993.
Dr. Mort is currently the chair of Particle Formation area in IFPRI (International Fine Particle Research Institute), and is active in sponsoring linkages between industry and academia. He has published a number of papers on topics relevant to Powder Technology including agglomeration, mixing, solid state reactivity, compaction and computer modeling of particulate processes.

Gabriel I. Tardos

Dr. G. Tardos received his early engineering education in Romania. He emigrated to Israel in 1973 and there continued his education and received a Ph.D. degree in Mechanical Engineering in 1978. He then moved to the U.S.A. and has dedicated his time to teaching and research in the Department of Chemical Engineering at the City University of New York where he is a Professor since 1979. He served as Chair of the department from 1987 to 1990.
Professor Tardos has more than 25 years experience in the fields of Particle Technology and Fluid-Particle systems. He spent five years doing research in industry on such topics as coal powder transport and burning, electrostatic precipitation and heat transfer. At CCNY, since 1978, he did research on filtration in granular and fibrous filters, fluidization, powder storage and transport, granulation, electrostatic effects and pneumatic conveying. He has published more than fifty papers on these subjects in major national and international journals and wrote several chapters in books related to Powder Technology.
Dr. Tardos is involved in promoting the development of Powder Science in industry and academia and was the first to introduce the subject into an undergraduate Chemical Engineering curriculum in the US. He is at present in the process of publishing an undergraduate/graduate textbook in Powder Science and Technology.

A Technical Review of the Proceedings of the '97 Fine Powder Processing Technology Conference†

Raj K. Rajamani and Luis A.C. Klujszo
University of Utah
*Department of Metallurgical Engineering**

1. Introduction

Powder processing technology is of interest to a variety of industries including among others chemical, pharmaceutical, food, ceramics, metals, and minerals. Powder processing alone is pushing the envelope of new technologies in a significant manner. Modern materials, nanoparticles, and aerosols are a few examples that seem to pave the way for emerging technologies. Given the importance of this field, Hosokawa Micron Powder Technologies Inc. in conjunction with the Pennsylvania State University put together a conference on fine powder processing technology. The meeting was held in August 1997 at the Pennsylvania State University's conference center. It was organized by Prof. Richard Hogg of PSU and Dr. C. C. Huang of Hosokawa Micron Powder Systems and well attended by engineering professionals from the industry, plants, consulting groups, academia, and sales groups.

The broad spectrum of fine particle processing was touched upon by speakers at the conference, which included particle characterization, grinding, size classification, agglomeration, flocculation, powder mixing, powder flow, rheology, particle deposition, particle compaction, and slurry flow. A total of 44 scientific articles were presented.

In this manuscript, we have succinctly written the essential content of each paper presented at the conference. So, the reader if interested in further information can go directly to the original article. The reference list at the end of this manuscript gives the proper titles and respective authors. The subject matter for the sake of this technical review is divided into eight different categories as follows: (1) grinding systems, (2) grinding mechanisms and processes, (3) powder production and synthesis, (4) particle characterization, (5) particle classification, (6) agglomeration, (7) powder mixing, and (8) powder flow, rheology, and consolidation.

* 135 South 1460 East Room 412, Salt Lake City, Utah, 84112, USA
Fax: +1 801 581 4937
† Received July 20, 1999

2. Proceedings Review

2.1 Grinding Systems

Schurr (1) opened the conference by presenting a view from the industry regarding the current stage of comminution technology and the important role universities play in developing and transferring new technologies to the process equipment industry. He posed a few challenging questions:

(a) State precise grindability criteria based on material properties so that a reliable process can be prescribed for size reduction.
(b) Understand the mechano-chemistry of polymer grinding so that desired polymer morphology can be arrived at via size reduction.
(c) Is there a classification device that can cut at micron sizes while maintaining high capacity?
(d) Can we develop a cost-effective size reduction process, which is able to produce narrow-sized, uncontaminated powders at nanosize scale to support an industrial production process?

Additionally, he suggested that industry and government agencies should work together to attract innovative engineers to work on such challenging problems. This opening address shows how the trends in industrial technology are beckoning the researchers to come up with an even better understanding of comminution, a field that is a century old now.

The long forgotten planetary mill seems to have made a reemergence. Designs of the past relied on meshing gears between the sun axis and planet axis and hence turned out to be cumbersome and noisy. Two newer designs were introduced at this conference. Rajamani et al. (2) describe a planetary mill in which the speed of the gyration shaft and canister shaft can be independently set. The continuous operation of this mill is implemented via rotary joints at the respective shafts. Gamblin (4) describes a planetary mill that is meant for continuous operation. While the cylinder or canister rotates about a sun axis, the inlet and outlet tubes maintain their stationary position on the canister. In other words, the net speed of the canister is zero with respect to the ground. This feature

facilitates inflow and outflow of slurry. Both mills clearly show that particles in the size range of 0.25−0.5 microns can be routinely produced, perhaps emphasizing the importance of planetary mills in the emerging nanoparticle production technology.

A complete description of the performance of a milling circuit by modeling has always been the fancy of both academic and industrial researchers as such models would be amenable for simulation later on. Gommeren et al. (3) attempt this difficult task for opposed jet mills. Furthermore, these authors use the selection function and breakage function concepts to model the mill. An understanding of internal classification and breakage developed via this detailed modeling is useful for tuning the performance of the jet mill as well as for the development of newer designs.

Becker, Kwade, and Schwedes (7) point out that variables such as circumferential velocity of discs, grinding bead size, and bead density principally alter the stress intensity on the particles caught between beads in stirred ball mills. Hence, they argue that the product size of these mills can be described with just two factors – stress intensity and specific energy. The stress intensity in turn depends on the elastic moduli of the beads and powder. The authors present a coherent picture of the performance of the stirred mill in terms of these two factors.

In a two part paper, Austin and Aplan (5, 6) analyze the Bond work index and Hardgrove grindability index as they apply to ball mills, roller-race mills, and high-pressure grinding roll mills. It is concluded that the index determined at a laboratory scale needs to be calibrated before applying it to full-scale plants. Hence, several indices instead of a lone one might lead to a more precise design. Furthermore, the accuracy of inter-conversion of one index to the other is not high.

2.2 Grinding Mechanisms and Processes

Huang (8) analyzes the motion of powder and hammers in a Mikro-pulverizer or hammer mill and shows that the general motion is affected by the way the feed is introduced into the mill. In a series of experiments, the author shows that the feeder type – either it be screw type, rotary type, or slot type – each has its own influence on the product fineness produced by this mill.

Mill power draft is the prime indicator of mill capacity and product fineness in ball mills. Yildirim, Cho, and Austin (9) show a power draft simulation model for a 2.8-m diameter silica flour-grinding mill based on power-draft data obtained in a 0.27-m laboratory batch mill. A comprehensive set of powder data is given for the laboratory mill.

More often than not, fine powder produced during grinding tends to agglomerate and so the size distribution of the product actually gets coarser. Kaya and Hogg (10) examine the production of fines in three distinct mills and conclude that the way to avoid agglomeration is to remove fines by maintaining a high circulation ratio through the classifier. They also show the shape differences produced by retention type mills and once-through mills.

Arastoopour et al. (11) show a curiously new device, an extruder, for the grinding of polyethylene and rubber. The key concept behind this device is the thin film of polyethylene caught between the screw and the barrel wall. These films are subjected to high compressive and shear forces, which cause unusual physical and chemical transformations. The authors exploit this phenomenon to bring about grinding of plastic materials, but the temperature rise in the extruder seems to be an impediment.

Weller, Gao, and Wilhelmsson (12) give valuable data on the media wear in a laboratory size stirred mill. They compare the wear of steel, ceramic natural material, glass, and ore media. The numerical data given in terms of total number of stirrer revolutions, energy input, and media size is most useful for a cost study.

Most grinding applications are conducted in wet mode, and hence a direct simulation approach to modeling grinding would be to use computational fluid dynamics. In such a scheme, the particles would be tracked throughout the mill allowing inter-particle collision and particle-wall collision forces to be readily computed. This is precisely what Theuerkauf, Schwedes, and Feise (13) tried. Using one-way-coupling of particles to the turbulent field, these authors predict the size distribution of particles for the ground product. Surprisingly, these distributions follow the expected trend even though there are some vagaries about the model for probability of breakage.

Hogg, Harrison, and Dynys (14) show that by simply examining the rate of disappearance of primary fragments one can identify the modes of breakage: catastrophic fracture, chipping, or simple fracture. This information could be used as a diagnostic tool for process evaluation.

It is well known that polyacrylic acid when added to solid suspension increases the fluidity due to the surfactant nature of the acid. Zheng, Harris, and Somasundaran (15) studied the grinding of high purity limestone with and without polyacrylic acid in a laboratory stirred mill. It is shown that a more than

100% increase in both specific surface and energy efficiency is achieved with the additive.

2.3 Powder Production and Synthesis

Fandrich (16), for the very first time, using the population balance model for particle bed breakage, shows the coupling between fracture and mineral liberation. Liberation refers to the release of valuable mineral grains from host particles. Hence, the differential breakage properties of the respective phases influence energy consumption and, consequently, liberation. The link between energy and liberation shown in this paper is a new branch off the well-known link between energy and particle size.

The influence of an impact mill and a bowl mill on the product fineness of coal grinding and the subsequent combustion of coal powder in a test combustion facility was shown by Maier and Hein (17). Using different coals ranging from low to high volatile, the authors proved that fine coal grinding could be effectively used to reduce the unburned carbon content in the flue ash as well as NO emissions.

A far off-field technology discussed in this volume is that by Meloy, Williams, and Whaley (18) who look at the problem of designing a coring device to be used on the 2001 Mars Lander project. The authors argue that this is not a trivial problem when considering the low gravity and the safety of the Martian Rover.

It is very rare one encounters the whole gamut of data from grinding to final strength of sintered ceramics in a single manuscript. Defying this rule, Wittmer and Holgesson (19) discuss the grinding of silicon nitride in a turbomill giving detailed data about media wear, mill torque, pulp viscosity, particle size, and specific and surface areas. The authors present properties of the ceramic cast before and after sintering, including density, four-point flexural strength, and fracture toughness.

The delicate processing of lead titanate via attrition milling, dispersing and pressing into monolithic devices is described by Kucera, Randall, Shrout, Kim and Hackenberger (20). Particular attention is paid to the dispersants that were pivotal in bringing about the enhanced properties of piezoelectric devices.

Likewise, Gao, Kear, and Seegopaul (21) describe a one-step reduction and carburization of ammonium paratungstate to tungstate carbide. The final powder exhibits a nanostructure of size 10 nm. Gas phase condensation reactions can be conducted in a variety of ways to form nanophase condensate of a particular structure. Skandan et al. (22) introduce a more efficient heat source called a flat flame combustor. The end process, called Low Pressure Flame Deposition is shown to deposit nanostructured films of SiO_2 and Al_2O_3 at a rapid rate.

A new technology known as Chemical Mechanical Polishing or Chemical Mechanical Planarization is used to flatten the films of metal deposited on semiconductor chip so that subsequent layers can be carefully laid on existing layers without encountering bleeding of one layer into another. Gandhi, Griffiths, and Pohl (23) give very critical insight into this process originally developed by IBM.

2.4 Particle Characterization

Kaye (24) reviews the developments in shape characterization techniques for irregularly shaped powders. A more thorough description becomes necessary for the case of irregular shapes, since particle size distributions originating from different measuring techniques (sieving, image analysis, optical difractometry, and aerosol spectrometry) will differ significantly. In recent years, the popularization of image analysis tools made it possible to better evaluate texture or shape of particles. For that purpose, techniques such as domain plotting, geometric signature waveform, edge (facet) measurement, and fractal dimensioning can all be employed to add an extra dimension to powder description.

Iacocca and German (25) compare in a statistical fashion the particle size distributions originating from several different techniques (i.e., laser diffraction with wet and dry dispersion, aerodynamic time-of-flight, electrical zone sensing, dynamic light scattering or photon correlation spectroscopy, and optical image analysis) for eight regularly shaped, metallic as well as non-metallic, powders. As long as proper dispersion is achieved (i.e., no agglomerates are present in the measuring system), all techniques are able to generate very consistent size distribution data. In other words, the authors emphasize that powder dispersion should be given more importance than the actual measuring technique.

2.5 Particle Classification

Galk and Peukert (26) discuss the operational characteristics and advantages of two impeller wheel air classifiers for the production of fine and ultrafine powders down to the submicron range. They are the MIKROCLASSIFIER CC and MIKROCUT MC. The former performs similarly but better for the coarser size ranges than standard cyclones with a range of classification between 7 and 100 microns. The latter handles ultrafine powders in the range of 0.3 to 20

microns. Very impressive circumferential velocity and centrifugal acceleration of the order of 100 m/sec and 15,000 g, respectively, are generated during MIKROCUT's operation, enabling the production of acrylate powders for paints (ρ=1100 kg/m^3) with top size of 20 microns. Mineral powders, with higher densities, such as limestone and talc can be produced with top sizes of the order of 2 microns.

In another paper (27), the same authors describe the production of powders with well-defined top sizes as well as narrow particle size distributions in impact mills containing internal classifiers known as air classifier mills. Powders with a well-defined top size are important for paint pigments, plastics, and the mineral industry in general, whereas narrow size distribution powders are sought for coatings and toners. Worldwide, air classifier mills are readily adopted due to their small compact design and flexibility to meet given specifications. They are suitable to operate in the range of 10 to 100 microns for throughputs up to 24 tph. The resulting size distribution is a function of the rotor and classifiers speeds, type of grinding elements, type of liner, height and type of classifier rotor, and air flow rate.

2.6 Agglomeration

Pietsch (28) starts by making a review of the effect of particle size on important characteristics of fine particulate solids either in single particle or bulk mass forms. Unfortunately, interactions of small particles with each other or other components in bulk masses cause a number of problems. Size enlargement can improve the behavior of bulk masses consisting of or containing small particles. When fine particulate solids are produced for the purpose of benefiting from specific characteristics of the single particles, size enlargement must be carried out such that these particle characteristics are maintained in the structure of the larger unit. By selecting the proper binding mechanism and granulation method, instant food products – which wet, disperse, and dissolve easily in liquids – can be tailor made for the respective application. The most commonly used methods for the manufacturing of instant products apply agglomeration techniques such as rewetting agglomeration, spray drying and agglomeration, a combination of the former and the latter, and press agglomeration.

Population balance is a conservation statement that accounts for all processes that give rise to the formation, growth, and disintegration of particles. It allows for the prediction of the time evolution of size distributions given that all processes that contribute to the growth and depletion of size classes in a particular system are known. A novel constant-N Monte Carlo method for the integration of population balances with agglomeration or fragmentation terms is presented by Tang and Matsoukas (29). In this method, the total number of particles in the simulation remains constant by refilling the particle array whenever vacancies are formed (agglomeration) or by removing particles from the array whenever new particles are formed (fragmentation), permitting indefinitely long times with modest computing power. The method is demonstrated by examining agglomeration and fragmentation models for which analytical solutions are available. Excellent agreement between simulation and theory is verified from the comparison between results yielded by the proposed Monte Carlo method and analytical solutions for a few ideal cases.

A model for continuous particle-liquid agglomeration using mixers of varying residence time distributions has been offered in the paper by Taylor (30). The target of this work is to gain a better knowledge of the effects of particle size distribution and agglomeration kinetics on agglomerate properties. The model is based upon mass balances and uses experimentally determined residence time distributions (through tracer techniques) curves. Validation efforts are undertaken by comparing model predictions with experimental data and literature reports. The model is able to show how the residence time distribution, step changes, and other agglomerate system dynamics affect agglomerate size distributions.

Superior storage, handling, and metering capabilities can be achieved in processes by using relatively large agglomerates instead of fine powders. A number of particle size enlargement techniques (i.e., agitation, pressure, thermal, or spray principles) are currently available. As requirements on shape and size distribution of particulates get more stringent, the need for developing novel approaches for agglomeration persists. Such an approach is presented by Atre et al. (31). The aqueous slurry process provides significant control over final particle size distribution, shape, porosity, and strength, and is of relevance to a number of areas including milling, die compaction, heterogeneous catalysis, and solid phase synthesis.

Flocculation is an important unit process for the removal of fine particulate matter and suspended solids from water and industrial domestic waste streams. The liquid suspension is treated with a chemical, the flocculant, that causes the particles to coagulate into flocs, which can be effectively removed

from the liquid by settling, filtration, or flotation. Application of bubble column technology in fine particle flocculation is a relatively new development. Both the rapid and quiescent mixing zones required for effective flocculation are combined in a properly designed and operated bubble column. The objective of the study by Ityokumbul et al. (32) is to determine the viability of such a bubble column flocculation process. The authors address the effect of flocculant addition time, gas velocity, and frother on the flocculation process in columns.

Wauters et al. (33) carried out the challenging task of modeling agglomeration with the population balance concept and verifying the model experimentally. A series of experiments were conducted in a horizontal high shear mixer to investigate the effect of binder liquid on granule growth. Three stages of growth were established: nucleation phase, compaction phase, and coalescence phase. The results of these experiments were then used for simulation attempts with a population balance equation for growth. The kinetics of growth was modeled with a volume-independent random kernel in the nucleation phase, zero growth in the compaction phase, and a volume-dependent Golovin kernel in the coalescence stage. Simulation results agreed fairly well with experiments, indicating the possibility of modeling granule growth in a high shear mixer with the population balance concept.

2.7 Powder Mixing

Ahmed and Shah (34) review the process of powder mixing aiming at the production of pharmaceutical solid dosage forms. Theories of powder mixing including random mixing, nonrandom mixing, ordered mixing, and total mixing are defined and discussed. By this same token, the authors make reference to the main mechanisms by which segregation of random powder mixes occurs: trajectory segregation, percolation segregation, and densification segregation. An analogous discussion is conducted for the mechanisms by which segregation of ordered mixes takes place: ordered unit segregation and constituent segregation. Finally, suggestions as how to improve powder mixing through enhancements of particle interaction in pharmaceutical mixes are listed.

Characterization of the physico-chemical properties of different pharmaceutical excipients becomes necessary in order to minimize the possibility of a batch of tablets or capsules failing a content uniformity test. The objective of this study (35) by the same authors is to seek optimum homogeneity and physical stability (resistance to segregation) for a low dose formulation by comparing the use of three distinct excipients: lactose anhydrous, starch 1500, and microcrystalline cellulose. Experimental determination of content uniformity and segregation profiles showed the best option being starch 1500 as a carrier excipient.

2.8 Powder Flow, Rheology, and Consolidation

Dr. Puri of Pennsylvania State University is a leading specialist in powder flow and rheology. In a series of three papers, Dr. Puri's research group presents their findings in that regard. In the first paper, the authors (36) use a novel, indigenously developed computer controlled shear cell (CCSC) to determine the flow properties of particulate materials by means of two tests: computer controlled Jenike test (CCJT) and dynamic yield locus test (DYLT). The importance of such an investigation lies in the fact that the flow of particulate materials during grain storage in bins is intimately related to the proper design of these structures. For instance, the Jenike method, usually employed for the design task, requires precise knowledge of flow properties of powders at low pressures. Using BCR limestone with a mean size of 3 microns as a test sample, yield loci for both CCJT and DYLT at low consolidation stresses (below 5 kPa) turned out to be close to each other and previously published values. This occurrence demonstrates the effectiveness of the computer controlled shear cell as a tool for conducting shear tests and gathering data for practical applications. In the second paper (37), five test materials (i.e., BCR limestone, glass fibers, ground silica, microcrystaline cellulose, and wheat flour) were submitted to the computer controlled dynamic yield locus tester (DYLT) and the computer controlled Jenike tester (CCJT). Flow parameters such as cohesion and angle of internal friction, which directly determine the flow of powders, were recorded at three consolidation stresses and statistically compared to each other and published values in order to assess the consistency of both methodologies. At 5% significance level and with few exceptions, both experimental techniques, CCJT and DYLT, were proven similar with regard to cohesion and angle of internal friction.

The determination of mechanical properties of powders is of vital importance when dealing with storage, flow, handling, and processing. Such properties are needed for the implementation of constitutive models to evaluate and predict the stress-strain behavior of powders as well as input for finite element methodology calculations concerning powder response to different levels of stress loads. The third paper of Dr.

Puri's group's series (38) deals with the development of a new medium pressure (up to 35 MPa) flexible boundary cubical triaxial tester capable of measuring stress-strain and time-dependent stress-strain behavior, shear strength, and material flow properties of powders over wide stress range and paths. In order to prove the applicability of this new device, hydrostatic triaxial compression tests were conducted in microcrystalline cellulose and KY3500 ceramic powders. The tester worked satisfactorily in terms of pressure control, loading rate control, loading boundary conditions, and deformation measurements during the experimental testing.

A fluidized bed containing powder and air should behave as a fluid. Quite often, a fluidized bed is used for pneumatic conveying of powder through a transport duct to achieve a uniform mass flow rate of material. If powders are cohesive, however, a uniform flow rate becomes difficult, since the flow of granules is intimately related to the degree of fluidization, which in turn, is a function of particle size and charge distribution of the powder. Cohesiveness, which prevents fluidization, may be produced by inter-particle electrostatic forces, which are generated by the injection of a gas during the fluidization process. The degree of fluidization or, inversely, cohesiveness will be clearly affected by these charging mechanisms. The main goal of the investigation by Mazumder et al. (39) is to experimentally quantify the influence of particle size distribution and charge of powders on fluidization and flow properties.

While researchers have studied the effects of filling methods on fundamental particulate properties and load distributions in large storage systems (bins and silos), there is a lack of quantitative analysis of the process of deposition of particulate materials into small storage systems such as dies. This study conducted by Dhanoa and Puri (40), still in very preliminary stages, deals with the effect of die filling methods and other related factors (i.e., die cross-section, die aspect ratio, and rate of die filling) on the spatial precompaction powder density distribution within the die volume. For such a task, a test apparatus to determine spatial in-situ fill density distribution in confined spaces, called real-time spatial particulate mass deposition tester, was designed, fabricated, and validated. After approval, it served the purpose of determining the influence of the above-mentioned filling and die related parameters on the fill density distribution of five powders: food (wheat flour), ceramic (alumina), metallic (silicon nitride), pharmaceutical (microcrystalline cellulose), and glass (beads). By analyzing the experimental data produced by the real-time spatial mass deposition device, the authors concluded that all these factors substantially affect the die filling density distributions.

The attributes of a generalized particulate mechanics model should include path dependence, physically meaningful parameters, three-dimensional anisotropic capability, time dependence, capability to predict cyclic loading response, and application of the model to industrial settings. Huang and Puri (41), after a careful literature review process, selected a modified Cam-clay (elastoplastic) model due to Desay and Siriwardane and an elasto-viscoplastic rheological model due to Adachi and Oka to work on here. Material parameter determination for these constitutive models (i.e., bulk modulus, loading index, and unloading index) for a microcrystalline cellulose (d_{50}=90 μm and ρ=1520 kg/m^3) at three different loading rates and two loading-unloading cycles was accomplished by means of the flexible boundary cubical triaxial tester. Finally, a three-dimensional finite element methodology is then employed to implement these models to determine powder compression characteristics.

In pressure filtration, cake porosity and resistance are determined by the fluid suspension. Therefore, rheology is of great importance to identify the state of aggregation of the suspension as well as to assess the effect of reagents on suspension properties. This paper by Sis and Chandler (42) evaluates the effectiveness of three surfactants (i.e., L-64, citric acid, and dicarboxylic acid) on the rheology and pressure filtration behavior of concentrated alumina slurries. The correlation between viscosity and pressure filtration turned out to be dependent on the type of reagent. An inverse relationship between specific cake resistance and viscosity was observed for slurries containing citric acid and dicarboxylic acid, but not those containing the nonionic L-64 block copolymer.

Reducing the amount of fat required in milk chocolate can make it more economical to produce and lower its caloric density, both very desirable factors. However, reduction in fat content to low levels may lead to a very high-viscosity product with poor texture. Fat fills the voids between the solid particles and reduces the resistance to the flow. The void volume in a packed bed of solids depends on the particle shape, size distribution (modality), and packing arrangement of the particles. For a given distribution of particles, the packing efficiency increases by adding solid particles of sizes corresponding to the sizes of the voids. Filling of these voids by smaller solid particles allows

for a higher amount of solids to be present per unit volume of the suspension and reduces the amount of space to be filled by the suspending medium (fat). Thus, the article by Mongia and Ziegler (43) address the effect of size distribution of suspended particles on milk chocolate flow properties. It is generally accepted that a decrease in particle size of suspended solids results in an increase in viscosity. Nevertheless, minimum viscosity for a particular volume of solids in suspension results when the particles are present in multimodal particle size distribution (higher packing efficiency is achieved). In order to elucidate all these claims, five milk chocolates with same composition but different particle distributions were produced and had their bulk densities and flow behavior parameters determined. Experimental results led the authors to the important conclusion that the viscosity of milk chocolate can be controlled by manipulating its particle size distribution. This feature can be applied industrially to produce lower viscosity with lower fat contents without compromising the flow properties of the chocolate.

Homogenization is a method for imparting high level of shearing forces and kinetic energy to mixes in order to disperse raw materials effectively. The objective of this article by Escaloni (44) is to illustrate a phenomenological design approach for a single orifice homogenizer required for optimal dispersion of oil and water emulsions. A flow solver called Flowplus, which follows finite element methodology, was used to solve the governing partial differential equations (i.e., fluid flow and heat transfer). The dependent flow variables were time-averaged and the resulting Reynolds stress components were accounted for by the isotropic Boussinesq approximation. Eddy viscosity and eddy conductivity were modeled by means of the standard κ-ε model. Four different orifice and plate configurations were simulated to discern the effects of the shapes on flow patterns and process variables. The use of velocity, stream function, shear, turbulent kinetic energy, and turbulent dissipation rate plots proved to be tremendously helpful to arrive at an optimized design for the homogenizer. The importance of the computational fluid dynamics modeling work lies in the fact that testing concepts before implementing the final design and manufacturing parts becomes just a matter of computer simulations, which brings about cost savings, while learning which properties should be adjusted.

3. Closing Remarks

The conference covered the spectrum of processes in powder production. Valuable information in the processes described above can be found in the original proceedings. Although there are many meetings held on the theme of nanoparticles, aerosols, and others, this conference fills a void – it brings together the front-end powder processing industry to share knowledge. A sequel to this important scientific meeting will be held at the same location in the year of 1999.

4. References

- FINE POWDER PROCESSING TECHNOLOGY PROCEEDINGS – Ed. Richard Hogg, Robert G. Cornwall, and C. C. Huang, Pennsylvania State University, 1998.

1) Schurr, G. A., "Comminution Technology Challenges – One View from Industry," pp. 3-9.
2) Rajamani, R. K., Ding, P., and Tillu, S. S., "Ultrafine Grinding in Planetary Mills," pp. 10-20.
3) Gommeren, H. J. C., Heitzmann, D. A., and Scarlett, B., "Prediction of Operating Ranges of Opposed Jet Mills Using Dynamic Modelling," pp. 21-27.
4) Gamblin, R. L., "Results with a High G Cyclomill," pp. 28-32.
5) Austin, L. G. and Aplan, F. F., "The Powder Technology of Standard Grinding Tests: Part I, Ball Milling and Roller-Race Milling," pp. 33-41.
6) Austin, L. G. and Aplan, F. F., "The Powder Technology of Standard Grinding Tests: Part II, High Pressure Roll Milling and Correlation of Grinding Indices," pp. 42-50.
7) Becker M., Kwade, A., and Schwedes, J., "Influence of Stress Intensity on the Comminution of Ceramics in Stirred Ball Mills," pp. 51-58.
8) Huang, C. C., "The Effect of Feeding Mechanism on the Grinding Efficiency of Pulverizers," pp. 61-68.
9) Yildirim, K., Cho, H., and Austin, L. G., "Mill Power for Smooth-Lined Mills as a Function of Media Type and Shape," pp. 69-77.
10) Kaya, E. and Hogg, R., "Control of Particle Characteristics in the Production of Fine Powder by Grinding," pp. 78-86.
11) Arastoopour, H., Riahi, A., Venerus, D., Bernstein, B., Schocke, D., and Bilgili, E., "Pulverization of Low Density Polyethylene and Rubber Under High Shear and Normal Forces," pp. 87-93.
12) Weller, K. R., Gao, M., and Wilhelmsson, B., "Media Wear in Stirred Milling," pp. 94-101.
13) Theuerkauf, J., Schwedes, J., and Feise, H. J., "Two Phase Flow Simulation and an Application for Comminution," pp. 102-109.
14) Hogg, R., Harrison, C., and Dynys, A., "The Effect of Particle Structure and Stress Application on Breakage Behavior in Fine Grinding," pp. 110-119.

15) Zheng, J., Harris, C. C., and Somasundaran, P., "Mechano-Chemical Interactions in the Use of Polyacrylic Acid as Grinding Aids in Fine Grinding in Stirred Media Mills," pp. 120-128.
16) Fandrich, R. G., "A Mineral Liberation Model for Confined Particle Bed Breakage," pp. 131-139.
17) Maier, H. and Hein, K. R. G., "The Effect of Coal Grinding to the Combustion in a Power Plant," pp. 140-147.
18) Meloy, T. P., Williams, M. C., and Whaley, D., "Comminution, Coring and the Martian Surface," pp. 148-155.
19) Wittmer, D. E. and Holgesson, P. M., "The Effect of Milling Media on Properties of Turbomilled Silicon Nitride Slurries," pp. 156-166.
20) Kucera, J. P., Randall, C. A., Shrout, T. R., Kim, N., and Hackenberger, W., "Ultrafine Particle Processing for Fine-Grain Piezoelectric Ceramics," pp. 167-172.
21) Gao, L., Kear, B. H., and Seegopaul, P., "Displacement Reaction Processing of Nanophase WC Powder," pp. 173-179.
22) Skandan, G., Glumac, N., Chen, Y. J., Cosandey, F., and Kear, B. H., "Chemical Vapor Condensation of Nanophase Oxide Powders and Films," pp. 180-188.
23) Gandhi, D. B., Griffiths, D. A., and Pohl, M. C., "Recent Developments in Fine Abrasives Used in Advanced Electronics Manufacturing," pp. 189-195.
24) Kaye, B. H., "New Developments in Shape Characterization Technology," pp. 199-206.
25) Iacocca, R. G. and German, R. M., "A Comparison of Particle Size Measuring Instruments Using Fine Metal and Ceramic Powders," pp. 207-216.
26) Galk, J. and Peukert, W., "Classification of Fine Powders," pp. 217-222.
27) Galk, J. and Peukert, W., "Production of Narrow Size Distributions in Air Classifier Mills," pp. 223-230.
28) Pietsch, W., "Agglomeration Techniques for the Manufacturing of Instant Granules from Fine Powder Mixtures," pp. 233-242.
29) Tang, Y. and Matsoukas, T., "A New Monte Carlo Method for Simulations of Agglomeration and Grinding," pp. 243-250.
30) Taylor, T., "Agglomerate Size Control in Continuous Systems," pp. 251-257.
31) Atre, S. V., Halls, S. D., Shivashankar, T. S., Thomas, J. A., and German, R. M., "A Novel Process for Particle Size Enlargement," pp. 258-264.
32) Ityokumbul, M. T., Ramani, D. V., and Kissel, M. M., "Bubble Column Flocculation of a Clay Suspension," pp. 265-272.
33) Wauters, P. A. L., Meesters, G. M. H., Pratsinis, S. E., and Scarlett, B., "Modeling Agglomeration in a High Shear Mixer," pp. 273-278.
34) Ahmed, H. and Shah, N., "Pharmaceutical Powder Mixing from Randomization to Homogenization," pp. 279-286.
35) Shah, N. and Ahmed, H., "Effect of Pharmaceutical Carrier Excipient Properties on Drug Homogeneity and Segregation Tendency of Low Dose Formulations," pp. 287-293.
36) Kandala, R. N. and Puri, V. M., "Measurement of Flow Properties of BCR Limestone at Low Pressures Using the Computer Controlled Shear Cell," pp. 297-304.
37) Duffy, S. P. and Puri, V. M., "Evaluation of the Computer Controlled Dynamic Yield Locus Tester," pp. 305-312.
38) Li, F. and Puri, V. M., "Development of a Medium Pressure Flexible Boundary Cubical Triaxial Tester for Measuring Mechanical Behavior of Particulate Materials," pp. 313-320.
39) Mazumder, M. K., Mountain, J. R., Wankum, D. L., Zheng, Q. J., Chasser, T., and Jones, D., "Fluidity and Flow Properties of Fine Powders," pp. 321-336.
40) Dhanoa, P. S. and Puri, V. M., "Experimental Analysis of Deposition of Particulate Materials into Confined Spaces," pp. 337-360.
41) Huang, L. and Puri, V. M., "Determination of Constitutive Model Parameters and Three-Dimensional Finite Element Formulation for Powder Compaction Process," pp. 361-368.
42) Sis, H. and Chandler, S., "Effect of Surface Modification on Flow Properties and Pressure Filtration of Alumina Slurries," pp. 369-376.
43) Mongia, G. and Ziegler, G. R., "Controlling the Flow Ability of Molten Milk Chocolate with Its Particle Size Distribution," pp. 377-384.
44) Escaloni, L., "Computational Fluid Dynamics of a Single Orifice Device Homogenizer," pp. 385-422.

Author's short biography

Raj K. Rajamani

Dr. Raj K. Rajamani earned B.S. and M.S. degrees in chemical engineering at Annamalai University, India and Indian Institute of Technology, Kanpur, India, respectively. Then, he studied metallurgical engineering for his Ph.D. at the University of Utah. Currently, he is a professor of metallurgical engineering at the University of Utah. His research interests include ultrafine particle production by comminution, simulation of charge motion in tumbling mills, and eddy current separation.

Luis Augusto Colembergue Klujszo

Dr. Luis Klujszo is currently a post-doctoral fellow in the Department of Metallurgical Engineering of the University of Utah conducting research on nanoparticle production. He received his B.S. in mining engineering (1990) and M.S. in metallurgical engineering (1993) from the Federal University of Rio Grande do Sul (UFRGS), Brazil, and his Ph.D. in metallurgical engineering (1998) from the University of Utah, USA. His research interests include mineral processing, application of computational fluid dynamics to separation processes, and production of particles in the submicron size range.

Review on the Vapour-Phase Synthesis of Aluminum Nitride Powder Using Thermal Plasmas†

A.C. Da Cruz[1,2] and R.J. Munz[1]

[1)] *Department of Chemical Engineering, Plasma Technology Research Centre (CRTP)**

[2)] *presently with the Division of Mechanics and Electricity, IPT***

Abstract

Production of high purity aluminum nitride powder which can be processed into electronic packages at a cost competitive with existing lower performance ceramic packages has promoted the development of many different synthesis methods. A survey of the synthesis of ultrafine AlN powders using thermal plasmas is presented. Laboratory scale experiments, applying inductively coupled and transferred-arc plasma systems, have been used to produce nanosize powders by vapour-phase reaction between aluminum vapour and ammonia, using a reduced number of steps. The specific surface area of the powders reported are in the 12 to 280 m^2/g range. Sinterability experiments have demonstrated that these powders can be compacted to full density at lower temperatures than powders produced by conventional methods.

1. Introduction

A noticeable progress has been made in the past few decades in the field of ceramic materials, based mainly on a better understanding of microstructure and its development during processing. Because of the key role that the starting material plays in the determination of the properties of the finished ceramic, this progress has been followed by a growing interest in the production of high quality ceramic powders [1], [2]. Many innovative powder synthesis methods have been proposed, addressing the fulfillment of requirements such as purity, particle size, particle size distribution, and particle morphology. One such method uses thermal plasma as the processing medium. The application of this technique to the production of powders of many different compositions has been demonstrated at the laboratory scale since the early 60's. Its most explored feature in these applications is the ability to carry out high temperature vapour phase reactions, which are followed by a fast quenching resulting in the formation of finely dispersed powders. Other highly valued features associated with the plasma synthesis are the reduced number of processing steps, and a clean processing environment that contributes to the production of high purity materials.

The application of thermal plasmas to the synthesis of refractory ceramic powders, which invariably require high temperature processing, is of particular interest. Ceramic powders such as oxides, carbides and nitrides have been successfully synthesized using this technique. Literature reviews on this subject were carried out by Hamblyn [3] (1975), Fauchais et al. [4] (1983), Akashi [5] (1987), and Kong and Lau [6] (1990). The plasma synthesis of aluminum nitride (AlN) has attracted a great deal of attention. Its current and future potential were reviewed by Sheppard [2] (1989), Mroz [7] (1993), and Knudsen [8] (1995). AlN synthesis methods were reviewed by Selvaduray and Sheet [9] (1993). AlN is a covalent ceramic that has a high thermal conductivity and good dielectric properties. It has a thermal expansion coefficient closely matching that of silicon. This unique combination of properties makes AlN especially useful as a substrate material for electronic packagings. Compared with conventional alumina (Al_2O_3) substrates, the high thermal conductivity of AlN provides a higher energy dissipation that allows the development of electronic packages with higher density of components. Because AlN exhibits high strength and high temperature stability associated with most non-oxide materials, a

* H3A 2B2, McGill University, Montreal, Quebec, Canada

** P.O. Box 0141-CEP 01064-970–São Paulo, S.P., Brazil

† Received July 20, 1999

variety of other applications also exist for AlN as structural ceramic [7]. Armour for aircraft and vehicles are currently the predominant structural application. High temperature applications involve AlN crucibles and hardware to process a wide variety of molten metals and salts. In metals like aluminum, AlN can be used to strengthen the matrix. In polymers, it can be used to increase stiffness, reduce the thermal expansion, or increase the thermal conductivity. Also, optical applications exist for AlN since it can be made translucent [10], or it can be added to alumina (Al_2O_3) to produce transparency in visible light [11].

It is recognized that AlN powder synthesis as well as its sintering procedure still need to be technologically and economically improved before these ceramics can be used to their full capability [7]. AlN powers are currently produced by two main processes: (a) the carbothermal reduction of alumina in the presence of nitrogen (N_2); and (b) the direct nitridation of Al powder. The major barriers to the large scale use of AlN are: the high cost of AlN powders [8]; and due to the presence of impurities, producing high thermal conductivity AlN is a major technological challenge [12]. Oxygen in the AlN lattice is considered the principal impurity responsible for lowering its thermal conductivity [7], [12].

Notwithstanding the large amount of research work in this field, scaling up of plasma reactors from the few grams/hr of lab scale experiments to the rates needed for industrial scale production is still a major problem. A technological barrier encountered in these developments is the limited availability of gas-phase metal precursors. The most commonly used reactants for plasma synthesis are solids which have to be evaporated. Another major obstacle is the still poor understanding of the mechanisms by which gas-to-condensed phase transition proceeds in these systems. In this respect, only more recently with the aid of numerical simulation, are the phenomena involving vapour phase nucleation and growth in these high temperature processes being better understood.

This paper presents a review of the research work that has been reported on the thermal plasma synthesis of AlN. It includes the most recent results on the developement of a two-stage transferred-arc reactor, and the results of the investigation of the sinterability of the ultrafine AlN powder produced by this method.

2. The thermal plasma synthesis

A gaseous plasma consists of a mixture of electrons, ions, neutral species in the ground state, excited species, and photons [13]. Overall, negative and positive charges in a plasma balance each other, to produce *quasi-neutrality*. Due to their small mass, electrons have a higher mobility and a natural tendency to have a higher temperature than ions and neutrals (heavy species). Thermal plasma is one type of plasma for which one of the basic conditions to be met is that the temperature of heavy particles approaches the temperature of electrons. The vapour synthesis of AlN using thermal plasmas has been studied by several workers. A summary of the experiments reported in the literature is given in **Table I**. Most of the research

Table I Summary of experimental results reported in the literature for the plasma synthesis of AlN.

Author(s)	Type of Plasma	Power (kW)	Plasma gas		Quenching gas (lpm)	SSA (m^2/g)	Particle size (nm)
			Comp.	Flow rate (lpm)			
Canteloup and Mocellin (1974)	RF	10	Ar	36	NH_3 10.5	220–260	7–8
Baba et al. (1987)	RF	20	Ar/N_2	42/18	NH_3 5~20	50–80	23–37
Wehling et al. (1991)	RF	13	Ar	40	$N_2/NH_3/Ar$ 75	115	30
Etemadi (1991)	DC-TA	2	Ar/N_2 Ar/NH_3	18	Not used	N.A.	30
Godin et al. (1991)	DC-TA	350	Ar/NH_3 NH_3	N.A.	Not used	N.A.	<200
Ageorges et al (1997)	DC-TA	69	N_2/Ar	80/25	NH_3 (100)	12–16	135
Moura and Munz (1997)	DC-TA	8	Ar	15	NH_3/Ar 2/3.6	80–100	23
Da Cruz and Munz (1997)	DC-TA	8.3–12.5	Ar or Ar/H_2	20 18/2	NH_3/Ar (2/2 to 7)	38–270	7–46

RF = Radio frequency induction coupled plasma.
DC-TA = Direct current transferred-arc.
(1) calculated based on reported data.

has been carried out using Al metal solid precursor, either as a powder or as pieces which are melted and evaporated in the plasma and reacted with nitrogen originating from nitrogen gas or ammonia (NH_3). Because of the presence of free charge carriers, in contrast to an ordinary gas, a plasma is electrically conducting. Radio frequency inductively coupled (RF) and transferred-arc plasmas are the two forms of plasma generation that have been most used in vapour phase synthesis applications. A RF plasma, schematically shown in **Figure 1**, operates at frequencies ranging from kHz to MHz. These are electrodeless devices which provide a very clean environment suitable for the production of high purity materials. However, RF plasma generators are usually limited to a few hundred kilowatts of power, and their thermal efficiency rarely exceeds 45%. A free-burning high intensity transferred-arc, schematically shown in **Figure 2**, which most commonly operates on direct current, is one of the simplest forms of thermal plasma generation. Because of their high energy transfer to the anode, transferred-arcs can be efficiently used to melt and evaporate clean metal. Also, transferred-arc systems can be easily scaled up to more than 1 MW with an energy efficiency of more than 85%.

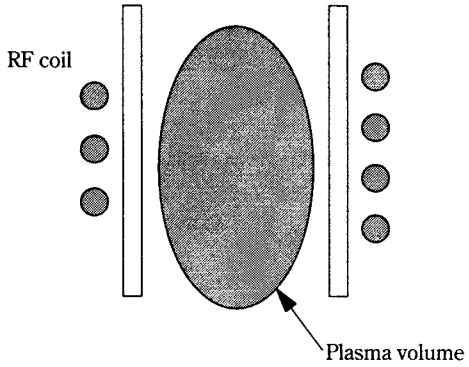

Fig. 1 Radio frequency (RF) plasma.

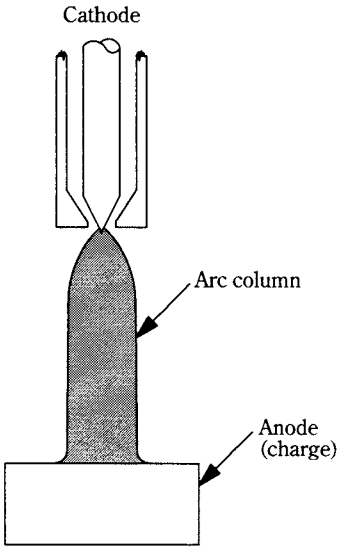

Fig. 2 Transferred-arc plasma.

The use of RF plasma for the preparation of AlN powder from Al powder was reported by Canteloup and Mocellin [14] (1974) and Wehling et al. [15] (1991). A common feature of these two works was the injection of aluminum powder above the fire ball where it evaporated in a non nitriding atmosphere. The nitriding reaction was carried out in a subsequent step, with the injection of NH_3 or NH_3/N_2 mixture in the tail flame. In the reactor used by Canteloup and Mocellin, NH_3 was injected in the tail flame and the reaction products were rapidly quenched. In the reactor used by Wehling et al., NH_3 was also injected in the tail flame, but quenching was not as fast since the reacting mixture flowed in a tube until it was quenched in a large chamber. The faster cooling seems to be the reason why the surface area of the powder produced in the first case was about twice as great. Baba et al. [16] (1987) prepared AlN ultrafine powder using a RF plasma, but used pieces of Al placed on a water cooled copper support which was lifted into the tail flame. Ammonia was injected between the RF coil and the aluminum support.

The use of transferred-arc plasma in nitrogen atmosphere (formed by N_2 or a mixture of N_2 and NH_3) was reported by Etemadi [17] (1991), Godin et al. [18] (1991), and Ageorges et al. [19], [20] (1991, 1993), with the anode formed by an aluminum bath. The AlN produced in these experiments was reported to range from ultrafine particles, collected from the exhaust gases and reactor walls, to large crystal lumps which grew around the anode. Vissokov et al. [21] (1981, 1983) produced ultrafine AlN powder by injecting Al powder near the anode attachment of an electric arc, using a mixture of argon and nitrogen as the plasma forming gas. Cusick (1989) [22] produced AlN using an off-axis transferred-arc reactor with aluminum fed by a consumable anode and N_2 used as plasma gas and nitriding agent. The powder produced by Cusick was reported to be formed of Al and AlN particles. Ageorges et al. [20] reported the use of two different arc devices: (a) transferred-arc on aluminum in N_2 and N_2/NH_3 atmosphere; and (b) cathode and anode arcs coupled together above the aluminum bath. In the second case, NH_3 was inject through a central tube placed above the junction of two arcs.

A great scatter for the particle sizes reported by different authors is observed in the data shown in **Table I**. In the transferred-arc experiments, for which

the metal evaporation and reaction were carried out in the same chamber, longer residence times at high temperatures (as opposed to reaction followed by fast quenching reported for most of the RF systems), and possibly higher concentrations of metal vapour, were available. Both factors might have contributed to producing larger particles than in the RF experiments. Also, because of the nitriding nature of the plasma gas, in these transferred-arc systems, reaction occurred on the surface of the aluminum bath forming undesirable lumps of AlN. Accordingly, the geometry reported by Ageorges et al. for the two arcs coupled above the aluminum bath, allowed for a great deal of recirculation in the plasma chamber. This possibly contributed to the formation of the larger particle sizes reported. Etemadi [17], who used a transferred-arc in a water cooled chamber, and the other authors who used RF equipment, reported smaller particle sizes and more uniform particle size distributions. In general, the use of pure nitrogen gas as the nitriding agent produced low conversion [14], [20]. The examination of the data reported for the above transferred-arc experiments suggests that the control of particle size becomes difficult when the reaction is carried out inside of the plasma chamber. This is due to the steep temperature and concentration gradients which develop around the plasma arc, resulting in different histories for the growth process of individual particles, and to nitridation on the surface of the aluminum bath. Based on these observations, Moura and Munz [23] (1997) proposed a novel concept of transferred-arc reactor for which the reaction was carried out outside the plasma chamber. The powder characteristics reported from their work and the work of Da Cruz and Munz [24] (1997) in a modified version of this reactor concept are also included in **Table I**. This reactor and its reported results are discussed next.

3. Two-stage transferred-arc reactor

The transferred-arc plasma generation system was chosen because it can be easily scaled up to MW power capacity, with a high efficiency [23] – a requirement which has to be met in order to scale up this technology to the many kg/h needed for industrial scale production of these powders. This reactor design provided for the reaction between aluminum vapour and ammonia to be carried out outside the plasma chamber, using NH_3 and Al vapour as reactants. A schematic diagram of the reactor used is shown in **Figure 3**. Al was evaporated from a graphite crucible by a transferred-arc in inert Ar atmosphere. The Al vapour produced in the plasma chamber was transported by the plasma gas into a tubular synthesis reactor. There it reacted with a NH_3/Ar mixture introduced at room temperature through radial jets distributed in the circumference of the tube, close to the entrance of the synthesis reactor. The reaction was further quenched at the end of the reactor by an outward radial flow of room temperature nitrogen. The ultrafine AlN powder produced was collected in a porous stainless steel filter. The production of a 100% converted AlN was reported, with the particles having spherical shape, and specific surface area in the 80 to 100 m^2/g range. These results show that the particle size produced by this reactor configuration was of the same order as that obtained using inductively coupled plasma systems. The mixing conditions at which full conversion could be achieved with this reactor configuration were investigated. It was concluded that the reaction was essentially complete within the mixing zone located a few reactor diameters downstream of the ammonia injection.

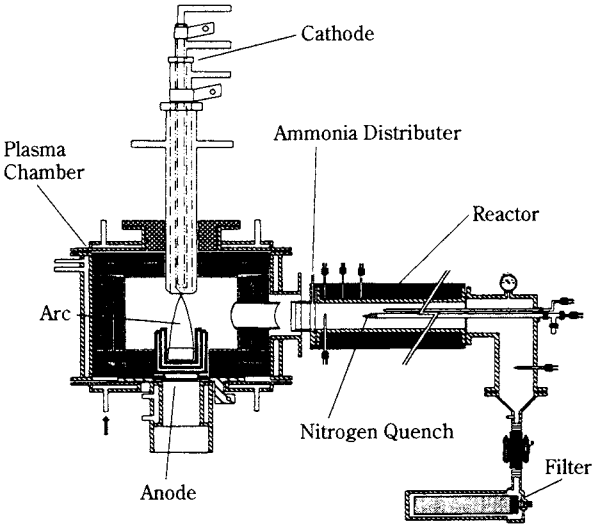

Fig. 3 Schematic diagram of the two-stage transferred arc reactor used by Moura and Munz [23] for the synthesis of AlN ultrafine powder.

The schematic diagram of a more recent design [24] of this reactor concept is shown in **Figure 4**. In this version the transferred-arc chamber and reaction tube were vertically aligned. Modifications were introduced to produce evaporation of Al over relatively long periods of time (from 3 to 5 hr), to promote an homogeneous outflow of the hot gas from the plasma chamber, and to provide space for the introduction of Al vapour concentration and temperature measurement probes. The plasma gas laden with Al(v) flowed through the annular space between the crucible and the plasma chamber wall into the reac-

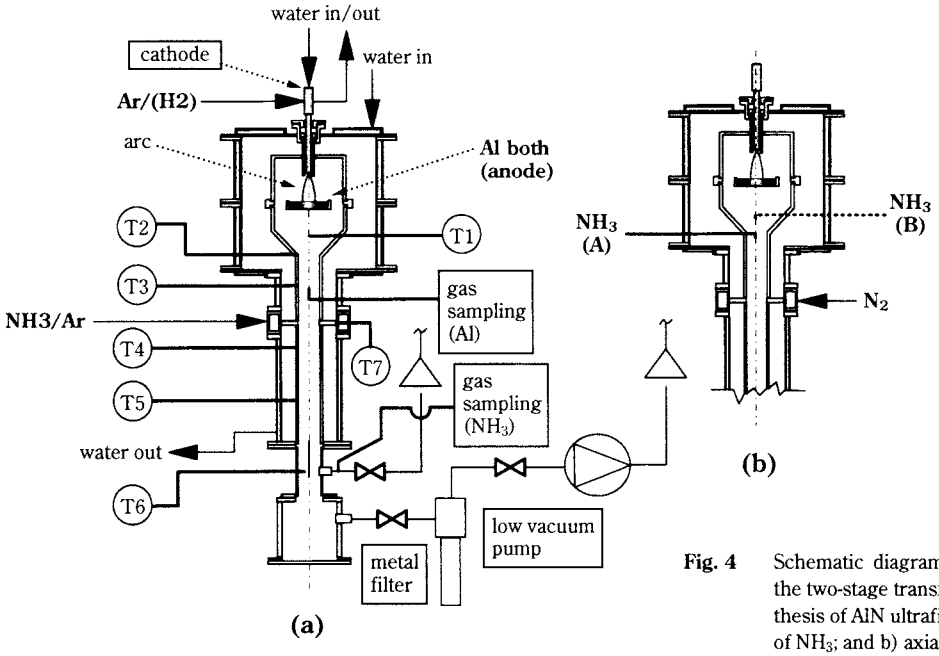

Fig. 4 Schematic diagram of the modified version of the two-stage transferred arc reactor for the synthesis of AlN ultrafine powder: a) radial injection of NH_3; and b) axial injection of NH_3. After [25].

tion tube where it was mixed with NH_3 and quenched by a radial jet of cold gas. This reactor allowed the use of two distinct gas mixing geometries: (a) using radial jets of NH_3/Ar; and (b) the axial injection of NH_3 upstream of the radial quenching point. Typical operating parameters of this reactor are shown in **Table II**. A wide range of particle sizes (38-270 m^2/g) could be produced by modifying the operating parameters such as: plasma gas composition, gas temperature, metal vapour concentration, and nitriding gas mixing geometry.

Table II Typical operating parameters of the transferred-arc plasma and reactive radial gas quenching.

	Radial Injection					Axial Injection	
Plasma gas composition	Ar	Ar		Ar/H_2		Ar	
Plasma gas flow rate (lpm, 298 K)	20	20		18/2		25	25
Temperature T1[1] (K)	1,500	1,800	2,000	1,800	2,000	1,800	2,000
Temperature T3[1] (K)	1,070	1,270	1,410	1,190	1,330	1,300	1,420
Arc length (cm)	5	7	7	5	5	8	8
Arc voltage (V)	29	30	34	50	55	34	36
Arc current (A)	185	275	360	180	250	340	360
Arc Power (kW)	5.4	8.3	12.2	9.0	13.8	11.5	13.0
Quenching:							
Ar (lpm, 298 K)	—	2 to 7				—	
NH_3 (lpm, 298 K)	—	2				—	
N_2 (lpm, 298 K)		—				6	
Pressure	100 kPa						

[1] Thermocouples were positioned according to Figure 4.

The specific surface area of the powders produced under different conditions with the radial and axial injection of NH_3 is shown in **Figures 5** and **6**, respectively. The finest powders were produced with the radial injection of ammonia, using Ar plasma gas with a temperature of 1800 K, and low quenching intensity. The coarsest powders were produced with a plasma chamber off-gas temperature of 2000 K, and the axial injection of pure (not mixed with Ar) NH_3 at a position that provided the longest residence time of particles at the high temperature region.

A theoretical analysis of these operating conditions was carried out using a numerical model [25]. The model, which accounted for the nucleation of particles from the gas phase and growth by condensation, reaction, and coagulation, showed that the nucleation rate in the AlN system is largely dominated by heterogeneous reaction, possibly on the surface of subcritical particles. The many experimental trends were studied in light of the modelling analysis. The opposing trends observed with the radial injection of NH_3 (**Figure 5**) were shown to be associated with the nucleation of particles under different concentrations of nitriding agent. Typical modelling results for the nucleation rate using the radial injection of NH_3 are shown in **Figure 7**. Except for the plasma gas composition, the operating conditions used in the simulation were: gas temperature of 2000 K at the entrance of the tubular reactor and a radial jet formed by 2 lpm of NH_3 and 5 lpm of Ar. Temperature gradients caused by heat loss upstream the point where NH_3 is injected result in the nucleation of pure Al particles near the

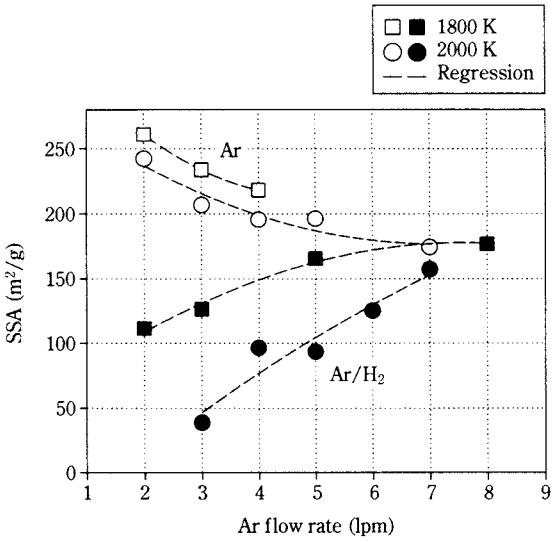

Fig. 5 Specific surface area of powders produced with the radial injection of NH_3, as a function of the impinging jet intensity, and plasma gas temperature and composition. NH_3 flow rate is kept constant at 2 lpm, and the jet intensity is modified by changing the amount of also injected Ar.

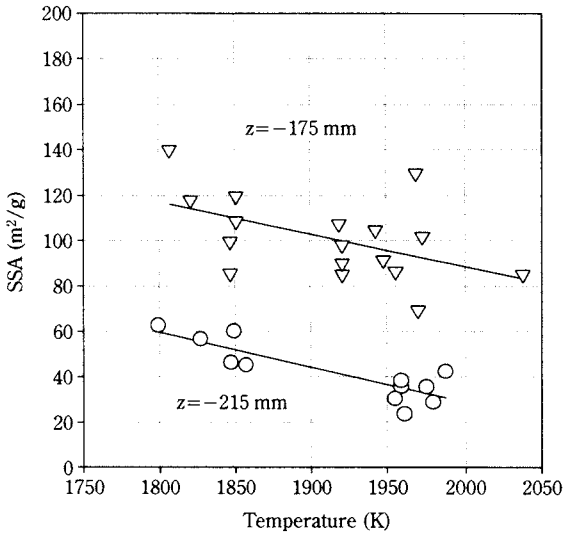

Fig. 6 Specific surface area of powders produced with the axial injection of NH_3, as a function of the gas temperature at the entrance of the tubular reactor, and position of NH_3 injection upstream of the quenching jet (z=0 mm).

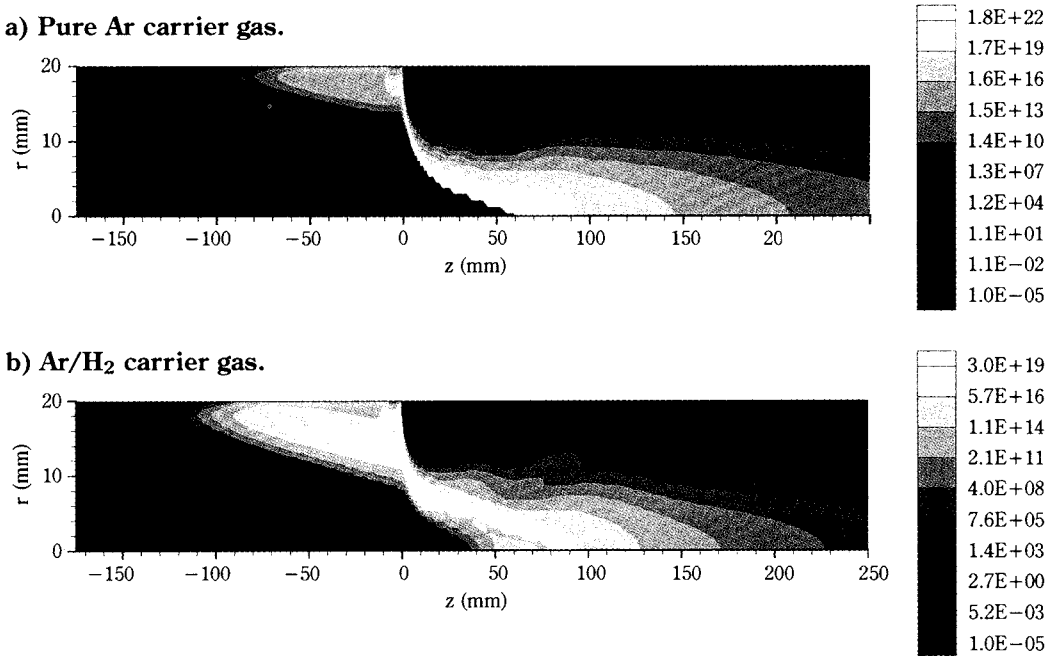

Fig. 7 Nucleation rate ($1/m^3/s$) predicted for different plasma gas compositions.

tube wall, in the absence of nitriding agent. A higher heat loss produced by the greater thermal conductivity of the Ar/H_2 gas mixture (in contrast with pure Ar) causes nucleation in a broader volume in this region [**Figure 7 (b)**]. The modelling analysis also showed that the change of particle size with temperature resulted from the greater Al(v) concentration produced with higher temperatures of the plasma chamber off-gas.

The modelling predicted weight percentage of AlN in the forming particles along the reaction zone for the radial and axial injection of ammonia of pure Ar plasma gas at 2000 K are shown in **Figure 8 (a)** and **(b)**, respectively. Particles which nucleate near the wall upstream of the jet do so in total absence of NH_3. Those particles which pass the injection point and remain near the wall where the NH_3 concentration is high, but temperature and Al concentration are rather

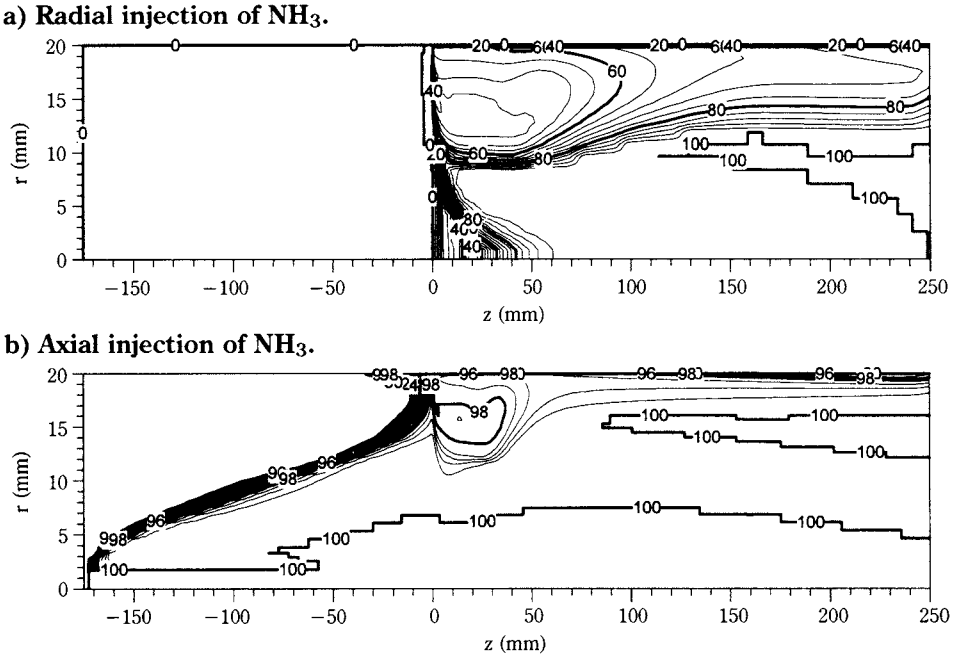

Fig. 8 AlN content in the powder predicted by the numerical simulation (Ar plasma, 2000 K): a) with the radial injection of NH_3 (2 lpm); and b) with the axial injection of NH_3 at $z=-175$ mm, and radial injection of N_2 (6 lpm) at $z=0$ mm.

low, have their already condensed Al only partially converted to AlN. Those particles which form in the higher temperature central portion, will become fully nitrided far before the end of the exit of the calculation domain. On the other hand, in the axial injection model [**Figure 8 (b)**], it is observed that full conversion is readily achieved in the high temperature and high NH_3 concentration core. As in the the radial injection, because of the lower temperatures near the tube wall, the particles which form in this region are difficult to nitride fully. However, in contrast with the radial injection, the conversion at this region is still better than 96%. Since most of the gas-to-condensed phase transition occurs in the hot core, a conversion of 99.9% is predicted for the average of the powder at the exit of the calculation domain in the 2000 K temperature level. The modelling results of the 1800 K temperature level showed similar distributions. These results, which are in full agreement with the experiments, confirm the importance of avoiding excessive cooling rates in the mixing zone in order to obtain fully converted powders.

3.2. Powder characterization

The examination of the AlN ultrafine powders produced by plasma using Scanning Electrons Microscopy (SEM) [15], [23] and Atomic Force Microscopy (AFM) [23] showed loose agglomerates of rounded particles. TEM micrographs of AlN powders synthesized by plasma are shown in **Figure 9** [25]. The larger sizes and broader size distribution observed in **Figure 9 (b)** are typical of longer residense times in a hot reaction zone. In contrast, the TEM micrograph

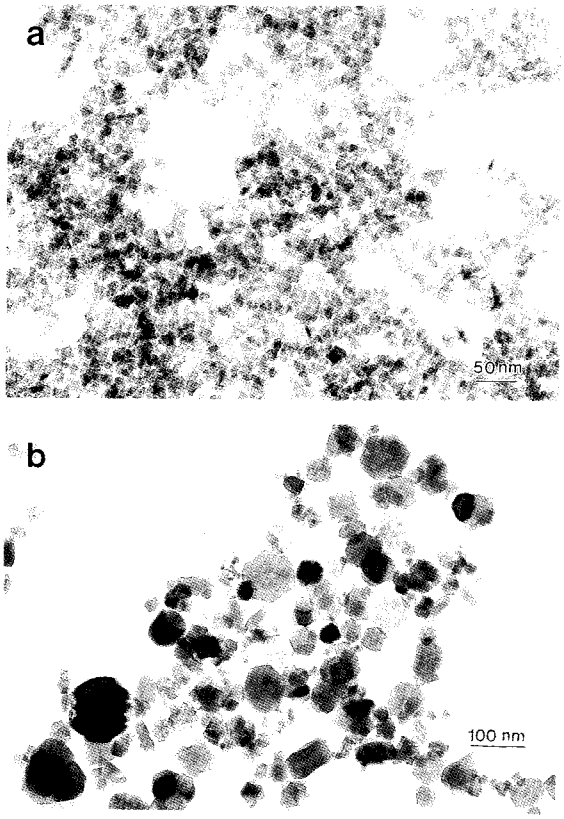

Fig. 9 TEM micrographs of powder produced with: a) the axial injection of NH_3 in the central portion of a tubular reactor; and b) the radial injection of NH_3 mixed with Ar. After [25].

of powders which where produced with a more stringent cooling condition, and therefore shorter residence times, shows smaller particles of a narrower size distribution [**Figure 9 (a)**].

Oxygen is the major impurity commonly found in these ultrafine powders; most authors have attributed this to contamination during handling in atmospheric air, after the powder has been produced. The oxygen content of nanosize AlN powders, plotted as a function of their specific surface area, is shown in **Figure 10**. For illustration, the data reported by Hashimoto and Yoden [26] (1992), who synthesized AlN ultrafine powders from aluminum chloride and glucose, is also included in this figure. The positive correlation between oxygen and surface area is evident. The results of Fourier Transform Infrared Spectroscopy (FTIR) [16], [23], [25] showed broad peaks of the O-H bond on the surface of the powder, suggesting that the high specific surface area of AlN might make it very reactive with moisture in the air. The presence of carbon, reported for the powders produced with transferred-arc systems, was attributed to the erosion of the graphite crucible by the plasma arc. The x-ray photoelectron spectroscopy (XPS) analysis of the AlN powders produced using the two-stage transferred-arc reactor also showed the presence of carbon contamination resulting from the graphite crucible erosion [25].

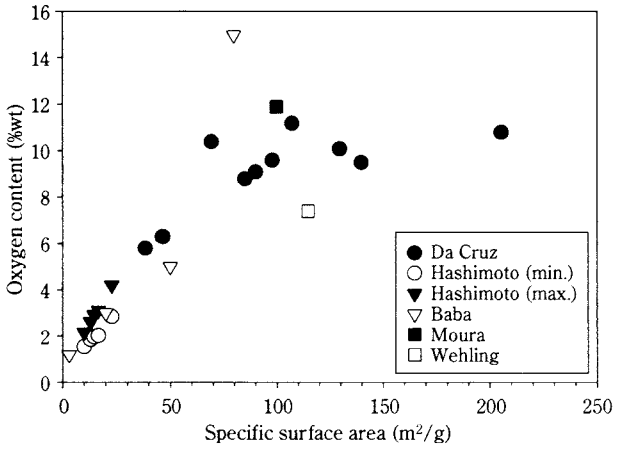

Fig. 10 Oxygen content of nanosize AlN powders, plotted as a function of their specific surface area.

3.3. Powder sinterability

Commercially available powders produced by the carbothermal reduction of Al_2O_3 have been reported to sinter at temperatures above 1850°C, using hot pressing sintering [12]. The preparation of full density AlN ceramics by pressureless sintering of AlN ultrafine powders produced by plasma, with and without sintering aids, has been reported [15], [16], [20], [27]. Presureless sintering without additives at temperatures as low as 1530°C has been reported [15].

The densification and microstructure development of AlN powders with a specific surface area in the 85-108 m^2/g range, produced in the two-stage transferred-arc plasma reactor, were reported by Da Cruz et al. [29]. Powder samples were compacted as produced, and pressureless sintered in the 1250°C to 1750°C range, for 3 hours. The fractured surface of a sample sintered at 1350°C, examined by TEM using the Pt/C replica and shadowing technique, is shown in **Figure 11**. This represents an intermediate stage of the sintering process in which fine grains of the starting powder and a plate-like structure, observed to develop at scattered domains, are present. Sintering at 1750°C resulted in the fully densified structure shown in **Figure 12**. The XRD patterns of the starting powder and of samples which have been sintered at 1750°C are shown in **Figure 13**. Peaks of a second

Fig. 11 TEM image of Pt/C replica of the surface of a fragment of AlN ultrafine powder sintered at 1350°C. A plate like structure is observed to develop. The arrow indicates the shadowing direction.

Fig. 12 TEM image of Pt/C replica of the surface of a fragment of AlN ultrafine powder sintered at 1750°C. The arrow indicates the shadowing direction.

a) AlN powder.

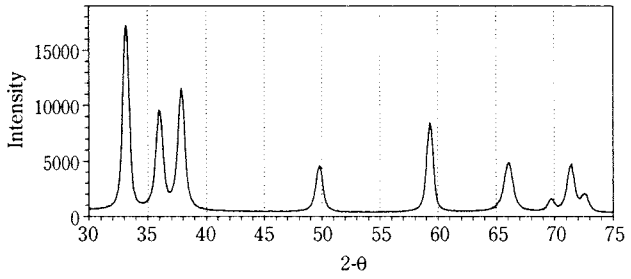

b) Compact sintered at 1750°C.

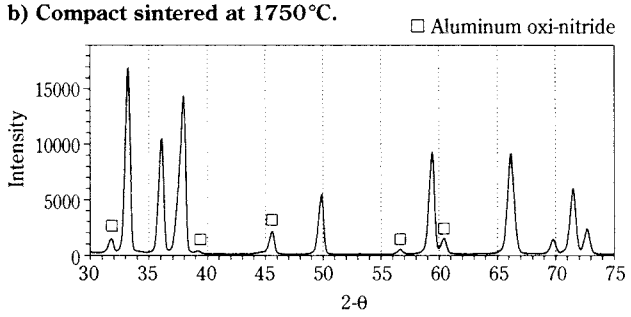

Fig. 13 X-ray diffraction pattern: a) AlN powder; b) sample sintered at 1750°C.

phase, identified as $Al_{8/3-x/3}O_{4-x}N_x$ (JCPD card 18-52), observed in the pattern of the sintered sample [**Figure 13 (b)**], possibly resulted from the incorporation of the oxygen from the surface of the starting particles into the sintered material structure during densification. Because the pseudo-binary solution AlN-Al_2O_3 presents high melting points at any composition [28], and oxygen content has been observed to exert little influence on AlN densification [26], it is believed that the densification of these fine powders occurs by solid state sintering, driven by the large surface free-energy change upon sintering rather than by liquid phase formation associated with their relatively high oxygen content.

4. Conclusions

An overview of the thermal plasma synthesis of ultrafine AlN powders has been presented. Laboratory scale experiments, using inductively coupled and transferred-arc plasma systems, have been used to produce very fine powders. Sinterability experiments have demonstrated that these powders can be sintered at lower temperatures than powders produced by conventional methods. The FTIR exam of the powder surface suggests that the high specific surface area of AlN may make it very reactive with moisture in the air. Therefore, to produce commercially acceptable powders aimed to high conductivity application, surface oxidation must be prevented by avoiding contact of the powder with atmosphere before final parts are produced. The presence of carbon observed in powders prepared with transferred-arc systems remains a problem to be solved, possibly with improved design of molten metal holders.

References

1) Richerson, D.W., Modern Ceramic Engineering, Marcel Dekker, Inc., New York, 1992.
2) Sheppard, L.M., International trends in powder technology, Ceramic Bulletin, Vol. 68, No. 5, p. 979, 1989.
3) Hamblyn, S.M.L., and Reuben, B.G., Use of radio-frequency plasma in chemical synthesis, Advances in Inorganic Chemistry and Radiochemistry 17, p. 89, 1975.
4) Fauchais, P., Bourdin, E., Coudert, J.F., and McPherson, R., High pressure plasmas and their application to ceramic technology, in Topics in Current Chemistry, F. L. Boschke (ed.), Plasma Chemistry IV, Springer-Verlag, pp. 59-183, Berlin, 1983.
5) Akashi, K., Application of plasma to processing for ceramics, Techno Japan, Vol. 20, No. 3, pp. 7-26, 1987.
6) Kong, P.C. and Lau, Y.C., Plasma synthesis of ceramic powders, Pure and Applied Chemistry, Vol. 62, No. 9, pp. 1809-1816, 1990.
7) Mroz, T.J., Aluminum nitride, American Ceramic Society Bulletin, Vol. 72, No. 6, pp. 78-80, 1993.
8) Knudsen, A.K., Aluminum nitride, American Ceramic Society Bulletin, Vol. 74, No. 6, pp. 97-101, 1995.
9) Selvaduray, G., and Sheet, L., Aluminum nitride: review of synthesis methods, Materials Science and Technology, Vol. 9, pp. 463-473, 1993.
10) Kuramoto, N., Taniguchi, H., and Aso, I., Development of translucent aluminum nitride ceramics, American Ceramic Society Bulletin, Vol. 68, No. 4, pp. 920-928, 1992.
11) McCauley, J.W., and Corbin, N.D., Phase relations and reaction sintering of transparent cubic aluminum oxynitride spinel (ALON), Journal of the American Ceramic Society, Vol. 62, pp. 476-479, 1979.
12) Jackson, T.B., Virkar, A.V., More, K.L., Dinviddie-Jr., R.B., and Cutler, R.A., High-thermal-conductivity aluminum nitride ceramis: the effect of thermodynamic, kinetic, and microstructural factors, J. Am. Ceram. Soc., Vol. 80, No. 6, pp. 1421-1435, 1997.
13) Boulos, M.I., Fauchais, P., and Pfender, E., Thermal Plasmas: Fundamentals and Applications, Vol. 1, Plenum Press, New York, 1994.
14) Canteloup, J. and Mocellin, A., Synthesis of ultrafine nitrides and oxynitrides in an R.F. plasma, Special Ceramics, Vol. 6, pp. 209-222, 1974.
15) Wehling, C., Heitz, F., and Hausner, H., Synthesis of ceramic powders from metals in an inductively coupled plasma, Symp. Proc.-Int. Symp. Plasma Chem. 10, Brochum, p. 1.4-5 p.1, 1991.
16) Baba, K., Shohata, N., and Yonezawa, M., Preparation of ultrafine AlN powder using RF plasma, Symp. Proc.-Int.

Symp. Plasma Chem. 8, Tokyo, pp. 2034-2039, 1987.
17) Etemadi, K., Formation of aluminum nitrides in thermal plasmas, Plasma Chemistry and Plasma Processing, Vol. 11, No. 1, p. 41-56, 1991.
18) Godin, M.F., Chevallier, F., Amouroux, J., and Morvan, D., Synthesis of aluminum nitride powders by thermal plasma, Symp. Proc.-Int. Symp. Plasma Chem. 10, Brochum, p. 1.4-4 p.1, 1991.
19) Ageorges, H., Kun, C., Mergy, S., Baronnet, J.M., Willians, J.K., and Chapman, C., Synthesis of aluminum nitride in transferred arc plasma furnaces, Symp. Proc.-Int. Symp. Plasma Chem. 10, Brochum, p. 1.4, 1991.
20) Ageorges, H., Megy, S., Chang, K., Baronnet, J.M., Williams, J.K., and Chapman, C., Synthesis of aluminum nitride in transferred arc plasma furnaces, Plasma Chemistry and Plasma Processing, Vol. 13, No. 4, p. 613-632, 1993.
21) Vissokov, G.P., and Brakalov, L.B., Chemical preparation of ultra-fine aluminum nitride by electric-arc plasma, J. Mater. Sci., Vol. 18, pp. 2011-2016, 1983.
22) Cusick, M.J., Plasma-arc synthesis of ultrafine aluminum-nitride powder for electronic packaging applications, Ph.D. thesis, Colorado School of Mines, 1989.
23) Moura, F.J., and Munz, R.J., Vapour-phase synthesis of nanosize aluminum nitride particles using a two-stage transferred arc reactor, J. Am. Ceram. Soc., Vol. 80, No. 9, pp. 2425-2428, 1997.
24) Da Cruz, A.C., and Munz, R.J, Vapor phase synthesis of fine particles, IEEE Transactions on Plasma Science, Vol. 25, No. 5, pp. 1008-1016, 1997.
25) Da Cruz, A.C., Experimental and modelling study of the plasma vapour-phase synthesis of ultrafine powders, Ph.D. thesis, Mcgill University, Montreal, Canada, 1997.
26) Hashimoto, N., and Yoden, H., Sintering behavior of fine aluminum nitride powder synthesized from aluminum polynuclear complexes, J. Am. Ceram. Soc., Vol. 75, No. 8, pp. 2098-2106, 1992.
27) Da Cruz, A.C., Munz, R.J., and Vali, H.. The densification and microstructure development of sintered aluminum nitride ultrafine powder produced in a two-stage transferred-arc plasma reactor, J. Mat. Sci. Letters 17, pp. 1255-1261, 1998.
28) McCauley, J.W., and Corbin, N.D., High temperature reactions and microstructures in the Al_2O_3-AlN system, in Progress in Nitrogen Ceramics, F.L. Riley (Ed.), Martinus Nijhoff Publishers, Boston, pp. 111-118, 1983.

Author's short biography

A.C. Da Cruz

Antonio Carlos da Cruz received the B.A.Sc. degree in mechanical engineering and the M.A.Sc. degree in chemical engineering from the University of São Paulo, São Paulo, Brazil, in 1978 and 1993, respectively. He received the Ph.D. degree in chemical engineering in 1998, from McGill University, Montreal, P.Q., Canada (plasma synthesis of aluminum nitride ultra-fine particles).
He worked as Project Engineer for steel plant equipment until 1982, when he joined the Institute for Technological Researches of São Paulo State, Brazil (IPT) as a Research Engineer. At IPT, he participates in the development of thermal plasma equipment and processes related to metal alloys and ceramics since 1986. His main area of interest is the thermal plasma processing of materials, the synthesis of ultra-fine particles, and the development of thermal plasma reactors.

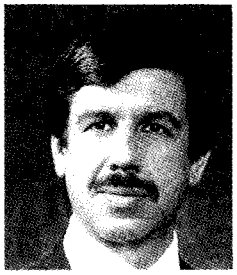

R.J. Munz

R.J. Munz has been involved in thermal plasma research since 1970. He is Professor and Chair of the Department of Chemical Engineering, McGill University and is Associate Director of CRTP.

Simulations for Powder Materials and Production Process Design†

Jusuke Hidaka
*Department of Chemical Engineering and Materials Science, Faculty of Engineering, Doshisha University**

Introduction

Owing to advances in powder simulation, exponential progress is being made in powder processing operations and in the design level of powder processes, but as process design becomes more sophisticated, it is necessary to set forth the design conditions (objectives) of a process more quantitatively and definitely than before, which is creating new challenges. Let us explain this problem with the example of designing a manufacturing process for functional ceramic materials.

Functional materials are also known as energy conversion materials because when mechanical, electromagnetic, thermal, optical, or chemical energy is applied to them, they convert it into a different form of energy. One well-known type of functional ceramic material is barium titanate ceramics, which convert applied mechanical energy to electrical energy because they are piezoelectric.

Barium titanate ceramics' permittivity and piezoelectric characteristics basically arise from spontaneous polarization that occurs owing to the perovskite crystal structure of $BaTiO_3$. But because that ceramic material is a kind of composite material comprising the three phases of crystal grains, grain boundaries, and pores, the material texture makes for great changes in the characteristics of the ceramic material. Hence the $BaTiO_3$ ceramics manufacturing process creates a constitutive texture (microstructure) that is optimum for providing the ceramics with the desired permittivity and piezoelectric properties through the three processes of powder raw material processing, forming, and sintering.

Accordingly, it is necessary in designing ceramic manufacturing processes to fully understand the relationship of ceramic materials' permittivity and piezoelectric properties to the materials' microstructure, and to have a clearly defined microstructure for the ceramics that are to be made in that manufacturing process. Even now, however, there is hardly an instance in which the relationship between ceramic material characteristics and microstructure is quantitatively known, and it is impossible to set forth a quantitative and definite ultimate objective for the design of processes whose main purpose is optimum microstructure formation.

Powder engineering is an academic discipline concerned with the creation of materials in which powders are involved, and the design of processes to bring that about. This discipline must for the next century hurry to establish an engineering system that covers powder materials from design to production. In doing so, powder simulation will play a very great role, and simulation will certainly serve as a tool in achieving these aims.

This paper shall use $BaTiO_3$ ceramic materials as a specific example in giving an overview of the use of powder simulation in the microstructure design and process design of powder materials.

1. Powder Simulation

For some time people have insisted on the need to organically use the three methods of experimentation, theory, and simulation (**Fig. 1**) in order to understand natural phenomena. This is especially impor-

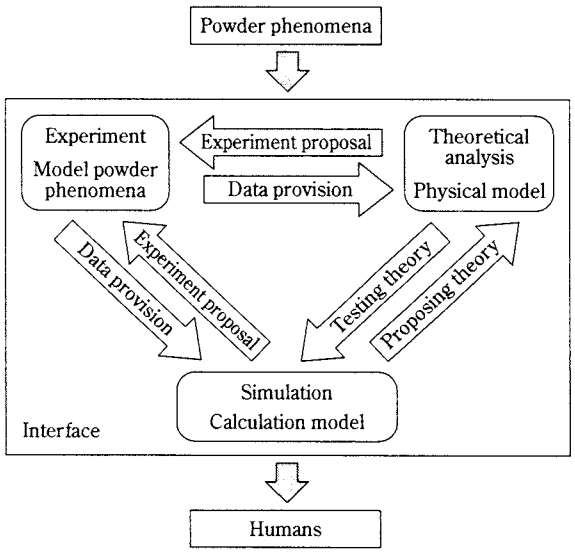

Fig. 1 Understanding of Powder Phenomena (the role of simulations)

* 1-3, Tataramiyakodani, Kyotanabe, Kyoto 610-0394, Japan
† Received August 9, 1999

tant for the understanding and engineering analysis of powder phenomena, which appear complex because many parameters are intricately involved. But as powders are aggregates of many solid particles, their behavior exhibits a strong tendency for dispersing. This makes it difficult to apply simulation methods based on continuum dynamics, which has seriously delayed the application of simulations to powders.

But the amazing advances in computers over the last 10-odd years now allow individuals to easily use workstations with powerful calculating capacities, and that makes it possible to perform not only continuum dynamics simulations, but also discrete element simulations such as those based on molecular dynamics. Inspired by this, discrete element simulations have been developed for the behavior of powders, which have a strong dispersive nature, which has catalyzed vigorous efforts to simulate powder phenomena and realized considerable achievements.

Currently researchers use a variety of powder simulation methods including molecular simulations, continuum dynamics simulations, and discrete element simulations, as well as hybrid simulations that combine these, for the purposes of designing the desired powder particles and materials, and analyzing powder behavior.

2. Microstructure Design of Ceramic Materials [1]

In the design of ceramic manufacturing processes, it is necessary to design microstructures according to the law of mixtures, which indicates the relationship between the characteristics and microstructures of ceramic materials, as noted above, and to design unit operations and processes. Thus as an example of simulation for microstructure design, we shall use a simulation to elucidate the relationship between permittivity and microstructure in barium titanate ($BaTiO_3$), and show that the microstructure design of dielectric ceramics is possible.

2.1 Permittivity Estimation Model

The microstructure of sintered barium titanate varies considerably depending on powder material characteristics, whether or not binders are used, and forming or sintering conditions, with the resulting microstructure greatly affecting permittivity. It being difficult to experimentally determine the relationship between permittivity and the divers changes in microstructure, a prediction method based on an appropriate estimation model is necessary. The equivalent circuit model has long been used to represent the electrical characteristics of ceramic materials [2, 3]. We therefore propose a permittivity estimation method that applies this equivalent circuit model and gives permittivity, sizes of crystal grains, pores, and grain boundaries in the sintered structure, and how their distributions are related.

2.1.1 Unit Cell: A Constituent Element of Microstructure

As shown in **Fig. 2**, the sintered structure consists of grains, grain boundaries, and pores. We shall consider as the constituent elements of this structure the unit cell, which as shown in **Fig. 3(a)** comprises grains that are the ferroelectric phase, grain boundaries that are the paraelectric phase, and pores that are the air phase. As shown in **Fig. 3(b)**, this unit cell is stacked three dimensionally, and then the sizes of the grains and pores and the grain boundary thickness in the unit cells are juxtaposed against the sizes of the grains and pores and the grain boundary thickness, as well as their distributions, in an actual sintered product, thereby representing the sintered product's microstructure. Because the unit cells are stacked on one another, the grain boundaries that surround the cells are placed along three surfaces of each cell as shown in **Fig. 4(a)**, whereby the grain boundary effects in the cells are concentrated on these three faces. These unit cells are an improvement over the

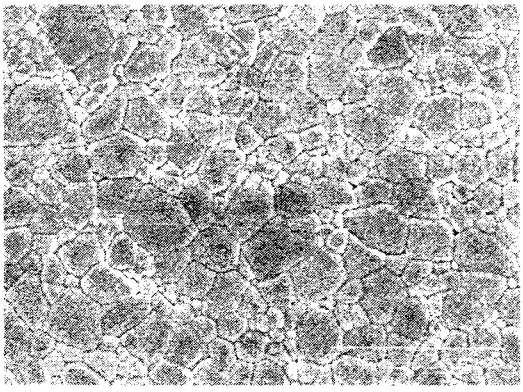

(a) SEM photograph of microstructure in $BaTiO_3$ ceramics

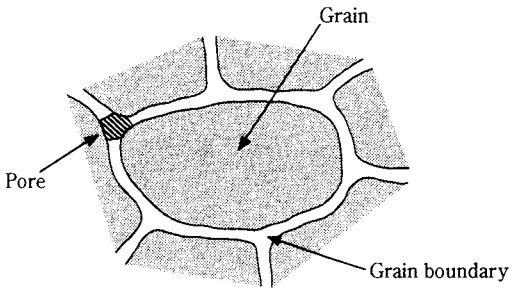

(b) Rough sketch of microstructure

Fig. 2 Microstructure of Ceramic Materials

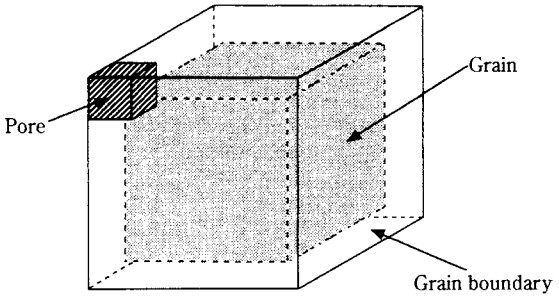

(a) Unit cell

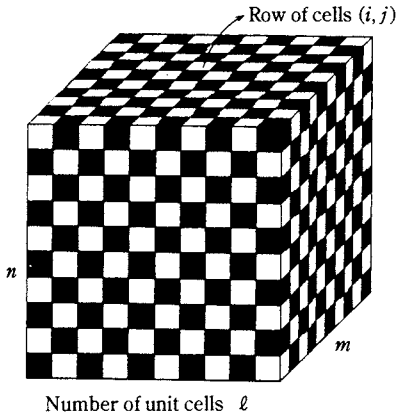

(b) Stack of unit cells

Fig. 3 Unit Cells and Representation of Microstructure

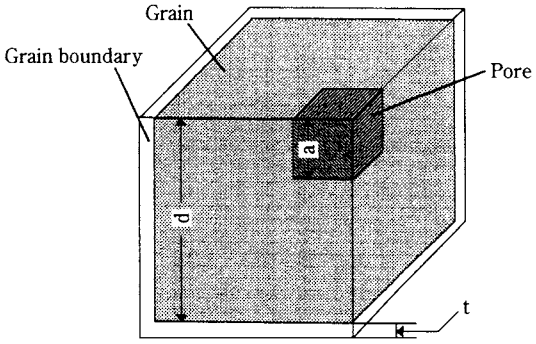

(a) Modified unit cell

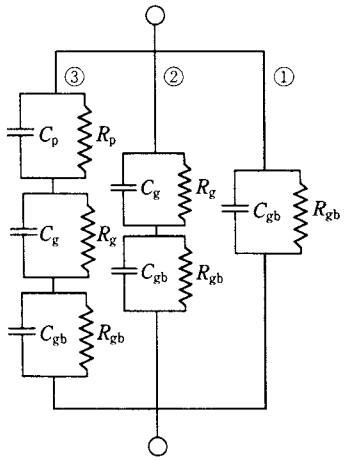

(b) Equivalent circuit

Fig. 4 Modified Unit Cell and Equivalent Circuit

so-called cubes model [4, 5], and their equivalent circuit appears in **Fig. 4(b)**. In this circuit there are three circuits connected in parallel: (1) the grain boundary alone, (2) the grain and boundary connected in series, and (3) the pore, grain, and boundary connected in series. If the resistance R of each part is assumed to be infinite [3], the permittivity of a unit cell can be derived as follows.

Generally when there is a substance in which k phases, from phase 1 to phase k, whose volume ratios and permittivities are, respectively, v_1, v_2, ... v_k and ε_1, ε_2, ... ε_k, are connected in series or parallel, the entire substance's permittivity $\bar{\varepsilon}$ is indicated by these equations.

a) Series

$$\bar{\varepsilon} = \frac{1}{\sum_{i=1}^{k}\left(\frac{v_i}{\varepsilon_i}\right)} \tag{1}$$

b) Parallel

$$\bar{\varepsilon} = \sum_{i=1}^{k} \varepsilon_i \cdot v_i \tag{2}$$

Then if grain size is d, pore size is a, grain boundary thickness is t, and their permittivities are ε_g, ε_p, and ε_a, respectively, the permittivity ε_{ga} of the portion comprising grain and pore combined in **Fig. 3(a)** is given by the following equation.

$$\varepsilon_{ga} = \varepsilon_p \left[\left\{ \frac{a^2}{d} \frac{\varepsilon_p}{(d-a)\varepsilon_p + a\varepsilon_g} \right\} + \left(1 - \frac{a}{d}\right)^2 \right] \tag{3}$$

The grain and pore portion is connected to the grain boundary in series on its bottom and in parallel on its side. In consideration of this, the following equation gives the permittivity of the unit cell as a whole.

$$\bar{\varepsilon_c} = \left(1 + \frac{d}{t}\right)^2 \frac{\varepsilon_{ga}\varepsilon_b(d+t)}{\varepsilon_b d + t\varepsilon_{ga}} + \frac{t(2d+t)}{(d+t)^2} \tag{4}$$

2.1.2 Sintered Product Permittivity

In a unit cell stack as shown in **Fig. 3(a)** the sizes of grains and pores and the thickness of boundaries differ from one cell to the next. Thus the geometric size of each unit cell would ordinarily be different, but in order to facilitate cell stacking this model assumes that individual cells each having their own unique characteristics are incorporated into a cell whose geometric size is uniform, and that each individual cell is interlinked with its surrounding cells. If a large enough number of cells is used to estimate permittiv-

ity, the error due to this stacking method is thought to be small.

If we create a cube in which the numbers of cells l, m, and n are arranged along axes x, y, and z as in **Fig. 3(b)**, the permittivity against an electric field in the z direction of the entire cubical stack is given by Eq. (6). In other words, in the z direction n unit cells are connected in series, and $1 \times m$ cell rows connected in series are connected with one another in parallel. Here the permittivity $\overline{\varepsilon_{ij}}$ of the cell row connected in series in the z direction (i, j) is given by this equation.

$$\overline{\varepsilon_{ij}} = \frac{\prod_{k=1}^{n} \varepsilon_{ijk}^{c}}{\prod_{k=1}^{n} \varepsilon_{ijk}^{c} \cdot \sum_{k=1}^{n} \left(\frac{v_{ijk}}{\varepsilon_{ijk}^{c}} \right)} = \frac{1}{\sum_{k=1}^{n} \left(\frac{v_{ijk}}{\varepsilon_{ijk}^{c}} \right)} \tag{5}$$

Accordingly, the permittivity of the entire cell stack $\overline{\varepsilon_T}$ connected in parallel with cell row (i, j) is given by this equation.

$$\overline{\varepsilon_T} = \sum_{i,j=1}^{l,m} \overline{\varepsilon_{ij}} \cdot v_{ij} \tag{6}$$

2.1.3 Estimating Permittivity

As crystal particle distributions obtained through experimentation generally have a normal logarithmic distribution, we decided that the particle size of each unit cell would assume a normal logarithmic distribution using random numbers and based on the average, minimum, and maximum particle sizes d_{av}, d_{min}, and d_{max}, and on the standard geometric deviation σ_g. Similarly for pore size as well, we randomly placed pores of varying sizes within each unit cell based on pore size distribution and relative density.

Particle permittivity, meanwhile, depends on particle size. We therefore established the permittivity corresponding to each particle diameter based on the relationship between particle size and permittivity reported by Arlt et al. [6]. Additionally, as Takeuchi et al. [3] report that sintered $BaTiO_3$ has a boundary thickness of 4 nm and permittivity of 100, we used those values in the calculations below.

2.2 Permittivity According to the Estimation Model

Fig. 5 shows the experimental results for the relative density and permittivity of $BaTiO_3$ ceramics. In this experiment a sintered product whose relative density was under 93% had an average grain size of about 1 μm, standard geometric deviation σ_g of 1.4, and average pore size of 0.012 μm. The solid curve in the graph represents the relationship between permittivity and relative density, which was calculated by varying the pore ratio on the basis of the values given above. Similarly, **Figs. 6** and **7** show the relationship of average grain size and its distribution to permittivity. These three examples of calculated values all conform closely to calculated results, which indicates that the estimation model proposed above can estimate

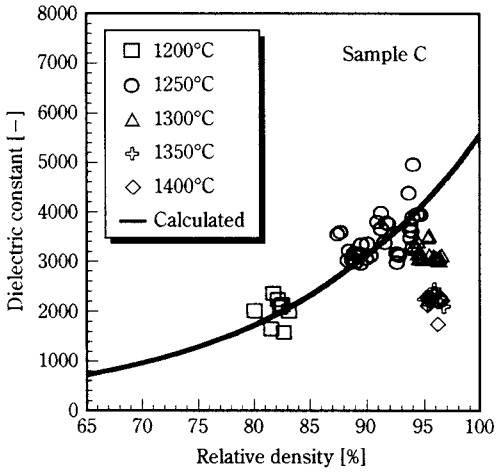

Fig. 5 Relative Density and Permittivity (temperature is sintering temperature)

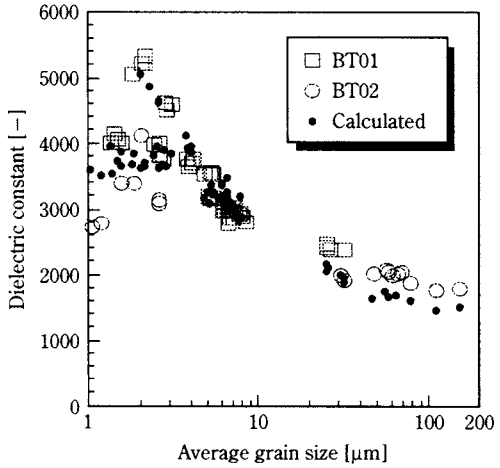

Fig. 6 Relationship Between Average Grain Size and Permittivity

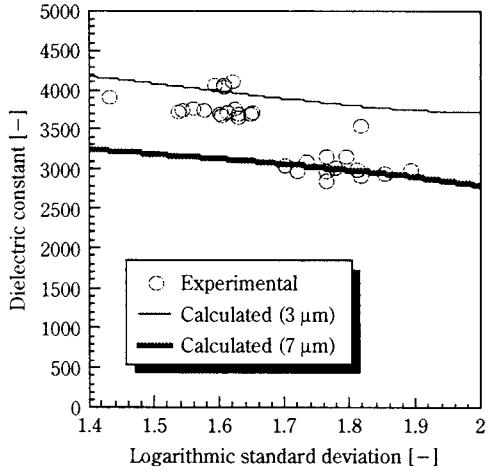

Fig. 7 Broadness of Grain Size Distribution and Permittivity

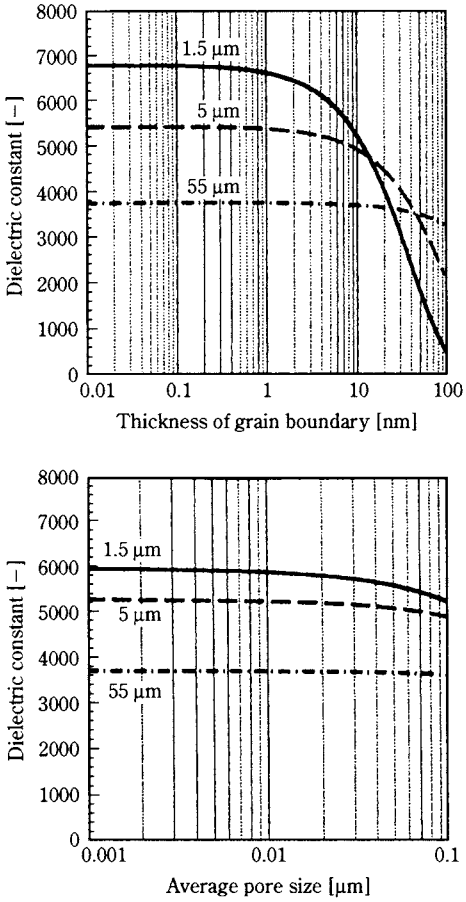

Fig. 8 Effects of Grain Boundary Thickness and Pore Size on Permittivity

the permittivity of sintered $BaTiO_3$.

As indicated by **Fig. 5**, if one performs fine-textured sintering without inducing an increase in grain size, it is possible for the sintered product to achieve a permittivity of about 5800, and to gain detailed knowledge about the effects of boundary and pore characteristics, as shown in **Fig. 8**. While this is but one example, this permittivity simulation provides detailed information about the relationship between the microstructure and permittivity of ceramics, and makes it possible to quantitatively design a microstructure in order to obtain the desired permittivity.

3. Sintering Behavior Simulation

Once one determines the microstructure of ceramics with the desired characteristics, it is necessary to design a process that will unfailingly deliver that microstructure. For that reason we shall next perform a simulation of the sintering phenomenon, which has a major influence on the formation of ceramic microstructures, and elucidate the relationship between sintering behavior and operating conditions.

3.1 The Sintering Phenomenon [7]

When placing two solid particles in a temperature field below the melting point of the solid, a neck forms between the particles as shown in **Fig. 9**, and the particles' surface areas are reduced. This phenomenon is called sintering, and it is a basic and important phenomenon in making ceramic materials.

Much research has been performed on this sintering mechanism for many years. A neck is formed by the dispersive movement mechanism of atoms as illustrated in **Fig. 10**. Many sintering speed equations

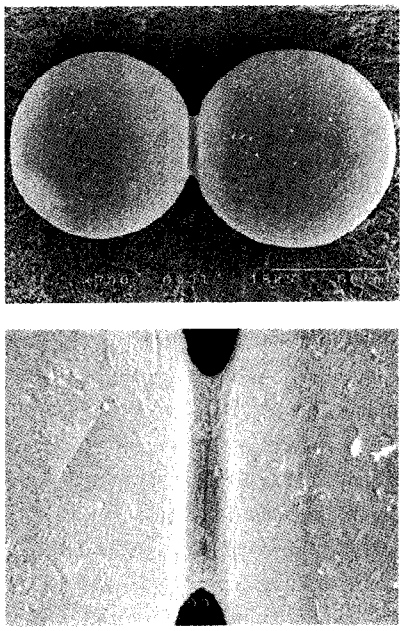

Fig. 9 Initial Sintering Behavior of Cu Particles

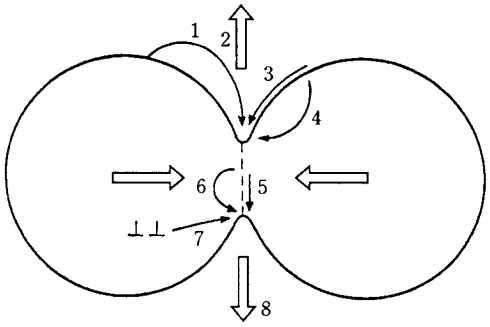

Material movement mechanism	Route
1. Evaporation-condensation	Surface → neck
2. Dissolution-precipitation	Surface → neck
3. Surface diffusion	Surface → neck
4. Volume diffusion	Surface → neck
5. Boundary diffusion	Grain boundary → neck
6. Volume diffusion	Grain boundary → neck
7. Volume diffusion	Transposition → neck
8. Flowing	Bulk → neck

Fig. 10 Atomic Movement Mechanism During Initial Sintering Phase

have been proposed in correspondence to the dispersion paths of atoms and molecules, but sintering never proceeds under a single mechanism, instead always requiring a complex of two or more. It is therefore difficult to obtain guidelines for actual sintering operations from the sintering speed equations now proposed.

For this reason we carried out a computer simulation of the composite sintering behavior of particles. Material movement occurring in the initial stage of the sintering process is conceived as two separate processes, agglomeration and densification. The agglomeration process is a material movement mechanism involving no change in the distance between the centers of two particles (evaporation-condensation, surface dispersion, surface volume dispersion), and densification is the process by which atoms move according to a mechanism that reduces the distance between the centers of two particles (grain boundary dispersion, grain boundary volume dispersion). If one assumes that the volume of atoms that move in the condensation and densification processes is preserved in the neck, and that sintering time is quantized by microtime Δt, and then repeatedly calculates the amount of atomic movement in the condensation and densification processes, it is possible to simulate a composite sintering process.

Fig. 11 compares experimental and simulation results for the relationship between neck radius and sintering time. Nearly all the experimental values fall within the range predicted by calculations, showing that simulation results were excellent. **Fig. 12** shows the quantities of atoms that moved in accordance with the various movement mechanisms. This simulation provided detailed information on sintering conditions and atomic movement mechanisms.

3.2 Microstructure Formation [8]

Large numbers of powder particles are involved in the formation of ceramic microstructures, and many parameters such as sintering temperature, temperature increase rate, and cooling rate also contribute to the outcome. We therefore used the Monte Carlo method in conducting a simulation of microstructure formation behavior, and examined the relationship of microstructure formation to the powder characteristics and sintering conditions of ceramic materials. The simulation principle is as follows.

Triangular lattices are placed on a two-dimensional coordinate system, and the lattice aggregation used to represent grains. We provided interface energy corresponding to boundary-boundary, boundary-grain interior, and interior-interior interfaces, and also took into account anisotropy relating to grain growth. To begin with, the simulation randomly selected and moved one lattice in the sintered product, and used the following Monte Carlo algorithm on the pre-/post-movement energy difference.

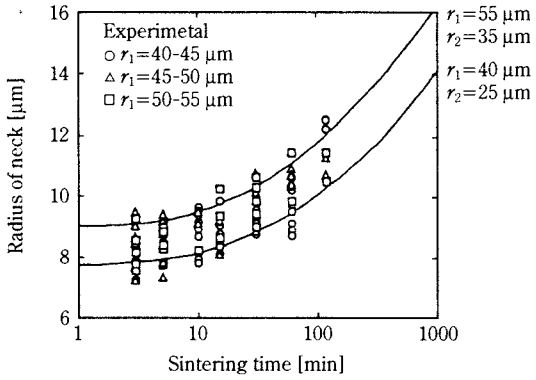

Fig. 11 Neck Radius and Sintering Time

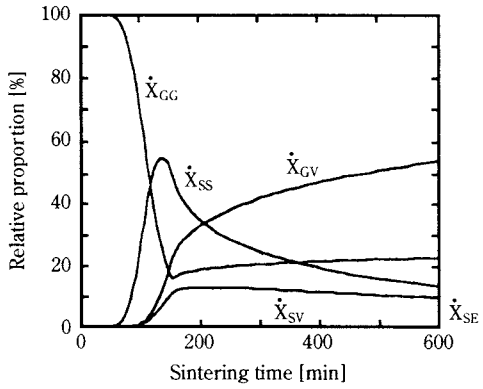

(b) Different diameter particles (r_1=40, r_2=25 μm)

Fig. 12 Relative Proportion of Atomic Movement in the Sintering Process
(X_{GG}: boundary diffusion; X_{SS}: surface diffusion; X_{GV}: boundary volume diffusion; X_{SV}: surface volume diffusion; X_{SE}: evaporation-condensation)

When the system's potential energy U_i becomes U_j due to movement, state j is adopted if (i) $U_j<U_i$. (ii) If $U_j>U_i$, a uniform random number η between 0 and 1 is generated; if (a), state j is adopted, but if (b), movement is not recognized. Here k_B is the Boltzmann constant and T is absolute zero.

Fig. 13 shows the change in microstructure when a Ni plate is heated. By contrast, Monte Carlo simulation results appear in **Fig. 14**. Both show that grains grow as sintering time lengthens (Monte Carlo step). Although the Monte Carlo simulation does not include the concept of time, a little innovation makes it possible to consider the correspondence with sintering time. **Fig. 15** graphs the relationship between average grain size D_{50} and sintering time, and **Fig. 16**

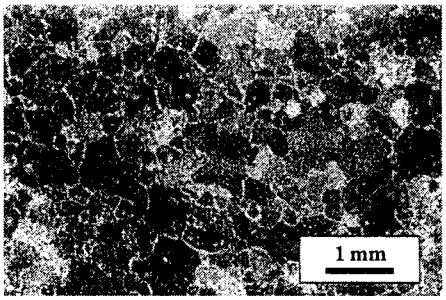

300°C/hr at 1100°C for 10 min

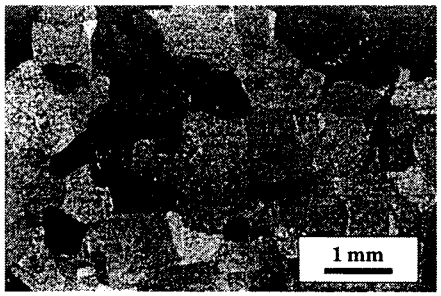

300°C/hr at 1100°C for 100 min

Fig. 13 Ni Plate Sintering

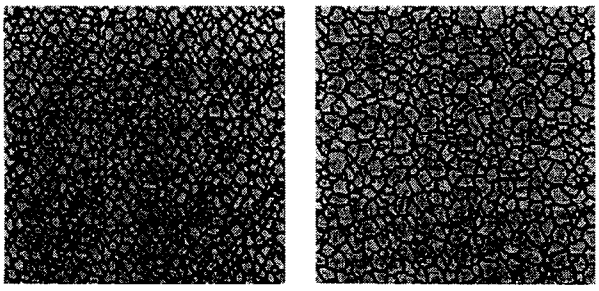

0 MCS 10000 MCS

Fig. 14 Monte Carlo Simulation of Microstructure Formation Behavior

shows the standard geometric deviation σ_g of grain size distribution. As experimental and simulation results closely coincide, it is evident that a Monte Carlo simulation can examine the relationship between microstructure formation and sintering conditions.

4. Designing Powder Operations

The ceramic manufacturing process includes powder operations such as the powder material processing and formation before sintering operations, thereby making powder flow simulation necessary. Powder simulation methods are the (1) finite difference method (FDM), (2) finite element method (FEM), and particle element method (PEM), also known as the distinct element method (DEM). Especially representative are FEM and PEM.

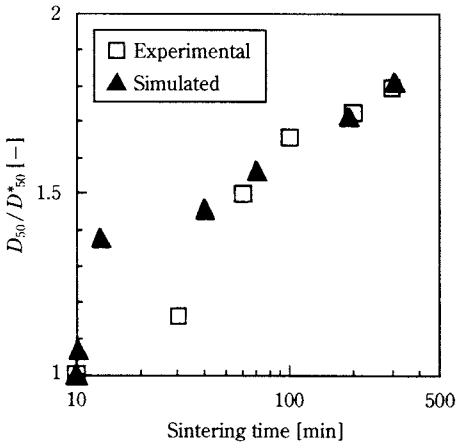

Fig. 15 Change in Average Grain Size

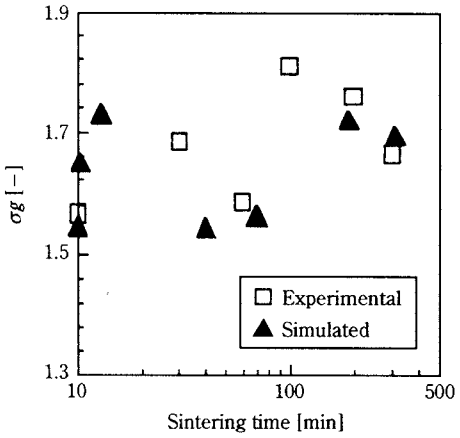

Fig. 16 Grain Size Distribution

4.1 PEM Simulation of Powder Compression Formation Behavior [9]

When small-particle powders are packed very densely and particles move little, as in powder compression, it is possible to use FEM, a continuum dynamics simulation. Using FEM necessitates three basic equations: (1) a stress equilibrium equation, (2) a conformity conditions equation, and (3) a composition equation. Generally (1) and (2) are easily obtained, but the difficulty of finding the composition equation, which shows the relationship between a powder's state of existence and its dynamic nature, calls for resourcefulness.

For powder compression formation, the example given here, we obtain the composition equation by assuming that the powder bed is an elastoplastic continuum. Additionally, the dynamic characteristics of the powder bed interior, where compression increases, change from moment to moment. Then we indicate the powder's interior friction coefficient by the bulk density function, and Young's modulus and strain

hardening rate by the minimum principal stress function, thereby making it possible to consider the moment-by-moment state change that happens as powder compression proceeds.

Fig. 17 is the stress-distortion curve in the powder compression process, and **Fig. 18** shows the development of stress distribution in a powder bed during the compression formation process.

The stress-strain curve obtained by the simulation coincides closely to measured values, and the simulation therefore provides detailed information on the stress distribution that develops during the compression formation process. In operations for the compression formation of ceramics the particle structure of the formed product must be highly uniform. For that reason it is necessary to limit as much as possible the development of stress distribution in the powder bed during the compression formation process.

This FEM simulation makes it possible to select the optimum operational parameters involved in the compression formation of ceramics, such as powder characteristics, shape of the compression formation vessel, compression rate, compression method, and wall friction coefficient, thereby making it possible to design compression formation operations.

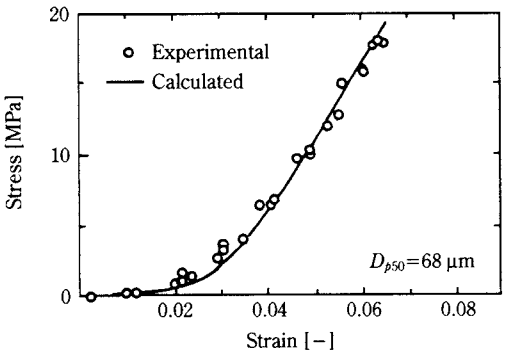

Fig. 17 Stress-Strain Curve for Powder Compression (Material: Al_2O_3)

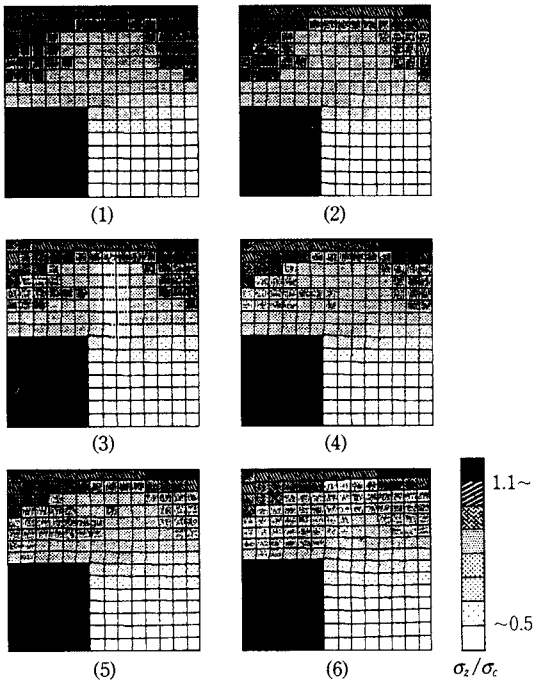

Fig. 18 Development of Strain Distribution in the Powder Compression Formation Process (black area at lower left is rigid body)

4.2 Powder Behavior Simulation by PEM [10, 11, 12, 13, 14]

The Navier-Stokes equation describes powder flow, but since no fundamental equation had been found for powder flow, it was impossible to simulate it. However, computer advances now make it possible to use the discrete element method, making PEM simulations common, and used also in designing powder processes.

The simulation principle for this method is very simple. Let us assume that the particle group in **Fig. 19(a)** is flowing in the arrow's direction. Focusing our attention on one of the particles in the flowing group reveals that its movement is caused by forces imposed by the surrounding particles in contact with it. If it is possible to find the contact force F imposed by surrounding particles from moment to moment, then the movement of the affected particle, which has mass m, is given by Newton's equation of motion ($F=m\alpha$). Because F and m are known, we can solve the equation of motion and obtain particle acceleration α. Integrating the obtained acceleration by time gives the particle's velocity v, and further integration gives its displacement u, thereby allowing us to calculate the flowing particle's trajectory. Because this method gives the trajectories for all the particles involved in fluid movement, it shows the fluid motion behavior of the particle group.

Fig. 20 presents the results obtained when studying the reliability of this simulation method [7].

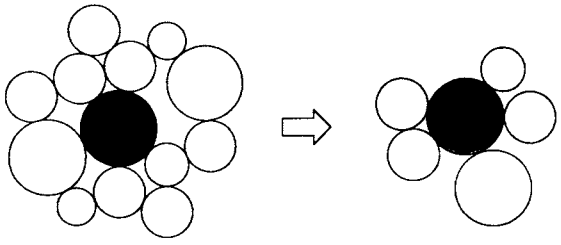

(a) Flowing particles

(b) Adjacent particles in contact with observed particle

Fig. 19 Flowing Particles

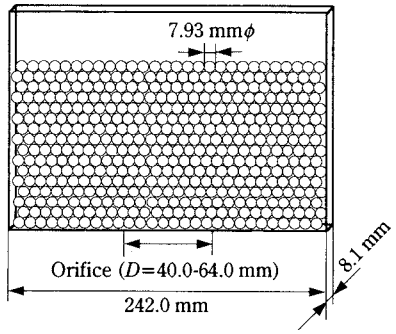

(a) Experimental hopper with vertically single layered monosize particles

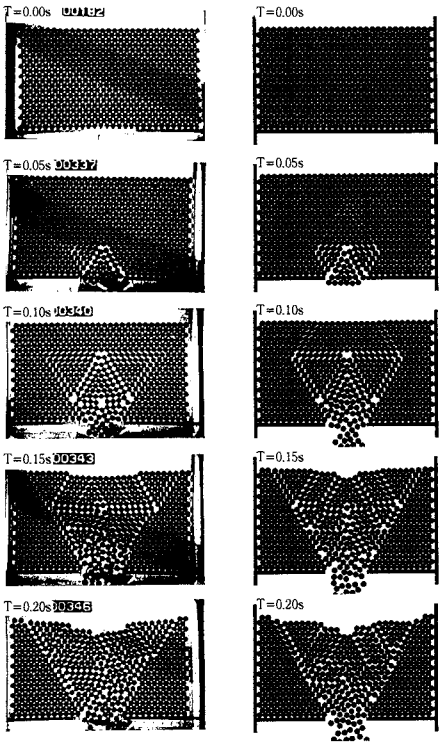

(b) Experimental (c) Simulated

Fig. 20 Simulation Reliability

As shown in **Fig. 20(a)** we put cylindrical particles in a transparent hopper and discharged them through the bottom orifice. **Fig. 20(b)** shows the results of recording the cylindrical particles' fluid behavior with a high-speed video camera, while **Fig. 20(c)** shows the results of simulating fluid behavior using the same conditions as the experiment. These results represent a comparison in which we accurately matched times from the start of movement, and the excellent coincidence demonstrates the great reliability of this simulation. As an example of PEM application, **Fig. 21** presents a simulation of particles discharged from a powder hopper. For a long time there have been several puzzles about powder flows in storage hoppers: (1) Wall pressure when the powder bed is

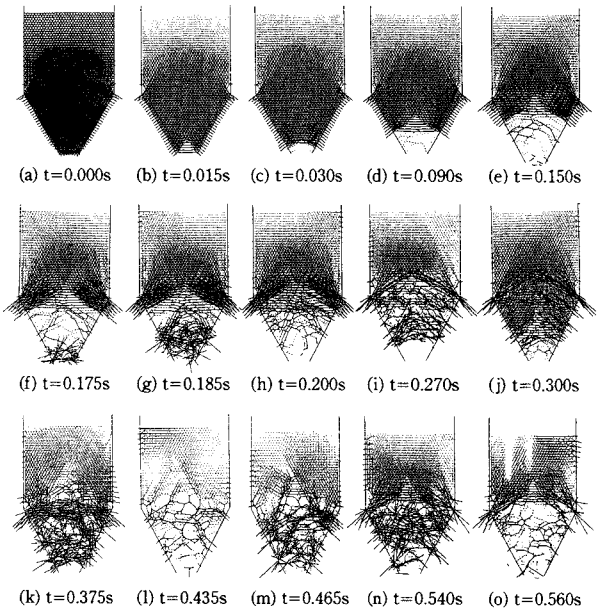

Fig. 21 Simulation of Particle Flow in a Powder Hopper

stationary in the hopper is not proportional to bed height, but comes to a certain constant value as bed height rises. (2) When opening the orifice at the hopper's bottom and allowing powder to flow out, great pressure is exerted on the hopper wall. (3) The outflow rate and wall pressure vary periodically. (4) The outflow rate is not proportional to the orifice's cross section, but rather proportional to the orifice's diameter to the 2.5-3.0 power. (5) The outflow velocity is constant regardless to the powder bed height.

One advantage of PEM simulations is that, because moment-by-moment information on all flowing particles is calculated, it allows very detailed observations of powder phenomena, which facilitates model analyses of the phenomena. In a study of the aforementioned puzzles about the flow of particles in hoppers, the authors proposed a flow model based on PEM simulation results, and offered an explanation according to dynamics [5].

One more PEM simulation advantage is that it allows one to perform powder experiments in a simple manner for the purpose of process design. **Fig. 22** is an example of a screening experiment, and **Fig. 22(b)** plots the relationship between frequency of the screening apparatus and the residual rate curve. Particle screening is sensitive to frequency, and in this example screening was fastest when frequency f was 14 Hz. In an actual experiment one must conduct tests by preparing a powder sample and making a screening apparatus that conforms to vibration conditions, but computer simulations make it possible to freely vary particle properties and the vibration

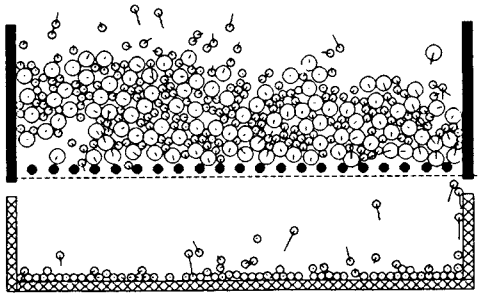

(a) Screening behavior

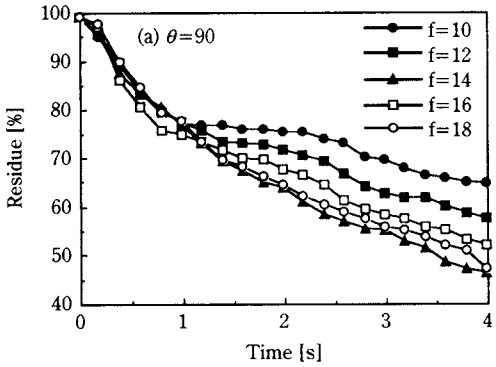

(b) Curve for residual rate above screen (effect of frequency on screening rate; vertical vibration $\theta=90°$, amplitude is 10 mm)

Fig. 22 Particle Screening

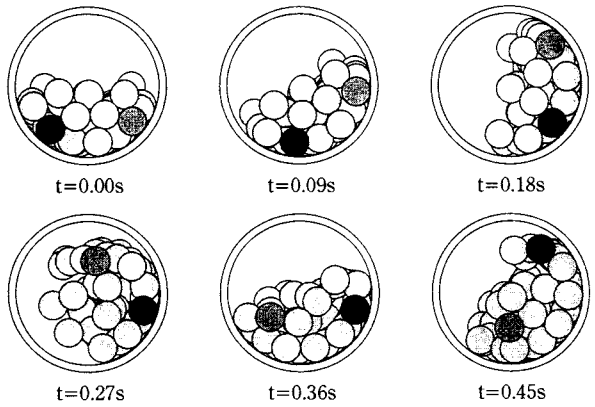

Fig. 23 Ball Behavior in a Ball Mill

characteristics of the screening apparatus, and to easily determine the optimum screening conditions for that powder.

Fig. 23 is a simulation of ball movement in a ball mill. This simulation makes it possible to obtain information on, for example, the energy input into the pulverized particles [15]. PEM simulations often use cylindrical and spherical elements, but simulations that take particle shape into consideration are also possible.

PEM simulations allow detailed observations of powder phenomena, and provide useful information for analyses of powder phenomena and for designing processes. On the other hand, just as with the molecular dynamics method it is difficult to perform large-scale simulations, and it is impossible for the PEM method to directly simulate the behavior of powder in an actual large powder apparatus. In order to get around this drawback, the authors are developing ways to use new simulation methods called the smoothed particle element method and the cellular automaton method [16, 17].

5. Conclusion

This has been an overview of powder simulations for designing powder processes. Especially with more advanced simulations of the powder processing operations included in processes, and with the higher level of production process design, it is necessary to elucidate the relationship between the characteristics of materials produced in processes, and the structure of the materials formed in processes. For that reason we described methods to simulate the relationship between material structure and permittivity, and discussed simulation of sintering, formation, and other processes that form those material structures.

Powder engineering will likely be systematized as a field of engineering pertaining to materials relating to powders and the design of systems for their production processes. It is anticipated that for that purpose powder simulations will become increasingly important. At the same time, the development of computers and improvements in simulation algorithms will proceed at a quickening pace, so that in the near future it will be possible to design powder materials and production process systems with computer simulations.

References

1) Hidaka, J., et al. MS submitted to *Kagaku Kogaku Ronbunshu*.
2) Chiou, B. S., and S. T. Lin. "Equivalent Circuit Model in Grain-Boundary Barrier Layer Capacitors," *J. Am. Ceram. Soc.*, **72**, 1967-1975 (1989).
3) Takeuchi, T., K. Ado, H. Kageyama, K. Honjyo, Y. Saito, C. Masquelier and O. Nakamura. "Analysis of Double Layered Structure of Submicron $BaTiO_3$ Grains Using Equivalent Circuit Model," *J. Ceram. Soc. Japan*, **102**, 1177-1181 (1994).
4) Banno, H. "Theoretical Equations for Dielectric and Piezoelectric Properties of Ferroelectric Composites Based on Modified Cubes Model," *Japanese J. Appl. Phys.*, **24**, 445-447 (1985).
5) Lee, H. G. and H. G. Kim. "Ceramic Particle Size Dependence of Dielectric and Piezoelectric Properties

of Piezoelectric Ceramic-polymer Composites," *J. Appl. Phys.*, **67**, 2024-2028 (1990).
6) Arlt, G., D. Hennings and G. de With. "Dielectric Properties of Fine-grained Barium Titanate Ceramics," *J. Appl. Phys.*, **58**, 1619-1625 (1985).
7) Shimosaka, A., et al. "Computer Simulation of Initial Particle Sintering Behavior," *J.Soc.Powder Technol., Japan*, **32**, 667-674 (1995).
8) Sugie, S., et al. *Summaries of Presentations at the 62nd Chemical Engineering Society Conference* (two vols.), p. 62 (1997).[1]
9) Hidaka, J. "Simulation and the Automation of Powder Processes," *Funtai to Kogyo*, **25**, [12] 27-36 (1993).
10) Hidaka, J. "Numerical Experiments with Powder Systems and Their Application," *J.Soc.Powder Technol., Japan*, **29**, 465-471 (1992).
11) Hidaka, J., et al. "Acoustic Emission Characteristics in the Powder Compression Process," *J.Soc.Powder Technol., Japan*, **26**, 238-244 (1992).
12) Hidaka, J., et al. "Simulation of Particle Behavior in an Inclined Trough," *J.Soc.Powder Technol., Japan*, **30**, 188-193 (1993).
13) Hidaka, J., et al. "Flow Mechanism of Particles When Ejected from a Hopper," *Kagaku Kogaku Ronbunshu*, **20**, 397-404 (1994).
14) Hidaka, J., et al. "Wall Pressure Change and Outflow Rate in Flow Behavior of Particles When Ejected from a Hopper," *Kagaku Kogaku Ronbunshu*, **21**, 581-587 (1994).
15) Kano, J., et al. "Two- and Three-Dimensional Particle Element Method Simulations, and Their Differences, of Particle Movement Behavior in a Vibration Field," *Kagaku Kogaku Ronbunshu*, **23**, 687-693 (1997).
16) Hidaka, J., et al. "New Simulation Method of Flow Behavior of Granular Materials Using Smoothed Particle Method," *Proc. McNU '97*, 626 (1997).
17) Hidaka, J., et al. MS submitted to *Kagaku Kogaku Ronbunshu*.

[1] Should say which volume.

Author's short biography

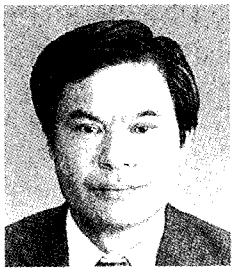

Jusuke Hidaka

Prof. Jusuke Hidaka has been at Doshisha University since 1976. His major research interests lie in mechanical analysis of powder flow using computer simulation, classification and instrumentation of powder industrial processes using acoustic emission. He is the secretary of the Society of Powder Technology, Japan.

Characterization of Changes in Particle Size Distribution by the PaRMAC Evaluation Method†

S.P.E. Forsmo[1], S-E Forsmo[1] and P-O Samskog[1,2]
[1] *LKAB, Malmberget, Sweden*
[2] *Luleå University of Technology, Sweden*

Abstract

PaRMAC is a newly developed evaluation method for the particle size distribution in agglomeration. The particle number distribution is divided into three size categories: 1-10 μm ("sand"), 10-40 μm ("stones") and 40-100 μm ("block"). The "stones" form the basic framework of the pellets. The "sand" is needed to fill in the voids. The relationship between the size categories is quantified by comparing each smaller size to the next larger. Two ratio factors are obtained and used as x-y coordinates. The obtained point defines the status of the sample. By following changes in the position of this point, changes in the original size distribution can be traced. The PaRMAC method allows us to visualise and compare hundreds of samples at the same time.

Changes in the particle size distribution of LKAB iron ore concentrates are tracked as the agglomeration process advances. The magnetite concentrates begin to agglomerate as early as during filtration. The bentonite binder redisperses the agglomerates. The dispersion grade varies due to changes in the efficiency of the bentonite mixer.

1. Introduction

The pelletizing process of iron ore concentrates includes wet grinding of the concentrate to the desired fineness, addition of additives, filtration to about 9% humidity, addition of binder, balling to a mean pellet size of 11 mm, and finally drying and induration at high temperatures to achieve the desired mechanical strength and metallurgical properties. The iron ore mined at LKAB, Sweden, is magnetite which oxidises to hematite during induration. This oxidation is an exothermic reaction releasing a large amount of energy. As much as two-thirds of the energy used for pelletization comes from the magnetite oxidation to hematite. The particle size distribution affects the pellet properties in a complex manner because it not only changes the porosity and packing properties, but also the oxidation pattern and the temperature profile in the pellet bed during induration.

The packing properties of dry powders have been widely studied [1,2]. A comprehensive review regarding both experimental work and mathematical models in this area was given by Yu and Zou [3] in the previous volume of this journal. The target when optimising the agglomeration properties of magnetite concentrates is not necessarily a high packing density as often seems to be the case in the area of packing dry powders. The pellet porosity should be a compromise between the pellet's mechanical strength and an open inner structure for better gas transfer during oxidation and reduction.

Traditionally, the particle size distribution of iron ore concentrate is measured by screening (weight distribution) or by laser diffraction methods (volume distribution). Also, the specific pressure drop through a packed bed of particles (Blaine index or Svensson surface) is commonly used to describe the fineness of materials. When this agglomeration research was started, we knew from practical experience that none of these methods successfully predicts the pelletizing process behaviour or the pellet quality as a function of the particle size distribution.

The formation of a green pellet can be regarded as masonry work on a micro scale. A specific number of particles with suitable size ratios is needed to do the work, a strong and at the same time open green pellet. Upon looking for a measuring instrument that could measure the size distribution of the number of

[1] Research and development, LKAB, 98381 Malmberget, Sweden
[2] Lulea University of Technology, 97187 Lulea, Sweden
† Received: May 12, 1999

particles instead of weight or volume distributions, the scanning laser microscope was found.

Another difficulty that was faced was to evaluate changes in the particle size distribution when a large number of samples is to be considered. Visual inspection of the size distribution curves can cope with maybe five to ten samples at a time. Numerical inspection of the curves by using, for example, k_{90} values reduces the inspection to only one, or a few points on the size distribution curve, and information on crossing curves is easily lost. A better evaluation method was needed and the PaRMAC method was developed. The name PaRMAC stands for Particle Ratios Method for Agglomeration Characterization.

With the PaRMAC method, the suitability of a particle mixture as masonry raw material is described by dividing the size distribution curve into three size categories. They are ratioed to each other and the ratio factors are used as x-y coordinates. This point describes the original particle size distribution of the sample. The PaRMAC method allows us to inspect and compare hundreds of samples at the same time and to visualise the differences in a simple and practical manner. PaRMAC has proved to be a good help in understanding how to accomplish desired changes in the size distribution. In this article, the PaRMAC method is described in detail and some practical applications of the method are given.

2. Measuring methods

The particle size distribution is measured using the Partec 100 instrument by Lasentec. It uses scanning laser microscope technology. The laser beam is focussed to a small beam spot with a high intensity at the focal point. The laser beam scans at a high and constant velocity, and the time it takes for the beam to scan across a particular particle is a direct measure of the particle size.

The Partec 100 instrument measures a random chord across the particle. The iron ore particles have shapes which are complex and irregular. As they are often somewhat needle-shaped, they show fairly short chord values more frequently. The additive particles, olivine and dolomite, are quite round and show about the same chord value in all directions. Depending on this difference in particle shape, screening, PaRMAC and laser diffraction all give different results. The magnetite concentrate and the additives are ground to the same fineness measured by sieving (% <45 μm). PaRMAC describes the additive particles as large compared to magnetite. In the Malvern diffraction pattern measurement, the additive particles are small and practically disappear under changes in the large magnetite particles [4]. This discrepancy between different measuring methods is a well-known problem when measuring the size distribution of particle mixtures with different particle shapes.

The particle number distribution measured by the Partec 100 can be mathematically recalculated to mass and volume distributions. At present, however, the raw data from the measurements are used. Possibly, in future, calculation of the volume distribution could be performed as a complement to the particle number distribution in order to collect additional information about changes in the large particles. This applies especially to the new digital instrument versions, where the counting time can be increased to also obtain good reproducibility for the largest particles.

The measuring range of 1.9 to 1000 μm is divided into 37 measuring channels, of which about 30 are active when measuring iron ore concentrates.

The Partec 100 measurements are made in a slurry containing 50 wt-% solids under high-shear mixing conditions. Moist samples such as filter cakes and green pellets can be measured directly without drying. The binding agent, bentonite, is invisible to the Partec 100 when it is added in amounts of 0.5 weight-%. Therefore, even green pellets can be measured. The possibility of measuring the particle size distribution in the natural process water environment, without drying and redispersion, has proved to be especially valuable.

Maintaining a constant measuring geometry, mixing speed and slurry solids content are prerequisites for a successful measurement. Reproducible results also require special care in sampling, sample preparation and dispersion.

3. The PaRMAC evaluation method

PaRMAC stands for Particle Ratios Method for Agglomeration Characterization. It was published in the proceedings of the XXth IMPC conference in Aachen, 1997 [4]. Our aim is to use the PaRMAC method in correlating and optimising the particle size distribution in pellet feed with respect to the pellet properties. The same principle of ratioing desired size fractions can, of course, be used in other applications as well as for mass and volume distributions.

With the PaRMAC method, the particle mixture is considered as a ternary particle system. The size classes are chosen empirically to describe the different behaviour of the particles.

The three size categories were selected and designated as follows:

- "sand" about 1-10 μm
- "stone" about 10-40 μm
- "block" about 40-100 μm

The designations sand, stone and block were chosen to describe the use of these different fractions as building materials for the green pellets. The "stones" form the basic framework in the pellet, the "sand" is needed to fill in the holes between the stones. The "blocks" are baked inside the green pellet with enough of both sand and stone. The names simplify discussions over changes in the size distributions. Also, they associate the complicated science of balling green pellets to the art of making sand cakes, well known by all small children. A firm sand cake can be created by mixing the three components in varying proportions and by adding a suitable amount of water.

The "sand" category was chosen to describe the particles that show nearly colloidal behaviour and have a comparably large surface area. Therefore, this fraction is expected to be a good indicator of surface chemical reactions such as flocculation, dispersion and topochemical oxidation. The measuring range of the Partec 100 instrument sets the lower limit of the sand fraction at about 1 μm. This was considered acceptable from the agglomeration point of view, because the average pore size in green pellets is around 1-2 μm.

LKAB produces pellets at both their Malmberget and Kiruna operations. For the Kiruna pellet concentrates, most of the particles are between 10 and 40 μm in size. The upper limit of 40 μm is set by the cut-off size of the hydro-cyclones in closed-circuit grinding. This size range was chosen for the category designated as "stones".

The upper limit for the "block" designation was chosen to be about 100 μm because in pellet concentrates, particles larger than this are few and of minor interest. The blocks probably show characteristic oxidation behaviour, because the oxygen needs to diffuse longer distances inside the particles.

The relationship between these three size categories is quantified by comparing each smaller size category to the next-larger size category. The following ratios are calculated:

$$\text{sand factor (x)} = (\%\text{sand}/\%\text{stone}) \times 100 - 100$$
$$\text{stone factor (y)} = (\%\text{stone}/\%\text{block}) \times 100 - 600$$

The constants of 100 and 600 have been chosen so that the normal values for the Malmberget pellet feed lie near the origin.

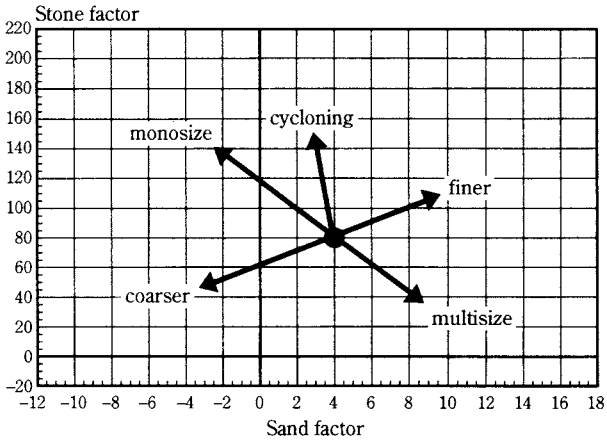

Fig. 1 Broad outlines for typical directions of changes in the PaRMAC chart.

These two factors are used as x and y coordinates and the resulting (x,y) point describes the overall size status of the sample in the PaRMAC chart. Changes in the position of this point describe changes in the original size distribution curve. Typical directions of changes are shown in **Figure 1**. In open circuit-grinding, the PaRMAC point moves towards higher positive x and y values as the material becomes finer. Cycloning lifts, typically, the PaRMAC point upward towards higher stone factor values. The exact direction of the change depends on the cut-off size of the hydro-cyclones.

The changes in the slope of the cumulative particle size distribution curve can also be interpreted from the PaRMAC chart. The steeper the curve, the further up and to the left the point moves. The particle size distribution becomes more "monosize" and obviously, more difficult to agglomerate.

The precision (defined as 2σ) is ± 0.5 units for the sand factor (x) and ± 10 units for the stone factor (y). The chosen limits for the three different size categories have been successful for our application.

4. Applications of the PaRMAC evaluation method

4.1 A comparison of pellet concentrates from different LKAB concentrating plants

A set-up of magnetite pellet concentrates from different LKAB concentrating plants is shown in the PaRMAC chart in **Figure 2**. The quality variations for different concentrates do not describe comparable process quality variations because of different sampling intervals.

The PaRMAC points for the Kiruna and Svappavaara pellet concentrates (KPC and SPC) lie at lower sand factor (x) values and higher stone factor (y) values

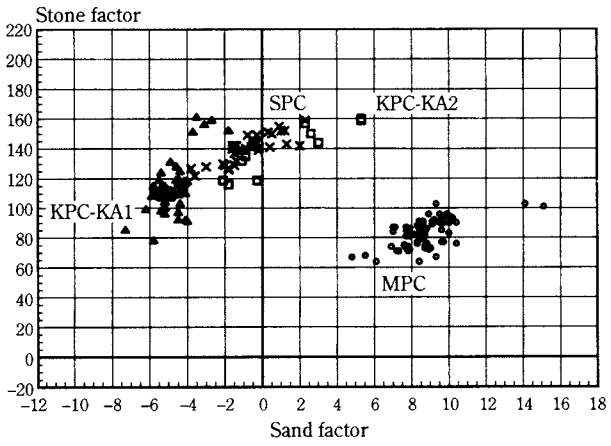

Fig. 2 A PaRMAC chart on magnetite pellet concentrates from different concentrating plants in LKAB. (△) Kiruna KPC-KA1, (□) Kiruna KPC-KA2, (×) Svappavaara SPC and (○) Malmberget MPC.

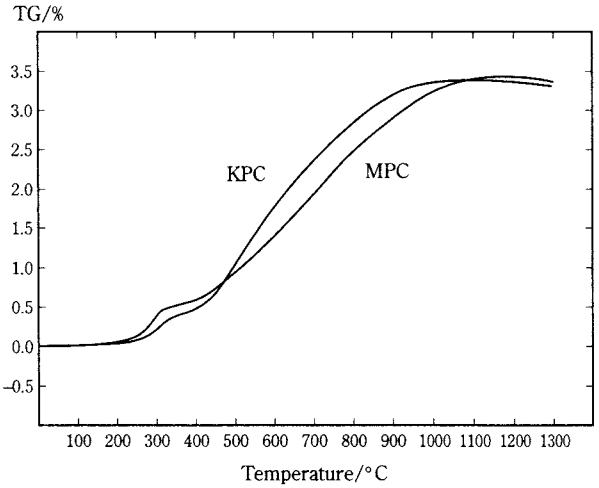

Fig. 3 A typical dynamic oxidation run for MPC and KPC. Scan rate 5°C/min, 110 mg of sample in an open platinum crucible.

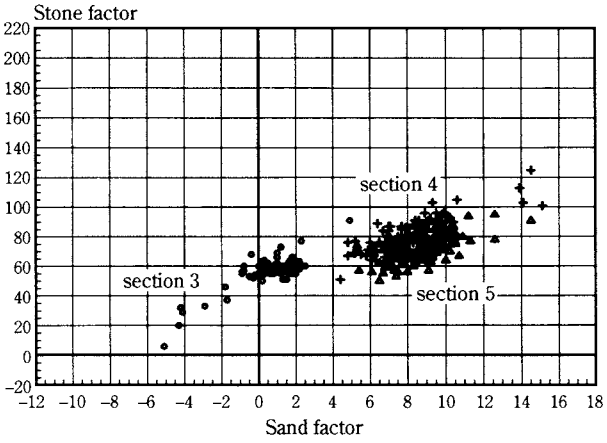

Fig. 4 PaRMAC chart on Malmberget pellet concentrate (MPC) produced in three production sections. (○) Section 3, (+) section 4 and (□) section 5.

compared with the Malmberget pellet concentrate (MPC). This is due to closed-circuit grinding in Kiruna and Svappavaara. In Malmberget, we have open-circuit grinding in three steps. The KPC and SPC are much finer by screening compared with the MPC (KPC 84% and MPC 68% <45 μm, respectively). However, the size distribution curve for KPC is much steeper due to cycloning. The proportion of "sand" to "stone" decreases and "stone" to "block" increases, the distribution becomes more monosize.

A more monosize distribution should result in higher porosity in the green pellets. This is indeed the case. The porosity in Kiruna and Svappavaara green pellets is typically somewhat higher than in the Malmberget pellets (32% and 30%, respectively).

The differences in the particle size distribution between KPC and MPC can also be seen in the oxidation pattern of these materials. Typical thermogravimetric analysis (TG) results for KPC and MPC are shown in **Figure 3**. MPC with higher PaRMAC x-values oxidises at low temperatures (<400°C) more to maghemite than KPC. This low-temperature oxidation of magnetite to maghemite is generally agreed to be topochemical in the literature. KPC with higher PaRMAC y-values gains in the oxidation rate when the large number of medium-sized particles is oxidised.

4.2 The benefit of visualising a large number of near-similar samples in the PaRMAC chart

In our earlier publication [4], an example was given regarding the visualisation of a large number of samples at the same time in the PaRMAC chart. This is shown in **Figure 4.**

In Malmberget, three open-circuit grinding sections were used to produce the pellet concentrate, MPC. The control value for all three sections was 68% <45 μm by sieving. The PaRMAC points for samples from section 3 differ significantly to those from sections 4 and 5 although they all showed similar values by sieving. The reason is a flow of screened oversize particles connected to the primary mill in section 3.

In **Table 1** screen analysis, Malvern and PaRMAC values are given for two sets of samples from these three sections. When sampling, the control values were 66% (section 3) and 64% (sections 4 and 5) <45 μm by sieving. The table describes six samples altogether. It demonstrates the difficulty of comparing particle size distributions expressed in figures, especially if the curves cross each other. The PaRMAC chart in **Figure 4** shows 326 samples altogether. By only glancing at the PaRMAC chart, one can directly point out the samples that differ.

Table 1 Sieve analysis, Malvern and PaRMAC values for Malmberget pellet concentrates (MPC) produced in three parallel production sections.

	Screening	Malvern	Malvern	Malvern	PaRMAC
	% <45 µm	K_{10}/µm	K_{50}/µm	K_{90}/µm	(x, y)
Sample pair 1:					
Section 3	66.3	5.2	46	138	+0.7, +59
Section 4	63.5	5	51	175	+7.5, +80
Section 5	63.9	5.1	51	162	+5.3, +70
Sample pair 2:					
Section 3	67.5	4.4	47	173	+0.5, +59
Section 4	61.8	4.6	48	162	+5.2, +59
Section 5	63.5	4.4	42	134	+6.2, +72

4.3 Particle size distribution in real process conditions interpreted by PaRMAC

Because the measurements are performed on a slurry with 50 weight-% solids, moist samples such as filter cakes and green pellets can be measured directly without drying. This allows us to study the particle size distribution and dispersion in real process conditions. In the case of green pellets which contain the bentonite binder, it is in general not possible to measure the particle size distribution at all, if the pellets need to be dried first. The bentonite binds the dried particles together so hard that redispersion is not possible.

The PaRMAC charts in **Figure 5** compare the dried pellet concentrates, the moist and dry filter cakes and the green pellets at the concentrating and pelletising plants of LKAB located in Malmberget (MPC), two plants in Kiruna (KPC-KA1 and KPC-KA2) and in Svappavaara (SPC). The pellet concentrates contain only magnetite, the filter cakes contain magnetite and olivine, and the green pellets contain magnetite, olivine and bentonite. The individual sample sets do not represent contemporary material flows. However, the PaRMAC charts give an interesting picture of how the particle size distribution changes due to different unit operations and different process design.

The pellet concentrates mixed with olivine are stored in large slurry buffer tanks before filtration. Therefore, the filter cakes show less variation in the PaRMAC co-ordinates than the pellet concentrates.

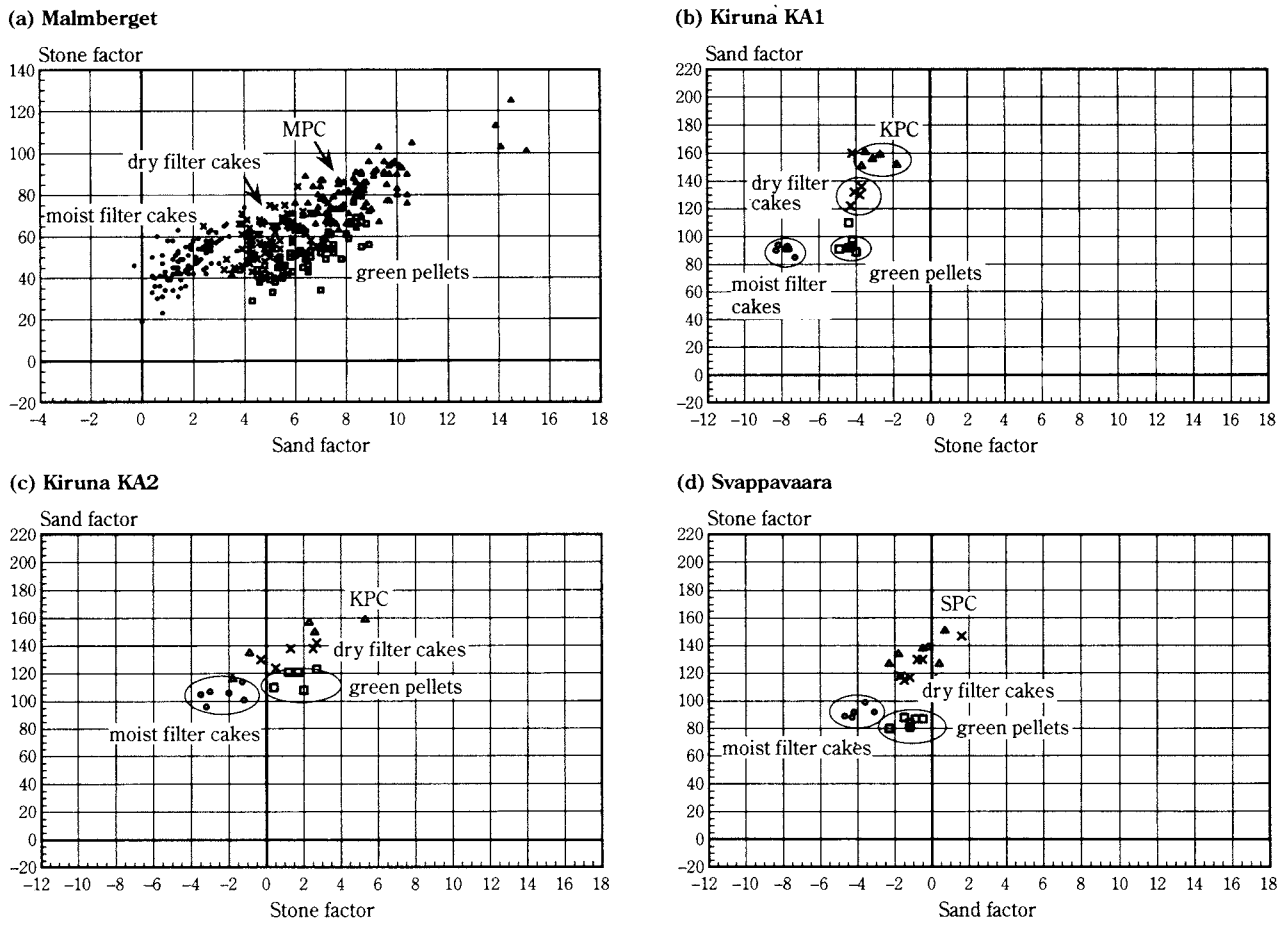

Fig. 5 PaRMAC chart on (△) dried pellet concentrates, (○) moist filter cakes, (×) dry filter cakes and (□) green pellets at LKAB Malmberget, Kiruna (2 plants) and Svappavaara.

This can be seen in **Figure 5a**, where the number of samples is large enough to describe real process variations.

The addition of olivine to the magnetite concentrate changes the PaRMAC coordinates. According to laboratory tests, addition of 3.6% olivine to the pellet concentrate slurry results in 10-20 units lower PaRMAC y-values. Therefore, the filtered pellet feeds should lie at somewhat lower y-values than the magnetite concentrates. This is the case for the dried filter cake samples. However, the moist filter cake samples measured directly without drying lie at much lower x- and y-values. This applies to all plants in varying degrees. This difference in the PaRMAC coordinates of humid and dried filter cake samples is explained by agglomeration during filtration. These agglomerates, which do not contain any bentonite binder, need to be dispersed before balling. Otherwise, it would lead to problems in pellet quality.

The addition of bentonite disperses the agglomerates formed during filtration. However, the degree of redispersion depends on the strength of the agglomerates, the effectiveness of the bentonite mixer, and also on the energy input in the balling circuits.

In Malmberget, we had the opportunity to follow this redispersion pattern when the old bentonite mixer in the pellet plant was changed to a new Eirich mixer [5]. After the new mixer was installed, the green pellet coordinates in the PaRMAC chart were shifted further to the right towards higher sand factor (x) values, indicating more effective dispersion in the bentonite mixer, see **Figure 6**.

The flotated pellet concentrate in Kiruna KPC-KA2 shows less agglomeration due to filtration than the unflotated concentrate KPC-KA1, see **Figures 5b** and **5c**. This can be explained by flotation reagent adsorption on magnetite surfaces. This difference in surface characteristics between the flotated and unflotated concentrates can also be seen visually during sample division. The moist, flotated pellet feed is more free-flowing and shows less tendency to agglomeration.

The PaRMAC measurements on samples containing bentonite are carried out by diluting the samples to 50 weight-% solids by the process water. When parallel samples of green pellets were prepared using a combination of process water and distilled water, the PaRMAC coordinates in clean water were systematically lower in both x- and y-values, indicating a lower degree of dispersion, see **Figure 7**. This could be either due to higher pH or the high salt content in the process water. The pH and the salt content in the process water show periodical variations, and the water quality is also different at different plants [6]. These variations might not be of great interest from the agglomeration point of view in the production scale, but they do play a role in the precision of the PaRMAC laboratory measurements. Therefore, samples containing bentonite are always diluted with filtered process water. For samples without bentonite, the quality of the water used in sample preparation is irrelevant.

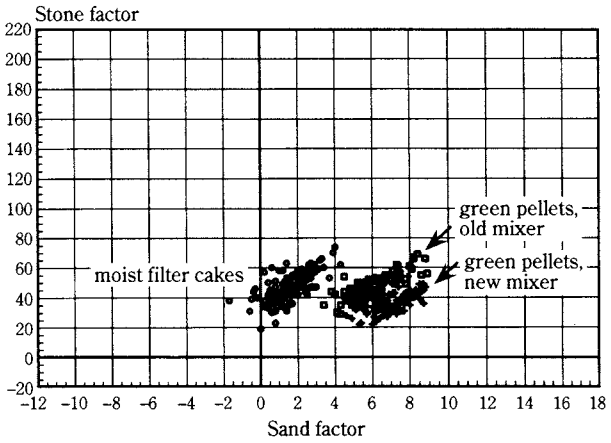

Fig. 6 PaRMAC chart from Malmberget before and after installing a new bentonite mixer. (○) Moist filter cakes, (□) green pellets with the old mixer and (+) green pellets with the new mixer.

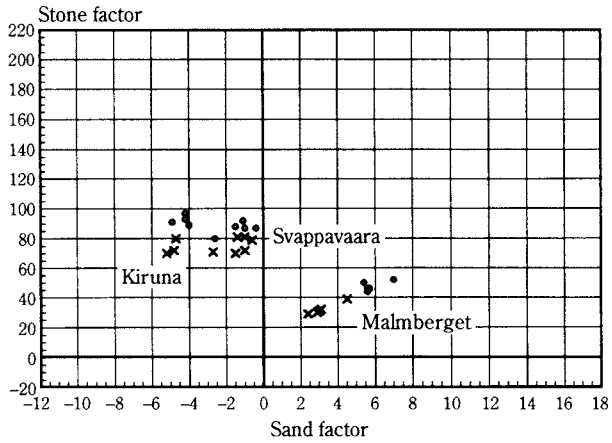

Fig. 7 PaRMAC co-ordinates on green pellets from Malmberget, Kiruna and Svappavaara measured after dilution by (×) distilled water and by (○) process water.

This example shows that the concept of particle size distribution in pellet feeds is somewhat ambiguous. The question that arises is whether the pellet properties should be correlated to the primary particle distribution or to the actual size distribution of agglomerates found in real process conditions. The oxidation rate in single particles could be expected to correlate with the fineness of primary particles measured in dried concentrates. The packing properties and the oxidation behaviour inside a single pellet

could, however, also depend on the material's tendency to agglomerate during filtration, on bentonite mixing efficiency, and on the dimensions of the balling drums. These phenomena are difficult to simulate on a small scale. They need to be considered when results from small-scale studies are scaled up to the production scale.

5. Discussion

The examples given above show the versatility of the PaRMAC method. It is a great help for a scientist to be able to view a large number of size distributions on a single chart and to be able to rapidly obtain an impression of deviating samples or sample groups.

The use of size distributions based on the number of particles has given more information about the behaviour of those size fractions which are significant for the pelletising process. Most of the unit operations in the concentrating plant lead to varying degrees of skewness in the size distribution curves. Changes in the process lay-out at the early stages of the concentrating process have been shown to affect the size distribution in the final pellet concentrate. Combined with process knowledge, the PaRMAC chart will show both optimal working areas and areas to be avoided.

The use of proportions between size fractions instead of absolute particle sizes seems to give a fair correlation to the pellet porosity and also to the magnetite oxidation behaviour. We are intensively studying this further.

The possibility of measuring the particle size distribution in real process conditions has shown that although the distribution of primary particles would be constant, variations in aggregate size distribution could occur because of variations in bentonite mixing efficiency or changes in balling circuits. These variations have previously not been detectable.

References

1) D.J. Cumberland, R.J. Crawford: The Packing of Particles, Elsevier Science, Amsterdam, The Netherlands, 1987.
2) R.M. German: Particle Packing Characteristics, Metal Powder Industries Federation, Princeton, New Jersey, 1989.
3) A.B. Yu, R.P. Zou: Prediction of the Porosity of Particle Mixtures, KONA 16 (1998), 68...81.
4) S.P.E. Forsmo, S-E Forsmo: PaRMAC – A New Method of Evaluating the Particle Size Distribution for Agglomeration, XXth IMPC, Aachen, Germany, 21-26 September 1997, 347...353.
5) S.P.E. Forsmo, S-E Forsmo: PaRMAC – A New Method of Evaluating the Particle Size Distribution for Agglomeration, Mineral Technical Conferance in Luleå, Sweden, 10-11 February, 1998, 75...86.
6) A. Lundkvist: The Process Water Geochemistry of the Kiirunavaara Magnetite Ore, Licenciate thesis, Luleå University of Technology, Department of Environmental Engineering, Division of Applied Geophysics, 1998.

Author's short biography

Seija Forsmo

Seija Forsmo works as a senior research engineer in LKAB. She works presently to develop new analytical measuring methods for the characterization of the agglomeration properties of iron ores.

Sten-Evert Forsmo

Sten-Evert Forsmo works as a senior research engineer in LKAB. He works presently to correlate raw material properties to the pelletizing process and to the pellet quality.

Per-Olof Samskog

Per-Olof Samskog received his Ph.D. physical chemistry at the University of Stockholm 1979 and spent two years as visiting scientist at the University of Alabama US. He is currently manager of Systems Technology at the Swedish mining company LKAB and adjunct Professor at the Luleå University of Technology, Sweden.

Particle Mass Spectrometer (PMS) and its Application to Nano-Particle Sizing in Various Systems†

C. Janzen, M.G.D. Strecker and P. Roth
Institut für Verbrennung und Gasdynamik
*Gerhard-Mercator-Universität Duisburg**

Abstract

Particle mass spectrometry has been shown to be an effective diagnostic technique to determine particle size and size distribution of charged nano-particles originating from different reactive sources. In the present paper, the principle of the PMS is described in detail and examples of application to various particle formation systems are presented. A spark generator, a microwave reactor, and a low-pressure premixed flame burner were used to produce particles of different materials in different size ranges between 1 and 10 nm. The resolution and sensitivity of the PMS has been improved by the adaptation of a preamplifier consisting of a secondary electron multiplier coupled to an external conversion dynode. The particle mass – being the main parameter of the measurements – is not influenced by the additional acceleration due to the conversion current. The use of a secondary electron multiplier leads to a signal gain of 10^4 compared with measurements without the preamplifier.

Introduction

A large number of commercial powders, e.g. for the semiconductor industry, pigments, carbon blacks, and high-purity materials for optical fibers and thin films, are produced via aerosol routes, see for example [1] – [4]. The control of the process is necessary in order to determine the powder characteristics and to specifically influence the properties of the product particles, [5]. Consequently, *in-situ* analysis is desired to follow the formation process and to control the characteristics of the particles. Available techniques for sizing and detecting aerosol particles are often limited to operation near atmospheric pressure (e.g. differential mobility analyser, condensation nuclei counter, diffusion batteries, etc.). Furthermore, most of the methods require sampling and dilution prior to analysis [6], which may change the powder characteristics. It is thus necessary to realize a continuous sampling method which has no effect on the particle characteristics and which is effective in size determination.

Molecular beam sampling, which is widely known from conventional time-of-flight mass spectrometry, can fulfill the requirements of almost undisturbed, continuous sampling, thus giving a clear image of the reactive environment in the probe. Disturbances are avoided by an expansion into the free-molecular regime with coinciding rapid freezing of the sample. The particle mass spectrometer described here [7] allows the determination of the particle size and size distribution by combining measured particle kinetic energy and particle velocity. In contrast to the particle beam mass spectrometer used by Ziemann et al. [8], the PMS does not require any calibration and is applicable for particles down to 1 nm and large molecules.

Measurement Principles

The basic principle of the particle beam mass spectrometer is the behavior of charged particles in an electric field. The situation is shown schematically in **Fig. 1**. The particle beam enters a uniform electric field in a capacitor of length l_C and width b_C supplied with a voltage U_C. The lines of force of the electric field are assumed to exist only inside the capacitor and are perpendicular to the electrode surfaces. The field strength therefore is $E=U_C/b_C$. An individual charged particle entering the capacitor is deflected by a force $F_y=z\,e\,U_C/b_C$. It causes an acceleration in the y-direction in relation to its mass $\ddot{y}=z\cdot e\cdot U_C/(b_C\cdot m_P)$. The trajectories of the particles inside the capacitor can be described as follows:

$$y_P=\frac{1}{2}\cdot\frac{z\cdot e\cdot U_C}{m_P\cdot b_C}\cdot t^2 \qquad x_P=v_P\cdot t$$
$$\dot{y}_P=\frac{z\cdot e\cdot U_C}{m_P\cdot b_C}\cdot t \qquad \dot{x}_P=v_P. \tag{1}$$

* 47048 Duisburg, Germany
† Received: May 17, 1999

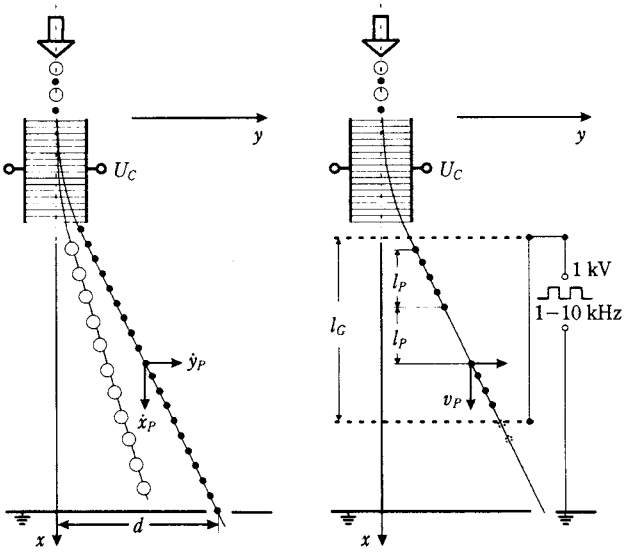

Fig. 1 Left-hand side: deflection of charged particles in an electric field and resultant particle trajectories in a vacuum containment. Right-hand side: formation of particle packages and operation of the electrical filter supplied with synchronously pulsed high voltage.

After leaving the capacitor, the particles move along straight lines as indicated on the left side of **Fig. 1**. Assuming constant velocity components $\dot{y}_P$ and $\dot{x}_P$, the trajectory of an individual particle is therefore given by:

$$y_P = \frac{z \cdot e \cdot U_C}{m_P \cdot v_P^2} \cdot \frac{l_C}{b_C} \cdot \left(x_P - \frac{l_C}{2} \right) \quad \text{for} \quad x_P \geq l_C. \tag{2}$$

Since every particle of mass m_P and charge z has its individual trajectory, the originally uniform and well-focused particle beam is split up into a fan-shaped beam. The mass classification is now realized by introducing a "monochromator" slit which selects particles of one distinct mass whereas the others are blocked. The slit is located at a distance of $x=l$ downstream of the capacitor, has a slit width Δd, and a position $y=d$ from the beam axis. By rearranging Eq. (2) and introducing $y_P=d$ and $x_P=l$, the kinetic energy selecting operation of the whole arrangement is:

$$E_{kin} = \frac{m_P}{z \cdot e} \cdot \frac{v_P^2}{2} = U_C \cdot \frac{l_C}{b_C} \cdot \left(\frac{2 \cdot l}{d} - \frac{l_C}{d} \right). \tag{3}$$

The equation above indicates that for known values of l_C, b_C, d, and l, the voltage U_C selects particles of kinetic energies $m_P \cdot v_P^2/2$ carrying z elementary charges. By varying the deflection voltage U_C, particles of various kinetic energies can be made to pass the "monochromator" slit. Thus:

$$U_C = \text{const.} \cdot \frac{m_P}{z \cdot e} \cdot \frac{v_P^2}{2}. \tag{4}$$

The particle mass m_P can be determined from the deflection voltage U_C, if the velocity of the particles is known. The set-up shown on the right side of **Fig. 1** is used to measure the required velocity of the particles. The selected beam of charged particles passes two grids supplied with a synchronously pulsed repelling potential. The upper grid forms packages of length l_P which depend on the frequency f of the grid voltage and the particle velocity v_P. Only very few or no particles can pass the second grid if the particle package length l_P is an odd-numbered multiple of the distance l_G between the grids. By changing the frequency of the deflection voltage U_C, a fluctuating particle current with maxima and minima is obtained. These minima and maxima of the particle current I_P obey the following conditions:

$$\begin{aligned} v_P &= 2 \cdot f_{min,i} \cdot l_{p,i} \\ l_{p,i} &= l_G, l_G/3, l_G/5, \text{ etc.} \end{aligned} \tag{5}$$

Combination of Eqs. (4) and (5) leads to

$$U_C = \text{const.} \cdot \frac{m_P}{z \cdot e}. \tag{6}$$

The resultant signals are current/voltage spectra of the kinetic energy of the particles. From the principle of the particle mass spectrometer (PMS), it is also clear that the current/voltage spectra are not the probability density function (PDF) of the particle mass or the kinetic energy, because the sensitivity of the PMS depends on the deflection voltage. Roth and Hospital [9] have shown the following relation between the measured particle current, the deflection voltage U_C, and the PDF to be valid:

$$\text{PDF}(m_P) = \text{const.} \frac{I(U_C)}{U_C} \tag{7}$$

The realization of the particle mass spectrometer is schematically shown in **Fig. 2**. It consists of a molecular beam sampling system by which a small sample taken from the respective aerosol generator is supersonically expanded through a silver-plated and electrically grounded glass nozzle ***a*** into a vacuum chamber where the pressure is kept at about 10^{-3} mbar. The supersonic free jet formed by the nozzle expansion flow contains both particles and gas molecules. The flow conditions are such that the gas temperature decreases very rapidly, freezing any physical and chemical reactions inside the expanding sample almost completely. The center of the free jet is extracted by a sharp-edged skimmer ***b*** and moves as a "particle-loaded" molecular beam into the second vacuum chamber. The molecular beam is directed through a

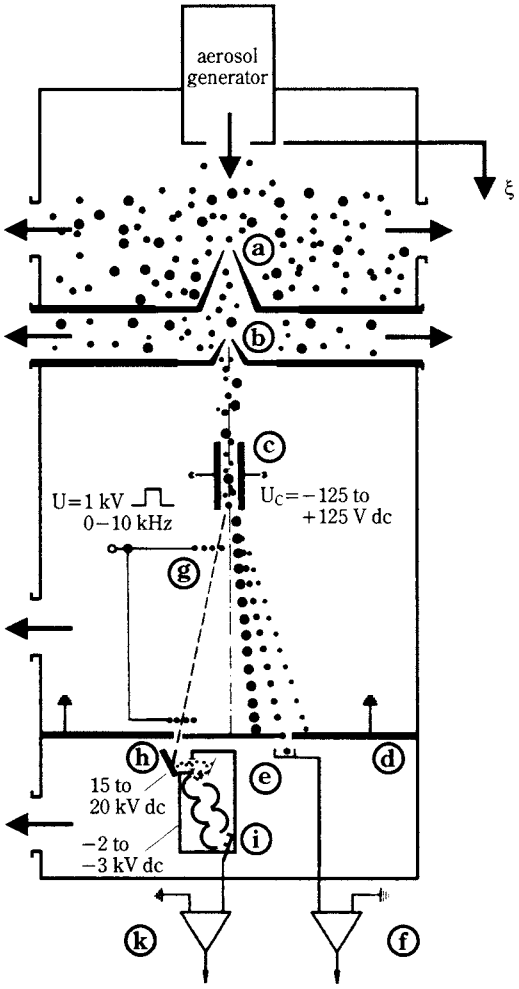

Fig. 2 Schematics of the PMS. ***a*** nozzle, ***b*** skimmer, ***c*** electrostatic deflection plates, ***d*** electrically grounded blend with slits, ***e*** Faraday-Cup, ***f*** electrometric amplifier, ***g*** repelling grids, ***h*** conversion dynode, ***i*** secondary electron amplifier, ***k*** electrometric amplifier.

deflection capacitor ***c***, where charged particles are deflected from the beam axis and analysed due to their kinetic energy, as described above. The particles deliver their charge to a Faraday-Cup ***e***, which is connected to an ultra-sensitive amplifier ***f***.

In order to improve the sensitivity of the PMS, a third vacuum chamber ***d*** is added to the PMS. The pressure in this chamber was maintained at about 10^{-8} mbar by a turbomolecular pump in order to obtain a further signal amplification compared with the Faraday-Cup. It consists of a conversion dynode ***h*** and a secondary electron multiplier ***i***. The dynode is supplied with a high positive voltage of 15 to 20 kV. This high electric field accelerates negatively charged particles from an initial kinetic energy of some hundred eV to some keV. The energy of the particles is then high enough to produce secondary electrons or ions when impacting on the surface of the dynode. The secondary charge carriers are further accelerated towards the cathode of the secondary electron multiplier which consists of 17 dynodes, causing an exponential electron increase by a factor of about 10^6 to 10^8. The generated current can be further amplified by an ultra-sensitive amplifier ***k***.

Experimental Study and Results

In this study, four different types of particle sources have been connected to the PMS, and the respective mass evolutions of the nano-sized particles have been studied in:

- premixed low-pressure $H_2/O_2/Ar$ flames doped with SiH_4 to produce SiO_2 particles,
- a spark generator to produce charged particles at different spark frequencies 10 Hz$\leq f \leq$ 1000 Hz from different materials,
- a microwave plasma burning in C_2H_2/Ar mixtures to generate nano-sized soot particles,
- premixed low-pressure $C_2H_2/O_2/Ar$ flames to produce soot particles.

In the case of soot particle formation in low-pressure hydrocarbon flames, Faraday-Cup measurements were compared with results obtained from secondary-electron multiplier measurements.

In the first series of experiments, the PMS was connected to a low-pressure flame reactor. Mixtures of hydrogen, oxygen, and argon were doped with small amounts of SiH_4 to produce ultrafine silica particles [10]. The pressure was held between 25 and 30 mbar providing an extended reaction and particle formation zone, thus ensuring a higher spatial resolution. The gases were premixed and supplied to the burner head by mass-flow controllers. The low-pressure burner was movable in the horizontal direction to vary the distance between the burner head and the probing nozzle, i.e., the flow coordinate ξ. Examples of simultaneously measured current/voltage spectra and current/frequency spectra of positively charged particles, from which the particle mass can be determined, are shown in **Fig. 3**. Samples containing silica particles were taken from the low-pressure burner at a flow coordinate of ξ=60 mm. The flame conditions are given in the figure caption. The upper part of **Fig. 3** shows the particle current measured with the Faraday-Cup as a function of the deflection voltage. The curve shows one distinct maximum at U_C=11 V. According to Eq. (6), the deflection voltage can be directly related to the particle kinetic energy. For a singly charged particle, a voltage of U_C=11 V results in a kinetic energy of $E_{kin}=4.7\cdot10^{-17}$ J. The measurement for the

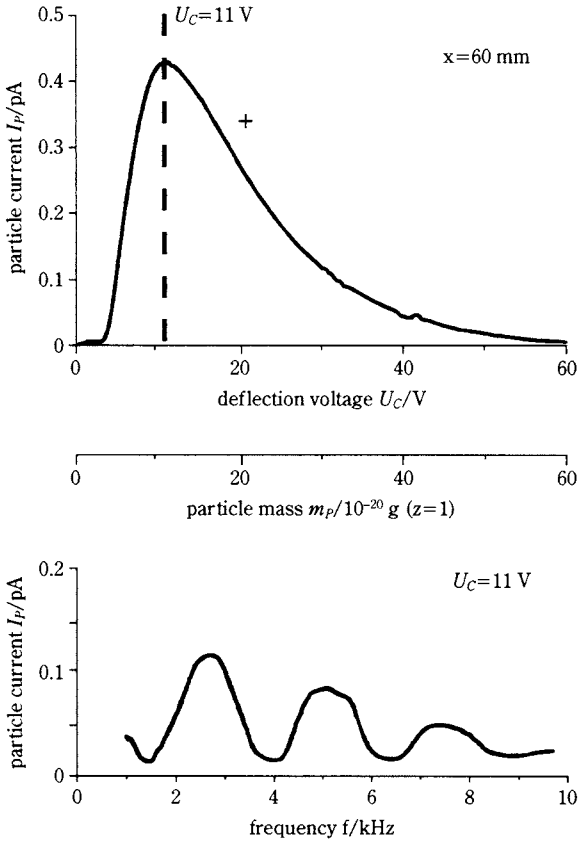

Fig. 3 Example of simultaneously measured kinetic energy and velocity of positively charged particles. Flame conditions: ξ=60 mm, v_u=1.44 m s^{-1}, p=27.5 mbar, H_2/O_2=1.69, $Ar/(H_2+O_2)$=1.36, 262 ppm SiH_4.

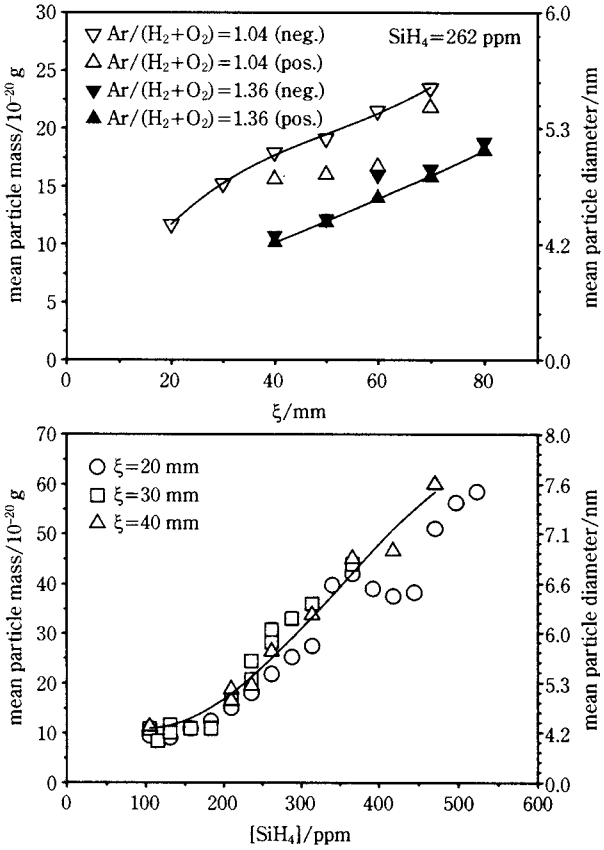

Fig. 4 Particle size measurements of SiO_2 particles as a function of the flow coordinate ξ (upper part) and precursor concentration (lower part). Flame conditions: H_2/O_2=1.69, p=30 mbar, v_u=1.32 m s^{-1}.

determination of the particle velocity shown in the lower part of **Fig. 3** was performed for particles deflected at U_C=11 V. The measured currents plotted as a function of the frequency of the repelling grid's voltage exhibit minima at f_{min1}=1.3 kHz, f_{min2}=3.9 kHz, and f_{min3}=6.5 kHz. Applying Eq. (5) leads to a particle velocity of about 650 m s^{-1}. Combination of Eq. (4) and (5) results in a mean particle mass of $22 \cdot 10^{-20}$ g, from which in turn a mean particle diameter of d_P=5.4 nm can be determined, assuming a density for the silica particles of ρ=2.65 g cm^{-3}.

Fig. 4 summarizes the measured mean particle mass as a function of the flow coordinate (upper part) and as a function of the precursor concentration (lower part) for the SiH_4-doped flames. The pressure was kept constant at p=30 mbar, the velocity of the unburnt gases was v_u=1.32 m s^{-1}, H_2/O_2=1.69, and the ratio of the inert gas to the fuel gases $Ar/(H_2+O_2)$ =1.36 and 1.04, respectively. As can be seen in the upper part of **Fig. 4**, particles formed in the hotter flame (open triangles) show an evolution of the mean particle mass from about $m_P=10 \cdot 10^{-20}$ g at ξ=20 mm to about $m_P=22 \cdot 10^{-20}$ g at ξ=70 mm, whereas the particles generated in the cooler flame (closed symbols) are smaller by a factor of about 1.7. The mean particle mass was measured at three different positions in the flame as a function of initial precursor concentration, see lower part of **Fig. 4**. The dependence of mean particle mass on the sampling position is not very distinct in the range 20 mm $\leq \xi \leq$ 40 mm, whereas it is obvious that the mean mass increases with increasing initial concentration of the dopant.

In the next series of experiments, the PMS was applied to particles generated by a spark generator using three different types of electrode materials. Conventional spark plug material was operated at atmospheric pressure, a silver electrode was used at 400 mbar, and for glassy carbon (Sigradur-G), the pressure was held between 20 and 30 mbar. **Fig. 5** shows results of the measured probability density of the particle diameter obtained from the three materials at a spark frequency of f=1000 Hz. All particles show a very narrow size distribution with mean particle sizes between 2 and 4 nm. **Fig. 6** shows the dependence of particle size on both the spark frequency and the ignition voltage. The mean particle diameter

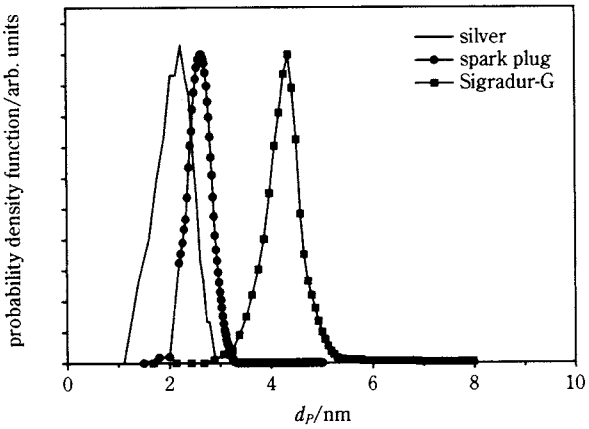

Fig. 5 Diameter-PDF of silver, glassy carbon (Sigradur-G), and conventional spark plug material. Spark frequency: f=1000 Hz.

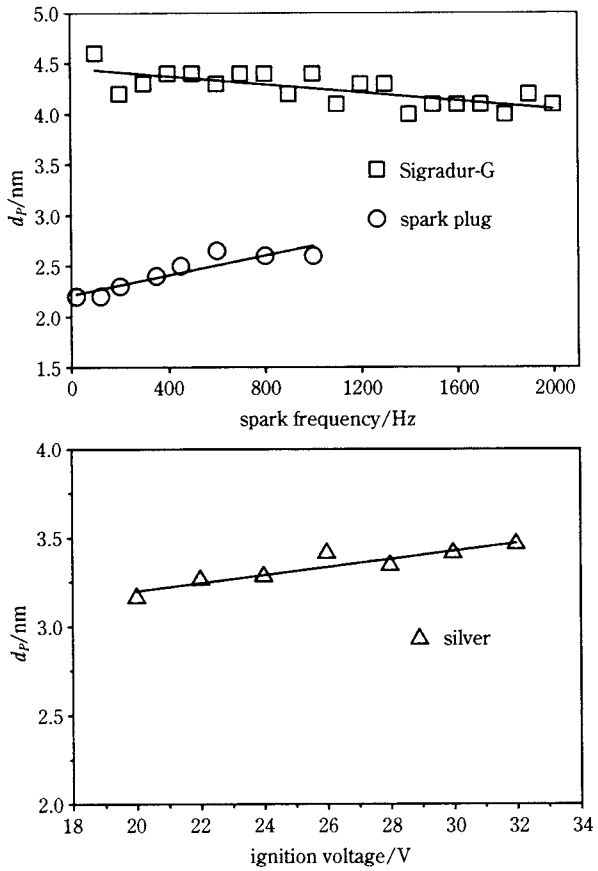

Fig. 6 Influence of spark frequency on the mean particle diameter of Sigradur-G and spark plug material (upper part) and of the ignition voltage on the mean diameter of silver (lower part).

increases slightly from 2.2 nm to 2.6 nm with spark frequency for normal spark material (open circles), and decreases from 4.5 nm to 4.2 nm for Sigradur-G, see upper part of **Fig. 6**. For silver electrodes, the frequency has almost no influence on the particle size. On the other hand, the ignition voltage and thus the spark energy is the main parameter determining the

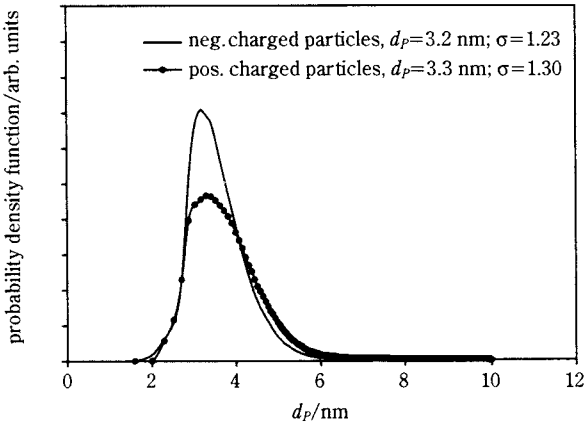

Fig. 7 Diameter-PDF of positively and negatively charged soot particles produced in a microwave reactor.

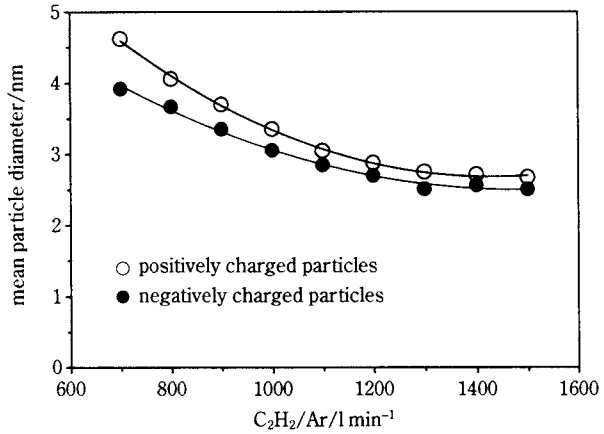

Fig. 8 Influence of the carrier gas flow on the mean particle diameter of soot from the microwave reactor.

mean size of the silver particles, see lower part of **Fig. 6**. The mean size shows linear behavior, increasing from 3.1 to 3.4 nm.

Next, soot particles formed during pyrolysis of a C_2H_2/Ar mixture in a microwave reactor were investigated. **Fig. 7** shows the measured probability density function of the particle diameter for negatively and positively charged particles. According to **Fig. 7**, the mean diameter for both polarities is almost the same, but the standard deviation is slightly different. An increase in the flow velocity of the C_2H_2/Ar mixture through the microwave reactor causes a decrease in the residence time of the particles in the reaction zone. **Fig. 8** shows the expected trends of decreasing particle diameter with increasing mixture volume flow.

The last series of experiments was conducted on particles generated in sooting C_2H_2/O_2/Ar flames. The aim was to compare Faraday-Cup measurements with those performed with an external dynode and the secondary electron multiplier. The main parameter for signal amplification is the voltage applied to

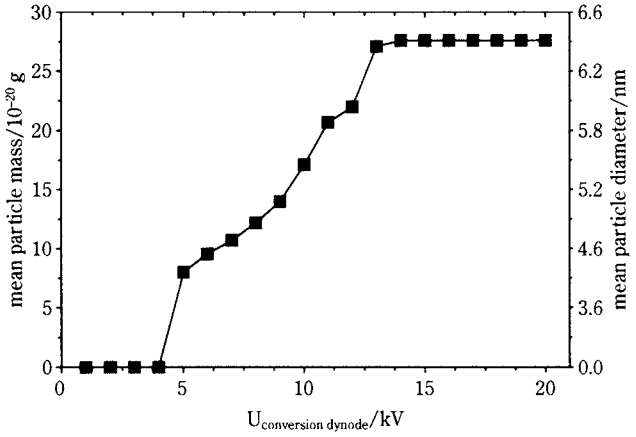

Fig. 9 Measured apparent mean mass and diameter of soot particles originating from a $C_2H_2/O_2/Ar$ flame (C/O=1.2, p=30 mbar, ξ=30 mm) as a function of the conversion dynode voltage.

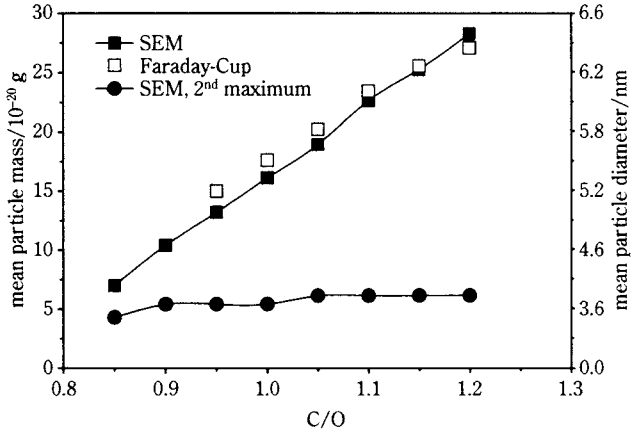

Fig. 10 Mean mass and diameter of negatively charged soot particles generated in $C_2H_2/O_2/Ar$ flames with various C/O ratios measured with the SEM as well as with Faraday-Cup.

the external dynode, which is proportional to the strength of the electric field between the dynode and the multiplier. The acceleration of the particles in the electric field must be high enough to produce secondary electrons by impaction on the surface of the dynode. Initially, the influence of the dynode voltage on the mean properties of soot particles was investigated. A flame burning with a C/O ratio of 1.2 was employed, and particles were extracted from a flow coordinate of ξ=30 mm above the burner head. As shown in **Fig. 9**, the apparent mean particle mass first increases with increasing voltage and then remains constant at over 13 kV. The voltage-independent size of d_P=6.41 nm is in agreement with the Faraday-Cup measurement of d_P=6.36 nm. From these experiments, the minimum external dynode voltage was determined, which yields a particle mass that is independent of the acceleration voltage. **Fig. 10** shows the mean mass and diameter of negatively charged

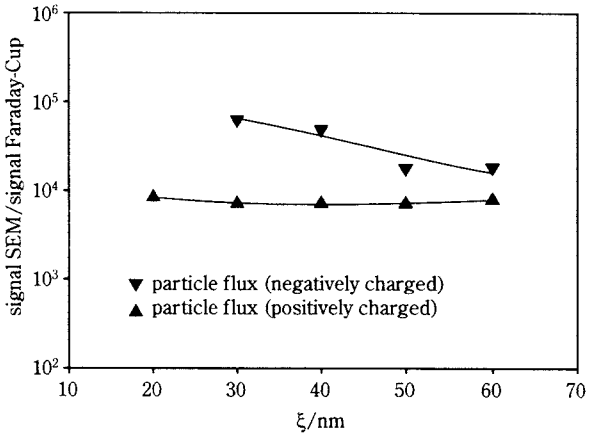

Fig. 11 Relative signal gain ($I_{P\text{-}SEM}/I_{P\text{-}Faraday\text{-}Cup}$) as a function of the flow coordinate.

soot particles, generated in $C_2H_2/O_2/Ar$ flames with C/O ratios of $0.85 \leq C/O \leq 1.2$. The flames were burned at 30 mbar and the samples were taken at a fixed flow coordinate of ξ=30 mm. The secondary electron multiplier (closed symbols) and the Faraday-Cup (open symbols) measurements show no significant differences in size for $C/O > 0.95$, indicating the correctness of the multiplier transfer function. Due to the much larger signal of the multiplier compared with the Faraday-Cup measurements, it was also possible to detect soot particles for extremely mild sooting conditions. Furthermore, an additional particle fraction of d_P=3.6 nm was identified, which could not be resolved by the Faraday-Cup device. The size of this particle class seems to be independent of the burning conditions of the sooting flames. The overall gain in the particle current obtained by the multiplier technique is summarized in **Fig. 11**. The particle flux measured with the SEM is related to the particle flux measured with the Faraday-Cup as a function of the flow coordinate ξ. The signal gain for positively charged particles is about 10^4, whereas negatively charged particles lead to a multiplier current which is always larger than 10^4.

Conclusion

The particle mass spectrometer (PMS) has been successfully applied to four different aerosols generated under different conditions in various pressure ranges. Soot as well as ceramic or metallic particles were generated in low-pressure flames, microwave plasma, and electric sparks, yielding particles in the size range of 1 to 10 nm. The only conditions of operation are that the process is stationary over a sample time of about two minutes and that the process results

in charged particles. The use of a secondary electron multiplier with an external dynode as a preamplifier leads to a clear increase in the sensitivity of the PMS. As expected, the particle diameter, being the most important parameter, is not affected by the multiplier. The signal could be increased by a factor of 10^4. It would be possible to additionally improve the sensitivity by further lowering the pressure in the detection chamber, which has a twofold influence. On the one hand, the signal-to-noise-ratio will increase due to the reduced gas in the vacuum chamber, and on the other hand, the reduced pressure will allow the use of a higher voltage applied to the conversion dynode which would lead to a higher degree of conversion, and hence an additional signal gain.

Acknowledgment

Financial support from the German National Science Foundation (DFG) is gratefully acknowledged.

Nomenclature

b_C	: deflection capacitor width	[cm]
d_P	: particle diameter	[nm]
e	: elementary charge	[C]
E	: kinetic energy	[J]
I_P	: particle current	[fA]
l_C	: deflection capacitor length	[cm]
l_G	: distance between repelling grids	[m]
l_P	: length of particle package	[m]
m_P	: particle mass	[g]
t	: time	[s]
U_C	: deflection voltage	[V]
v_P	: particle velocity	[m s^{-1}]
x_P	: x coordinate of a particle	[m]
$\dot{x}_P$	: particle velocity in x-direction	[m s^{-1}]
y_P	: y coordinate of a particle	[m]
$\dot{y}_P$	: particle velocity in y-direction	[m s^{-1}]
z	: number of elementary charges on a particle	[−]
ξ	: flow coordinate	[mm]

References

1) Chen, Y.; Glumac, N.; Kear, B.H.; and Skandan, G.: High rate synthesis of nanophase materials. *Nanostructured Materials* 9, 1997, pp. 101−104
2) Ulrich, G.D.: Flame synthesis of fine particles. *C&EN* 62, 1984, pp. 22−29
3) Lindackers, D.; Janzen, C.; Rellinghaus, B.; Wassermann, E.F.; and Roth, P.: Synthesis of Al_2O_3 and SnO_2 particles by oxidation of metalorganic precursors in premixed H_2/O_2/Ar low-pressure flames. *Nanostructured Materials* 10, 1998, pp. 1247−1270
4) Kobata, A.; Kusababe, K.; and Morooka, S.: Growth and transformation of TiO_2 crystallites in aerosol reactor. *AIChE Journal* 37, 1991, pp. 347−356
5) Kusters, K.A. and Pratsinis, S.E.: Strategies for control of ceramic powder synthesis by gas-to-particle conversion. *Powder Technology* 82, 1995, pp. 79−91
6) Whitby, E. and Hoshino, M.: Development of a low-pressure aerosol sampler. *Rev. Sci. Instrum.* 66, 1995, pp. 3955−3965
7) Roth, P. and Hospital, A.: Mass growth and coagulation of soot particles in low-pressure flames. *24th Symposium (International) on Combustion.* The Combustion Institute, Pittsburgh, 1992, pp. 981−989
8) Ziemann, P.J.; Liu, P.; Rao, N.P.; Kittelson, D.B.; McMurry, P.H.: Particle Beam Mass Spectrometry of Submicron Particles Charged to Saturation in an Electron Beam. *J. Aerosol Sci.*, 26, 1995, pp. 745−756
9) Roth, P. and Hosptial, A.: Design and test of a particle mass spectrometer (PMS). *J. Aerosol Sci.* 25, 1994, pp. 61−73
10) Lindackers, D.; Strecker, M.G.D.; Roth, P.; Janzen, C.; Pratsinis, S.E.: Formation and Growth of SiO_2 Particles in Low-Pressure H_2/O_2/Ar Flames Doped with SiH_4. *Combust. Sci. Technol.*, 123, 1997, pp. 287−315

Author's short biography

C. Janzen

Christian Janzen graduated in Mechanical Engineering at the University of Duisburg, Germany, in 1996. He is currently working on a Ph.D. project in the Sonderforschungsbreich 445. The subject of his thesis deals with formation and characterization of nanoparticles from low pressure flame reactors.

M.G.D. Strecker

Marc G. D. Strecker received is Diploma in Mechanical Engineering from the University of Duisburg, Germany, in 1991. He was working on a Ph.D. project on nanoparticle generation and measuring methods in low pressure reactors in the DFG Schwerpunktprogramm "Feinste, feste Partikeln" since 1992. Since 1998 he is working as a Software Engineer at the "software design & management AG".

P. Roth

Dr. Paul Roth is Professor of Combustion and Gasdynamics and director of the respective Institute at the Gerhard-Mercator-Universität in Duisburg. He received his diploma in mechanical engineering from Technical University in Aachen and got his Ph.D. also from Aachen in thermo- and fluiddynamics. He worked for about 10 years as a research assistant and later as a senior scientist at the German Aerospace Research Center (DLR) and moved there after to University of Duisburg. He was for about 15 years speaker of the Aerosol Research Program at Duisburg supported by the German Science Foundation. He is currently heading a new long term program on "Nanoparticles from the gasphase" (SFB 445). He has authored more than 250 articles on reaction kinetics, combustion, aerosols, gasdynamics, engine combustion, and on gas-to-particle conversion processes. Prof. Roth is an editorial board member of the J. Aerosol Science and of the Shock Wave Journal.

Extrusion Pressure Estimation in Axisymmetric Paste Extrusion†

D. J. Horrobin
*University of Melbourne, Australia**
and R.M. Nedderman
*University of Cambridge, UK***

Abstract

Paste extrusion is an important process used for manufacturing products based on particulate materials. From a theoretical viewpoint, paste extrusion resembles solid metal extrusion, for which extensive theory has been developed. In particular, exact solutions are available for many extrusion processes involving plane strain deformations, allowing extrusion pressures to be accurately determined in these situations. However, axisymmetric extrusion is more common in a paste flow context, and in this case simple alternative methods for estimating extrusion pressures are desirable.

In this article, we describe how exact solutions for plane strain extrusion can be applied empirically to axisymmetric geometries, to provide accurate estimates for extrusion pressures. The nominal extrusion pressures for plane strain and axisymmetric extrusions with equal area reductions appear to be similar, for both smooth- and rough-walled square-entry dies. The axisymmetric extrusion pressure can be estimated directly in the smooth wall case, while for rough walls, the contribution due to rigid sliding, away from the deforming zone, must also be considered.

Some new correlations describing combined results from slipline field solutions for plane strain extrusion are also presented.

1. Introduction

Paste extrusion is a common method for manufacturing objects from particulate materials. The process involves liquid addition to a powder to produce a deformable soft solid paste, which then undergoes extrusion to create the desired cross-sectional shape. This is typically followed by further processing, which might involve liquid removal to obtain a hard final product. Many materials not derived from dry powders, notably various foodstuffs, are also processed in a soft solid state, and so soft solid extrusion has a wider significance.

Typical pastes are dense, solid-liquid mixtures that exhibit yield behaviour when subjected to deforming loads, *i.e.* deformation does not begin (at least at an appreciable rate) until the load has reached a critical magnitude. The yield stress is found to be largely independent of hydrostatic pressure [1], and in many cases the stress in a deforming sample is only weakly dependent on the deformation rate and accumulated strain. In this sense, pastes resemble solid metals, both materials being perfectly plastic to a first approximation.

For plane strain extrusion, the slipline field method allows extrusion pressures to be accurately determined for perfectly plastic materials, and plane strain slipline field results are often tabulated in standard metal-forming texts [*e.g.* 2]. The plane strain geometry can be visualised from **Figure 1** by imagining the wall to extend for a large distance perpendicular to the page. However, axisymmetric extrusion, where the entering and exiting flows have concentric circular cross-sections, is rather more common in paste processing.

The slipline field approach is difficult to apply to axisymmetric geometries, and so to obtain accurate solutions, numerical methods must be employed. In particular, the finite element method has been widely used for analysing extrusion processes. Numerical calculations can be costly and time-consuming, however, and simple methods for estimating forming loads are thus desirable. Extrusion pressures can be estimated, for both plane strain and axisymmetric deformations, using the limit analysis (upper and lower bound theorem) approach. Although these estimates are very accurate for plane strain extrusion, comparisons with finite element results have indicated that this is not generally the case for the axisymmetric geometry [3].

In this article, we briefly describe the perfect plasticity model, and some slipline field solutions for plane strain extrusion through square-entry dies. The upper

* Department of Mathematics and Statics, Victoria, 3010, Australia
**Department of Chemical Engineering, Pembroke Street, Cambridge, CB2 3RA, UK
† Received: May 21, 1999

bound approach is also illustrated by some plane strain examples. We then show how plane strain slipline field results can be applied to axisymmetric extrusion, to produce better agreement with finite element extrusion pressures than is obtained from axisymmetric upper bound solutions. We shall consider problems involving Tresca boundary conditions, where the wall shear stress has a constant value where sliding occurs. If this value is zero, the walls are said to be perfectly smooth, and if it is equal to the material's shear yield stress, they are said to be perfectly rough. We shall only consider these two limiting cases, but the conclusions are expected to hold for intermediate, partly rough walls.

As a side issue, we also present some new correlations (equations 1, 7 and 9) describing combined slipline field results for plane strain extrusion through square-entry dies.

2. Perfectly plastic materials

As with other problems in continuum mechanics, the flow of a perfectly plastic material is described by a set of force equilibrium equations (body forces usually being neglected) and a set of constitutive relationships, which in this case comprise a yield criterion and a flow rule. The yield criterion determines the deviatoric stress magnitude at which deformation can occur. This critical stress cannot be exceeded, and below it the material is rigid. For a von Mises material, the appropriate measure of the stress magnitude is the sum of the squares of the deviatoric stress components.

The flow rule determines the ratios of the strain rate components, and for a von Mises material obeying the associated flow rule, these are equal to the ratios of the corresponding deviatoric stress components. Consequently, the deformation is volume conserving, *i.e.* the material is incompressible. The magnitudes of the strain rate components are independent of the stress components, and are determined by the kinematic boundary conditions, in this case the ram velocity. The extrusion pressure is therefore independent of extrusion rate.

3. Slipline field solutions

Under plane strain conditions, the velocity and strain rate in a given direction are both zero, and it is possible to obtain exact solutions for many problems using the slipline field method. This is an application of the method of characteristics, and is described in standard metal-forming texts [e.g. 2, 4, 5]; its details will not be discussed here. A number of slipline field solutions have been presented for extrusion with Tresca boundary conditions. The flow patterns are characterised by well-defined deforming zones separating the rigid material entering and exiting the die entry region. Depending on geometry and boundary conditions, there may also be a well-defined static zone on the die face, and surfaces within the deforming zone across which the velocity is discontinuous. These features can all be seen in the solutions described below.

Figure 1 shows the deforming zones, and associated static zones and velocity discontinuities, for plane strain extrusion through perfectly smooth, square-entry dies with two different fractional thickness reductions (denoted by r). **Figure 1(a)** corresponds to a solution due to Hill [6] for extrusion through dies with small thickness reductions, the maximum reduction for which this solution is valid

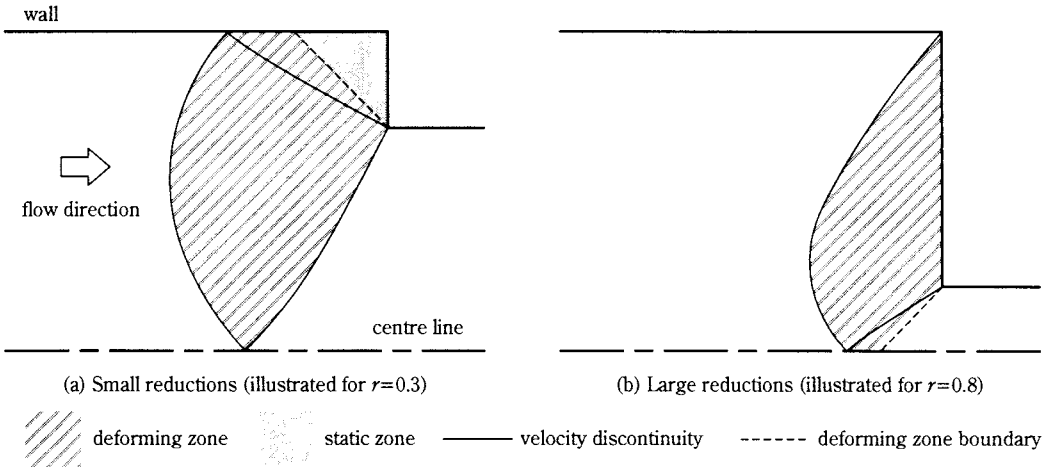

Fig. 1 Deforming zones, static zones and velocity discontinuities for plane strain extrusion through smooth, square-entry dies; from slipline field solutions.

being $r=1/2$. **Figure 1(b)** corresponds to a solution due to Johnson [7] for extrusion through dies with large thickness reductions, the minimum reduction for which this solution is valid being $r=2/3$. Two solutions covering the range $1/2<r<2/3$ have been given by Green [8].

The extrusion pressures derived from these solutions are tabulated in standard texts [2] or can be calculated relatively quickly using a computer. (The solutions described in this article were all calculated on a PC using the *Mathematica* package.) These extrusion pressures are plotted in **Figure 2** against the logarithm of the thickness ratio (entry thickness divided by exit thickness). They are made dimensionless by dividing by $\sqrt{3}k$, where k is the material's shear yield stress; $\sqrt{3}k$ is equal to the uniaxial yield stress for a von Mises material. The results are found to lie approximately on two parabolic arcs with equations

$$\begin{aligned} \frac{P}{\sqrt{3}k} &= 0.520\left(\sqrt{20.2\xi+1}-1\right) && r\le 0.75 \\ &= 0.0468\xi^2+0.845\xi+1.02 && r\ge 0.75 \end{aligned} \tag{1}$$

where $\xi=\ln\left|1/(1-r)\right|$.

4. Plane strain upper bound solutions

Extrusion pressures can be estimated for both plane strain and axisymmetric extrusion using the upper bound approach. An upper bound solution comprises a velocity field that satisfies the incompressibility constraint and the velocity boundary conditions for the problem. The rate of energy dissipation associated with this velocity field can be calculated without detailed knowledge of the stress field, as the flow rule and yield criterion uniquely determine the energy dissipation rate per unit volume at each point. The extrusion pressure is then obtained from an energy balance, and the upper bound theorem, due to Hill [9], states that this extrusion pressure is greater than or equal to the exact extrusion pressure. In other words, the material adopts the flow pattern that minimises the forming load. By examining different velocity fields, that with the lowest energy dissipation rate can be selected, and a close approximation to the exact extrusion pressure hopefully obtained.

Simple upper bound solutions for plane strain extrusion can be constructed by dividing the deforming zone into triangular sub-regions, within which the material moves rigidly. The incompressibility constraint requires that the velocity component normal to

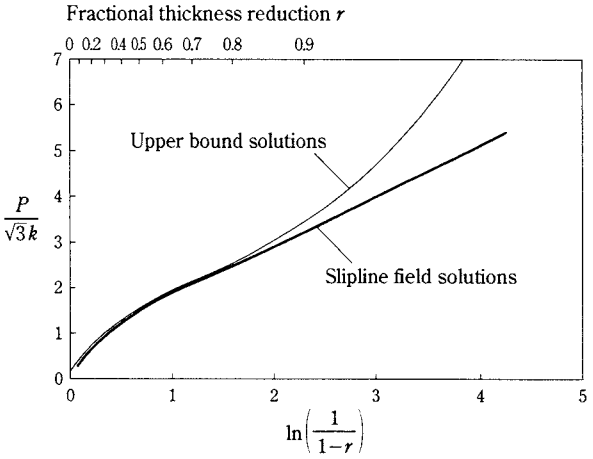

Fig. 2 Extrusion pressures for plane strain extrusion through smooth, square-entry dies.

an interface between sub-regions must be continuous, although the tangential velocity component can be different on either side. The interfaces are therefore velocity discontinuities. Energy dissipation only takes place at the discontinuities, and at external boundaries if the wall shear stress is non-zero.

Two such upper bound solutions, due to Kudo [10, 11], are shown in **Figure 3**. In each case, the length parameter a is adjustable, and its value can be selected to give the lowest extrusion pressure. Similarly, the angles in the triangular sub-regions can be optimised, the most suitable triangular shapes being indicated in the figure. The velocity field in **Figure 3(a)** produces a lower extrusion pressure when the reduction is small (less than 60.2%), and the optimum value for a is

$$a=4\sqrt{\frac{r(1-r)}{7}} \tag{2}$$

The resulting extrusion pressure is

$$\frac{P}{\sqrt{3}k}=\sqrt{\frac{7r}{3(1-r)}} \tag{3}$$

The velocity field in **Figure 3(b)** produces a lower extrusion pressure for larger reductions, with a and P given by

$$a=\sqrt{r(1-r)} \tag{4}$$

$$\frac{P}{\sqrt{3}k}=\frac{16-9r}{4}\sqrt{\frac{r}{3(1-r)}} \tag{5}$$

Equations (3) and (5) are also plotted in **Figure 2**, where it is seen that the upper bound solutions provide very good estimates for the extrusion pressure over a wide reduction range, specifically for reductions less than about 85%. At larger reductions, the upper bound and slipline field results diverge, although

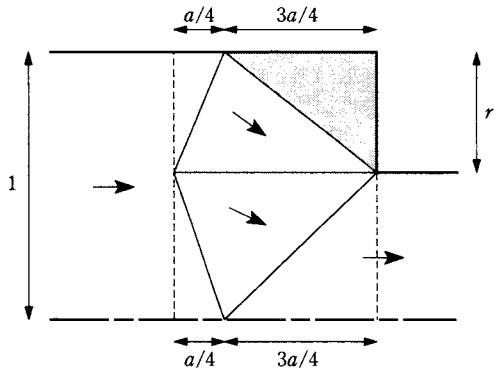

(a) Velocity field for $r \leq 60.2\%$

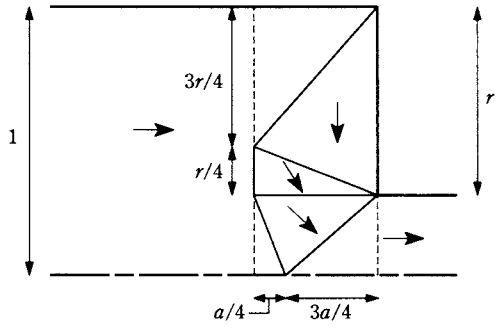

(b) Velocity field for $r \geq 60.2\%$

Fig. 3 Velocity fields used in upper bound solutions for plane strain extrusion through smooth, square-entry dies.

it should be pointed out that the solution depicted in **Figure 3(b)** does not represent the best available upper bound solution in this region. Simple modifications to this solution result in lower extrusion pressure estimates at very large reductions, although agreement is still not as close as for reductions less than 85%.

5. Axisymmetric extrusion

The slipline field method is not easily applied to axisymmetric extrusion, but accurate solutions to the equations of motion can still be obtained, at higher computational cost, by performing numerical calculations. For example, in a paste extrusion context, references [3] and [12] present some finite element results for extrusion of a perfectly plastic material through dies with various geometries and boundary conditions. The finite element extrusion pressures plotted in **Figure 4**, for axisymmetric extrusion through smooth, square-entry dies with diameter reductions between 4 and 92%, are taken from these sources. The values are made dimensionless by dividing by the material's uniaxial yield stress $\sqrt{3}k$ and are plotted against $\xi = \ln|1/(1-r)|$, where r is again the linear reduction (in this case the fractional diameter reduction). The

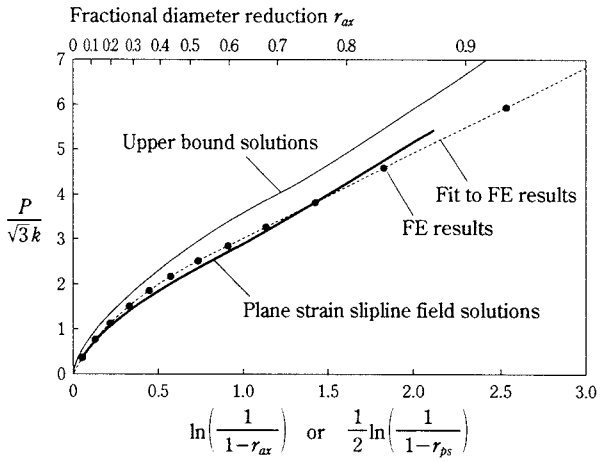

Fig. 4 Extrusion pressures for axisymmetric extrusion through smooth, square-entry dies.

dotted line in the figure is an empirical fit to the finite element data given by

$$\frac{P}{\sqrt{3}k} = 0.700\left(\sqrt{26.8\xi+1}-1\right) \qquad r \leq 0.60$$
$$= 1.92\xi + 1.08 \qquad r \geq 0.60 \tag{6}$$

Since finite element analyses can be costly and time-consuming, it is desirable to find alternative procedures for determining forming loads with sufficient accuracy. Upper bound solutions exist for axisymmetric extrusion, but in this case it is not possible to construct deformation modes based on (axisymmetric) rigid blocks, due to the need to accommodate circumferential straining. The velocity fields employed therefore comprise *deforming* sub-regions, again separated by velocity discontinuities. As a result, calculation of the rate of energy dissipation is more complicated, and expressions for the extrusion pressure are generally more cumbersome than for plane strain extrusion [3, 12].

Among the better upper bound solutions for axisymmetric extrusion through square-entry dies are those due to Kudo [13]. These were developed before numerical solutions for extrusion problems were available, in the belief that they might provide accurate estimates for the extrusion pressure, over a wide reduction range, as in the plane strain case. The solutions will not be discussed in detail here (the details can be found in reference 12), but give rise to the upper bound curve shown in **Figure 4**. Comparison with the finite element results indicates that the axisymmetric upper bound solutions are less accurate than the upper bound solutions for plane strain extrusion shown in **Figure 2**.

6. Correspondence between plane strain and axisymmetric extrusion pressures

Hill suggested in 1948 [6] that reliable estimates for axisymmetric extrusion pressures could be obtained from plane strain slipline field solutions if the area reductions were the same in both cases. Hill's comments were based on agreement between plane strain slipline field results and measured extrusion pressures for axisymmetric metal extrusion, but the hypothesis can now be tested against numerical results. (We shall now adopt the subscripts *ps* and *ax* to distinguish, where necessary, between quantities associated with plane strain and axisymmetric deformations.) The plane strain slipline field extrusion pressures from **Figure 2** have been replotted in **Figure 4**, but this time against $\frac{1}{2}\ln\{1/(1-r_{ps})\}$, for comparison with axisymmetric extrusion pressures for equal area reductions. The slipline field results are seen to provide much better predictions for the axisymmetric extrusion pressures than the upper bound solutions. Furthermore, a similar correspondence can be found for rough-walled dies, as we shall now demonstrate.

7. Perfectly rough dies

Plane strain extrusion

At a perfectly rough wall, the wall shear stress is equal to the material's shear yield stress. The flow patterns for plane strain extrusion through perfectly rough, square-entry dies show less variation with reduction than those for perfectly smooth dies. A single slipline field solution, given by Hill [6], covers reductions up to $r=0.925$, and a similar solution, due to Johnson [7], covers the range $0.925 \leq r \leq 0.980$. **Figure 5** shows the deforming zone, static zone and velocity discontinuity in Hill's solution, illustrated for a 60% thickness reduction. Comparison with **Figure 1** reveals that the deforming zone is generally much larger for perfectly rough dies. In the discussion that follows, we shall describe the distance between the die face and the position where the deforming zone boundary meets the container wall as the deforming zone length d (made dimensionless by dividing by the initial half-thickness); this is indicated in **Figure 5**. The perfectly rough die has a large static zone on the die face, with a curved boundary that coincides with a strong velocity discontinuity. In this case, the deforming zone length is equal to the static zone length, but this is not always true for smooth or partly rough dies.

The extrusion pressure for a rough-walled die depends on the total length of material upstream from the die face, which we term the upstream length L (again relative to the initial half-thickness), and so extrusion pressure results need to be reported more carefully than for smooth-walled dies. The extrusion pressure also depends on the length of material downstream from the die face, but we shall assume that this is zero; the correction for a non-zero downstream length is straightforward. Extrusion pressures obtained from slipline field solutions are often reported as *nominal* extrusion pressures P_{nom}, which correspond to the energy dissipation associated with the deforming zone only, and do not take into account the energy dissipation due to rigid sliding against the rough container wall. The nominal extrusion pressures for plane strain extrusion through perfectly rough, square-entry dies are plotted against $\ln\{1/(1-r)\}$ in **Figure 6**. These results, calculated from Hill's and Johnson's solutions, are accurately described by the equation

$$\frac{P_{nom}}{\sqrt{3}k} = 0.01845\xi^3 - 0.1314\xi^2 + 1.638\xi + 0.8248 \qquad (7)$$

To determine the actual extrusion pressure for a given upstream length (and zero downstream length), an additional term must be added to include the effect of rigid sliding in the container:

$$P = P_{nom} + (L-d)k \qquad (8)$$

This correction involves the deforming zone length d, which can also be obtained from the slipline field solutions, and is plotted in **Figure 6** against the right-hand ordinate axis. The deforming zone length does not vary substantially with reduction, being slightly less than 1.5 times the initial half-thickness in all

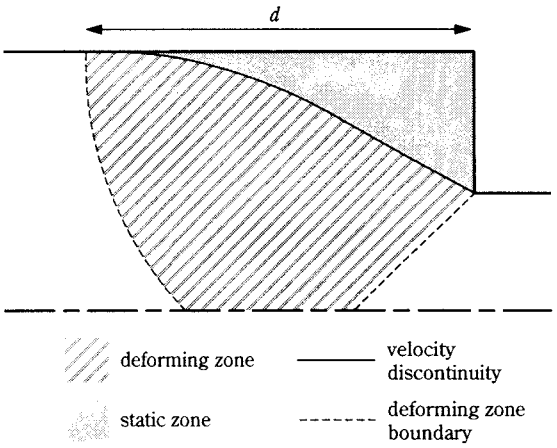

Fig. 5 Deforming zone, static zone and velocity discontinuity for plane strain extrusion through a perfectly rough, square-entry die; from slipline field solution (illustrated for $r=0.6$).

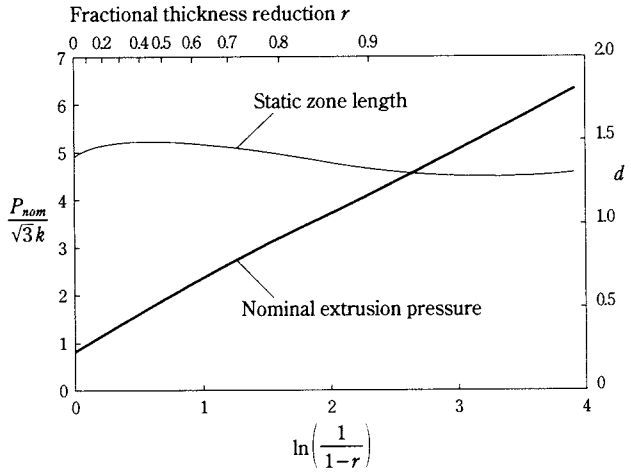

Fig. 6 Nominal extrusion pressures and deforming zone lengths for plane strain extrusion through perfectly rough, square-entry dies; from slipline field solutions.

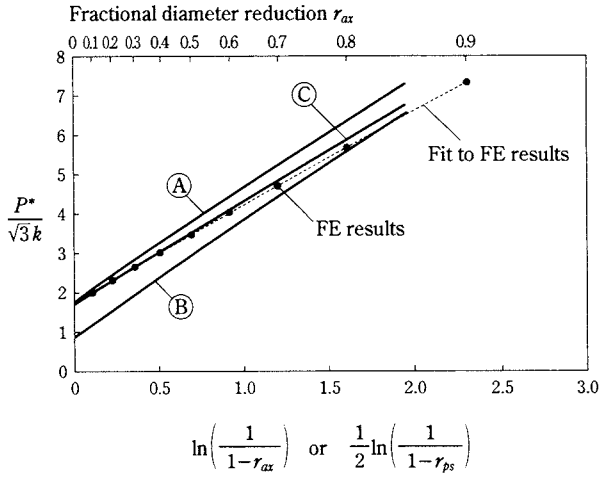

Fig. 7 Standard extrusion pressures for axisymmetric extrusion through perfectly rough, square-entry dies.

cases. A suitable correlation describing these results can be constructed from two polynomial arcs:

$$d = 1.42 + 0.310\xi - 0.377\xi^2 + 0.142\xi^3 - 0.0192\xi^4 \quad r \le 0.925$$
$$= 1.41 - 0.0789\xi + 0.0135\xi^2 \quad r \ge 0.925 \qquad (9)$$

Axisymmetric extrusion

A disadvantage with reporting extrusion pressures as nominal values is that these correspond to slightly different upstream lengths depending on reduction and wall friction (and may not correspond to a real extrusion pressure at all if the furthest deforming material from the die face is not located at the container wall). Furthermore, it is difficult to determine the deforming zone length precisely from numerical solutions, which are usually the only accurate solutions available for axisymmetric extrusion. An alternative is to quote extrusion pressures based on a standard upstream length L^*, and we shall denote the resulting standard extrusion pressure by P^*. The finite element results plotted in **Figure 7** are standard extrusion pressures taken from reference [12] for axisymmetric extrusion through perfectly rough, square-entry dies. In this case, L^* was chosen to be 1.5 initial radii from the die face. This is approximately equal to the deforming zone length, and so the contribution to the extrusion pressure from rigid sliding in the container is small. The finite element results are represented well by the straight line fit

$$\frac{P^*}{\sqrt{3}k} = 2.41\xi + 1.79 \qquad (10)$$

Correspondence between plane strain and axisymmetric extrusion pressures

Kudo's upper bound solutions for axisymmetric extrusion [13] can also be applied to perfectly rough, square-entry dies, but as before only provide a good approximation to the finite element results when the reduction is small [12]. A close correspondence between plane strain and axisymmetric results for equal area reductions is therefore valuable. For rough-walled dies, it is necessary to choose an appropriate upstream length to use when evaluating the plane strain extrusion pressures. This was not required for the smooth-wall calculation.

When the upstream length is large, the plane strain value should approach twice the axisymmetric value to account for the different surface area to cross-sectional area ratio in the container in the two cases. Any rule relating the plane strain and axisymmetric upstream lengths must reproduce this behaviour. The simplest hypothesis is to make the plane strain upstream length exactly equal to twice the axisymmetric value, even when the upstream length is small. Line A in **Figure 7**, calculated from equation (8), is based on this hypothesis, with L_{ps} equal to 3, twice the L^* value used when plotting the axisymmetric results. There is good agreement between plane strain and axisymmetric extrusion pressures at small reductions, but the plane strain values are significantly greater than the axisymmetric values at large reductions.

An alternative rule for determining L_{ps}, which also produces the correct behaviour when the upstream length is large, is to assume that the difference $(L - d)$ in the plane strain case is twice that in the axisymmetric case. This is equivalent to the assumption that the nominal extrusion pressures for equal area reductions are similar, which was found to work well for smooth-walled dies. We must now estimate the axisymmetric

deforming zone length, and the two most obvious possibilities are that it is approximately equal to (i) the plane strain deforming zone length for an equal *area* reduction, or (ii) the plane strain deforming zone length for an equal *linear* reduction. In fact, because d_{ps} does not vary greatly with reduction, both choices produce similar results. Line B in **Figure 7** is based on choice (i), and the plane strain extrusion pressures are found to be in good agreement with the axisymmetric extrusion pressures at large reductions, but significantly less than the axisymmetric values at small reductions.

If the nominal extrusion pressures for equal area reductions are indeed similar, then we can deduce that d_{ax} is approximately equal to d_{ps} at large reductions, but is less than d_{ps} at small reductions. The velocity fields obtained from finite element calculations support this conclusion [12], which provides some justification for the following method for estimating the axisymmetric deforming zone length. Since the linear reduction for an axisymmetric extrusion is smaller than for a plane strain extrusion with an equal area reduction, the axisymmetric deforming zone length can be estimated from the plane strain deforming zone length by scaling according to the ratio of the linear reductions:

$$\frac{d_{ax}}{d_{ps}} \approx \frac{r_{ax}}{r_{ps}} = \frac{1}{1+\sqrt{1-r_{ps}}} \tag{11}$$

The axisymmetric standard extrusion pressure is then estimated from

$$P^*_{ax} \approx P_{nom,ps} + 2\left(L^*_{ax} - \frac{d_{ps}}{1+\sqrt{1-r_{ps}}}\right)k \tag{12}$$

where the plane strain quantities all correspond to an equal area reduction. Line C in **Figure 7** is calculated from this equation, and provides good estimates for the axisymmetric extrusion pressures at all reductions.

8. Conclusions

Nominal extrusion pressures appear to be similar for plane strain and axisymmetric extrusions with equal area reductions, for both perfectly smooth and perfectly rough square-entry dies. Since plane strain slipline field extrusion pressures are widely reported, this fact allows axisymmetric extrusion pressures to be rapidly estimated. Even where plane strain extrusion pressures must be specially calculated from slipline field solutions, these calculations are much quicker than a finite element analysis for the axisymmetric problem. When the walls are rough, the need to determine the axisymmetric deforming zone length complicates matters, but an empirical rule for estimating this quantity for perfectly rough, square-entry dies has been described.

This method for estimating axisymmetric extrusion pressures could prove useful in situations where forming loads must be determined quickly and without extreme precision, and where no additional information regarding the stress and velocity fields is required. The method is expected to produce good results for dies with intermediate Tresca boundary conditions, in addition to the perfectly smooth and perfectly rough cases. Furthermore, plane strain slipline field solutions exist for many more complicated extrusion problems. For example, different wall shear stress values can be accommodated on the die face and container wall, and the die geometry itself can also be quite different; solutions are available for tapered and curved die entries, and for unsymmetrical extrusion. Agreement between nominal extrusion pressures for plane strain and axisymmetric (or, in the unsymmetrical case, three-dimensional) extrusions with equal area reductions might also exist in these situations. Such agreement is purely empirical, however, and can only be established by further comparisons between plane strain slipline field results, and numerically or experimentally derived axisymmetric extrusion pressures.

Nomenclature

Roman

- a Length parameter in upper bound solutions, relative to initial half-thickness
- d Static zone length, relative to initial half-thickness or radius
- k Shear yield stress
- L Upstream length, relative to initial half-thickness or radius
- L^* Standard upstream length
- P Extrusion pressure
- P^* Standard extrusion pressure, based on upstream length L^*
- P_{nom} Nominal extrusion pressure
- r Linear reduction

Greek

- ξ Logarithm of the thickness or diameter ratio, $\xi = \ln[1/(1-r)]$

General subscripts

- *ax* Quantity associated with axisymmetric extrusion
- *ps* Quantity associated with plane strain extrusion

References

1) Oliver, D.R. and Whiskens, M.: "The effect of absolute pressure on the processing parameters of ceramic pastes", British Ceramic Proceedings, no. 55 (1996), 87-97.
2) Chakrabarty, J.: "Theory of Plasticity", McGraw-Hill Book Company, New York, U.S.A. (1987).
3) Horrobin, D.J. and Nedderman, R.M.: "Die entry pressure drops in paste extrusion", Chemical Engineering Science, **53** (1998), 3215-3225.
4) Hill, R.: "The Mathematical Theory of Plasticity", Clarendon Press, Oxford, U.K. (1950).
5) Johnson, W.; Sowerby, R. and Venter, R.D.: "Plane-strain Slip-line fields for Metal-Deformation Processes: a Source Book and Bibliography", Pergamon Press, Oxford, U.K. (1982).
6) Hill, R.: "A theoretical analysis of the stresses and strains in extrusion and piercing", Journal of the Iron and Steel Institute, **158** (1948), 177-185.
7) Johnson, W.: "Extrusion through square dies of large reduction", Journal of the Mechanics and Physics of Solids, **4** (1956), 191-198.
8) Green, W.A.: "Extrusion through smooth square dies of medium reduction", Journal of the Mechanics and Physics of Solids, **10** (1962), 225-233.
9) Hill, R.: "On the state of stress in a plastic-rigid body at the yield point", Philosophical Magazine, **42** (1951), 868-875.
10) Kudo, H.: "An upper-bound approach to plane-strain forging and extrusion-I", International Journal of Mechanical Sciences, **1** (1960), 57-83.
11) Kudo, H.: "An upper-bound approach to plane-strain forging and extrusion-II", International Journal of Mechanical Sciences, **1** (1960), 229-252.
12) Horrobin, D.J.: "Theoretical Aspects of Paste Extrusion", Ph.D. Dissertation, University of Cambridge, Cambridge, U.K. (1999).
13) Kudo, H.: "Some analytical and experimental studies of axi-symmetric cold forging and extrusion-I", International Journal of Mechanical Sciences, **2** (1960), 102-127.

Author's short biography

D.J. Horrobin

D.J. Horrobin studied Chemical Engineering as an undergraduate at Queens' College, Cambridge, and has recently completed a Ph.D. in the Department of Chemical Engineering at Cambridge University. His Ph.D. dissertation was concerned with modelling the flow of perfectly plastic materials through extrusion dies, with particular reference to the extrusion of soft solid pastes.
In August 1999 he took up a position as a Research Fellow in the Department of Mathematics and Statistics at The University of Melbourne, Australia.

R.M. Nedderman

R.M. Nedderman has been a lecturer in the Department of Chemical Engineering at Cambridge University since 1960. He was appointed Ely Fellow of Trinity College, Cambridge in 1981, and is due to retire in July 1999.
His research and teaching has been mainly concerned with Fluid Mechanics and Granular Materials. Up to about 1975, he worked on the Two-Phase Flow of gas/liquid mixtures. Since that date, he has concentrated on the prediction and measurement of stress and velocity distributions in granular materials discharging from hoppers. His recent involvement with the study of the extrusion of plastics results from the similarity between the governing equations for plastic and granular materials.

Nano-Process Technology for Synthesis and Handling of Nanoparticles†

F.E. Kruis and H. Fissan
*Gerhard-Mercator-Universität Duisburg, Germany**

Abstract

The term nanoparticle is used nowadays to indicate particles with diameters smaller than 100 nm. The reduced size of nanoparticles is responsible for changed electronic, optical and magnetic properties of nanoparticles and nanostructured materials in comparison with the bulk material. This can be used for new applications such as quantum dots, luminescent materials, gas sensors, conductive films, and capacitive, resistive, magnetic and optical materials.

An overview is given of the different synthesis processes used to provide nanoparticles with the required properties for functional applications, especially electronic and optical ones. We will concentrate on gas-phase processes to show their advantages. Apart from the synthesis techniques, handling techniques are described. Some examples from our own research are given, in which the use of electrical forces plays a central role: size fractionation, deposition and mixing can all be controlled by using charged particles.

1. Introduction

Nanoparticles have attracted the attention of an increasing number of researchers from several disciplines in the last ten years. The term "nanoparticle" came into frequent use in the early 1990s together with the related concepts, "nanoscaled" or "nanosized" particle. Until then, the more general terms "submicron" and "ultrafine" particles were used. The term nanoparticle is generally used now in the materials science community to indicate particles with diameters smaller than 100 nm.

Nanoparticles can be used to prepare nanophase materials, which are materials with a three-dimensional structure and a domain size smaller than 100 nm. Nanophase materials are usually produced by compaction of a powder of nanoparticles. They are characterised by a large number of grain boundary interfaces in which the local atomic arrangements are different from those of the crystal lattice. "Nanocomposites" consist of nanoparticles dispersed in a continuous matrix, creating a compositional heterogeneity of the final structure. The nanocomposites usually involve a ceramic or polymeric matrix and are not restricted exclusively to thin films.

Most of the synthesis methods are based on the production of disperse materials systems, a domain of chemical engineering. This is also true for the conditioning processes, necessary for bringing the nanoparticles in a form which is suitable for application, which can be thought of as specialised unit operations. The experience and the special methods developed by chemical engineers with respect to dispersed materials systems are needed to understand, optimise, and scale-up the processes used for the synthesis and applications of nanoparticles. This field can be described as nano-process technology.

2. Properties of nanoparticles

The small size of nanoparticles, which is responsible for the different properties (electronic, optical, electrical, magnetic, chemical and mechanical) of nanoparticles and nanostructured materials with respect to the bulk material, makes them suitable for new applications. Of a size between the molecular and bulk solid-state structures, nanoparticles have hybrid properties which are incompletely understood today, creating a challenge for theoreticians as well. Some examples of these properties are lower melting temperature, increased solid-solid phase transition pressure, quantum effects, non-linear optical properties, lower effective Debye temperature, decreased ferroelectric phase transition temperature, higher self-diffusion coefficient, luminescence and catalytic activity [1].

* Process and Aerosol Measurement Technology, Gerhard-Mercator-Universität Duisburg, D-47057 Duisburg, Germany
† Received: May 31, 1999

3. Functional applications of nanoparticles

Structural applications of nanoparticles are based on the mechanical properties of the nanophase materials, leading to, e.g., superplastic ceramics or extremely hard metals, using the nanoparticles rather as passive basic building units. Functional applications, however, rely on a transformation of external signals such as the filtering of incident light, the change of electrical resistance in different gas concentrations, and luminescent behaviour when electrically activated. Even before the 1990s, nanoscale catalysts and pigments were used, based mainly on the large surface area to volume ratio in these systems. After 1980, a renewed interest took place in nanomaterials research. Brus [2] suggested that quantum confinement effects occur specifically in semiconductor nanoparticles. Birringer *et al.* [3] developed a method for synthesising amounts of weakly agglomerated nanoparticles for producing nanophase materials.

In this paper, the use of nanoparticles for electronic and optical applications is discussed [1]. A broad spectrum of materials including insulators, semiconductors, superconductors, metals and alloys, optical active materials, and artificially structured materials can be used for these purposes. Most applications use films composed of nanoparticles, supported by a substrate material.

When electrons are confined to a small domain such as a nanoparticle, the system is called a "quantum dot" or zero-dimensional (0-D) structure. In this case, the electrons behave like "particles-in-a-box", and their resulting new energy levels are determined by quantum "confinement" effects. These new energy levels give rise to a modification of the optoelectronic properties as compared with the corresponding properties determined by the bulk material electronic structure [2]. Quantum confinement effects lead, for example, to higher energy level transitions as compared with the bulk material observed as a shorter wavelength optical absorption edge, indicated by a spectral "blue shift". Quantum dots can be also used to produce light emitters of various colours by "band gap tuning" using particle size effects. As an example, light-emitting diodes (LEDs), which have a voltage-controlled, tuneable output colour, were produced [4].

Although these applications seem very attractive, the processes for producing quantum dot devices are technologically very demanding, as the nanoparticles should be of controlled size, monodisperse within a few percent, spherical, monocrystalline, and should have a stable and passivated surface. A current technological approach to circumvent the inherent reactivity and instability of nanoparticles is to embed them in a glass or in a semiconductor which has a wider band gap. These nanocomposite structures can then be used in real-life optical and electrooptical applications. For semiconductor applications other than optical, the nanoparticles should be efficiently electrically contacted. Since attaching electrical leads to an array of quantum dots is a formidable technological task, one way of making an efficient contact is to use a semiconductor structure consisting of an ensemble of quantum dots. Increasing the contact area between nanoparticles and electrode to increase the signals is possible by depositing the nanoparticles on a very porous TiO_2 electrode [5].

In microelectronics, the need for faster switching times calls for a reduction in the size of the electronic components. At present, one switching cycle in a transistor gives rise to the movement of many thousands of electrons, requiring a considerable amount of switching energy and producing excessive heat which can hardly be dissipated in high-frequency applications. This calls for the development of single-electron devices, in which the switching occurs with the motion of only a single electron. Such a device can be realised by a quantum dot in which the charge of an added electron effectively blocks the flow of other electrons by the so-called "Coulomb blockade". Both switching – which performs logic operations – and storage of information are possible with these devices. The problem here is also how to contact the nanoparticles electrically.

The interest in luminescent Si is due to the desire for the integration of optoelectronic devices, now based mainly on III-V semiconductors which are not yet integrable monolithically with the dominant Si microelectronics. Hence light-emitting Si would open the way for optical and electrical functionality on one integrated monolithic Si chip. Si in its bulk form is not luminescent but luminescence has been obtained from Si nanoparticles.

A gas sensor consists quite generally of a material with measurable physical properties, e.g. electrical or optical, which change when a gas is present. The simplest "nanomaterials"-based sensor concept involves measuring the changes in the electrical resistance of a nanocrystalline material when exposed to hydrogen. It has been shown that gas sensors based on nanoparticles are more sensitive than their bulk counterparts.

Nanometre particles have also found new applications in the production of resistors and varistors. Granular films consisting of small conducting particles embedded in an insulating matrix of ceramic or

glass exhibit a great variability of the electrical conductivity by a proper control of the volume fraction [6]. They can be used as thick-film resistors. They were also shown to increase the breakdown voltage of varistors due to their large volume of grain boundaries.

Nanometre-structured, polycrystalline conducting thin films have also found potential in the production of transparent conductive electrodes for photoconductor and solar cell applications, where a large surface area is needed and epitaxial films are not feasible. By spraying a colloid of 3-nm nanoparticles on a heated substrate, Pehnt *et al.* [7] produced very smooth conducting thin CdTe films without gaps and with a roughness smaller than 5 nm, for use in solar cells. Transparent conducting films based on nanoparticles, usually SnO_2 and In_2O_3, have the advantage that they display minimal light absorption and scattering.

Dielectric elements based on nanometre structures are of recent interest due to the reduction in capacitance caused by the continuing scaling down of dynamic random access memories (DRAMs), which causes materials with ever larger dielectric permittivities to be sought. One method for increasing the dielectric permittivity is to disperse conductive particles in a dielectric matrix. Using nanoparticles keeps the dissipation factor low.

Other applications of nanoparticles include their use to improve high-temperature superconductors (HTS), thermoelectric materials, optical materials for attenuating UV radiation, electrochromic materials which can be used for smart windows and magnetics.

4. Synthesis methods of nanoparticles

At present, there are many synthesis routes which lead to nanoparticles, but they can be divided into three main groups: gas-phase synthesis, colloidal synthesis, and high-energy milling. Gas-phase processing systems have several inherent advantages:

- a very good control over size, shape and crystallinity
- a higher purity than in the case of liquid synthesis brought about by an improved control over the composition of the environment
- possibilities to synthesise multicomponent nanoparticles because of the convenient way in which the reactants are supplied and mixed
- cost advantages in comparison with – for instance – vacuum synthesis techniques due to the use of atmospheric or low-pressure conditions
- easier control over the reaction rate and the reaction mechanism through temperature variation of the gas.

Most synthesis routes presently in use are based on the production of condensable monomers. A supersaturation should therefore be achieved. This is made possible by physical or chemical methods. The physical methods involve some form of cooling of the vapour. Supersaturation can also be achieved by chemical reactions which produce a non-volatile condensable product. These reactions are usually decomposition reactions initiated by a rise in temperature.

Various heating and evaporation methods are possible. They are shown schematically in **Figure 1.** The

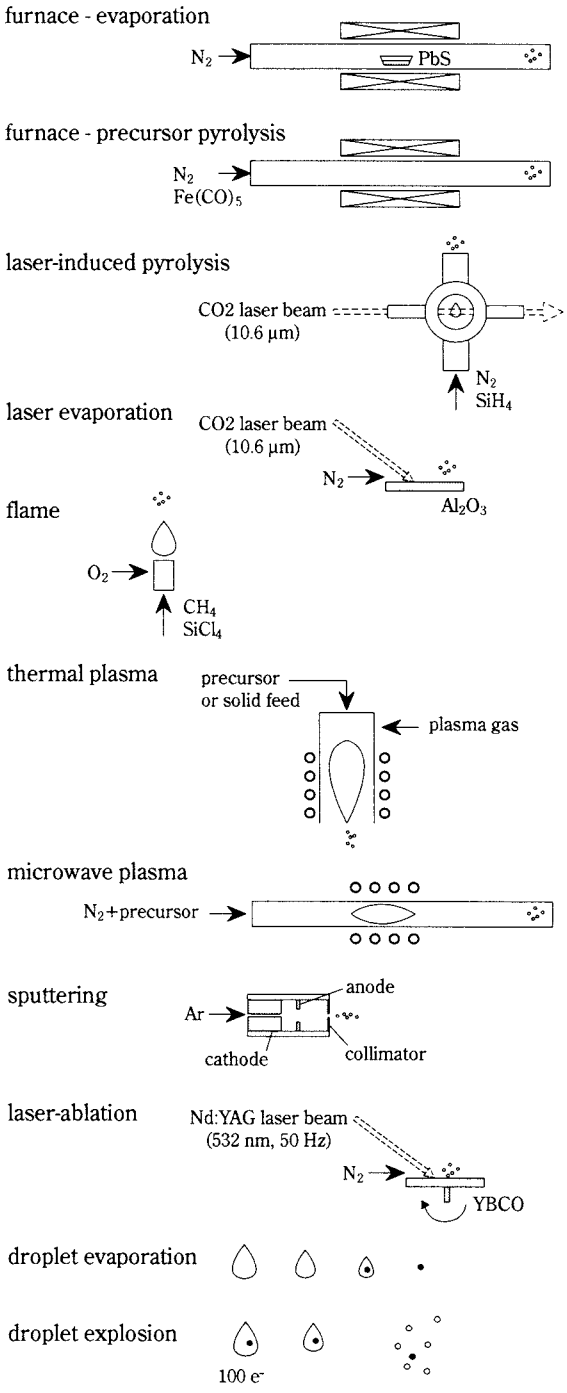

Fig. 1 Possible routes for synthesising nanoparticles

simplest method is to heat a crucible containing the material in a furnace in a flowing inert gas. Nanoparticles are formed by subsequent cooling such as natural cooling or dilution cooling. Materials whose vapour pressure is too low to obtain appreciable particle density have to be fed into the furnace in the form of suitable precursors such as organometallics or metal carbonyls. These decompose in the oven to yield a condensable material.

In the laser pyrolysis technique, a flowing reactant gas is heated rapidly with an IR laser such as a cw CO_2 laser. The source molecules are heated selectively by absorption of the laser beam energy. A gas-phase decomposition of the reactants takes place due to the temperature increase, and supersaturation is created. As an example, SiH_4 pyrolysis results in Si nanoparticle formation and $Fe(CO)_5$ decomposition leads to Fe nanoparticles. The main advantage of laser-heating in gas-flow systems is the absence of heated walls, which reduces the danger of product contamination.

Laser vaporisation of solids uses a laser which evaporates locally a small area from a solid target in an inert gas-flow reactor. It is useful in the case of materials with a very high melting point and low vapour pressure such as refractory oxides.

Flame reactors employ the flame heat to initiate chemical reactions to produce condensable monomers. The flame route has the advantage of being an inexpensive method, however, it usually yields agglomerated particles and there is a risk of carbon contamination. Most flame reactors are operated at normal pressure, but they can also be operated at reduced pressures in order to decrease the particle size. Complex products such as nanocomposites can also be obtained.

A plasma reactor can also deliver the energy necessary to cause evaporation or initiate chemical reactions. The plasma temperatures are in the order of 10^4 °C, decomposing the reactants into ions and dissociating atoms and radicals. Solid powder feeds and droplets can also be decomposed by the plasma. Nanoparticles form upon cooling while exiting the plasma region. Complex materials such as multicomponent oxides, e.g. $BaFe_{12}O_{19}$, can be obtained by using appropriate combinations of solutions. Another method uses a microwave-generated plasma. The plasma enhances the kinetics of the chemical reactions leading to nanoparticle formation due to ionisation and dissociation of the reactive molecules. The charges on the particles might prevent further collisions and growth. A related method uses a high-current spark between two solid electrodes to evaporate the electrode material for creating nanoparticles. A plasma forms at the electrodes. This technique is used for materials with a high melting point such as Si or C.

Sputtering is a method of vaporising materials from a solid surface by bombardment with high-velocity ions of an inert gas, e.g. Ar or Kr, causing an ejection of atoms and clusters. Sputter sources are normally used in vacuum systems, below 10^{-3} mbar. It was shown, however, that a DC/RF magnetron sputter source can be operated in the mbar range, ejecting nanoparticles of sizes between 5 and 20 nm. Sputtering has the advantage that it is mainly the target material which is heated and that the composition of the sputtered material is the same as that of the target.

Nanoparticle formation does not always rely on homogeneous nucleation from the gas phase. The ablation of a solid source with a pulsed laser can also yield nanoparticles, but the formation mechanism does not necessarily involve a homogeneous nucleation step. Instead, clusters or even larger particles are ejected from the surface which may undergo coagulation. One important characteristic of this method is that the nanoparticles have the same stoichiometry as the substrate, which is difficult to achieve for some materials using normal evaporation sources. A micron-sized aerosol droplet may also yield nanoparticles by evaporating a solute-containing droplet. By choosing a sufficiently dilute solute, nanoparticles consisting of the solid residue can be obtained. Electrospray systems are often applied as droplet generators, as they produce very small droplets which are quite monodisperse in comparison with other spray processes. Additionally, droplet explosion due to an electrical charge which exceeds the Rayleigh limit during evaporation may yield even smaller droplets. Finally, initiating homogeneous nucleation inside aerosol droplets can result in many nano-sized nuclei in the droplet, which upon drying and ultimate fragmentation in the gas will yield nanoparticles. A more complete review of synthesis techniques can be found in [1].

5. Methods to synthesise monosized nanoparticles

Size control is of course necessary when size-dependent properties are sought. Gas-phase processes yield particles with a polydisperse size distribution, with standard deviations of 1.3 to 1.6. When a narrow size distribution is required, the first process requirement is to make sure that all the particles experience the same time-temperature history. This method is used

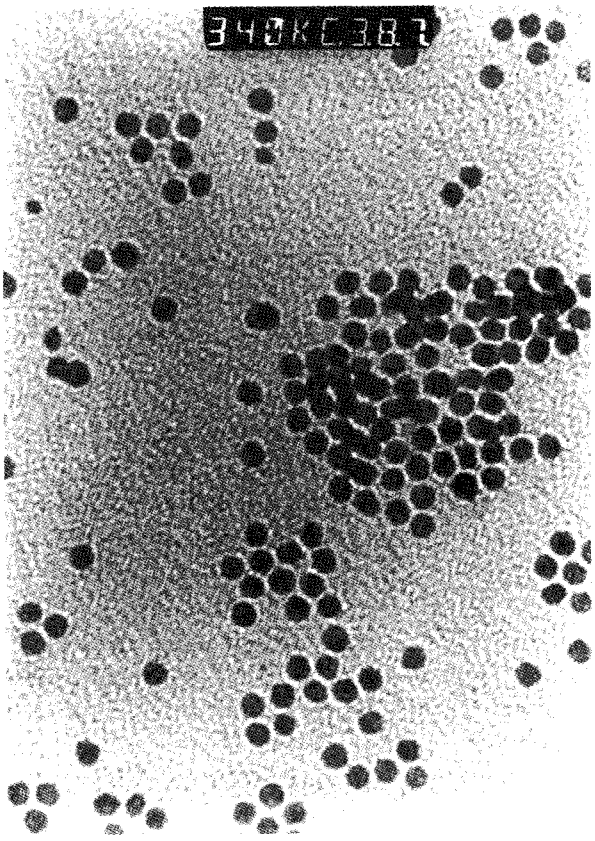

Fig. 2 Ag nanoparticles with a mobility diameter of 10 nm, obtained by size fractionation using a Differential Mobility Analyser.

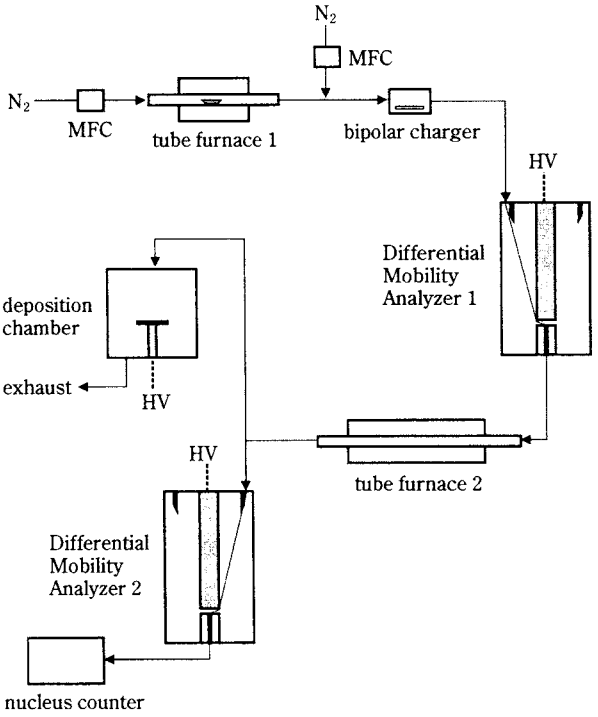

Fig. 3 Experimental set-up for synthesising monosized PbS nanoparticles.

in the so-called cluster machine [8] which is commercially available in Japan. When operated correctly, geometrical standard deviations of about 1.2 – 1.3 can be obtained. Another method is to produce in a first step small nuclei and then to let them grow by controlled condensation [9]. This can yield still smaller standard deviations Monodisperse nanoparticles with standard deviations of around 1.1 can also be obtained by size classification techniques. The only technique currently being employed, apart from high-vacuum mass spectrometry, is the classification of single-charged particles in an electric field. This so-called Differential Mobility Analysis (DMA) technique has been applied to produce monodisperse Ag (**Figure 2**), Si [10], Ga, GaAs, InP [11]and PbS [12] nanoparticles. Our work on the synthesis of PbS nanoparticles will be summarised in the remainder of this paper.

5.1 Experimental technique for the synthesis of monodisperse PbS nanoparticles

In the present work, a gas-phase synthesis method at normal pressure was developed for the preparation of sub-20 nm, crystalline, quasi-spherical, monodisperse PbS particles [12]. The experimental set-up is depicted in **Figure 3**. It contains six elements: a nanocrystal source, an aerosol charger, a size classifier, a tube furnace, an electrostatic precipitator, and a particle size measurement system consisting of a Differential Mobility Analyser (DMA) and a condensation nucleus counter (3025, TSI, Minneapolis, USA). After an experimental comparison of four DMAs [13], a nanometre aerosol DMA (Nano-DMA) [14] was designed, optimised for the size range 3 to 50 nm, see **Figure 4**.

A PbS aerosol is formed by sublimating a PbS powder in a tube furnace and after dilution (1:2), charged by a radioactive source (Kr^{85}). Nitrogen obtained from evaporating liquid nitrogen is used as the carrier gas. The total gas flow was kept at 1.5 l/min by means of mass flow controllers (MFC), and the system was operated at atmospheric pressure. In a Differential Mobility Analyser, the charged particles are fractionated on the basis of their electric mobility, which is a function of their charge level, mass, and shape. The DMA (NANO-DMA, TSI, Minneapolis, USA) is capable of delivering monodisperse aerosols with sizes adjustable between 2 and 50 nm and standard deviations between 1.05 and 1.20, depending on the flow conditions in the apparatus. In our studies, the flow ratio was chosen to provide a theoretical distribution in diameter of $\pm 0.1\ D_m$. An electrostatic precipitator enables the aerosol to be deposited with almost 100%

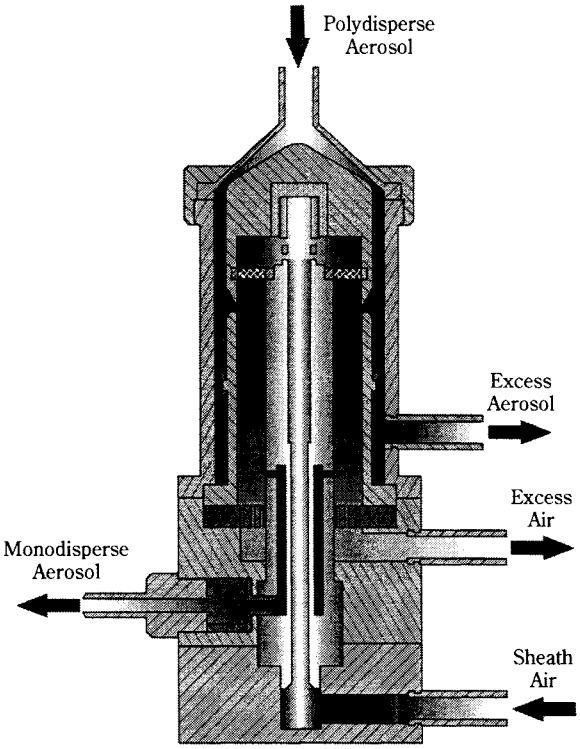

Fig. 4 Design of the Nano-DMA.

efficiency on a substrate. A condensation nucleus counter (3025, TSI, Minneapolis, USA) with a lower detection limit of 3 nm enables the monitoring of the aerosol number concentration.

5.2 Evaluation of the particle formation mechanisms

Using a Differential Mobility Particle Sizer after the second furnace, a decrease in the mean mobility equivalent diameter was experimentally observed when increasing the temperature of the second furnace (**Figure 5**). This can be attributed to two mechanisms. The first is a compaction process caused by restructuring, sintering and crystallisation. Restructuring and sintering processes are known to lead to a smaller mobility equivalent diameter with increasing temperature. This is due to increased solid-state diffusion coefficients. The negative slope of the curves increases with increasing particle diameter, indicating an increased compaction rate. This is confirmed by TEM microscopy, from which we observe a more porous and open structure containing tens of primary particles for the larger aggregates, which can be compacted more strongly due to sintering. The sintering effect can be clearly seen on the TEM micrographs in **Figure 6**. The second mechanism is evaporation of the particles, which is responsible for the increased negative slope of the curves at higher temperatures.

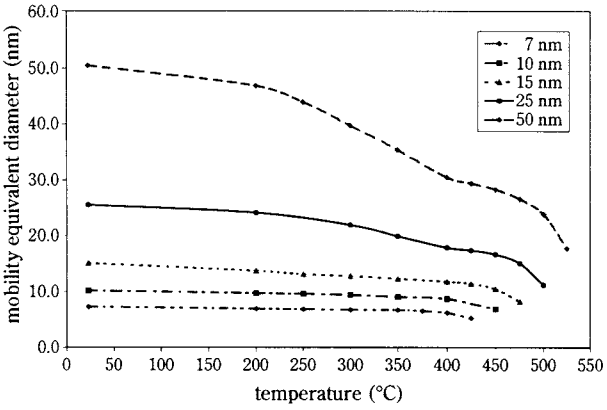

Fig. 5 Particle diameter of PbS based on electrical mobility as a function of the temperature in the second furnace, for different initial diameters.

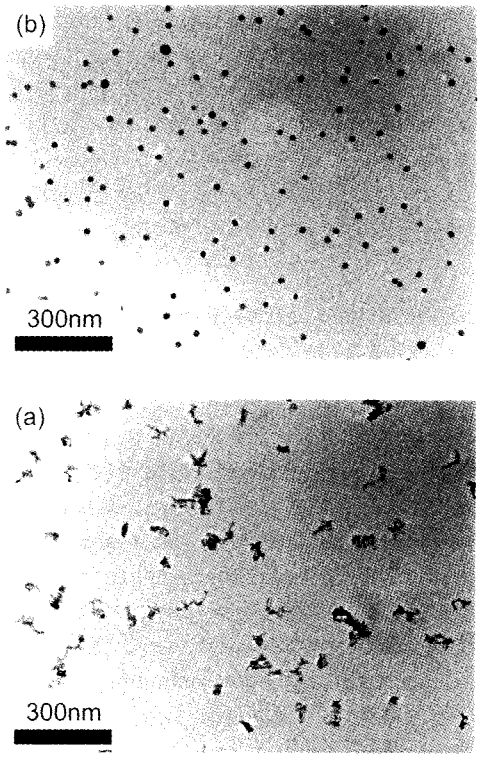

Fig. 6 TEM micrographs showing the sintering of PbS agglomerates (initial mobility diameter: 50 nm) [12]: with a sinter temperature of 300°C (a) and 500°C (b), respectively. They were produced by sublimation in a furnace, charged using a radioactive source, size-fractionated in a DMA and deposited onto a substrate by using an electrostatic precipitator.

With a residence time of 6 s in the second furnace, the calculations on the evaporation rate of the PbS nanoparticles predict a decrease in particle diameter of 2.2 nm (T=450°C), 7.2 nm (T=475°C), 23 nm (T=500°C) and 65 nm (T=525°C).

From the experimental results, it becomes clear that the sublimation and sintering temperatures have

to meet the following conditions:

$$T_{\text{high nucleation rate}} < T_{\text{furnace for sublimation}} < T_{\text{stoichiometric evaporation}} \quad (1)$$

and

$$T_{\text{appreciable sintering}} < T_{\text{furnace for sintering}} < T_{\text{appreciable evaporation}} \quad (2)$$

Fulfilling the first condition ensures that a sufficient number of particles is formed by homogeneous nucleation at temperatures lower than the temperature where off-stoichiometric evaporation starts. For InP and GaAs e.g., this relation is not fulfilled [15]. The second relation is clear from the earlier description of the experiments: crystalline and quasi-spherical particles have to be obtained by sintering at temperatures which do not cause extensive evaporation. For PbS, there is for each particle size a temperature range of some 50 K where the sintering rate is appreciable, while at the same time the evaporation rate is such that the particles shrink but do not disappear. The optimum sintering temperature turns out to be 400°C for particles which have a mobility equivalent diameter of 15 nm and 500°C for particles which have a mobility equivalent diameter of 50 nm.

6. Handling methods of nanoparticles in the gas phase

Nanoparticles leaving the reactor are not always suited to be directly integrated into their application. There are different conditioning steps possible which are indicated schematically in **Figure 7**.

Decreasing the degree of agglomeration is essential when nanoparticles have to be synthesised and when the formation of hard agglomerates has to be avoided. These agglomerates are formed by partial sintering of coagulated particles, forming material bridges which cannot be broken or dissolved. The most simple method is to dilute rapidly with a cool gas. One of the most successful cooling methods is the so-called inert-gas condensation, in which the nanoparticles are collected on a liquid N_2 cooled surface (a "cold finger") and continuously scraped off in a funnel. The powder can be compacted in the reactor, which avoids exposure to air and oxidation. This method has been scaled up and is already being applied in industry, yielding up to 40 tons/month. Expansion of a condensable gas through a nozzle leads to very high cooling rates. Special nozzle design can result in a one-dimensional temperature gradient. This leads to a highly uniform quench rate and thus to nanoparticles with a narrow size distribution.

Chemical and physical transformations are applied in order to obtain the desired product. In some cases,

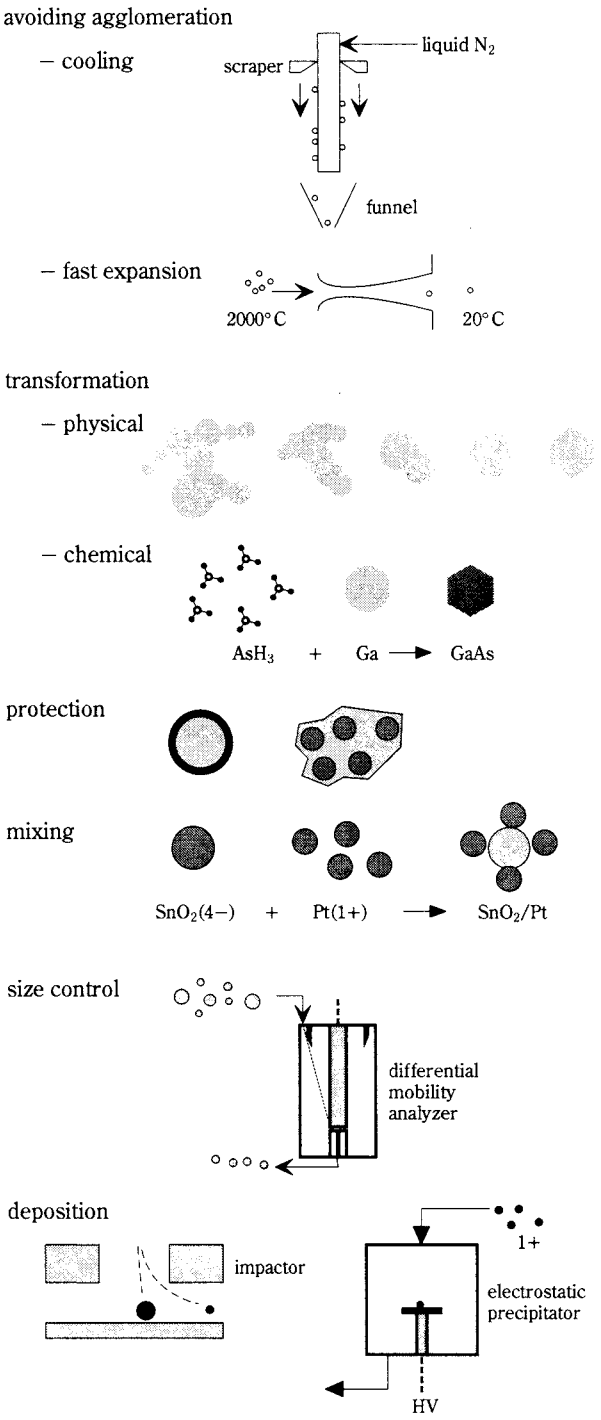

Fig. 7 Possible handling methods for nanoparticles.

chemical reactions are used in order. As an example, in the case of GaAs synthesis, direct sublimation is not possible due to incongruent evaporation. Therefore Ga nanoparticles are synthesised by evaporation in a first furnace and then reacted in a second furnace with AsH_3, resulting in GaAs nanoparticles [11]. Apart from chemical composition, the crystallinity is also important. Usually crystalline particles are required. In our PbS nanoparticle synthesis work [12], the as-

formed nanoparticles are amorphous and not spherical and have to be sintered in order to obtain monocrystalline and spherical particles.

Protection of nanoparticles is important as they are very reactive due to their large surface area. This is the main handling problem. In order to protect them for oxidation, they can be embedded, e.g. in a polymer or glassy host, handled in an inert atmosphere or protected by a thin coating. As an example, a method to avoid oxidation of flame-generated nanoparticles is to encapsulate them in the reactor within a material, e.g. a protective layer of NaCl, which can be removed later by washing or sublimation.

Nanocomposites demand a mixing of the components on the nano-scale. Usually this is no longer possible when the components are separately collected as powder, due to the presence of big aggregates. A mixing during the reaction or shortly afterwards, when the nanoparticles are still unaggregated or only slightly aggregated, is necessary to obtain a homogeneous mixing. A controlled mixing can be obtained by electrical bipolar mixing, in which two aerosols of different chemical composition are separately charged with opposite polarities and then mixed. The aggregation rate of particles of the same component is thereby slowed down, while the aggregation rate of particles of unequal components increases. This is shown in **Figure 8**, where this selectivity is shown as a function of particle size for singly charged particles. It can be seen that the two unequal charged particles have a 15-times-higher probability to aggregate than two equal charged particles. An example is the bipolar mixing of $BaZrO_3$ with $YBa_2Cu_3O_{7-x}$ [16], in which it was possible to control the number of $BaZrO_3$ particles combining with one $YBa_2Cu_3O_{7-x}$ particles by the charge level on the $BaZrO_3$ particles.

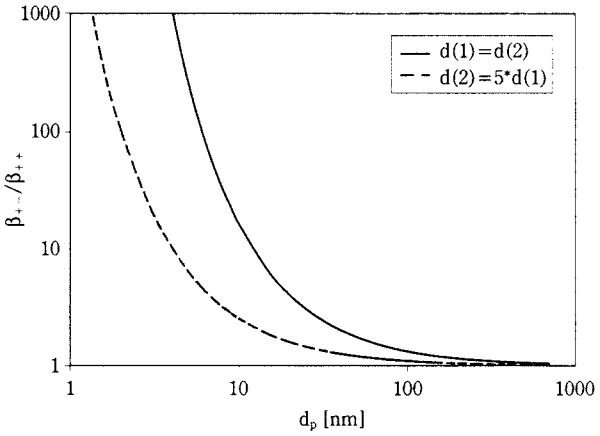

Fig. 8 Selectivity for aggregation of unequal components: ratio of collision rate of unequal charged particles and collision rate of equal charged particles (for singly charged particles)

7. Deposition of nanoparticles

After the synthesis, the particles have to be collected as a powder or brought onto a substrate. Powder collection can be accomplished by filtration, electrostatic precipitation or thermophoresis (the net movement of particles towards regions with a lower temperature) onto a cold surface. When thin or thick films of nanoparticles are required on a substrate, the usual way is to insert the substrate into the aerosol flow. The nanoparticles, which are often aggregated in micron-sized particles, will deposit due to the combination of thermophoresis and impaction due to inertia. A large part of the aerosol will, however, pass by. A higher deposition efficiency can be obtained by unipolarly charging the particles, and depositing them on a substrate placed on the central electrode in an electrostatic precipitator. A new type of unipolar charger we developed is shown in **Figure 9** [17], which can be called a twin-Hewitt charger. Here, two corona discharge zones are connected by a charging zone. The aerosol flow is parallel to the corona wires and the wire mesh. The first main advantage of this new charger is that due to the use of a square-wave voltage, ions are drawn into the charging zone alternately from each corona discharging zone. This increases the mean ion concentration considerably, resulting in a higher *Nt*-product. As a second advantage, the relatively low residence time in the inlet and outlet regions (some 10-20% of the total residence time) should be mentioned. This is especially important for nanoparticles with potentially high diffusional losses.

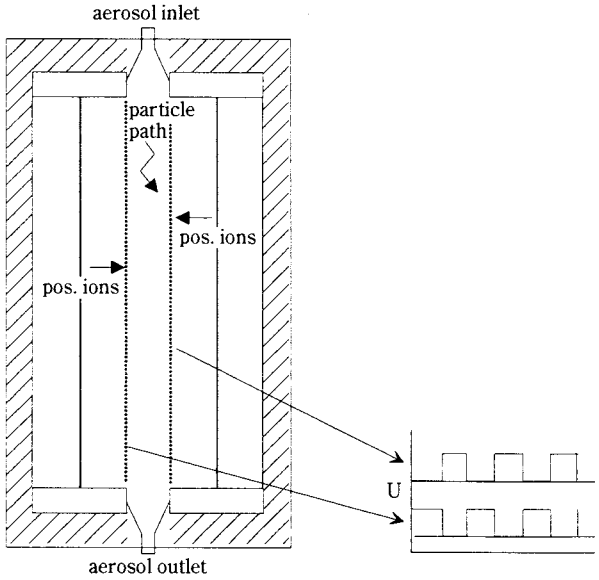

Fig. 9 Schematic design of the new unipolar charger for nanoparticles.

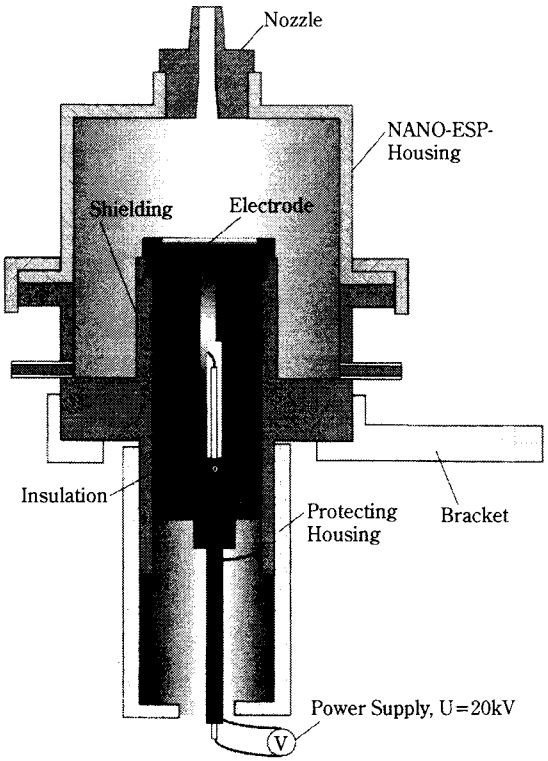

Fig. 10 Schematic design of the electrostatic precipitator.

Deposition of charged particles is achieved most efficiently by means of an electrostatic precipitator, which was specially developed [18] and is shown in **Figure 10**. Requirements for the ESP-design were almost complete particle sampling on a flat substrate and at least nearly homogeneous particle distribution on the substrate. To achieve better control of the particle deposition process, the charging and the deposition processes were separated. In the centre of the aerosol flow, the particle concentration distribution is homogeneous. If we put a round plate into the aerosol flow, the particles spread out because the flow goes around the obstacle. This affects the deposition pattern. On the other hand, an electric field with converging field lines on the plate competes with the flow-field effect on the particles. Thus both mechanisms may be used to achieve complete sampling on the one side and a homogeneous distribution on the other side. The voltage is applied between the central electrode and the walls of the electrically earthed expansion chamber. The design was guided by a complete numerical model. Particles up to 220 nm in diameter carrying one elementary charge can be sampled with the ESP with 100% efficiency.

Controlling the deposition pattern of nanoparticles on surfaces is another step towards the use of nanoparticles in functional applications. Nanoparticles were deposited in an electrostatic precipitator on microelectronic substrates with metal electrodes of micron-sized spacing. Control over particle deposition was obtained by creating a lateral electric field between the electrodes, resulting in the particles depositing preferentially on one electrode. Another method uses photoresist patterns on the substrate. The particles deposit preferentially on the areas without photoresist, probably due to charging of the photoresist. The photoresist is removed afterwards without visible loss of particles. As a first device application, metal-semiconductor-metal photodetectors with multifinger interdigitated electrodes were produced. After nanoparticle deposition, the detectors show a higher sensitivity, 4x on a GaAs substrate and 60x on a Si substrate [19].

8. Conclusions

Without doubt, nanoparticles show interesting properties of practical importance. We have listed some of the possible applications in the field of electronics and (electro)-optics. Many types of gaseous synthesis techniques exist. Essential for applications involving nanoparticles is the use of suitable handling techniques. Chemical engineering methods concerning dispersed materials systems are needed to understand, optimise and scale-up the processes used for the synthesis and applications of nanoparticles. This field can be described as nano-process technology. We have shown here some examples of handling techniques based on the use of electrical forces, which allows the use of monodisperse nanoparticles, controlled mixing of different nanoparticle components, and deposition control.

9. References

1) Kruis, F.E., H. Fissan and A. Peled: J.Aerosol Sci., **29** 511 (1998)
2) Brus, L.E.: J.Chem.Phys. **79** 5566 (1983)
3) Birringer, R., H. Gleiter, H.P. Klein, and P. Marquardt: Phys.Lett **102A** 365 (1984)
4) Colvin, V.L., M.C. Schlamp, and A.P. Alivisatos: Nature **370** 354 (1994)
5) Weller, H.: Angew.Chem.Int.Ed.Engl. **32** 41 (1993)
6) Abeles, B., H.L. Pinch and J.L. Gittleman: Phys.Rev.Lett. **35** 247 (1975)
7) Pehnt, M., D.L Schulz, C.J. Curtis, K.M. Jones and D.S. Ginley: Appl.Phys.Lett. **7** 2176 (1995)
8) Hayashi, C.: Mat. Sci. Forum **246** 153(1997)
9) Bowles, R.S., J.J. Kolstad, J.M. Calo and R.P. Andres: Surf. Sci **106** 117 (1981)
10) Camata, R.P., H.A. Atwater, K.J. Vahala and R.C. Flagan:

Appl.Phys.Lett. **68** 3162 (1996)
11) Deppert, K., J.-O. Bovin, J.-O. Malm and L. Samuelson: J.Crystal Growth **169** 13 (1996)
12) Kruis, F.E., K. Nielsch, H. Fissan, B. Rellinghaus and E.F. Wassermann: Appl.Phys.Lett. **73** 547 (1998)
13) Fissan, H., D. Hummes, F. Stratmann, P. Büscher, S. Neumann, D.Y.H. Pui and D.R. Chen: Aerosol Sci. Technol. **24** 1 (1996)
14) Chen, D.R., D.Y.H., Pui, D. Hummes, H. Fissan, F.R. Quant, and G.J. Sem: J. Aerosol Sci. **29** 497(1998)
15) Deppert, K., K. Nielsch, M.H. Magnusson, G. Dumpich, E. Kruis and H. Fissan: Nanostruct. Matls.**10** 565 (1998)
16) Takao, Y., M. Awano, Y. Kuwahara and Y. Murase.: Sensors and Actuators B **31** 131 (1996)
17) Kruis, F.E., F. Otten, F. Jordan and H. Fissan: J. Aerosol Sci. **29** S1021 (1998)
18) Dixkens, J. and H. Fissan. Design of a sampling system for off-line particle analysis, pp. 214-222 *in* Fine Solid Particles (ed. J. Schwedes, S. Bernotat), Shaker Verlag, Aachen, Germany (1997)
19) Prost, W., F.E. Kruis, F. Otten, K. Nielsch, B. Rellinghaus, U. Auer, A. Peled, E.F. Wassermann, H. Fissan and F.J. Tegude: J. Microelect. Eng. **41/42** 535 (1998)

Author's short biography

F.E. Kruis

Einar Kruis graduated in Chemical Engineering from Delft University of Technology in 1988. In 1993 he completed his Ph.D. research on the laser-assisted synthesis of ultrafine ceramic particles, performed in the Particle Technology Group of Prof. B. Scarlett and the inorganic Chemistry Group of Prof. J. Schoonman. During this time he also worked with Prof. S. Pratsinis in Cincinnati, USA. He pursued his academic carrier from 1993 to 1995 in the Reactor Engineering Institute of the late Prof. J. Villermaux at the ENSIC in Nancy, France as post-doctoral fellow in the Human Capital and Mobility program of the EC.
Since 1995 he is an assistant professor in the Institute for Process- and Aerosol Measurement Technology at the Gerhard Mercator University in Duisburg, Germany. He currently works on synthesis and handling techniques of nanoparticles.

H. Fissan

Heinz Fissan is Professor at the Electrical Engineering Department and Director of the Institute for Process- and Aerosol Measurement Technology at the Gerhard Mercator University in Duisburg, Germany. His research deals with aerosols and their application in different fields of technology. Fields covered are aerosol measurement technology, gas filtration, atmospheric aerosols, clean technology and nanostructured materials. The last field includes the synthesis of nanostructures, the in-situ and off-line analysis of nanoparticles and nanostructures, the simulation of structure development and the application of nanoparticles and nanostructures in sensors and electronic and opto-electronic devices.
He is author/co-author of approximately 200 publications on these subjects. He is a fellow of the International Aerosol Research Assembly since 1990 and obtained the Max Planck Research Award in 1993. In 1998 he received the David Sinclair Award from the American Association for Aerosol Research (AAAR).

Generation of Fine Solid Particles by Desublimation in a Subsonic Nozzle Expansion†

Alexander Wagner, Dieter Mewes
*Universität Hannover, Germany**

Abstract

The generation of fine solid particles by heterogeneous desublimation of succinic acid vapor is investigated experimentally and theoretically. In the experimental investigations, a gas mixture consisting of air and succinic acid vapor is cooled by means of subsonic nozzle expansion and is directly cooled by mixing. As a result of the cooling process, the gas mixture is supersaturated and the succinic acid vapor desublimes to fine particles. The number concentrations and particle size distribution of the powders generated are measured with an optical particle counter. The particle growth by desublimation is calculated with an Eulerian-Eulerian approach in a two-dimensional flow field. The population balance for the particle size distribution is solved and the mass and energy balance equations for each particle class are implemented in a CFD program (CFX 4.2).

Introduction

Gas-to-particle conversion processes can be used to produce very fine solid particles with narrow size distributions and of high purity. In the process, the particle formation is driven by the cooling of a supersaturated vapor or by the generation of atoms or molecules by chemical reactions of gaseous precursors. The use of gas-phase reactions is well established, for example, in flame synthesis processes used to produce submicron particles of titanium dioxide, silica or carbon black [1].

One method of gas-to-particle conversion is the desublimation process, which is the direct conversion from the vapor state to the solid state without passing through the liquid state. Desublimation can be used to separate a single desublimable component from a mixture of gaseous components. On account of the high purity and the good appearance (morphology) of the solid product, desublimation is widely employed to purify chemicals such as salicylic acid, naphthalene, anthracene or anthraquinone [2].

To desublime a single component from a mixture of gaseous components, the vapor phase must be supersaturated with the component that is to desublime. This can be achieved by cooling a saturated gas mixture. In this case, the cooling method and the process conditions determine whether nucleation, particle growth or coagulation will be the dominant mechanism in the process of particle formation. Thus, within limits, it is possible to control the number concentration, the particle size distribution and the surface structure of the desublimed particles. Direct cooling by mixing with an inert cooling gas leads to the formation of very small particles [3], [4]. Monodisperse particles are obtained if the gas mixture is cooled by a subsonic nozzle expansion [5]. Though desublimation by direct cooling and cooling due to expansion can be used to produce fine solid particles in a continuous process, little is found in the literature regarding these processes.

In the present experimental and theoretical work, the particle growth by desublimation due to expansion and direct cooling by mixing is investigated.

Experimental set-up

The experimental set-up to investigate the particle growth by desublimation due to expansion and direct cooling is shown schematically in **Fig. 1**. A filtered flow of pressurized ambient air is divided into a flow of carrier gas and a flow of cooling gas. One part of the carrier gas flows through a heated sublimer, in which solid succinic acid is sublimed into the carrier gas. The second gas flow is transported to an aerosol generator.

In the aerosol generator, sodium chloride nuclei are formed by means of an electrically heated platinum wire, which is coated with sodium chloride. The sodium chloride is vaporized into the gas flow, where the formation of solid nuclei subsequently takes place.

* Institut für Verfahrenstechnik der Universität Hannover
Callinstr. 36, 30167 Hannover, Germany
Email: wagner@c36.uni-hannover.de
† Received: May 31, 1999

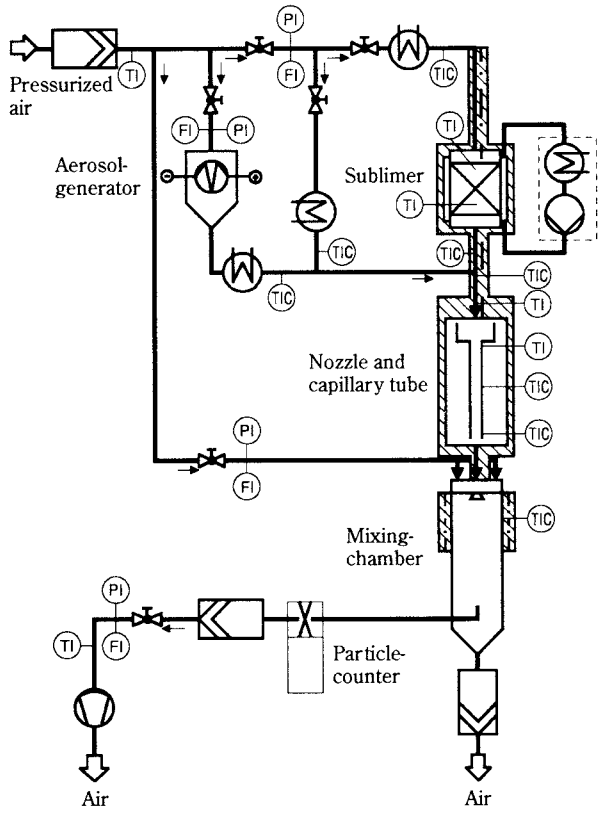

Fig. 1 Experimental set-up

The nuclei formed are to a large extent smaller than 100 nm, and number concentrations of 10^6 nuclei per cm^3 of air are achievable [6]. After heating the gas flow containing the sodium chloride nuclei, it is mixed with the gas flow containing the desublimable vapor.

The resultant gas mixture containing air, succinic acid vapor and nuclei is then expanded in a nozzle and a capillary tube. Due to the expansion, the gas mixture is cooled. Therefore, the gas mixture is supersaturated and the heterogeneous particle growth on the nuclei is initiated in the nozzle and the capillary tube. The residence time in this section of the set-up depends on the length of the capillary tube. The design of this section was calculated with a one-dimensional model of the particle growth in the nozzle and the capillary tube [7], [8]. In the experimental investigation, the length of the capillary tube is 0.5 m. The diameter is 1 mm and the diameter of the nozzle inlet is 6 mm.

After entering the mixing chamber, the remaining succinic acid vapor is desublimed due to direct cooling by mixing with the flow of cooling gas. The walls are heated in order to avoid desublimation of succinic acid vapor at the walls of the chamber. The diameter of the mixing chamber is 40 mm and it has a length of 0.6 m. At the bottom of the mixing chamber, a sample is taken from the gas flow and the number concentration and the particle size distribution of the particles are measured by means of an optical particle counter.

Experimental results

In the experimental investigations, the change of state of the gas mixture in the nozzle and capillary tube is adiabatic. In **Fig. 2**, experimental results are given for the measured mean particle diameter of the volume distribution of the powder generated depending on the partial pressure of the succinic acid at the inlet of the nozzle. The number concentration of the particles varies. The gas flow through the nozzle is 3 l/min and the cooling gas flow amounts to 6 l/min. The total pressure at the inlet of the nozzle is 145 kPa. An increase of the mean particle diameter is achieved by increasing the partial pressure. For a constant number concentration of particles, the measured points are represented by the continuous lines. These curves describe the expected relationship between the particle diameter and the partial pressure. For a constant partial pressure and an increasing number concentration, the mean particle diameter decreases.

Fig. 3 shows the measured sum of the number distribution of the powder generated. The partial pres-

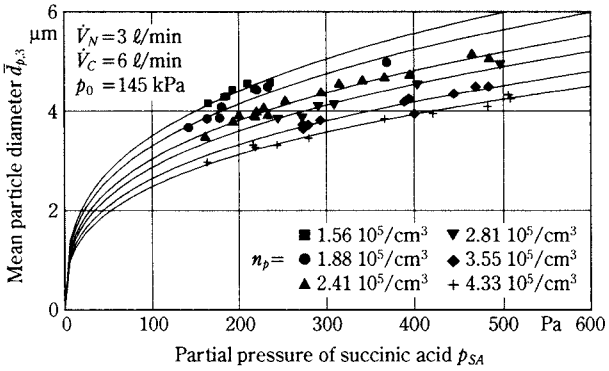

Fig. 2 Measured mean particle diameter of the generated powder

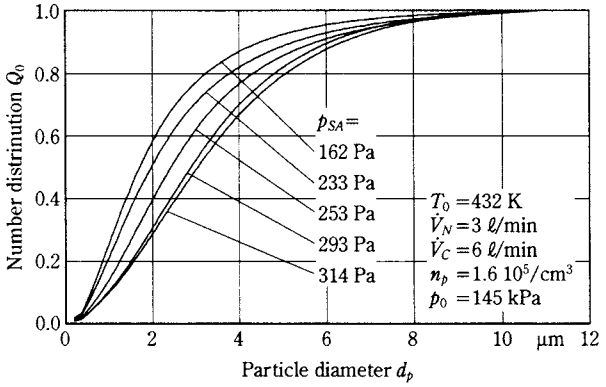

Fig. 3 Measured sum of the number distribution of the powder for constant number concentration

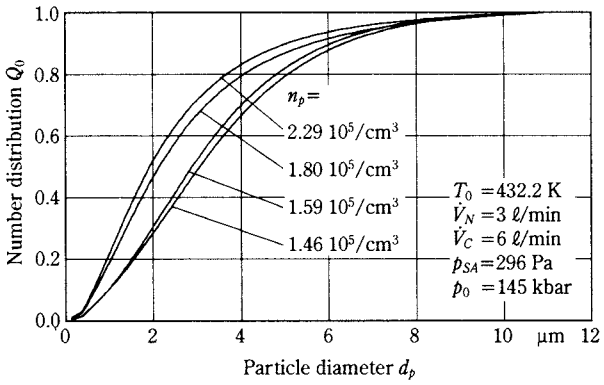

Fig. 4 Measured sum of the number distribution of the powder for constant initial partial pressure

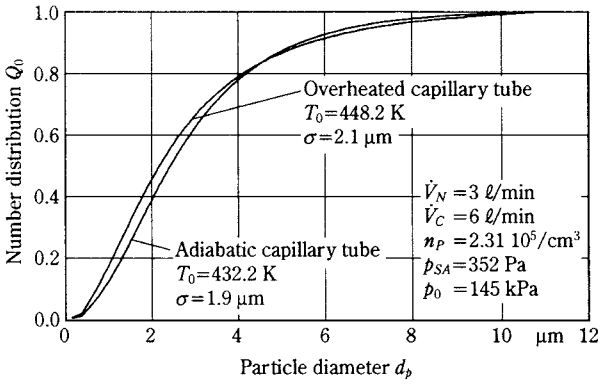

Fig. 5 Measured sum of the number distribution for two different operating points of the set-up

sure of the succinic acid varies. The number concentration of particles is kept constant. The temperature at the nozzle inlet is 432 K. For an increasing partial pressure, the curve for the number distribution is shifted to the right and to greater particle diameters.

This can be explained by the increasing amount of vapor available for the growth of every single particle. Additionally, the number distribution becomes wider for an increasing partial pressure. The duration of particle growth increases and therefore there is a greater influence on the particle growth of inhomogeneities of the flow field in the mixing chamber.

In **Fig. 4**, the sum of the number distribution is shown for a varied number concentration of the particles. The initial partial pressure of succinic acid is kept constant. For greater number concentrations smaller particles are generated. An increasing number concentration has the same effect as a decreasing partial pressure. Accordingly, the number distribution of the particles becomes narrower for an increasing number concentration.

The influence of the expansion on the particle size distribution of the particles generated cannot be investigated using the experimental results described. At the end of the capillary tube the particle growth is not finished and the particles are not in thermodynamic equilibrium. Therefore, no sample can be taken at the outlet of the capillary tube to measure the particle size distribution. To investigate the influence of the expansion, two different operating points of the experimental set-up are compared. On the one hand, the experiments are performed with an adiabatic nozzle and capillary tube, and on the other hand, the capillary tube is overheated. The latter has the consequence that there is no supersaturation in the capillary tube and, accordingly, no particle growth takes place. In **Fig. 5**, the sum of the number distribution of the particles generated are shown for both cases, the adiabatic and the overheated capillary tube.

In the case of the adiabatic capillary tube, the standard deviation of the particle size distribution is approximately 10% smaller than in the case of the overheated tube. The reason for the reduction in the case of an adiabatic tube can be explained by the particle growth in the homogeneous flow field of the capillary tube. The particles are enlarged by about one decade in the homogeneous flow field of the capillary tube [7], [8], before entering the inhomogeneous flow field of the mixing chamber.

Theoretical results

On the basis of the calculated two or three-dimensional flow field, the particle growth by desublimation is evaluated by solving a population balance for the particle size distribution. It is presumed that the particles are small enough to travel at the same velocity as the local gas mixture at any point. Furthermore, the density of the solid phase is presumed to be much greater than that of the gas. Thus, the presence of the solid particles makes no contribution to the specific volume of the mixture. If there is no particle diffusion at any point, the balance equations for mass and energy of a particle class can be written as:

$$\frac{\partial r_j}{\partial t} + \nabla(r_j \vec{v}) = S_{r,j} \tag{1}$$

$$\frac{\partial r_j h_j}{\partial t} + \nabla(r_j h_j \vec{v}) = S_{rh,j} \tag{2}$$

Here, r_j is the volume fraction and h_j is the total specific enthalpy of the particle class. $S_{r,j}$ and $S_{rh,j}$ are source terms for mass and energy, respectively. In order to determine these terms, the following population balance for the particle size distribution $n=f(s,t)$

has to be evaluated [9]:

$$\dot{n} = \frac{\partial n}{\partial t} + \dot{s}\frac{\partial n}{\partial s} + n\frac{\partial \dot{s}}{\partial s} \tag{3}$$

Here, s is the squared radius of the particles and n is the number of particles per unit volume having sizes between s and $s+ds$. Multiplying the population balance with the volume of the particles, V_p, and introducing the volume fraction of the particles in this range, v, gives:

$$v = V_p n, \tag{4}$$

Eq. (3) can be transformed into the following differential equation:

$$V_p\dot{n} = \frac{\partial v}{\partial t} - \frac{v}{V_p}\frac{\partial V_p}{\partial t} + \dot{s}\frac{\partial v}{\partial s} - \dot{s}\frac{v}{V_p}\frac{\partial V_p}{\partial s} + v\frac{\partial \dot{s}}{\partial s}. \tag{5}$$

Assuming that the particles are spherical and that the growth rate is limited by the mass transfer in the gas phase, a mass balance at the surface of the particles leads to the equation for the change of the particle surface, $\dot{s}$, [4]:

$$\dot{s} = 2r_p\frac{\partial r_p}{\partial t} = \frac{\beta_M Sh D}{\rho_p}\frac{\pi M_v}{R}\left(\frac{p_{v,\infty}}{T_\infty} - \frac{p_{v,p}}{T_p}\right) \tag{6}$$

Here, β_m is a function of the Knudsen number and takes into account the conditions in the entire range of continuum, transition and free molecules regimes [10], [11]. Sh is the Sherwood number, D is the diffusion coefficient, r_p is the particle density, M_v is the molecular weight of the vapor and R is the universal gas constant. $p_{v,p}$ and $p_{v,\infty}$ are the vapor pressures at the particle surface and in the gas mixture, respectively. T is the temperature.

If the temperature of the particles is independent of their size, then so is the change of particle size, $\dot{s}$. Taking also into account the fact that the volume of the particles, V_p, is independent of time, Eq. (5) can be simplified:

$$V_p\dot{n} = \frac{\partial v}{\partial t} + \dot{s}\frac{\partial v}{\partial s} - \dot{s}\frac{v}{V_p}\frac{\partial V_p}{\partial s}. \tag{7}$$

Also

$$r_j = \int_{s_{j-1}}^{s_j} v\,ds, \tag{8}$$

Integration with respect to s and with some rearrangement, the source term for the mass balance of a particle class can be derived:

$$S_{r,j} = -\dot{s}(v_j - v_{j-1}) + \dot{s}\frac{3}{2}\int_{s_{j-1}}^{s_j}\frac{v}{s}ds + \int_{s_{j-1}}^{s_j} V_p\dot{n}\,ds \tag{9}$$

For the integration, spherical particles are presumed. s_j and s_{j-1} are the upper and lower boundaries of the particle class j. If there is no agglomeration of the particles in the flow field, the last integral on the right-hand side of Eq. (9) describes the change of the volume fraction r_j of the particle class due to homogeneous nucleation. At a certain point in the flow field, the rate of nucleation, I, is calculated for one critical radius of the particles, $r_{p,crit}$. Therefore, the integral can be replaced by:

$$\int_{s_{j-1}}^{s_j} V_p\dot{n}\,ds \approx \frac{\pi}{6}I\left(s_j^{1/2} + s_{j-1}^{1/2}\right)^3 \text{ with } s_{j-1} < r_{p,crit}^2 \le s_j, \tag{10}$$

The source term for mass can be written as:

$$S_{r,j} = -\dot{s}(v_j - v_{j-1}) + \dot{s}\frac{3}{2}\int_{s_{j-1}}^{s_j}\frac{v}{s}ds + \frac{\pi}{6}I\left(s_j^{1/2} + s_{j-1}^{1/2}\right)^3 \tag{11}$$

The remaining integral on the right-hand side can only be solved if the dependency of the volume fraction, v, on the particle size, s, is known. Therefore, a step function for the volume fraction is assumed as shown in **Fig. 6**. This means that the volume fraction is constant between the upper and lower boundary of a particle class. With

$$v_j = \frac{r_j}{s_j - s_{j-1}} \tag{12}$$

the source term reads:

$$S_{r,j} = -\dot{s}_j\frac{r_j}{s_j - s_{j-1}} + \dot{s}_{j-1}\frac{r_{j-1}}{s_{j-1} - s_{j-2}} + \dot{s}_j\frac{3}{2}\frac{r_j}{s_j - s_{j-1}}$$
$$\ln\left(\frac{s_j}{s_{j-1}}\right) + \frac{\pi}{6}I\left(s_j^{1/2} + s_{j-1}^{1/2}\right)^3 \tag{13}$$

The last two terms in Eq. (13) stand for the mass transfer between the gas phase and the specific particle class. The mass transfer into the particle class containing bigger particles is described by the first

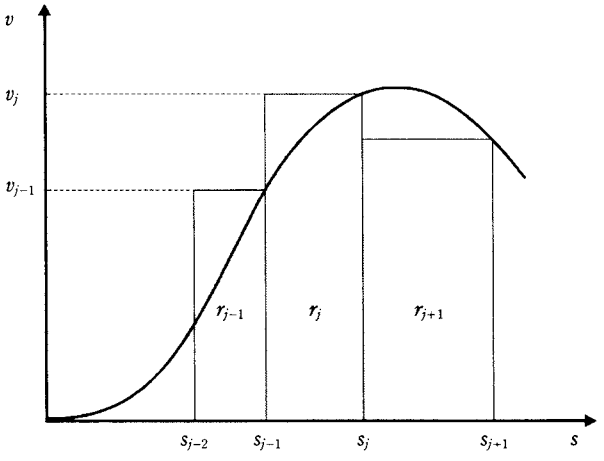

Fig. 6 Discretized particle size distribution

term. The second describes the mass transfer into the class containing smaller particles. The source term of the energy can be derived in the same way.

In order to calculate the particle growth in a two or three-dimensional flow field, the equations 1, 2 and 6 are implemented in a CFD program (CFX 4.2).

Fig. 7 shows the rotationally symmetrical rescaled geometry of the calculated flow field. The inlet of the saturated gas mixture consisting of gas, vapor and nuclei is at the top, and the cooling gas flows through an annular nozzle. The nozzle and capillary tube are insulated, which means there is no heat flux through the walls. The walls in the upper part of the mixing chamber are heated in order to avoid desublimation at the walls.

Fig. 8 shows the calculated flow field in the upper part of the mixing chamber. The gas mixture containing the particles flows downward out of the capillary tube into the mixing chamber. The gas mixture is directly cooled by mixing with the inert flow of cooling gas. The cooling gas flow enters the chamber through an annular nozzle. Due to the free jet in the center of the mixing chamber, a vortex develops.

Fig. 9 shows the calculated number distribution density for different axial positions in the capillary tube and the mixing chamber. The calculation predicts a growth rate in the capillary tube which allows an enlargement of the nuclei by about a decade. The flow enters the mixing chamber at 0.5 m. At this point the gas flow is mixed with the cooling gas and the particles therefore grow rapidly. Because of the inhomogeneous concentration and the temperature fields in the mixing chamber, the standard deviation of the number distribution becomes wider.

The calculated particle size distribution is compared with the measured size distribution at the outlet

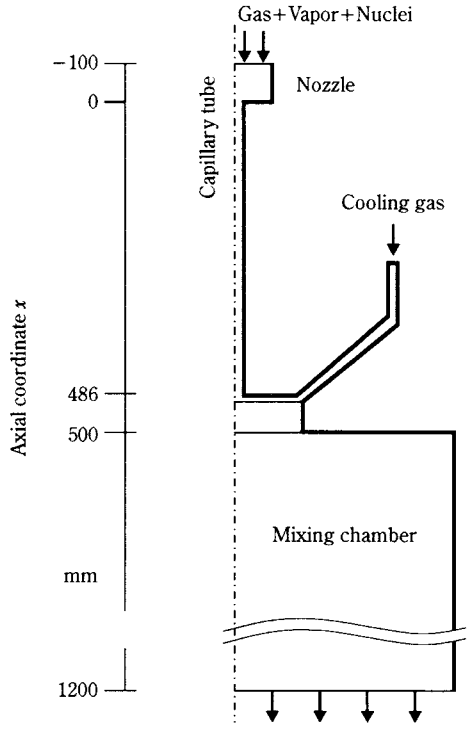

Fig. 7 Rescaled geometry of the calculated flow field

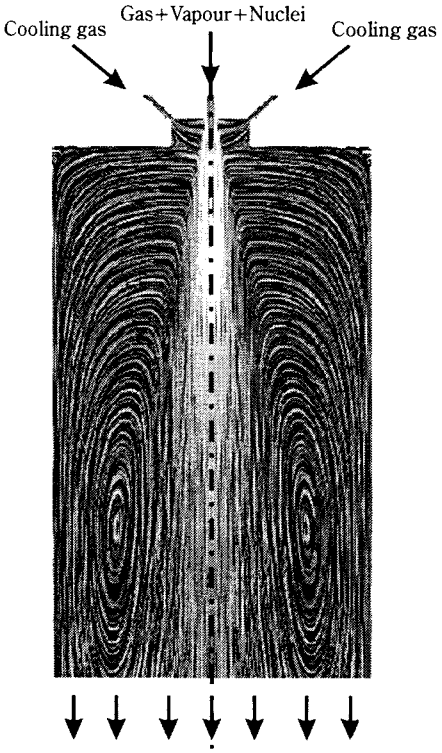

Fig. 8 Calculated flow field in the upper part of the mixing chamber

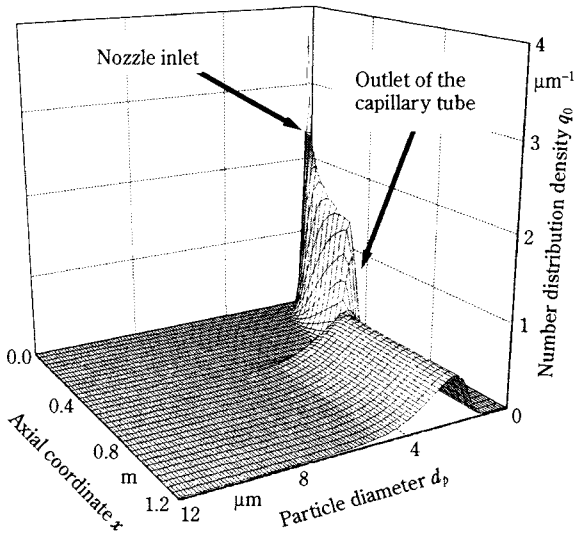

Fig. 9 Calculated density of the number distribution in the center of the flow field

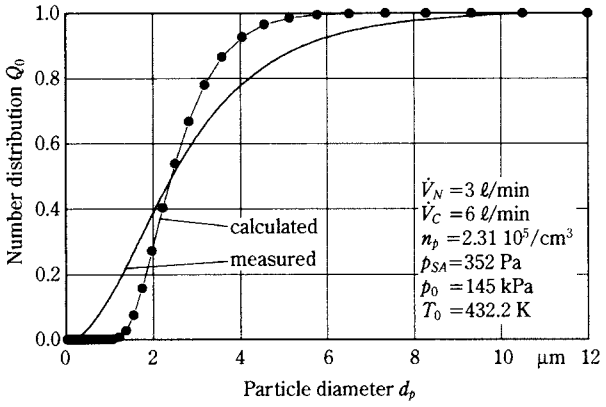

Fig. 10 Measured and calculated cumulative number distributions at the outlet of the mixing chamber

of the mixing chamber in **Fig. 10**. For the calculation, it is presumed that the temperature of the particles equals the local gas temperature at any time. Homogeneous nucleation is neglected at any point of the flow field. The calculations are performed with 50 particle classes, which are shown by the dots in the diagram. The measured number distribution is shown by the continuous line. The mean particle diameter of the measured and calculated particle size distribution is in good agreement, although the measured distribution is wider than that calculated.

Conclusion

Desublimation by direct cooling of a mixture of gaseous components is a suitable process to produce fine solid particles in a continuous process. The number concentration and the particle size distribution of the desublimed particles can be influenced by various process parameters. On the one hand, increasing vapor concentration leads to increased mean diameters of the particles. And on the other hand, an increasing number concentration of the desublimed particles results in a decrease to the mean diameters of the particles. For inhomogeneous concentration and temperature fields, the standard deviation of the particle size distribution is wide. The standard deviation of the particle size distribution can be reduced by 10% if the gas mixture is first expanded in a subsonic nozzle expansion. Theoretical simulation of the particle growth in the subsonic nozzle expansion predicts a growth rate which allows an enlargement of the particles by about a decade in the capillary tube. The calculated number distribution of the particles generated is in agreement with the measured distribution.

Acknowledgement

The financial support of the Deutsche Forschungsgemeinschaft (DFG) is greatfully acknowledged.

Nomenclature

D	m^2/s	diffusion coefficient
$\bar{d}_{p,3}$	m	mean particle diameter of the volume distribution of the particles
h	J/kg	total specific enthalpy
I	1/m^{3}s	nucleation rate
j		counter
Kn		*Knudsen number*
M	kg/kmol	molecular weight
n	1/m^3	number concentration
n	1/m^5	number concentration related to the particle surface
p	Pa	pressure
Q_0		cumulative number distribution of particles
q_0	1/m	number density distribution of particles
r		volume fraction
R	J/kmolK	universal gas constant
r	m	radius of particle
s	m^2	surface of particles
Sh		Sherwood number
S_{rh}	J/kgs	source term for the energy of a particle class
S_{rj}	1/s	source term for the mass of a particle class
T	K	temperature
t	s	time
V	m^3	volume
$\dot{V}$	m^3/s	volume flow
$\vec{v}$	m/s	local velocity of the fluid
x	m	axial coordinate
β_m		$=f(Kn)$
ρ	kg/m^3	density
σ	m	standard deviation

Subscripts

∞	infinity
0	initial state
crit	critical
C	capillary tube
j	number of particle class
N	nozzle
p	particle
SA	succinic acid
v	vapor

References

1) Gurav, A.; Kodas, T.; Pluym, T.; Xiong, Y.: Aerosol Processing of Materials, Aerosol Sci. Technol. 19 (1993), 411-452
2) Bilik, J.; Krupiczka, R.: Heat Transfer in the Desublimation of Phthalic Anhydride, Chem. Engng. J. 26 (1983) 3, 169-180
3) Kudela, L.; Sampson, M. J.: Understanding Sublimation Technology, Chem. Engng. 93 (1986) 12, 93-98
4) Kodde, M.: Partikelbildung durch Desublimation infolge direkter Kühlung, VDI Fortschrittberichte Reihe 3 Nr. 451 (1996)
5) Turner, J. R.; Kodas T. T.; Friedlander, S. K.: Monodisperse Particle Production by Vapor Condensation in Nozzles, J. Chem. Phys. 88 (1988) 1, 457-465
6) Stahlhofen, W.; Gebhart, J.; Heyder, J.; Roth, C.: Generation and Properties of a Condensation Aerosol of Di-2-Ethylhexyl Sebacate (DES) – Part I; J. Aerosol Sci. 6 (1975), 161-167
7) Wagner, A.; Mewes, D.: Enlargement of Particles by Continuous Desublimation, PARTEC 98, March 10-12, 1998, Nürnberg, Germany.
8) Wagner A., Mewes, A.: Generation of Fine Solid Particles by Continuous Desublimation in a Gas Mixture, Fine Solid Particles, Shaker-Verlag Aachen, 1997
9) Spalding, D. B.: Notes on the PARMIX Program, Imperial College Heat Transfer Section Report BL/TN/A/35, 1970
10) Fuchs, N. A.; Sutugin, A. G.: Highly Dispersed Aerosols, Ann Arbor Sci. Publ., Ann Arbor 1970
11) Wagner, P. E.: Aerosol Growth by Condensation; In: W. H. Marlow (ed.): Aerosol Microphysics II, Springer Verlag, Berlin 1982, 129-178

Author's short biography

Alexander Wagner

- Research Assistant, Institute of Process Engineering, University of Hannover, Germany, since 1996
- 1995 Dipl.-Ing. (RWTH Aachen, Process Engineering)

Dieter Mewes

- Professor, Institute of Process Engineering, University of Hannover, Germany, since 1983
- 1966 Dipl.-Ing. (TU-Berlin), 1970 Dr.-Ing., 1972 Dr.-Ing. habil. (TU Berlin, Prof. Brauer, Chemical Engineering)
- 1973 Degussa AG, Frankfurt, 1978 Degussa Antwerpen NV, 1978 – 1981 Degussa Corp., USA (Vice President Engineering), 1981 Degussa AG, Director
- Member of the Berlin-Brandenburg Academy of Science, Editor of Heat and Mass Transfer, Springer Verlag, Berlin, numerous assignments to scientific and governmental committees
- Research interests in multiphase flow, heat and mass transfer, optical and tomographic measurement methods, applications in polymer techniques, process and equipment design, safety systems for nuclear and chemical industry, multiphase transport of oil and gas, medical engineering

Computational Fluid Dynamics Model of a Swirler Separator for Gas Cleaning†

Luis A.C. Klujszo, Polycarpe K. Songfack and Raj K. Rajamani
University of Utah
*Department of Metallurgical Engineering**
Menachem Rafaelof
*MJR Scientific Corporation***

Abstract

This work is concerned with the development of a computational fluid dynamics model for a two-phase, turbulent, swirling flow produced by stationary guide vanes. The swirling flow causes separation of particles in the air stream and hence the device is called swirler separator. The Reynolds-averaged continuity and Navier-Stokes equations are solved along with the Boussinesq hypothesis to describe the stress distribution throughout the flow field in a body-fitted coordinate system. The κ-ε model is used to determine turbulent viscosity. Finite volume methodology is adopted to discretize the system of governing partial differential equations and the semi-implicit method for pressure linked equations consistent to deal with the pressure-velocity coupling. The dilute phase is accounted for by following a Lagrangian methodology in which a Newtonian force balance tracks the particles throughout the flow field. A stochastic method is employed to model the dispersion of particles due to turbulence of the fluid-phase. The phenomenological model is then successfully used to predict velocity and pressure fields created by the guide vanes as well as particle classification curves brought about by the swirler separator.

1. Introduction

A number of practical applications involve the cleaning of a stream of air contaminated with particles in dilute concentration. As few examples of application areas, one can mention among others the industrial treatment of effluent gases, clean room technology, mine ventilation, and coal dust separation. The swirler device in study here is suitable for just about any application in which a particle-laden air has to be freed of solids.

For separating particles from a stream of air, a few devices other than swirlers are also available [1]. Standard cyclones, linear cleaners, also referred to as settling chambers, electrostatic separators, and filters with reverse fan can all be employed to separate particles from air in practical situations. Cyclones and their variants are very efficient, but the pressure drops across these units are not very promising. Electrostatic separators and filters are able to provide excellent separation sizes and overall cleaning efficiencies, but, at the same time, require large power inputs as well as installation space. Linear cleaners are effective in terms of pressure drops, but the space requirements are huge, and cleaning efficiencies are not satisfactory for most targeted processes. Trade-off always exists among all these options, but the swirler device, if properly designed, exhibits the combined advantage of separation of low-micron range particle sizes and compact device size per unit volume of dusty air processed, while maintaining low pressure drop. Since the swirler uses existing pressure drop in the gas flow line for self-operation, it is important that the pressure drop be as low as possible while producing the best possible separation.

In some instances, the proper design and operation of the device employed to accomplish just the air-solid separation task are crucial to the performance of the overall industrial flowsheet. Therefore, such an important feature should be looked at from a fundamental standpoint.

The design and operation of air-solid separators require characterization and optimization of very

* 135 South 1460 East Room 412, Salt Lake City, Utah, 84112, USA
Fax: +1 801 581 4937
** 1439 Sherman Avenue, Salt Lake City, Utah, 84105 USA
Fax: +1 801 582 9483
† Received July 20, 1999

complex phenomena. Nowadays, empiricism is not adequate to elucidate many of the aspects of interest in the separation process; rather, mathematical modeling based purely on physics has become more attractive with the development of powerful computers and reliable computational fluid dynamics (CFD) software.

The main goal of this work is to develop a CFD model for the swirler separator, which can then be used later on to investigate improved designs. The swirler separator consists basically of a cylindrical tube fitted with static blades at the entry. At the outlet, a slightly smaller-diameter tube is attached so that an annular slit is formed (collection ring, collection gap). A typical single-cell swirler separator is shown schematically in **Figure 1**. The incoming particle-laden air passes through the fixed vanes, gaining angular momentum, thus creating centrifugal force, which causes particles to be thrown to the periphery of the tube wall. Thus, dust particles migrate to the wall, get discharged through the slit due to the axial motion of the swirling flow, and settle in the closed collection chamber.

As emphasized earlier, an efficient design to fully accomplish the air-solid separation should offer as low a pressure drop across the unit as possible, while maintaining reasonable cleaning efficiency. Computer simulations come into play at this stage. Instead of trying to answer a whole range of questions by means of experiments, the development of a reliable model describing the physics of the separator is attempted. In this model, the fluid flow is predicted by solving the averaged conservation (continuity) and momentum (Navier-Stokes) equations along with the Boussinesq hypothesis [2] to describe the stress distribution in the flow field and the standard κ-ε model [3] to calculate the turbulent viscosity. The solid-phase is modeled by solving a Newtonian force balance plus dispersion of particles due to the turbulence of the fluid-phase over each particle fed to the system throughout the flow field.

Successful development of the CFD model for both phases translates into a powerful simulation tool. The assessment of success can be made through comparisons between model predictions and experimental data, including pressure drop and velocity field to validate the fluid-phase model as well as particle collection to verify the particulate-phase model.

Finally, after verification of the model, it can be safely used to determine a final configuration for the swirler separator capable of fulfilling the constraints of any particular task.

A literature survey on the topic of swirler separators employed to clean particle-laden airflows reveals that very little work has been conducted on the matter up to this point. A few reports of experimental investigations can be found in Daniels [4], Akiyama et al. [5], and Akiyama and Marui [6]. The main goal of these literature reports was to experimentally correlate design and operational variables to the response of the separator in terms of pressure drop and collection efficiency. Ramachandran et al. [7] pioneered attempts to arrive at a mathematical model able to describe the main variables of interest of a similar separator (i.e., pressure drop and collection efficiency). More recently, Klujszo [8, 9] performed extensive

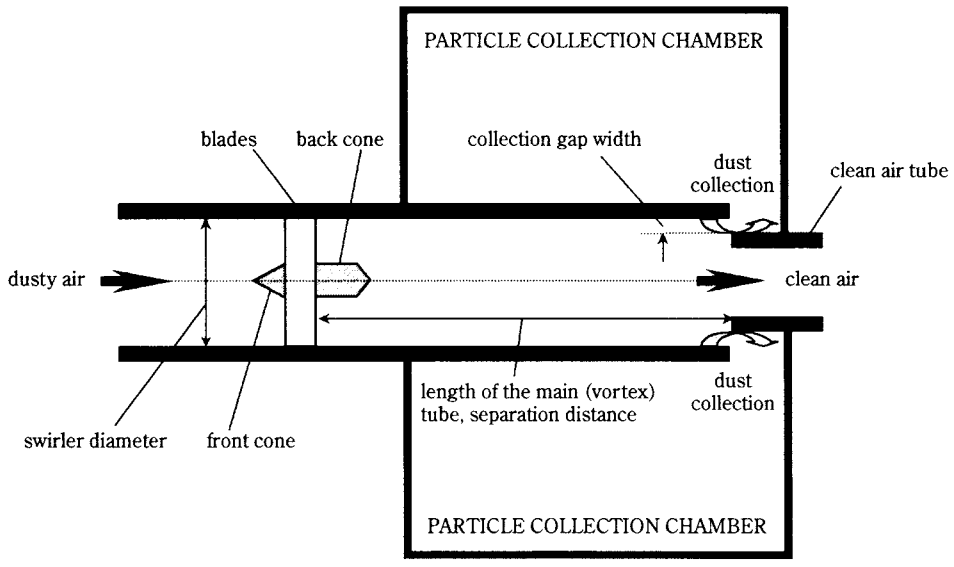

Fig. 1 Schematic of a single-cell swirler separator

work on this type of separator, including phenomenological modeling (i.e., transport equations) of the two-phase flow and a series of particle-laden airflow separation experiments.

2. Model Development

2.1 General Considerations

The task of modeling any flow situation automatically implies the knowledge of the main features of the flow, since the particular set of equations to be solved is directly determined by the characteristics of the flow. Therefore, some questions have to be addressed before work is started. A few examples of the issues to be addressed are presented below.

- Geometry: two-dimensional, axially symmetric, or three-dimensional.
- Time dependence: steady or unsteady.
- Fluid: Newtonian or non-Newtonian.
- Flow: compressible or incompressible, laminar or turbulent (if turbulent, which modeling strategy should be followed for turbulence), one-phase or two-phase (if two-phase, which approach should be used to model the dispersed-phase).

Once all the above questions are answered, the basic governing equations, which are nothing but mathematical representations of principles of conservation of mass and momentum, can be framed. The flow inside the swirler separator falls into the category of steady-state, incompressible, turbulent, and two-phase. Incompressibility is assumed since the flow velocities involved in this problem are much smaller than the speed of the sound, causing no effect on the density of the fluid medium. A fully three-dimensional geometry is chosen as flow domain to cut short simplifications and, therefore, enhance model predictions. Regarding turbulence, the standard κ-ε model is believed to give reasonably good predictions for this type of flow and is the one followed. A no-coupling-between-phases approach is used to account for the two-phase flow due to the dilute nature of the concentration of particles in the system. Additionally, the randomness of turbulence prohibits direct numerical simulation of the governing equations and analytical solution is not possible because of the high non-linearity of the partial differential equations. Thus, averaging procedures are employed and instantaneous information is lost in favor of averaged quantities.

2.2 Basic Governing Equations

The conservation principles (mass and momentum) can be expressed for this case by the Reynolds-averaged continuity (1) and Navier-Stokes (2) equations as follows:

$$\frac{\partial}{\partial x_j}u_j = 0 \tag{1}$$

$$\rho\frac{\partial}{\partial x_j}(u_i u_j) = -\frac{\partial p}{\partial x_i} + \frac{\partial}{\partial x_j}\left[\mu\left(\frac{\partial u_i}{\partial x_j} + \frac{\partial u_j}{\partial x_i} - \frac{2}{3}\frac{\partial u_k}{\partial x_k}\delta_{ij}\right)\right] + \frac{\partial}{\partial x_j}(-\rho u_i' u_j') \tag{2}$$

where u_i, u_j, and u_k are the components of the velocity vector, p and μ are the static pressure and laminar viscosity, respectively, and δ_{ij} is the kronecker delta. Prime indicates fluctuations over mean quantities. The kronecker delta function is defined as follows:

$\delta_{ij} = 1$ if i = j
$\delta_{ij} = 0$ if i ≠ j.

2.3 Turbulence Modeling

Due to the averaging process, additional unknown terms $-\rho u_i' u_j'$, called Reynolds stresses [10], are generated. A brief explanation on the Reynolds stress tensor is useful here. This term represents the transport of momentum due to turbulent fluctuations. Reynolds first noticed that these fluctuation products effectively augmented the viscous stress due to random molecular motion. The presumption that an analogy could be drawn between Reynolds and viscous stresses implied that the former quantity could also be expressed as a linear relationship in terms of the mean rate of strain and an effective coefficient of viscosity. This hypothesis is commonly known in fluid dynamics as the generalized Boussinesq eddy viscosity concept [2]. That is:

$$-\rho u_i' u_j' = \mu_t\left(\frac{\partial u_i}{\partial x_j} + \frac{\partial u_i}{\partial x_i} - \frac{2}{3}\frac{\partial u_k}{\partial x_k}\delta_{ij}\right) - \frac{2}{3}\rho\kappa\,\delta_{ij}. \tag{3}$$

The proportionality parameter, μ_t, is termed the eddy (or turbulent) viscosity. Unlike the molecular viscosity, μ, which is a fluid property, μ_t depends on the turbulence levels of the flow (flow property), and hence is a function of position. In equation (3), κ is the turbulent kinetic energy.

By substituting equation (3) into equation (2), the final form of the time-averaged Navier-Stokes equations is obtained, which is:

$$\rho\frac{\partial}{\partial x_j}(u_i u_j) = -\frac{\partial p}{\partial x_i} + \frac{\partial}{\partial x_j}\left[(\mu+\mu_t)\left(\frac{\partial u_i}{\partial x_j} + \frac{\partial u_j}{\partial x_i} - \frac{2}{3}\frac{\partial u_k}{\partial x_k}\right)\right] - \frac{2}{3}\frac{\partial}{\partial x_i}(\rho\kappa). \tag{4}$$

At this stage, μ_t has to be determined, and this is accomplished by choosing a proper eddy viscosity-based turbulence model.

The model used in this work, proposed by Launder and Spalding [3], employs two partial differential equations (i.e., two-equation model) to estimate velocity scales and lengths of energy-containing eddies. These equations are the κ- and ε- equations, which govern the transport of turbulent kinetic energy and its dissipation rate:

$$\rho\frac{\partial}{\partial x_j}(u_j\kappa)=\rho P-\rho\varepsilon+\frac{\partial}{\partial x_j}\left[\frac{\mu+\mu_t}{\sigma_\kappa}\frac{\partial\kappa}{\partial x_j}\right] \tag{5}$$

$$\rho\frac{\partial}{\partial x_j}(u_j\varepsilon)=C_{\varepsilon_1}\frac{\rho P\varepsilon}{\kappa}-C_{\varepsilon_2}\frac{\rho\varepsilon^2}{\kappa}+\frac{\partial}{\partial x_j}\left[\frac{\mu+\mu_t}{\sigma_\varepsilon}\frac{\partial\varepsilon}{\partial x_j}\right] \tag{6}$$

with the production P defined as:

$$P=v_t\left(\frac{\partial u_i}{\partial x_j}+\frac{\partial u_j}{\partial x_i}-\frac{2}{3}\frac{\partial u_k}{\partial x_k}\delta_{ij}\right)\frac{\partial u_i}{\partial x_j}-\frac{2}{3}\kappa\frac{\partial u_k}{\partial x_k}. \tag{7}$$

The expression for eddy or turbulent viscosity is then computed as:

$$v_t=\frac{C_\mu\kappa^2}{\varepsilon}\quad\text{or}\quad\mu_t=\rho C_\mu\frac{\kappa^2}{\varepsilon}. \tag{8}$$

The five constants present in the model are depicted in **Table 1**, below.

Table 1 Constants in the κ-ε model

Constant	Numerical Value
C_μ	0.09
C_{ε_1}	1.44
C_{ε_2}	1.92
σ_κ	1.0
σ_ε	1.3

Both equations that make up this model are derived from principles of conservation, as are the Navier-Stokes equations. In other words, one can just start from the Navier-Stokes equations and end up with the κ-ε equations. The constants that appear in the derivation process are determined by reference to the results of various laboratory experiments.

In the context of turbulence modeling, it is worthwhile to point out the importance of the distribution of stresses and the turbulence description throughout the flow field. Swirling flows are very difficult to model in terms of stress distribution due to the anisotropy imposed by a strong swirl component of velocity. A dilemma arises on which approach to follow to describe the stress distribution. Isotropic eddy viscosity and the modified Boussinesq hypothesis may not capture the full extent of the heterogeneous behavior of the stress field. On the other hand, higher order closure schemes such as the differential Reynolds stress model [11] greatly increase computational complexity and time requirements. Furthermore, they have not been sufficiently developed and proven for applied studies. The choice of the approach to be followed for describing the turbulent character of the flow generated by the guide vanes is not straightforward. Too many differences exist about the applicability of certain techniques to difficult flow situations such as those exhibiting swirling motion. However, the main intent of this work is not to investigate the fundamental aspects of the flow field, but to be able to predict it sufficiently well for engineering applications. Therefore, the investigation being pursued here accommodates the use of the Boussinesq hypothesis with a suitable turbulence model for the eddy or turbulent viscosity. Among several turbulence models proposed by different authors, it seems that the most acceptable for this case is the two-equation standard κ-ε model presented above.

2.4 Near-Wall Modeling Approach

When simulating turbulent flows, it is particularly challenging to model the effective viscosity in near-wall regions (i.e., regions adjacent to solid boundaries that contain the viscous sub-layer). A major reason is that, in order to resolve the sharply varying flow variables in near-wall regions, a disproportionately large number of grid points would be required in the immediate vicinity of the solid boundary. For most typical flow scenarios, this leads to prohibitively expensive computations. A second difficulty is of a primarily fundamental nature and is directly related to the type of turbulence model used to determine the effects of viscosity on the turbulence field in the viscous sub-layer (the so-called low-Reynolds number effect on turbulence). The standard κ-ε model is of the high-Reynolds number type, and therefore cannot be used in near-wall regions.

In this work, the law-of-the-wall approach according to Van Driest [12] has been employed. The following expression for the velocity profile between the wall and the first grid point away from the wall is assumed:

$$\begin{aligned} u^+&=y^+ && \text{for} \quad y^+<11.5\\ u^+&=\frac{u_\tau}{K}\ln(Ey^+) && \text{for} \quad y^+\geq 11.5 \end{aligned} \tag{9}$$

where the constants K (von Karman) and E have values of 0.4 and 9.0, and y^+ and u^+, normalized distance from the wall and velocity, respectively, are defined as:

$$y^+ = \frac{\rho y u_\tau}{\mu} \tag{10}$$

$$u^+ = \frac{u}{u_\tau}. \tag{11}$$

The friction velocity, u_τ, is defined as:

$$\mu_t = \left(\frac{\tau_w}{\rho} \right)^{\frac{1}{2}} \tag{12}$$

where τ_w is the wall shear stress.

From known y and u at the first grid point, u_τ is iteratively determined from preceding equations (9) through (12).

For the first cell adjacent to the wall, κ and ε equations are not numerically integrated either. Instead, semi-empirical relations for κ and ε at the first grid point are applied to the flow:

$$\kappa = \frac{u_\tau^2}{\sqrt{C_\mu}} \tag{13}$$

$$\varepsilon = C_\mu^{3/4} \frac{\kappa^{3/2}}{Ky} \tag{14}$$

where y is the normal distance of the first grid point from the wall.

In this modeling technique, the standard κ-ε model is solved for almost the entire flow domain, while wall functions are employed in near-wall regions. Thus, the wall functions are essentially an integral model connecting conditions at some distance from the wall with those at the wall.

2.5 Discretization

Finite volume methodology is followed for the discretization of the governing equations in a body-fitted coordinate (BFC) system. Interpolation of cell-face values of variables is accomplished by the first order upwind scheme. The velocity-pressure coupling is taken care of by the SIMPLEC algorithm due to Van Doormal and Raithby [13]. The resulting system of algebraic equations is solved by a numerical method known as whole-field solver. Under-relaxation is applied to all variables of interest to ensure the stability of the SIMPLEC loops. The solution of the governing equations as stated above yields pressure, turbulence, and velocity fields, which in turn are used in the calculations of the second-phase trajectories.

2.6 Initial and Boundary Conditions

At this point, the basic equations governing the flow have been determined. In order to have a well-posed problem, initial guesses as well as values at the boundaries must be provided. Since the solution is steady-state, initial conditions can be arbitrarily chosen. However, in several situations, they are closely linked with ease of convergence. The attribution of nonzero initial guesses, mainly for turbulence quantities, sometimes, improves convergence. On the other hand, proper setting of all boundary conditions is related to the quality of the solution. Considering the flow domain in study, the following boundary conditions were set:

2.6.1. Inlet: Since the flow is well known at the inlet region, a specified mass-flow-type (Dirichlet prescribed) boundary condition is applied. Thus, the axial component of the velocity is required, because the flow exhibits only axial momentum prior to the vanes. Regarding turbulence quantities, the levels and shapes of the profiles of turbulent kinetic energy (κ) and its dissipation rate (ε) at the inlet plane are unique for each flow problem, and these should ideally be obtained from experimental measurements. Unfortunately, these values are seldom available, and a precise set of laws does not exist from which appropriate profiles for κ and ε can be arrived at for all possible flow scenarios. However, some values for both quantities are required and expressions for fully developed pipe flow [14] can be used, namely:

$$\kappa = 0.02 v_{inlet}^2 \tag{15}$$

$$\varepsilon = C_\mu^{3/4} \frac{\kappa^{3/2}}{l_{inlet}} \tag{16}$$

where v_{inlet} is the inlet axial velocity, l_{inlet} is the inlet length scale, generally taken as a fraction of the inlet diameter, and $C\mu$ is 0.09.

2.6.2. Outlet: Fixed-pressure-type boundary condition is applied to the outlet. This boundary condition anchors the system pressure and allows inflow and outflow so as to satisfy continuity. It is important to provide realistic values of velocities and turbulent quantities at the boundary, since this kind of boundary condition can also allow inflow.

2.6.3. Solid walls: Impermeability and no-slip conditions are assumed at the walls. As a result, all velocity components are set to zero. As a reminder, the wall function approach is employed for regions adjacent to the walls (boundary layer). Blades and cones, internal to the flow domain, are given wall boundary conditions too.

2.6.4. Symmetry: The axis of the swirler system receives a symmetry boundary condition. At a symmetry boundary, the velocity component normal to the boundary is set to zero, whereas for all other variables, the gradient normal to the boundary is set to zero (Newmann zero-gradient boundary condition).

2.7 Particulate-Phase Modeling

As swirlers are devices meant to clean particle-laden air streams, the ultimate goal of this investigation is to determine what happens to particles carried into the swirling flow. The simulation of two-phase flows demands a mathematical model that appropriately extends the classical system of equations of single-phase flows. There are two basic approaches to modeling two-phase flows, commonly referred to as Eulerian and Lagrangian.

The Eulerian approach considers each phase as a continuum. The governing equations are written in averaged terms for each phase along with appropriate boundary conditions. The information between phases is then transferred through averaged momentum transfer terms in the governing equations.

In the alternative followed in this work, Lagrangian approach, the underlying concept is what is usually called dispersed or particulate two-phase flow. That is, one of the phases is dispersed throughout the other phase, and the latter acts as a carrier of the former. Two different methodologies can be followed in the Lagrangian approach: coupling or no-coupling between phases.

The Lagrangian approach represents the dispersed-phase by a continuum stream of particles moving through the carrier-phase. The conservation equations for the carrier-phase are described by the standard transport equations, while the motion of the particles is described in a Lagrangian frame of reference. The momentum gain or loss along the particle path accounts for the information transfer between phases.

The underlying assumption in this modeling strategy is that particle-particle interactions are nonexistent. This means that local forces determine the motion of the particles, that is, the particles have enough time to respond to these forces before colliding with other particles.

If there is no-coupling between phases, the basic governing equations are solved for the carrier-phase, and the results originated are used to track particles throughout the flow domain by solving a Newtonian force balance: mass-acceleration of the particle equals the net force on it. The dispersed-phase will generate no source term for the momentum equations of the continuous-phase. In other words, no momentum gain or loss along the particle trajectory is considered, and there is only one-way interaction. This approach is ideal for dilute system, which is the case in this study.

Mathematically speaking, the equation of motion for spherical particles is described as in Crowe et al. [15]:

$$\frac{dV^P}{dt} = \frac{3}{4}\frac{\mathrm{Re}C_D\mu}{\rho_p d_p^2}(U-V^P) - \frac{\nabla p}{\rho_p} + g \qquad (17)$$

where $V^P = u\vec{i} + v\vec{j} + w\vec{k}$ is the velocity vector of particles, Re is the Reynolds number, C_D is the drag coefficient, μ, U, and ∇p are the viscosity, velocity, and pressure gradient of the carrier fluid, and ρ_p and d_p are the particle density and diameter. The gravity vector is represented by g. Equation (17) accounts for the acceleration/deceleration of the particle due to combined effects of drag, local pressure gradients, and body forces.

2.7.1. Drag coefficient correlation: Several correlations for C_D, the drag coefficient, are available in the literature. The correlation followed in this work, by Schuller and Naumann [16], is expressed following:

$$\begin{aligned} C_D &= \frac{24}{\mathrm{Re}} && \text{for} \quad \mathrm{Re} \le 1 \\ C_D &= \frac{24}{\mathrm{Re}}\left[1+0.15\mathrm{Re}^{0.687}\right] && \text{for} \quad 1 < \mathrm{Re} \le 1000 \\ C_D &= 0.44 && \text{for} \quad \mathrm{Re} > 1000. \end{aligned} \qquad (18)$$

Integration of the acceleration term produced by equation (17) yields the particle velocity. Finally, a kinematics equation from which the trajectory is obtained is applied to the velocity term, namely:

$$\frac{dr}{dt} = V^P \qquad (19)$$

where r is the position vector of a particle at a given time.

2.7.2. Turbulent dispersion: In addition to the particle's equation of motion, dispersion of particles due to carrier-phase turbulence is also taken into account in the second-phase model by following a stochastic method by Gosman and Ioannides [17]. The underlying hypothesis behind this modeling methodology is that turbulence is assumed to be isotropic and to possess a Gaussian probability distribution in the fluctuating velocity. An instantaneous carrier-phase velocity, evaluated by adding a fluctuating part to the mean, is used in place of U in the particle motion

calculations (equation (17)). The fluctuating velocity components are calculated as:

$$U' = \left(\frac{2}{3}\kappa\right)^{1/2} erf^{-1}(R) \tag{20}$$

where κ is the local turbulent kinetic energy, erf^{-1} is the inverse error function, and R is a random number between -1 and $+1$.

The ultimate goal of tracking particles throughout the flow domain is to obtain theoretical classification curves to compare with the ones determined experimentally. As mentioned earlier, a Newtonian force balance over a particle fed to the system gives a net force (magnitude and direction) on that particle, which can be easily translated into particle acceleration. This acceleration term can be integrated twice with respect to time to give that particle's displacement in the direction of the net force. These calculations are started by positioning particles of given size at a prescribed location at the swirler's inlet plane. Sizes are varied in increments of 1 μm starting with particles of 1 μm. The computations are carried out for small increments of time and repeated until the particles travel either to the collection chamber or to the outlet plane where the clean air stream exits the device. The entries in the classification curves are then the ratio of particles collected in the chamber to the total injected into the separator for a given particle size. Special attention must be paid to the amount of particles injected at a particular initial location, as there is an area effect. For instance, if the inlet plane is divided into 50 concentric circles, the number (or mass) of particles entering the outer rings is much higher than that entering the inner rings. Particle trajectory calculations were actually performed by injecting particles in each of the 50 radial positions. Then, by summing the mass of particles of a size class arriving at the collection chamber, the fractional collection efficiency of the separator was computed.

2.8 Model Implementation

The procedure followed to solve the fluid dynamics model highlighted in the previous sections was implemented in a CFD software package called CFD – GEOM, ACE, VIEW developed by the Computational Fluid Dynamics Research Corporation (CFDRC) of Huntsville, Alabama. This package consists of three distinct modules: CFD-GEOM for grid generation and boundary condition specification, CFD-ACE for physical model input and strategies for the numerical solution, and CFD-VIEW for visualization of results.

The package was installed in a HP 735/125 workstation with 160 megabytes of RAM. In terms of CPU times, when only the fluid-phase with a simplified flow domain is simulated, typical runs can take anywhere from 12 to 24 hours, depending on the grid size and quality. Computational grids contain about 40,000 to 45,000 cells. Simulations for the whole swirler device, including both phases and particle collection facility, took up to 100 hours of CPU time.

3. Experimental Apparatus and Procedure

Experiments in this work were performed to gather data to validate the model in development. For such, pressure drop and velocity measurements were taken to evaluate the fluid portion of the model. Regarding the particulate-phase model, dust collection experiments were carried out for the determination of classification (recovery versus particle size) curves for the separator device. A representation of the setups used for these validation experiments is shown in **Figures 2** (pressure drop and velocity measurements) and **3** (particle collection).

The apparatus for pressure drop and velocity measurements consists of a blower, flow straightener, 50.8-mm Plexiglas™ tube, and replaceable 50.8-mm diameter swirlers. On the other hand, the apparatus for particle collection experiments is more complex, since facilities for particle collection were needed. The separator itself consists of 50.8-mm diameter Plexiglas™ tube, a 50.8-mm diameter swirler made up of a variable number and shape of stationary guide vanes, slightly smaller diameter tube to form the collection gap, and a 152.4-mm diameter closed collection chamber. The length of the Plexiglas™ tube, which translates into separation distance, the diameter of the slightly smaller diameter tube, which in turn translates into collection gap size, as well as the geometry of the stationary vanes were all varied from experiment to experiment. Accessories such as a blower to feed air into the swirler system, 50.8-mm diameter Plexiglas™ tubes, and flexible hose for connection purposes were all integral part of the particle collection apparatus as well.

3.1 Pressure Drop

Two different swirler designs were used to obtain pressure data for validation of the fluid-phase model. In the first, an 8-straight blade, 50.8-mm diameter swirler fitted with a 25.4-mm diameter, 12.7-mm long parabolic front cone and a 25.4-mm diameter, 50.8-mm long parabolic back cone was attached to the setup shown in **Figure 2**. Average inlet velocities

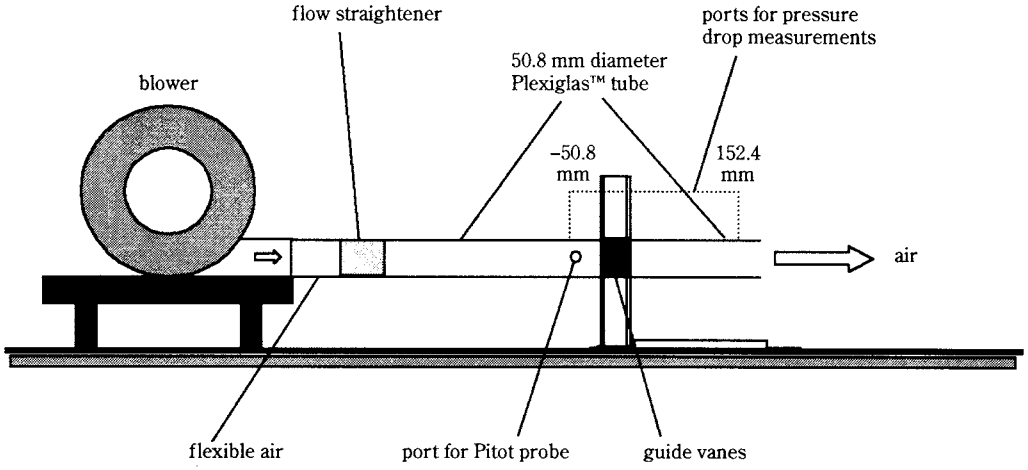

Fig. 2 Setup for pressure drop and velocity measurements

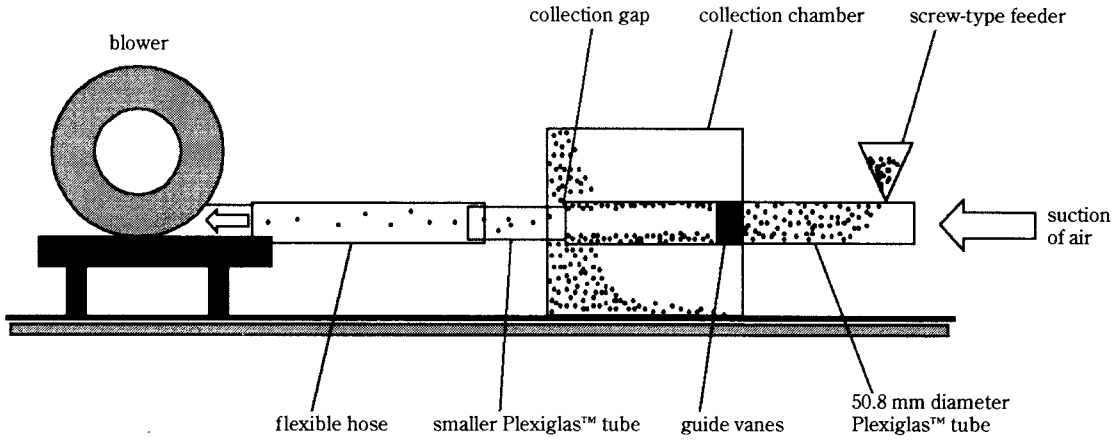

Fig. 3 Setup for particle collection experiments

were varied in the range of 3.5 to approximately 9.0 m/sec. For the second set of measurements, the apparatus received an 8-3-plane-(20°-20°-20°) blade, 50.8-mm diameter swirler fitted with a smaller 12.7-mm diameter, 2.5-mm long front cone (true cone) and a 12.7-mm diameter, 25.4-mm long back cone (cylinder+cone). At this time, average inlet velocities were varied from about 4.0 to 9.0 m/sec. Average inlet velocities were set with a Pitot tube by measuring the centerline velocity of the flow. A careful calibration procedure was carried out to relate centerline to average velocity. Ports for pressure measurements were located 50.8 mm upstream and 152.4 mm downstream of the front of the swirler blades.

As far as blade geometry is concerned, straight blades are the ones in which the entire blade surface is contained in a single plane and the angle formed between the blade plane and the axial direction is constant (kept at 60° throughout this work), whereas 3-plane-(20°-20°-20°) blades are composed of three different planes – the first plane forms an angle of 20° with the axial direction, the second turns 20° with respect to the first, and the third an extra 20° with respect to the second. Thus, the last plane of the blade forms the same 60° with relation to the axis as in the case of straight blades.

3.2 Velocity

Experimental measurements of the axial component of the fluid velocity vector were performed with a single-channel, dual-beam, 100-milliwatt argon ion Laser Doppler Velocimeter (LDV) manufactured by Thermal Systems Incorporated (TSI) of Saint Paul, Minnesota. Laser Doppler Velocimetry is an optical, nonintrusive technique. Many problems encountered by the use of probes and hot-wire anemometry in complex turbulent swirling flow field measurements are overcome by this technique. The only external physical interaction with the flow in LDV is the one due to seeding. Very small seeds of the order of 2 to 5 μm are introduced into the flow to scatter the incoming laser light. The determination of velocity values

does not take into account any interaction of these small seeds with the carrier fluid. In other words, the seed velocities represent the local fluid velocities.

The operation of the LDV is based upon the Doppler frequency of the light scattered by seeding particles travelling with the fluid. The scattered light will have a frequency proportional to the velocity of the particles that scattered it. A series of 1024 observations is made at each position of the measuring volume, which is adjusted with an x-y-z traverse system. The light forward-scattered into the processing components of the LDV for each and every observation is converted into velocity and displayed on a computer monitor as a histogram from which mean values are recorded. Low values of velocities as well as flow reversals can be detected with the aid of a frequency shifter. A careful alignment of the entire optics system will assure a good beam crossing and measuring volume, and is fundamental for the proper operation of the device.

The swirler was mounted on a three-dimensional traverse system with plenty of freedom in all three directions. Thus, the measuring volume could be positioned at any location within the swirler experimental setup with an accuracy of ±0.5 mm.

A 12-straight blade, 50.8-mm diameter swirler fitted with a 25.4-mm diameter, 25.4-mm long front cone and a 25.4-mm diameter, 50.8-mm long back cone was attached to the experimental setup shown in **Figure 2**. Average velocity of 5.70 m/sec was set at the inlet plane. Point measurements were taken at four distinct planes at distances 75, 100, 125, and 150 mm from the swirler front. Radial spacing in each plane was fixed at 2 mm with the first measurement taken 4 mm from the wall. Therefore, 22 observations in each of the four planes resulted from the adopted procedure.

Direct measurements of tangential velocity were not taken. However, the particulate-phase calculations rely heavily on centrifugal acceleration, which is a direct function of the tangential component of the velocity vector.

3.3 Particle Collection

The particles were fed into the system shown in **Figure 3** via a screw-type feeder. A variable-voltage power supply was used to provide power to an electrical motor that drove the screw. The voltage supplied to the electrical motor used to power the feeder determined the flowrate of particles fed into the system. The average airflow velocity supplied by the blower was adjusted in the same fashion as for the pressure and velocity measurements.

In all cases, particle concentration in the feed was always kept below 5 g per m^3 of air. The sample used in the experiments was a classified dust from the Arizona desert prepared by the AC Spark Plug Division of the General Motors Corporation in Flint, Michigan. It is named AC Coarse and has a specific gravity of approximately 2500 kg/m^3. Its particle size distribution, by mass, is presented in **Figure 4**. Exactly 30 g of dust material were used in each test.

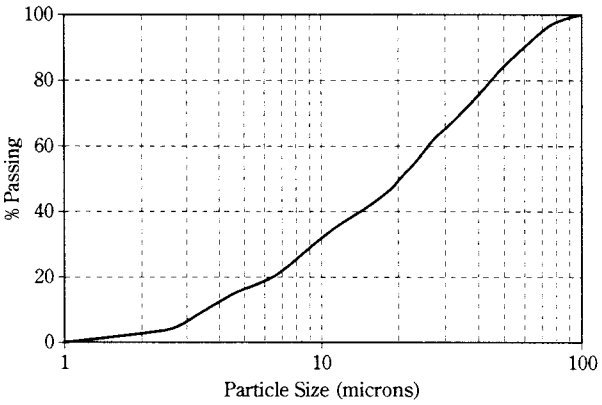

Fig. 4 Particle size distribution of AC Coarse

After each experiment, the portion of the dust settled in the closed collection chamber, referred to as collected sample, was recovered in a straightforward way. The portion of the feed that escaped with the clean air stream, referred to as clean air sample, was recovered either from the inside of the flexible hose downstream of the separator or by a filter placed at the blower outlet. Thus, after weighing the portion of the feeding sample coming from each of the streams, mass recoveries could be easily recorded. In order to relate collection efficiency with particle size (i.e., determination of classification curves), size analyses were performed with a Microtrac™ SRA model 7995-12 by Leeds & Northrup Instruments. The Microtrac™ analyzer utilizes the phenomenon of low-angle, forward-scattering light from a laser beam projected through a stream of particles to measure size. The instrument is composed of three distinct parts: optical system module, which contains all the optics for detection of scattering as well as the laser source; control module, which allows the user to control the analysis; and sample handling module, which allows for the circulation of the suspension through the measuring cell.

A total of six particle collection tests were carried out to determine classification curves to be compared to the ones provided by the particulate-phase model. The size entries in the experimental classification curves were chosen as the midpoint of each size interval measured by the size analyzer equipment.

Table 2 Conditions for particle collection experiments

	TEST 1	TEST 2	TEST 3	TEST 4	TEST 5	TEST 6
Inlet velocity	4.2 m/sec	5.7 m/sec	4.2 m/sec	5.3 m/sec	4.2 m/sec	5.1 m/sec
Blade number and shape	8 (20°-20°-20°)	8 (20°-20°-20°)	6 (30°-20°-10°)	6 (30°-20°-10°)	6 (30°-20°-10°)	6 (30°-20°-10°)
Separation distance	88.9 mm	88.9 mm	57.2 mm	57.2 mm	57.2 mm	57.2 mm
Collection gap	6.4 mm	6.4 mm	6.4 mm	6.4 mm	8.9 mm	8.9 mm

Table 2 presents the conditions in which each test was run. Inlet velocity, blade design (number and shape), separation distance, and collection gap size were all varied in this set of experiments. Swirler diameter was fixed at 50.8 mm and so was blade angle (i.e., angle formed between the blade and the axis of the swirler) at 60°. The same front and back cones were attached to the blades in all six tests (2.5-mm long, 12.7-mm diameter front cone and 25.4-mm long, 12.7-mm diameter back cone). Cones are attached to the front and backsides of the blades for two distinct reasons. The front cone's main function is to direct the incoming flow away from the central region of the swirler tube. The presence of the back cone is much more important. The strong swirling motion produced by the stationary guide vanes causes a zone of flow reversal in the core region just behind the blades. This reversal would bring dust particles back toward the blades, causing unwanted mixing exactly where actual air-solid separation is supposed to occur. A cone is then used in that region to cover this zone of negative axial velocity.

A new blade design was tried in some of the particle experiments (tests 4 through 6). It is called 3-plane-(30°-20°-10°) blade, and the 60° turn is made in gradual steps of 30°, 20°, and 10°. As mentioned before, a collection gap is originated between the two concentric tubes in the outlet of the separator, and the gap size is the width of the annulus ring formed. Separation distance is the distance between the swirler blades and the collection gap, as shown in **Figure 1**.

4. Results and Discussion

Regarding the fluid-phase predictions, plots of experimentally-measured against model-predicted pressure drops are presented in **Figures 5** and **6**. The pressure drop predictions are consistently higher than experimental values for the whole extent of velocities considered for the 8-straight blade case (**Figure 5**). The percentage error in the model prediction with respect to experimental data is around 20% for average inlet velocities ranging from 4 to 8.25 m/sec.

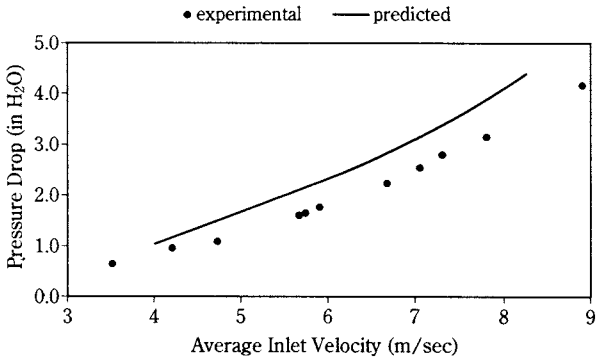

Fig. 5 Comparison between experimental and predicted pressure drops – 8-straight blade, 50.8-mm diameter swirler fitted with a 25.4-mm diameter, 12.7-mm long front cone and a 25.4-mm diameter, 50.8-mm long back cone

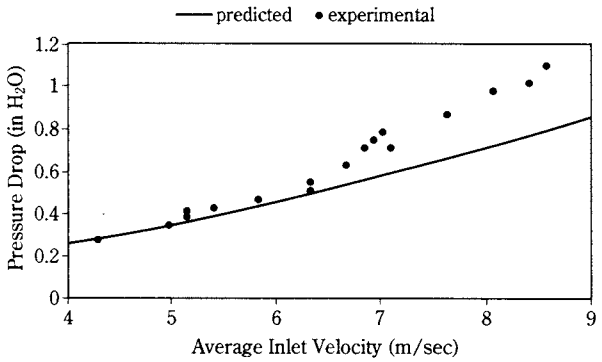

Fig. 6 Comparison between experimental and predicted pressure drops – 8-3-plane-(20°-20°-20°) blade, 50.8-mm diameter swirler fitted with a 12.7-mm diameter, 2.5-mm long front cone and a 12.7-mm diameter, 25.4-mm long back cone

These predictions are acceptable given that both turbulence model and grid size were chosen to minimize the computational burden. In general terms, discrepancies of 20% are acceptable for simulations of highly swirling flows.

Figure 6 illustrates the experimental pressure drops and the corresponding predictions for the 3-plane-(20°-20°-20°) design. For this design, at 6 m/sec, the experimentally measured pressure drop falls almost exactly on the prediction. Furthermore, in the useful range of inlet velocities between 4 and 6 m/sec, model predictions agree closely with experimental observations. At higher velocities, discrepancies get

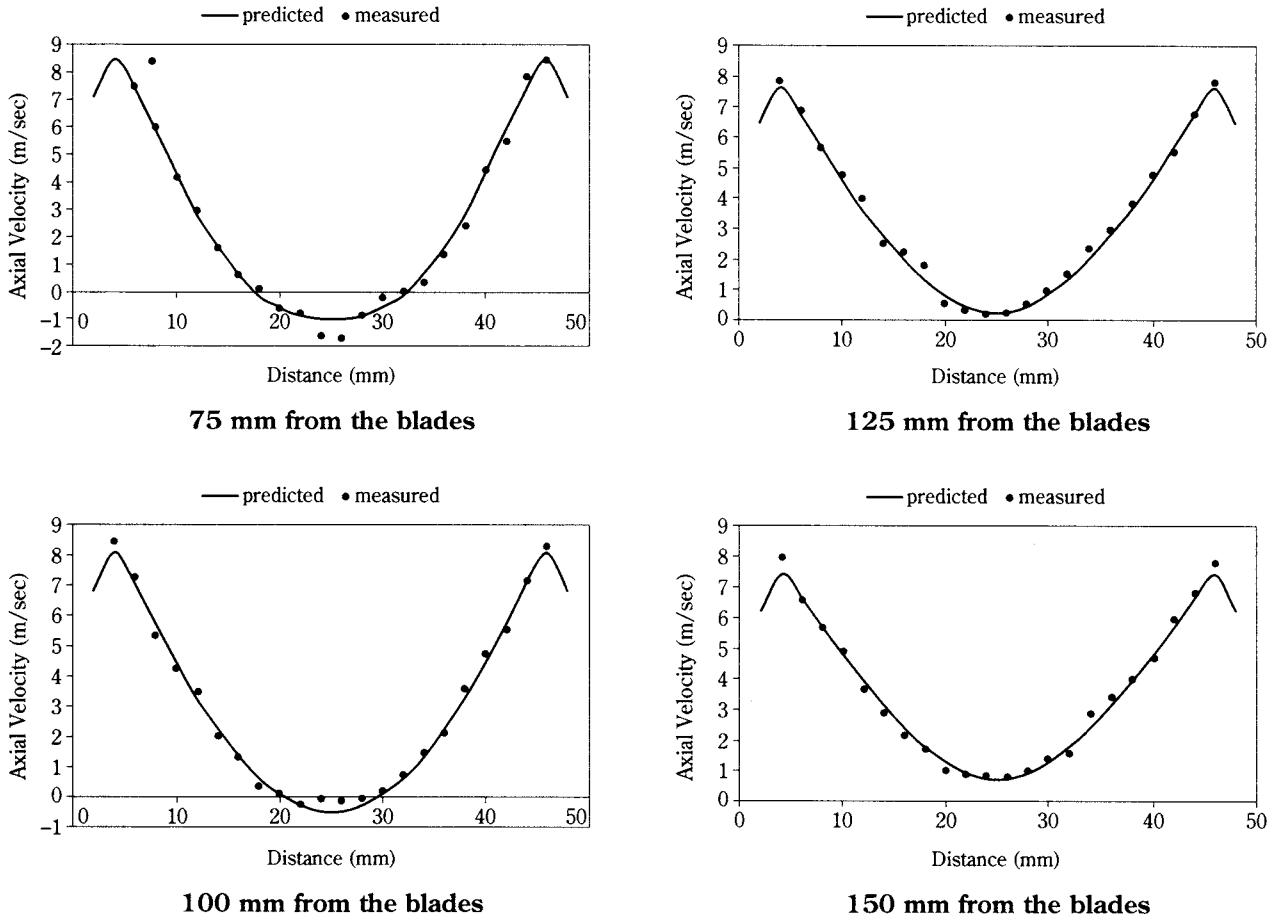

Fig. 7 Measured against predicted axial velocity for a 12-straight blade swirler at 5.70 m/sec inlet velocity

larger. An error of 26% was verified for an inlet velocity of 8 m/sec.

Next, axial velocities measured with an LDV system are compared to those computed by the CFD model in **Figure 7**. Some characteristics of confined swirling flows can be observed in these graphs right away. Due to swirl, there is flow retardation towards the axis of the swirler tube, resulting in parabolic-shaped profiles for axial velocity. Since the angle of the blades with respect to the axial direction is large (60°), the swirling motion is strong enough to cause flow reversal in the core region. When the inflow velocity is set at 5.70 m/sec, negative axial velocities as high as about 1.5 m/sec are observed at a plane 75 mm away from the blades. Another verification is that the decay of the swirling motion makes the flow reversal core disappear at a distance of approximately 100 mm from the blades.

A close analysis of **Figure 7** points to a very successful modeling work. Experimental measurements and model predictions are extremely close to each other. Not only was the shape of the profiles described closely, but also axial velocity magnitudes are very well predicted. Even the flow-reversal zone was pinpointed extremely precisely.

As explained earlier, the CFD model's ability to predict the tangential component of velocity was assessed indirectly through measured versus predicted classification curves. Good prediction of classification characteristics implies good prediction of velocity field, because axial, tangential, and radial components of the velocity vector are needed in the particle's equation of motion. Moreover, one of the very significant forces acting on particles in a swirling motion, the centrifugal force, is a strong function of tangential velocity. As will be shown next, the computed classification curves compare fairly well with experimental data. Also, computed axial velocities and pressure drops agree closely with experimental findings. Hence, we conclude that the tangential velocity too should have been in good agreement with experimental data had this been measured.

Regarding the second-phase present in the system (very fine solid particles in a dilute concentration), the validation work was carried out through the use of mass and size distribution of particles reporting to

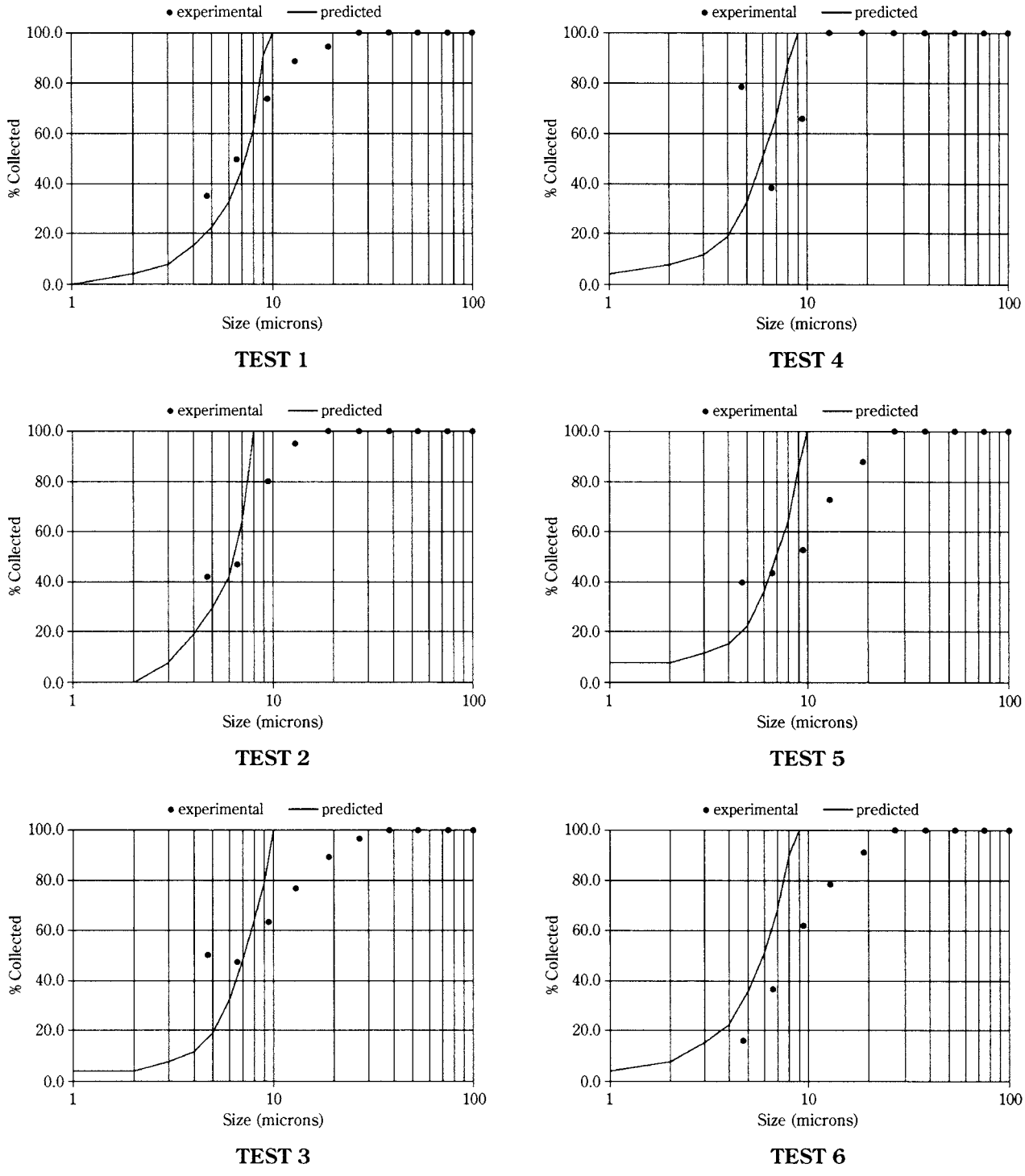

Fig. 8 Measured against predicted particle classification curves

the products of the separator. A series of six particle collection tests were carried out, whose conditions are summarized in **Table 2**. **Figure 8** shows compares experimental and predicted classification curves for these tests.

Definitely, there are some positive aspects about the model predictions. For five out of six tests, experimental and theoretical classification curves agree perfectly well for particle sizes above 27 μm (an exception being test 3). In test 4, for example, the experimentally-determined and predicted particle sizes totally separated from the stream of air, that is, critical size, are very close to each other (9 μm predicted against 13 μm measured). Another strong point of the predictions is that d_{50}, the size at which 50% of the particles report to the collection chamber, was closely deter-

Table 3 Measured and predicted d_{50} values for particle collection tests 1 through 6

Test	Measured d_{50} (μm)	Predicted d_{50} (μm)
1	6	7
2	7	6
3	7	7
4	8	6
5	8	7
6	8	6

Table 4 Measured and predicted overall mass recoveries for particle collection tests 1 through 6

Test	Measured Recovery (%)	Predicted Recovery (%)
1	81.3	82.3
2	81.5	83.9
3	80.3	85.0
4	81.3	83.2
5	80.3	87.5
6	80.7	89.5

mined by the model in all six tests. **Table 3** tabulates measured and predicted d_{50} values.

With regard to overall mass efficiencies, experimental and calculated recoveries are within a reasonable distance of each other for tests 1 through 4. Larger discrepancies are verified in the last two tests, which are overpredicted. Whenever the gap was maintained at 6.4 mm (tests 1 through 4), the response of the model was very good. It deteriorated when the gap was increased to 8.9 mm. **Table 4** presents such measured and predicted mass recoveries.

The differences between model computations and experimental results bring out some key points. As shown earlier, the CFD model offers good predictions for the fluid-phase. This implies that there is high enough centrifugal field to carry even 10-μm particles to the wall of the swirler tube. However, experiments show that only particles 27 μm and above (for five tests) are completely separated from the clean air stream. A number of numerical simulations carried out from different angles failed to reveal any source of error in the numerical modeling. Therefore, the discrepancies can only be due to phenomena that are not modeled, as well as some inherent difficulties in the experiments themselves, as explained below:

- Each experiment was conducted with 30 g of sample. Ideally, one would like to distribute the sample uniformly across the inlet plane, but, in the experiments, the particles were dropped through a hole in the wall of the feeding tube. The model presumes a number of particles of given size is present at all radial locations.
- Sampling of the clean air stream is by no means an easy task. Some particles, particularly at a lower size range, could have freely escaped along with the air.
- Particles in the modeling work are assumed to be perfectly spherical. There could be a shape factor difference between the particle size in the model and the actual particle size used in the experiments.
- The model does not include particle collisions with the wall. There are many reasons to suspect that particles move outward from the center of the swirler tube and strike the wall, reflecting back toward the center. Likewise, collisions against the annular tube are also suspected. This is a very critical suspicion that could not be verified either experimentally or theoretically with the facilities available.
- As all the particles collected by centrifugal force along the swirler tube wall exit through a narrow collection ring, there could be some crowding effect at the gap despite the dilute nature of the flow, which could bring about interparticle collisions. These collisions can scatter particles in all directions, and some could be carried off by the intense inward radial velocity in the vicinity of the gap.
- The turbulent diffusion of particles was modeled following the methodology of Gosman and Ioannides. There is no assurance that this model fully depicts the diffusion that occurs in the experiments.
- The dispersed-phase calculations take advantage of the velocity and pressure fields generated by the solution of the fluid-phase equations. Although fair, the predictions are not perfect by any means. Thus, any discrepancies in fluid predictions will produce discrepancies in the particle calculations.

In summary, the dispersed-phase model predicts experimental classification curves reasonably well. It predicts the d_{50} size closely. Also, the overall mass recovery of particles in the collection chamber is fairly predicted. While the model has all the attributes pointed out above, it underpredicts particle sizes below 27 μm. At a considerable expense in modeling complexity and computations, these discrepancies can be overcome.

5. Conclusions

A comprehensive computational fluid dynamics model for the fluid-phase was developed and validated through pressure drop and velocity measurements. This model was mathematically expressed by the Reynolds-averaged continuity and Navier-Stokes

equations along with the Boussinesq hypothesis to describe the Reynolds stress tensor of the flow field, and the standard κ-ε model was employed to calculate turbulent viscosity. The behavior of the fluid-phase inside the separator was predicted well by the CFD computations.

Cleaning efficiency is the other main factor to look at when studying a separator device. A comprehensive computational fluid dynamics model for the dispersed-phase of the two-phase flow was also developed. Since the concentration of particles in the airflow is very dilute for the case in study, there is no necessity to consider coupling of phases in the calculations. Hence, the particulate-phase does not interfere with the continuum-phase, and both can be solved separately. Velocity and pressure fields from the fluid-phase calculations are used to track particles inside the flow domain via a Newtonian force balance until they leave the system through one of the outlets – either they settle in the collection chamber or they escape with the clean air. A stochastic discrete droplet approach due to Gosman and Ioannides was followed to account for the dispersion of particles due to the turbulence field of the fluid-phase. Validation of the dispersed-phase model was accomplished through comparisons between experimentally-determined and model-predicted classification curves. The model was capable of estimating very well the behavior of particles larger than 27 μm and d_{50} size. Overall mass recoveries were also predicted closely.

The success of the model can be measured by its future use in design studies. The CFD model developed here was successfully used to reduce pressure drops in the original swirler design by about 75%. After careful simulation studies, the replacement of straight blades by three-plane blades with each plane turning the flow by 20° brought about a significant reduction in pressure drop. In order to prove the point that the model was generating reliable results, an 8-blade swirler of this design was built, and it exhibited pressure drops very close to numerical predictions.

6. Notation

C_D	drag coefficient in the particle equation of motion
C_{ε_1}	coefficient of production of ε in the ε-equation
C_{ε_2}	coefficient of destruction of ε in the ε-equation
C_μ	coefficient in the eddy viscosity relation in the κ-ε model
d_{50}	50% passing size (median size)
d_p	particle diameter
E	constant in the near-wall velocity profile law to account for wall roughness
g	acceleration due to gravity
i, j, k	unit vectors of Cartesian x-, y-, and z- coordinate directions
K	von Karman's constant in the near-wall velocity profile law
l_{inlet}	length scale associated with inlet
P	production term in the turbulence model equations
p	static pressure
R	random number between −1 and +1, overall mass recovery
Re	particle slip Reynolds number
r	position vector
t	time increment for particle trajectory calculations
U	fluid velocity in particle trajectory calculations
U′	fluctuating component of fluid velocity in particle trajectory calculations
u, v, w	x-, y-, and z- components of velocity vector
$u_{i,j,k}$	velocity components
u^+	normalized velocity in wall units
u_τ	friction velcoity
$u_i'u_j'$	Reynolds stresses
V^p	particle velocity vector
v_{inlet}	inlet fluid velocity
$x_{i,j,k}$	directions in the Cartesian coordinate system
y	normal distance of the first grid point to the wall
y^+	normalized distance from the wall in wall units
δ_{ij}	kronecker delta
ε	dissipation rate of turbulent kinetic energy
κ	turbulent kinetic energy
μ	dynamic laminar or molecular viscosity
μ_t	turbulent or eddy viscosity
ν_t	kinematic turbulent or eddy viscosity
ρ	fluid density
ρ_p	particle density
σ_ε	Prandtl number for dissipation rate of turbulent kinetic energy
σ_κ	Prandtl number for turbulent kinetic energy
τ_w	wall shear stress

7. Acknowledgments

One of the authors, Luis A. C. Klujszo, would like to thank the ***"Conselho Nacional de Desenvolvimento Científico e Tecnológico – CNPq – Brazil"*** for partially sponsoring this investigation.

8. References

1) Perry, R. H. and Green, D. W.: "Chemical Engineers' Handbook," Ed. McGraw-Hill, New York, USA (1997).
2) Boussinesq, J.: Mem. Pre. Par. Div. Sav., 23 (1877).
3) Launder, B. E. and Spalding, D. B.: Comp. Met. App. Mech. and Eng., 3. 269 (1974).
4) Daniels, T. C.: Engineer, 203. 356 (1957).
5) Akiyama, T., Marul, T., and Kono, M.: Ind. Eng. Chem. Proc. Des. Dev., 25. 914 (1986).
6) Akiyama, T. and Marui, T.: Powder Technology, 58. 181 (1989).
7) Ramachandran, G., Raynor, P. C., and Leith, D.: Filtration and Separation, 631 (1994).
8) Klujszo, L. A. C.: Ph.D. Dissertation, University of Utah, UT, USA (1998).
9) Klujszo, L. A. C., Rafaelof, M., and Rajamani, R. K.: Powder Technology, *in press* (1999).
10) Reynolds, O.: Phil. Trans. R. Soc., A186, 123 (1895).
11) Launder, B. E., Reece, G. J., and Rodi, W.: J. Fluid Mech., 68. 537 (1975).
12) Van Driest, E. R.: Journal of the Aeronautical Sciences, 23. 1007 (1956).
13) Van Doormal, J. P. and Raithby, G. D.: Numerical Heat Transfer, 7. 147 (1984).
14) CFDRC: ACE user's guide manual (1996).
15) Crowe, C. T., Sharma, M. P., and Stock, D. E.: ASME J. of Fluids Eng., 325 (1977).
16) Heiskanen, K.: "Particle Classification," Ed. Chapman & Hall, New York, USA (1993).
17) Gosman, A. D. and Ioannides, E.: Journal of Energy, 7. 482 (1983).

Author's short biography

Luis Augusto Colembergue Klujszo

Dr. Luis Klujszo is currently a post-doctoral fellow in the Department of Metallurgical Engineering of the University of Utah conducting research on nanoparticle production. He received his B.S. in mining engineering (1990) and M.S. in metallurgical engineering (1993) from the Federal University of Rio Grande do Sul (UFRGS), Brazil, and his Ph.D. in metallurgical engineering (1998) from the University of Utah, USA. His research interests include mineral processing, application of computational fluid dynamics to separation processes, and production of particles in the submicron size range.

Polycarpe K. Songfack

Dr. Poly Songfack is currently a post-doctoral fellow at the University of Utah, Department of Metallurgical Engineering. His research interests include computational fluid dynamics, discrete element method, mineral processing, and SAG mill optimization with the Millsoft® simulation software. He received his B.S. in chemical engineering from the UCL, Belgium, in 1989 and his Ph.D. in metallurgical engineering from the University of Utah in 1996. He is a recipient of several awards and distinctions.

Menachem Rafaelof

Menachem Rafaelof received a M.S. degree in mechanical engineering from the University of Utah in 1987. He served as a design engineer and later as an adjunct instructor at the University of Utah's Department of Mechanical Engineering between 1987 and 1998. He is currently the vice president of MJR Scientific Corporation in Salt Lake City, Utah. His interests are micro electro systems (MEMS), drug delivery devices, robotics, and active structures.

Raj K. Rajamani

Dr. Raj K. Rajamani earned B.S. and M.S. degrees in chemical engineering at Annamalai University, India and Indian Institute of Technology, Kanpur, India, respectively. Then, he studied metallurgical engineering for his Ph.D. at the University of Utah. Currently, he is a professor of metallurgical engineering at the University of Utah. His research interests include ultrafine particle production by comminution, simulation of charge motion in tumbling mills, and eddy current separation.

Evaluation of Thermally-Assisted Fracture of Particles Using Microscale Fracture Measurements†

L.M. Tavares
*Dept. of Metallurgical and Materials Engineering, Universidade Federal do Rio de Janeiro**
R.P. King
*Comminution Center, University of Utah***

Abstract

Thermal pretreatment can significantly improve industrial comminution operations by reducing energy requirements. The effect of pretreatment using conventional and dielectric heating followed by quenching on the microstructure and on the fracture characteristics of selected single-phase and multiphase materials has been investigated using single-particle fracture experiments, crack density measurements and indentation fracture. It was shown that measurements of the crack density from polished sections correlated very well to a parameter related to material integrity, called damage, which makes the latter a very good tool to assess pretreatment. It has been observed that very significant reductions in both fracture energy and material integrity were achieved by heating followed by water quenching.

1. Introduction

Thermal pretreatment was identified early as a potential method to improve comminution and liberation characteristics of ores by weakening the rock and inducing grain-boundary fracture. It takes advantage of the differences in thermal expansion and contraction in single anisotropic grains or in adjacent grains as well as on rapid contraction produced by quenching, resulting in the development of localized stresses and damage.

Thermally assisted comminution has attracted the attention of several researchers since the 1920's, and many studies have been published on a variety of geological materials including quartz, tin ore and iron ores. Comprehensive reviews of the literature can be found elsewhere (Geller and Tervo, 1975; Fitzgibbon and Veasey, 1990). Most recently, interest in thermal treatment has been renewed due to the capabilities of microwave energy in promoting rapid and selective heating of different mineral phases. Improvements in the grindability of iron ores, including taconite, have been reported and the results are encouraging (Walkiewicz et al., 1995).

Although several aspects of the effect of thermal pretreatment on comminution were demonstrated, the techniques used did not provide any direct information on its effect on the ore microstructure. Further, one common method of quantitatively assessing the effect of thermal pretreatment – the Bond Work index method – has several shortcomings (Austin et al., 1984), particularly regarding the assumption that the shape of the size distribution during grinding does not change such that only the 80% passing size is considered. This is a particularly severe assumption as changes in fragmentation pattern have been often observed in thermally treated products (Brown et al., 1958).

An alternative to standard crushing and grinding experiments is single-particle fracture. Single-particle fracture experiments are conducted under controlled, reproducible experimental conditions and provide fundamental information that characterizes particle fracture. A device, called Ultrafast Load Cell (UFLC), developed at the Utah Comminution Center, allows fast and accurate measurement of fracture characteristics of brittle material subjected to impact fracture (King and Bourgeois, 1993a; Tavares and King, 1998). In particular, it provides a method for the measurement of the minimum energy to fracture (also called the particle fracture energy), the damage parameter

* Cx. Postal 68505, Rio de Janeiro, RJ, 21945-970, Brazil.
**135 South 1460 East Room 306, Salt Lake City, UT 84112, USA
† Received July 20, 1999

and the single-particle breakage function. Data measured using the UFLC provides a basis for the calculation of the rate of breakage and the breakage function (King and Bourgeois, 1993b), which are used in the modeling and simulation of large-scale comminution machines.

In a recent work it was demonstrated that particle fracture energy measurements with the UFLC were consistent with Bond Work index measurements for a thermally treated quartzite (Pocock et al., 1998). Reductions in particle fracture energy were, however, significantly greater than reductions in Bond Work index. This shows that smaller but significant effects of pretreatment, that would not be detected using standard grindability experiments, can be accurately measured given the high resolution of the UFLC.

In the present work the effect of several variables involved in thermal pretreatment are studied and their effect on the breakage characteristics of materials is investigated through fracture experiments using the UFLC. The relevance of the damage parameter to assess internal material integrity is demonstrated and the effect of thermal pretreatment on the fragmentation pattern is investigated.

2. Experimental

2.1 Materials

Samples used in the experiments consisted of borossilicate glass spheres, quartz (Karlsruhe, Germany), fluor-apatite (Cantley, Québec), specular hematite (Québec), iron ore (Newfoundland), titanium ore (Norway) and copper ore (Utah). Examination of polished sections in an optical microscope indicated that the single-phase materials consisted mostly of single-grained, high-purity particles. The quartz sample was from a riverbed deposit and contained particles exhibiting nearly spherical shapes. Fluor-apatite particles presented a very high concentration of pre-existing micro-cracks in the original material. The iron ore sample consisted mostly of polycrystals of hematite, magnetite and quartz. More details can be found elsewhere (Tavares, 1997). Samples were screened in narrow size intervals using round-mesh precision sieves for thermal treatment and fracture testing.

2.2 Thermal treatment experiments

Conventional heating experiments were undertaken using a batch electric furnace (Thermoline 10500) where samples of about 10 grams were heated at variable temperatures in porcelain crucibles. Low heating rates (about 20°C/min) were used in the tests, ensuring uniform temperature throughout the sample. These heating rates were achieved by manually changing the furnace temperature setting by discrete increments. Samples were immediately withdrawn from the furnace upon reaching the set temperature (within ±5°C).

Dielectric heating tests were only used for samples containing high-loss minerals. Experiments were carried out in an LBM 1.2A batch laboratory microwave oven (by Cober Electronics, Inc.), which operates at 2.45 GHz and allows continuous control of power from 0 to 1.2 kW. The sample volume and position of the mode-stirring fan were carefully selected prior to each pretreatment experiment in order to achieve maximum heating rates. In the present study, microwave heating experiments were conducted at 1200 W for 30 seconds.

Sample temperatures during both microwave and conventional heating experiments were monitored using a type K thermocouple with an ungrounded tip sheathed in stainless steel. Samples were quenched immediately upon withdrawal from the furnace in still air or by immersion in water (or salt solution) at room temperature (15-25°C).

More details on the equipment and procedure used in the thermal treatment experiments can be found elsewhere (Tavares, 1997).

2.3 Microfracture experiments

Apparent crack density measurements were undertaken using an optical image analysis system. It consisted of an optical microscope, a CCD camera and a microcomputer. The digital images were analyzed using VIDAS, a PC image analysis software by Kontron Systems, Inc. The procedure used to measure the apparent crack density consisted of background correction, delineation, segmentation, skeletization, filtering, feature identification and crack length measurement. Apparent crack densities were then given from the ratio between the total crack length measured and the scanned area.

Indentation fracture experiments were carried out using a Leco M-400 micro-hardness tester. A sharp Vickers indenter, with loads ranging from 50 to 500 g, was used in the experiments. Both the indent dimensions and the lateral extent of cracks associated with the indents were measured using the calibrated eyepiece mounted on the hardness tester within about one minute of the indentation. Indentation tests were used to calculate the Vickers hardness and the surface fracture energy, given by

$$H_v = 1.854\frac{F}{\bar{d}^2} \quad (1)$$

and

$$r_f = \frac{K_c^2 Y}{2(1-\mu^2)}, \text{ with } K_c = \chi\frac{F}{\bar{c}^{3/2}} \quad (2)$$

where F is the indentation force, $\bar{d}$ is the average diagonal of the plastic indentation, Y is the modulus of elasticity of the material, μ is the Poisson's ratio, and $\bar{c}$ is the average distance, measured along the diagonal of the indent, from the center of the indent to the extremity of the crack. χ is a term that incorporates factors involving the indenter geometry, friction and free-surface effects (Lawn, 1993; Middlemiss and King, 1994).

Sample preparation for both crack density measurements and indentation fracture tests consisted of mounting several grams of the material in epoxy and polishing using abrasive materials down to 0.3 μm alumina.

Impact-fracture experiments were undertaken using the Ultrafast Load Cell (UFLC). The UFLC is a hybrid between the drop weight apparatus and the split Hopkinson pressure bar (King and Bourgeois, 1993; Tavares and King, 1998). Tests are conducted using individual particles and are used to estimate quantities such as the mass-specific fracture energy and the particle stiffness (Tavares and King, 1998). The size distribution of the progeny was determined using round-mesh precision sieves.

3. Effect of thermal shock pretreatment on particle microstructure

In order to gain insights into the role of thermal pretreatment on the fracture of particulate materials, selected single-phase materials were subject to thermal-shock pretreatment, and their microfracture as well as their single-particle fracture characteristics were examined. Samples of riverbed quartz (4.0-4.75 mm), hematite (2.0-2.8 mm) and glass (3 mm) – an ideal model material – were subject to conventional heating at different preheat temperatures followed by water quenching at room temperature.

Examination of polished sections of quartz under the optical microscope (**Fig. 1**) shows that pretreatment is able to induce cracks that can be identified and also that the severity of the thermal pretreatment determines the intensity of the cracking. In order to assess quantitatively these effects, the image analysis system was used to estimate the apparent crack density in the polished section. Results given in **Figure 2** show that the density of cracks is, indeed, function of

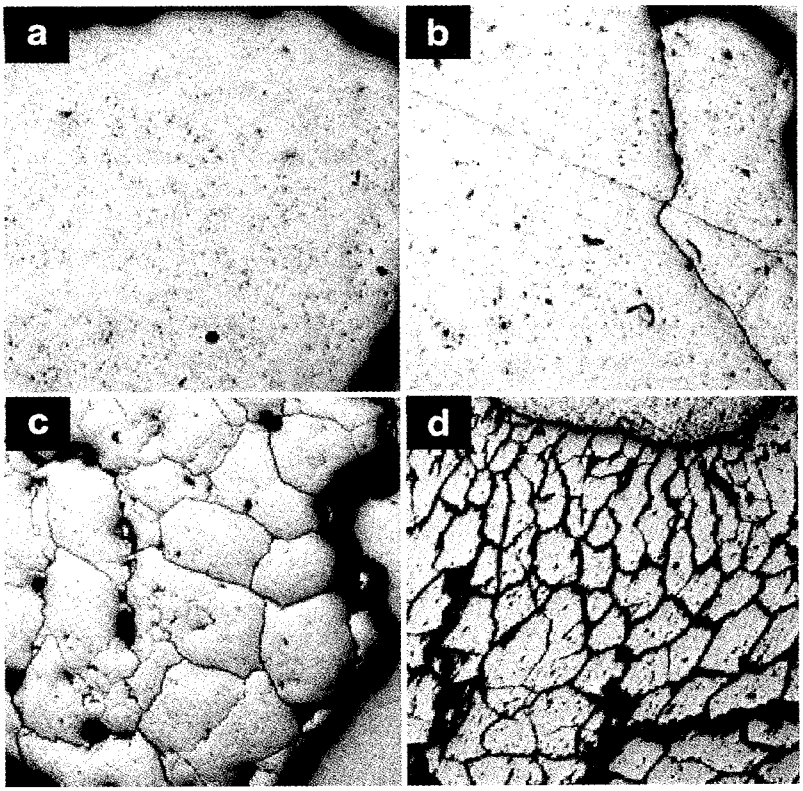

Fig. 1 Micrographs of untreated (a) and heated and water quenched quartz particles: (b) heated to 200°C, (c) heated to 600°C, and (d) heated to 1000°C. Horizontal distance in each micrograph is 1.2 mm.

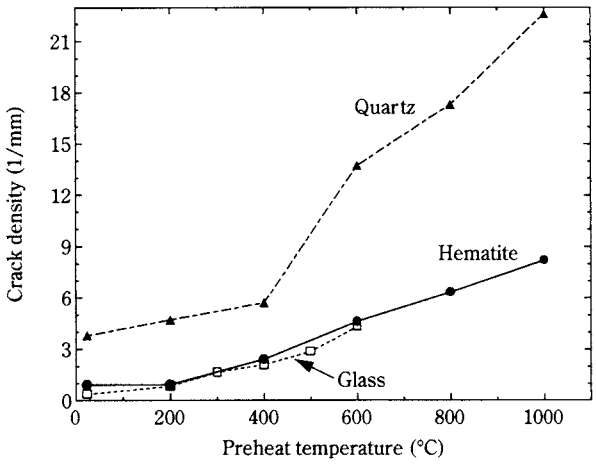

Fig. 2 Effect of heat treatment at different temperatures and water quenching on the apparent crack density of selected materials.

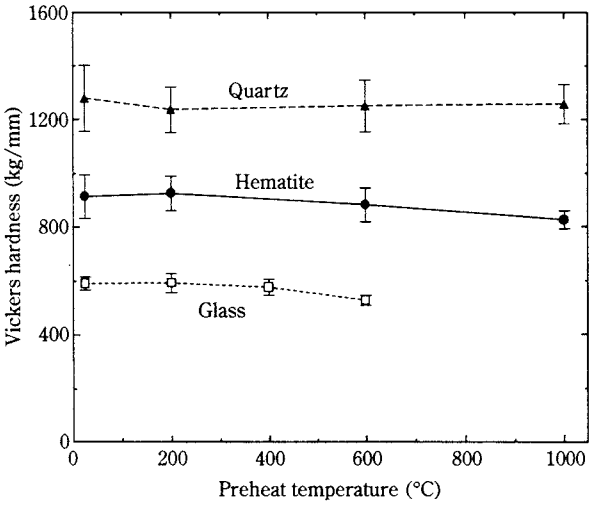

Fig. 3 Effect of heat treatment at different temperatures and water quenching on Vickers hardness of selected materials.

the severity of the pretreatment used. The greater the severity of the shock, the higher the density of crack induced. At the magnification used, however, it appears that regions between the cracks appear intact. This is particularly relevant when thermal pretreatment is used prior to size reduction, because it would mean that as grinding progresses and fragments become smaller than the regions fully surrounded by cracks, they would essentially behave as intact particles and would, therefore, require as much grinding energy for additional size reduction. It is possible, however, that thin – and closed – cracks were present but could not be detected with the optical system and that heat treatment released residual stresses in the material.

Indentation is a very good probe of the material microstructure and is here used to characterize the integrity of regions of the material that were apparently undamaged by pretreatment. Using small indents (with diagonals of 16 μm for quartz, 43 μm for hematite and 55 μm for glass) surface-fracture energies and Vickers hardness were determined. Results summarized in **Figure 3** show that the Vickers hardness was little or not affected by thermal pretreatment. Similar results were observed for the surface-fracture energy and are given elsewhere (Tavares, 1997). Therefore, in the scale of the indents, the microstructure did not appear to be significantly affected by pretreatment and that it was largely limited to inducing a macroscopic array of cracks in the particles, as is shown in **Figure 1** for quartz. This may suggest that thermal shock essentially only extends preexisting cracks in the material and does not apparently nucleate new ones. Nevertheless, small reductions in the hardness and surface fracture energy of glass and hematite, as well as the smaller fraction of ideal indents in some heat-treated samples (1/5 for glass heated to 600°C and quenched versus about 4/5 for untreated glass, for example) suggest that some relief of residual stresses may have occurred, and/or that closed cracks may still be present in the material.

Measurement of crack density, therefore, gives a good indication on how the material is affected by thermal-shock pretreatment. However, these measurements have several limitations: they are critically dependent on the sensitivity of the optical method of detecting cracks, on surface preparation, illumination and magnification. Further, they represent an invasive measurement and are not a convenient tool to systematically assess pretreatment.

Cracked solids are more compliant (have lower stiffness) than intact solids. This is illustrated in **Figure 4**, which shows impact-breakage results for quartz before and after thermal pretreatment. By measuring the stiffness of a material before and after pretreatment, the fractional reduction of the cross-sectional area that has been stress-relieved by cracks and that is unable to withstand load can be estimated by (Tavares and King, 1998; Kachanov, 1958)

$$D = 1 - \frac{k_d}{k_u} \tag{3}$$

where k_u and k_d are the stiffness of the particles before and after pretreatment.

For the data in **Figure 4** and Equation 3, we can calculate the damage induced in the particle as 0.62, which shows that thermal pretreatment destroyed the integrity of 62% of any cross section of the particle. This is consistent with the intense cracking observed in the micrographs from **Figure 1**.

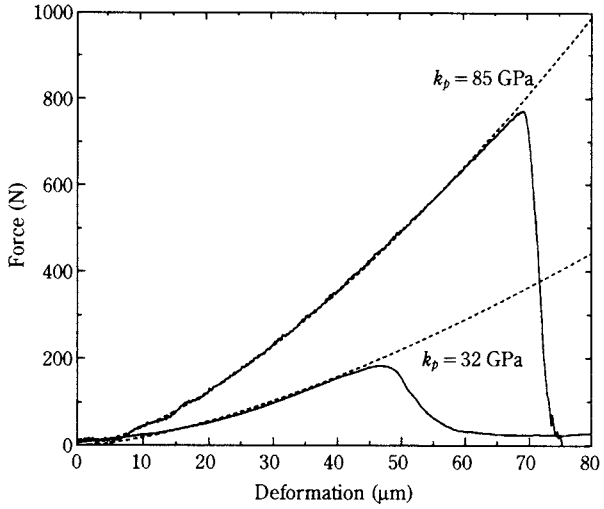

Fig. 4 Force-deformation profiles for untreated and heated to 1000°C and water quenched quartz particles (4.0-4.75 mm).

Data from **Figure 4** represent only two experiments and the estimated damage value is only valid for illustration purposes. In practice, considerable scatter exists in the fracture characteristics of single particles, requiring the testing of samples of at least 50 particles (Tavares and King, 1998). Damage values were then calculated from average particle stiffness for several materials and are compared to the measured crack densities in **Figure 5**. Although a unique (material-independent) relationship does not apparently exist, a good correspondence between the measured damage values and the apparent crack density is evident. The significance of this correspondence is that the extent of the microcracking induced by any given pretreatment method could be assessed simply from testing untreated and pretreated samples in the UFLC. This is significant not only when the enormous effort involved in measuring crack densities from polished sections is considered, but also considering the non-absolute character of those measurements, given their invasive nature.

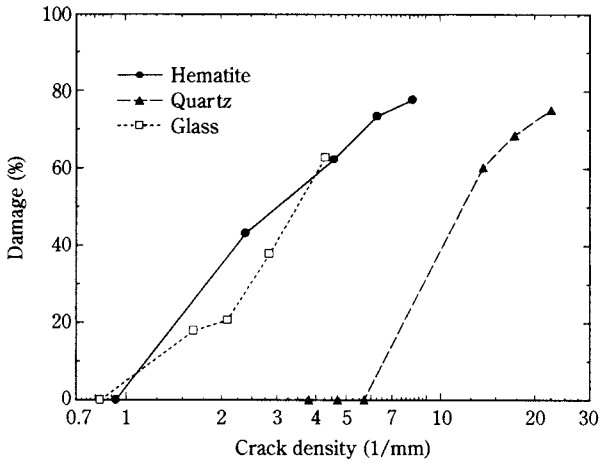

Fig. 5 Relationship between apparent crack densities and damage parameters of selected materials.

4. Effect of thermal treatment on fracture characteristics

With the use of the damage parameter (Equation 3) and the particle fracture energy, the effect of relevant thermal pretreatment variables such as temperature, quenching medium and particle size on the weakening could be studied in detail.

4.1 Effect of heating temperature

Heating temperature is recognized as the most important variable affecting thermal-shock weakening. It not only controls the magnitude of the thermal stresses induced during rapid cooling but also determines the energy expenditure in heating, which ultimately establishes the feasibility of thermally assisted comminution.

Fracture characteristics of selected single- and multiphase materials heated to a range of temperatures and quenched in water have been measured, and results are summarized in **Figures 6** and **7**. Residual fracture energy is here defined as the ratio between the mean particle fracture energy of the pretreated particles and mean particle fracture of the untreated particles. **Figure 6** shows that heat treatment produces significant reductions in particle fracture energy even at moderate preheat temperatures, result of the superficial cracks induced that offer sites for crack propagation leading to fracture, particularly in the more brittle solids. In some instances, however, little

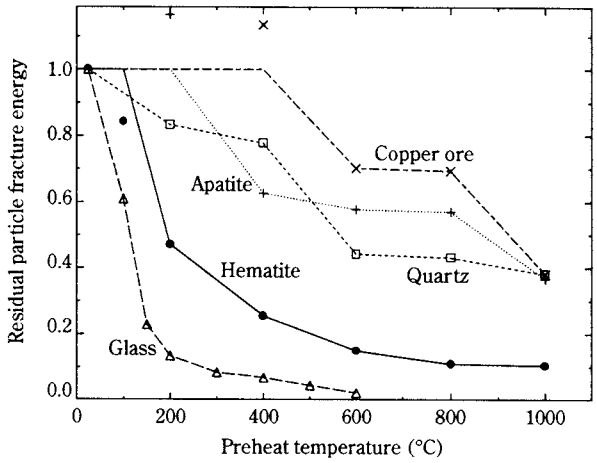

Fig. 6 Effect of heat treatment at different temperatures and water quenching on the residual fracture energy of different materials. Lines in the figure take into account whether the particle fracture energy distributions after pretreatment are statistically different from that before pretreatment (Milin and King, 1994).

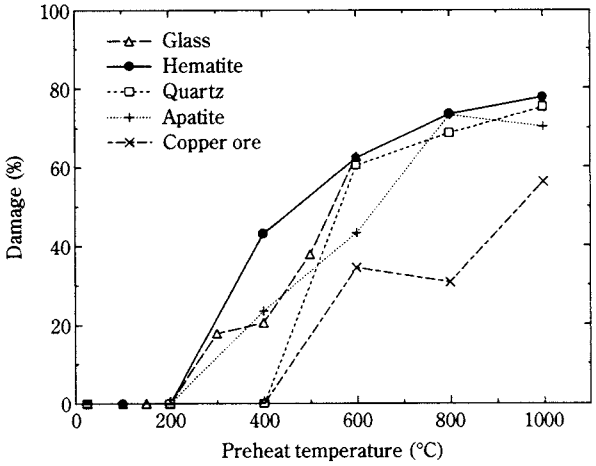

Fig. 7 Effect of heat treatment at different temperatures and water quenching on the damage parameter of different materials

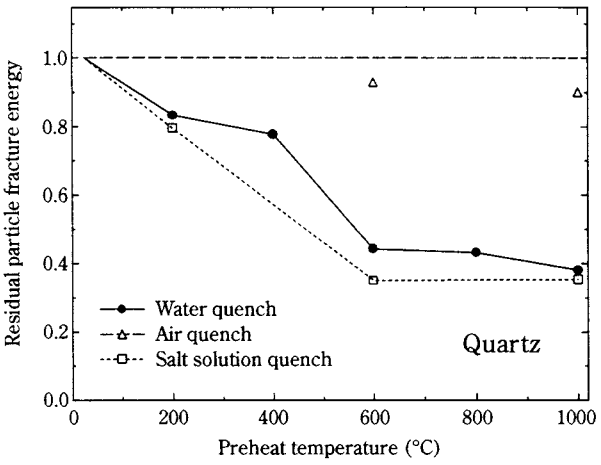

Fig. 8 Effect of quenching medium on the fracture characteristics of 4.0-4.75 mm quartz.

additional reduction in fracture energy is achieved by increasing the heating temperatures above a certain level, in spite of the greater proportion of crack-initiating sites present, as evident from the higher damage values. A possible explanation is that, in highly cracked solids, fracture is not controlled by crack initiation. A crack that initiates in the particle may arrest in the microstructure and not contribute to failure. Fracture of these materials will only occur when a significant number of pre-existing cracks are activated, thus allowing the propagation of a crack through the entire particle.

Lowering the particle fracture energy as a result of pretreatment only ensures higher breakage rate of the parent in a comminution machine and does not necessarily lead to a reduction in overall comminution energy. Substantial volume cracking, on the other hand, ensures lower energy expenditures not only in breakage of the parent particle but also in the breakage of several generations of progeny fragments. Therefore, substantial energy savings do require a substantial increase in the proportion of damage in addition to the reduction in fracture energy. **Figure 7** shows that significant damage occurs only after pretreatment at higher temperatures. The significance of this result is that, in order to achieve substantial gains in comminution greater expenditures in heating must be made. Incidentally, this has been the major limitation for the industrial application of thermally assisted comminution.

4.2 Effect of quenching medium

A promising approach to reducing energy expenditure in thermal pretreatment is the use of more severe quenching media that could allow greater weakening at lower temperatures. Several quenching media exist that allow greater heat transfer and faster cooling than water (Luty, 1993). Brines (salt solutions at high concentrations) have up to 75% higher heat-transfer coefficients and therefore allow significantly higher cooling rates than pure water (Luty, 1993). This is because the duration of the less efficient stage in quenching with liquids that boil – called vapor blanket – is reduced and almost eliminated. The effect of quenching in a 10% sodium chloride solution (in weight) on the fracture energies of quartz and copper ore particles is compared to water quenching, and results are summarized in **Figure 8**. No significant difference was found between water and salt-solution quenching, so that the application of the corrosive sodium chloride-containing solution as quenching media is not justified. Similarly, no statistically significant increase in the amount of damage was observed with salt quenching compared to water quenching.

In spite of its lower heat-transfer coefficient in comparison to water, air-cooling has the advantage of more effectively allowing partial recovery of the input energy when, for example, vertical shaft furnaces are used. The energy recovered could then be recycled and reduce energy input in thermally assisted comminution. Comparisons between air and water quenching are given in **Figure 9**. Comparable fracture energy reductions are obtained for copper ore with air and water quenching. The mismatch between the various crystals in the polycrystalline copper ore particles appear to be responsible for the weakening even without a severe thermal shock. Nevertheless, greater reductions in fracture energy are still achieved with water quenching. On the other hand, no statistically significant weakening was observed after heating and

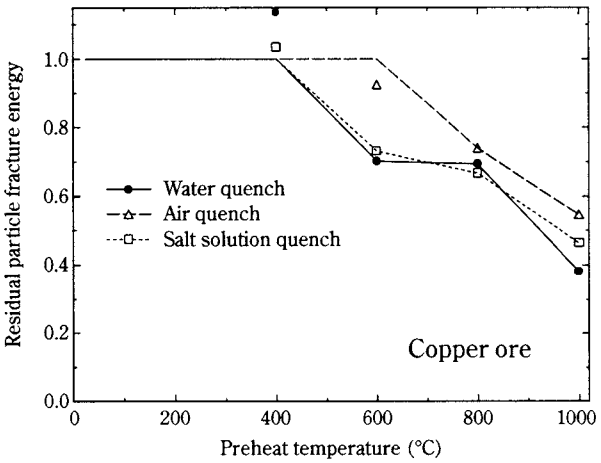

Fig. 9 Effect of quenching medium on the fracture characteristics of 4.0-5.0 mm copper ore.

cooling the monolithic quartz particles in still air. This is true even after heated above its α-β transformation temperature, generally considered as the reason for the greater susceptibility of quartz to thermally assisted comminution (Kanellopoupos and Ball, 1975; Hariharam and Venkatachalam, 1977). In the absence of chemical degradation, single-phase materials consisting of single crystals would essentially expand and contract elastically during heating and cooling, respectively, and therefore would not sustain permanent damage.

4.3 Effect of particle size

The effect of particle size has been studied by subjecting narrow size fractions of riverbed quartz to heating and water quenching and testing in the UFLC. **Figures 10** and **11** show that the magnitude of the weakening is relatively little affected by particle size in the interval studied (0.25 to 5 mm). The amount of damage induced by thermal pretreatment, on the other hand, generally decreases for smaller particle sizes.

4.4 Effect of heating method

Microwave heating offers an alternative to conventional heating as it allows fast and selective heating of the high-loss phase in the ore. The rapid expansion of the absorbing phase produces stresses that can lead to internal cracking and ultimately lower energy consumption in size reduction.

Both dielectric and conventional heating experiments were undertaken with selected ores containing high-loss minerals, and results are summarized in **Table 1**. The ores were heated to about 600°C and were subsequently either cooled in air or quenched in water. Moderate heating rates were achieved, with the iron ore sample being heated for 30 s to 612°C, taconite to 588°C, and titanium ore to 566°C during the microwave heating experiments. Significant reductions in particle fracture energy and increases in damage were obtained for the thermal-shock samples,

Table 1 Variation of particle fracture energy and damage resulting from different heating methods. Samples were heated to 600°C

Material and size	Heating method	Quenching Medium	Reduction in fracture energy (%)	Damage (%)
Iron ore 4.5-5.35 mm	Conventional	Air	25	29
	Microwave	Air	36	0
	Conventional	Water	24	47
Titanium ore 4.0-4.75 mm	Conventional	Air	29	0
	Microwave	Air	28	51
	Conventional	Water	50	52
Taconite 5.0-5.95 mm	Conventional	Air	28	0
	Microwave	Air	29	0
	Conventional	Water	56	51

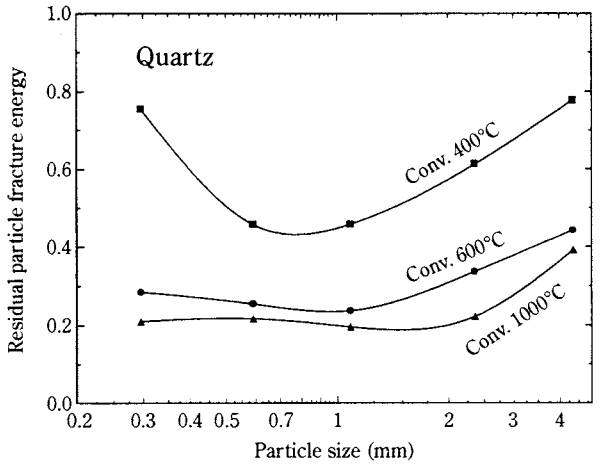

Fig. 10 Effect of particle size and heat treatment and water quenching, on the residual fracture energy of quartz.

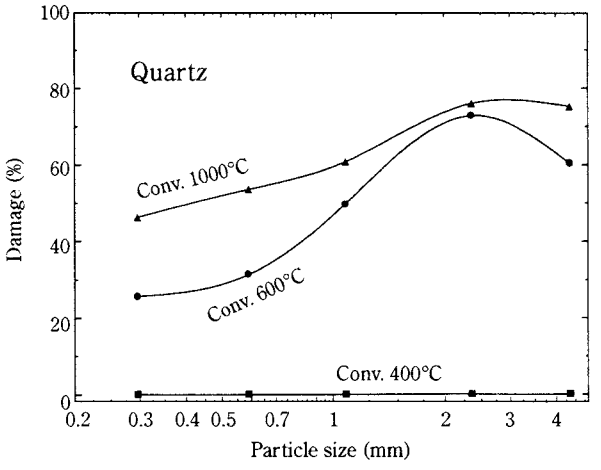

Fig. 11 Effect of particle size and heat treatment on the damage parameter of quartz.

while limited weakening was observed for air-cooled specimens. Such reductions in fracture energy, however, were comparable to those obtained by heating slowly (at about 20°C/min) in the muffle furnace. Further, no damage was induced by heating taconite and iron ore samples with microwaves, while substantial damage resulted from microwave heating the titanium ore.

Thermomechanical stresses that led to weakening during microwave pretreatment result from the interplay between the thermal expansion of the high-loss mineral and the dissipation of heat by conduction to the neighboring grains. It has been shown (Salsman et al., 1996) that the magnitude of the tensile stresses in the boundary between the high-loss and the gangue mineral would depend critically on the heating rate that can be achieved during heating. The temperature rise depends on the power dissipated in the mineral, which in turn is proportional to the electrical field strength. Therefore, higher powers of the microwave heating system must be used to enhance the weakening and therefore make microwave pretreatment a viable proposition.

5. Effect of Thermal Treatment on Fragmentation and Comminution

Progeny size distributions from breakage of single particles of untreated and heat-treated hematite particles are shown in **Figure 12**. Similar trends were observed for the others materials tested. Consistently with measurements of internal damage and particle fracture energy (**Figures 7** and **8**), increases in heating temperature produced greater breakage. However, the fragmentation pattern resulting from breakage of heat-treated particles differed significantly from that found with untreated particles. Heating to higher temperatures produced a significant increase in the fragmentation of coarser sizes with little or no increase in the proportion of fines. This confirms observations from polished sections, which show that as soon as fragments become smaller than the regions fully surrounded by cracks, the effect of thermal pretreatment vanishes.

These were, indeed, confirmed by batch grinding experiments, carried out on a 19-cm ball mill with 1.9-cm, 30-gram steel balls operating at 75% critical speed (**Figure 13**). Breakage of the heat-treated material results in bimodal size distributions with greater spread of sizes in the product.

Although thermal pretreatment can induce significant cracking and reduce energy expenditure in comminution, the net energy expenditure is usually not favorable (a rough estimation based on thermal capacities shows that heating above 600°C would require well over 100 kW-hr/ton). Therefore, thermal pretreatment cannot be justified on the basis of reduction in grinding energy alone. It could be used in some specialty applications. Excessively competent pebbles only suffer wear inside the mill and do not break. Preconditioning the pebbles using conventional or microwave heating could be used to control their competency, thus allowing an optimum performance of the mill

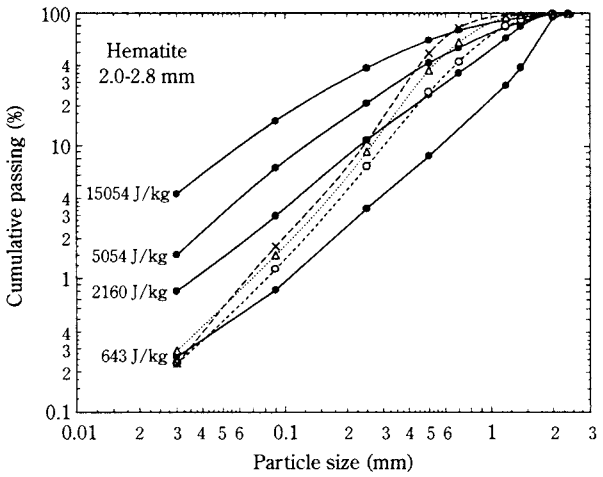

Fig. 12 Effect of heating to the target temperature and water quenching on the fragmentation behavior of hematite. Heat-treated particles were all impacted at 643 J/kg.

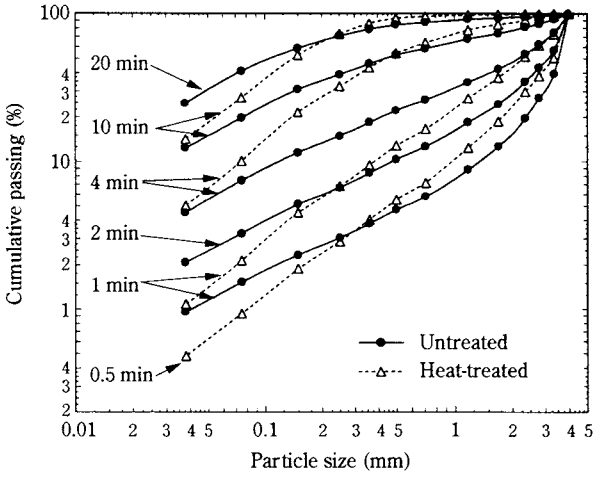

Fig. 13 Batch grinding results of untreated and heat-treated (heated to 600°C and water-quenched) quartz particles (4.0-4.75 mm). Grinding conditions: 190 mm diameter ball mill, 75% critical speed, 30% mill filling, with a charge of steel balls of 19 mm diameter.

6. Summary and Conclusions

The application of thermal predamage to improve comminution has been studied using a microscale approach involving precise single-particle breakage measurements with the UFLC and microscopic examination. It was shown that pretreatment was essentially responsible to inducing an array of cracks in the solid, with its concentration depending on the severity of the treatment. It was found that a correspondence exists between the crack density and the reduction in material stiffness, given by the damage parameter. Weakening was higher for coarser particles and for severe quenching, with water or salt solution.

Reductions in the measured particle fracture energy indicate weakening of the parent particle due to induced crack-like damage but, in spite of this, substantial reduction in comminution energy can be achieved only if substantial numbers of the progeny fragments are themselves weaker than the undamaged material. When this occurs, substantial damage can be measured in the particle in addition to reductions in particle fracture energy.

The studies showed that limited reductions in fracture energy can occur after thermal-shock pretreatment to temperatures as low as 200°C. However, substantial damage was found to occur at temperatures of 600°C and above. The amount of damage induced was found to decrease with a reduction in particle size. Microwave heating experiments at 1.2 kW showed little or no improvement when compared to thermal pretreatment by conventional heating.

Acknowledgements

This research has been supported by the Department of the Interior's Mineral Institute program administered by the US Bureau of Mines through the Generic Mineral Center for Comminution under grant numbers G1125249 and G1135249. The assistance of Mr. Ludovic Milin on the batch grinding experiments and of Mr. Stewart Middlemiss on the microfracture experiments is acknowledged.

References

1) Austin, L.G., Klimpel, R.R. and Luckie, P.T., The Process Engineering of Size Reduction, Society of Mining Engineers, 1984, New York.
2) Brown, J.H., Gaudin, A.M. and Loeb, C.M., Intergranular comminution by heating. Trans. SME-AIME, 1958, **211**, 490-496.
3) Fitzgibbon, K.E. and Veasey, T.J., Thermally assisted liberation – a review. Miner. Eng., 1990, **3**, 181-185.
4) Geller, L.B. and Tervo, R.O., Grinding of preheated rocks. Trans., Instn. Min. Metall., Sec. C, 1975, **84**, 25-33.
5) Hariharam, K. and Venkatachalam, S., Influence of thermal treatments upon the grindability of quartz. Min. Mag., 1977, **136**, 105-108.
6) Kachanov, L.M., Time of the rupture process under creep conditions (in russian), Izv. Akac Nauk AN SSSR, 1958, **8**, 26-31.
7) Kanellopoupos, A. and Ball, A., The fracture and thermal weakening of quartzite in relation to comminution. J. S. Afr. Inst. Min. Metall., 1975, **76**, 45-52.
8) King, R.P. and Bourgeois, F., Measurement of fracture energy during single-particle fracture. Miner. Engineering, 1993a, **4**, 353-367.
9) King, R.P. and Bourgeois, F., A new conceptual model of ball milling. Proc. 18th Int. Miner. Process. Congr., Vol. 1, Sydney, 1993b, pp. 81-86.
10) Lawn, B.R., Fracture of Brittle Solids, 2nd edition, Cambridge, University Press, 1993.
11) Luty, W., Types of cooling media and their properties. In Theory and Technology of Quenching, ed. B. Liscic, H.M. Tensi and W. Luty. Springer-Verlag, Berlin, 1992, pp. 248-340.
12) Middlemiss, S. and King, R.P., Investigation of the Microfracture Characteristics of Geological Materials by Indentation Techniques. Presented at AIME/SME Annual Meeting, Albuquerque, New Mexico, 1994.
13) Milin, L. and King, R.P., Testing the equality of two independent distributions of data measured on the Ultrafast Load Cell, Technical Report, Utah Comminution Center, 1994.
14) Pocock, J., Veasey, T.J., Tavares, L.M. and King, R.P., The effect of heating and quenching on grinding characteristics of quartzite, Powder Tech., 1998, **95**, 137-142.
15) Salsman, J.B., Williamson, R.L., Tolley, W.K. and Rice, D.A., Short-pulse microwave treatment of disseminated sulfide ores. Miner. Eng., 1996, **9**, 43-54.
16) Tavares, L.M., Microscale Investigation of particle breakage applied to the study of thermal and mechanical predamage, Ph.D. Thesis, University of Utah, 1997.
17) Tavares, L.M. and King, R.P., Single-particle fracture under impact loading. Int. J. Min. Process., 1998, **54**, 1-28.
18) Walkiewicz, J.W., Lindroth, D.P. and Clark, A.E., Improved grindability of taconite ore by microwave heating. Report of Investigations, USBM RI 9559, 1995.

Author's short biography

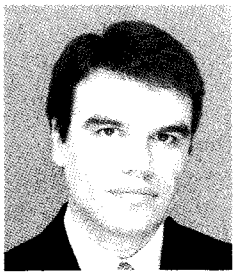

Luís Marcelo Tavares

Marcelo Tavares graduated with First Class Honors in Mining Engineering from the Universidade Federal do Rio Grande do Sul, Brazil. In 1991 he obtained a MSc degree in Metallurgical Engineering at the same university. He joined the Comminution Center in the University of Utah, where he obtained his PhD degree in 1997. He is currently an assistant professor in the Department of Metallurgical and Materials Engineering at the Universidade Federal do Rio de Janeiro, where he is involved in both teaching and research in several topics in mineral processing, particularly comminution and gravity concentration.

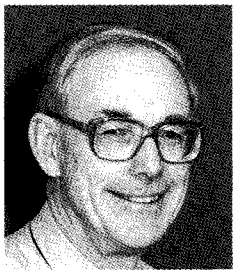

R.P. King

Professor was born in South Africa and received BSc and MSc degrees from the University of the Witwatersrand. He received the PhD degree from the University of Manchester, England in 1963. He has lectured at the universities of Manchester, Natal, Witwatersrand, Utah and at the Camborne School of Mines. He established and led Mintek's Chemical Engineering Research Group at the University of Natal for 7 years and was Head of the Department of Metallurgy and Materials Engineering from 1975 to 1990. He is now professor of Metallurgical Engineering and Director of the Comminution Center at the University of Utah. Professor King has researched and published widely in the field of quantitative modeling of process engineering systems and has contributed particularly to the development of computer simulation techniques for the minerals processing industry. Professor King is an Honorary Life Member of the South African Institute of Mining and Metallurgy and he was President of that institute in 1982 – 1983. He is a member of SME and a member of the Society for Industrial and Applied Mathematics. Since 1999 he has been the Editor-in-Chief of the International Journal of Mineral Processing.

Nanometric Dry Powder Coatings Using a Novel Process†

J. M. Fitz-Gerald
*Naval Research Laboratory**
R. K. Singh and H. Gao
*Department of Materials Science and Engineering, University of Florida***
S. J. Pennycook
*Solid State Division, Oak Ridge National Laboratory****

Abstract

A wide range of advanced technology for existing and emerging products based on high temperature metal-ceramic composites used in aircrafts, cutting tools, lithium-ion based rechargeable batteries, superconductors, field emission based flat-panel displays, etc. employ micron to submicron sized (0.1−10 microns) particulate precursors in their manufacturing process. Although there has been a significant emphasis given to control of the particle characteristics (shape, size, surface chemistry, adsorption, etc.), relatively little or no attention has been paid to concomitant designing desirable surface and bulk properties at the particulate level, which can ultimately lead to enhanced properties of the product. By attaching atomic to nano-sized inorganic, multi-elernental clusters either in discrete or continuous from onto the surface of the core particles, i.e nano-functionalization of the particulate surface, materials and products with significantly enhanced properties can be obtained. In this paper, we demonstrate for the first time the synthesis of artificially structured, nano-functionalized particulate materials with unique optical, cathodoluminescent, superconducting and electrical properties. In this paper, we show the feasibility of the pulsed laser ablation technique to make very thin, uniformly distributed and discrete coatings in particulate systems so that the properties of the core particles can be suitably modified. Experiments were conducted for laser deposition of Ag nano particles on Al_2O_3 and SiO_2 core particles by pulsed excimer laser (wavelength=248 nm and pulse duration=25 nanosecond) irradiation of a Ag, Y_2O_3:Eu^{3+}, and $TaSi_2$ sputtering targets.

Analytical techniques using scanning electron microscopy (SEM), wavelength dispersive x-ray mapping (WDX), transmission electron microscopy (TEM), scanning transmission electron microscopy with z contrast (STEMZ), and photoluminesence (PL) were utilized to examine the structural, chemical, and morphological characteristics of the nanometric coatings. Qualitative surface uniformity measurements by WDX mapping techniques showed a high degree of coating uniformity on the core particulate. Structural TEM and STEMZ imaging showed both continuous and discrete polycrystalline, multiply twinned nano particle coatings ranging from 5-40 nm in thickness.

Introduction

Sub-micron to micron sized metallic and ceramic particles (100 nm to 10 microns) act at principal precursor materials for a wide range of existing and emerging products involving advanced ceramics, metals, composites which spans several industries such as aerospace, automobile, machining, vacuum electronics, batteries, data storage, catalysis, etc [1-2]. Particulate materials, as core technologies impact over 1 trillion dollar yearly on a worldwide basis [3]. To achieve desirable properties in the final product, typically the properties of the particles such as shape, size, composition, surface charge, flowability, etc., have been controlled. These characteristics play an important role in determining the final microstructure, and thus the product's properties. However with the rapid advancements in non-particulate technologies such as computers, telecommunications and electronics, there is a strong need to need to develop novel particulate systems which can results in value-added products with enhanced properties [4].

Increasing interest in the recent years has been focused on a *wide variety of nanostructured materials*,

* Code 6372, Washington, District of Columbia 20375, USA
** Gainesville, Florida 32611, USA
***Oak Ridge, Tennessee 37831, USA
† Received July 20, 1999

which possess grain or phase structures modulated on a length scale of less than 100 nm, because it is anticipated that their properties will be different from and often superior to conventional materials that have phase or grain boundaries over a coarser size scale [5-6]. Using artificial engineered nanostructured materials, it may also be possible to engineer the properties by controlling the size of the constituent domains and the manner in which they are assembled. Some of the recent efforts have been focused on synthesizing atom clusters, zero dimensionality quantum well structures, one dimensional modulated multilayered materials, and three dimensional modulated nanophase materials and nanocomposite materials [3-7]. These artificially engineered nanostructured materials may possess novel properties, however typically *they cannot be used along with the submicron to micron sized (100 nm to 10 micron) sized materials which constitutes the bulk of the existing commercial technologies.*

By synthesizing nano-functionalized particulates, or *artificially engineered materials formed by attachment of nanosized particles of complex stoichiometries onto core particles in different architectural forms (porous to compact, discrete to continuous)*, it is possible to produce particulate materials which concomitantly exhibit, distinct, disparate and unique properties. A schematic diagram of two types of nano-functionalized particulate materials is shown in **Fig. 1**. This figure shows both discrete and continuous nanofunctionalized layers onto core particles. **Table I** shows some of the unique characteristics of nano-functionalized particulate materials. For example, thin, conducting continuous clusters (<2 nm) are required for field emission display flat panel powders, so that the surface electrical charge can be dissipated, and electron beam induced surface oxidation can be prevented for long-life cathodoluminescent properties [8-9]. Similarly continuous nanoparticle intermetallics (such as TiAl) clusters of size <2 nm may be ideal for WC core particles, so that defect-free, high-toughness, high-temperature strength composite materials may be synthesized for next generation high speed (>1500 m/min) cutting tool applications [10]. In contrast, thick (20-30 nm) discontinuous CoO clusters may be ideal for Ni(OH)2/CoO composites, in which the surface exposure of the core material is essential of efficient charging and discharging kinetics for high capacity rechargeable nickel metal hydride battery applications. It should be noted that in all these applications, it is imperative that the *functionalized surface*

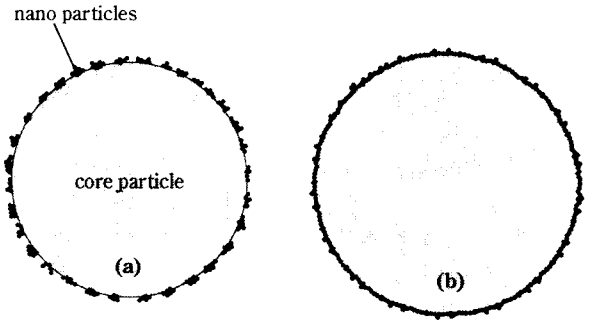

Fig. 1 Schematic diagram of a nanofunctional particulate consisting of a core particle coated with nano particles. Fig. 1 (a) illustrates a discrete or porous coating while (b) shows a continuous nanoparticle coating.

Table I Various Examples of nano functionalized particulate materials showing the surface architecture, the nature of surface functionalization, and potential desirable applications.

Nano Phase Compound	Core Particle	Nano Phase Architecture	Surface Functionalization	Applications
Co	WC	Continuous, Compact, Thin	Fracture Toughness	Cutting Tools
TiAl	WC	Continuous, Compact, Thin	Fracture Toughness, High Temp. Strength	Aircraft, High Speed Cutting Tools
Y_2O_3	Si_3N_4	Thin, Compact, Phase Sintering	Controlled Liquid Ball Bearings	High Strength Ceramic
SiO_2	Al_2O_3	Thin, Continuous, Compact	Solid Phase Reaction Sintering	Advanced High Strength, High Toughness Ceramics
CoO	$Ni(OH)_2$	Discrete, Porous, Thin	High Surface Conductivity	Rechargeable Batteries
Y_2O_3:Eu^{3+}	SiO_2	Continuous, Compact, Thick	Cathodoluminescent Surfaces	Spherical, Mono sized Red Phosphor Particles
$TaSi_2$	Y_2O_2S:Eu^{3+}	Thin, Compact	Surface Degradation Protection	Low Degradation Phosphor Particles
$Ni(OH)_2$	SiO_2	Thin, Discrete, Porous	Bacteria Absorption from Water	Efficient Filtration Systems
$YBa_2Cu_3O_{7-\delta}$	Al_2O_3	Thin, Continuous, Compact	Superconducting Surfaces	Electromagnetic Shielding
TiO_2	SiO_2	Thick, Discrete, Porous	Catalytic Surfaces	Environmental Clean Up

should be in the nanometric dimensions, otherwise the thick layer masks the useful bulk property of the core particle e.g phosphorescence, mechanical strength, etc. These examples clearly show that nano-functionalized particulates can have *wide ranging impact in existing and emerging technologies* and can replace existing particulate materials.

Although the synthesis of nanofunctionalized particulates is highly desirable from both fundamental and technological viewpoint, significant progress has not been made in this field due to several complicating factors [13-15]. Some of the cluster materials are in the form of multicomponent stochiometric materials such as high T_c superconductors (Y-Ba-Cu-O), colossal magnetoresistance (CMR) materials (such as La-Ca-Mn-O), phosphorescent materials (e.g, Eu doped yttrium oxide, sulphide). This complicates the uniformly deposition of these species onto the core particle [11-12]. In addition, the functionalized surface should typically have nanometric dimensionality control for optimum interaction between bulk and surface properties. Techniques presently used in the literature such as fluidized bed coating, powder blending, mechanofusion processing, chemical precipitation and chemical vapor phase condensation are not capable of overcoming the above mentioned barriers [13-15]. Thus, the state of the art methods cannot be utilized to synthesize nano-functionalized particulates with uniformly distributed multicomponent coatings in nanometric dimensions.

Experimental

The use of atomic to nano-sized particle fluxes to coat particulate materials has several advantages. Typically nano particles (5-30 nm) are very reactive and when brought into close contact with each other, aggregate to form larger particles, thus substantially decreasing the observed surface area. By adhering the nano particles to larger particles, the aggregation of the nano particles is prevented, thus significantly increasing their utilization. It should also be noted that the formation of a composite particle with atomic or nano particles will lead to improved adherence of the coating due to its size and reactivity of the nano particle. Another advantage of using nano particles to synthesize a composite particle is the small amount of material required in the vapor form. For example if 1% surface coverage is required, 1 gm of nano particles (<10 nm) can coat more than 100 kg of 10 μm core particles, if 100% efficiency of the coating process is assumed. Thus, the formation of nano thin coatings on particulate materials not only provides unique properties but can be manufactured in large quantities. The pulsed laser deposition (PLD) technique has emerged as one of the most popular methods to deposit complex oxide thin films and deposition of compositionally varying multilayer systems [16-19]. Presently, most of the thin film deposition has been conducted on flat substrates which are normally kept parallel to the substrate at a distance of 3-10 cm from the target. The flux generated by the laser interaction with the target and the ablated material, is composed of active atomic and molecular species. The background gas has been found to play a significant role in the film formation process. If the background gas chamber pressure consists of reactive gases such as oxygen, ammonia, nitrous oxide etc., a higher concentration of molecular species is observed in the plasma. At high background pressures (>200 mTorr), nano particles, (>3 nm) size in the plasma have been reported [20-22]. The formation of these clusters is due to increased collisions of the ablated species in the gas phase. Also, if the background gas is reactive (e.g. oxygen etc.), the ablated species may react to form new compound species [22]. Composite particulates which have been surface modified with a thin continuous or discontinuous layer have a large number of applications in existing and emerging technologies [23-24]. An example of a composite particulate material is shown in **Fig. 1**. This figure shows that the surface of the core particle is modified by the attachment of the secondary particles.

In this paper, we show the feasibility of the pulsed laser ablation technique to form discrete Ag nano particle coatings on core particles of Al_2O_3 and SiO_2. **Fig. 2** shows a schematic diagram of the experimental setup to fabricate the particulate coatings. Except for the core particle suspension system, this deposition system resembles a standard PLD thin film deposition system. An excimer laser irradiates the target material through the ultraviolet transparent quartz window. Typical energy densities employed in the experiments were approximately 2-3 J/cm^2. The laser plume is directed perpendicular to the target material to an agitated bed to core particles. The core particles are suspended in the system by a mechanical agitation method. The thickness and surface coverage of the coating is controlled primarily by the repetition rate of the laser and the residence time of the suspension. By controlling the energy as well as the background pressure in the system, the composition and size of the nano particles can be controlled. Earlier work has shown a correlation between the cluster

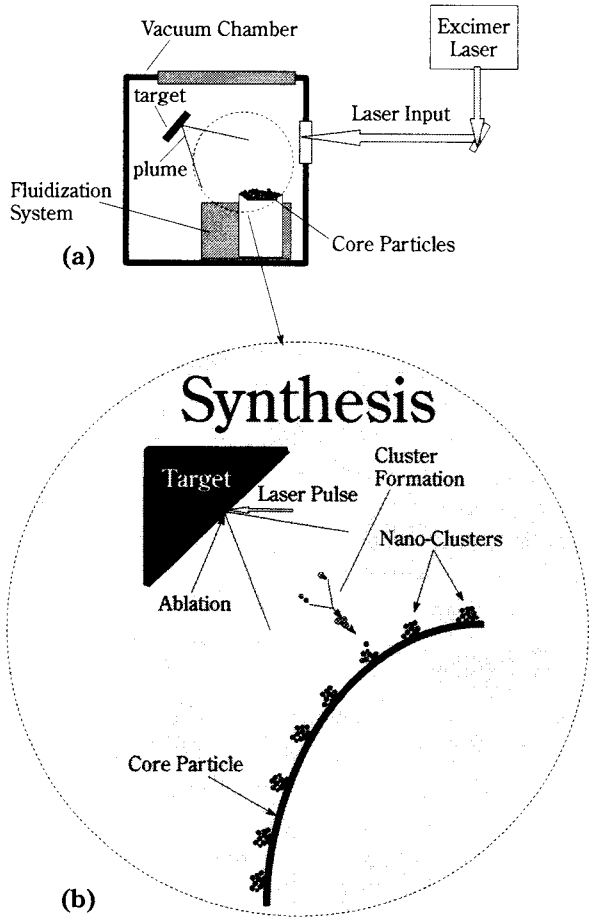

Fig. 2 Schematic diagram of the system employed to synthesize nano-cluster coatings. Fig. 2 (a) is a schematic of the overall processing system, including the pulsed excimer laser heat source, (b) shows an enlarged schematic of the nano particle growth process.

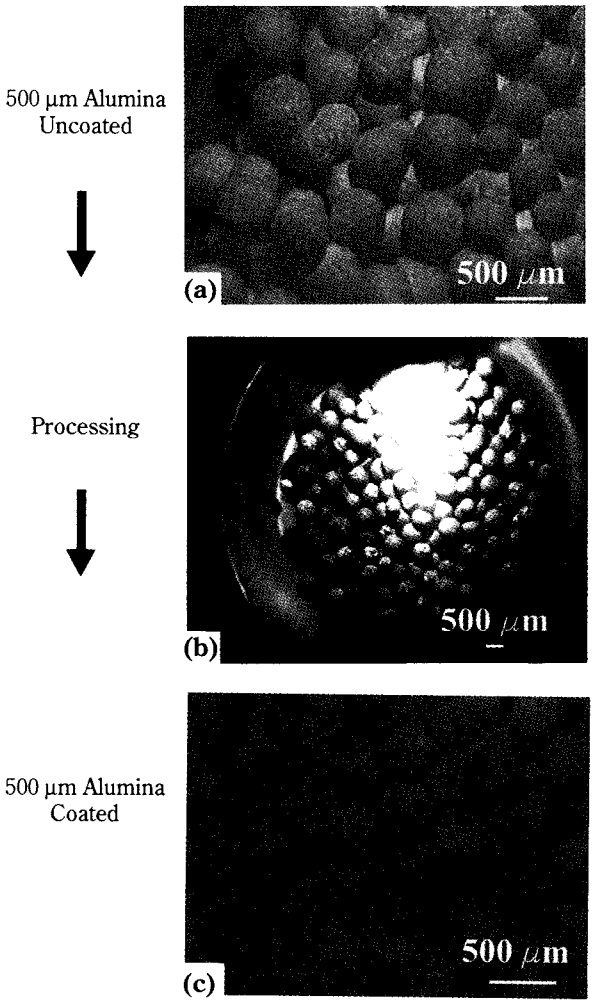

Fig. 3 CCD camera images during laser coating of 500 μm Al_2O_3 particles. Figures 3. (a), (c) show CCD images of uncoated and coated samples respectively. Fig. 3. (b) shows a CCD image during processing, where optical emission from the plume is clearly visible.

size and the background gas pressure. When the background gas pressure is increased, the cluster size changes from a few atoms to nanometer dimensions. The experiments have been conducted using Al_2O_3 and SiO_2 core particles with a high purity Ag, Y_2O_3:Eu^{3+}, and $TaSi_2$ sputtering targets as sources. **Figure 3** shows in-situ CCD images obtained during processing coating of 500 μm Al_2O_3 particles.

Results and Discussion

As shown in **Fig. 4. (a)**, the size of the ablated nano particles is below the resolution of the SEM, therefore the presence of the coating on the surface was determined by chemical analysis. **Figures 4 (b), (c)**, respectively show SEM and Ag chemical images of Ag/Al_2O_3 composite particles synthesized by the laser ablation process. The SEM micrograph shows approximately 18 μm faceted alumina particles, however as in (a), it does not reveal the presence of a nano particle film on the surface. From the WDX Ag chemical map shown in **figure 4 (c)**, it appears that the Ag is distributed uniformly on the surface of the Al_2O_3 particles. To determine the structure as well as the spatial distribution of the nano-functionalized layer, high resolution transmission electron microscopy and scanning transmission electron microscopy (HRTEM) with dark field contrast (STEM-Z) were conducted on these samples. The contrast in STEM-Z occurs due to incoherent Rutherford scattering, thus the intensity is proportional to the atomic number of the element [26-27]. **Figure 4 (d)** shows the STEM-Z micrograph of the surface morphology of the Ag/Al_2O_3 nano-functionalized particulate system. This figure shows that the surface of the core particle is partially covered with a dis-continuous layer of silver nanoparticles. To

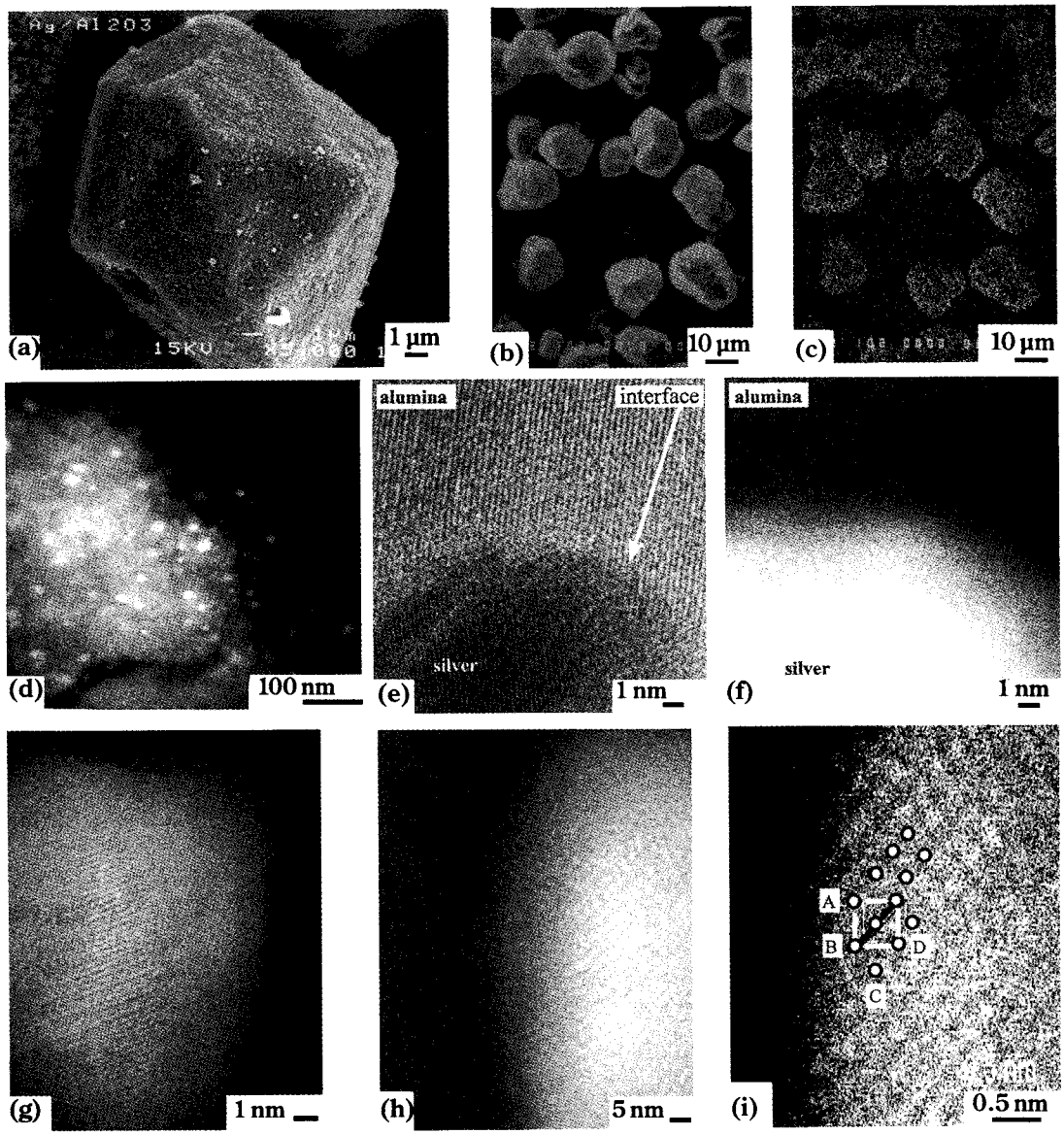

Fig. 4 (a) SEM of an Al_2O_3 particle coated with Ag nano particles, (b) SEM of Al_2O_3 particles coated with Ag nano particles and (c) corresponding WDX chemical map for Ag on (b) showing the 1 : 1 correlation of the Ag coating, (d) represents a dark field image of Ag on the Al_2O_3 particle surface, at higher magnification, (e), (f) present dark field and bright field images of the Ag nano particle-Al_2O_3 interface respectively, (g) shows a multiply twinned Ag nano particle on the Al_2O_3 particle substrate, (h), (i) show STEM structure reconstruction of a (110) twinned Ag nano particle on Al_2O_3.

investigate the interface further, the sample was tilted to look at the interface between the Ag nano particle and the Al_2O_3 core particle. **Fig. 4. (e), (f)** show dark and bright field STEM-Z images of the interface respectively. From **Fig. 4. (f)**, the brighter area corresponds to Ag and the darker Al_2O_3. It appears that there is little if any intermixing between the Ag nano particles and the core Al_2O_3 particle surface. **Fig. 4. (g)** shows a dark field image of a multiply twinned Ag nano particle on the surface of the core Al_2O_3 particle. **Fig. 4. (h)** and **(i)** show dark field images of a Ag nano particle on Al_2O_3, subsequent structure reconstruction showed prevalent (110) twinning behavior.

X-ray photo electron spectroscopy (XPS) was used to examine the relative surface coverage of Ag nano particles on Al_2O_3 core particles as a function of background gas molecular weight and pressure. **Figure 5 (a)** shows the results of quantitative analysis of Ag surface coverage. Both the molecular weight and pressure of the backfilled gas appear to modify the deposition characteristics with respect to surface coverage in this system. Mean Ag nano particle size distributions, shown in **Fig. 5 (b)** were gathered by collecting nanoparticles on TEM grids. Subsequent CCD camera time-gated Ag plume imaging at long times after the initial laser pulse are shown in

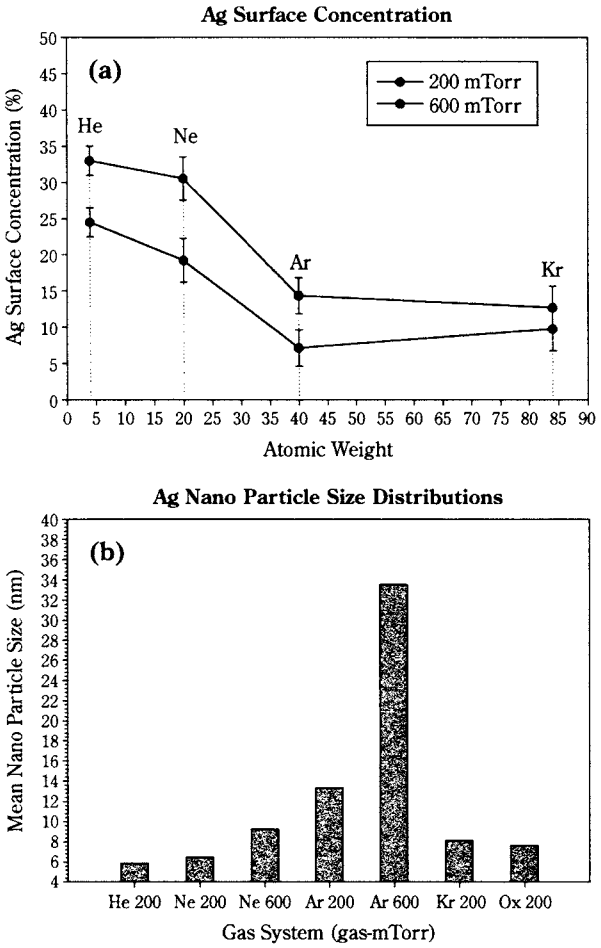

Fig. 5 (a) XPS measurements of the Ag surface concentration taken as a function of backfill gas pressure and molecular weight, (b) Ag nanoparticle size distributions obtained from deposition onto mesh TEM grids.

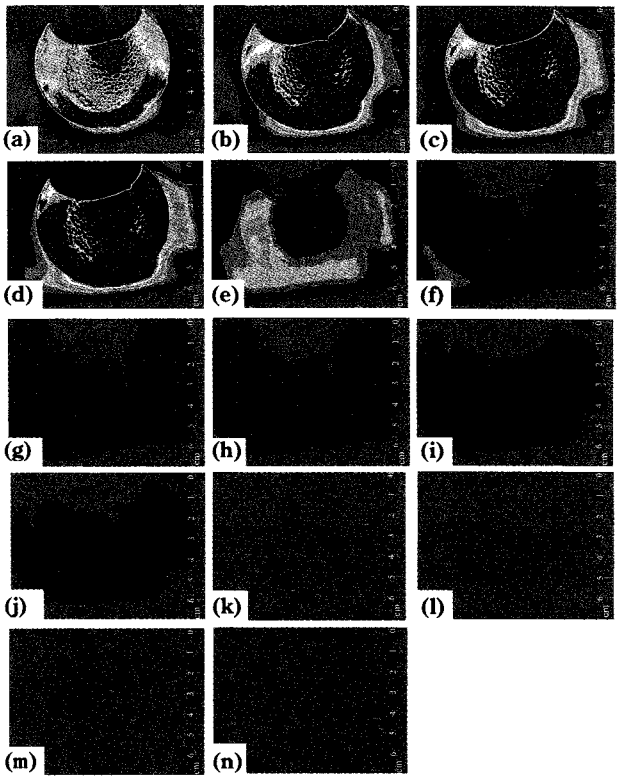

Fig. 6 Plume evolution behavior in the presence of Helium at 200 mTorr. CCD imaging was time gated at 20 μsec intervals. Optical emission lasts for ≈75 μsec.

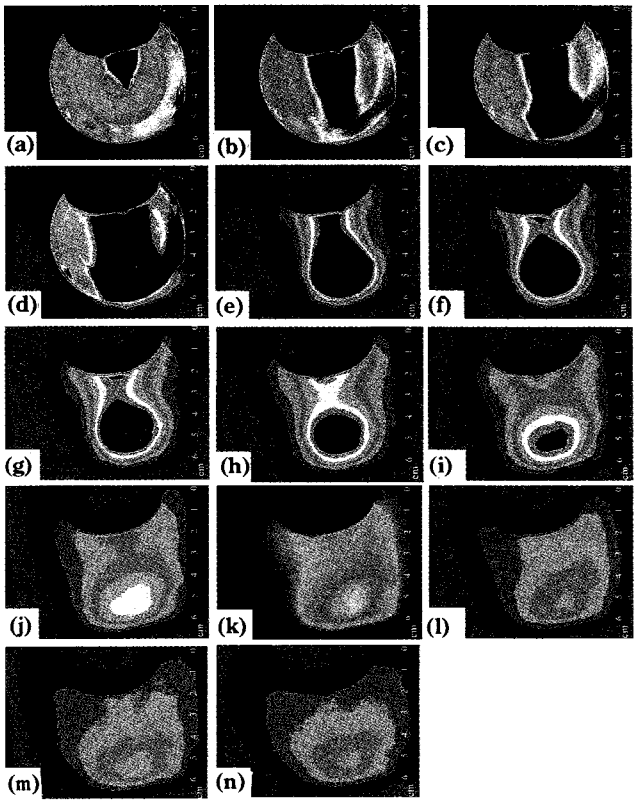

Fig. 7 Plume evolution behavior in the presence of Krypton at 200 mTorr. CCD imaging was time gated at 20 μsec intervals. Optical emission is sustained out to ≈300 μsec, with confinement of the ablated species.

Figures 6, 7. **Figure 6** shows the plume evolution of the plume in the presence of Helium at 200 mTorr. Optical emission due to collisional heating and electron-ion recombination lasts for ≈70 μsec, in comparison to sustained emission lifetimes of ≈300 μsec in the presence of Krypton. Further analysis of the CCD imaging have shown that the molecular weight of the backfill gas controls both the nanoparticle formation and deposition characteristics by the formation of a semi stationary confined plasma (SSCP) [28].

Nano-functional particulate materials *can be designed to achieve properties which cannot be obtained with existing particulate materials*. An example of this is shown for particulate requirements for field emission based flat panel display applications [9]. This emerging technology has several advantages in terms of low power consumption, high brightness, low power consumption, large viewing angle and is expected to replace liquid based crystal technology in specific applications [9]. In this application, the multiple field

emission electron beam sources directly strike a phosphor particulate based screens possessing red blue or green activators to produce light which is emitted out of the surface. The phosphor screens are typically made from powder materials which exhibit a multitude of shapes and sizes distributions, thus causing non-uniformity in the thick film microstructure. Additionally, upon continuous irradiation with intense electron beams, the brightness of the screens degrade thus limiting its usefulness and have become a major impediment for commercialization [9]. **Fig. 8 (a)** shows the SEM image of a continuous nano-functionalized Y_2O_3:Eu layer on 1 μm mono-sized silica particles. These nano-functionalized particulates were heat treated at 700°C for 1 hr in air to activate the phosphor layer. The silica particles, prepared by sol-gel techniques are typically spherical in shape, thus leading to the spherical morphology of the nano-functionalized particulates. The TEM micrograph in **Fig. 8 (b)** and its corresponding diffraction pattern, **(8c)**, shows two important microstructural characteristics of the nano-functionalized Y_2O_3:Eu layer, namely (i) the layer forms a continuous film on the surface and (ii) a single crystal like electron diffraction pattern is obtained from nano-functionalized surface layer. The single crystal nature of the surface layer on a curvilinear substrate possibly suggests new mechanisms for stabilization of single crystal growth on curved surfaces. More studies are presently being conducted to understand the nature of layer growth on curved interfaces. **Fig. 8 (d)** shows the typical photoluminesence spectrum obtained from $Y_2O_3:Eu^{3+}$/silica nano-functionalized particles. The figure shows that the particles yield a dominant red light emission peak at 611 nm due to $^5D_0$-$^7F_2$ transition. Due to shielding effect of $4f^6$ electrons by $5s^2$ and $5p^6$ electrons in outer shells of Eu ion, one expects a sharp emission within Eu ions. The photoluminesence brightness was significantly higher when the samples were annealed in air at 700°C for 1 hour.

Another potential application of nano-functionalized particulates is shown in **Fig. 9**. This example is related to reduction in the degradation in the brightness of the flat-panel phosphors due to aging effects. This fig-

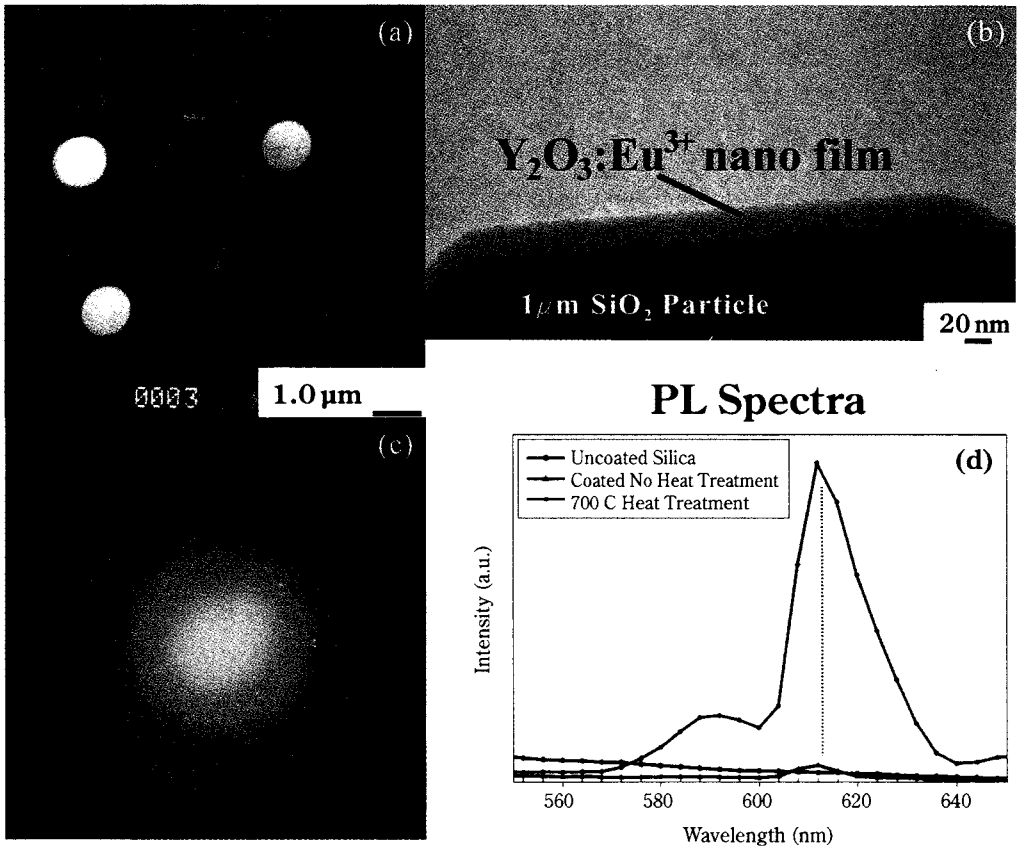

Fig. 8 (a) SEM of 1 μm mono sized SiO_2 core particles, (b) TEM image showing a continuous thin film of $Y_2O_3:Eu^{3+}$ deposited on the core particle, (c) selected area diffraction pattern of the thin film showing single crystal like behavior from the nano-functionalized surface layer, (d) PL spectra from coated core particles showing the standard Eu peak at 611 nm.

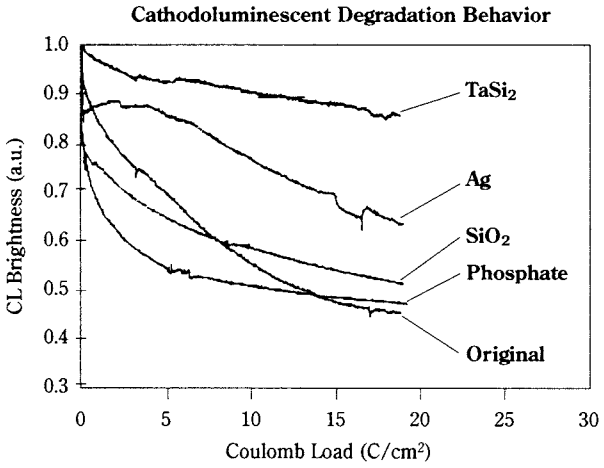

Fig. 9 This figure shows that during cathodoluminescent degradation, the uncoated phosphor material ($Y_2O_2S:Eu^{3+}$) degraded to approximately 50% of its original brightness if the total dose exceeds 15 C/cm^2 (standard industrial conditions for a phosphor lifetime). However, the application of very thin nano-functionalized tantalum di silicide ($TaSi_2$) and Ag layers by the laser ablation process reduces the degradation of this phosphor material by a factor of 5 and 2 respectively. Results of wet coatings with SiO_2 and phosphate materials are shown for comparison.

ure shows the change in brightness of an yttrium oxysulphide phosphor powder as a function of cumulative electron dose. This figure shows that the phosphor degraded to approximately 50% of its original brightness if the total dose exceeds 15 C/cm^2. However, the application of a very thin nano-functionalized tantalum di silicide ($TaSi_2$) layer reduces the degradation of this phosphor material by a factor of 5. This reduction in degradation has been attributed to the reduced oxidation of the surface layer in presence of the protective nano-thin layer. It should be noted that nanometric dimensions of the layer is essential to ensure electron transparency of the surface.

Conclusions

A novel technique coupling pulsed laser ablation to synthesize engineered particulate materials has been presented. TEM observations have shown that the backfill gas pressure and molecular weight have significant effects on Ag nano particle formation during ablation. Ag nano particles formed during laser ablation have a multiply twinned, high defect structure. STEM investigations of the interface between the Al_2O_3 core and the Ag nano particles contains very little intermixing with adhesion mechanisms most probably due to long range Van de Waals bonding. Further STEM characterization of the interfaces is presently underway. In short, it is felt that PLD method represents a viable method to surface modify particulate systems, which are required for a wide variety of current and future applications.

Acknowledgements

Part of this research is sponsored by the National Science Foundation funded Engineering Research Center on Particle Science and Technology via grant #ERC 94-0929 and the Division of Materials Sciences, U.S. Department of Energy under contract No. DE-AC05-96OR22464 with Lockheed Martin Energy Research Corp. The authors would also like to thank Troy Trottier at Motorola Flat Panel Display Division for providing data and characterization on the phosphor degradation.

References

1) Tom Forester, The Materials Revolution, MIT Press (1988).
2) Materials Science & Engineering for the 1990s, National Academy Press, Washington DC 1990.
3) U.S Department of Commerce Annual Report, 1992.
4) Scientific American, May, 1997 pg. 38-39.
5) H. Glieter, *Advanced Materials*, 4, 474 (1992).
6) R.W. Seigel, *Nanostructured Materials*, 4, 121 (1994).
7) See for example, E. Gonsalves, J. Baraton, R.K. Singh, H. Hofmann, J. Akarra, editors, "Surface Modification of Nanomaterials for Value of Added Application", Proceedings of the November, 1997 Materials Research Society, Fall Meeting (1998).
8) R.K. Singh, A. Ata. J. Fitz-Gerald, Kona,.
9) J. Fitz-Gerald, R.K. Singh, T. Trottier and P.H. Holloway, App. Phys. Lett, Vol 72, 15 (1998).
10) R. Darolia, D.F. Lahrman, R.D. Field, and A.J. Freeman, MRS Society Proceeding on High Temperature Ordered Intermetallic Alloys III, eds, C.T. Liu Pittsburgh (1989).
11) Y. Kousaka, Y. Endo, M. Alonso, H. Ichitoubo, A. Fukui, Advanced Powder Tech., 6, 11 (1995).
12) I. Saito, M. Senna, Kona, 13, 191 (1993).
13) K. Higashitani, T. Yamamura, Y. Ishiki, A. Kage, A. Kondo, Kona 12, 119 (1994).
14) S. Jin, T.H. Tifel, M. McCormack, R.A Fastnatch, R. Romish, and L.H. Chen, Science, 264 413 (1994).
15) See for example, "Pulsed Laser Processing of Materials: Fundamentals and Applications", Editors R.K. Singh, D.P. Norton, J. Narayan, M. Hanabusa, Materials Research Society Proceedings, Vol 347 (1997).
16) R.K. Singh and J. Narayan, Phys. Rev B, 43, 8843 (1990).
17) R.K. Singh, J. Narayan, A.K. Singh and J. Krishnaswamy, Appl. Phys. Lett.
18) R.K. Singh and D. Kumar, Mat. Sci. and Rep, (in press), 1998.
19) D.B. Geohegan and A.A. Putretsky, Mat. Sci Soc Symposia, Eds R.K. Singh et. al.

20) K.D. Rinnen, K.D. Kolenbrabder, A.M. DeSantioolo, M.L. Mandich, J. Chem Phy. 96, 4088 (1992).
22) T. Yoshida, S. Takeyama, Y. Yamada, K. Mutoh, Appl. Phys. Lett, 68, 1772 (1996).
23) D.L. Lowdnes, D.B. Geohegan, A.A. Puretsky, D.P. Norton and C.M. Rouleau, Science, 273, 898 (1996).
24) R.K. Singh, A. Ata, J. Fitz-Gerald, Y. Rabinovich, W. Hendrickson, *Kona* **15**, 121-131 (1997).
25) R.K. Singh, A. Ata, J. Fitz-Gerald, Y. Rabinovich, W. Hendrickson, *Surface Modification Technologies X, Proceedings of the Tenth International Conference on Surface Modification Technologies*, 909-917 (1997).
26) N.D. Browning, M.F. Chisholm, and S.J. Pennycook, Nature 366 (1993) 143.
27) A.J. McGibbon, S.J. Pennycook, and J.E. Angelo Science, 269, 519-521 1995.
28) J. Fitz-Gerald and R.K. Singh, "Synthesis and Nano Particle Formation of Nanofunctionalized Particulates by Pulsed Laser Deposition", J. of Mat. Res., (to be published).

Author's short biography

J. M. Fitz-Gerald

James Fitz-Gerald is currently a Post Doctoral Research Fellow at the Naval Research Laboratory performing research in the areas of thin film devices, flat panel display materials, pulmonary drug delivery, laser direct-write processing, and bio-electronic materials. Prior to his appointment at NRL, he received a BSME degree from the University of Lowell in 1993 and his MS and PhD degrees from the University of Florida in 1995 and 1998 respectively. His interests cover adhesion of diamond thin films, formation of large area surface structures by pulsed laser processing for electronic materials, nano functional material synthesis via pulsed laser processing of novel biomedical and electronic materials. He is the author of over 40 publications, 10 invited talks and has 6 patents pending. He has recently accepted a faculty position in the Department of Materials Science and Engineering at the University of Virginia, starting in May, 2000. Fitz-Gerald can be reached at the Naval Research Laboratory, Code 6372, Bldg. 74, 4555 Overlook Ave S.W. Washington, D.C. 20375 USA; e-mail: jfitz@ccsalpha2.nrl.navy.mil.

R. K. Singh

Dr. Rajiv K. Singh, is a Professor of Materials Science and Engineering and is also the Associate Director of the Particle Science and Technology Center at the University of Florida. He obtained his Ph.D. in 1989, in Materials Science and Engineering from North Carolina State University. He has nearly 300 publications in the area of innovative processing of materials including laser processing of materials, thin films and particle coatings. He has been issued over 10 patents and edited 4 books in this area. He is the recipient of several awards, including the National Science Foundation Young Investigator Award and the Hardy Gold Medal from TMS/AIME.

Author's short biography

H. Gao

Hongjun Gao, received his Ph.D at Peking University in 1994, for his work on ultra-high density data storage, which was selected as the best Ph.D dissertation of the year in China. He then moved to the Beijing Laboratory of Vacuum Physics, Institute of Physics, Chinese Academy of Sciences, and became an associate Professor and full Professor in 1994 and 1995, respectively. He was conference secretary for the Fourth International Conference on Nanometer-Scale Science and Technology (NANO IV), held in Beijing, China in 1996. Since 1997, he has been a guest scientist working in the Solid State Division, Oak Ridge National Laboratory. Gao has two invited book chapters and about 50 Journal articles. His research work covers structure and properties of organic-inorganic complexes, ultrahigh density data storage on organic thin films by scanning probe microscopy, molecular beam expitaxial growth of metals, and characterization of ferroelectric, collosal magnetoresistant, cathodoluminescent, mesoporous and nanoparticulate materials by TEM, Z-contrast STEM, and electron energy loss spectroscopy (EELS).

S.J. Pennycook

Stephen J. Pennycook is a corporate fellow in the Solid State Division at Oak Ridge National Laboratory and leader of the Electron Microscopy Group. He obtained his Ph.D. in Physics from the University of Cambridge, England, in 1978, joining the staff at Oak Ridge National Laboratory in 1982. His main research interest is the study of materials through the technique of Z-contrast scanning transmission electron microscopy. Pennycook is a fellow of the American Physical Society and is author or coauthor of over 300 publications. Awards for his work include two DOE Awards for Outstanding Achievement in Solid State Sciences and Metallurgy and Ceramics, an R&D 100 Award, the Heinrich Award from the Microbeam Analysis Society, and the Materials Research Society Medal.

Developing an Effective Control Strategy for Granulation Processes†

A. Adetayo, B.A. Ogunnaike and M. Pottmann
*E.I. duPont de Nemours and co.**

Abstract

The main objective of granulation processes is to produce granules with specific physical properties based on the end usage. The numerous disturbances associated with most granulation processes causes significant variations in first pass yield. Development and application of a yield based on-line control strategy is essential to maintaining consistent product quality. This paper highlights the problems associated with, and the need for, the development and online implementation of a yield based control scheme that controls appropriate physical properties of the granules exiting the granulator. A multi-level control scheme using process models of varying complexity is proposed. This paper discusses some of the results from online implementation of a section of this control scheme on a continuous granulation unit.

Introduction

Granulation is a particle size enlargement process that is widely used in the agricultural, pharmaceutical, food, metallurgical and ceramic industries. Granules have better handling properties, are free flowing, less dusty and have significantly lower explosion potential.

In a typical industrial granulation process, the objective is to produce granules with consistent product quality. For Agro-chemicals, these physical properties include attrition, bulk density, breakage resistance, size uniformity and dispersion rate. These properties are related directly or indirectly, to two fundamental quantities: particle size distribution and bulk density. Maximizing the product yield defined as the percentage of manufactured product having the required physical property is the main economic objective. Although product specification on granule size may vary from product to product and from plant to plant, they are typically of the form of an upper limit d_u and a lower limit d_L, as specified by the screen sizes used in product classification. Granules exceeding d_u in size are classified as *oversize* while those below d_L are classified as *undersize*. Acceptable product granules are those within these size classes that have the desired physical properties. As a result of this strict product specification, a first pass yield of less than 40% is not uncommon.

Up until now, online control of granulation processes has been restricted to stabilizing process flow rates. Quality control is typically achieved by adjusting the liquid flowrates through the different nozzles, the point of liquid addition and the specific amount of liquid introduced at each location. Product quality control is performed manually with particle size measurements taken rather infrequently, typically via sieve analysis. On-line size characterization of wet granules is desirable for many reasons. Firstly, granule densification, breakage and coalescence that occur on the sieves and in the drier are eliminated from the analysis. Secondly, measurement dead time is significantly reduced from approximately 60 minutes (depending on the size of the drier) to less than 2 minutes making it easier to monitor the response of the process to changes in the operating variables. Recent advances in light scattering technology makes on-line size characterization of free-flowing granules possible. Commercially available instruments like the Sympatec Helos® can now measure granule sizes up to 3.5mm in diameter paving the way for the development and on-line implementation of advanced process control schemes.

In addition to the challenges of obtaining reliable online particle size measurements, there are many factors that make implementation of online particle size

* Experimental Station, E308/225, Wilmington, DE 19880, USA
† Received July 20, 1999

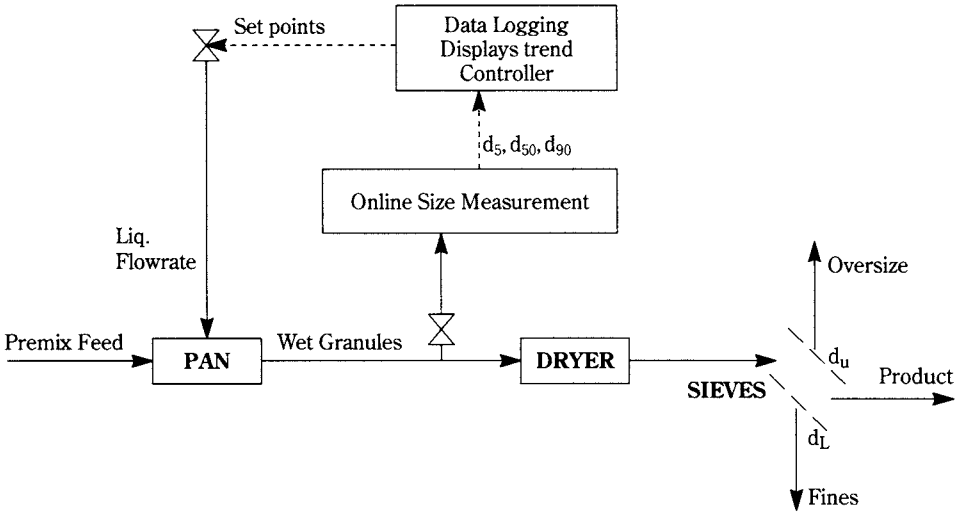

Fig. 1 Schematic Diagram of the Experimental Setup

control difficult [4]. For most granulation processes, especially those involving recycle streams, a complex interaction exists between the operating variables, the unit operations and the product yield [1]. For such systems, a plant-wide control strategy is desirable. Prior to designing a plant-wide control scheme, one needs to be able to control the granulation unit.

This paper presents a summary of the development and successful implementation of a yield based model predictive control (MPC) scheme on a pan granulation unit. Results from on-line characterization of both the size distribution and, the bulk density of the granules exiting the pan are used in the feedback loop of the MPC. For the feed-forward/feedback analysis, the feedrate is taken as the measured disturbance. Note, this yield-based scheme is applicable to other granulation processes: In the drum granulation circuit [1], the optimization section might use a model that accounts for the effects of drum speed, drum angle and spray zones while the control section uses the liquid flowrate as the manipulated variable. Similarly, in a fluid bed granulation unit, the optimal section can be used to optimize nozzle location, air velocity, liquid droplet size etc. while the control section uses the liquid flowrates to achieve the desired control objectives.

The Pan Granulation Process

In the pan granulation process, powder feed, 10±8μm in diameter, is continuously fed into a rotaring pan. Liquid binder (e.g. water) is introduced into the pan from one or more strategically chosen position(s). The liquid binder contacts the premix powder forming small particles known as nuclei which subsequently grow by layering/coalescence [2]. The flowrates through the nozzles can be used to adjust both the size and bulk density of the granules thus produced. The experimental setup is schematically depicted in **Figure 1**.

Representative samples of the wet granules exiting the pan are collected at regular intervals for online size measurement using a forward laser scattering instrument. With the help of a data acquisition program, information on d_5, d_{50} and d_{90} is transmitted to and graphically displayed on a computer screen. The terms d_5, d_{50} and d_{90} represent the 5^{th}, 50^{th} and 90^{th} percentile of the granule size distribution respectively. With this setup, it is easy to quantify the effect of the total moisture content and its distribution in the pan on the sizes of the granules produced. **Figure 2** shows an example of how results from the online size analyzer compares with off-line classification by the sieving of the same sample. There is a good agreement between the two methods for a broad granule size distribution typically obtained in a process like this.

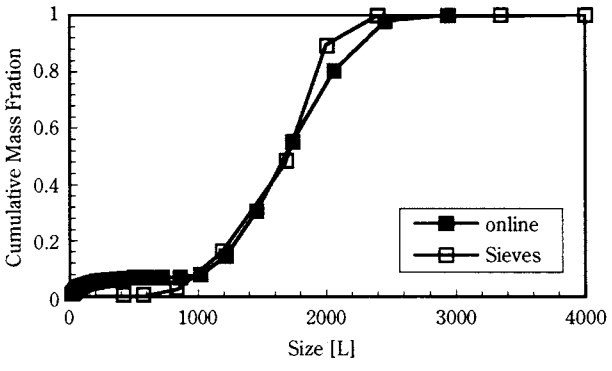

Fig. 2 Comparison of online/off-line Measurement

The Bulk Density

Figure 3 is an indication of the strong correlation that exists between the bulk density of the wet granules and that of the product. The product's bulk density lags behind the wet one by the estimated average residence time of the granules in the drier. An indirect control of the product's bulk density can therefore be achieved by controlling the bulk density of the wet granules.

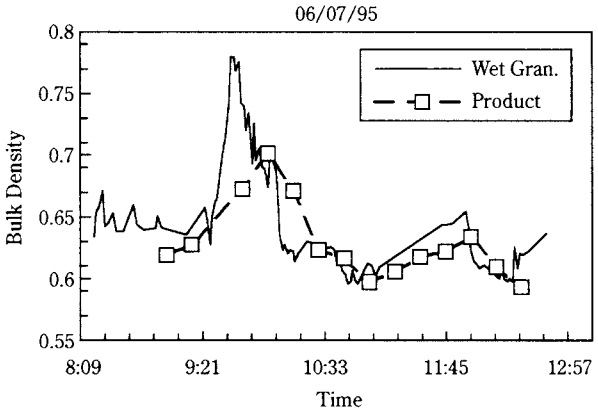

Fig. 3 A comparison of the Wet and Dry Bulk Densities

The Model Development

Model identification was done by making step changes to the liquid flowrates through each nozzle while keeping all other process variables constant. Open loop response data shows that while the 90th and 50th percentiles of the exiting granule size distribution go through a minimum as binder content increases [2, 3], the 5th percentile, an indication of the amount of 'fines' produced increases monotonically with liquid content [2]. This indicates the existence of an operating region where the granule size distribution has the lowest spread. Day-to-day variations in the attained steady states under otherwise constant operating conditions were also noticed. These factors present significant challenges to the development and online implementation of an effective control strategy. A yield based multi-level, model predictive control scheme is proposed for optimal operation of this process. **Figure 4** shows the block diagram of the proposed control scheme which has two sections; the optimization and control sections.

The Model Predictive Control Scheme

A dynamic non-linear model that accounts for the significant interactions among the variables such as pan angle, pan speed and nozzle positions affect the product properties is required at the optimization level. The effectiveness of this level depends on one's understanding of the process and, the model's accuracy. This level can be used to specify the optimal pan speed, pan angle, nozzle position for a given formulation during startup. The optimization level can also be called upon when the control section cannot achieve the desired control objectives at the current operating condition. Online comparison of the non-linear model prediction and the measured size distribution is used to determine the accuracy of the model and the effect of unmeasured disturbances.

At the control level, liquid flowrates through the nozzles, N_i are manipulated by the control scheme to achieve the control objectives outlined below. Depending on the process dynamics, a linear or multi-linear (to take care of the negative steady state gain of the d_{90}-liquid content relationship) empirical model is sufficient. A summary of the linear first order transfer function model with time delay used for this application is given below. Detailed description of the control scheme and model development is presented elsewhere [5, 6]

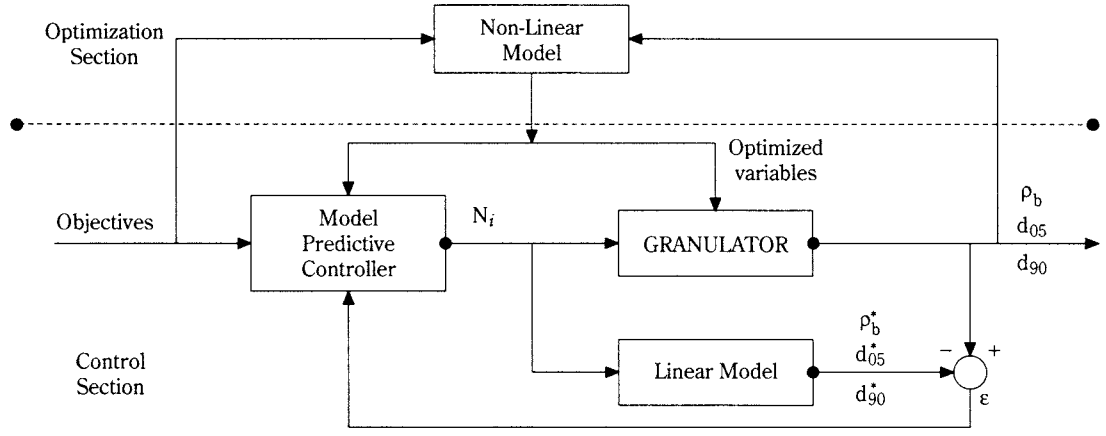

Fig. 4 Schematic Diagram of the Multi-Level Control Strategy

The Linear Model

Introducing model inputs and outputs as deviations from their nominal respective values,

$$u_i = N_i - N_i^o \qquad i = 1, 2, 3$$
$$y_1 = \rho_B - \rho_B^o$$
$$y_2 = d_5 - d_5^o$$
$$y_3 = d_{90} - d_{90}^o$$

where N_i represent the liquid flowrates through nozzle i. This granulation process is equipped with three spray nozzles. ρ_B represents the granules bulk density and the superscript 'o' represents the nominal (steady state) values of the variables. The linear discrete-time model is of the form:

$$\begin{bmatrix} y_1^*(z^{-1}) \\ y_2^*(z^{-1}) \\ y_3^*(z^{-1}) \end{bmatrix} = \begin{bmatrix} g_{11}(z^{-1}) & g_{12}(z^{-1}) & g_{13}(z^{-1}) \\ g_{21}(z^{-1}) & g_{22}(z^{-1}) & g_{23}(z^{-1}) \\ g_{31}(z^{-1}) & g_{32}(z^{-1}) & g_{33}(z^{-1}) \end{bmatrix} \begin{bmatrix} u_1(z^{-1}) \\ u_2(z^{-1}) \\ u_3(z^{-1}) \end{bmatrix}$$

Here, y_i^* represents the model prediction which is different from the actual process data, y_i. The experimental step response data indicate that simple first-order plus time-delay transfer functions, g_{ij}, are adequate to represent the behavior observed in each of the responses, at least for moderate deviations from the nominal operating point.

$$g_{ij}(z^{-1}) = \frac{k_{ij} z^{-\theta_{ij}}}{1 + \tau_{ij} z^{-1}}$$

k_{ij} and τ_{ij} are the gain and time constants respectively.

The Model Predictive Control Scheme

Due to the limited capacity of the nozzles, lower and upper bounds are imposed on their flowrates. The overall yield based process control strategy adopted for this study is;

1. Monitor and control the bulk density, ρ_B around its setpoint, ρ_B^*
2. Maintain d_{90}, the 90th percentile of the granule size distribution below the upper limit, d_u.
3. Maintain d_5, the 5th percentile of the size distribution above the lower limit, d_L.

The control objectives at every sampling instance can be represented mathematically as,

$$\rho_B(t) = \rho_B^r(t) \pm \varepsilon_B$$
$$d_5(t) \geq d_L$$
$$d_{90}(t) \leq d_U$$

subject to

$$N_i^{\min} \leq N_i(t) \leq N_i^{\max} \qquad i = 1, 2, 3$$

ρ_B^r is a reference trajectory for the granule's bulk density and ε_B is the allowable deviation in ρ_B.

Note that this strategy guarantees a product yield of at least 85%. The decision on the percentiles of interest depends on one's knowledge of the physics of the process, the material being granulated, the reliability of the measuring instrument and the targeted yield increment. It is practically impossible to control a size distribution. Granulation processes do not have enough actuators to arbitrarily "shape" the particle size distribution. The approach taken here to control two points on the PSD requires at least two input variables that have a significantly different effect on the chosen percentiles.

Results and Discussions

Experiments were conducted with both the feedback-feedforward and feedback only control actions. For the feedback only control scheme, information on feedrate changes is not communicated to the controller. This simulates cases of unmeasured disturbances. The second scheme combines a feedforward action using a simple ratio controller that maintains a constant liquid flowrate to feedrate ratio and a feedback action using feedback information from online granule characterization. The performance of the controller using the combined feedback/feedforward action can be greatly improved if a better model is used.

Feedback Control

Figure 5 shows the closed-loop response to a change in the powder feed rate from 320 to 350 [MT^{-1}] when feedback control alone is used. The response is rather sluggish because a small weight [5, 6] is used for density tracking, and neither d_5 nor d_{90} initially violates their constraints. Significant changes in the nozzle flowrates are initiated as d_5 approaches and subsequently violates its lower bound at 400μm. Although the nozzles saturate at their upper bound, (i.e. the valves are fully opened), the control system returns the pan back to acceptable operating conditions.

Combined Feedback/Feedforward Control Scheme

Figure 6 shows the rejection of a step disturbance in the feed rate from 350 to 320 [MT^{-1}] when the combined feedback/feedforward control scheme is used.

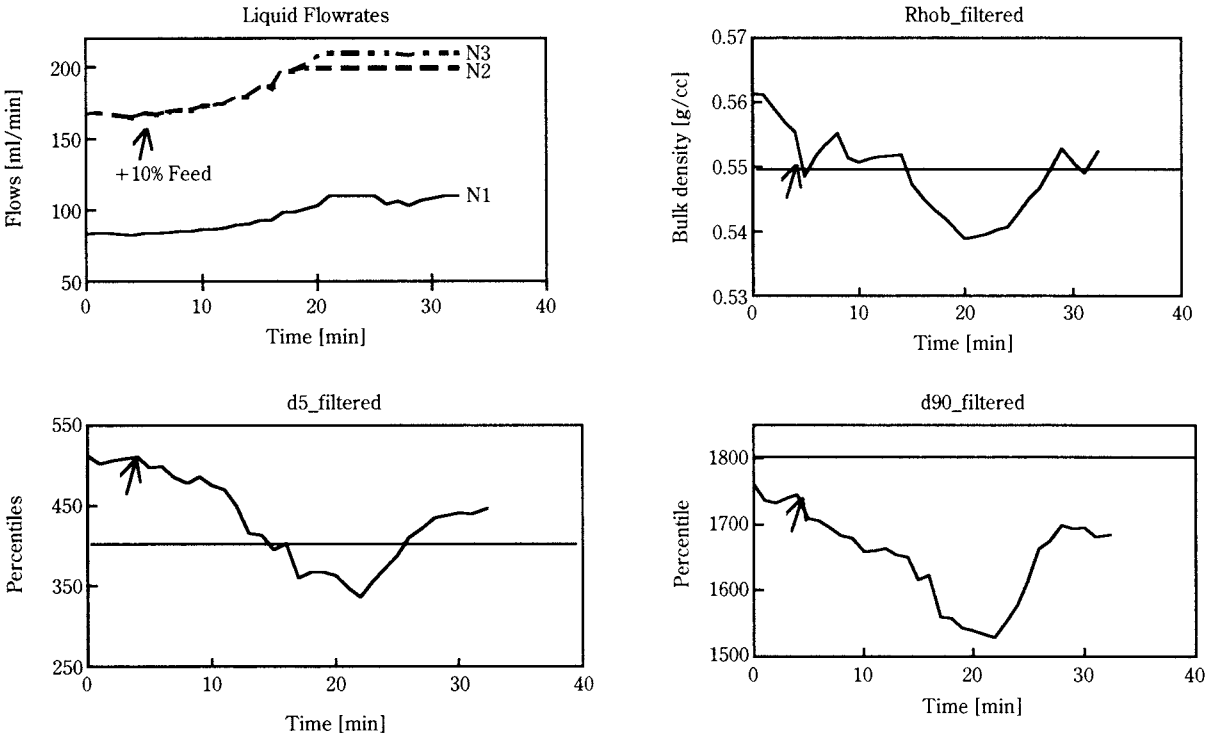

Fig. 5 Feedback control rejection of a Feedrate disturbance [5]

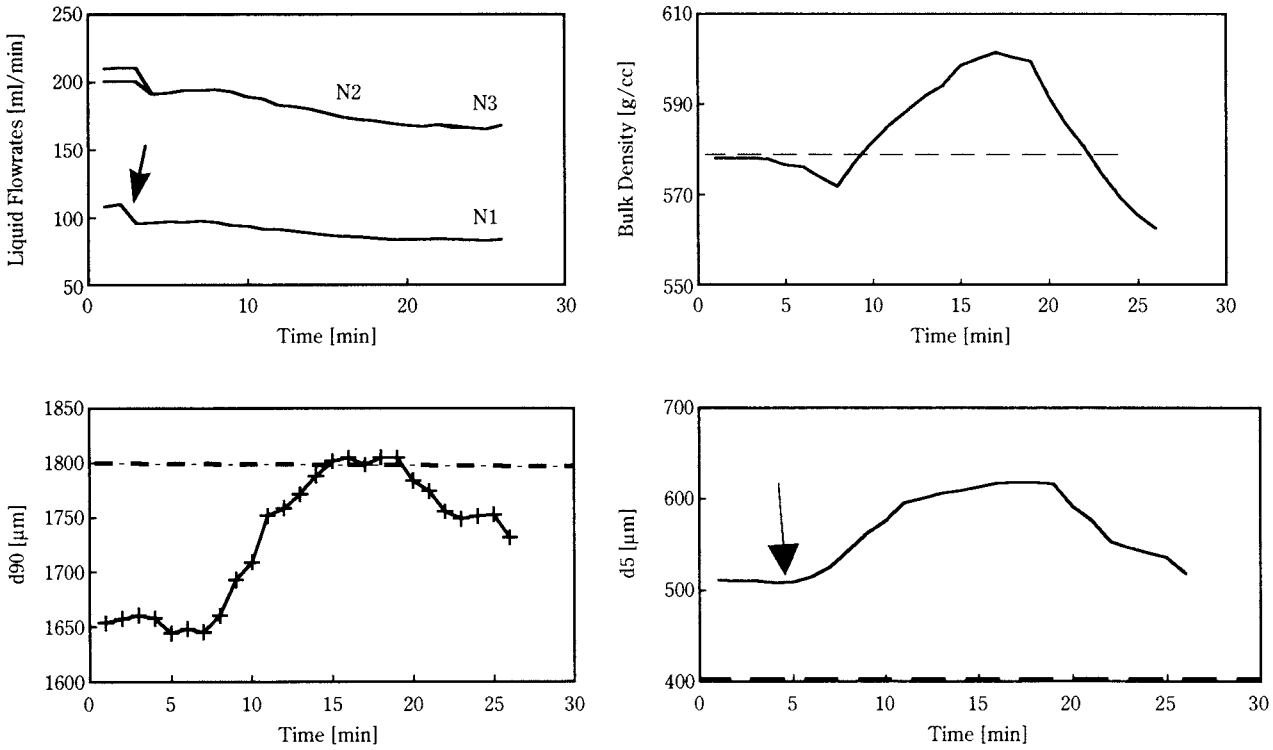

Fig. 6 Feedback/Feedforward rejection of a Feedrate Disturbance [6]

The arrow indicates the position of the step change. The feed-forward action is based on premise of maintaining constant liquid flowrate to feedrate ratio. The drop in the feed rate causes an immediate step change in the nozzle flowrates of identical relative magnitude. However, this decrease is not sufficient to compensate for the decreased feed rate, as both d_5 and d_{90} starts to increase considerably. Additional decreases in the nozzle flow rates are required to eventually return the pan to its nominal operating conditions.

This additional decrease in liquid flowrate shows the premise of a constant total moisture/feedrate ratio, on which the feed-forward control action is based on, is not a good approximation, at least not for the magnitude of feed rate changes implement here. The fact that the moisture content had to be reduced by more than the expected amount can be explained by the well known observation that a reduced feed rate results in a longer residence time in the pan. The particles then have more time to grow. For this reason, the total moisture has to be reduced even more to compensate for the additional factor that favors particle growth. Note, without these control actions, these disturbances would have resulted in a significant reduction in the first pass yield.

Conclusions

This report presents a successful demonstration of on-line granule size and bulk density characterization. With the on-line particle sizer, effects of process disturbance due to changes in input or disturbance variables can be monitored within a few minutes! This is a vast improvement over what is currently possible i.e. granule characterization after drying and screening, a process which, depending on the granule's residence time in the dryer could take up to 60 minutes. In addition to the shorter dead time, the current approach eliminates the screen and dryer dynamics from the analysis.

A yield based multi-level control scheme that ensures a predefined yield is maintained is successfully implemented on a pilot plant granulation unit. This control scheme uses different models of varying complexities at its control and optimization section. This paper shows that *effective control of key process variables using on-line particle size measurements is feasible.*

Acknowledgements

G. Sunshine, K. Pyada and the operating technicians of Ag product's Semi-works for their help in data acquisition.

References

1) Adetayo, A.A., Litster, J.D. and Cameron, I.T., "Steady State Modeling and Simulation of a Fertilizer Granulation Circuit", *J. Comp. and Chem. Eng.*, 19,4, (1995) 383-393.
2) Adetayo A.A. and Pottmann, M., "Experimental Verification Of Steady-State Multiplicities in Pan Granulation", *Second Israel Conference for Conveying and Handling of Particulate Solids, Beer Sheva, Israel* (1997).
3) Fillipova, K.I., Bochkarev, V.M. and Sinegribov, V.A., *Soviet Chem. Ind.*, 2(1972)114-117.
4) Heiskanen, K., "On the difficulties of implementing particle size control in particulate processes", Powder Tech., 83, (1995) 13-19
5) Pottmann, M., Ogunnaike, B.A., Adetayo, A.A. and Ennis, B.J., "Model Based Control of a Continuous Granulation Process", (1998) in preparation.
6) Pottmann, M., Ogunnaike, B.A., Adetayo, A.A. and Ennis, B.J., "Model Based Control of a Granulation System", *Preprints of the Control of Particulate Processes IV, Alberta, Canada* (1995).

Author's short biography

Anthony Adetayo

Anthony Adetayo is a Senior Research Engineer at DuPont's Ag Enterprise. He received a degree in Chemical Engineering from the University of Lagos, Nigeria in 1988. He joined DuPont's Central Research and Development group after obtaining a PhD in Chemical Engineering from the University of Queensland, Australia in 1993. His research interests include granulation, material handling, granule segregation and, modeling, simulation and control of particulate processes.

Babatunde A. Ogunnaike

Babatunde A. Ogunnaike, B.S. (Chemical Engineering), M.S (Statistics), Ph.D. (Chemical Engineering), is currently a Research Fellow in the Advanced Control and Modeling group, DuPont Central Research and Development; he is also an adjunct professor in the Chemical Engineering Department, University of Delaware. His research interests include identification and control of nonlinear systems, modeling and control of polymer reactors and distillation columns, applied statistics, and biosystems analysis and control.

Martin Portmann

Martin Portmann is a Senior Engineer with DuPont DACRON. He received his doctoral degree from the University of Technology, Vienna, in 1993, and a M.S. degree in Chemical Engineering from the University of California at Santa Barbara in 1991. He joined DuPont's Central Research and Development Department in 1993, and has been involved in a variety of research and application projects in process modeling and advanced control.

A Model of Liquid-phase Homogeneous Nucleation in a System Containing Seed Particles†

Yasuo Kousaka, Toshiyuki Nomura, Shinji Hasebe and Ken Tanaka
*Chemical Engineering Department, Osaka Prefecture University**
Manuel Alonso
*National Center of Metallurgical Research, Avda Gregorio del Amo***

Abstract

This paper deals with particle formation by homogeneous nucleation in a system containing seed particles. A model of homogeneous nucleation previously developed by the present authors[1] is here extended to include the effect of the presence of seed particles. To this end, the cell model upon which the original model was based has been modified to account for the random distribution of the inter-particle distances in the medium. Liquid-phase experiments, in which particles have been generated by a chemical reduction method with varying number concentrations of seed particles and generation rates of precursor monomers, have confirmed the validity of the model. The proposed model enables determination of the operating conditions where 1) homogeneous nucleation is predominant, 2) particle growth is predominant, and 3) homogeneous nucleation and particle growth coexist.

1. Introduction

In order to selectively promote the enlargement of particles present in a medium by means of precursor monomer nucleation onto their surfaces, it is necessary to avoid the formation of new particles by self-nucleation. Presently, however, there is no theory for determining under which conditions self-nucleation is suppressed. We have recently developed, and successfully verified, a new model of homogeneous nucleation in the absence of seeds.[1] The objective of this paper is to extend this analysis to account for the effect of the presence of seeds on new particle formation by self-nucleation. The predictions of the proposed model will then be compared with experimental results obtained for liquid-phase particle formation by a chemical reduction method.

2. Theory

2.1 Conditions for Self-Nucleation in the Presence of Seed Particles

In our previous investigation[1] we arrived at the following relationship between the number concentration n^* of nucleated particles and the critical monomer generation rate G^*:

$$G^* = 4\pi r^* D C^* n^*. \quad (1)$$

In this expression, r^* is the radius of the critical nucleus ($r^* \approx 1$ nm), D the diffusion coefficient of monomers (atoms or molecules of the precursor material), and C^* the critical saturation concentration of monomers, i.e. the minimum concentration required for the appearance of new nuclei. When the particle concentration in the system is n^*, the monomer generation rate G must be larger than G^* in order to have further particle formation by self-nucleation. Thus, when the number of nucleated particles has become so large that $G < G^*$, homogeneous nucleation stops, no new nuclei can be formed, and the particle number concentration remains constant thereafter.

When seed particles of radius r_p and number concentration n_p are present in the medium, we can write an expression similar to the above:

* 599-8531 Sakai, Japan
** 8, 28029 Madrid, Spain
† This report was originally printed in Kagaku Kogaku Ronbunshu, **23**, 673-678 (1997) in Japanese, before being translated into English by KONA Editorial Committee with the permission of the editorial committee of the Soc. Chemical Engineers, Japan.

$$G_p = 4\pi r_p D C^* n_p. \quad (2)$$

Equating equations (1) and (2) yields

$$n^*/n_p = R,\ R = r_p/r^*. \quad (3)$$

Therefore, the attainable number concentration of nucleated particles in a system without seeds is R times that in a system with seeds, other conditions being equal. The reason is that the depletion rate of monomers per seed is R times larger than the depletion rate per nucleus.

When $G > G_p$, the depletion of monomers by seeds is low enough so that $C > C^*$ and new particles can be formed by homogenous nucleation. In this case, monomers are used for new particle formation as well as for particle growth, and hence we can write

$$G = G_p + G^* = 4\pi D C^* r^* (R n_p + n^*). \quad (4)$$

In these circumstances, the number concentration of nucleated particles and the total number concentration of particles become

$$n^* = \frac{G}{4\pi r^* D C^*} - R n_p, \quad (5)$$

$$n_T = n^* + n_p = \frac{G}{4\pi r^* D C^*} + (1-R) n_p, \quad (6)$$

respectively. Equations (5) and (6) are valid when $G > G_p$, and cannot be used for the reverse case of $G < G_p$. Obviously, in the latter situation no new particles can be formed by self-nucleation. Clearly, the condition required for new particle formation by homogeneous nucleation ($n^* > 0$) is readily obtained from equations (4) or (5) as

$$G > 4\pi D C^* r^* R n_p. \quad (7)$$

This implies that homogeneous nucleation is suppressed when the number concentration of seed particles is larger than $1/R$ (< 1) times the attainable number concentration of nucleated particles in a system without seeds. It further follows from equation (7) that the conditions for homogeneous nucleation suppression depend essentially on the monomer diffusion coefficient, the critical supersaturation concentration of monomers, the size and number concentration of seed particles, and the conditions under which monomer generation takes place (temperature, reaction rate).

Figure 1 illustrates the variation with reaction time of variables such as the seed radius r_p, the radius of the nucleated particles r^*, the total number concentration of particles n_T, the monomer concentration C, and the monomer concentration C_m that would result if neither nucleation nor particle growth had taken place. **Figure 1 (a)** describes what happens when $G < G_p$, that is, when no particles can be formed by self-nucleation because the monomers are consumed solely in seed particle growth, thereby always keeping the monomer concentration below the critical concentration C^*. **Figure 1 (b)** corresponds to $G > G_p$, that is, when conditions are favorable to new particle formation by homogeneous nucleation. The time t^* at which the monomer concentration in the liquid medium attains the critical value C^* is the starting point of self-nucleation. During a certain time interval Δt^* the monomer concentration is still high enough to produce new particles; at the same time, however, the rate of monomer depletion by diffusion toward particle surfaces steadily increases as new particles are being formed. Thus a time $t^* + \Delta t^*$ is reached at which the depletion rate has become so large that the monomer concentration in the medium falls below the critical value C^*, stopping homogeneous nucle-

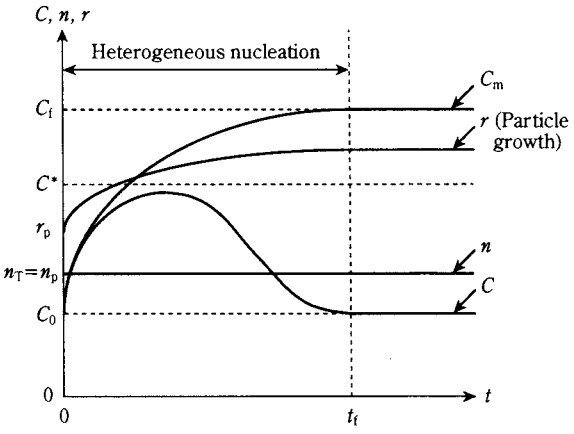

(a) No homogeneous nucleation takes place

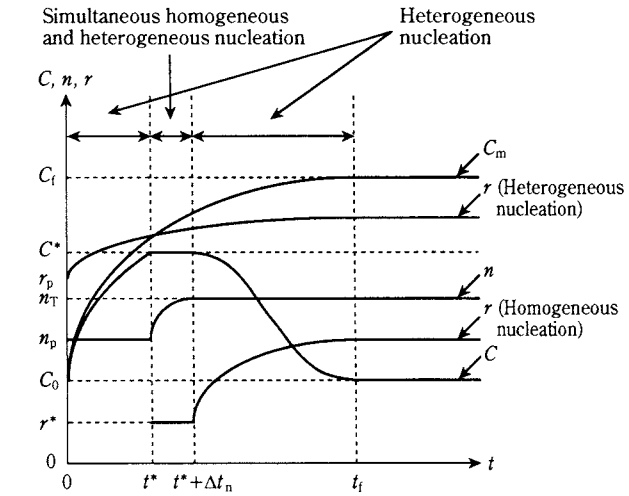

(b) New particle formation by homogeneous nucleation takes place

Fig. 1 Illustration of homogeneous and heterogeneous nucleation in a system containing seed particles

ation. From this point on the generated monomers are consumed exclusively in particle growth, until the monomer concentration finally attains the saturation value C_0.

Consider first the absence of seed particles from the system. When the number concentration of nucleated particles is n_0^*, the critical monomer generation rate G_0^*, above which new particles can be formed in the absence of seeds, is given by

$$G_0^* = 4\pi r^* D C^* n_0^*. \tag{8}$$

(This is the same as equation (1) except that we have attached a subscript 0 to the appropriate variables to indicate that they refer to a condition in which seeds are absent from the system.) If, under the same operating conditions, seed particles (radius r_p, number concentration n_p) are also present in the medium, we can use equation (4) with G_0^* instead of G, and solve for the number concentration of nucleated particles, resulting in

$$\frac{n^*}{n_0^*} = 1 - R\frac{n_p}{n_0^*}. \tag{9}$$

The total number of particles thus becomes

$$\frac{n_T}{n_0^*} = \frac{n^*}{n_0^*} + \frac{n_p}{n_0^*} = 1 + \frac{n_p}{n_0^*}(1-R) \tag{10}$$

Equations (9) and (10) are plotted in **Figure 2**. Consider, for instance, the curve for the seed-to-nucleus size ratio $R=100$: when the seed number concentration is such that $n_p/n_0^* > 10^{-2}$, no new particles can be formed by homogeneous nucleation, but as the seed number concentration is reduced, the total number concentration of particles n_T gradually approaches the limiting value n_0^*, which corresponds to a system without seeds.

2.2 Modification of the Cell-Model to Account for the Presence of Seeds

So far, the model for simultaneous homogeneous and heterogeneous nucleation has been based on our original development using a cell-model with constant cell radius b[1]. However, a modification of the cell-model is necessary in order to reproduce the experimental results of nucleation in the presence of seeds. The constant-size cell model assumes that all the particles are equally spaced. Actually, the particles are randomly distributed in the medium, so that the distance between neighboring particles follows a certain distribution law. As illustrated in **Figure 3**, monomers generated in regions where the seeds are separated by very small distances are depleted through condensation onto seed surfaces. Conversely, new nuclei can only be formed in those places where the distance between particles is larger. Therefore, one must somehow consider the random distribution of seeds in the medium in order to arrive at a more realistic description of the nucleation process.

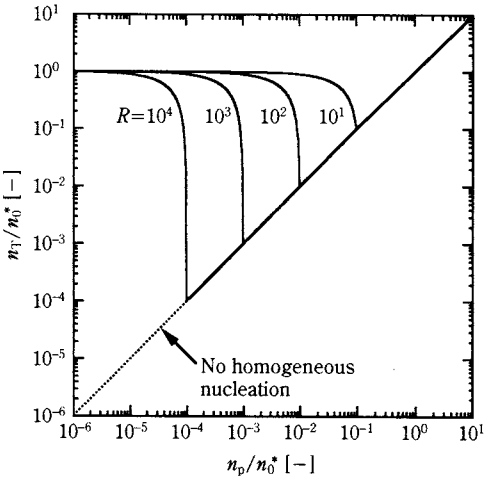

Fig. 2 Relationship between total number concentration of particles n_T and number concentration of seeds n_p as a function of the seed-to-nucleus size ratio R

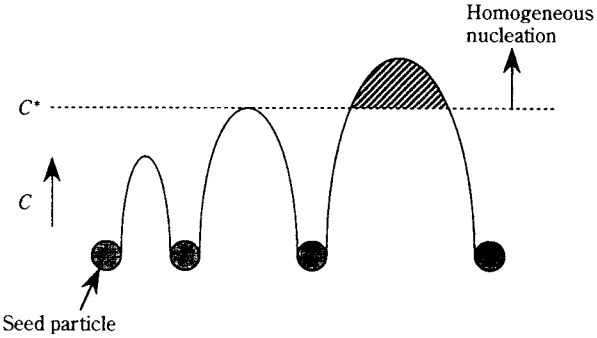

Fig. 3 Effect of the random spatial distribution of seeds on the monomer concentration profile in their vicinity

The cell-model modification we propose is to assume that, contrary to the above equations, new nuclei can still be formed (i.e. $C > C^*$) even when $G < G_p$, but only in a fraction v^* of the total number of cells. Hence, the number concentration of self-nucleated particles can be written as $v^* n_0^*$ when the seed concentration is so large that $G < G_p$. An estimation based on kinetic theory arguments led to a value of $v^* = 0.16$ for the number fraction of cells where homogeneous nucleation can occur.[2] Accordingly, the total number concentration of particles (seeds plus self-nucleated) should be rewritten as

$$\frac{n_T}{n_0^*} = \frac{n^*}{n_0^*} + \frac{n_p}{n_0^*} = \begin{cases} 1 + (1-R)\dfrac{n_p}{n_0^*} & \text{for } Rn_p < n_0^*(1-v^*) \\ v^* + \dfrac{n_p}{n_0^*} & \text{for } Rn_p > n_0^*(1-v^*) \end{cases} \tag{11}$$

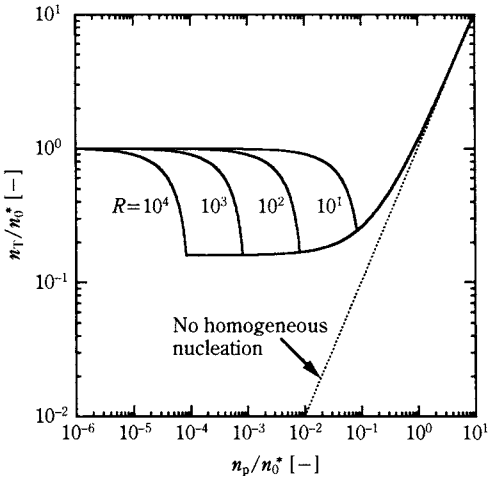

Fig. 4 Effect of the seed-to-nucleus size ratio R on the relative importance of homogeneous and heterogeneous nucleation

Equation (11) is plotted in **Figure 4** for several values of the seed-to-nucleus size ratio R. According to the cell-model modification just introduced, homogeneous nucleation is never completely suppressed, no matter how large the seed number concentration is, although for quite high seed concentrations the relative importance of self-nucleation is certainly insignificant.

3. Experimental Method

Silver particles were generated by the liquid-phase chemical reduction reaction

$$4AgNO_3+N_2H_4 \rightarrow 4Ag+N_2+4HNO_3 \qquad (12)$$

Three solutions were prepared: (A) 0.2 g of sodium polyacrylate in 1 ℓ of ultrapure water, (B) silver nitrate in ultrapure water, and (C) hydrazine in ultrapure water. The solution (C) was prepared with an amount of hydrazine larger than required by stoichiometry. 25 ml of each solution were placed in separate beakers in a water bath at 293 K. First, Ag seed particles were generated by pouring the solutions B and C simultaneously into a beaker containing solution A under agitation (particles obtained: diameter 0.3 μm, geometric standard deviation 1.5, number concentration 3×10^{17} m^{-3}); the number concentration of seed particles could then be changed at will by adding the required amount of ultrapure water. The solution containing the seed particles called D. In order to modify the size of the silver seed particles, 25 ml of solution B was added to 25 ml of solution D under agitation. Two types of experiments were then carried out: 1) varying the concentration of silver nitrate in solution B, thereby modifying the monomer generation rate G (this rate is proportional to the concentration of silver nitrate), and 2) varying the size of the seed particles, thereby modifying the depletion rate of monomers by diffusion toward the particles' surfaces. Furthermore, in the type 1) experiments we employed different seed particle sizes, which were prepared by adding to solution D (diameter 0.3 μm, geometric standard deviation 1.5, number concentration 3×10^{17} m^{-3}) a solution of high-concentration silver nitrate. Using this procedure we were able to obtain seeds with average diameters 0.5 and 1.0 μm, both of which had a geometric standard deviation of 1.5. The reason for using ultrapure water in the experiments was to prevent the presence of contaminants that could act as undesired nucleation seeds. The zeta potentials of the solutions were measured before and after particle generation by nucleation. The measured values were always above 20 mV, which means that particle coagulation did not occur in the medium during the experiments. The number concentration and size of the generated silver particles were measured following the same procedure described in our previous works.[1,2]

4. Results and Discussion

Figure 5 shows the results of the experiments carried out by adding silver nitrate solutions of different concentrations to a suspension of 0.3 μm seed particles. As explained above, varying the concentration of silver nitrate is equivalent to modifying the monomer generation rate G. The straight dotted line in this Figure corresponds to the extreme case in which homogeneous nucleation does not occur at all, so that the total number concentration of particles in the system is simply equal to the number concentration of seeds,

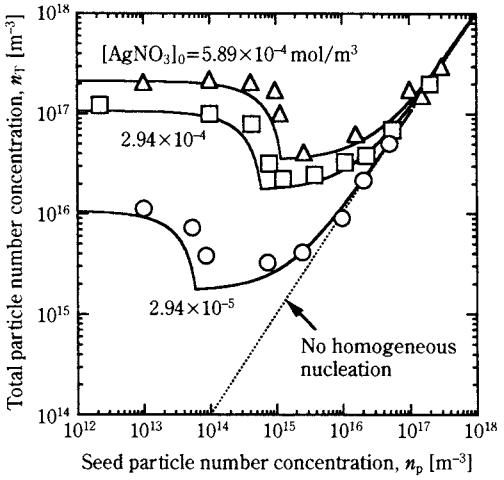

Fig. 5 Comparison of experimental and calculated results (seed-to-nucleus size ratio R=150 [r_p=0.3 μm]; initial $AgNO_3$ concentration [mol/m^3] ○: 2.94×10^{-5}, □: 2.94×10^{-4}, △: 5.89×10^{-4})

i.e., monomers are only used for seed growth ($n^*=0$). From our previous experiments[1] we know the number concentration n_0^* of nucleated particles in the absence of seeds as a function of the concentration of silver nitrate in the solution. The curves plotted in **Figure 5** were calculated with equation (11) using the previously known values of n_0^*, the theoretically estimated value of the fraction of cells of sizes larger than the average ($v^*=0.16$), and the seed-to-nucleus size ratio $R=r_p/r^*=150$ ($r_p=150$ nm, $r^*=1$ nm). As seen in the Figure, when the seed number concentration n_p is very low, the total number concentration of particles in the system is practically constant, independent of n_p. The reason is that when n_p is very low, the generation rate of monomers G is much larger than the monomer depletion rate by diffusion toward seeds ($G \gg G_p$) and homogeneous nucleation is predominant. At the other extreme, when the seed number concentration is very high, homogeneous nucleation is practically suppressed. At intermediate levels of seed concentration both mechanisms – self-nucleation and particle growth – coexist. The existence of these three different situations, namely, predominant homogeneous nucleation, coexistence of nucleation and growth, and predominant particle growth, has been also verified in gas-phase systems.[3] According to the theoretical curves plotted in **Figure 2**, homogeneous nucleation is suddenly suppressed at a certain value of the seed number concentration, and this causes a sharp decrease in the total number of particles in the system. This is, however, in clear contradiction to the experimental data plotted in **Figure 4**. Modification of the cell-model to account for the number fraction of cells with sizes larger than the average ($v^*=0.16$) produces a theoretical picture markedly different from that of **Figure 2**. That is, now the suppression of self-nucleation with an increasing number concentration of seeds is not a clear-cut phenomenon, but rather one which takes place gradually in such a manner that, in fact, homogeneous nucleation is never completely suppressed. The reason for this is found in the random spatial distribution of seeds in the medium whereby some interparticle voids are sufficiently large to permit the formation of new nuclei. This is also observed in **Figure 6**, which plots the same data as **Figure 5** but in non-dimensional form.

Figure 7 shows the results obtained in the experiments carried out at a constant monomer generation rate (i.e. a constant concentration of the silver nitrate solution) and a varying seed particle size. The diameters of the seeds used were 0.3, 0.5, and 1.0 μm, giving seed-to-nucleus size ratios R of 150, 250 and 500,

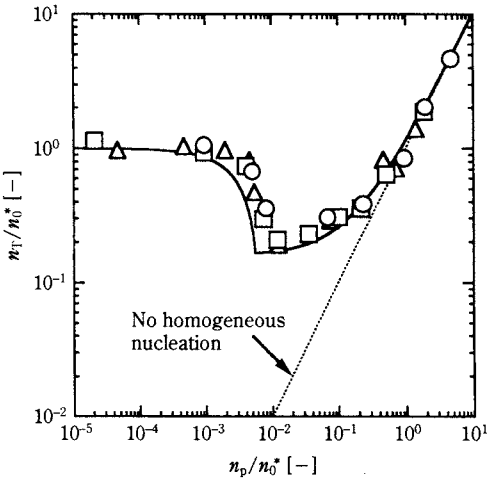

Fig. 6 Comparison of experimental and calculated results using non-dimensional variables (seed-to-nucleus size ratio R= 150 [r_p=0.3 μm]; initial $AgNO_3$ concentration [mol/m^3] ○: 2.94×10^{-5}, □: 2.94×10^{-4}, △: 5.89×10^{-4})

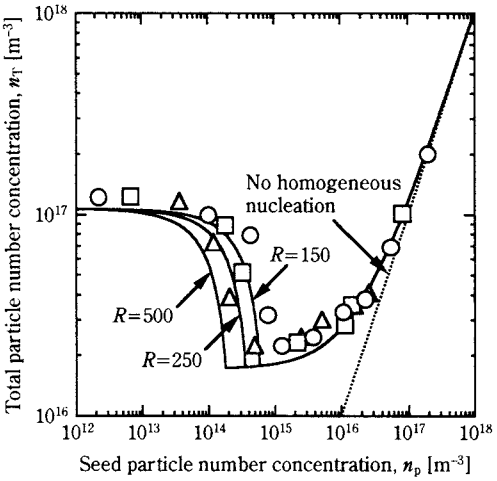

Fig. 7 Comparison of experimental and calculated results (initial $AgNO_3$ concentration 2.94×10^{-4} mol/m^3; seed-to-nucleus size ratio R ○: 150, □: 250, △: 500).

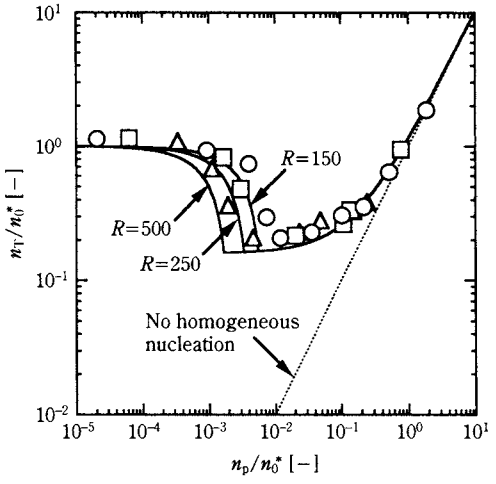

Fig. 8 Comparison of experimental and calculated results using non-dimensional variables (initial $AgNO_3$ concentration 2.94×10^{-4} mol/m^3; seed-to-nucleus size ratio R ○: 150, □: 250, △: 500).

respectively. The straight line has the same meaning as explained for **Figure 5**. The same data is plotted in non-dimensional form in **Figure 8**. From any of these two figures, we observe again the presence of three regions according to the level of seed particle number concentration: a region with predominant homogeneous nucleation and practically no particle growth (low n_p), a region with predominant particle growth and insignificant new particle formation by self-nucleation (high n_p), and an intermediate region where both phenomena coexist.

In summary, we have seen that the data obtained from two different types of nucleation experiments in the presence of seeds can be accurately predicted with the proposed modified-cell model, in which the random size distribution of the empty space between seeds has been taken into account.

5. Conclusions

Based on our previous work,[1] we have developed a practical model of homogeneous nucleation in the presence of seed particles, including the effect of the randomly-sized empty space among particles. We demonstrated that the model predictions are in excellent agreement with the results of experiments performed with varying monomer generation rates, and sizes and concentrations of seed particles. The model allows assessment of the operating conditions under which 1) homogeneous nucleation is predominant, 2) particle growth is predominant, and 3) both phenomena, self-nucleation and particle growth, coexist.

Nomenclature

b	: radius of unit cell	[m]
C	: monomer concentration	[kg/kg-liquid]
C_m	: monomer concentration without nucleation	[kg/kg-liquid]
C_0	: critical monomer saturation concentration	[kg/kg-liquid]
C^*	: critical monomer supersaturation concentration	[kg/kg-liquid]
D	: monomer diffusion coefficient	[m^2/s]
G	: monomer generation rate	[kg/(kg-liquid.s)]
G_p	: monomer generation rate with seed particles	[kg/(kg-liquid.s)]
G^*	: monomer generation rate when $n=n^*$	[kg/(kg-liquid.s)]
G_0^*	: monomer generation rate without seeds	[kg/(kg-liquid.s)]
n_p	: number concentration of seed particles	[m^{-3}]
n_T	: total number concentration of particles	[m^{-3}]
n^*	: number concentration of self-nucleated particles	[m^{-3}]
n_0^*	: number concentration of self-nucleated particles without seeds	[m^{-3}]
R	: seed-to-nucleus size ratio	[−]
r_p	: radius of seed particles	[m]
r^*	: radius of critical nucleus	[m]
t	: time	[s]
t^*	: time at which $C=C^*$	[s]
v^*	: number fraction of cells with radius larger than the average	[−]

References

1) Kousaka, Y. and T. Nomura, "Engineering model for homogeneous nucleation," *Kagaku Kogaku Ronbunshu*, **23**, 666-672, (1997).
2) Nomura, T., M. Alonso, K. Kousaka and K. Tanaka, "A model for simultaneous homogeneous and heterogeneous nucleation," *J. Colloid Interface Sci.*, **203**, 170-176, (1998).
3) Okuyama, K., R. Ushio and K. Kousaka, "Particle generation in a chemical vapor deposition process with seed particles," *AIChE J.*, **36**, 409-419, (1990).

Author's short biography

Yasuo Kousaka

The author is Professor of Chemical Engineering Department at Osaka Prefecture University since 1979. His major research interests are dynamic behavior of aerosol particles, sizing techniques of aerosol particles and powders, dispersion of aggregate particles in air and water, and particle formation by homogeneous and heterogeneous nucleation. He is currently the vice president of the Association of Powder Process Industry and Engineering, Japan.

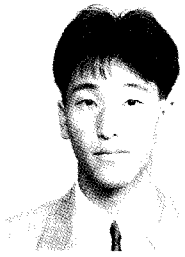

Toshiyuki Nomura

The author received his B.S. and M.S. degrees from Kyoto University in 1993 and 1995, respectively. He earned his Ph.D. degree in Chemical Engineering in 1999 from Osaka Prefecture University. He is Research Instructor of Chemical Engineering Department at Osaka Prefecture University since 1996. His major research interests are particle formation by homogeneous and heterogeneous nucleation, dynamic behavior of aerosol particles and electrostatic characteristics of powder.

Manuel Alonso

The author received his B.S. and M.S. degrees from the University of Malaga, Spain, in 1984 and 1985, respectively. He earned his Ph.D. degree in Chemical Engineering in 1991 from Osaka Prefecture University, where he later stayed as a Research Associate in 1994-1996. Since 1996 he is a tenured scientist at the National Center of Metallurgical Research in Spain. His research activities have ranged from Powder Technology in the past (powder mixing and coating, particle packings) to Aerosol Science at present (aerosol particle formation, coagulation, charging, size measurement, and filtration).

The Granulation Mechanism of a Tapered Fluidized Bed†

Yasushi Okada,
*Dept. of Chem. Eng. Nagoya Univ.***
Takaaki Sakai, Ryohei Yamazaki and Shigekatsu Mori
*Dept. of Pharmaceutical Res. & Technol., Eisai Co., Ltd.**

Abstract

Fluidized bed granulation is used widely in the manufacturing processes for solid drug products. It is known that optimum granulation conditions are not determined simply by the complexity of the operation factors. This study investigated the effects of manufacturing factors on the physical properties of granules in order to understand the granulation mechanism. Experiment results indicated that granule moisture content determines average particle size. A granulation model is proposed in accordance with a theoretical consideration of the physical properties of granules. The model was found to simulate granule density and bulk density. Also discussed is the scale effect of the experimental apparatus on the physical properties of granules.

1. Introduction

Fluidized bed granulators are widely used as solid drug product manufacturing machines that comply with good manufacturing practices (GMP). Especially because granules obtained with the fluidized bed granulation method are porous and have a comparatively uniform particle size distribution, this technique is often used to manufacture fine-grain and dry syrup preparations. Further, in recent years the validation of manufacturing methods has been required by law in order to guarantee the quality of pharmaceuticals, and that has necessitated a more scientific approach to manufacturing processes than before. As granulation is the most important process in the manufacture of solid pharmaceuticals, it is not an overstatement to say that drug manufacturing quality is determined by that process. However, the complexity of operational factors in the fluidized bed granulation process creates difficulty in setting the optimum manufacturing conditions, and results in frequent quality problems when increasing manufacturing scale. Several past studies have investigated operational factors in fluidized bed granulation, such as kinds of binders[1,2], amount of moisture adhering to particles[3], and diameter of spray droplets[4], and they report on these factors' effects on the granules formed. But as few reports take up the granulation mechanism itself, the particle agglomeration process has yet to be completely elucidated. Focusing on the fluid state in the fluidized bed granulation method, the authors have investigated the dynamic equilibrium of the agglomeration and disintegration effects of particles in granulation processes[5,6]. Fukumori et al. conducted simulations on droplet diameter at the granulation threshold and on the particle size dependence of separation force.[7] Watano et al. investigated granule agglomeration in view of inter-particle fluid bridging force and separation force that is proportional to particle momentum[8], and they also examined particle growth rate[9] using population balance. As this shows, recently there are a number of studies that attempt to model granulation, but they are still few in number and the granulation mechanism is not yet fully understood. The authors focused on the agglomeration morphology of raw material particles during granulation in a tapered fluidized bed, which is the most widely used, and proposed a granulation model. We also elucidated the granulation mechanism by simulating the particle density and bulk density of the formed granules. Here we also discuss the differences in granulation due to apparatus size.

2. Experimental

2.1 Experimental Apparatus and Conditions

Fig. 1 is a diagram of the experimental apparatus used, which was a tapered fluidized bed granulator

* 1-Takehaya, Kawashima-cho, Hashima-gun, Gifu. 501-61 TEL. 0586-89-4716
** Furo-cho, Chikusa-ku, Nagoya 464-01 TEL. 052-789-3379
† This report was originally printed in J. Soc. Powder Technology, Japan. **34**, 586-591 (1997) in Japanese, before being translated into English by KONA Editorial Committee with the permission of the editorial committee of the Soc. Powder Technology, Japan.

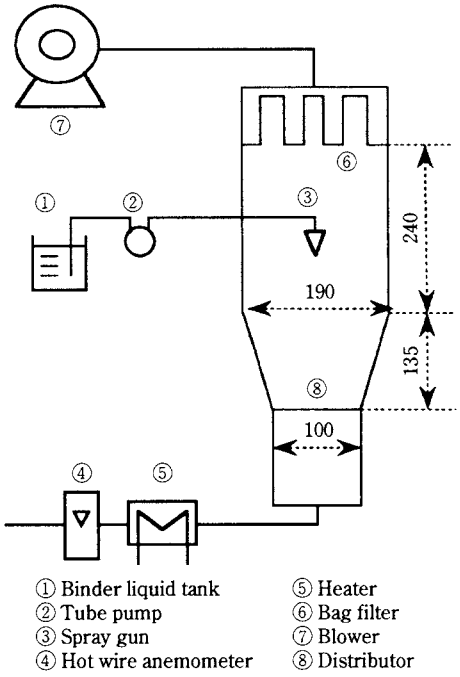

Fig. 1 Schematic diagram of experimental apparatus

having a column diameter of 190 mm and a distributor diameter of 100 mm. The distributor had a stainless steel wire mesh, and the spray nozzle was binary (model O made by the Freund Co.). The sample powder for granulation was formulated by mixing two materials generally used in the pharmaceutical field, lactose and cornstarch, in a 7:3 ratio. **Table 1** presents the powder's physical properties. The experiment was conducted while varying two of the granulation conditions: the spray solution rate and the fluidizing gas rate. **Table 2** presents the other granulation conditions.

2.2 Experimental Method

The granulation experiment proceeded by loading 500 g of the mixed powder and using a 5% W/V solution of hydroxypropyl cellulose (HPC-L) as the binder. Powder was sampled at intervals during granulation, and moisture content was measured by calculating it on a wet basis from the change in weight after drying the powder samples at 80°C for 30 min. Particle size distribution, bulk density, and particle density were measured after stationary drying of the powder samples at 80°C for 2 hr. Particle size distribution was calculated on a weight basis using the standard screen prescribed by JIS Z 8801, and average particle size D_{50} was determined on logarithmic normal probability paper. Bulk density was measured in accordance with JIS K 5101. Particle density was measured in the following manner: In consideration of the reliability of data, the granule particle size range measured was set at 200 to 350 μm and determined to be the representative particle density value. We began by selecting samples whose average particle sizes fell into the range of 200 to 350 μm, then used a standard screen to take from each sample some granules that fell into the 200 to 350 μm range. The total weight of about 100 granules was measured, and photomicrographs taken. The numbers of granules were counted in the photomicrographs, and the average weight of one granule was determined by dividing total weight by the number of granules. Average particle size was 294 μm, as calculated from volumetric standard particle size, and the average volume of one granule was calculated as equivalent spherical volume. Granule density was determined to be the value obtained when dividing the average weight of one granule by the average volume of one granule, as obtained above.

Table 1 Physical properties of powder

Powder	Physical properties	
Lactose	Average particle size (μm)	40.1
	Bulk density (kg/m^3)	590
Cornstarch	Average particle size (μm)	12.0
	Bulk density (kg/m^3)	480
Mixed Powder	Average particle size (μm)	25.8
	Bulk density (kg/m^3)	550
	True density (kg/m^3)	1530
	Moisture content (−)	0.053

Table 2 Experimental conditions of fluidized bed granulation

Experimental material	Lactose-cornstarch = 7:3
Bed material inventory (kg)	0.5
Binder solution	5% (w/v) HPC-L
Nozzle diameter (mm)	0.71
Type of spraynozzle	Binary
Position of spray nozzle (mm)	260 (above distributor)
Air pressure of spraynozzle (kPa)	15.7
Air temperature (°C)	60
Feeding rate of binder solution (m^3/s)	10.8×10^{-8} – 24.3×10^{-8}
Air velocity at distributor (m/s)	0.25 – 1.61

3. Experimental Results

3.1 Change in Moisture Content of Powder

By choosing the desired spray solution rate and fluidization gas rate as granulation was in progress, we varied the powder moisture content while forming granules. **Fig. 2** shows the diachronic change in powder moisture content during granulation. Comparisons made at the same point in time show that the higher the spray solution rate, and the lower the fluidization gas rate, the greater the powder moisture content becomes. This shows that moisture content is governed by a balance between the moistening effect of the spray solution and the drying effect of the fluidization gas.

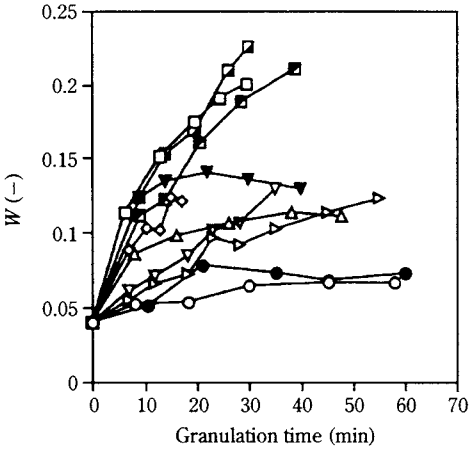

	$f\times10^{-8}$ (m^3/s)	u (m/s)
EX-1	10.8	0.62
EX-2	17.2	0.62
EX-3	23.0	0.62
EX-4	15.8	0.25
EX-5	15.8	0.44
EX-6	15.8	0.66
EX-7	15.8	0.90
EX-8	24.3	1.61
EX-9	24.3	1.20
EX-10	24.3	0.90

Fig. 2 Changes in moisture content during granulation

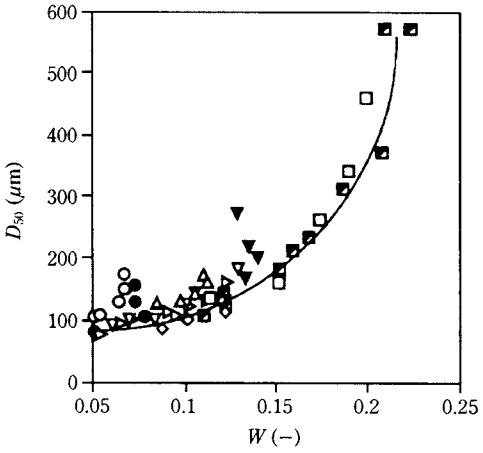

	$f\times10^{-8}$ (m^3/s)	u (m/s)
EX-1	10.8	0.62
EX-2	17.2	0.62
EX-3	23.0	0.62
EX-4	15.8	0.25
EX-5	15.8	0.44
EX-6	15.8	0.66
EX-7	15.8	0.90
EX-8	24.3	1.61
EX-9	24.3	1.20
EX-10	24.3	0.90

Fig. 3 Relationship between average granule size and moisture content

3.2 Physical Property Values of Powder

3.2.1 Average Granule Size

Fig. 3 shows the relationship between powder moisture content W and average granule size D_{50} during granulation. We noted a trend in which average granule size became larger as moisture content increased, and the trend was pronounced in the high-moisture-content region. Additionally, the existence of a moisture content envelope corresponding to average particle diameter suggested that there is a granulation region in which average granule size is determined by moisture content alone. At the same time, we discerned a phenomenon in which the D_{50} of EX-1, 7, and 8 diverged from the envelope in **Fig. 3**, where water content during granulation was for the most part constant with respect to time. This is likely because as the HPC-L concentration in the powder bed increased, the aqueous binder solution increased in viscosity, which facilitated the growth of particle agglomerates.

3.2.2 Bulk Density of Granules

In order to investigate the variation factors affecting granule bulk density, we plotted the relationship between powder moisture content and fluidization gas rate, and bulk density, in **Fig. 4**. Bulk density value

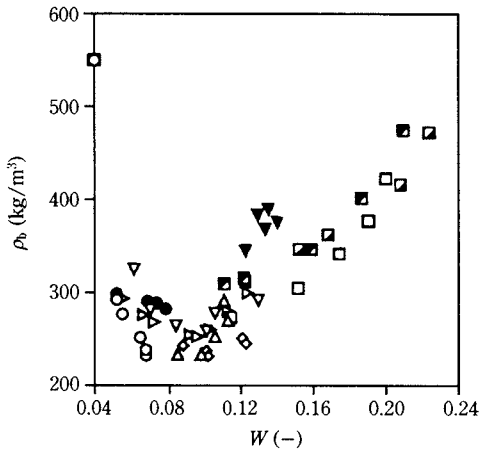

	$f\times10^{-8}$ (m^3/s)	u (m/s)
EX-1	10.8	0.62
EX-2	17.2	0.62
EX-3	23.0	0.62
EX-4	15.8	0.25
EX-5	15.8	0.44
EX-6	15.8	0.66
EX-7	15.8	0.90
EX-8	24.3	1.61
EX-9	24.3	1.20
EX-10	24.3	0.90

Fig. 4 Relationship between bulk density and moisture content

was exceedingly small at a moisture content of about 0.1. Decreasing bulk density in the 0.05 to 0.1 moisture content range despite the large average granule size suggests a dendrite-type granule growth mechanism. Bulk growth increased when moisture content exceeded 0.1, and with an increase in average granule size the trend became more pronounced. Additionally, bulk density tended to increase when the gas flow rate was high, and this tendency became pronounced when moisture content exceeded 0.1.

4. Discussion

4.1 Granulation Model

On the basis of experimental findings to date we studied a granulation model for granulation in a fluidized bed. **Fig. 5** illustrates the granulation model.

(1) $W < 0.1$

Droplets and powder particles associate, and the aqueous binder solution penetrates the powder by capillary suction. The locations where particles bind to each other are limited because the aqueous binder solution adheres to isolated places on particle surfaces. Under these conditions, the agglomeration of particles occurs within a dynamic equilibrium of adhesion and separation forces, which results in dendrite-like particle growth. And because average granule size is only about 100 μm, bulk density is heavily influenced by the roughness of primary particles on the granule's shell. That is to say, granule size increases, while bulk density decreases.

(2) $0.1 \leq W$

At this moisture content the void inside powder particles is almost completely filled with water, the force of capillary suction becomes weak, and there is much aqueous binder solution on particle surfaces. Because particle surfaces are covered with the aqueous binder solution, there are more locations on particles that are capable of binding with other particles. Under the influence of external force created by the fluidization gas, the particles move in such a way that they bond with others in the most stable configuration. As a result, the void inside agglomerated particles becomes smaller, which increases bulk density. It also appears that because variation in gas flow rate changes the magnitude of external force on particles, the void rate in agglomerated particles changes, making for differences in bulk density. Average granule size becomes larger as moisture content rises, which reduces the ratio of roughness due to primary particles on the shells of granules. As a result, bulk density increases and one can discern a correlation with the average size of agglomerated granules.

4.2 Particle Agglomeration Mechanism and Calculating Granule Physical Property Values

4.2.1 Simulation and Assessment of Bulk Density

To simulate bulk density we used Eq. (1) below to determine inter-granular voidage ε from the measured values of granule density and bulk density.

$$\varepsilon = 1 - \rho_b / \rho_p \qquad (1)$$

Fig. 6 shows the inter-granular voidage calculated in Eq. (1). The horizontal axis is average granule size D_{50}. We discerned no systematic change due to the D_{50} value, and the average value of ε was 0.47. Based on the granulation model we conceived the form of particle agglomeration in the fluidized bed in the following manner. To begin with, we assume that the raw

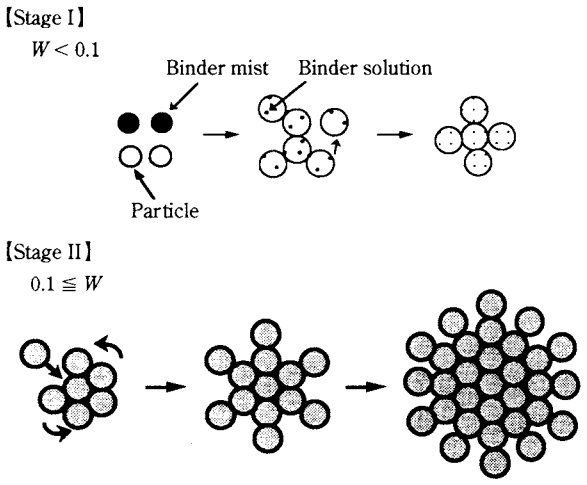

Fig. 5 Granulation model

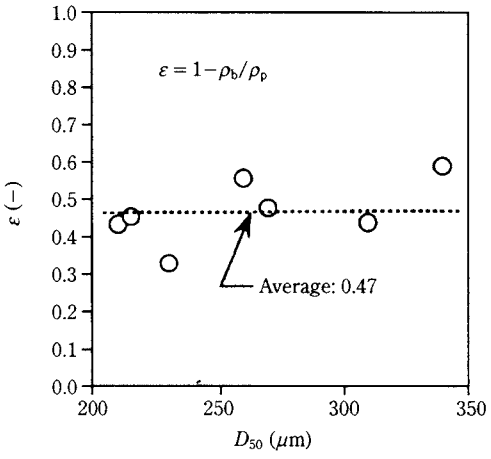

Fig. 6 Calculation of inter-granular voidage

material's primary particles are spherical. Agglomerating particles grow while giving roughness to granule surfaces, with that roughness being about the size of primary particles in the raw material, but unrelated to the size of agglomerated particles. Further, the model assumes that the particle fraction of the shell of agglomerated particles is one-half the interior particle fraction. **Fig. 7** illustrates the particle agglomeration model. d_p is the primary particle size of the raw material, while d_i indicates the size of interior agglomerated particles excluding the granule shell. If ε_i is the voidage of interior granules excluding the shell (ε_{si} is the particle fraction), the number of interior primary particles N_{si} is given by Eq. (2).

$$N_{si} = d_i^3 \cdot \varepsilon_{si} / d_p^3 \tag{2}$$

Eq. (3) gives the number of particles in the shell, N_{so}.

$$N_{so} = (\varepsilon_{si}/2) \times \frac{(d_i+2d_p)^3 - d_i^3}{d_p^3} \tag{3}$$

Eq. (4) gives the particle fraction ε_s including the shell.

$$\varepsilon_s = \frac{d_p^3 (N_{so}+N_{si})}{(d_i+2d_p)^3} \tag{4}$$

If one substitutes Eqs. (2) and (3) in Eq. (4), ε_s is given by Eq. (5).

$$\varepsilon_s = \varepsilon_{si} \frac{1+3d_p/d_i+6(d_p/d_i)^2+4(d_p/d_i)^3}{(1+2d_p/d_i)^3} \tag{5}$$

Using Eq. (5) we found the particle fraction for agglomerated particle size from the d_p/d_i ratio, and multiplied by the true density of the raw material to calculate granule density. We then compared experimental values with the values for bulk density calculated using the above equation for determining granule density, and the results appear in **Fig. 8**. In calculating bulk density, we used the spherical equivalent random maximum packing rate of 0.64[10] for the granular internal fraction ε_{si}, and the value of 0.47 obtained in **Fig. 6** for inter-granular voidage ε. The reason that bulk density experimental values were larger than calculated values for a D_{50} value of around 100 μm is probably because there were raw material particles not yet formed into granules, making the actual inter-granular voidage smaller than 0.47. On the other hand, the reason that experimental values became larger than calculated values at a D_{50} of about 550 μm is probably because the greater moisture content within agglomerated particles caused some of the primary particles to partially dissolve and deform, thereby enlarging ε_{si}.

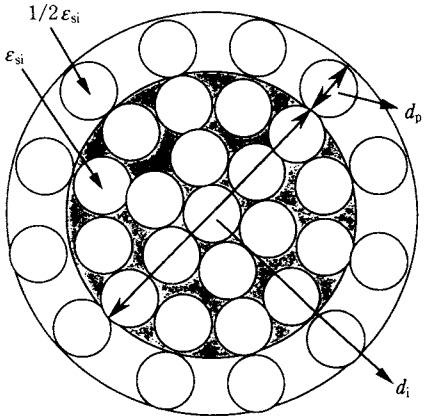

Fig. 7 Illustration of particle agglomeration model

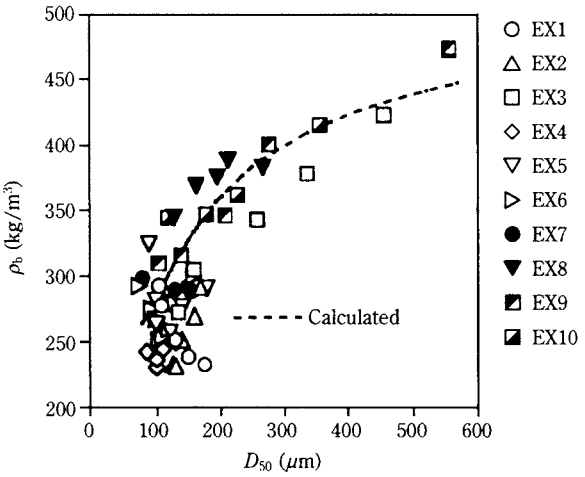

Fig. 8 Relationship between bulk density and average granule size

4.2.2 Effects on the Agglomeration Mechanism by Differences in Apparatus Scale

It is known that differences of scale in fluidized bed granulators greatly affect the physical properties of their granular products. For that reason, in order to investigate the effects of granulator scale, we organized and compared the experimental results obtained in previous work[6] with the experimental results obtained in the present research. Comparison results appear in **Fig. 9**. The data used in this comparison were the results obtained with a tapered fluidized bed granulator that loaded 10 times the bed material (5 kg) and had a column twice the size. Granulation conditions in the experiment were a spray solution rate of 16.7×10^{-7} m^3/s and a fluidization gas rate of 1.2–1.6 m/s, with other fixed conditions being the same. We discerned no great difference, between the two apparatus scales, in the average size of formed granules due to powder moisture content, but scale made a marked difference in bulk density. Specifically, despite the same average granule size, a large scale made for

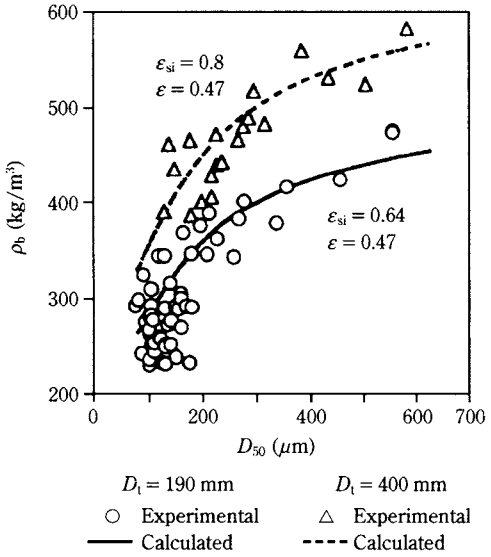

Fig. 9 Effects of experimental apparatus scale on physical properties of granules

a large bulk density value. Because it is nearly inconceivable that scale makes a big difference in granule surface morphology, we surmised that the difference in bulk density due to scale is caused by a difference in granule density. Assuming that inter-granular voidage is 0.47 and calculating the internal granular ε_{si} from bulk density, we arrived at an internal granular fraction ε_{si} for large-scale granulators of 0.8, which is about 1.25 times the value for small-scale granulators. In consideration of the change in bulk density in response to change in the gas flow rate during granulation found in this research, we conjectured that the difference in bulk density due to scale arises from the difference in the fluidization states of the two granulators. The findings of this research could provide useful information when designing equipment for manufacturing pharmaceutical preparations using the fluidized bed granulation method, and might be useful in validation and other industrial research. By elucidating the effects on the particle agglomeration process, future studies, such as on the effects of column diameter on the fluidization state of powder, should lead to the establishment of scale-increasing technologies of truly great practicality.

5. Conclusion

The authors conducted a tapered fluidized bed granulation experiment using lactose and corn starch as the raw material and an aqueous solution of hydroxypropyl cellulose as the binder. Results were as follows.

(1) We investigated the variation factors that affect the physical characteristics of granules at the time of granulation, and found that it is possible to adjust average granule size and bulk density by changing the moisture content of powder during granulation.

(2) By assessing the relationship between granule moisture at the time of granulation and granule physical characteristics, we proposed a granulation model and elucidated the particle agglomeration mechanism in a fluidized bed.

(3) We found a highly precise simulation method for granule density and bulk density, and showed that it is possible to estimate the values for granule physical characteristics. We also showed that granule density changes in response to differences in granulator scale.

Nomenclature

d_i	: internal agglomerated granule diameter	(μm)
d_p	: particle diameter of raw material	(μm)
D_{50}	: average particle diameter	(μm)
D_t	: column diameter	(mm)
f	: feed rate of binder solution	(m^3/s)
N_{si}	: number of constituent particles in internal agglomerated granule	(−)
N_{so}	: number of constituent particles in granule shell	(−)
u	: gas velocity at distributor	(m/s)
W	: moisture content	(−)
ε	: inter-granular voidage	(−)
ε_s	: solid fraction of granule	(−)
ε_{si}	: solid fraction of internal agglomerated granule	(−)
ρ_b	: bulk density	(kg/m^3)
ρ_p	: particle density	(kg/m^3)

References

1) Davis, W. L. and W. T. Gloor, Jr. "Effects of Process Variables on Physical Properties of Final Granulation," *J. Pharm. Sci.* 60, 1869-1874 (1971).
2) Davis, W. L. and W. T. Gloor, Jr. "Effects of Various Binders and Their Concentrations on Granulations and Compressed Tablets," ibid. 61, 618-622 (1972).
3) Shinoda, A., T. Nasu, M. Furukawa, S. Sakashita, K. Uesugi, Y. Miyake, and S. Toyoshima. "Growth of Particles in Fluidized Granulation," *Yakuzaigaku*. 36, 83-88 (1976).
4) Nishimura, K., H. Kakizawa, T. Fukazawa, S. Kishitani, K. Kasahara, and T. Asai. "Particle Size of Binder Droplets and Granulation Efficiency in Fluidized Bed Granulation," *Yakuzaigaku*. 38, 196 (1978).

5) Okada, Y., T. Ohwaki, Y. Ishibashi, Y. Taguchi, H. Ozawa, R. Yamazaki, and G. Jimbo. "Influence of Distributor Types on the Fluidizing Characteristics of a Tapered-Fluidized Bed," *J. Soc. Powder Technol., Japan.* 29, 886-890 (1992).
6) Okada, Y., T. Ohwaki, K. Uesugi, Y. Taguchi, H. Ozawa, T. Suzuki, R. Yamazaki, and G. Jimbo. "Granulation in a Tapered-Fluidized Bed and Its Dominant Factors," ibid. 29, 891-896 (1992).
7) Fukumori, Y., H. Ichikawa, K. Jono, Y. Takeuchi, and T. Fukuda. "Computer Simulation of Agglomeration in the Wurster Process," *Chem. Pharm. Bull.* 40, 2159-2163 (1992).
8) Watano, S., T. Fukushima, and K. Miyanami. "Computer Simulation of Fluidized Bed Granulation by a Two-Dimensional Random Coalescence Model," *J. Chem. Eng. Japan.* 28, 171-176 (1995).
9) Watano, S., T. Morikawa, and K. Miyanami. "Mathematical Model in the Kinetics of Agitation Fluidized Bed Granulation," *Chem. Pharm. Bull.* 44, 409-415 (1996).
10) Iinoya, K. *Funtai Kogaku Binran*, p. 103, Nikkan Kogyou Shinbunsha (1988).

Author's short biography

Yasushi Okada

Yasushi Okada is born 1959 in Wakayama, Japan. He graduated from Nagoya University, Japan (1977) with the degree of Bachelor of Engineering. He entered EISAI company, Ltd.. He was served in Department of Pharmaceutical Research and Technology in Gifu, Japan. He got Doctor of Engineer (1998) from Nagoya University, Japan for a thesis entitled : Studies on Fluidizing Characteristics and Granulation Mechanism in Tapered-Fluidized Bed. He employed as senior researcher in Formulation Research Laboratories in Gifu, Japan and he is in that position at present.

Takaaki Sakai

Takaaki Sakai is born 1973 in Aichi. He graduated from Nagoya University, Japan and got Master of Eng. (1998) He works in TOYODA GOSEI CO., LTD now.
He belongs to Elastomer Material Engineering Dept. in Material Engineering DIV.
His present work is to develop the material of rubber part of cars.

Ryohei Yamazaki

Ryohei Yamazaki is born 1942 in Tokyo. He graduated from Yokohama National University, Japan and received MSc (1968). He got Dr. of Eng. (1974) from Nagoya University, Japan. He is Associate Professor of Chemical Engineering at Nagoya University and his research activity is mostly oriented to fluidization and particle technology.

Shigekatsu Mori

Shigekatsu Mori graduated in Chemical Engineering at Nagoya University in 1965. MS and PhD were also received from Nagoya University.
He has been the professor of department of chemical engineering in Nagoya University from 1993.
His research field involves gas-solid multiphase process, coal conversion technology and wasted material utilization.

Dispersion Behavior of Coarse Particles by Lateral Vibration under Microgravity†

Yasushi Ohyama, Hiromi Takeuchi, A. T. Pyatenko and Shigeo Chiba
*Hokkaido National Ind. Res. Institute**
Kunio Shinohara
*Division of Materials Sci. & Eng. Hokkaido Univ.***

Abstract

We studied coarse particle behavior in a laterally vibrated vessel under microgravity. Vibration conditions were a frequency of 75-150 Hz and a displacement amplitude of 86-310 μm. The two-dimensional displacement distribution of particles moving in three dimensions was measured by particle image sampling within the depth of field. Observations revealed a saddle-shaped distribution in which concentration was higher at the center in the lateral direction and the ends in the longitudinal direction. This tendency became distinct with increasing total particle concentration. The round corners of the vessel made the distribution more uniform due to enhanced circulation. We also found that particle concentration increased with velocity amplitude.

1. Introduction

In a microgravitational field it is easy to obtain a uniform state in processes such as for material synthesis when working with multi-component raw materials owing to the lack of transport phenomena caused by matter density differences, such as the convection of fluids or the separation of ingredients, and there are expectations for the synthesis of new materials by taking advantage of this. Fully eliciting the characteristics of microgravity in such material synthesis requires that we establish methods of manipulating powders used as raw materials, and especially needed is study of particle dispersion in order to resolve a problem of particle adhesion. External forces are always required for powder operations under microgravity, which makes it necessary to start by studying the basic characteristics of the particle assembly that are subject to external forces. While applied vibration is an excellent external force that is independent of environment because it can be used in a vacuum and under high and low temperatures, there are few reports on vibrated powder beds and particle assemblies under microgravity,[1] and the behavior is not well understood. Ohyama et al.[2] reported that a particle assembly vibrated under microgravity exhibit dispersion behavior that differs according to particle size. It would seem that explaining this difference will require determining the respective dispersion mechanisms for coarse and fine particles. In that consideration, this research involved measuring the two-dimensional particle distribution of coarse particles in a vibrated vessel, with parameters being the concentration of the particles in the vessel, displacement amplitude, and frequency; determining the effects on particle behavior when applying vibration under microgravity; and investigating the conditions needed to obtain a state of homogeneous dispersion.

* 2-17-2-1 Tsukisamu-Higashi, Toyohira-ku, Sapporo, 062-0052, Japan
**Kita 13-Nishi 8, Kita-ku, Sapporo, 060-0813, Japan
† This report was originally printed in J. Soc. Powder Technology, Japan. **34**, 834-839 (1997) in Japanese, before being translated into English by KONA Editorial Committee with the permission of the editorial committee of the Soc. Powder Technology, Japan.

2. Experimental

2.1 Experimental Apparatus and Method

Fig. 1 is a schematic diagram of the apparatus. An observation cell mounted to the stage of an electric vibrator (PET-05-05A made by IMV) consists of a glass box (W×D×H=20×20×28 mm) in an aluminum cell holder. While the top corners are round, those at the bottom are square, thereby allowing comparison of effects on dispersion state due to local container shape. Our experiments used the Japan Microgravity Center (JAMIC) in Kamisunagawa Town (10^{-4} G grav-

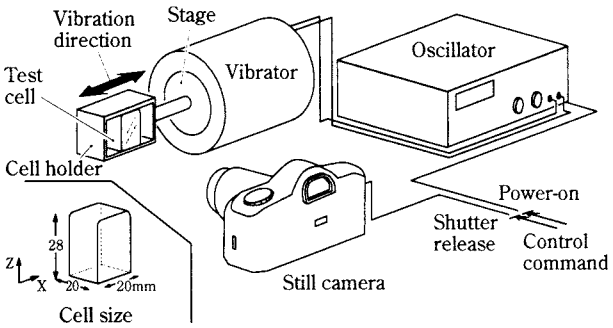

Fig. 1 Experimental Apparatus

ity level, microgravity state sustained approximately 10 s). The observation cell was loaded with lead particles having a particle size d_p of 362 μm (density ρ was 1.066×10^4 kg/m^3). Using an oscillator that began operating with a control command, we put the container into a microgravity state while applying lateral vibration with the vibrator, within the ranges of 75-150 Hz for frequency f, and 86-310 μm for displacement amplitude A_d. Behavior of the particles in the test cell was photographed continuously by means of a control command with a still camera (Canon EOS-1N with RS and EF 100 mm macrolens) every one-third second beginning 1 to 3 seconds before the cell entered a microgravity state. To make sure of vibration conditions a laser Doppler vibration meter (Ono-sokki model LV-1500) was used to measure the test cell's velocity amplitude under normal gravity.

Longitudinal direction z was chosen for the direction of normal gravity, and lateral direction x for the direction in line with vibration displacement.

2.2 Analysis Method

Positions of individual particles suspended in the cell was measured in order to determine the relationship between the state of particle dispersion inside the cell and operational conditions. Specifically, the camera was placed about 30 cm away from the observation cell on the same level, focus was set to the central region of the cell, and the aperture was set at f 2.8, which gives the shallowest depth of field. This arrangement allowed us to measure particle coordinates on a two-dimensional plane in the central region of the test cell where there is little wall influence, and no hindrance to the three-dimensional movement of the particles. This method is illustrated in **Fig. 2**. While the focal plane is actually a spherical surface whose radius is the distance to the subject, we regarded it as a longitudinal plane within the cell because of its small size. If particle concentration in the system is low, particles scattered in front of and behind the focal plane will appear indistinct in photographs, or be

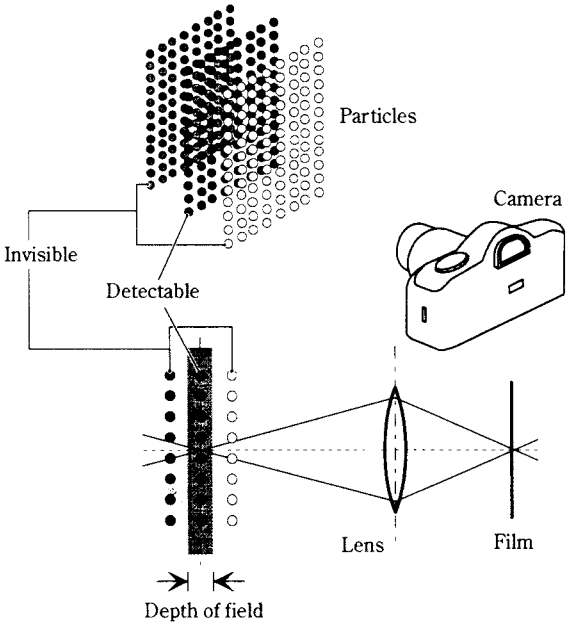

Fig. 2 Method of particle sampling in depth of field

entirely invisible, while only particles within the region whose thickness is that of the depth of field will appear distinct. Particles thus caught on film were considered to be in the cell's longitudinal section. This plane was divided into 12 zones longitudinally and 8 zones laterally, the number of individual particles was visually chosen and counted in each zone, and divided by the theoretical number of particles if the cell is filled to maximum density to determine the two-dimensional particle concentration distribution. Our actual depth of field in this experiment was 0.66 mm. This observation method shall henceforth be called the depth of field particle extraction method.

3. Results and Discussion

3.1 Observation Results

The photographs in **Fig. 3** show the particle dispersion state at 1 s intervals and at a particle concentra-

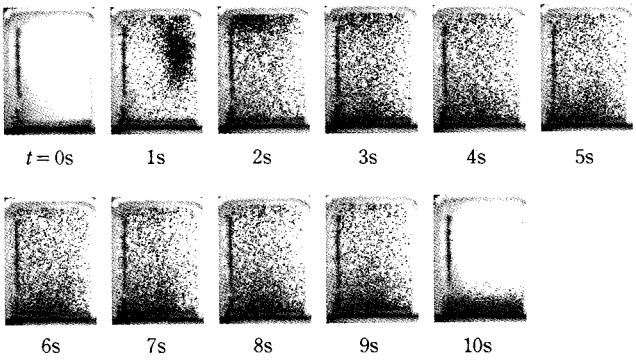

Fig. 3 Photographs of particle behavior
d_p=362 μm, C_p=7.76×10^8 m^{-3}, A_d=86 μm and f=150 Hz

tion C_p of 7.76×10^8 m^{-3}, displacement amplitude A_d of 86 μm, and a frequency f of 150 Hz. t is elapsed time, which began with the first photograph taken after the capsule containing the experimental apparatus began its descent and attained microgravity. During the approximately 2 s until the powder bed reached the upper surface of the cell, it floated upward as the apparatus made the transition to microgravity, and disintegrated as the particles repeatedly collided with the walls and other particles. Subsequently it remained in a dispersed state. Each time the experiment was conducted we took 27 to 31 photographs during the approximately 10 s of microgravity, but in order to compare the stable dispersed states attained after the initial stage of powder bed ascent and disintegration, analyses with the depth of field particle extraction method used the average particle distribution obtained from the last three photographs taken under microgravity, i.e., those from the 8th though the 10th seconds of each run.

3.2 Particle Concentration Effects and Distribution Structure

As a means of investigating the effects of collision frequency, we plotted the two-dimensional particle concentration distribution under different initial loading concentrations, C_p in **Fig. 4**. z is the longitudinal position, x is the lateral position, and these coordinates have been rendered dimensionless with, respectively, the height and width of the cell. The distribution tended to be saddle-shaped, with the ends high in the longitudinal z direction and the center high in the lateral x direction, and we found that this tendency became more pronounced as the initial powder loading concentration increased. **Fig. 5** shows the results obtained when comparing the average values for the

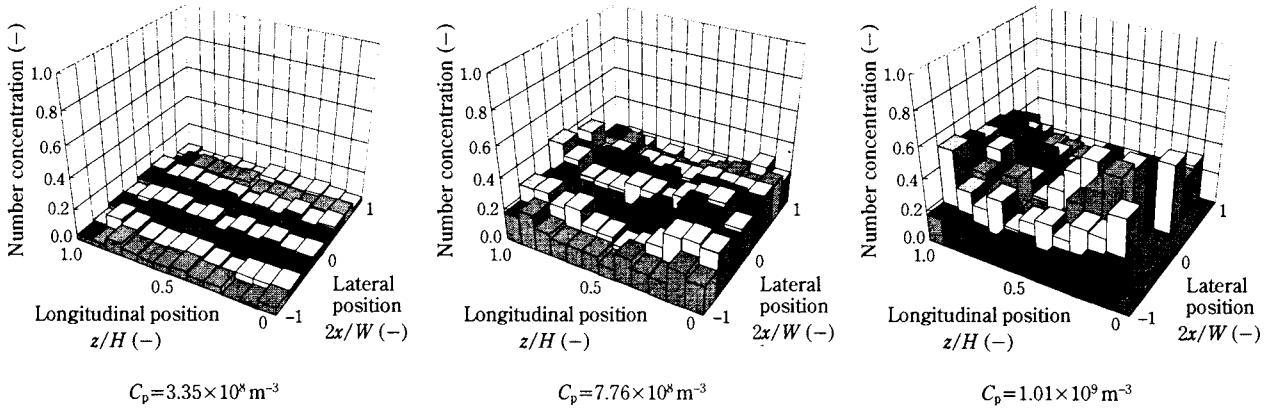

Fig. 4 Two-dimensional concentration distribution in vertical cross section d_p=362 μm, f=150 Hz, A_d=86 μm in t=8.7−9.7s

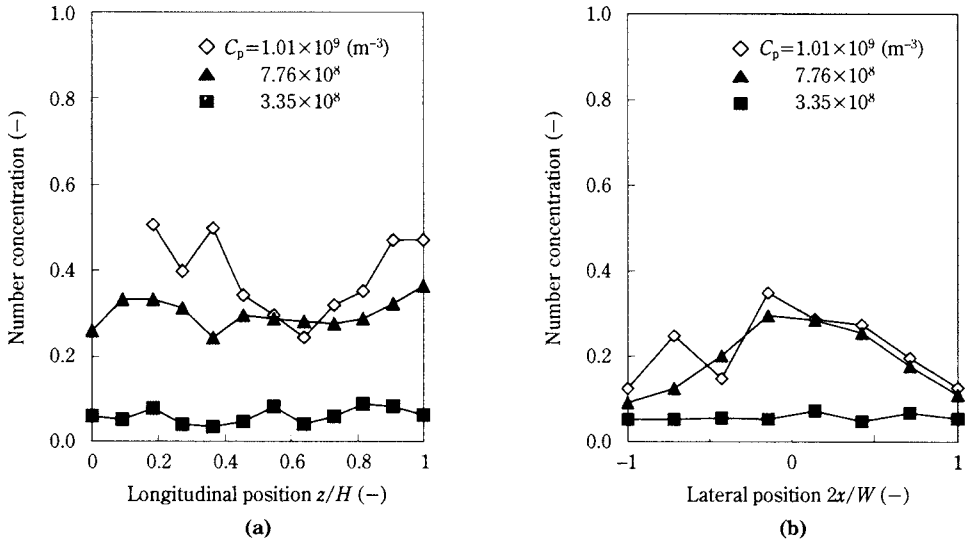

Fig. 5 Effect of total particle concentration C_p
(a) on longitudinal particle concentration distribution at lateral position 0.38−0.63, (b) on lateral particle concentration distribution at longitudinal position 0.42−0.58: d_p=362 μm, f=150 Hz, A_d=86 μm

two center rows in the longitudinal and lateral directions. When C_p was 3.35×10^8 m^{-3} the distribution was uniform, but when C_p was 7.76×10^8 m^{-3} the concentration distribution assumed a saddle shape, with the upper and lower ends high as shown in **Fig. 5 (a)** for the longitudinal direction, and the central area high as shown in **Fig. 5 (b)** for the lateral direction. One can see that this tendency toward uneven distribution became even more pronounced when C_p was 1.01×10^9 m^{-3}, even though we could not measure this in photographs due to insufficient lighting in the longitudinal position region below 0.1.

Thus when particle concentration becomes high, the dispersion structure exhibiting a tendency toward uneven distribution can be interpreted as in **Fig. 6**. To begin with, particles near the vibrating walls are given lateral momentum by the wall surfaces, and disperse into the cell interior while colliding repeatedly with other particles. Because particles lose velocity owing to friction in the collision process, the farther they are from the vibrating walls, i.e., the closer they are to the cell center, the smaller that inter-particle distances become, and the higher the concentration. Next, because of the influx of particles toward the center from both lateral directions, upward and downward flows arise in the cell's central region as particles try to escape. These flows push the particles against the top and bottom walls where they stagnate momentarily, then arrive at the right and left vibrating walls where vibration again gives them horizontal momentum. It appears that macroscopically the particles repeat this cycle while colliding with one another over and over, and that the aforementioned concentration distribution arises due to the velocity loss in the central region and the stagnation near the top and bottom walls that occur during this cyclical flow, in which the particle velocity vector, which initially has only the x direction component, then picks up the z direction component due to inter-particle collisions, resulting in a flow that becomes more distinct as the collision frequency increases. The relationship between initial loading particle concentration and concentration distribution revealed in **Figs. 4** and **5** presumably correspond to this behavior.

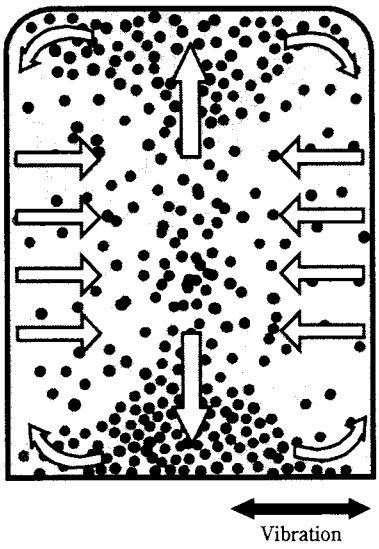

Fig. 6 Model of particle circulation by vibration

These results indicate that although there was an adaptive concentration range, the depth of field particle extraction method used in this research is effective for two-dimensional observation of suspended particles. There are expectations that using a computer will enable this method to make still more precise selective extractions. Further, the use of a flashing light source instead of a steady one would perhaps make it possible to use this method to measure three-dimensional velocity.

3.3 Effects of Vibration Conditions

Fig. 7 shows the particle concentration distribution when frequency f was 95 Hz and displacement amplitude A_d was 86 and 310 μm. The saddle-shaped distribution pattern is distinct even when A_d was 86 μm. When A_d was 310 μm, a high-low concentration difference appeared in addition to the saddle distribution tendency. That is to say, the regions where there were no data for the lower part of the vertical cross section were places where the depth of field particle extraction method was unable to perform measurements because of blockage by high-concentration particles. This means that concentration was very high in those regions, with results showing that in the longitudinal direction the lower the position, the higher the concentration. **Fig. 8** is a comparison using average values for the two center rows in the longitudinal and lateral directions. The dotted lines in the graphs represent the average dispersion concentration calculated from the initial particle load. Both distributions in the lateral direction were high in the center and about the same magnitude. Although both distributions in the longitudinal direction tended to be high at the ends, there was a difference according to amplitude in which at low amplitude the ends were symmetrical, while at high amplitude the lower end has a high concentration.

Fig. 9 shows the particle concentration distribution when A_d was 86 μm and f was set to 95 and 150 Hz. The distribution shapes are similar despite the frequency difference. Comparing average values for the

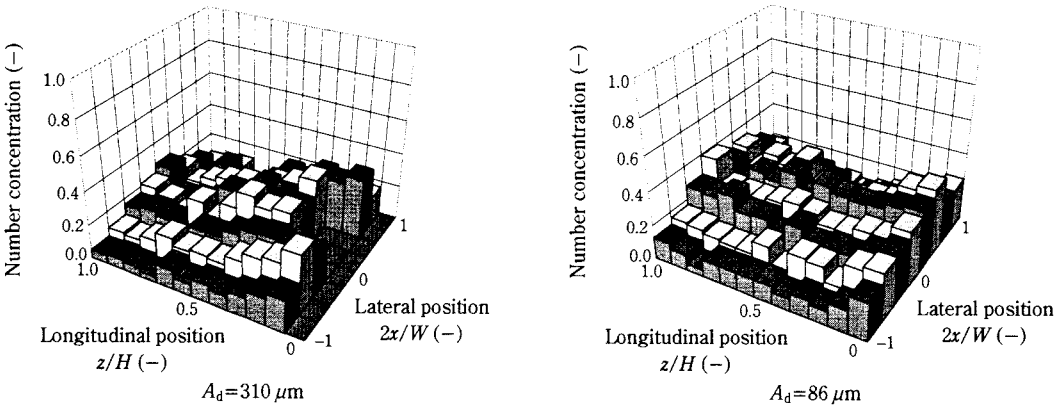

Fig. 7 Two-dimensional concentration distribution in vertical cross section at different displacement amplitudes d_p=362 μm, C_p=7.76×10⁸ m⁻³, f=95 Hz in t=9.0−9.7s

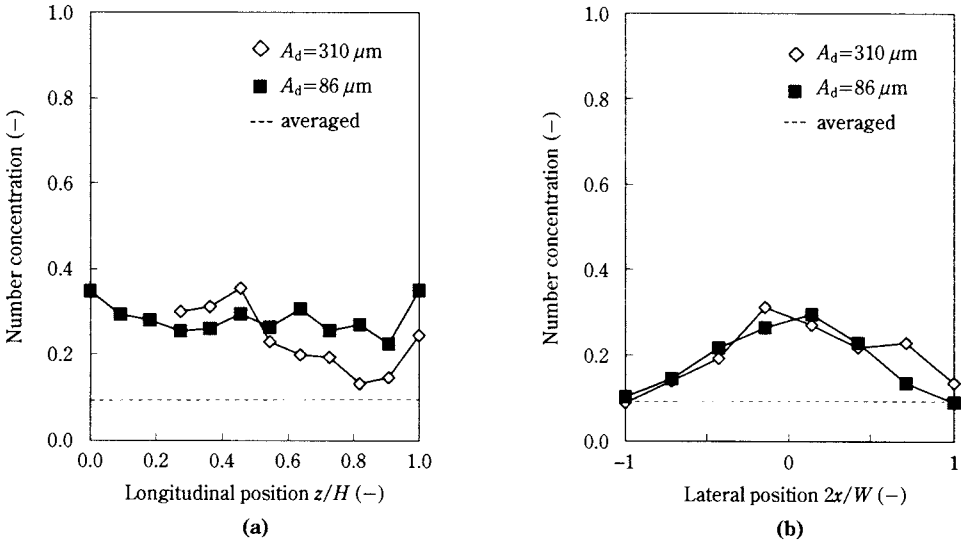

Fig. 8 Effect of displacement amplitude A_d
(a) on longitudinal particle concentration distribution at lateral position 0.38−0.63, (b) on lateral particle concentration distribution at longitudinal position 0.42−0.58: d_p=362 μm, f=150 Hz, C_p=7.76×10⁸ m⁻³

two center rows in the longitudinal and lateral directions in **Fig. 10** shows that the distributions coincided closely, and thus the influence of frequency difference in the displacement amplitude region was not manifested. The dotted lines in the graphs represent the average dispersion concentration.

3.4 Discussion

Assuming that uneven concentration distribution arises in the process illustrated in the macroscopic cyclical movement in **Fig. 6**, the velocity at which the cell walls drive particles toward the cell's central region, strongly influences both the velocity loss process until particles reach the cell's central region, and the influx velocity in the stagnation area. We therefore compared the effect of velocity amplitude A_v, i.e., the maximum cell wall velocity, on dispersion structure at a constant initial particle load concentration, and showed the results in **Fig. 11**, which plots the average particle concentration values in the three zones H, M, and L, shown in the graph, that are part of the observed region. The dotted line in the graph represents the average distribution concentration. In zones M and L particle concentration gradually increased in relation to velocity amplitude, showing that velocity amplitude promoted uneven distribution with concentration higher in the cell's central region. By contrast, as far as our experiment showed, in zone H concentration decreased as velocity amplitude increased, revealing a difference in dependence on velocity amplitude in the cell's longitudinal direction. The top and bottom corner configurations of the cell were different, with top corners being round, but no other differences in conditions in the longitudinal direction were discerned. As **Fig. 12** shows, round corners act to expel particles from the stagnation area

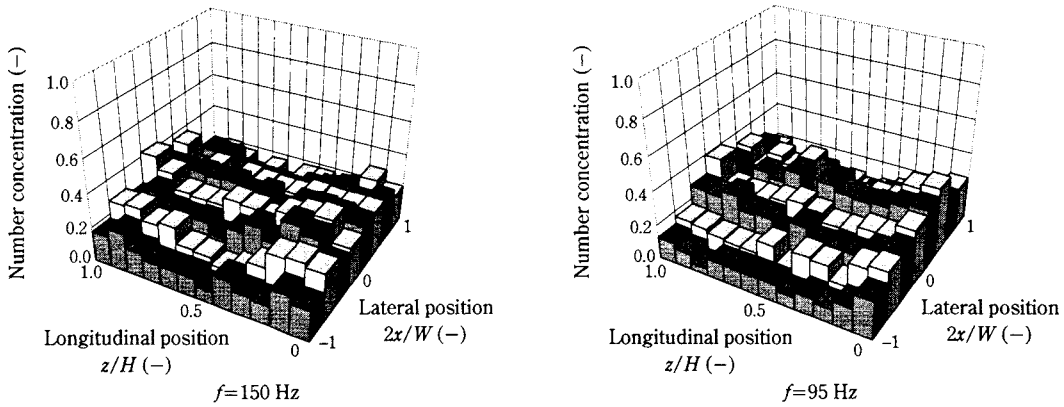

Fig. 9 Two-dimensional concentration distribution in vertical cross section at different frequencies f
d_p=362 μm, C_p=7.76×10^8 m^{-3}, A_d=86 μm in t=9.0−9.7s

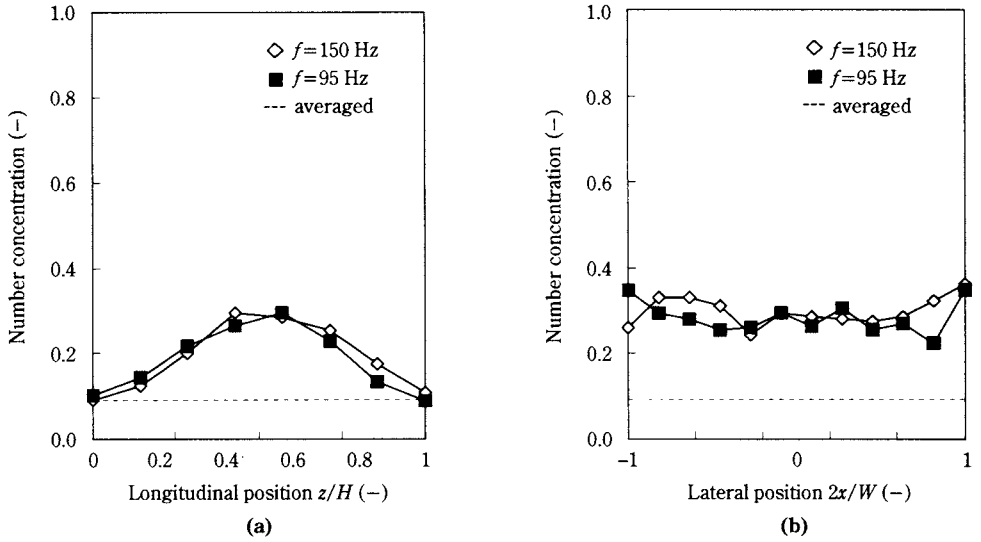

Fig. 10 Effect of frequency f
(a) on longitudinal particle concentration distribution at lateral position 0.38−0.63, (b) on lateral particle concentration distribution at longitudinal position 0.42−0.58: d_p=362 μm, f=150 Hz, C_p=7.76×10^8 m^{-3}

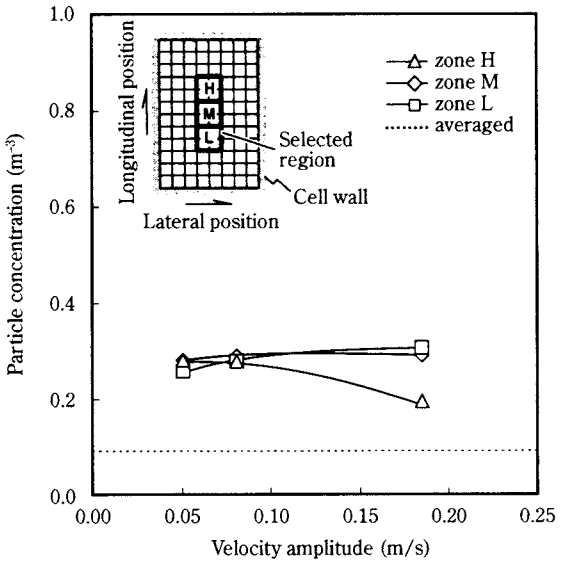

Fig. 11 Effect of velocity amplitude on particle concentration

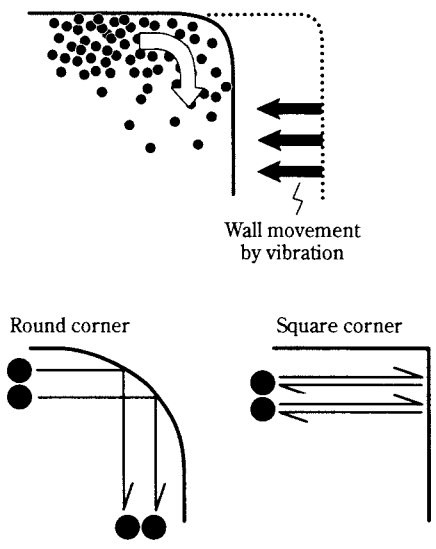

Fig. 12 Effect of corner shape on particle convection

at the top surface of the cell. At square corners vibrating laterally, particle movement is primarily in the x direction alone, but particles that collide with round corners have a post-collision z-direction velocity component, and move downward along the side walls. Because this effect cannot be expected very much at the cell's square bottom corners, it appears that this difference was manifested as the concentration difference in the longitudinal direction. This particle expulsion effect by round corners presumably increases as wall velocity increases, and the dependence on velocity amplitude of particle concentration in zone H of **Fig. 11** would seem to be an indication of this. These results suggest that it is possible to control the direction of particle movement in a vibration field by using container shape, and it is possible that this effect could be applied during transport and supply manipulation under microgravity.

4. Conclusion

We used the depth of field particle extraction method to measure the two-dimensional dispersion structure of 362 μm lead particles in a cell vibrated laterally under microgravity, and examined the effect of vibration conditions on particle dispersion, arriving at the following results.

(1) Under microgravity, particles came into contact with walls vibrating in the x direction, gained momentum, and dispersed throughout the cell by inter-particle collisions.

(2) Under microgravity we obtained an uneven, saddle-shaped two-dimensional particle concentration distribution, a tendency that became more pronounced as the initial particle load concentration increased. This was presumably due to emergence of a macroscopic cyclical flow inside the cell, and the velocity loss and stagnation area that arose in conjunction with that flow.

(3) We discerned a difference along the cell's longitudinal direction in the relationship of dependence between the vibrating walls' velocity amplitude A_v and the dispersion structure, in which, as velocity amplitude increased, concentration increased and uneven distribution was promoted in the regions at the square corners, while concentration decreased in the regions near round corners. This is presumably because the repulsion of particles at the round corners promoted expulsion of particles from the stagnation area near the cell top, thereby heightening dispersiveness.

(4) We found that, although simple, the depth of field particle extraction method used in this experiment is an effective way to make two-dimensional measurements of suspended particles without restricting their three-dimensional movement.

Acknowledgments

The authors express their gratitude to Ms. Izumi Uchidate, and to Masahiro Ohshima of Kawasaki Heavy Industries' Gifu Technical Institute for their cooperation in preparations for the experiment, data analysis, and other tasks associated with this research. We should also like to express our thanks by noting that part of this experiment was financed with a grant from the Hokkaido Technology Advancement Center, while another part was performed as research commissioned by the Japan Space Utilization Promotion Center.

Nomenclature

A_d	: displacement amplitude	(μm)
A_v	: velocity amplitude	(m/s)
C_p	: particle concentration	(m^{-3})
d_p	: particle diameter	(μm)
f	: frequency	(Hz)
t	: microgravity duration	(s)
x	: lateral position	(m)
z	: longitudinal position	(m)
ρ	: density	(kg/m^3)

References

1) Yamanaka, K., K. Hashimoto, N. Kamehara and T. Kotani. "Powder-mixing process under microgravity for oxide superconductors," Proc. of the 3rd IUMRS Internat. Conf. on Advanced Materials (1993).
(IUMRS: International Union of Materials Research Societies)

2) Ohyama, Y., S. Chiba, H. Takeuchi, O. Muragishi and Y. Sakakida. "Vibrated Powder Beds under Microgravity Conditions," Proc. of the 8th Japan Soc. of Microgravity Application Conference, 101 (1992).

Author's short biography

Yasushi Ohyama

Yasushi Ohyama obtained a bachelor of engineering and a master of engineering degree in Chemical Process Engineering from Hokkaido University, Japan in 1989 and 1991. He joined Hokkaido National Industrial Research Institute in 1991 as a researcher. He has been engaged in research work on powder handling in microgravity.

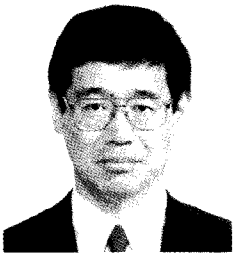

Hiromi Takeuchi

Hiromi Takeuchi graduated in Chemical Engineering from the Kyoto University, Japan, in 1980. And then, he studied at the same university as an assistant researcher for 3 years. In 1983, he obtained a Ph.D. and the title of the thesis is "Gross behavior of vertical buoyant jet". In 1983 he moved to the Hokkaido National Industrial Research Institute and started research on circulating fluidized bed. Since 1996, he has been a chief of microgravity section. Takeuchi specialises in heat transfer and hydrodynamics in fluidized bed, but has carried out, or supervised, projects in a variety of other areas such as cold energy transportation and humidity control under the freezing point.

Alexandr T. Pyatenko

A. Pyatenko graduated in Chemical Physics from Moscow Institute of Physics and Technology, Russia in 1978. After completed his doctor course at the same Institute he was awarded a Ph.D. in 1981. From 1981 to 1991 he worked as a researcher, then a senior researcher at the Institute for High Temperatures Academy of Science of the USSR. Since April 1993 up to now he is working as a senior researcher at HNIRI. He specializes in a study of powder handling process under microgravity, as well in a study of low-temperature (~0°C) – high humidity process.

Shigeo Chiba

Shigeo Chiba graduated in Chemical Engineering from the Murolan Institute of Technology in 1975, and completed his Masters degree in Chemical Process Engineering at Hokkaido University in 1977 and was awarded a Dr. tech. degree by the University for his thesis entitled "Basic Study on Solid Mixing and Segregation in Gas-Fluidised Beds" in 1981. He jointed Hokkaido National Industrial Research Institute (HNIRI) under AIST, MITI, immediately afterwards, and was late awarded a Post-Doctoral Researchship to study on solid particle behavior in fluidised bed systems by the Fluidised Bed Cooperative Research Center at West Virginia University in 1984. Since 1995, he has been a chief of Functional Materials Laboratory at HNIRI. Chiba specialises in powder processing and synthesis for functional materials, but has carried out projects in areas such as powder handling in microgravity and development of a centrifugal fluidised bed heat exchanger.

Author's short biography

Kunio Shinohara

Kunio Shinohara graduated in Chemical Process Engineering from Hokkaido University, Sapporo, Japan, in 1965. He got M.Sc in the course of Powder Technology, King's College London, England in 1970. He was awarded D.Eng. from Hokkaido University in 1973 for a thesis entitled "Mechanism of Gravity Flow of Particulate Materials". He has been a research and teaching staff at Hokkaido University since 1965 and become a full professor at the same Department and University in 1992. During these periods he made research visits to NRC in Canada and CMI & Telemark College in Norway.

He has been working on the following research topics:

- Fine particle preparation by attrition & jet millings, rotational impact blending and chemical vapor deposition.
- Analyses on powder flow and packing characteristics and on gravity flow mechanisms including segregation and new pneumatic transport.
- Production of functional and coated particulate materials by mechanical and chemical treatments with a moving bed reactor.

Simulation of Composite Particle Growth in the Dispersion and Compounding Processes of Alloy Particles and Ceramic Powder†

Tomohiro Iwasaki, Takeshi Yanagida and Munetake Satoh
*Dept. of Chem. Eng., Osaka Pref. Univ.**

Abstract

The authors investigated a compounding process in which fine WC powder is uniformly dispersed into particulate Ag-Ni alloy with a high-speed elliptical-rotor-type powder mixer. The growth of composite particles is observed as processing time elapses. A model for the growth phenomenon is constructed on the basis of the theory of powder grinding with a ball mill, and of the dynamics of the plastic deformation of metal particles. In the model, a function of the probability that composite particles grow is expressed in terms of three factors that include the compounding conditions as parameters: (1) the probability that particles are caught between a pair of medium balls (zirconia beads), (2) that they have undergone plastic deformation, and (3) the frequency with which the mixture of composite particles and beads is compressed by the elliptical rotor at the minimum clearance per unit time. Temporal change in the size distribution of composite particles has been calculated by using model equations. Comparison of calculated values with the experimental data for particle median diameter shows that they agree closely. It was demonstrated that the model is valid and that it is possible to accurately estimate and control particle size.

1. Introduction

In the powder processing in which the particle size changes, such as granulation, comminution, and others, formulating the size distribution of products in time series makes it possible to control the products' physical properties and estimate the processing time in which products of a required state are obtained. Recently in the field of powder metallurgy there has been active study of mechanical alloying (MA), mechanical grinding (MG), and other processes in which materials are compounded mechanically. However, there has been little research analyzing temporal changes in the size of composite particles on the basis of kinetics.

The authors have evaluated processing in which fine ceramic powder (tungsten carbide) is dispersed uniformly into a particulate alloy of silver and nickel with a high-speed elliptical-rotor-type powder mixer. Effects of compounding conditions on the state of the composite particles obtained were investigated by measuring the temporal change in the lightness and size of composite particles.[1,2] A simplified model of chemical reaction between two species was applied to the growth phenomenon of composite particles as time passed during the process. It was found that experimental conditions, such as the volume ratio of the powder mixture to the medium (zirconia beads) and the amount of ceramic powder added, had a great qualitative influence on the rate of particle growth and the degree of compounding.[2]

In this paper, a kinetics model of particle growth has been constructed on the basis of the theory of powder grinding with a ball mill[3] and of the dynamics of the plastic deformation of metal particles. This model takes into account the operating conditions of the powder mixer, the physical properties of powders, and the effects of ceramic powder in composite particles on plastic deformation. Temporal changes in the size distribution of composite particles have been simulated in terms of the model equations.

2. Model of particle growth

2.1 Kinetics model

The frequency distribution function $f(D_p, t)$ of the composite particles with diameter D_p (area basis) at

* 1-1 Gakuen-cho, Sakai, Osaka 599-8531, Japan
TEL. 0722-54-9307 FAX. 0722-54-9911

† This report was originally printed in J. of Japan Soc. of Powder and Powder Metallurgy, **45**, No. 4 362-367 (1998) in Japanese, before being translated into English by KONA Editorial Committee with the permission of the editorial committee of the Japan Society of Powder and Powder Metallurgy.

processing time t is derived from the population balance as follows:

$$\frac{d}{dt}[S(t)\cdot f(D_p, t)\cdot dD_p] = S_{in} - S_{out} \quad (1)$$

where $S(t)$ indicates the total projected area of composite particles. S_{in} and S_{out} are the projected areas of the composite particles, the sizes of which are within and without the size range between D_p and D_p+dD_p per unit time, respectively.

Observations of composite particles with a scanning electron microscope confirmed that composite particles were discoidal and that their thickness was uniform in the compounding process.[2] We proposed a simplified model for the particle growth phenomenon of the process. As illustrated in **Figure 1**, the model indicates that composite particles grow in the following manner: (1) a pair of colliding beads holds two disk-shaped particles (diameter $D_p/\sqrt{2}$ and thickness h) and sticks the particles together, and (2) a particle of diameter D_p (particle density and thickness are same as those of the particles before growth) is newly formed by the fused particles, causing plastic deformation. S_{in} and S_{out} are given by Eqs. (2) and (3):

$$S_{in} = P_z(D_p/\sqrt{2})\cdot S(t)\cdot f(D_p/\sqrt{2}, t)\cdot dD_p \quad (2)$$

$$S_{out} = P_z(D_p)\cdot S(t)\cdot f(D_p, t)\cdot dD_p \quad (3)$$

where $P_z(D_p)$ is a function of the probability that a particle of diameter D_p will grow per unit time.

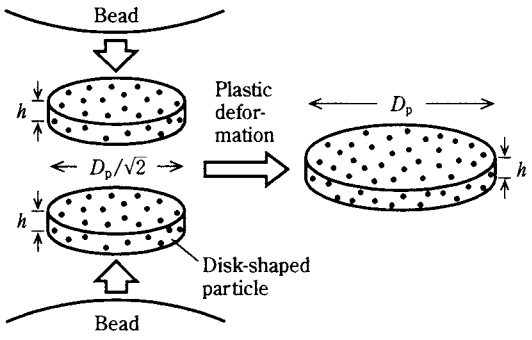

Fig. 1 Compounding model for disk-shaped particles

2.2 Theoretical analysis of the probability function $P_z(D_p)$ of particle growth

The probability function $P_z(D_p)$ of particle growth is defined as the product of a function $P_n(D_p)$ of the probability that two particles are held between a pair of beads, $P_{pl}(D_p)$ that plastic deformation occurs, and the frequency Z with which the mixture of composite particles and beads is compressed by the rotor at the minimum clearance per unit time.

$$P_z(D_p) = P_n(D_p)\cdot P_{pl}(D_p)\cdot Z \quad (4)$$

Z is given by

$$Z = 2(N_r + N_v) \quad (5)$$

where N_r and N_v are the rotational speeds of the rotor and the vessel, respectively.

Probability of holding composite particles

The apparent volume V_a of the mixture of metal particles and ceramic powder in the vessel is expressed on the basis of the charging condition of the powder mixture and the beads as follows:

$$V_a = V_m f \frac{V_p/V_b}{1+V_p/V_b} \quad (6)$$

V_m is the effective volume of the vessel, and f is the charge volume ratio. V_p and V_b are the apparent charge volumes of the powder mixture and the beads, respectively.

By assuming that two composite particles held between a pair of beads adhere rapidly to each other and then form one particle in appearance, the apparent volume v_a of the composite particles existing in voids among the beads is expressed geometrically (see **Figure 2**).

$$v_a = \pi b^2 D_p \quad (7)$$

$$b^2 \cong \frac{1}{2} D_p D_b \quad (8)$$

where D_p and D_b are the diameters of the composite particle and the bead, respectively.

As illustrated in **Figure 2**, the forces $\mu F\cos^2\alpha$ and $F\cos\alpha\sin\alpha$ act simultaneously on the composite particles held between a pair of colliding beads: the former is the force by which composite particles are pulled in between the beads, and the latter repels the particles. F is the impact force of the beads and μ is coefficient of dynamic friction. The composite particles are

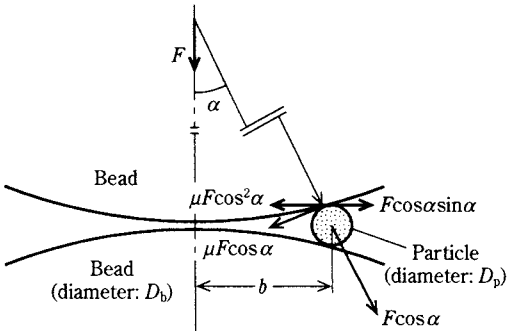

Fig. 2 Schematic diagram of a composite particle held between a pair of beads

caught by the beads when the following condition is satisfied:

$$\mu F\cos^2\alpha \geq F\cos\alpha\sin\alpha \tag{9}$$

$$\therefore \tan\alpha \leq \mu \tag{10}$$

The area ratio γ of the region where the composite particles are held and that where the forces act upon them is expressed by Eq. (11) in terms of $\xi=\tan^{-1}\mu$.

$$\gamma = \frac{[(D_b/2)\tan\xi]^2}{b^2} = \frac{\mu^2}{2}\left(\frac{D_b}{D_p}\right) \tag{11}$$

Therefore, $P_n(D_p)$ is expressed by Eq. (12).

$$P_n(D_p) = \frac{v_a}{V_a}\times\gamma = \frac{\pi\mu^2 D_p D_b^2}{4V_m f}\left(\frac{V_p/V_b}{1+V_p/V_b}\right)^{-1} \tag{12}$$

In consideration of the shape of composite particles in the compounding process, Eq. (12) is corrected with the shape factor ϕ.

$$P_n(D_p) = \frac{\pi\mu^2 D_p D_b^2}{4V_m f}\left(\frac{V_p/V_b}{1+V_p/V_b}\right)^{-\phi} \tag{13}$$

ϕ is defined by the following equation:

$$\phi = A/A_s \tag{14}$$

where A and A_s indicate the projected areas of composite particles and spherical particles, respectively, having volumes equal to that of the composite particle.

Probability of plastic deformation occurring

From the equilibrium of stress in the radial direction in the disk-shaped particle as shown in **Figure 3**, the following equation is obtained in terms of the approximation $\sin(d\theta/2)\approx d\theta/2$.

$$(\sigma_r h-\sigma_\theta h+2\tau r)dr+rhd\sigma_r=0 \tag{15}$$

If we assume that the composite particle is an ideal plastic solid and that the frictional condition between the composite particle and the bead is described by

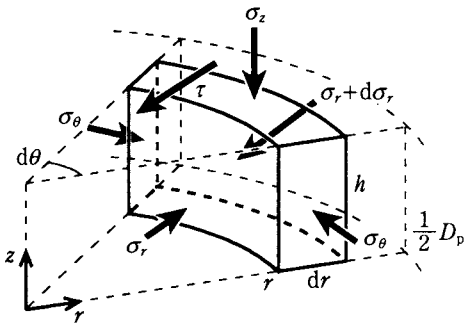

Fig. 3 Stresses acting on disk-shaped particles

using a constant coefficient of Coulomb friction without sliding, the relation $\sigma_\theta=\sigma_r$ holds from the Levy-Mises equation.[4] The shearing stress τ is expressed by Eq. (16) from von Mises' yield criterion.[4]

$$\tau = -\sigma_0/\sqrt{3} \tag{16}$$

σ_0 represents the yield stress of a composite particle. The following equation is obtained by substituting Eq. (16) into Eq. (15).

$$\frac{d\sigma_r}{dr} - \frac{2\sigma_0}{\sqrt{3}h} = 0 \tag{17}$$

By disregarding the effects of shearing stress at the edge of a composite particle on plastic deformation, σ_r is expressed by

$$\sigma_r = \sigma_0 - p \tag{18}$$

where p indicates the stress required to cause plastic deformation. The following equation is obtained by solving Eq. (17) (after substitution of Eq. (18)) with the boundary condition $p=\sigma_0$ at $r=D_p/2$.

$$p = \sigma_0\left[1+\frac{2}{\sqrt{3}h}\left(\frac{D_p}{2}-r\right)\right] \tag{19}$$

The average $\bar{p}$ of the stress p is given by Eq. (20).

$$\bar{p} = \frac{\int_0^{D_p/2} 2\pi p r dr}{\pi D_p^2/4} = \sigma_0\left(1+\frac{D_p}{3\sqrt{3}h}\right) \tag{20}$$

$P_{pl}(D_p)$ is defined as a function whose value decreases as diameter D_p of a composite particle increases because of a linear relation between $\bar{p}$ and D_p as indicated by Eq. (20).

$$P_{pl}(D_p) = kD_p^{-g(C_{WC})} \tag{21}$$

k is a constant that is dependent on physical properties of materials. $g(C_{WC})$ represents the magnitude of the effect of ceramic powder concentration C_{WC} in the composite particle on plastic deformation. The following equation is obtained by substituting Eq. (20) into Eq. (21).

$$P_{pl}(D_p) = k\left[3\sqrt{3}h\left(\frac{\bar{p}}{\sigma_0}-1\right)\right]^{-g(C_{WC})} \tag{22}$$

$P_{pl}(D_p)$ is calculated with Eq. (22) by assuming that the impact force between a pair of beads is equivalent to the centrifugal force generated by the rotational motion of the rotor.

Both the elastic modulus and strength of fine particle-dispersed metal material are proportional to the total volume of fine particles in the material. The movement of the dislocation line in the material,

which is necessary for causing plastic deformation, becomes more difficult as the amount of fine particles increases.[5] Accordingly, a simple formula is used to express $g(C_{WC})$.

$$g(C_{WC}) = c_1 + c_2 \cdot C_{WC} \quad (23)$$

c_1 and c_2 are constants that depend on the physical properties of materials.

3. Experimental and calculation methods

The appropriate amount of the mixture of gas-atomized Ag-Ni alloy particles (Ni content 3.2 wt%, median diameter 7 μm, true density 1.05×10^4 kg/m^3) and WC fine powder (median diameter 0.7 μm, true density 1.56×10^4 kg/m^3) was charged together with a medium (zirconia beads) into a high-speed elliptical-rotor-type powder mixer.[6] The charge volume ratio f (i.e., apparent volume of the powder-bead mixture divided by the effective volume of the vessel) was 0.2. The rotational speed of the vessel was maintained at 1.67s^{-1}, and rotor speed N_r was set at 25.0−41.7 s^{-1}. The volume ratio V_p/V_b of the powders to the beads was varied within the range of 0.3−1.5, the concentration C_{WC} of WC in the composite particles within the range of 1.0−10 wt%, and the size D_b of the beads in the range of 0.3−1.0 mm. An image analyzer mounted on a metallurgical microscope was used to measure more than 5,000 particles to determine the size distributions (area basis) of composite particles.

The constants k, c_1 and c_2, which were necessary to calculate size distribution, were determined ($k=5.00\times10^4$, $c_1=14.2$ and $c_2=3.54\times10^{-2}$) from the particle compounding experiments under the several conditions[2]. Calculations were based on the assumptions that WC powder was dispersed uniformly in the powder mixture at the processing time $t=0$ and that the yield stress of composite particles was dependent only on the WC concentration.

4. Results and discussion

4.1 Size distribution of composite particles

Figure 4 shows a typical example of calculation and experimental results for temporal change in the size distribution of composite particles. In the early stage of processing, the particle growth phenomenon caused by the plastic deformation of particles was highly evident. Particle growth reached the equilibrium state as processing progressed owing to the balance between the forces necessary for causing plastic deformation and acting on the composite particles.

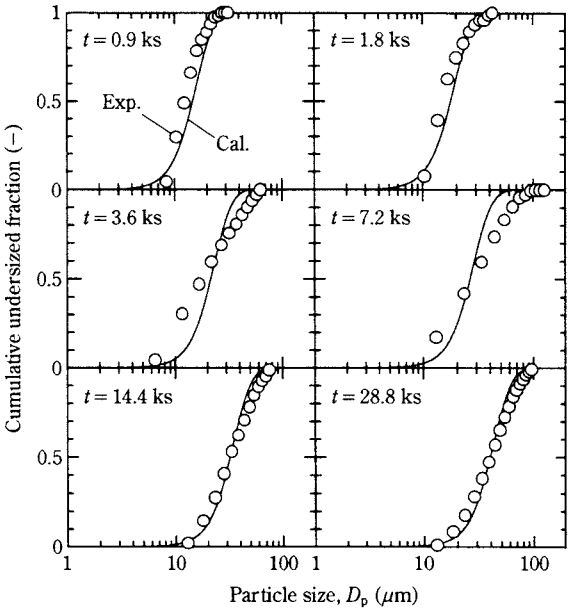

Fig. 4 Change in size distribution curves with the passage of processing time t (C_{WC}=10 wt%, D_b=1.0 mm, N_r=41.7 s^{-1}, V_p/V_b=0.3)

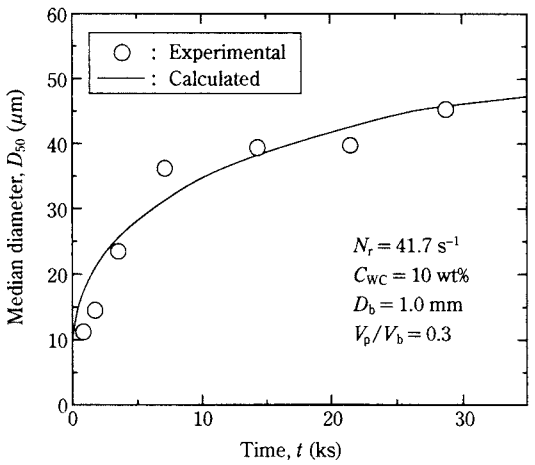

Fig. 5 Change in D_{50} with the passage of processing time t

Figure 5 shows the temporal change in median diameter D_{50} obtained from the data in **Figure 4**. Calculation results coincided closely with experimental results. In the following section, the validity of the proposed model is verified by comparing calculated values with the experimental data for D_{50}.

4.2 Effects of the compounding conditions

Figure 6 shows the relation between the median diameter D_{50} of composite particles and the processing time t when varying the powder-bead volume ratio V_p/V_b. In calculations and experimental results the particle growth rate decreased as V_p/V_b increased

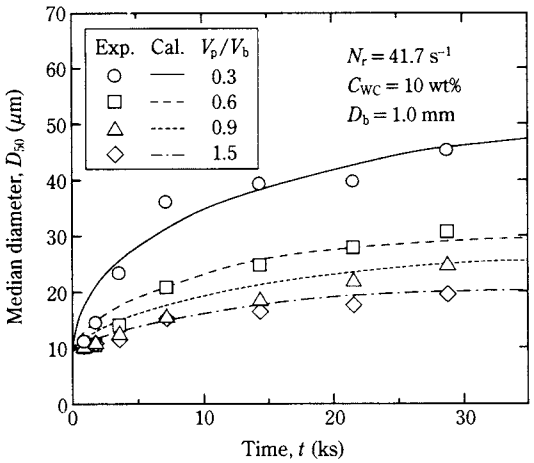

Fig. 6 Effect of volume ratio V_p/V_b on temporal change in D_{50}

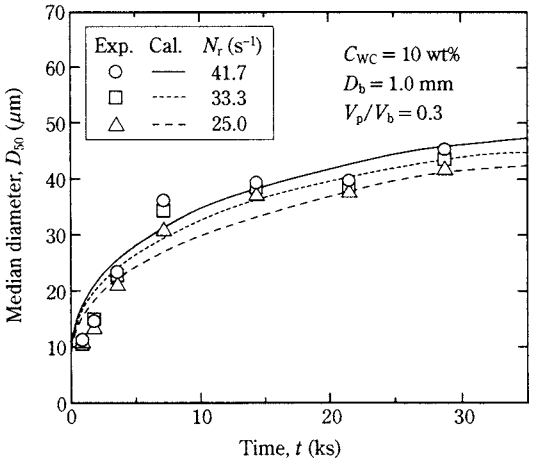

Fig. 8 Effect of rotor speed N_r on temporal change in D_{50}

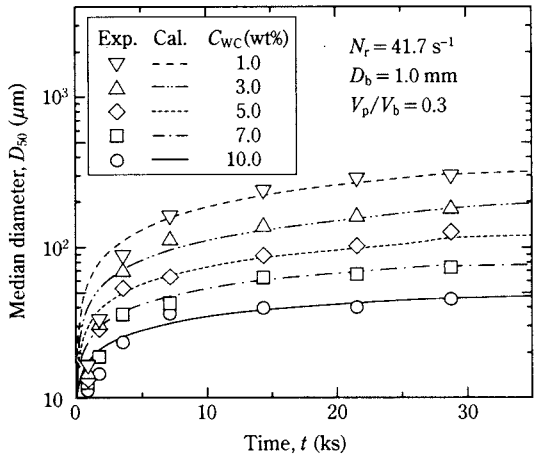

Fig. 7 Effect of WC concentration C_{WC} on temporal change in D_{50}

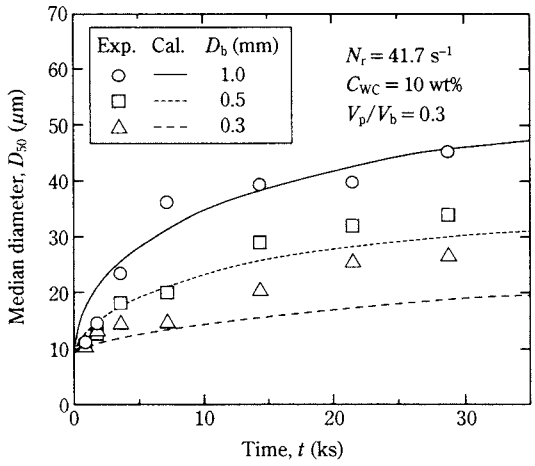

Fig. 9 Effect of bead diameter D_b on temporal change in D_{50}

because of the decreasing probability that composite particles were held by beads.

Figure 7 shows the effect of WC powder weight concentration C_{WC} on the temporal change in D_{50}. The size of composite particles in the late stage of processing declined with the increase in C_{WC}. This means that the presence of WC powder in composite particles prevented the composite particles from causing the plastic deformation that is necessary for growth.

Figure 8 shows the effect of rotor speed N_r on particle growth. At higher N_r, the particle growth rate increased due to the increase in the frequency per unit time with which the mixture of composite particles and beads was compressed by the rotor at the minimum clearance. However, comparing the results in **Figure 8** with those in **Figure 6** shows that the effect of N_r on particle growth was smaller than that of V_p/V_b. At higher rotor speeds, particle growth occurs only with difficulty even though the compression frequency increases more if the amount of beads is insufficient to cause plastic deformation.

Figure 9 shows the calculation and experimental results obtained when bead diameter D_b was varied. Composite particle size decreased when using smaller-sized beads because of change in the stress acting on composite particles and in the probability of holding a composite particle.[7]

Close agreement between calculated values and experimental data for particle size in **Figures 6** through **9** supports the validity of the proposed model.

5. Conclusion

We performed a kinetic analysis, and investigated the mechanism, of a composite particle growth phenomenon brought about by plastic deformation of composite particles occurring in a compounding process involving the uniform dispersion of fine

ceramic powder into alloy particles. The following conclusions can be drawn.

1) Particle growth in the compounding process has been conceived as a probability phenomenon in which composite particles are caught between a pair of media and subjected to plastic deformation. A simplified model of the phenomenon has been proposed in terms of the probability function of composite particle growth. The validity of the model has been confirmed by agreement between calculated values and experimental data.

2) Both the calculations and the experiments clarified the effects of compounding conditions, i.e., the powder-media volume ratio, the amount of ceramic powder added, rotor speed, and medium diameter, on particle growth.

Nomenclature

A	: projected area of composite particle	(m^2)
A_s	: projected area of spherical particle having volume equal to that of composite particle	(m^2)
b	: constant expressed by Eq. (8)	(m^2)
C_{WC}	: weight concentration of WC in composite particles	(%)
c_1, c_2	: constants in Eq. (23)	(−)
D_{50}	: area median diameter of composite particle	(m)
D_b	: bead diameter	(m)
D_p	: disk-shaped particle diameter	(m)
F	: impact force between a pair of beads	(N)
f	: charge volume ratio	(−)
$f(D_p, t)$	: frequency distribution function	(m^{-1})
$g(C_{WC})$	: function of C_{WC} defined by Eq. (23)	(−)
h	: height of disk-shaped particle	(m)
k	: constant in Eq. (21)	($\mu m^{g(C_{WC})}$)
N_r, N_v	: rotational speeds of rotor and vessel	(s^{-1})
$P_n(D_p)$	: probability function expressed by Eq. (13)	(−)
$P_{pl}(D_p)$	: probability function defined by Eq. (21)	(−)
$P_z(D_p)$	: probability function defined by Eq. (4)	(−)
p	: stress required to cause plastic deformation	(Pa)
S_{in}, S_{out}	: projected areas of composite particles expressed by Eqs. (2) and (3)	(m^2)
$S(t)$	: total projected area of composite particles	(m^2)
t	: processing time	(s)
V_a	: apparent volume of powder mixture	(m^3)
V_b	: apparent charge volume of beads	(m^3)
V_m	: effective volume of mixer vessel	(m^3)
V_p	: apparent charge volume of powder mixture	(m^3)
v_a	: apparent volume of composite particles present in voids among beads	(m^3)
Z	: frequency expressed by Eq. (5)	(−)
α	: angle representing contact point between composite particle and bead	(rad)
γ	: area ratio defined by Eq. (11)	(−)
μ	: coefficient of dynamic friction between composite particle and bead	(−)
σ_0	: yield stress of composite particle	(Pa)
σ_r, σ_θ	: stresses applied in directions of r and θ	(Pa)
τ	: shearing stress	(Pa)
ϕ	: shape factor defined by Eq. (14)	(−)

References

1) Satoh, M., T. Yanagida and T. Iwasaki, "Dispersion and Compounding Process of Particulate Ag-Ni Alloy and Fine WC Powder Using a High-speed Elliptical-rotor-type Powder Mill," *J. Jpn Soc. Powder and Powder Met.*, **44**, 618-621 (1997).

2) Iwasaki, T., T. Yanagida and M. Satoh, "Effect of Operating Conditions in Powder Metal Compounding Process on Particle Size Change," *J. Jpn Soc. Powder and Powder Met.*, **45**, 271-275 (1998).

3) Kuwahara, Y., F. Saito and S. Yashima, "An Analysis of Selection Function of Vibration Mill," *J. Res. Ass. Powder Technol., Japan*, **14**, 319-325 (1977).

4) Dieter, G. E., *Mechanical Metallurgy*, 3rd ed., McGraw-Hill, Inc. (1986).

5) Fukuda, H., R. Yokota and I. Shiota, *Fukugou Zairyou Kisokougaku*, Nikkan Kougyo (1994).

6) Satoh, M., T. Yoshida, K. Miyanami and Y. Okudaira, "Evaluation of the Performance of a High-speed Elliptical-rotor-type Powder Mixer," *J. Soc. Powder Technol., Japan*, **31**, 789-794 (1994).

7) Yamauchi, K, Y. H. Park, H. Hashimoto and R. Watanabe, "Change in Morphology and Some Properties of Ti-Al Powder Particles during Mechanical Alloying by Vibratory Ball Milling," *J. Jpn Soc. Powder and Powder Met.*, **38**, 42-46 (1991).

Author's short biography

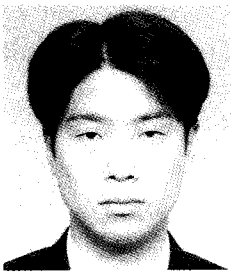

Tomohiro Iwasaki

Tomohiro Iwasaki received the master degree in chemical engineering from the Osaka Prefecture University in 1996. He joined the Department of Chemical Engineering, the Osaka Prefecture University, as an Assistant Professor in 1997. His major research interests are design of functional composite particle, evaluation of manufacturing process of composite particles, simulation of behavior of particle in compounding process, measurement and evaluation of dynamic physical properties of powder, and analysis of stress in powder bed.

Experimental Study on the Grinding Rate Constant of a Ball Mill: Effects of Feed Size and Ball Diameter†

Yoshiteru Kanda, Kiichi Simodaira, Naoya Kotake and Yasushi Abe
*Dept. of Materials Science and Eng. Yamagata Univ.**

Abstract

The grinding rate constant is one of the important factors needed to measure or evaluate a grinding process. It has been found that the decreasing rate of the feed size is described by a first-order equation in the initial grinding stage of various mill types.

In this study we conducted grinding tests on silica glass using a ball mill, and measured the grinding rate constant of the feed size decrease. We investigated the effects of ball diameter and feed size on the rate constant when the ball mass, feed mass, and the mill's rotational speed were constant.

The results indicated that the grinding rate constant can be expressed by modifying the equation that was proposed by Snow as the function of ball diameter and feed size.

1. Introduction

Grinding is put to effective use in the manufacture of fine and ultra-fine powders for the development of new materials and for improving product quality. For a long time grinding processes have been subjected to statistical and kinetic analyses,[1-3] and have been widely investigated especially on ball mills.

When a grinding rate is examined in terms of material balance, there are two basic functions: the selection function, which indicates the fracture probability of a particle, and the breakage function, which shows the size distribution of fractured particle. Using these functions makes it possible to express the material balance equation for a particle size in the following way.[4,5]

$$\frac{dm_i(t)}{dt} = -S_i m_i(t) + \sum_{\substack{j=1 \\ j<i}}^{i-1} b_{i,j} S_j m_j(t) \qquad (1)$$

$i = 1, 2, \cdots \cdots n$

where:

$m_i(t)$ is the mass fraction of the particles of component i,

S_i is the selection function,

$b_{i,j}$ is the rate at which particles of the ground component j become particles of component i, and

t is the grinding time.

Additionally, i=1 in Eq. (1), for it is often the case that the decrease rate of the largest particle group is shown by the following first-order equation.

$$\frac{dm_1(t)}{dt} = -S_1 m_1(t) \qquad (2)$$

In particular the selection function S_1 has been subject to investigation by many researchers using a variety of grinding machines and conditions,[6-12] and even now this is an item of great interest when considering the problems of grinding efficiency and small amount of coarse particles in products.

In this study, Eq. (2) corresponds to the decrease rate of feed material, we expressed $m_1(t)$ as the mass fraction of feed size R, and S_1 as grinding rate constant K_1 in Eq. (3). Silica glass was ground with a ball mill while varying the feed size and ball diameter, and measured K_1.

$$-\frac{dR}{dt} = K_1 R \qquad (3)$$

An experimental equation was obtained by expressing K_1 as a function of feed size and ball diameter.

2. Sample Used and Experimental Method

Material used in the experiment was silica glass with a density of 2,150 kg·m^{-3}, and a Hardgrove

* 4-3-16, Jonan, Yonezawa, Yamagata, 992-8510 Japan
TEL. 0238-26-3161

† This report was originally printed in J. Soc. Powder Technology, Japan. **35**, 12-17 (1998) in Japanese, before being translated into English by KONA Editorial Committee with the permission of the editorial committee of the Soc. Powder Technology, Japan.

Table 1 Grinding conditions

$d_B \times 10^3$ (m)	3	5	10	20	30
$x_f \times 10^3$ (m)	1.68~1.41 – 0.105~0.088	2.38~2.00 – 0.105~0.150	3.36~2.83 – 0.149~0.125	4.0~3.36 – 0.149~0.125	8.0~6.7 – 0.105~
Number of feed sizes	12	11	11	12	19
x_f/d_B (–)	0.515–0.032	0.438–0.023	0.31–0.0137	0.184–0.0069	0.245–0.0032

Grindability Index of 48. The experimental feed was prepared by using a Jaw crusher to make several cm of silica glass into coarse sizes, then using a standard sieve in a rotating and tapping shaker (Ro-Tap shaker) to classify the particles, and the ratio of aperture size of adjacent screens used was $2^{1/4}$. The mill was made of alumina with an inside diameter of 144 mm and a volume of 2.1 liters, and the grinding medium was also alumina. Five ball diameters ranging between 3 and 30 mm were used and feed size was varied on the order of 10^{-3} to 10^{-1} as a ratio of ball diameter. Feed sizes and ball diameters used in the experiment are shown in **Table 1**. Feed mass and ball mass were set at 200 g and 2 kg, respectively, in consideration of the optimum grinding conditions reported in a previous paper,[13] and mill rotational speed was constant at 108 rpm, i.e., about 90% of critical speed. Experiments were conducted for the three time spans of 1, 3, and 5 minutes for each set of conditions, and ground products were sieved with a rotating and tapping shaker, after which the mass of the unground feed was measured and put back in the mill, with grinding again continued for the prescribed length of time.

3. Experimental Results and Discussion

3.1 Measurement of Grinding Rate Constant

Figs. 1 through **3** show examples of the relationship between mass fraction of feed size and grinding time when using ball diameters of 10, 20, and 30 mm, respectively. They exhibit nearly linear relationships when plotted on semi-log graph paper, and it is possible to calculate the grinding rate constant K_1 of Eq. (3). The graphs indicate that K_1 varies according to feed size at all ball diameters.

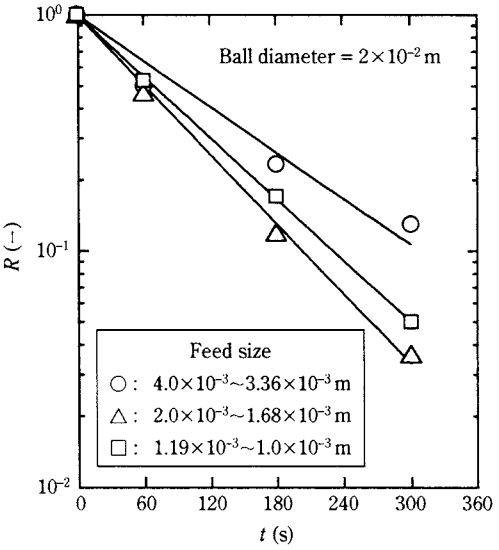

Fig. 2 First-order plots of feed fraction (d_B=2×10⁻² m)

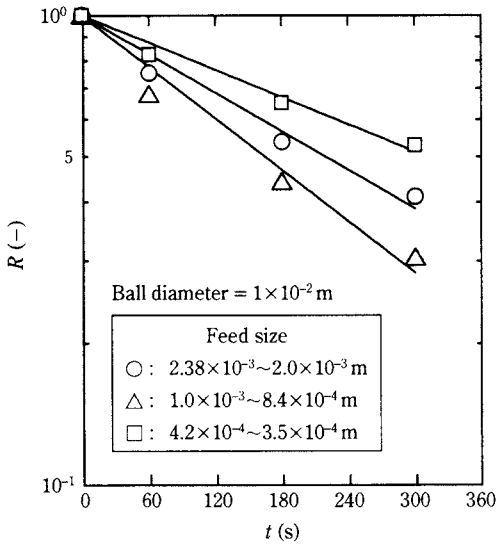

Fig. 1 First-order plots of feed fraction (d_B=1×10⁻² m)

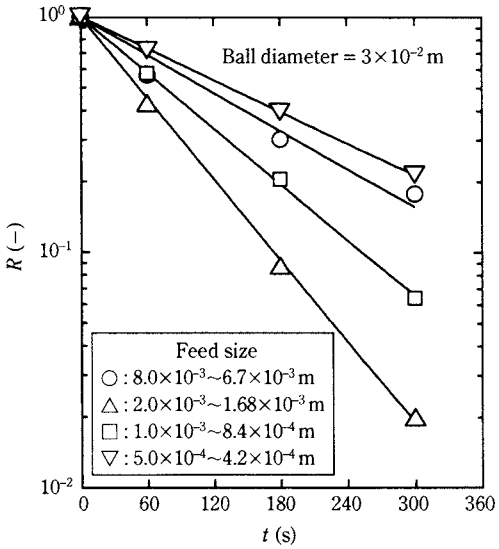

Fig. 3 First-order plots of feed fraction (d_B=3×10⁻² m)

3.2 Relationship between Grinding Rate Constant and Feed Size

Fig. 4 shows the relationship between K_1 and feed size which was plotted on log-log graph paper with ball diameter as a parameter. The feed size was the arithmetic mean of opening of sieves used to arrange the feed particles. K_1 increases as feed size increases, and is independent of the ball diameter used. There is an optimum feed size at which K_1 has a maximum. There is also a tendency for this optimum feed size to increase with ball diameter.

Austin[7] and Zhao et al.[11] used the following equation to show the change in the feed size of $K_1(=S_1)$.

$$S_1 = a x_f^{\alpha'} Q(z) = a x_f^{\alpha'} Q\left(\frac{\ln(x_f/\mu)}{\ln\sigma}\right) \tag{4}$$

where:
a and α' are constants,
$Q(z)$ is the Gaussian probability distribution function,
x_f is the feed size,
z is a dimensionless parameter,
μ is the feed size when $Q(z)=0.5$, and
$\ln\sigma$ is the standard deviation of $Q(z)$.

In both reports one notices that this formula matches experimental values in the fine particle range, but that calculated and actual values diverge considerably in the coarse particle range. Snow[14] quoted the data of Kelsall et al.[6] and showed that the relationship between S_1 and feed size was empirically shown by Eq. (5).

$$\frac{S_1}{S_m} = \left(\frac{x_f}{x_m}\right)^{\alpha} \exp\left(-\frac{x_f}{x_m}\right) \tag{5}$$

where:
α is a constant, and
x_m is the feed size at which S_1 is maximum, i.e., S_m.

From **Fig. 4** one can see that, variation in K_1 due to feed size is roughly analogous and independently of ball diameter. **Fig. 5** shows the result obtained when normalizing **Fig. 4** using x_m, the optimum feed size that maximizes K_1, and the grinding rate constant K_m at this time. As one can see from **Fig. 4**, owing to the difficulty of specifying x_m, at which K_1 has maximum. Then as shown by the black points we chose feed size averages that are within 10% of the values considered to be the K_1 maximum, and used them as the average values for K_m. From **Fig. 5** it is evident that the relationship between K_1 and feed size lies fairly well along a curve, and has no relation to ball diameter. The reason is thought to be that in the first stage of grinding silica glass with a ball mill, the grinding rate varies depending on ball diameter, but that the grinding mechanism makes little difference.

3.3 Relationship between Grinding Rate Constant and Feed Size According to Other Researchers

Figs. 6 through **8** show the grinding rate constant data for a ball mill according to Kelsall et al., a vibration mill according to Kuwahara[10], and for a planetary mill according to Zhao[11], plotted as in **Fig. 5**. From the graphs it is clear that the variation in the grinding rate constant due to feed size can be more or less normalized independently of ball diameter. This suggests that the base of the size reduction in ball media mills results from the interactions between the grinding media and the particles, and that this mechanism does not change even if the feed size and ball diameter are changed.

3.4 Revision and Application of Snow's Equation

As **Figs. 5** through **8** show, variation in the dimensionless grinding rate constant due to feed size is sim-

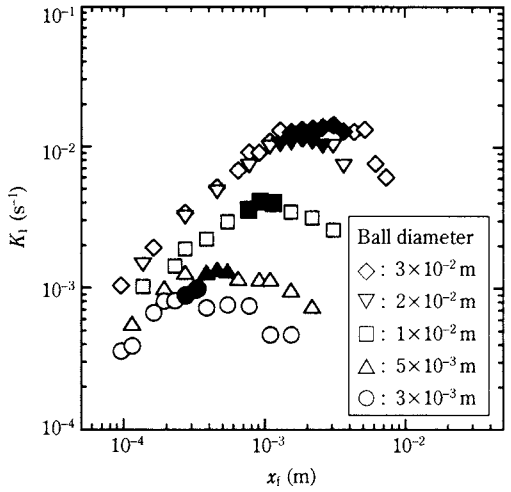

Fig. 4 Variation in grinding rate constant due to feed size

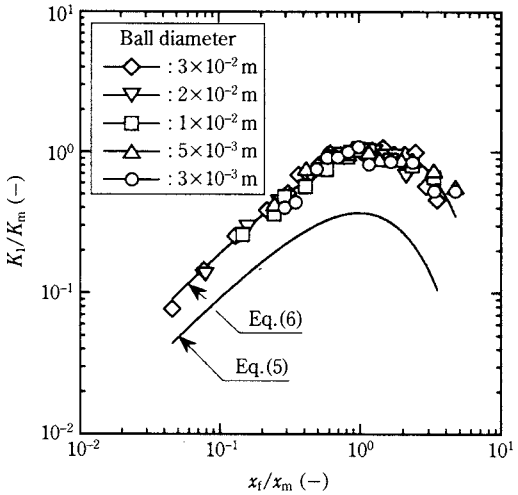

Fig. 5 Variation in dimensionless grinding rate constant due to dimensionless feed size

ilar to the variation indicated by Eq. (5) proposed by Snow, but the data plots do not indicate a good correspondence. The main reason appears to be that when $x_f = x_m$ in Eq. (5), S_1 does not equal S_m, so in our research we revised the decrease function term in Eq. (5) to yield Eq. (6), and fit curves to arrive at the results shown in **Figs. 5** through **8**.

$$\frac{K_1}{K_m} = \left(\frac{x_f}{x_m}\right)^{\alpha} \exp\left(-c\frac{x_f - x_m}{x_m}\right) \tag{6}$$

Eq. (6) does comparatively well at showing the experimental values. **Table 2** gives the parameters for Eq. (6) used in **Figs. 5** through **8**. As we discerned no definite trend in the values of either α or c with respect to the type of ball media mill or the kinds of feed materials, it will be necessary in the future to investigate more types of ball media mills and feed materials.

Table 2 Application of Eq. (6) to other studies

Author	Kind of mill	Ball material	Sample	α	c
Kelsall et al.(1967)	Ball mill (Wet grinding)	Steel	Quartz	1.44	1.1
Kuwahara (1985)	Vibration mill	Steel	Silica sand	1.0	0.6
Zhao et al. (1988)	Planetary mill	Steel, Alumina, Glass	Silica sand	1.28	1.04
This study	Ball mill	Alumina	Silica glass	1.0	0.7

3.5 Grinding Rate Constant for Silica Glass

Fig. 9 shows the relationship between ball diameter and optimum feed size on the one hand, and the

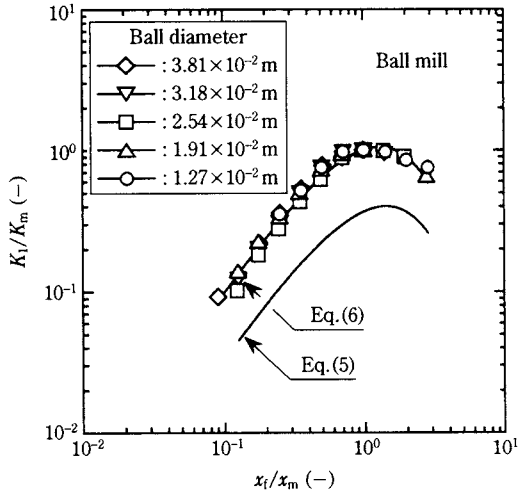

Fig. 6 Variation in dimensionless grinding rate constant due to dimensionless feed size (Kelsall et al.[6]; ball mill, wet grinding, quartz)

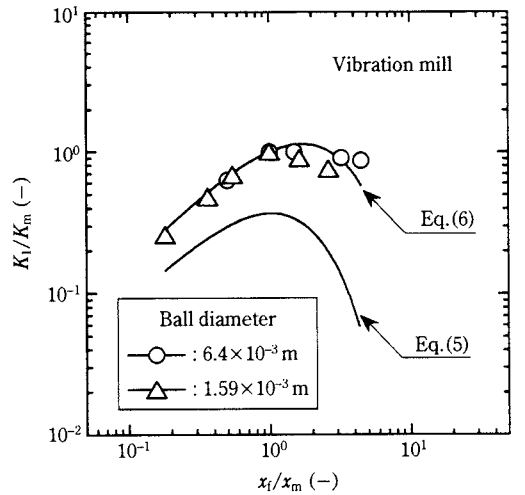

Fig. 7 Variation in dimensionless grinding rate constant due to dimensionless feed size (Kuwahara[10]; vibration mill, dry grinding, silica sand)

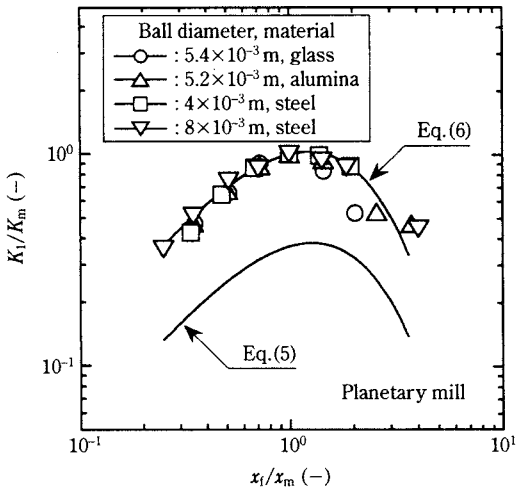

Fig. 8 Variation in dimensionless grinding rate constant due to dimensionless feed size (Zhao et al.[11]; planetary mill, dry grinding, silica sand)

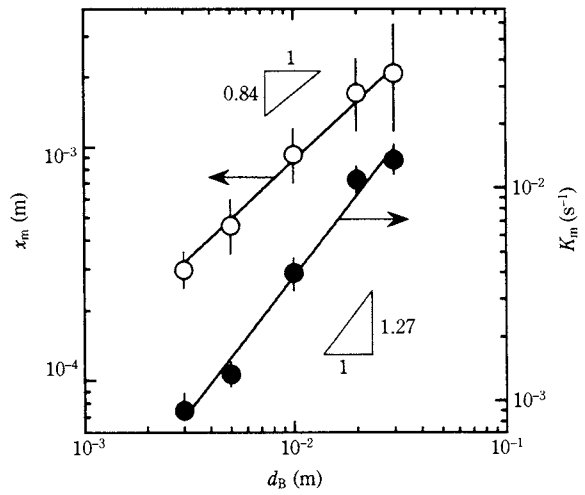

Fig. 9 Correlation of x_m and K_m with ball diameter

maximum value of the rate constant on the other, in relation to the silica glass used in this experiment. The relationship between ball diameter and optimum feed size is similar to that described by Zhao et al.[11] for grinding with ball media mills. In this experiment we obtained Eq. (7).

$$x_m = 0.042 d_B^{0.84} \tag{7}$$

Eq. (8) was obtained for the relationship between ball diameter and the maximum value for the rate constant.

$$K_m = 1.29 d_B^{1.27} \tag{8}$$

Substituting Eqs. (7) and (8) into Eq. (6), Eq. (9) is obtained.

$$K_1 = 61.9 d_B^{0.43} x_f \exp(-16.7 d_B^{-0.84} x_f) \tag{9}$$

Fig. 10 compares the experimental values for the grinding rate constant and the calculated values obtained with Eq. (9). As it is desirable to run a mill with feed material below the optimum feed size in actual operation, the graph uses circles to plot the rate constant for particle sizes smaller than the optimum feed size, and triangles to plot the rate constant for particle sizes larger than the optimum feed size. It is somewhat evident from the graph that when feed size is larger than the optimum value, there is a large difference between the experimental and calculated values. Eq. (9), however, largely satisfies the experimental values for a broad feed size range, and we believe that it is an effective method especially when evaluating the grinding rate in actual operation.

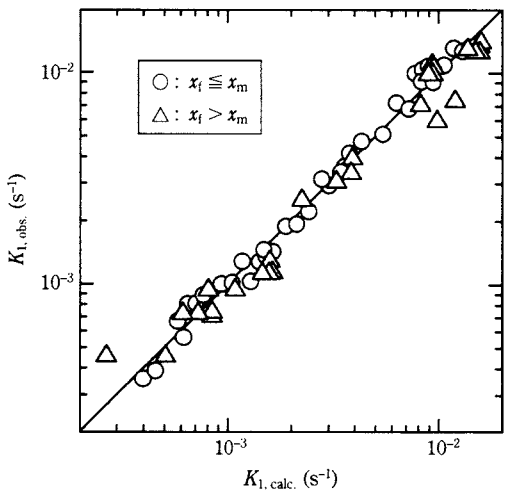

Fig. 10 Comparison of observed values and values calculated by Eq. (9)

4. Conclusion

In this paper, we performed dry grinding tests of silica glass with a ball mill and investigated the effects of feed size and ball diameter on the grinding rate constant (selection function). The results are summarized as follows.

1) Variation in the grinding rate constant due to feed size was roughly analogous, and it was independently of ball diameter. We were able to show this relationship by revising the equation proposed by Snow. By examining other researchers' data we confirmed that this relationship holds even when using different types of ball media mills and feed materials.

2) We obtained equations showing the relationships between ball diameter and optimum feed size, and between the ball diameter and the maximum grinding rate constant.

3) Using Snow's equation as revised in this research and the results in 2), we obtained an empirical equation for the grinding rate constant when grinding silica glass with a ball mill.

Nomenclature

a	: constant in Eq. (4)	($s^{-\alpha'}$)
$b_{i,j}$	: fraction of broken particles of size j which falls into particle size i	(−)
c	: constant in Eq. (6)	(−)
d_B	: ball diameter	(m)
K_1	: grinding rate constant of feed size decreasing ($=S_1$)	(s^{-1})
$K_{1,calc}$	: calculated value of K_1	(s^{-1})
$K_{1,obs}$	: observed value of K_1	(s^{-1})
K_m	: maximum value of K_1 ($=S_m$)	(s^{-1})
$m_1(t)$	: mass fraction of maximum particle size at time t	(−)
$m_i(t)$	: mass fraction of particle size i at time t	(−)
$m_j(t)$	: mass fraction of particle size j at time t	(−)
$Q(z)$	: Gaussian probability function	(−)
R	: mass fraction of feed size ($=m_1(t)$)	(−)
S_1	: selection function of maximum particle size	(s^{-1})
S_i	: selection function of particle size i	(s^{-1})
S_j	: selection function of particle size j	(s^{-1})
S_m	: maximum value of S_1	(s^{-1})
t	: grinding time	(s)
x_f	: feed size	(m)
x_m	: feed size for which the rate constant K_1 is maximum at a given ball diameter	(m)

z	: dimensionless parameter $(=\ln(x/\mu)/\ln\sigma)$	(−)
α	: constant in Eq. (6)	(−)
α'	: constant in Eq. (4)	(−)
μ	: feed size at $Q(z)=0.5$	(m)
$\ln\sigma$	: standard deviation of the probability function	(−)

References

1) Epstein, B.: "Logarithmic-normal Distribution in Breakage of Solids." *Ind. Eng. Chem.* **40**, 2289-2291 (1948).
2) Gardner, R. P. and L. G. Austin: "A Radioactive Tracer Technique for Determination of Breakage Functions." Proc. 1st Europ. Symp. p. 217 (1962).
3) Herbst, J. A. and D. W. Fuerstenau: "The Zero-order Production of Fine Sizes in Comminution and its Implications in Simulation.", *Trans. A.I.M.E.*, **241**, 538-549 (1968)
4) Gaudin, A. M. and T. P. Meloy: "Model and a Comminution Distribution Equation for Repeated Fracture." *Trans. A.I.M.E.*, **223**, 43-50 (1962).
5) Sedlatschek, K. and Bass. L.: "Contribution to the Theory of Ball Milling.", *Powder Metall. Bull.*, **6**, 148-153 (1953).
6) Kelsall, D. F., K. J. Reid and C. J. Restarick: "Continuous Grinding in a Small Wet Ball Mill, Part I, A Study of the Influence of Ball Diameter.", *Powder Technol.*, **1**, 291-300 (1968).
7) Austin, L. G., K. Shoji and P. T. Lukie: "The Effect of Ball Size on Mill Performance.", *Powder Technol.*, **14**, 71-79 (1976).
8) Kanda, Y., H. Gunji, H. Takeuchi and K. Sasaki: "Rate Constants of Wet and Dry Ball Mill Grinding.", *J. Soc. Mat. Sci., Japan.*, **27**, 663-666 (1978).
9) Tanaka, T.: "Funtai purosesu nyumon." Kougakutosyo. p. 205 (1981). (In Japanese)
10) Kuwahara, Y.: "Doctoral Thesis, Tohoku University." p. 67 (1985). (In Japanese)
11) Zhao, Q. Q. and G. Jimbo: "The Effect of Grinding Media on the Breakage Rate of Planetary Mill.", *J. Soc. Powder Technol., Japan.* **25**, 603-608 (1988).
12) Nomura, S., K. Hosoda and T. Tanaka: "An Analysis of the Selection Function for Mills using Balls as Grinding Media.", *Powder Technol.*, **68**, 1-12 (1991).
13) Kotake, N., K. Shimodaira, H. Nishihara, Y. Abe and Y. Kanda. "Production of Submicron Particles by Ball Milling and its Evaluation.", *J. Soc. Mat. Sci., Japan.* **42**, 1265-1270 (1993).
14) Snow, R. H.:"Grinding Mill Simulation and Scale-up of Ball Mills.", Proc. 1st Int. Conf. Particle Technol., IITRI. p. 28, Chicago (1973).

Author's short biography

Yoshiteru Kanda

- Professor, Department of Materials Science and Engineering, Yamagata University.
- 1964 B.S. (Yamagata Univ.), 1966 M.S. (Yamagata Univ.), 1970 Ph.D. (Tohoku Univ.)
- 1969 Lecturer (Yamagata Univ.), 1972 Associate Professor (Yamagata Univ.), 1989 Professor (Yamagata Univ.)
- Yamazaki Award by The Society of Materials Engineering for Resources of Japan (1997)
- Research Interests: Effect of particle shape on grindability of solid materials, Fine and ultrafine grinding and its evaluation, Control of size distribution in grinding process, Recycle of waste glass.

Kiichi Simodaira

Kiichi Simodaira graduated in Materials Science and Engineering of Yamagata University in 1991. He is engaging in optical related products division of Nitto Denko Corporation.

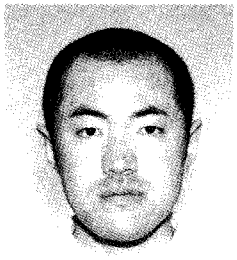

Naoya Kotake

- Research Assistant, Department of Materials Science and Engineering, Yamagata University.
- 1991 B.S. (Yamagata Univ.), 1993 M.S. (Yamagata Univ.), 1996 Ph.D. (Yamagata Univ.)
- Research Interests : Production of fine particles and control of its size distribution by grinding, Studies of evaluation method in fine grinding, Kinetics of size reduction.

Yasushi Abe

Yasushi Abe had been Technical Assistant of Department of Chemical Engineering, and Materials Science and Engineering of Yamagata University from 1961 to 1997.

Evaluation of a Direct Granulation Method for Liquid Materials with a Fluidized Bed Granulator†

Hiroyuki Tsujimoto, Toyokazu Yokoyama
*Hosokawa Micron Corporation**
Isao Sekiguchi
*Dept. of Applied Chemistry, Chuo Univ.***

Abstract

The authors propose a new granulation technique employing a spray fluidized bed granulator that directly produces granules from liquid materials. Instant coffee dissolved in water was used as the liquid material. In order to elucidate the agglomeration mechanisms in the granulator, changes in the physical properties of granules were measured at various liquid material feed rates. We proposed an index R that is related to the liquid feed rate and is capable of quantitatively evaluating the conditions of drying in the granulator.

Experimental results showed that granule formation depends on the R value in accordance with the following three mechanisms: 1) generation of fine particles by the spray drying effect, 2) agglomeration of fine particles, and 3) layering of fine particles onto the surface of individual agglomerates.

Spherical granule products with high bulk density were obtained especially with layering granulation in a stable fluidized bed. Further, an equation derived from the mass balance for coffee solids in the granulator accurately described the growth of granules during layering granulation.

1. Introduction

In general, spray driers are often used in processes that produce powders by drying a variety of liquid materials in fields such as food, pharmaceuticals, and chemical products. This drying process uses cyclones, filter bags, and other such means to capture spray-dried particles carried on air flows. Presently it is often the case that granulation processing is used to manufacture granules out of the fine spray-dried particles thus obtained in order to effect improvements in solubility, packing properties, formability, and other properties. Recently practicalized for this purpose is the integrated fluidized bed spray drier[1] made by adding a fluidized bed granulator to the lower end of a spray dryer and connecting to a finishing drier. This device makes particle agglomerations by creating a fluidized bed of spray-dried particles and spraying liquid materials and liquid binders into the bed with nozzles. It is used to manufacture irregularly shaped granules with a porous agglomerate structure. Other than this, a generally used method involves using an extrusion granulator to make spray-dried particles into cylindrical granules, process them by tumbling spheroidizing and drying, and make them into spherical granules for the purpose of obtaining visually pleasing spherical granules with excellent handling properties such as for transport, supply, and packaging.

Manufacturing granular products from liquid materials in this manner necessitated a number of single-function machines, which resulted in a long and large-scale manufacturing process, augmented capital outlays, and increased costs such as for running and maintenance. This especially tends to be so in the manufacture of spherical granule products, so there is a great demand for new granulation and drying processes that can shorten, and save labor in, manufacturing processes.

Based on our experience thus far in research and development for laborsaving in and multiple functions of fluidized bed granulators, the authors explored a new granulation method that involves using a spray nozzle fitted with a distributor to directly spray feed liquid materials into fluidizing air in a fluidized bed granulator whose empty column has no particulate material feed. As a result, it was possible to directly

* 1-9 Shoudai-Tajika, Hirakata Osaka 573-1132, Japan
** 1-13-27 Kasuga, Bunkyo-ku Tokyo 112-8551, Japan
† This report was originally printed in J. Soc. Powder Technology, Japan. **36**, 368-377 (1999) in Japanese, before being translated into English by KONA Editorial Committee with the permission of the editorial committee of the Soc. Powder Technology, Japan.

make spherical granules from liquid material with a single fluidized bed granulator, thereby considerably streamlining the manufacturing process.

For the purpose of elucidating the granule formation mechanism of this granulation method, here we experimentally examine the particle size and shape characteristics of granular products obtained under batch operating conditions and report the results.

2. Experimental Apparatus and Method

2.1 Experimental Apparatus and Method

Fig. 1 shows a fluidized bed granulator (AGM-SD, Hosokawa Micron). The fluidized bed unit comprises three polycarbonate chambers: The granulating section (a cylinder with a 200 mm inside diameter and 150 mm height), the freeboard section (a cone with a 400 to 200 mm inside diameter and 670 mm height), and filter bag section (a cylinder with a 400 mm inside diameter and 400 mm height). Urethane foam insulation was installed on the outside of the freeboard and filter bag chambers. After the dehumidifier (1) adjusts the temperature and humidity of the fluidizing air

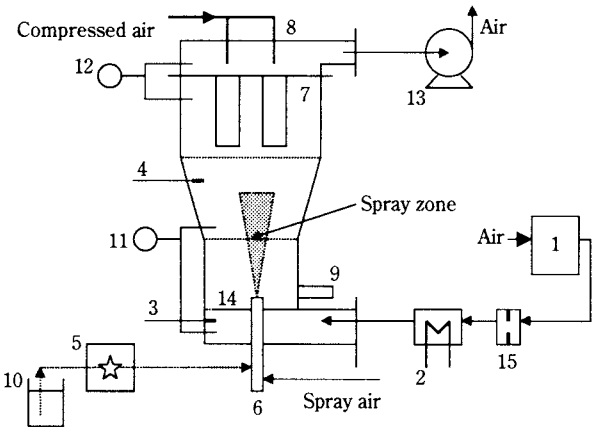

Fig. 1 Schematic diagram of the experimental apparatus
1. Dehumidifier 2. Heater 3. Thermometer 4. Thermometer
5. Pump 6. Spray nozzle 7. Filter bags 8. Jet nozzle 9. Sampler
10. Liquid material 11. Manometer 12. Manometer 13. Fan
14. Distributor 15. Orifice flow meter

(3.33×10^{-2} m^3·s^{-1}) to 290±1 K and 75.0±2% RH, the air is heated with the electric heater (2), and 393 K hot air is fed into the apparatus in accordance with directions from the thermometer (3) under the distributor. Exhaust air temperature is measured by thermometer (4) installed in the freeboard, and after it attains a steady state of 391-393 K, 5.0 kg of liquid material (1.75 kg in solid state) is sprayed at a constant flow rate through spray nozzle (6) via pump (5). This liquid material feed method is known as the bottom spray type, which uses a binary nozzle that is installed on the distributor. Atomized liquid material is sprayed toward the freeboard unit and flows along with the fluidizing air that is meant for drying. The spray nozzle's tip is fixed at a height 10 mm above the distributor (14), and the height of the freeboard was determined through preliminary experiments so that the liquid material sprayed up from the bottom can be captured on the filter bags after becoming dried particles. Exhaust was filtered by five filter bags (7) having a combined filtering area of 0.55 m^2. Pulsed jet backwashing was used to remove, one bag at a time, the particles adhering to these filter bags using regular bursts of 0.6 MPa compressed air at 5 s intervals from jet nozzles (8). Granules sampled diachronically from the sampler (9) during granulation were dried at rest for 120 min at 373 K in a thermostatic chamber, and then particle size distribution and bulk density were measured. After feeding in all the liquid material we recovered all the granules produced without any finishing drying in particular.

The model liquid material used in this granulation experiment was an aqueous solution of readily obtainable, commercially marketed instant coffee granules (Blendy, Ajinomoto General Foods) prepared at 35.0% solids concentration by weight. The solution's density and viscosity were, respectively, 1033 kg·m^{-3} and 1.62×10^{-3} kg·m^{-1}·s^{-1}, both at 290 K, while solid density was 1270 kg·m^{-3}.

Table 1 shows granulation conditions. For the purpose of assessing the effect of exhaust humidity on

Table 1 Experimental conditions

Granulation conditions		R-1	R-2	R-3	R-4	R-5	R-6	R-7	R-8
Flow rate of inlet air, Q_F	(m^3/s)	3.33E-02	3.33E-02	3.33E-02	3.33E-02	3.33E-02	3.33E-02	3.33E-02	3.33E-02
Inlet air temperature, T_i	(K)	393.0	393.0	393.0	393.0	393.0	393.0	393.0	393.0
Outlet air temperature, T_o	(K)	354.0	349.0	343.0	338.5	333.0	328.0	323.5	318.0
Theoretical outlet air temperature, $T_{o,t}$	(K)	355.0	350.0	343.5	340.0	334.5	330.0	326.5	321.0
Feed weight, W_F	(kg)	5.00	5.00	5.00	5.00	5.00	5.00	5.00	5.00
Solid concentration in coffee solution, x_L	(%)	35.0	35.0	35.0	35.0	35.0	35.0	35.0	35.0
Feed rate of coffee solution, L	(kg/s)	7.00E-04	7.92E-04	8.92E-04	9.83E-04	1.08E-03	1.18E-03	1.28E-03	1.38E-03
Flow rate of spray air, Q_S	(m^3/s)	8.75E-04	9.90E-04	1.11E-03	1.23E-03	1.35E-03	1.48E-03	1.60E-03	1.72E-03
Granulation time, θ	(s)	7.14E+03	6.32E+03	5.61E+03	5.08E+03	4.62E+03	4.23E+03	3.90E+03	3.64E+03

the way in which particles agglomerate, the experiment provided for constant thermal conditions (temperature, humidity, flow rate) at the air intake, and varied one of the granulation conditions, i.e., the liquid material feed rate (spray flow rate) from the spray nozzle. For the purpose of limiting the differences in spray droplet size among batches due to these variation conditions, we set the spray air rate so as to maintain the air-liquid flow ratio at a constant 1250 by volume ratio at the spray nozzle.

2.2 Bed Particle Behavior with this Granulation Method

As illustrated in **Fig. 2**, the present granulation method feeds liquid material by spraying into a fluidized bed that is initially empty, which means it is a non-steady granulation process. Specifically: (1) Aqueous solution droplets that are initially fed by spraying into the bed evaporate instantaneously, and all the solute solidifies to become fine particles that adhere to the filter bags above. Particles are then knocked off the bags by pulsed jet backwashing, whereupon they disperse while falling into the fluidized bed's lower spray zone by virtue of the inertial force gained from backwashing. (2) After a certain length of time, particle growth occurs in this spray zone due to particle agglomeration and to layering, i.e., the precipitation of liquid material solute on particle surfaces. The particles are once again transported by the fluidizing air and adhere to the filter bags. In this way the liquid material is consumed in the formation of new particles according to the principle of spray-dry granulation, and by the layering and agglomeration granulation of already formed particles. (3) Continuation of these phenomena results in the growth of particles over time, and a fluidized bed of granules forms after a while. As this process shows, non-steady granulation occurs in the bed and can be regarded as having three phases: a new particle formation phase, a phase of growth by particle agglomeration, and a phase of growth by particle layering.

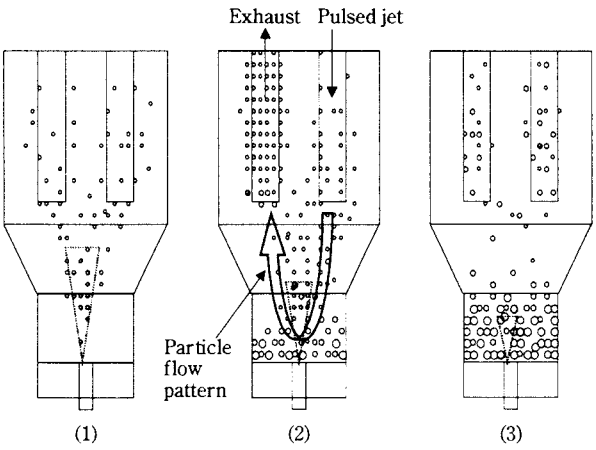

(1) Generation process of new fine particles
(2) Generation process of fine particles, and their agglomeration and layering process
(3) Layering granulation process

Fig. 2 Behavior of fluidized particles

3. Experimental Results

3.1 Characteristics of Spray Nozzle Liquid Droplets

The size of spray droplets is a crucial factor affecting the granule size and its size distribution.[2] **Fig. 3** shows the size distributions for spray droplets obtained according to spray conditions in each batch, and measured with a laser diffraction particle sizer (2600 Particle Sizer, Malvern). Within the scope of this experiment, the plot exhibits a normal logarithmic distribution (standard geometric deviation, 1.9) up to about 30 μm. As droplets with a volumetric median size of 15.1 to 17.7 μm formed, we discerned no great differences in droplet size distribution due to changes in spray flow rate.

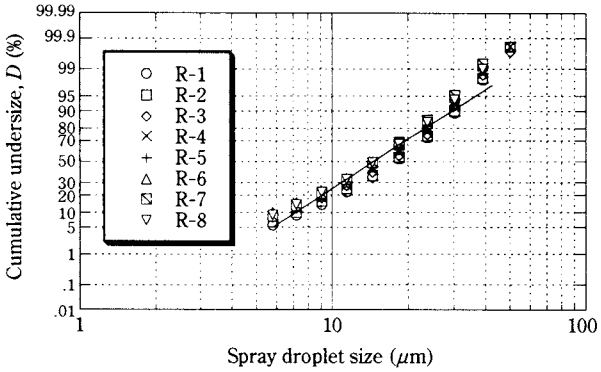

Fig. 3 Size distributions of spray droplets

3.2 Setting Integrated Index *R* for Thermal Operating Factors

If a fluidized bed coater can be conceived as an adiabatic humidification system, then fluidizing air is humidified by the fluid sprayed into the bed as it cools along an adiabatic cooling curve.[3] By making use of this relationship, it is possible for the coating efficiency of operations for the fine-particle coating of seed particles in tumbling fluidized beds,[3] internal circulation fluidized beds,[4,5] and vibro-fluidized beds[6] to be correlated with the operational conditions of the moisture feed rate by spraying, and by thermal operating factors such as the fluidizing air rate and fluidizing air temperature, provided that one uses an index

that assesses these factors in an integrated manner. Kage et al.[4–6] defined this index for assessing these thermal operating factors in an integrated manner as Eq. (1), which is the ratio between H_o, the humidity at the fluidizing air outlet, and H_s, saturation humidity, or the maximum humidity that this air can hold in the bed due to adiabatic humidification. By means of that assessment they showed H_o and H_s using Eqs. (2) and (3), respectively.

$$R = H_o / H_s \tag{1}$$

$$H_o = (W_i + W_p) / W_g \tag{2}$$

$$H_s = (W_i + W_t) / W_g \tag{3}$$

where:
W_g is the fluidizing air flow rate,
W_i is the amount of moisture carried by the fluidizing air and fed into the bed per unit time,
W_p is the feed rate of water by spraying, and
W_t is the maximum amount of moisture that can be held by the air inflow per unit time.

The relationship with H_i, the humidity of fluidizing air at the inlet, is shown by the following equations.

$$W_i = W_g \cdot H_i \tag{4}$$

$$W_p = W_g (H_o - H_i) \tag{5}$$

$$W_t = W_g (H_s - H_i) \tag{6}$$

In granulators that incorporate convective heat transfer and drying methods using devices such as for spray drying, pneumatic conveyer drying, and fluidized bed drying, the actual range for the moisture addition rate has an appropriate value, based on the device and the characteristics of the raw materials used, that corresponds to the maximum theoretical moisture evaporation rate of the drying air, and the setting of that value determines granule characteristics. It is likely that the foregoing equations can be used as an indicator to relate granule characteristics to the thermal operating factors of devices when performing such granulation operations. The primary granulation operating conditions in this experiment are the concentration and feed rate of the liquid material, fluidizing air volume and temperature, and the spray air flow rate. In order to increase the liquid material processing capacity for industrial applications, it is generally necessary to make these values large, but the upper limit of the liquid material concentration is prescribed by the solubility of the solids and the process by which liquid materials are synthesized. In the same way, inlet temperature and fluidizing air volume are determined as thermal degradation characteristics of granule quality, and as the air flow volume corresponding to the appropriate fluidization condition. When the thermal operating conditions of fluidizing air are set in this way, the liquid material feed rate is a factor that directly determines index R of Eq. (1), which is believed to influence the granule formation mechanism.

A problem that is peculiar to this device is that, in connection with the use of diverse liquid materials, for example when using highly viscous liquid materials, the spray air-liquid ratio is sometimes raised to about 4000 in order to create fine spray droplets, for which reason it becomes impossible to disregard the effects of the moisture from the liquid material that the spray air can contain. Even within the range of our experiment, in which we set the spray air-liquid ratio to 1250, we noted that the spray air had a dehumidifying effect of between 2 and 5%. Yet, the index R assessment according to Eqs. (2) and (3) takes no account whatsoever of this effect by spray air. In view of this problem, when processing our experimental data we devised the following equations for H_o and H_s values that take this spray air dehumidification effect into consideration, and carried out an index R assessment for the purpose of more accurately representing the state of drying as it occurs in the fluidized bed.

$$H_o = (W_i + W_p + W_{is}) / (W_g + W_s) \tag{7}$$

$$H_s = (W_i + W_t + W_{ts}) / (W_g + W_s) \tag{8}$$

where:
W_s is the amount of spray air,
W_{is} is the amount of moisture taken into the bed by the spray air per unit time, and
W_{ts} is the maximum amount of moisture that the spray air can contain.

The relationship in the following equations arises by using H_{is}, the humidity at the spray air inlet (this experiment used perfectly dry air; H_{is}=0.00 kg − H_2O/kg − dry air), and H_{ss}, the saturation humidity, i.e., the maximum amount that the spray air can contain when being adiabatically humidified within the device.

$$W_{is} = W_s \cdot H_{is} \tag{9}$$

$$W_{ts} = W_s (H_{ss} - H_{is}) \tag{10}$$

To begin with, in applying index R according to Eqs. (7) and (8), we used the same method as Abe et al.[3] by assuming the exhaust temperature and adiabatic humidification during granulation, and found the dif-

ference with the theoretical temperature obtained from a humidity diagram. As shown in **Table 1**, the result was in the neighborhood of 1.0 to 3.0 K, thereby confirming that likewise in our experimental device, inlet air was more or less adiabatically humidified in conjunction with the liquid material feed.

3.3 Physical Properties of Granules

Figs. 4 through **6** and **Table 2** show the physical properties of the granules made in this experiment, including size, bulk density, and moisture content. **Fig. 4** shows granule size distributions according to a logarithmic normal plot. R-1 and R-2 granule size distributions were measured with laser diffraction scattering (Microtrack HRA, Honeywell), and for other granule sizes we used JIS standard sieves. For all distributions we were able to very nearly approximate logarithmic normal distributions. **Fig. 5** shows the effects of Index R on the average granule size D_{50} and the geometric standard deviation σ_g, which indicates the slope of the particle size distribution obtained using **Fig. 4**. Granule moisture content M_p (Kett method; 373 K, 3600 s) is also plotted in this graph.

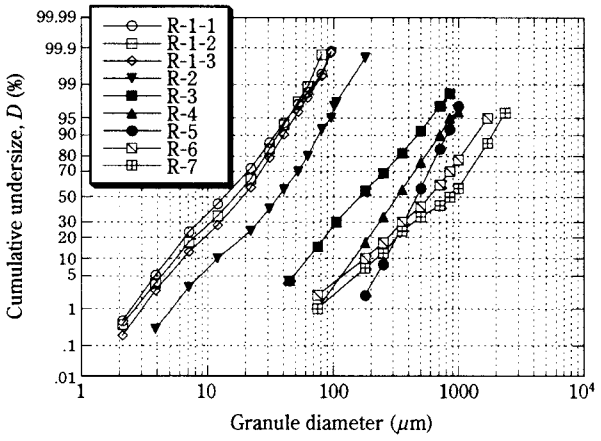

Fig. 4 Granule size distributions

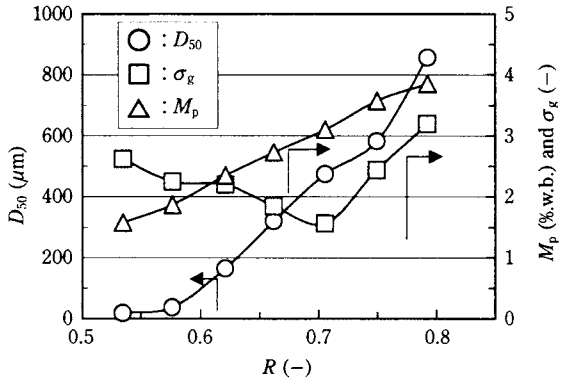

Fig. 5 Effects of Index R on mean diameter of granules, geometrical standard deviation, and moisture content

When increasing R by raising the liquid material feed rate, we discerned a tendency for D_{50} to increase, a tendency that becomes pronounced when R exceeds 0.58. In connection with this, granule moisture content M_p increased roughly proportionally. And as indicated by the results of Run 5 in **Fig. 11**, described below, the fact that granule moisture content during granulation was roughly constant regardless of time suggests that it was determined by a balance between humidification that occurs in conjunction with the liquid material feed, and drying caused by fluidizing air. In other words, it appears that the reason average particle size D_{50} increased with R is that when R was increased during granulation, particle moisture content increased and facilitated particle growth. Standard deviation σ_g decreased as R increased, reached a minimum at around 0.72, and then increased. **Fig. 6** shows the results of the loose bulk density ρ_b and the angle of repose α of granule products after drying at rest, measured with Powder Tester (PT-R, Hosokawa Micron). These correspond roughly to the tendency of change in σ_g, for in the range up to 0.72 for R we observed a tendency in which bulk density increased, the angle of repose decreased, and the fluidity of granule products increased, but when the value of R exceeded 0.72 there was a reversal in the change tendency.

Table 2 Physical properties of granules

Granulation conditions	R-1	R-2	R-3	R-4	R-5	R-6	R-7	R-8
Index R (−)	0.534	0.576	0.621	0.662	0.706	0.749	0.792	0.831
D_{50} (μm)	18.3	37.4	164	320	473	582	856	
σ_g (−)	2.61	2.24	2.19	1.84	1.56	2.43	3.19	
ρ_b (kg/m³)	372	410	544	742	811	577	519	Blocking occurred at t=16 min
α (deg.)	50	45	37	22	17	33	36	
M_p (%w.b.)	1.57	1.86	2.34	2.72	3.10	3.57	3.85	
P (−)	0.883	0.906	0.911	0.968	0.987	0.937	0.920	

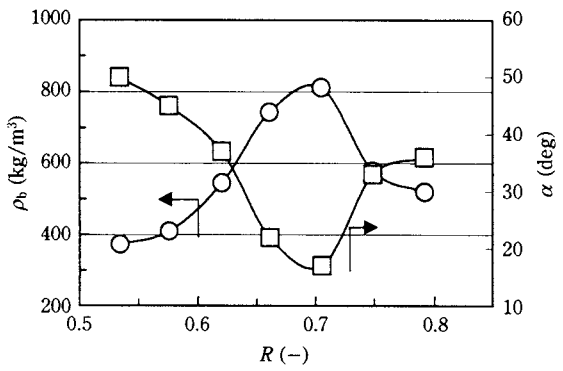

Fig. 6 Effects of Index R on bulk density and angle of repose

4. Discussion

When R exceeds 0.72 as noted above, the tendency for change in granule physical characteristics undergoes a major change. We conjectured that the reason for the broader granule size distribution, decreasing bulk density, and increasing angle of repose when R crosses the 0.72 mark is the different form of particle agglomeration. In proceeding with the following discussion, we observed all granule products with an electron microscope (SIGMA-I, Topcon) and found circularity P, which is defined with the following equation.

P= (circumference of a circle having an area equal to the projection area of a particle) / (circumference of projected particle) (11)

To measure circularity we used an image analyzer (Luzex F, Nireco) to analyze microscopic images of granules produced in R-3 through R-7, and a wet dispersion type flow particle image analyzer (FPIA-2000, Toa Medical Instruments) for the R-1 and R-2 granules, whose dry dispersion is difficult owing to small particle size. Measurement results appear in **Fig. 7** and are discussed below.

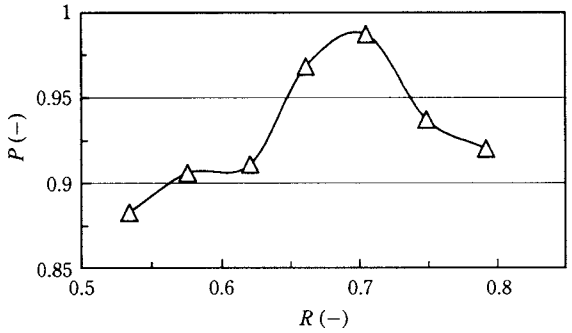

Fig. 7 Effects of Index R on granule circularity

4.1 Effects of R on Particle Agglomeration Form

(1) $R<0.58$ [Conditions: R-1 (P=0.833), R-2 (P=0.906)]

As an example of the granule products of this range, **Figs. 8 (a)** and **(b)** show electron micrographs of samples obtained in R-1 immediately after beginning granulation (θ=300 s, D_{50}=13.5 μm, σ_g=2.51) and at the end (θ=7140 s, D_{50}=18.3 μm, σ_g=2.61). **Fig. 4** shows these granule size results along with the granule size distributions when θ=3600 s (D_{50}=17.0 μm, σ_g=2.62). In the initial granulation stages of other batches as well, fine particles were formed as in **Fig. 8 (a)**. Observation of SEM photographs to examine R-1 results while taking into consideration the diachronic changes in particle size distribution, in which there is little σ_g fluctuation, shows that although a decrease in fine particles several μm in size as granulation proceeds can be discerned, hardly any agglomeration of particles is observed. This likely means that while on the one hand the continuous generation of new particles from spray liquid in this range dominated, the granulation mechanism occurring when granule product size increased somewhat was a layering granulation mechanism wherein fine particles that had been generated in the bed, or fine particles from spray liquid, adhered to the surface of particles larger than themselves. For this reason particle growth proceeded at a slow pace, with the granules produced constituting a fine powder with low bulk density, high angle of repose, and poor fluidity. We conjectured that the reason for particle size enlargement in R-2 was that, while the generation of new particles was dominant as in R-1, as R increased, the ratio of layering granulation to new particle generation became relatively higher, which resulted in the promotion of particle growth.

(2) $0.58 \leq R \leq 0.64$ [Conditions: R-3 (P=0.911)]

Figs. 8 (c) and **(d)** are SEM photographs of R-3 granule products. In this range there is a conspicuous presence of granules that have grown to 100 μm or larger. Observation of these large granules reveals that granules have formed by the agglomeration of particles that had grown to sizes on the order of several tens of μm (primary agglomeration). These granules' surfaces have localized unevenness due to the effects of agglomeration, and one can also discern what appears to be the result of layering by fine particles of about 10 μm in size that occurred subsequently. The reason is thought to be that inter-particle adhesive force heightens when moisture in the bed increases as the value of R rises, the rate of new particle generation from spray liquid falls to a level below that of the range in section (1), above, and particle growth by inter-particle agglomeration (primary agglomeration) was facilitated more. It also appears that the reason the proportion of fine particles declined, the σ_g of granule size distribution fell, bulk density increased, and the angle of repose fell as granules assumed a somewhat rounded shape was that the fluidization condition of particles that had grown to this comparatively large size made them relatively slower in movement than fine particles, thereby allowing the direct adhesion of fine particles from spray liquid to proceed more easily, and because higher moisture content on particle surfaces meant that fine particles in the bed

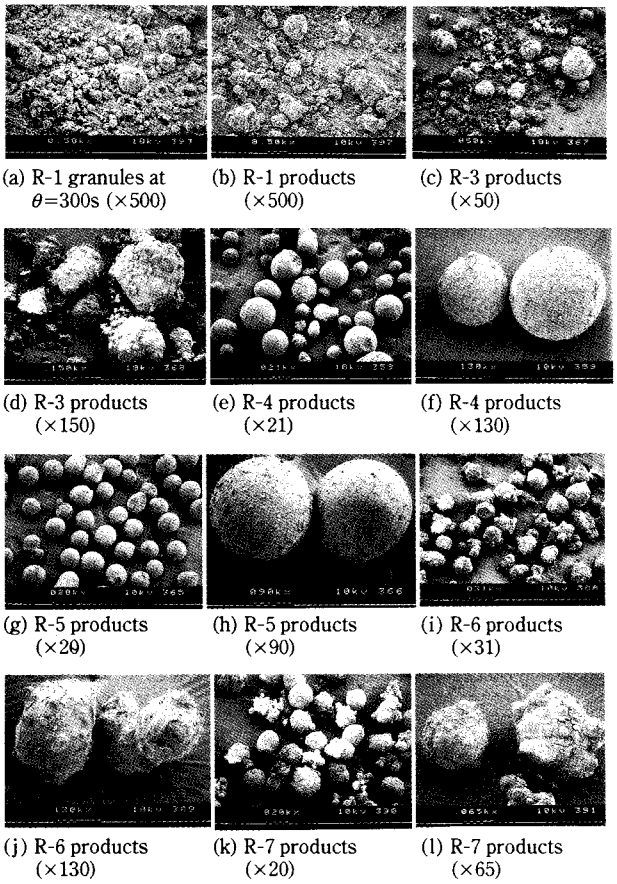

(a) R-1 granules at θ=300s (×500) (b) R-1 products (×500) (c) R-3 products (×50)

(d) R-3 products (×150) (e) R-4 products (×21) (f) R-4 products (×130)

(g) R-5 products (×20) (h) R-5 products (×90) (i) R-6 products (×31)

(j) R-6 products (×130) (k) R-7 products (×20) (l) R-7 products (×65)

Fig. 8 SEM photographs of granules (scale factor)

became involved in layering granulation easily and in a way providing for granule stability.

(3) $0.64 \leq R \leq 0.72$ [Conditions: R-4 (P=0.968), R-5 (P=0.987)]

Figs. 8 (e) through **(h)** show granule products from R-4 and R-5. Granules with very high circularity were observed in this range. Compared with the conditions in section (2) above, the still larger increase in bed moisture content engendered, at an earlier granulation stage, the agglomeration of particles that had grown due to the agglomeration of new particles and to fine particle layering (primary agglomeration), thereby forming large agglomerated granules as shown in (2). Subsequently the process was dominated by the layering of these granules' surfaces by fine particles in the bed and by fine particles from spray liquid, whereby fine particles adhered in a form in which granules were most stable. We conjectured this was the reason for the granules' very high circularity. The tendency toward a decrease in the σ_g of particle size distribution, an increase in bulk density, and a decline in the angle of repose in the granule products obtained were even more pronounced, which likely corresponded to granule sphericalization induced by the increase in R.

(4) $0.72 \leq R \leq 0.81$
[Conditions: R-6 (P=0.937), R-7 (P=0.920)]

Figs. 8 (i) through **(l)** show granule products for these ranges. The SEM photographs reveal that these granules were formed by the agglomeration of granules about the same size (on the order of several hundred μm) as the granules produced in the range in (3), i.e., by secondary agglomeration, and their surfaces are greatly affected by the shapes of the agglomerated particles. This means that, as a result of a further strengthening of inter-particle adhesive force in these ranges, there was no fine-particle layering by granules from spray liquid, which dominated the process in the final stage of (3), and spray liquid contributed to the secondary agglomeration of these granules. Thus when R exceeds the value of about 0.74, there is agglomeration by granules that had grown larger in the final granulation stage, which results in the switch to a tendency toward an increase in the σ_g of granule size distribution, a decrease in bulk density, an increase in the angle of repose, and lessened circularity.

(5) $R \geq 0.81$ [Conditions for R-8]

Under these conditions comparatively large particles agglomerated very actively at θ=960 s after starting granulation, and arrived at a defluidization (blocking) due to the unstable fluidized bed, which indicates that the highest R value that can be applied in granulation operations is about 0.81.

4.2 The Mechanism of Spherical Granule Formation

Direct granulation of liquid material by this granulator was investigated also by the use of surfactants, pharmaceuticals, food additives, beverage ingredients, and other materials in aqueous solutions, and in all instances we observed that, as R is increased, the properties of the granules produced tended to change as indicated by the results of our experiment, and as illustrated in **Fig. 9**. Especially if R was within the appropriate range, we noted that there was a stable fluidized bed in which secondary agglomeration was suppressed, and which yielded spherical granules of uniform size like those in **Figs. 8 (e)** through **(h)**. The greatest value of this granulator as an industrial device is that it provides spherical granules directly from liquid materials, thereby saving energy and streamlining processes.

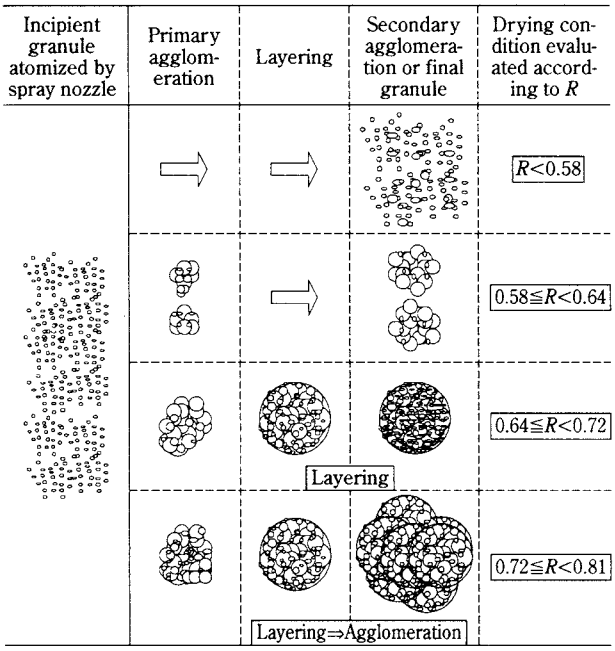

Fig. 9 Relationship between index R and granule growth mechanism

Getting a firm understanding of the mechanism that forms the desired spherical granules and of the fluidized bed characteristics prevailing when they are formed is of paramount importance when designing industrial devices, including their ancillary equipment. For this reason, in **Figs. 10** and **11** we show the diachronic change in granule size distribution and fluidized bed characteristics during granulation in R-5, in which spherical granules were obtained. A look at the change in granule size distribution shows that average granule size in the initial granulation stage at θ=300 s was small at 22.6 μm (σ_g=2.50). During this stage (θ=0 to 300 s in **Fig. 10**) the generation of new particles from spray liquid was dominant, but there was a modicum of particle size enlargement due to layering of fine particles onto particles in the bed.

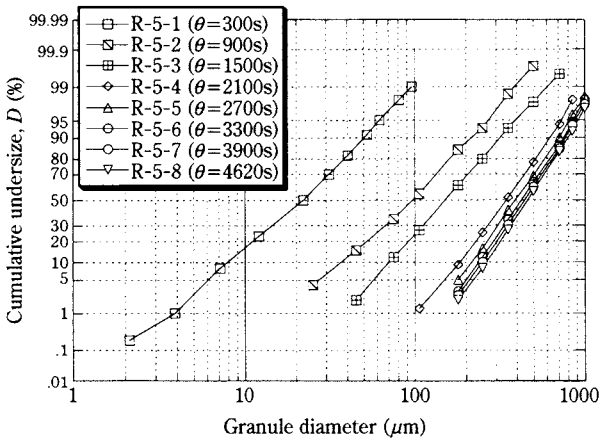

Fig. 10 Diachronic change in granule size distributions in R-5

This can also be seen from the results of fluidized bed observations. Behavior of particles in the bed during this time frame consisted in the continuously formed new particles being transported by the fluidizing air and adhering to the filter bags. These particles were knocked off the bags and periodically fell down into the spray zone while dispersing, but they did not achieve sufficient particle growth and were again transported by the fluidizing air, indicating that the bottom of the fluidized bed was not adequate for practical use. The filter bag pressure drop in the new particle generation region, ΔP_F, which exhibited this singular particle behavior, tended to increase as the amount of new particles generated increased. At the same time, the pressure drop of the fluidized bed formed by the granules, ΔP_B was smaller than the theoretical pressure drop indicated in the graph by the broken line (quantity of particles holdable in bed divided by distributor area). Exhaust temperature tended to fall under a balance between humidification by the spray liquid feed and drying by the fluidizing air, coming to a nearly constant value at θ=900 s and thereafter. Then rapid particle growth was observed upon entering the middle granulation stage (θ=900 to 2100 s). In this region new particle generation was limited by the increased amount of particles held in the bed, and it was the process in which the spray liquid was consumed in particle agglomeration from layering onto particles in the bed (primary agglomeration). Although ΔP_F tended to gradually decline, this was a manifestation of fewer fine particles from the bed flying up to the filter bags, i.e., a decrease in the amount of fine particles in the bed, which suggests the layering of those fine particles onto other, larger particles, or the occurrence of agglomeration among

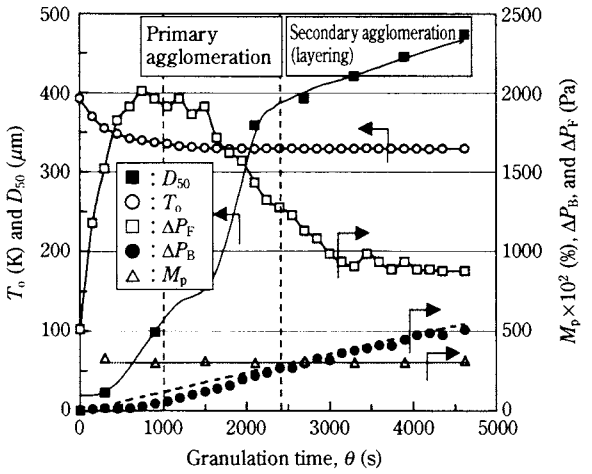

Fig. 11 Diachronic change in granule diameter, moisture content, outlet temperature, and pressure drop of filter bags and fluidized bed in Run 5

fine particles. In connection with this, ΔP_B gradually approached the theoretical pressure drop because formation of the fluidized bed proceeded as agglomerating granulation proceeded and granule size increased. Further, upon entering the final granulation stage (θ=2100 to 4620 s) there was a precipitous drop in the number of fine particles in the bed, and ΔP_F became the minimum stable pressure drop caused by clogging of the filter bags with the minimum practical number of fine particles, while the value of ΔP_B exhibited roughly the theoretical pressure drop owing to the formation of a dynamically stable fluidized bed of granules in which the separation force among granules was greater than agglomeration force, thereby suppressing secondary agglomeration.

Thus in a fluidized bed with stable granule behavior, the dominant process is layering granulation in which nearly all the spray liquid fed in from the bottom of the bed directly adheres to granule surfaces, with the result being particle growth whose σ_g is nearly constant. The next matter is to consider how average granule size in this region grows diachronically. In a coating granulation operation using deposition solution on seed particles in a fluidized bed, Harada et al.[7] derived, from the coating mass balance, the following equation on the relationship between operational conditions and coated particle size D_c.

$$\frac{L \cdot x_L \cdot \theta}{S_0} \cdot \frac{\rho_s}{\rho_c} = \frac{D_c}{D_0} - 1 \qquad (12)$$

where:
S_0 is the weight of seed particles in the bed,
ρ_s is the solid density of seed particles, and
ρ_c is the solid density of coating material.

Because the fluidized bed particles and coating material were the same in this experiment, we set ρ_s equal to ρ_b, and assumed that this equation is applicable in the region $\theta \geq 2100$ s, in which layering granulation is thought to be dominant, and set S_0 and D_0 to the quantity of particles holdable in the bed and the average particle size D_{50}, respectively, at the moment θ=2100 s. In the same manner, the layering granulation starting point in R-4, which provided spherical granules, was set at θ=2100 s, with results appearing in **Fig. 12**. Although the plot has high linearity, the plotted values' deviation from the dotted line increased as θ grew. This is because as layering granulation proceeded, there was a modicum of inter-granule agglomeration as observed in **Fig. 8 (e)**, so the average granule size measured because of these effects was larger than the theoretical size found with Eq. (12). However, our experiment's results were nearly the same as the ideal granulation model, and we determined that the change in granule size with granulation time in this region was due to the layering granulation mechanism.

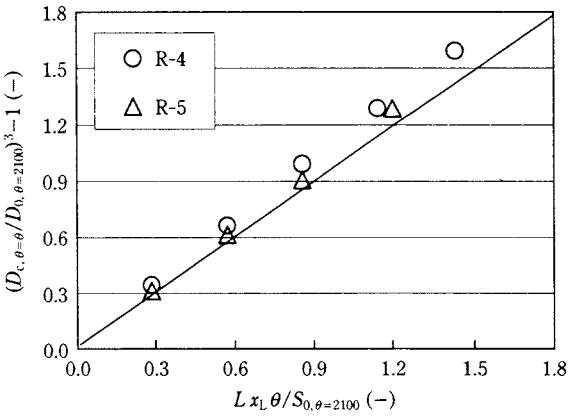

Fig. 12 Theoretical and experimental granule growth rates in layering region, Run 4 and Run 5

5. Conclusion

We proposed a new granulation method by directly spraying liquid material into the fluidized bed of an empty column to generate granules. For the purpose of elucidating the mechanism of granule agglomeration and the behavior of particles in the bed as they occur with this granulation method, we established the integrated index R for the thermal operating factors that indicate the drying condition in the fluidized bed, and examined the characteristics of the granules formed and of the fluidized bed. An integrated assessment of the relationship between granule physical properties and microscopic examination results revealed the relationship between the mechanism of granule formation and the characteristics of the fluidized bed. We ascertained that in the fluidized bed the generation of fine particles starts immediately after the initiation of granulation, the agglomeration size of fluidized particles increases thereby forming a primary agglomeration fluidized bed, and then it becomes a secondary agglomeration fluidized bed after the formation of a dynamically stable region in which agglomeration and dispersion are balanced. When the operation is performed while increasing the value of R, the conditions of the primary and secondary agglomeration fluidized beds appear earlier, and there is a tendency to readily attain defluidization from unstable fluidization. We discovered a characteristic in which, when granulating with an appropriate R setting, layering granulation proceeds in this stable region, and the

apparatus produces spherical granules of a uniform size that are of very high value in practical use. We also discovered that the rate of growth in granule size at this time is determined by the mass balance, with respect to the fluidized bed, of the liquid material fed into the bed.

Nomenclature

D	: cumulative undersize	(−)
D_c	: coated particle diameter	(μm)
D_0	: seed particle diameter	(μm)
D_{50}	: volume median diameter of granule	(μm)
H_i	: humidity of inlet air	(kg-H_2O/kg-dry air)
H_{is}	: humidity of inlet spray air	(kg-H_2O/kg-dry air)
H_o	: humidity of outlet air	(kg-H_2O/kg-dry air)
H_s	: humidity of saturated air	(kg-H_2O/kg-dry air)
H_{ss}	: humidity of saturated spray air	(kg-H_2O/kg-dry air)
L	: feed rate of liquid material	(kg/s)
M_p	: moisture content	(−)
P	: circularity	(−)
ΔP_B	: pressure drop of fluidized bed	(Pa)
ΔP_F	: pressure drop of filter bags	(Pa)
Q_F	: volumetric flow rate of fluidizing air	(m^3/s)
R	: index defined by Eq. (1)	(−)
S_0	: quantity of seed particles	(kg)
T_i	: inlet air temperature	(K)
T_o	: outlet air temperature	(K)
W_g	: mass flow rate of inlet air	(kg-dry air/s)
W_i	: feed rate of water with inlet air	(kg/s)
W_{is}	: feed rate of water with inlet spray air	(kg/s)
W_p	: feed rate of water with inlet air flow	(kg/s)
W_s	: mass flow rate of inlet spray air	(kg/s)
W_t	: additional maximum vapor content of inlet air	(kg/s)
W_{ts}	: additional maximum vapor content of inlet spray air	(kg/s)
x_L	: solid concentration in liquid material	(−)
α	: angle of repose	(deg)
ρ_c	: density of coating material	(kg/m^3)
ρ_b	: bulk density	(kg/m^3)
ρ_s	: density of seed particles	(kg/m^3)
σ_g	: geometrical standard deviation	(−)
θ	: operation time	(s)

References

1) Ashizawa, N. and K. Masters. "Integrated Fluid Bed Spray Dryers," Proc. 4th International Drying Symp., Kyoto, p. 364 (1984).
2) Tohata, H. and I. Sekiguchi. "Studies on Spray Granulation," *Kagaku-Kougaku*, **26**, 818 (1962).
3) Abe, E., H. Hirosue and H. Kikuchi. "Coating of Seed Particles in Tumbling Fluidized Bed by Atomizing the Suspensions of Clayey Particles," *J. Soc. Powder Technol., Japan*, **22**, 278 (1985).
4) Kage, H., T. Yoshida, H. Matsunaka and Y. Matsuno. "The Coating of Fluidizing Particles by Atomization of Fine Powder Suspensions," *J. Soc. Powder Technol., Japan*, **29**, 422 (1992).
5) Kage, H., T. Takahashi, T. Toshida, H. Ogura and Y. Matsuno. "The Coating Surface and Agglomeration of Seed Particles in a Fluidized Bed Coater," *J. Soc. Powder Technol., Japan*, **35**, 4 (1998).
6) Kage, H., M. Oba, H. Ishimatsu, H. Ogura and Y. Matsuno. "The Effects of Frequency and Amplitude on the Powder Coating of Fluidizing Particles in Vibro-Fluidized Bed," *J. Soc. Powder Technol., Japan*, **33**, 711 (1996).
7) Harada, K. and J. Fujita. "Ryuudousou niyoru Ryushi no Kochingu," *Kagaku-Kougaku*, **31**, 790 (1967)

Author's short biography

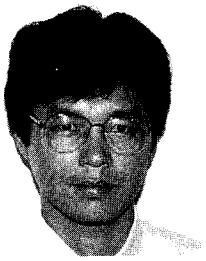

Hiroyuki Tsujimoto

Hiroyuki Tsujimoto graduated in Industrial Chemistry from Chuo University and received M.S. in 1988. His M.S. thesis focused on the research of agglomeration of polymeric powder in a hot fluidized bed granulator. Since his graduation he has been working mainly at R&D section of Hosokawa Micron Corporation, where he developed "Tumbling Fluidized Bed Granulator with Opposed Pulsed Jet Assembly" in 1994. His primary research interest is in new granulation technology of "Direct Granulation Method of Liquid Material in a Fluidized Bed Granulator".

Toyokazu Yokoyama

Toyokazu Yokoyama graduated in Chemical Engineering from Kyoto University and received M.S. in 1975. Then he spent six years in Europe to study powder technology at Karlsruhe University and to work as an engineer for Hosokawa Europe Ltd. in Cologne and near London. After another six year work in the engineering division and laboratory of Hosokawa Micron Corp. in Osaka, he was engaged in research at Nagoya University, where he received Ph.D. on the subject of fine wet grinding by ball media mills. Since 1992, he is a manager of Hosokawa Micromeritics Laboratory. His major interests are particle design and processing for advanced functioning by mechanical composing and granulation methods as well as fine grinding and particle characterization.

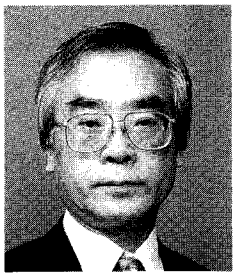

Isao Sekiguchi

Dr. Isao Sekiguchi graduated from the Department of Industrial Chemistry, Chuo University in 1958, and obtained the Doctor degree of Engineering from Tohoku University in 1975. Since 1977, he is a professor in the Department of Applied Chemistry, Chuo University. His main research in the field of granulation techniques is concerned with fundamentals and extended application which cover three areas: fluidized bed granulation, tumbling granulation and spray drying or prilling. Additional research topic being pursued at present is a new development in the use of microcapsuled asphalt powder as an auxiliary in soil stabilization.

Information Articles

The 33rd Symposium on Powder Technology

The 33rd Symposium on Powder Technology was held on Friday, August 20 at Senri Hankyu Hotel under the auspices of the Hosokawa Powder Technology Foundation with the support of Hosokawa Micron Corporation. The planning of this symposium including the selection of the main subject and speakers was made by the Council of Powder Technology, Japan, supported by Hosokawa Micron Corp.

The symposium this year was also very successful with the attendance of more than 250 with about 25 academic people. The main subject this year was "Powder Technology for the Creation of New Business". In the one-day symposium, there were six presentations including the one given by Mr. Masuo Hosokawa entitled "Globalization of Powder Technology and Its Future Prospect". He has been the vice-president of this Council for a long time.

The 33rd Symposium on Powder Technology

Theme: "Powder Technology for the Creation of New Business"

Session 1 To seek for the way for the Japanese Industries to take
Chairperson: Prof. K. Miyanami (Osaka Pref. Univ.)

• Point of view of industrial economical strategy for the future	Mr. Yuji Hosoya (The Ministry of Trade and Industry)
• Application of powder technology to pharmaceutical particle design	Prof. Yoshiaki Kawashima (Gifu College of Pharmacy)

Session 2 KONA award commemorative lectures
Chairperson: Prof. Yasuo Kousaka (Osaka Pref. Univ.)

• Research of particle electric charging and potentiality of its application	Prof. Hiroaki Masuda (Kyoto Univ.)
• Mechanism of soft mechanochemical reaction and new concept of creation of new material	Prof. Mamoru Senna (Keio Univ.)

Session 3 To learn from the successful cases
Chairperson: Prof. Hitoshi Emi (Kanazawa Univ.)

• Environmental problems and creation of new business	Mr. Negoro Isao (Negoro Sangyo)
• Globalization of Powder Technology and Its Future Prospect	Mr. Masuo Hosokawa (Hosokawa Micron Corp.)

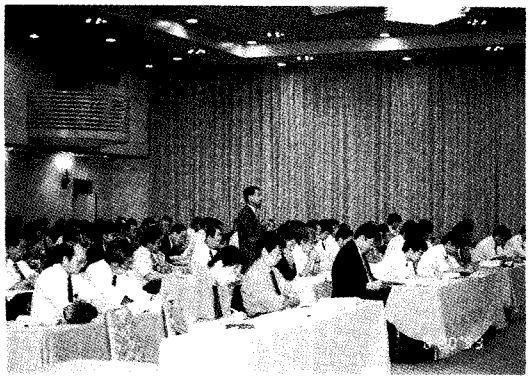

The 8th KONA Award

The 8th KONA Award sponsored by Hosokawa Powder Technology Foundation and given to the scientists or groups who have achieved excellence in the researches related to the basic powder technology, was presented to Professor Hiroaki Masuda of Kyoto University and to Professor Mamoru Senna of Keio University by Masuo Hosokawa, President of the Foundation on January 22, 1999 at the R&D Center of Hosokawa Micron Corporation in Hirakata.

Prof. Masuda's research achievements are related to studies on static electrification of particles, aerosol classification performance and particle reentrainment.

Prof. Senna's research achievements are related to studies on agglomeration and new fabrication technique via a soft mechanochemical route.

In these studies both professors obtained epoch-making results.

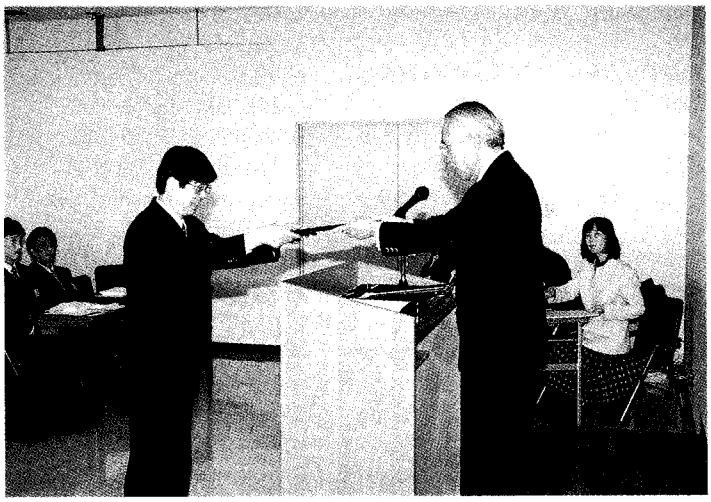

Academic publication concerning powder technology in Japan (1998)

Journal of the Society of Powder Technology, Japan Vol.35 (1998)

Title	Author(s)	Page
〈Research Papers〉		
• The Coating Surface and Agglomeration of Seed Particles in a Fluidized Bed Coater	H. Kage, T. Takahashi, T. Yoshida, H. Ogura and Y. Matsuno	4–11
• An Experimental Study on the Grinding Rate Constant of a Ball Mill –The Effects of Feed Size and Ball Diameter–	Y. Kanda, K. Simodaira, N. Kotake and Y. Abe	12–17
• The Influences of Operating Parameters on the Recovery of Coated Single-Core Particles by the Spray Drying of Suspensions	N. Yamada and E. Abe	18–24
• The Adsorption Behavior of Dispersant Molecules and Rheological Properties of Highly Concentrated Alumina Slurries	H. Unuma, Beyong-Hwan Ryu, I. Hatano and M. Takahashi	25–30
• A Study of the Hydroxyl Determination of Silica	S. Shioji, M. Kawaguchi, Y. Hayashi, K. Tokami and H. Yamamoto	98–105
• The Triboelectric Separation for Plastic Sheets	T. Takeshita, K. Atsumi, Y. Iwasaki and T. Harada	106–110
• The Fixation Effect of Fine Particles on the Coating Mechanism by Dry Impact Blending	K. Shinohara, Y. Otomura, T. Uchiyama and H. Minoshima	111–117
• The Effect of Vibration Ball-milling on the Reactivity during Firing of a SiO_2-MgO Powder Mixture	H. Shiomi, H. Hayashida and M. Nakamura	118–124
• Distinct Element Simulation of Vibrating Behavior of Adhesive Fine Powder	S. Matsusaka, M. Furutake and H. Masuda	168–173
• The Numerical Simulation of the Velocity and Stress Field for a Flowing Powder Using the Smoothed Particle (S.P.) Method and Experimental Verification	S. Yuu, M. Waki, A. Iwamasa and T. Umekage	174–182
• The Effects of Temperature on the Shear Properties of Fine Powder	M. Hirota, Y. Fujimoto, M. Suzuki and T. Ohshima	210–217
• Estimation of the Sieving Rate of Powders Using Computer Simulation	A. Shimosaka, S. Higashihara and J. Hidaka	242–249
• The Observation of the Process of Accumulation of Dust on a Rigid Ceramic Filter Surface and the Cleaning Mechanism of Dust from the Filter Surface	C. Kanaoka and T. Kishima	250–255
• The Characterization of Microgranules Produced by a Tumbling Fluidized Bed Granulator with an Opposed Pulsed Jet Assembly	H. Tsujimoto, T. Yokoyama and I. Sekiguchi	256–264
• The Evaluation of the Mixing Process for Dispersing Polymer Fiber Materials into a Powder Bed	Y. Sugita and M. Satoh	265–270
• The Effect of Characteristics of a Seed on Silica Removal from a Model Geothermal Brine by a Seeding Method Using Silica Gel	H. Sugita, Y. Sakurai, Y. Bando and M. Nakamura	338–345
• The Influences of the Multiple Counting of Particles on the Perticle Size Distribution Measured Using a Microscopy Method	J. Tsubaki, H. Mori, T. Sugimoto, S. Maeda and O. Hayakawa	346–352
• The Effect of Water Content and Crystallinity of the Heptakis-(2,6-di-*o*-methy1)-β-cyclodextrin on the Physicochemical Properties of a Sealed Heated Compound with Naphthalene	H. Kawashima, E. Yonemochi, T. Oguchi and K. Yamamoto	353–359
• The Effect of the Mixing Condition on the Microstructure and Electrical Properties of a Glass Composite Containing Semiconductive Sno2 Fine Particles Prepared by a Mechano-chemical Process	H. Shiomi, T. Goto and M. Nakamura	360–370
• Designing Toner Particles Using a Particle Coating Method and its Evaluation	K. Terashita, K. Okuda, T. Teshima and K. Miyanami	420–426

Kagaku Kougaku Ronbunnshu Vol.24 (1998)

Title	Author(s)	Page
• Dynamic Analysis and Control of Closed-Circuit Ball Mill Grinding System	K. Ozaki, O. Nakagawa and S. Ihara	5–11
• Effect of Packing Sttucture on Separation Performance of Packed Bed	H. Sakaguchi, K. Adachi, Y. Ishiki, K. Fukui, J. Ma, Chi-Mun Y., E. Shinoda and H. Yoshida	37–41
• Simulation Modeling of Fluidized Bed Coal Gasifier for New Topping Cycle System	Gui-Lin P., R. Yamazaki, S. Mor and Y. Fujima	42–45
• Estimation of Bubble Behavior and Particle Flow Pattern in Large Scale Rectangular Fluidized Bed	N. Kobayashi, R. Yamazaki and S. Mori	46–51
• Deposition of Fine Particles on Surface of Core Particles by High-speed Elliptical-Rotor-Type Mixer	M. Naito, T. Hotta, S. Asahi and T. Tanimoto	52–56
• Studies in Hold-up and Agglomeration of File Particles in a Powder -Particles Fluidized Bed	D. Taneda, H. Takahashi, S. Aoshika, N. Nakagawa and K. Kato	69–74
• Removal on Fine Particles from Various Surfaces by Consecutive Pulse Air Jets –Prediction of Particle Removal Efficiency with Resuspension Parameter–	N. Namiki, Y. Otani and H. Emi	86–92
• Effect of Processing Conditions on Particle Composite Process by a High-Speed Elliptical-Rotor-Type Mixer	M. Naito, T. Hotta, S. Asahi, T. Tanimoto and S. Endoh	99–103
• Development of Novel Magnetic Sensing for Brain Lesion Using Functional Magnetic Particles	M. Shinkai, A. Ohshima, M. Yanase, T. Uchiyama, K. Mohri, T. Wakabayashi, J. Yoshida, H. Honda and T. Kobayashi	174–178
• The Effect of Operating Conditions on SO_2 Removal in Semidry Desulfurization Process by Powder-Particle Spouted Bed	G. Qimin and K. Kato	279–284
• Desulfurization Characteristics in High-Temperature Powder-Particle Fluidized Bed Desulfurized	T. Tashimo, H. Machida, Y. Matsumoto, N. Nakagawa and K. Kato	324–328
• Conveying Characteristics Of Fine Particles Using Convering Nozzle	K. Ijichi, Y. Uemura, H. Yoshizawa, Y. Hatate and K. Yoshida	365–369
• Development of On-line Resin Pellet External Testing and Automatic Selecting Control Systems by using Image Processing Technology	T. Shizawa	380–384
• Wettability of Packed Bed of Surface Composite Fine Particles	K. Shinohara, K. Ueno and T. Uchiyama	407–412
• Studies on Elutration of Fine Particles in a Powder-Particle Fluidized Bed	D. Taneda, H. Takahagi, S. Aoshika, N. Nakagawa and K. Kato	418–424
• Influence of the Characteristics of Charge Relaxation for Tribo-Charging of Powder	T. Nomura, Y. Yamada and H. Masuda	585–590
• Preparation of Composite Particles Composed of Waste Polymer and Paper Fiber by Chemical Crush Method	H. Hori, Y. Taguchi and M. Tanaka	603–608
• Studies on Mean Residence Time of Fine Particles in a Powder-Particle Fluidized Bed –Effect of Particle Size Distribution, Static Electricity, and Humidity–	D. Taneda, T. Masagaki and K. Kato	628–632
• Preparation of Monodispersed Electroconductive Particled	M. Kimata, H. Kashiwaya and M. Hasegawa	660–664
• Environmental Assessment of PSP Tray and PET Bottle Recycling	E. Nakanishi and K. Kitamura	726–731
• Prediction of HEPA Filter Collection Efficiency with a Bimodal Fiber Size Distribution	L. Bao, Y. Otani, N. Namiki, J. Mori and H. Emi	766–771
• Influence of Internal Structure of Fibrous Filter on Collection Performance at Low Peclet Number	Y. Otani, L. Bao, N. Namiki, M. Hosaki and H. Emi	772–778
• Mixing and Segregation of Solid Wastes in a Fluidized Bed with an Inclined Distributor	T. Kita, H. Kamiya and M. Horio	901–906
• Evaluation of Shear and Friction Characteristics of Wet Powder by Intrusion Method Using Conical	T. Iwasaki, M. Kobayashi, M. Satoh and R. Tsuchiya	918–922

New Product

Mechano Fusion System AMS
Designed for particle-to-particle combination in order to enhance particle performance

The Mechano Fusion System explores possibilities for new materials.

Mechano Fusion refers to the process by which mechanical energy is applied to several different types of particles to induce a mechano-chemical reaction, thereby creating new materials. Since there is an infinite variety of possible particle combinations, various forms of particle designs and processing technology have now become a reality in a broad range of fields. Coupled with the above, Mechano Fusion technology has been employed to yield new materials with enhanced particle performance.

Main Features

The Mechano Fusion System can:

1. produce composite particles, control particle forms (making them spherical or flat) and mix particles in rigorous precision.
2. eliminate the need for pre-mixing particles during particle performance improvement processes (any addition of a pre-mixing process achieves a further cut in processing time.)
3. fuse higher volumes of particles while providing the same level of Mechano Fusion effect as the previous model.
4. allow for ease of loading and unloading powder materials (it is even possible to unload the entire amount of material.)
5. control product temperature by the use of a water-cooled jacket that is provided on the casing.
6. can substantially save space due to its reduced size compared with the previous version.

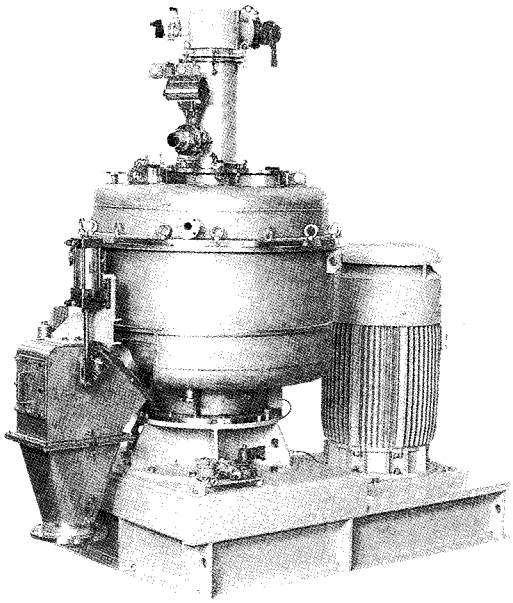

HOSOKAWA MICRON CORPORATION
5-14, 2-chome, Kawaramachi, Chuo-ku, Osaka 541-0048, JAPAN
Tel.: 06-6233-3968 Fax: 06-6229-9267

Principles & Structure

The basic operating principle of the Mechano Fusion System is shown in the left-hand diagram. The powder materials in the rotary container are subject to a centrifugal force and are securely pressed against the wall. The materials undergo strong compression and shearing forces when they are trapped between the wall and the inner piece with a different curvature.

In the new Mechano Fusion System (AMS Model), as indicated in the drawing below, the powder materials are delivered outside through slits on the rotary rotor walls. They are then carried up above the rotors by the rotor-mounted circulating blades. Subsequently, the materials return again to the rotors where they receive strong forces from the inner

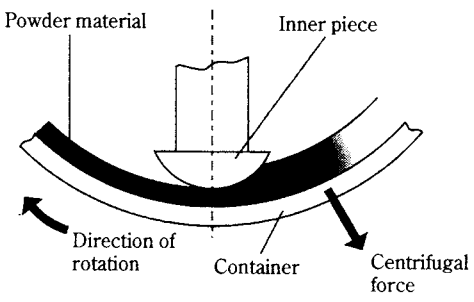

Basic Principle of the Mechano Fusion System

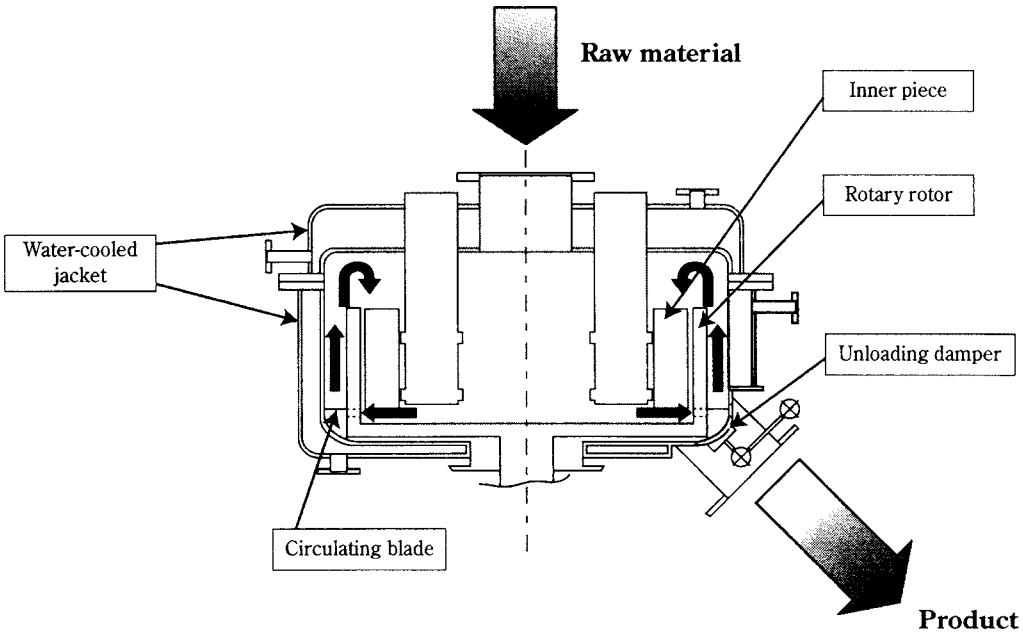

Schematic drawing of the circulation-type Mechano Fusion System (AMS Model)

pieces. This cycle of both three-dimensional circulation and effective compression/shearing of the powder materials are repeated at high speeds, thereby forming them into a composite material.

Applications

The Mechano Fusion System is capable of both preparing particles with enhanced performance and mechanically processing large quantities of new material particles. The processes employed include:

* combining particles of organic and inorganic substances, metals, ceramics and other similar materials;
* modifying the surface properties of these particles;
* controlling particle forms; and
* distributing and blending particles in a fine, precise manner.

Mechano Fusion

<Control techniques>	<Examples>
Control techniques	Examples
Particle surface chemical property control	Catalyst characteristics
Particle fusing and absorptivity control	Release control
Interfacial characteristics control	Wettability
Dispersibility and aggregate	
Optical property control	Light energy absorption
Shielding against ultraviolet ray	
Thermal characteristics control	Heat-resisting property
Dynamic characteristics control	Fluidity, dispersibility, adhesion property and extensibility of powder
Mechanical strength of a single particle	
Electrical property control	Electrification property
Magnetic property control	
Shielding of particles from other phases	Masking
	Deterioration prevention
Reduction in the use of useful material to carrier particles	Bonding of useful substances to carrier particles
Particle form control (formed into a spherical form)	Fluidity and packing
Particle form control (flattening)	Orientation effect
Fine precision dispersion and blending	Ordered mixture

Typical applications of the Mechano Fusion System include:

- Catalysts
- Ceramic parts
- Electrical parts
- Magnets
- Toner
- Electronic parts
- Cosmetics
- Medicine
- Pigments
- Li ion secondary cells
- Ni-MH secondary cells
- Fuel batteries
- Biochemical applications
- Cement materials
- Powder metallurgy
- Thermet materials

Application for cosmetics

Mechano Fusion can fuse nano-order particles onto the surfaces of particles as fine as several microns in both a quick and simple manner. For example, combining a titanium oxide particle (with a BET diameter of 15 nm) on the surface of a PMMA particle (with a mean diameter of 5 μm) produces a product that exhibits not only entirely different properties from those of the component particles, but also fluidity similar to liquid.

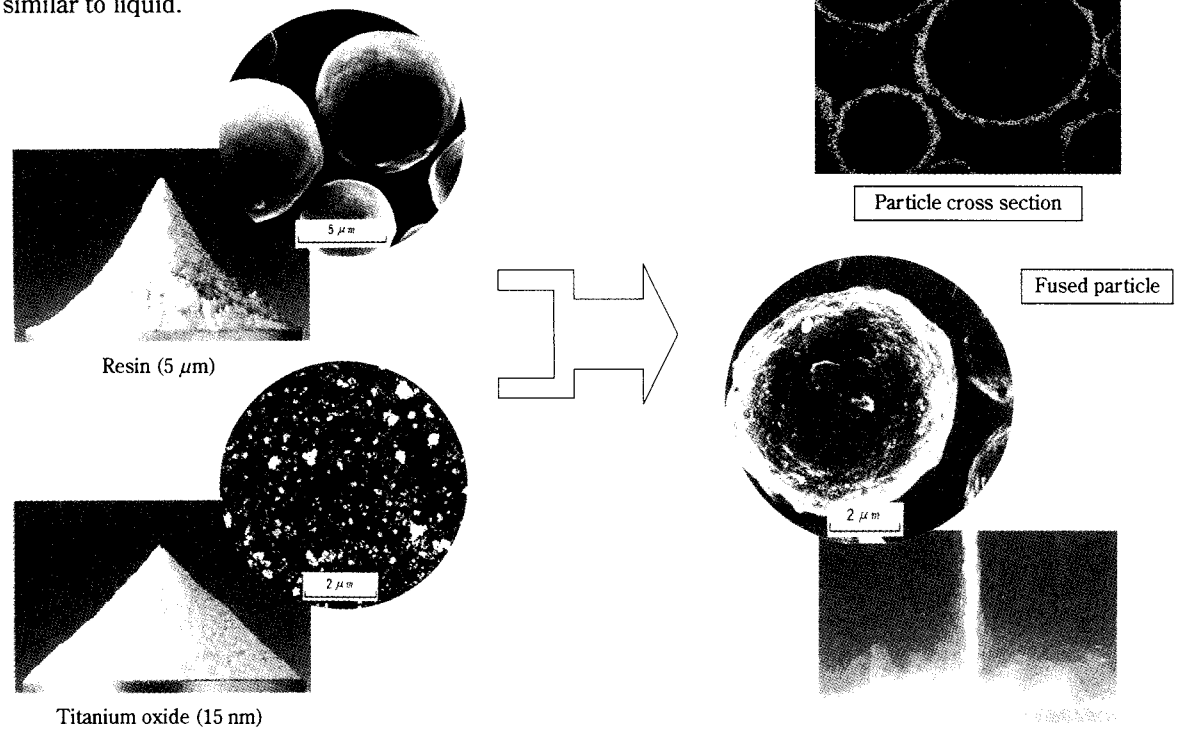

1. Combination of particles into a composite

1.1 Resin electrification control (resin to resin fusion)

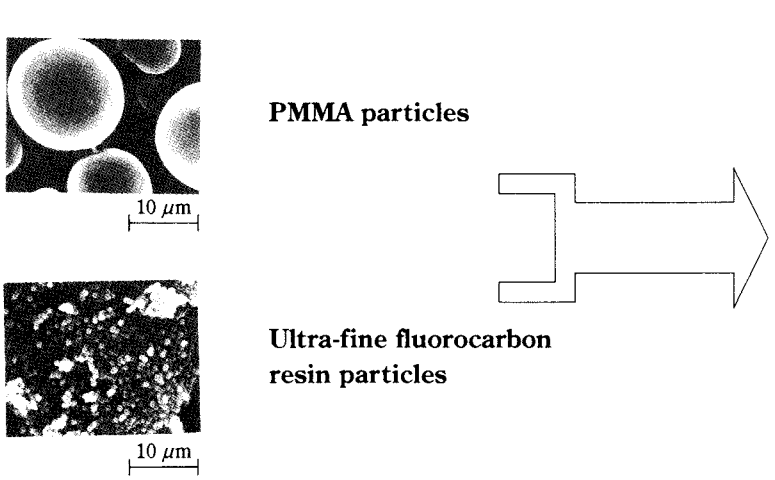

PMMA particles, with poor electrification quality, can be successfully modified into particles that have strong negative-electrode charging properties. This is accomplished by fusing the ultra-fine particles of the fluorocarbon resin to the surfaces of the PMMA.

1.2 Lightweight heat-resistant materials (metal to metal fusion)

Surface-coated particles

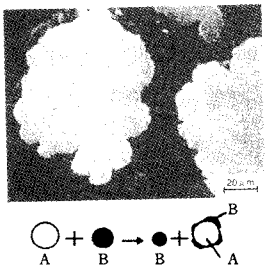

(1) This microscopic photograph shows a surface-coated structure resulting from mechano fusing nickel (bright) and aluminum (dark)

Particles in which other types of ultra-fine particles are dispersed

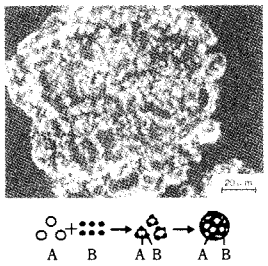

(2) Shown above is an aggregate structure that is produced by rotating micron-sized Ni-Al composite powder materials at high speeds for mechano fusing.

Lamella structure particles

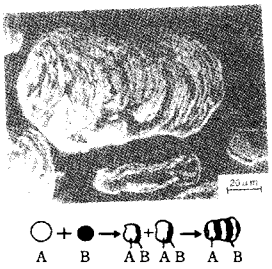

(3) This photograph depicts a lamella structure composed of Ni-Al composite powder materials that are mechano fused using a zirconia medium.

1.3 Application for electrical and electronic parts (metal to ceramics combination)

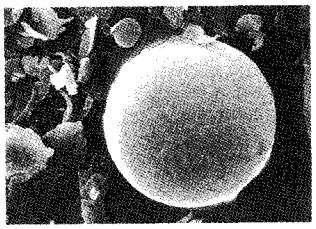

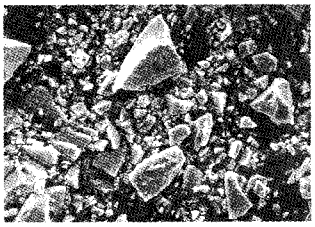

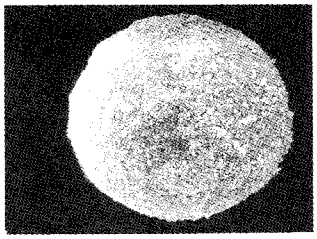

Ultra-fine ceramic particles are fused around the surfaces of the metal particles. This process yields a new material that combines the electromagnetic properties of the metal material with the electrical insulation qualities of the ceramics.

1.4 Application for high-performance structural materials (metal to ceramic polyphase coated composite particles)

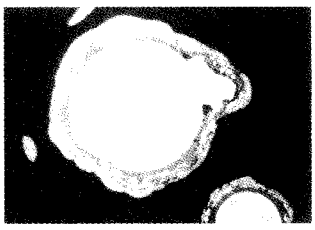

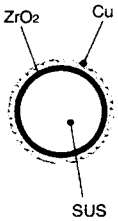

This is a double layered composite particle in which a layer of zirconia superfines and a layer of copper superfines are fused in two steps onto the surface of the stainless (SUS316L) spherical particles.

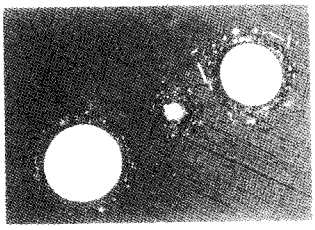

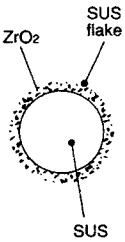

This is a polyphase coated layer composite particle in which a mixture of stainless flake particles and zirconia superfines are fused onto the surface of stainless spherical particles.

The Mechano Fusion System offers a broader array of potential for both various other particle combinations and morphological designs. (Typical applications: high-temperature, high-strength materials)

1.5 Control of the coating rate during the particle-to-particle combination process and that of the structure of a formed product

(a) Preparation of composite materials in which particles of another type are dispersed
(Ex. Ceramic particles fused on metal matrix particles)

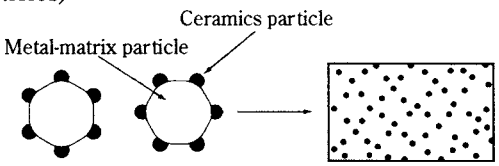

Fusing ceramic particles at various spots on the metal matrix particles, followed by incineration, produces a composite material in which the microscopic ceramic particles are dispersed in the matrix.

(b) Production of network structure composite material
(Ex. Metal particles fused onto ceramics-matrix particles)

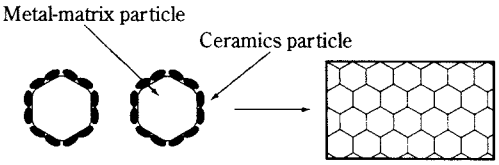

Composite particles in which superfines cover the entire surface of the ceramics-matrix particles can be employed to produce electrically conductive ceramics base materials and electrically insulative metal base materials.

2. Particle form control

2.1 Formation of particles into spherical forms (cell material)

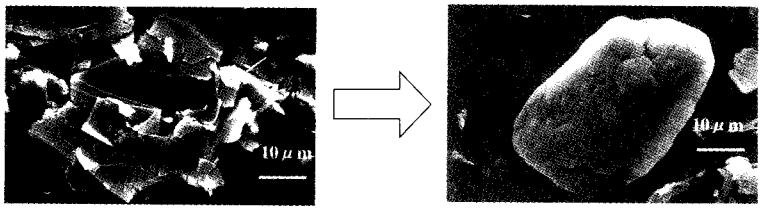

Before Mechano Fusion　　After Mechano Fusion

The Mechano Fusion technique generally serves to make particles more spherical in form, and is employed to improve particle fluidity and packing density, as well as particle electrification.

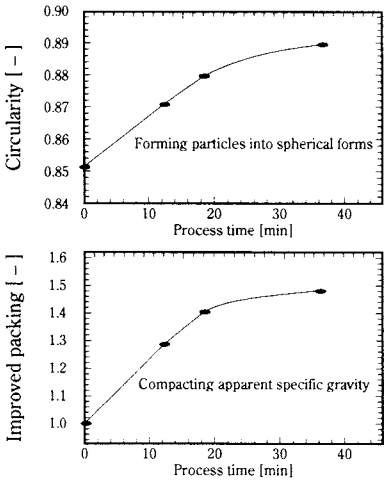

(in the case of AMS-60F)

2.2 Flattening (cell material)

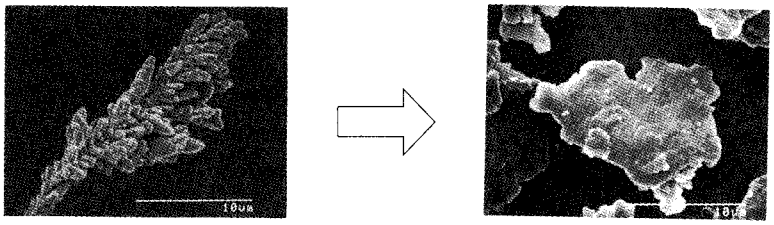

Before Mechano Fusion　　After Mechano Fusion

Flattening of copper particles

The proper setting of Mechano Fusion process conditions can permit the flattening of the metal particles being processed. Flat particles prove to be significantly effective in the enhancement of product quality when applied as electric cell materials, special paint for electronic parts and various types of fillers.

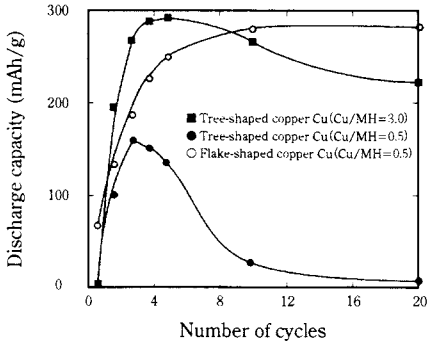

Addition of Cu to the hydrogen-occulding alloy for the negative electrode of a nickel-metal hydride battery and its impact on particle forms

2.3 Sphere formation performed simultaneously with particle combination (toner)

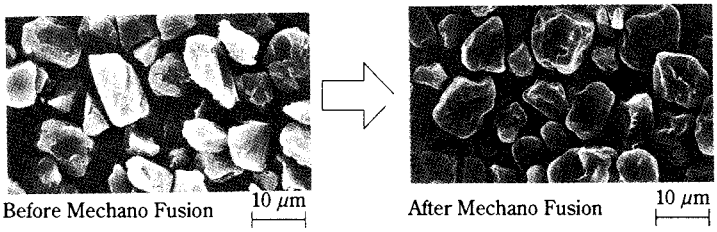

It is possible to prepare toner products that excel in fluidity and possess adequate electrification properties by shaping the square toner particles into spherical forms while fusing the static charge controlling and fluidity improving agents.

3. From precision to mechanical blending

3.1 Hue comparison

A blend of yellow iron oxide and blue dye (5 wt.%)

The product processed by a conventional high-speed mixer

The product processed by a Mechano Fusion process

The Mechano Fusion process generates strong compression and shear forces that disperse particle aggregates finely and blend the dispersed particles precisely. At the same time, this methodology can achieve the mechano-chemical modification of particle properties. Thus, the resultant product assumes different hues from those mixtures produced by a conventional high-speed mixer.

3.2 Comparison in terms of lightness

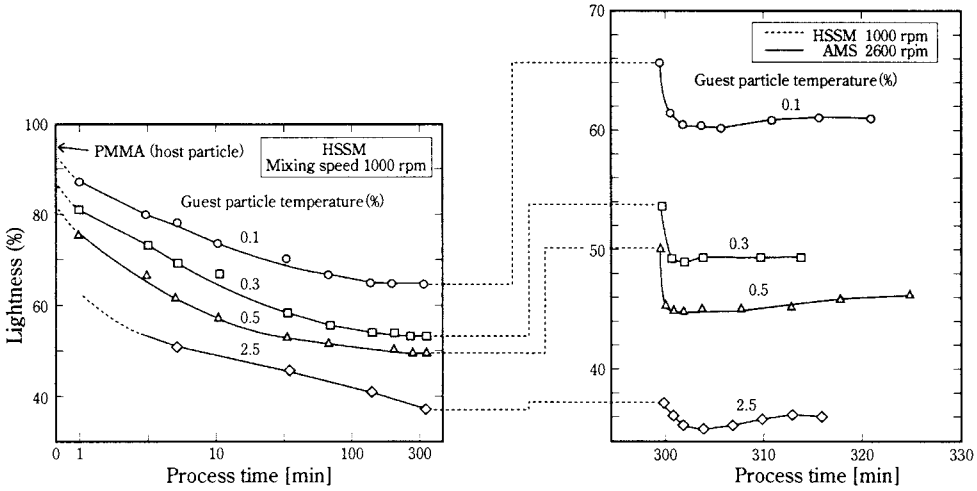

Process by high-speed mixer (HSSM)

Process by Mechano Fusion System (AMS) (using a product processed by HSSM 300min.)

Using black magnetite powder (as guest particles) and white PMMA powder (as host particles), an evaluation was carried out as to the mixing effects of a high-speed mixer and a Mechano Fusion System. This test was based on the optical lightness of the test mixture. The mixture produced by the conventional mixer in five hours was processed by the Mechano Fusion System in only a few minutes, which resulted in a substantial decrease of power lightness. This provides an unmistakable proof that Mechano Fusion is much more effective in finely blending and fusing powder particles.

New Product News

Mikro Classifier CC

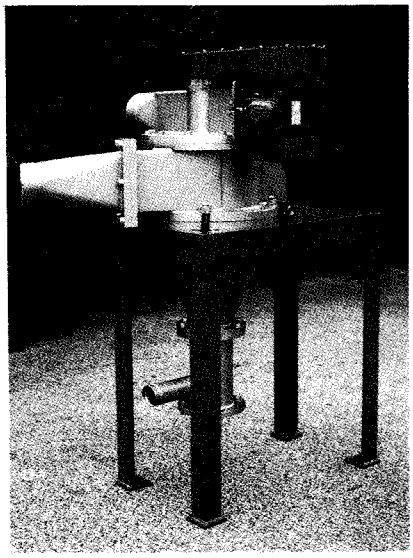

With this new classifier from Hosokawa MikroPul, powder coating production can be much more efficient. By using air classification with a high sharpness of cut, yield can considerably be increased, while losses decrease in similar scales.

An improved rotor design, secondary air flow and integrated central fittings create an optimum of material and air flow. As a result, agglomerates are significantly well dispersed.

The new MikroClassifier operates in a wide range of cut sizes between 5 µm and 100 µm. Off-line and Inline classification is possible.

Tests showed that this system is in an ideal way suitable for powder coating products (epoxy or acrylate based) with enormous positive appeal to production. Other products which can be processed are minerals, food (sugar) and other fine or finest materials.

MikroCut Air Classifier-MC

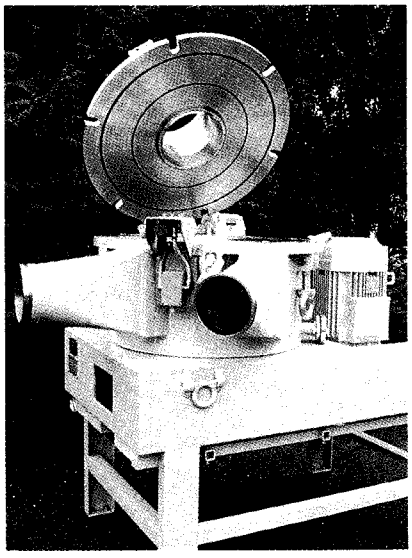

The MikroCut is a new developed air classifier for in- and off-line operation. Due to its special design a high sharpness of classification, even in the range of 1 μm, can be achieved. The MikroCut is available in various sizes that are adapted to the throughput of the ACM-grinding systems of Hosokawa MikroPul. Typical applications are classification of powder coatings, pharmaceutical products, fillers, fine mineral materials etc.

Features:

- cut sizes from a few ten micron down to the submicron range
- high sharpness of classification
- no coarse particles in the fine
- high yield of product
- low energy consumption due to optimised rotor design
- easily cleanable

For more information contact; **HOSOKAWA MIKROPUL GmbH**
Welserstraße 9-11
D-51149 Köln, Germany
Tel.: +49-2203-308-0
Fax: +49-2203-308-293
E-mail: info@hmgmbh. hosokawa. com

HOSOKAWA MICRON

Hosokawa Micron Ltd. is a member of the Hosokawa Micron Group, responding to global needs through an emphasis on materials science and engineering. The Group is an international provider of equipment and Technology for powder and particle processing, product recovery, plastics processing and confectionery products. The Group maintains facilities for research, engineering, manufacturing, and service in each of the world's major industrial markets.

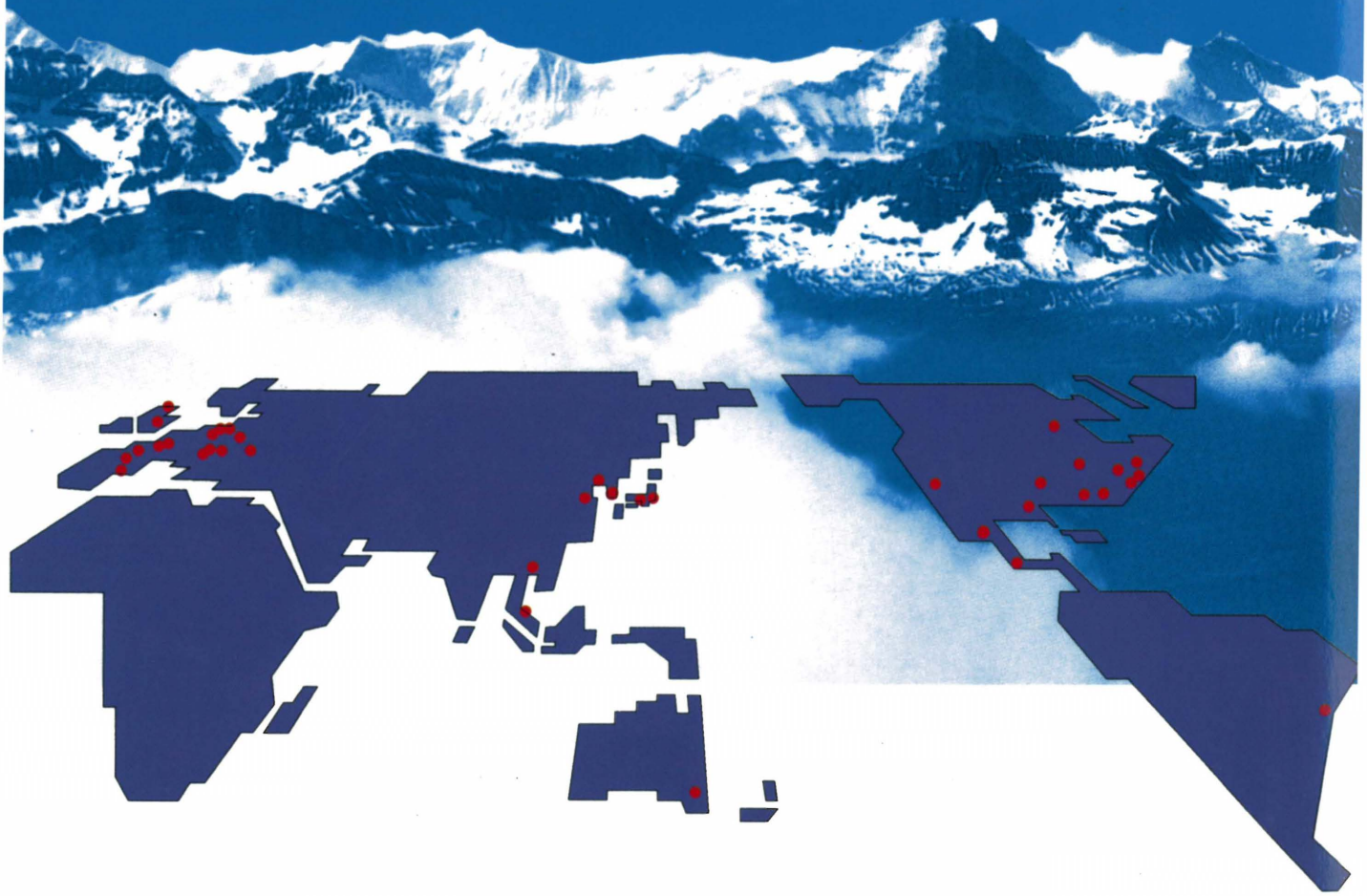

Process Technologies for Tomorrow

HOSOKAWA MICRON

Headquarter Locations;

HOSOKAWA MICRON CORPORATION

5-14, 2-chome, Kawaramachi, Chuo-ku,
Osaka 541-0048, Japan
Tel: 81-6-6233-3968
Fax: 81-6-6229-9267
http://www.hosokawamicron.com/japan

HOSOKAWA MICRON INTERNATIONAL INC.

780 Third Avenue, New York,
NY 10017, U.S.A
Tel: 1-212-826-3830
Fax: 1-212-826-6612
http://www.hosokawamicron.com